universität wien

DISSERTATION | DOCTORAL THESIS

Titel | Title

Post-transcriptional regulation of endoplasmic reticulum homeostasis: IGF2BP3 as a dual regulator of the unfolded protein response

verfasst von | submitted by

Aleksandra Anisimova

angestrebter akademischer Grad | in partial fulfilment of the requirements for the degree of

Doctor of Philosophy (PhD)

Wien | Vienna, 2025

Studienkennzahl lt. Studienblatt | Degree programme code as it appears on the student record sheet:	UA 794 685 490
Dissertationsgebiet lt. Studienblatt | Field of study as it appears on the student record sheet:	Molekulare Biologie
Betreut von | Supervisor:	Gülsün Elif Karagöz PhD

Acknowledgements

My PhD has been a journey full of challenging questions and rewarding discoveries. It gave me the chance to explore new ideas, learn and develop complex methods, discover different perspectives, and connect with wonderful people along the way. This experience has been deeply encouraging and, at the same time, humbling. I am deeply thankful to my supervisor Elif for her trust and guidance throughout my PhD. Her curiosity, encouragement, and enthusiasm for science have been a constant source of inspiration, while her determination and persistence drove my project forward, and her support allowed me to grow both scientifically and personally.

This work would not have been possible without the collaborative environment of the Vienna BioCenter. I am thankful for the essential support from the NGS, BioOptics, and MassSpec facilities, and multiple laboratories (especially the Dagdas, Versteeg, Erinc, Otsuka, Foisner, Köhler, Martinez, and Moll labs) whose members helped me countless times along the way. I also would like to thank my TAC Gijs Versteeg, Stefan Ameres, and Anna Obenauf for their valuable input.

Huge thanks go to all current and former members of the Karagöz lab for being amazing colleagues and friends. Particularly, Harald, Milica, Greg, Sascha, Asja, Paulina, Arda, and Sabina, who brightened even the toughest days. And also, my trainees, Lisa, Ioanna, and Astrid for their trust and dedication.

I would not have started my PhD without my Specialist's Thesis supervisors Sergey Dmitriev, Ivan Kulakovskiy, and Vadim Gladyshev. To them, I owe a special gratitude for bringing the passion for molecular and systems biology to my heart.

Extra thanks go to my friends for all the fun and support during my PhD years, especially Mark, Zhenia, Artem, Polina, Sascha, Tsimafei, Nastya, Alisa, Fedya, Dimon, Denis, Lera, Julia, and Ranj.

A warm thank you to my family (my parents Olga and Sergey, sister Lera, and grandparents), who never stopped supporting me with love, patience, and encouragement, no matter the distance or challenges. With all my love, I thank my partner Alibek Abdrakhmanov and our dog Cindy who have been my constant source of strength and joy during the PhD and beyond.

Additionally, I would like to acknowledge ChatGPT (version 5.0) for its assistance in improving the clarity and grammar of the written text.

Abstract

Various physiological and pathological conditions lead to the accumulation of misfolded proteins in the endoplasmic reticulum (ER), perturbing cellular homeostasis and causing ER stress. Although the Unfolded Protein Response (UPR) primarily relies on the transcriptional response to counter the ER protein-folding overload, many UPR-associated mRNAs are post-transcriptionally regulated. Yet, the mechanisms of post-transcriptional regulation during ER stress are not fully understood. In this work, we discovered that the conserved RNA-binding protein IGF2BP3 binds to multiple transcripts encoding UPR effectors. ER stress shifts IGF2BP3 function toward promoting destabilization of its target transcripts, including those encoding UPR effectors. Mechanistically, this shift correlates with the increased association of IGF2BP3 with ER stress sensor RNase IRE1 and mRNA decapping complex. Strikingly, prolonged depletion of IGF2BP3 dampens the UPR through transcriptional downregulation of UPR target genes. Altogether, our results suggest a dual role for IGF2BP3 during ER stress: directly, it promotes mRNA degradation to reduce protein synthesis and alleviate folding overload, while indirectly supporting transcription of UPR effectors.

Zusammenfassung

Verschiedene physiologische und pathologische Bedingungen führen zur Anhäufung von fehlgefalteten Proteinen im Endoplasmatischen Retikulum (ER), wodurch die zelluläre Homöostase gestört wird und ER-Stress entsteht. Obwohl die Unfolded Protein Response (UPR) in erster Linie auf die Transkriptionsantwort angewiesen ist, um der Überlastung des ER durch Proteinfaltung entgegenzuwirken, werden viele UPR-assoziierte mRNAs posttranskriptionell reguliert. Die Mechanismen dieser posttranskriptionellen Regulation während des ER-Stresses sind jedoch noch nicht vollständig geklärt. In dieser Arbeit haben wir entdeckt, dass das konservierte RNA-bindende Protein IGF2BP3 an mehrere Transkripte bindet, die UPR-Effektoren kodieren. ER-Stress verschiebt die Funktion von IGF2BP3 in Richtung einer Destabilisierung seiner Zieltranskripte, einschließlich derjenigen, die UPR-Effektoren kodieren. Mechanistisch korreliert diese Verschiebung mit der erhöhten Assoziation von IGF2BP3 mit dem ER-Stresssensor RNase IRE1 und dem mRNA-Decapping-Komplex. Bemerkenswert ist, dass eine längere Depletion von IGF2BP3 die UPR durch transkriptionelle Herunterregulierung der UPR-Zielgene dämpft. Insgesamt deuten unsere Ergebnisse auf eine doppelte Rolle von IGF2BP3 während des ER-Stresses hin: Direkt fördert es den mRNA-Abbau, um die Proteinsynthese zu reduzieren und die Faltungsüberlastung zu verringern, während es indirekt die Transkription von UPR-Effektoren unterstützt.

Table of contents

1 Introduction

1.1 Endoplasmic Reticulum (ER) stress and the Unfolded Protein Response (UPR)

1.1.1 The UPR senses perturbations of ER proteostasis

The endoplasmic reticulum (ER) is the largest membrane-bound organelle in eukaryotic cells. It is essential for cellular function, as approximately one-third of the proteome is translated by the ribosomes into the ER [1–3]. One of the primary functions of the ER is to provide a proper folding environment for the maturation of the secreted, transmembrane, and endomembrane resident proteins [4,5]. Thus, ER is abundant in molecular chaperones and folding enzymes as well as protein quality control machineries. Moreover, unlike the cytosol, the ER has an oxidizing redox potential to facilitate disulfide bond formation [4–7]. Together, the unique enzymatic repertoire and chemical environment of the ER lumen support the folding of secreted and membrane proteins.

Despite being tailored for promoting the folding of its clients, ER lumen remains a challenging folding environment due to lower diffusion rates [8] and oxidizing redox potential [6]. In addition, cells must often cope with varying protein synthesis demand and damaging conditions. If the folding capacity of the ER is exceeded, unfolded polypeptides accumulate in the lumen, perturbing ER homeostasis. This state is referred to as “ER stress”. The resulting depletion of available chaperones and increase in the concentration of the unfolded polypeptides are directly detected by specialized sensors embedded in the ER membrane. In mammalian cells, three such sensors coordinate the response: the inositol-requiring enzyme 1 (IRE1), PKR-like kinase (PERK), and the activating transcription factor 6 (ATF6). Together they activate a conserved signaling cascade called the **u**nfolded **p**rotein **r**esponse (UPR; reviewed in [9,10]; **Fig. 1**).

1.1.2 The three branches of the UPR

The most conserved branch of the UPR is initiated by the ER stress sensor IRE1, which is conserved from fungi to plants and animals [11–14]. IRE1 is a type I transmembrane protein with an ER luminal domain that directly senses the unfolded polypeptides [15–17]. When ER proteostasis is perturbed, the cytosolic RNase domains

of IRE1 become allosterically activated, mediating its endoribonuclease activity. The direct outcome of IRE1 activation is the unconventional splicing of the *XBP1* mRNA [18–24]. In unstressed cells, the unspliced form, *XBP1u* mRNA is translated into a polypeptide containing a hydrophobic region that targets it to the ER membrane surface [25]. *XBP1u* mRNA contains two stem-loops that are specifically recognized and cleaved by the activated RNase domain of IRE1, initiating the unconventional splicing [18,21,26,27]. The spliced *XBP1* mRNA (*XBP1s*) encodes a potent transcription factor that induces transcription of ER chaperones, folding enzymes, and ER-associated degradation (ERAD) components, thereby increasing the folding capacity of the ER [28–30]. Although *XBP1u* mRNA is the only known substrate of IRE1 that undergoes unconventional splicing, IRE1 also cleaves a broader set of ER-localized mRNAs, leading to their degradation and reducing protein influx into the stressed ER. This function of IRE1 is called **r**egulated **I**RE1-**d**ependent **d**ecay (RIDD) [31,32]. Together, these mechanisms allow the IRE1 branch to promote cellular adaptation to ER stress [33,34]. However, if protein misfolding persists and stress cannot be resolved, prolonged RIDD activity shifts the balance toward apoptosis by targeting transcripts that support cell survival [34–36].

In addition to IRE1, mammalian cells rely on two other UPR branches, initiated by ATF6 and PERK, to respond to ER overload. Upon ER stress, ATF6 translocates to the Golgi, where it undergoes proteolytic cleavage to release its cytosolic N-terminal fragment [37–39]. This fragment functions as a transcription factor that induces ER chaperones and folding enzymes to facilitate folding in the ER [40–44]. PERK, on the other hand, is an ER-tethered kinase that, upon activation, phosphorylates the translation initiation factor eIF2α, leading to rapid and transient downregulation of global protein synthesis [45–47]. This lowers the influx of new proteins into the ER, while allowing translation of mRNAs encoding ER stress response proteins, such as transcription factor ATF4 [48–50]. Initially, the PERK–ATF4 branch supports adaptation to ER stress by enhancing amino acid metabolism and antioxidant responses [48]. However, if stress is excessive or prolonged, ATF4 induces transcription of pro-apoptotic genes, including *DDIT3* (CHOP), promoting cell death in parallel with the IRE1 branch [51,52].

The three UPR branches drastically remodel the transcriptome of stressed cells. Moreover, they partially overlap in their targets, employ feedback loops, and can

promote opposing cell fate outcomes [53–55]. As a result, the ultimate effect of the UPR depends not only on the severity of ER stress but also on the pre-existing state of the transcriptome. This is evident from the striking differences in sensitivity to ER stress and UPR activation observed across different cell types [56–59]. The importance of cellular context for UPR activation and outcome is further reflected at the organismal level [60,61], where the UPR is essential for diverse physiological processes during development [30,62–64] and in adulthood, including plasma cell differentiation [65], glucose homeostasis [66,67], hepatic lipid metabolism [68,69], gastrointestinal tract [70] and nervous system function [71–73]. Consequently, UPR dysregulation contributes to a variety of pathological conditions, including cancer (reviewed in [74–80]).

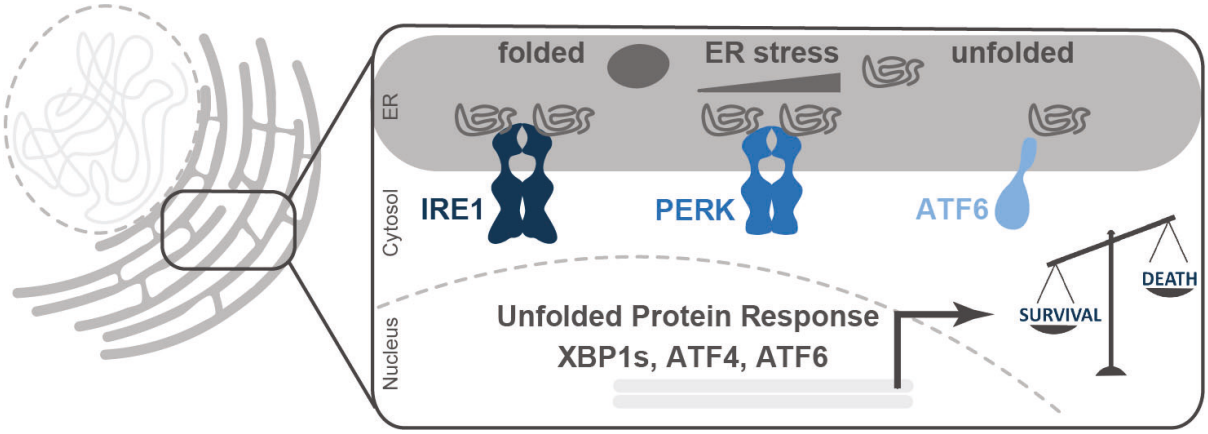

Figure 1. Schematic of the unfolded protein response (UPR) branches.

1.1.3 Regulation of mRNA stability during ER stress

Increasing evidence indicates that, in addition to transcriptional reprogramming driven by the UPR, cells also rely on post-transcriptional mechanisms to regulate mRNA levels during ER stress. Several genome-wide studies have addressed this indirectly by comparing changes in total mRNA levels either with nascent mRNA [81,82] or with a combination of translatome and proteome data [83], revealing hundreds of transcripts whose stability is differentially regulated. The diversity of these transcripts and the features defining their fate suggests that selective mRNA degradation and stabilization during ER stress are mediated by multiple mechanisms.

One of the key mechanisms to counteract ER folding overload during acute stress involves the stabilization of newly transcribed UPR-induced mRNAs. These mRNAs have longer poly(A) tails, which contribute to their increased translation rates and stabilization [82,84]. In parallel, bulk translation is suppressed through eIF2α phosphorylation by PERK [45–47]. The mRNAs are released from polysomes and assemble into messenger ribonucleoprotein granules (mRNPs) called stress granules (SGs) [85–88]. The SGs contain 40S ribosomal subunits, translation initiation factors, and multiple RNA-binding proteins that maintain the structure of this membraneless organelle through a mesh of multivalent interactions with mRNAs [89]. Interestingly, upon ER stress a subset of SGs co-localizes with the ER membrane and includes ER-targeted mRNAs [90]. Although SG formation is observed upon multiple stress conditions, their function is still debated [91]. While localization of particular mRNAs to SGs can correlate with increased stability [92,93], global analyses show that SG-enriched mRNAs are generally less stable than SG-depleted ones, and only ~10% of the transcriptome is associated with SGs at a given moment [94,95]. This suggests that the functional outcome for a particular mRNA is dictated more by the set of proteins interacting with it than by SG localization itself. Indeed, SG formation per se has been shown to be dispensable for stabilization of select mRNAs, which instead relies on interactions with specific RBPs [96].

Accumulating evidence suggests that RBPs are involved in the post-transcriptional response to ER stress. Since the extent and outcome of the UPR depend strongly on the transcriptome of the affected cell, and RBPs are powerful regulators of mRNA stability, localization, and translation, they are prominent candidates to shape the response. Transcriptome-wide non-ribosomal protein footprinting has shown that ER stress alters RBP binding to mRNA's untranslated regions (UTRs) [83], supporting their involvement in the regulation of the ER stress response. Nevertheless, the role of RBPs in the ER stress response has not yet been systematically explored. Instead, individual studies point to their function in regulating specific transcripts during stress. For instance, in *Drosophila,* RBP Pumilio binds *Xbp1* mRNA and protects spliced mRNA from further IRE1-mediated cleavage and degradation [97]. The RBP TIA-1 links hormonal control of the cardiovascular system with ER stress through differential regulation of the angiotensin II type 1 receptor (AT1R). Under homeostatic conditions,

TIA-1 binds *AT1R* mRNA and represses translation, while under ER stress, it releases the mRNA, leading to increased AT1R protein expression [98]. In another example, the RBP HuR mediates ER stress-induced stabilization of the liver hormone hepcidin, which controls iron transfer to plasma [99]. HuR also increases its binding to the 3′ UTR of *ATF3* mRNA during amino acid starvation, increasing its stability. A similar mechanism may function during ER stress as it also increases *ATF3* levels and half-life. At the same time, AUF1, a decay-promoting RBP, shows reduced binding to the *ATF3* 3′ UTR during stress, which may further stabilize the transcript [100].

One of the primary mechanisms by which RBPs regulate mRNA stability is through modulation of miRNA-mediated silencing and degradation. miRNAs guide the RNA-induced silencing complex (RISC) to complementary sequences in target mRNAs. RBPs can either counteract this process by binding to miRNA sites and shielding the mRNA from RISC, or facilitate it by modulating secondary structure to increase site accessibility and promoting recruitment of RISC and associated decay factors (reviewed in [101]). miRNA-mediated regulation is a broad and complex layer of UPR as miRNAs target components of all three UPR branches and are themselves subject to regulation [102–104]. The importance of miRNA pathways in the UPR is supported by findings that depletion of AGO2, the major component of the RISC, prevents ER stress-induced downregulation of multiple transcripts [105].

In response to ER stress, cells attempt to reduce the influx of newly synthesized proteins into the ER by limiting the number of mRNAs translated by ER-bound ribosomes. This is illustrated by the finding that ER stress induces the release of mRNAs from the ER surface [106]. In addition, IRE1 cleaves the mRNAs translated on the ER surface, which has been proposed to decrease protein folding load of the organelle. How IRE1 selects its targets among the ER-bound mRNAs is not yet completely understood. The canonical IRE1 substrates such as *XBP1u*, *BLOC1S1*, *CD59*, *TGOLN2*, and others are confirmed in multiple studies and contain a distinct hairpin structure with CNG|CAGN consensus sequence within the loop [27,31,32,107,108]. Yet, the presence of this hairpin motif is not the only determinant of IRE1 target selection, as for many ER-targeted mRNAs, it is not sufficient to induce cleavage [107]. Moreover, IRE1 also acts in a more promiscuous, motif-independent manner [34,109,110]. In this mode, it even targets UPR-induced transcripts, such as *HSPA5* (encoding BiP)

[34], counteracting the transcriptional UPR. The absence of strict determinants suggests that IRE1 substrate specificity is modulated by additional factors. For example, stress-induced reduction in translational initiation increases the accessibility of hairpin motifs in mRNA coding sequences to IRE1 [107]. Another layer of regulation may be provided by RBPs, which can influence the localization of IRE1 target mRNAs or the accessibility of cleavage sites within the target sequence. In line with this idea, IRE1 has been shown to associate with SGs, which facilitates XBP1 splicing [111]. However, it remains unclear whether this association also affects the cleavage of other IRE1 substrates.

The work of Acosta-Alvear and Karagöz et al. [112] combined IRE1 immunoprecipitation with proteomics to investigate how IRE1 recruits and selects its targets among the ER-bound mRNAs. Using protein-RNA crosslinking followed by immunoprecipitation under denaturing conditions with stringent washes, the authors discovered that IRE1 directly contacts the ribosome and monitors the dynamics of folding and translation to detect the mRNAs whose products fail to fold efficiently. This systematic and unbiased approach also captured proteins that associate closely with IRE1 in an RNA-dependent manner, plausibly either through their mutual binding to ribosome or their mRNA substrates. Among the identified interactors, RBP from Insulin-like growth factor 2 mRNA-binding proteins (IGF2BP) family, IGF2BP3, stood out as a specific mRNA binder that associates with IRE1 in an ER stress-dependent manner. These findings led us to hypothesize that IGF2BP3 may modulate IRE1 function or regulate the fate of IRE1 mRNA targets, including multiple UPR effectors.

1.2 Oncofetal proteins of the IGF2BP family are potent regulators of mRNA metabolism

The Insulin-like growth factor 2 mRNA-binding proteins (IGF2BPs) are a highly conserved family of RBPs (reviewed in [113,114]). Mammals express three IGF2BP paralogs IGF2BP1/2/3, while only single homologs have been described in *Xenopus laevis* (Vg1RBP/Vera, most closely related to IGF2BP3) and in *Drosophila* (dIMP). Several synonymous names are present in the literature for IGF2BP family proteins: Vg1RBP/Vera, IMP, CRD-BP, KOC, and ZBP, therefore the family is sometimes referred to as VICKZ. IGF2BP1 and 3 are expressed as single isoforms and share 73% amino acid identity, while IGF2BP2 is more distant (56%) and exists in two alternative splicing isoforms [113,114].

1.2.1 Functional roles of IGF2BPs

IGF2BPs belong to the class of so-called “oncofetal” proteins, which are expressed at high levels during embryogenesis, largely silenced in most adult tissues, and re-expressed in cancer [115,116]. Consistent with this patter, all three IGF2BP paralogs are abundant during early development [113,117–120], where they regulate mRNAs involved in cell growth and migration and are therefore necessary for embryo development [121–128]. In adult tissues, IGF2BP1 and IGF2BP3 are mostly down-regulated in an organ-specific manner, while IGF2BP2 remains highly expressed and displays a more uniform pattern across tissues [113,129,130]. Unlike IGF2BP1 and 3, IGF2BP2 has been linked to the regulation of metabolic processes. It regulates mRNAs involved in glycolysis [131], thermogenesis [132], and insulin responses [132,133], and the variants in its gene associate with type 2 diabetes risk [134]. The overexpression of IGF2BP paralogs contributes to carcinogenesis [113,114,124,135,136], [115,116]where their elevated levels are associated with increased tumor growth[137], therapy resistance [138], metastasis [139], and poor prognosis [140]. The most common mechanism by which IGF2BPs contribute to cancer is the upregulation of developmental oncogenic pathways through stabilization of oncogenic mRNAs, such as *KRAS* [141], *cMYC* [123], *HMGA2* [126], and *ABCB1* (MDR1) [142].

1.2.2 Domain architecture and RNA-binding specificity of IGF2BPs

IGF2BP homologs share a canonical RNA-binding protein architecture. Each ~65 kDa proteins contains two RNA recognition motifs (RRM1-2) followed by four hnRNP K homology domains (KH1-4), which are arranged in heterodimers (KH1-2) and (KH3-4). These heterodimer domains are separated by unstructured linkers of ~40 amino acids (between RRM1-2 and KH1-2) and ~60 amino acids (between KH1-2 and KH3-4) [120] . Each of the six domains has its own RNA binding surface with distinct sequence preferences and affinities [143–145]. This enables combinatorial recognition of clustered motifs with the target mRNA looping around the domains [144,146]. The first defined IGF2BP-binding element was a 54-nt sequence in chicken β-actin, termed the “zipcode” [147,148]. IGF2BP footprinting obtained with Photoactivatable-Ribonucleoside-Enhanced Crosslinking and Immunoprecipitation (PAR-CLIP) revealed short consensus motif CAUH (H = A, C, or U), which represents the most common sequence recognized by RNA binding sites within IGF2BP domains [149]. Later, Systematic

Evolution of Ligands by Exponential Enrichment (SELEX) experiments resulted in an extended consensus sequence for IGF2BP3: GGCA-N_{20}-CACA-N_{14}-CACA-N_{22}-CGGC-N_4-$(CA)_4$ [144] (**Fig. 2**). It has to be noted, however, that this sequence represents an optimal binding motif under *in vitro* selection, while *in vivo* recognition is more versatile [144]. Due to the combinatorial nature of RNA-binding motifs, IGF2BPs can bridge multiple mRNAs in multivalent interactions and recruit them into mRNPs [126,143,150]. This feature provides a structural basis for the diverse regulatory functions of IGF2BPs and their ability to coordinate transcript fate in diverse cellular contexts.

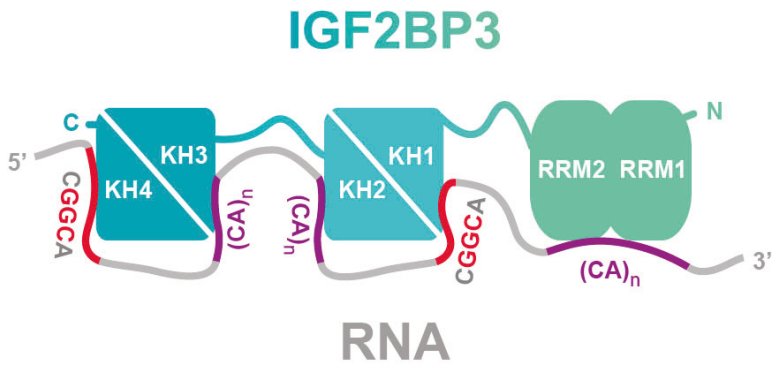

Figure 2. Schematic model of RNA binding by IGF2BP3 (adapted from Schneider et al. [144])

1.2.3 Mechanisms of IGF2BPs function

The ability of IGF2BPs to recognize flexible motifs allows them to bind a broad spectrum of transcripts. This is confirmed in RNA immunoprecipitation studies, which robustly identify around three thousand targets for each IGF2BP paralog [125,151]. However, transcriptome- and translatome-wide analyses following IGF2BP depletion indicate that binding does not necessarily results in regulation of the associated RNA [125,151]. Moreover, the high overlap between the bound transcripts further suggests that IGF2BP paralogs can compensate for one another [151,152]. As many of their targets encode transcriptional regulators [123,126,141,153,154], deciphering the downstream networks perturbed by IGF2BP loss and identifying the actual mechanisms of their function remain a challenging task.

Despite this complexity, several mechanisms of action have been described for IGF2BPs. In mammals, IGF2BPs have been characterized as translational inhibitors of IGF2 mRNA [120]. IGF2BP1 was later shown to regulate spatial translation of β-actin

to allow directed cell movement. Specifically, binding of IGF2BP1 to the 5'UTR of β-actin mRNA inhibits its translation in the cytosol and facilitates its delivery to the leading edge [155]. Once localized to the cell periphery, phosphorylation of IGF2BP1 by Src results in mRNA release and allows translation initiation [122]. This mechanism is not universal for all IGF2BP targets. For instance, IGF2BP2 binding has been shown to directly promote translation of *UCP1* mRNA, conferring resistance to obesity in mice [132]. In contrast, depletion of IGF2BP3 leads to a substantial increase in bulk translation [156]. Mechanistically, this has been linked to IGF2BP3-depletant sequestrations of mRNAs into processing bodies (P-bodies) [156].

All IGF2BPs can act as mRNA stabilizers [151]. IGF2BP1 was first identified as a stabilizer of mRNA encoding c-Myc [116,157,158]. Binding of IGF2BP1 to a region within the coding sequence protects the mRNA from cleavage by an endonuclease [142], later identified as APE1 [159]. Although depletion of each IGF2BP paralog results in *MYC* destabilization [151], the underlying mechanism has not yet been confirmed for IGF2BP2 and IGF2BP3.

The ability of IGF2BP1 and 3 to protect the mRNAs from cleavage has been extensively described in the context of miRNA-mediated degradation. Competition of IGF2BP1 with the miRNAs for overlapping binding sites results in stabilization of target transcripts, as shown for *BTRC* (βTrCP1, a substrate recognition subunit for the $SCF^{\beta TrCP}$ E3 ubiquitin ligases) [160] and *MITF* (microphthalmia-associated transcription factor) [161]. However, the primary mechanism by which IGF2BP1 and 3 interfere with miRNA-mediated mRNA degradation relies on the recruitment of their targets into mRNPs depleted of RISC [126,152]. This mechanism is employed to stabilize mRNAs of multiple oncogenic factors [126,152], including SRF (serum response factor) [153] and HMGA2 (high-mobility group AT-hook 2) [126,154].

mRNA modifications strongly influence the ability of IGF2BPs to bind their targets. All three IGF2BP paralogs recognize the most abundant internal mRNA modification - N6-methyladenosine (m6A) [151]. For multiple targets, including *MYC*, IGF2BP-mediated stabilization has been shown to depend on m6A [151]. Another abundant modification, internal N7-methylguanosine (m7G), also enhances IGF2BP binding. However, its functional outcome differs from that of m6A. While IGF2BP2 binding to m7G-modified

sites does not affect mRNA stability, binding of IGF2BP1 and, in particular, IGF2BP3 leads to destabilization of its targets [162].

In contrast to IGF2BP1 and IGF2BP2, several studies have shown that IGF2BP3 can promote degradation of its targets [162–165]. Nevertheless, the proposed mechanisms vary. Epistasis analysis revealed that IGF2BP3 acts in the same pathway as the endonucleases RRP4 (one component of the 3′-5′ exonuclease complex) and XRN2 (5′–3′ exonuclease) to promote decay of *EIF4E-BP2* mRNA [164]. These endonucleases and exosome components were also identified in IGF2BP3 co-immunoprecipitates [162,164]. In another study, IGF2BP3 was found to promote the association of its targets, including *ZFP36L1*, with RISC, promoting miRNA-mediated degradation [165]. Taken together, these studies show that IGF2BP binding results in diverse outcomes depending on the mRNAs and proteins it engages.

Altogether, IGF2BPs regulate mRNA translation, stability, and degradation via various mechanisms. IGF2BP1 and IGF2BP2 are mainly characterized as stabilizers, while IGF2BP3 can also promote decay, highlighting functional divergence within the family (**Fig. 3**). Given the large number of confirmed targets and the connection with miRNA pathways and mRNA modifications, the outcome of IGF2BP activity is likely to be highly context dependent. Thus, IGF2BPs can be regarded as adaptable post-transcriptional hubs whose regulatory output is dictated by the specific mRNAs and proteins they interact with, tailoring gene expression programs to cellular needs.

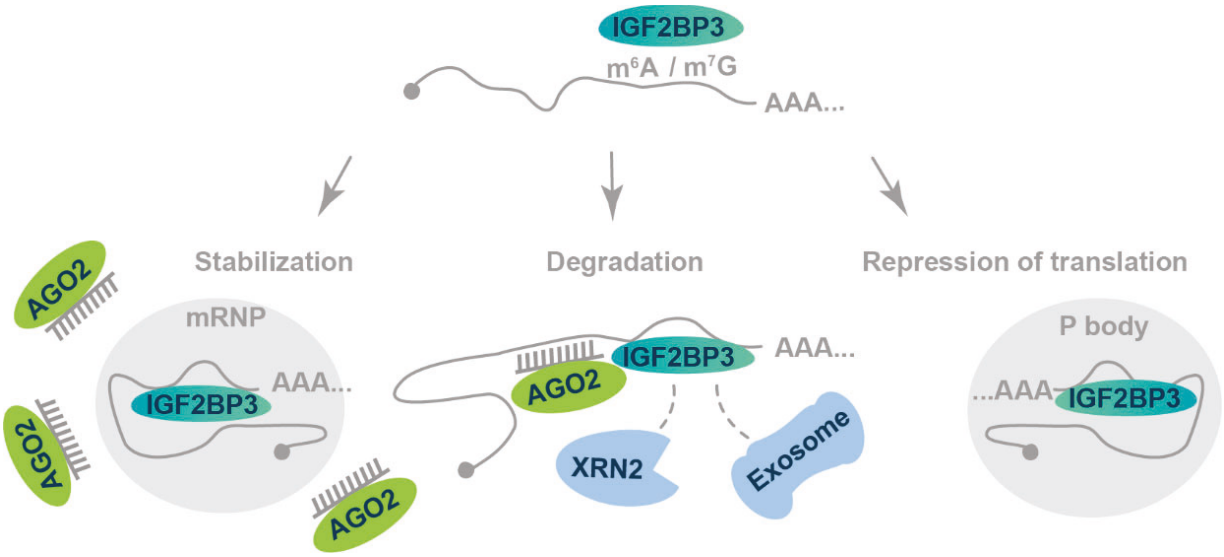

Figure 3. Overview of the mechanisms employed by IGF2BP3.

1.2.4 Regulation of IGF2BPs' functions by phosphorylation

Phosphorylation adds an additional layer to IGF2BP-mediated regulation. Src phosphorylates IGF2BP1 at Y396, located in the linker between the KH1-2 and KH3-4, interfering with mRNA binding and allowing for localized translation of β-actin mRNA [122]. IGF2BP1 can also be phosphorylated at S181 in the linker between the RRM1-2 and KH1-2 by mTORC2. In contrast to phosphorylation of Y396, S181 phosphorylation increases IGF2BP1's binding to its target mRNAs, best described is *IGF2* mRNA [166,167]. Similarly, phosphorylation of IGF2BP2 at S162 and S164 promotes its interaction with mRNA targets [168]. Much less is known about phosphorylation of IGF2BP3. One of the first studies describing IGF2BP3 reported its localization to the ER at the vegetal cortex in *Xenopus* oocytes, where it dictates the localization of mRNA Vg1 encoding transforming growth factor-β [128]. Phosphorylation of IGF2BP3 at S402, located between the KH2 and KH3 domains, by Erk2 MAPK releases the Vg1 mRNA from the cortex without affecting RNA binding, suggesting that this modification regulates protein-protein interactions with the cytoskeleton and/or ER [169]. Taken together, these findings suggest that phosphorylation modulates IGF2BP activity in a site- and paralog-specific manner, integrating signaling with post-transcriptional control and adding a spatial dimension to regulation.

1.2.5 IGF2BPs' functions during stress conditions

Several studies show that IGF2BPs contribute to the regulation of mRNA stability during cellular stress responses. Under stress-induced translational repression, IGF2BPs localize to SGs [93,170,171]. Partitioning of IGF2BP1 into SGs increases SG retention for several of its targets, such as *ACTB* (β-actin), *IGF2*, *MYC*, and *CD44*. Moreover, reporters containing the IGF2BP1 binding 'zipcode' sequence are stabilized during acute stress and recovery phases [93]. While IGF2BP1 depletion destabilized its targets, knockdown of core SG components (TIA1, TIAR, G3BP1), which prevents SG formation, had no effect [96]. This indicates that stabilization by IGF2BP1 does not require localization of its mRNA targets to SGs. Stress conditions such as oxidative stress or heat shock decrease the levels of select IGF2BP targets, including *MYC* [151,172], but overexpression of any IGF2BP paralog restores *MYC* expression [151,172]. Taken together, although current evidence for IGF2BP function during stress is limited,

available data suggest an important role in modulating mRNA fate during cellular adaptation to adverse conditions.

Because carcinogenesis is strongly linked to stress conditions such as ER stress [75,76,80] or oxidative stress [173], regulation of mRNA stability by IGF2BPs upon stress is highly relevant to tumor development and progression. Moreover, IGF2BPs are promising cancer therapeutic targets, as multiple small-molecule inhibitors that disrupt IGF2BP-RNA interactions have already been developed, and many demonstrate potent anti-cancer activity in various cancer models, including liver, non-small cell lung, ovarian, and colorectal cancer [174].

In summary, IGF2BPs act as versatile post-transcriptional regulators. They influence mRNA translation, stability, and decay through a variety of mechanisms, with outcomes determined by mRNA modifications, binding partners, and signaling cues. Phosphorylation provides an additional layer of regulation, which integrates extra- and intracellular signals and adds a spatial dimension to IGF2BPs' function. During stress, IGF2BPs safeguard critical transcripts, further emphasizing their role as adaptable hubs that regulate mRNA fate to meet cellular needs. This function becomes critical in cancer, where IGF2BP activity fuels malignant growth. The recent development of compounds that block IGF2BP-RNA interactions demonstrates that these proteins are highly attractive targets for anti-cancer therapies.

1.3 Aim of this study

In this work, I aimed to identify post-transcriptional mechanisms involved in restoring proteostasis during ER stress. An unbiased proteomic data by Acosta-Alvear and Karagöz et al. [112] revealed that RBP IGF2BP3 associates with IRE1 under stress conditions. This observation suggested that IGF2BP3 may interact with IRE1 target mRNAs and contribute to their regulation during stress. Guided by this finding, I focused on uncovering the role of IGF2BP3 in ER stress and its impact on the UPR.

IGF2BP3 binds a wide and context-dependent set of transcripts, which makes it essential to define its targets specifically in the model system used in the study. Therefore, my first aim was to establish a protocol capable of identifying IGF2BP3-bound transcripts with high precision. To this end, **in section 2,** I optimized the existing PAR-CLIP protocol to achieve radioactive-free, high-quality footprinting of IGF2BP3.

Importantly, I also optimized the immunoprecipitation conditions to capture endogenous IGF2BP3 efficiently and to avoid potential artifacts caused by tagging or overexpression. This approach enabled the identification of IGF2BP3-bound transcripts and the precise mapping of its binding sites.

In section 3, I investigated how IGF2BP3 contributes to the ER stress response. First, I aimed to determine how IGF2BP3 binding to its targets changes during stress. Using the optimized PAR-CLIP protocol, I discovered that IGF2BP3 binds transcripts encoding crucial UPR effectors. To assess whether IGF2BP3 regulates the UPR, I analyzed the transcriptome of stressed cells upon IGF2BP3 depletion using transcriptomics approaches that distinguish between transcriptional effects and changes in mRNA stability. Finally, to understand the mechanism by which IGF2BP3 influences mRNA stability during ER stress, I identified its protein interaction partners and tested the relevance of specific interaction interfaces. In conclusion, I deciphered a novel function of IGF2BP3 as a regulator of the UPR.

In section 4, we addressed whether IGF2BPs are specifically regulated under stress conditions. Because phosphorylation provides a rapid and reversible means of transient regulation, we focused on this modification as a potential mechanism of stress-specific adaptation. Our first goal was to determine whether cellular stress influences the phosphorylation pattern of IGF2BP1. To this end, we analyzed stress-induced changes in IGF2BP1 phosphorylation and identified the regulated sites. Next, we aimed to examine how phosphorylation of IGF2BP1 at these sites affects its properties by introducing phosphomimetic mutations. In particular, we addressed how these mutations influence IGF2BP1's RNA binding, phase separation, and mRNP granule properties both *in vitro* and *in vivo*, as well as their impact on the transcriptome during oxidative stress. Together, our findings establish phosphorylation as a mechanism that modulates IGF2BP1 function during stress.

By systematically dissecting distinct layers of the IGF2BP-mediated regulation during cellular stress, my work advances our understanding of how IGF2BPs integrate signaling with mRNA fate decisions, with implications for stress biology and cancer.

2 Results

2.1 Optimized infrared photoactivatable ribonucleoside-enhanced crosslinking and immunoprecipitation (IR-PAR-CLIP) protocol identifies novel IGF2BP3-interacting RNAs in colon cancer cells

2.1.1 Preamble

In this paper, I optimized the existing PAR-CLIP protocol to identify the RNA targets and precise RNA binding sites of endogenous human IGF2BP3. As a first step, I established immunoprecipitation conditions to isolate endogenous IGF2BP3-RNA complexes of high purity. To avoid the use of radioactive labeling, I then introduced infrared (IR) fluorescent dyes, which increased sensitivity and allowed direct visualization of crosslinked RNA fragments. The modified version of the method (IR-PAR-CLIP) provided a safer and easier-to-use alternative to the conventional protocol. I also tested alternative RNase digestion conditions and discovered that sequence preferences of the enzymes influence both the recovery of IGF2BP3 targets and the motifs detected. In addition, to improve the efficiency of library construction and reduce sequence bias, I used a single-adapter circular ligation strategy. Altogether, we established an optimized IR-PAR-CLIP protocol, which identified novel IGF2BP3 RNA targets in colorectal carcinoma cells.

This manuscript was published in *RNA* on August 15th, 2023.

2.1.2 Contribution statement

I contributed to the conceptualization, designed, and performed all experiments, including crosslinking-immunoprecipitation, cell line establishment, PAR-CLIP optimization, and computational analysis. I also wrote the first draft of the manuscript and was involved in the editing

METHOD

Optimized infrared photoactivatable ribonucleoside-enhanced crosslinking and immunoprecipitation (IR-PAR-CLIP) protocol identifies novel IGF2BP3-interacting RNAs in colon cancer cells

ALEKSANDRA S. ANISIMOVA[1,2,3] and G. ELIF KARAGÖZ[1,2]

[1]Max Perutz Labs, Vienna BioCenter Campus (VBC), 1030 Vienna, Austria
[2]Medical University of Vienna, Center for Medical Biochemistry, 1030 Vienna, Austria
[3]Vienna BioCenter PhD Program, a Doctoral School of the University of Vienna and the Medical University of Vienna, 1030 Vienna, Austria

ABSTRACT

The conserved family of RNA-binding proteins (RBPs), IGF2BPs, plays an essential role in posttranscriptional regulation controlling mRNA stability, localization, and translation. Mammalian cells express three isoforms of IGF2BPs: IGF2BP1-3. IGF2BP3 is highly overexpressed in cancer cells, and its expression correlates with a poor prognosis in various tumors. Therefore, revealing its target RNAs with high specificity in healthy tissues and in cancer cells is of crucial importance. Photoactivatable-ribonucleoside-enhanced crosslinking and immunoprecipitation (PAR-CLIP) identifies the binding sites of RBPs on their target RNAs at nucleotide resolution in a transcriptome-wide manner. Here, we optimized the PAR-CLIP protocol to study RNA targets of endogenous IGF2BP3 in a human colorectal carcinoma cell line. To this end, we first established an immunoprecipitation protocol to obtain highly pure endogenous IGF2BP3–RNA complexes. Second, we modified the protocol to use highly sensitive infrared (IR) fluorescent dyes instead of radioactive probes to visualize IGF2BP3-crosslinked RNAs. We named the modified method "IR-PAR-CLIP." Third, we compared RNase cleavage conditions and found that sequence preferences of the RNases impact the number of the identified IGF2BP3 targets and introduce a systematic bias in the identified RNA motifs. Fourth, we adapted the single adapter circular ligation approach to increase the efficiency in library preparation. The optimized IR-PAR-CLIP protocol revealed novel RNA targets of IGF2BP3 in a human colorectal carcinoma cell line. We anticipate that our IR-PAR-CLIP approach provides a framework for studies of other RBPs.

Keywords: IGF2BP3; PAR-CLIP; RNA stability; posttranscriptional regulation

INTRODUCTION

RNA-binding proteins (RBPs) play a crucial role in the posttranscriptional regulation of gene expression. They regulate fundamental steps in the RNA life cycle including RNA splicing, stabilization, subcellular localization, translation, and degradation (Nielsen et al. 1999; Ladd et al. 2001; Fallini et al. 2011; Mizutani et al. 2016). The insulin-like growth factor 2 mRNA-binding proteins (IGF2BPs/IMPs) are a family of RBPs conserved from insects to mammals (Bell et al. 2013). Originally IGF2BPs were identified as posttranscriptional regulators of mRNA encoding for growth factor IGF2 (Nielsen et al. 1999; Zhang et al. 1999). Mammals have three IGF2BP paralogs (IGF2BP1-3), which are oncofetal proteins expressed during early development and in various cancers. Their crucial role in early development was shown in Xenopus (Yaniv et al. 2003), mice (Hansen et al. 2004), and zebrafish (Ren et al. 2020; Vong et al. 2021). Whereas the expression of IGF2BP1/3 decreases in most adult tissues, IGF2BP2 retains its expression and was shown to regulate lipid and glucose metabolism in adults (Hansen et al. 2004; Hammer et al. 2005; Bell et al. 2013; Laggai et al. 2014; Dai et al. 2015; Regué et al. 2019; Lu et al. 2021).

Due to its overexpression in aggressive tumors, IGF2BP3 is currently heavily studied. IGF2BP3 was initially identified as a highly overexpressed gene in pancreatic cancer (Müeller-Pillasch et al. 1997). In addition to pancreatic cancers,

Corresponding author: guelsuen.karagoez@meduniwien.ac.at
Article is online at http://www.rnajournal.org/cgi/doi/10.1261/rna.079714.123. Freely available online through the *RNA* Open Access option.

IGF2BP3 is highly expressed in various cancers including lung, liver, breast, skin, and colon (Samanta et al. 2013; Zhao et al. 2017; Xu et al. 2019; Hanniford et al. 2020; Huang et al. 2020). Its overexpression is strongly correlated with tumor aggressiveness and poor patient prognosis (Ross et al. 2001; Dimitriadis et al. 2007). IGF2BP3 shuttles between the nucleus and cytosol (Rivera Vargas et al. 2014), yet it is mainly found in the cytosol. It regulates the stability of oncogenic mRNAs *MYC* and *HMGA2* (Jønson et al. 2014; Huang et al. 2018) and controls the protein levels of cyclins D1, D3, and G1 (Rivera Vargas et al. 2014). This regulation was suggested to promote cell proliferation and tumor growth. Moreover, since IGF2BP3 binds to a large number of mRNAs in cells, it is likely that it controls the stability of mRNAs participating in various pathways involved in cellular homeostasis, thereby additionally contributes to tumorigenesis. Therefore, identifying RNAs interacting with IGF2BPs in a transcriptome-wide manner is crucial. IGF2BP paralogs share a high sequence identity in the amino acid level (~60% among three paralogs). The sequence identity reaches 73% between IGF2BP1 and IGF2BP3 paralogs. Currently, the functional differences in IGF2BP paralogs remain largely uncovered.

Genome-wide crosslinking and immunoprecipitation (CLIP) methods have been instrumental in identifying the RNA targets of various RBPs. CLIP methods rely on in vivo photo-crosslinking of proteins to RNAs in cells followed by the immunoprecipitation of RBPs of interest to identify RNAs directly interacting with those RBPs (Lee and Ule 2018; Hafner et al. 2021). Over the years, several variations of CLIP methods have been introduced to increase the stringency, efficiency, and resolution of those approaches. The high-throughput sequencing of RNA isolated by crosslinking immunoprecipitation (HITS-CLIP) for the first time implemented the use of deep sequencing in the CLIP approaches allowing for genome-wide identification of RBP-binding sites in RNAs (Licatalosi et al. 2008). To increase the resolution in identifying RBP-binding sites in RNAs, alternative CLIP strategies were developed enabling precise mapping of the RBP-binding sites in their target RNAs at nucleotide resolution. The photoactivatable-ribonucleoside-enhanced crosslinking and immunoprecipitation (PAR-CLIP) relies on identifying the mutations introduced by the reverse transcriptase at the crosslink sites. In contrast, the individual-nucleotide resolution UV crosslinking and immunoprecipitation (iCLIP) leverages the termination of reverse transcription at the peptide–RNA crosslink sites (König et al. 2010).

PAR-CLIP methods revealed a large overlap of RNA targets of IGF2BP paralogs in human embryonic kidney (HEK) 293 cells (Hafner et al. 2010). In human pluripotent stem cells, a modified version of iCLIP, with improved library preparation, referred to as enhanced CLIP (eCLIP) (Van Nostrand et al. 2016), showed that while IGF2BP1 and IGF2BP2 were bound to a highly similar group of RNAs, IGF2BP3 displayed a binding preference that was distinct from the other paralogs (Conway et al. 2016). These results indicated that the paralogs play both redundant and distinct functions during early development and in different tissues. However, systematic characterization of RNA binding of the IGF2BP paralogs across cell types and tissues remains largely unexplored.

In recent years, significant improvements were made in the multistep CLIP methods, and several modifications were made to the protocols to overcome various challenges during the library preparation (Lee and Ule 2018; Hafner et al. 2021). Due to low input amounts, originally radioisotopes were used in these methods to visualize the RNA. Currently, the 3′ adapter conjugated to the fluorescent or infrared (IR) dye is being used to avoid radioactivity making these methods more accessible (Zarnegar et al. 2016; Kaczynski et al. 2019; Anastasakis et al. 2021). The low RNA input amounts represent a major challenge for the CLIP methods. To overcome this, increasing the efficiency of the library construction has been crucial. In addition to the low RNA input, the inefficient readthrough of the oligopeptide crosslink sites by the reverse transcriptase presents another challenge. The use of highly processive reverse transcriptases was shown to increase the efficiency of the library preparation and to produce libraries with higher complexity (Zarnegar et al. 2016; Van Nostrand et al. 2017). As the major goal of the CLIP methods is the identification of the RBP-binding sites with high precision, the interpretation of the results is highly influenced by the sequence bias introduced during small RNA library preparation. One of the sources of the sequence bias is the ligation of the adapters (Hafner et al. 2011). The single adapter strategy combined with circular ligation and the addition of the short random sequences to the 5′ ends of the adapter were shown to be effective in reducing sequence bias at this step in iCLIP (König et al. 2010), miRNA (Hafner et al. 2011; Barberán-Soler et al. 2018), and ribosome profiling (Lecanda et al. 2016) libraries. Another source of sequence bias in CLIP experiments is the selection of RNase treatment conditions to obtain short RNA sequences to precisely map the RBP-binding sites (Kishore et al. 2011). Importantly, different RNases were shown to produce very distinct read coverage profiles in ribosome profiling experiments, which rely on the mapping of short RNase-digested footprints similar to the CLIP methods (Gerashchenko and Gladyshev 2017). Therefore, the RNase selection and treatment conditions have to be carefully assessed and optimized.

To date, PAR-CLIP approaches have been instrumental in identifying RNAs interacting with several important RBPs in the cell (Hafner et al. 2010; Ascano et al. 2012; Gregersen et al. 2014). The PAR-CLIP relies on the incorporation of photoactivatable modified nucleoside analogs (4-thiouridine [4sU] or 6-thioguanine [6SG]) into cellular RNAs. Under UV light (365 nm) photoactivatable

nucleoside analogs, 4sU being the most commonly used, covalently crosslink with the interacting proteins. The 4sU incorporation leads to 100- to 1000-fold increased crosslinking efficiency compared to the UV crosslinking at 254 nm. The protein–RNA complexes are then immunoprecipitated in combination with the two-step RNase treatment: in-lysate and on-beads RNase to shorten the RNA fragments, and the protein is digested with proteinase K to remove the polypeptide. The peptide remnants of the protein at the crosslink site result in the T to C transitions in the final sequencing library allowing identification of the RBP-binding sites with single-nucleotide resolution (Hafner et al. 2010). Here, we describe a modified PAR-CLIP protocol optimized for immunoprecipitation of the endogenous human IGF2BP3 in colon carcinoma cell lines. Our modified PAR-CLIP strategy uses the IR-labeled 3′ adapter and circular ligation to increase the accessibility of the method and to decrease bias in library preparation. Importantly, by comparing the IGF2BP3-target transcripts identified in samples treated with different RNases, we revealed that RNase selection is crucial for both the identification of certain targets and the prediction of the RBP-binding sites. We anticipate that our modified PAR-CLIP protocol can be utilized for characterizing IGF2BP3 targets as well as studying other RBPs in various tissues and cancer cells.

RESULTS

Overview of the infrared PAR-CLIP protocol

In this work, we present a modified version of the PAR-CLIP protocol (Hafner et al. 2010; Danan et al. 2016). We optimized three crucial aspects in the protocol: (i) the immunoprecipitation (IP) of the endogenous protein (on the example of IGF2BP3), (ii) RNase treatment conditions to reduce sequence bias, and (iii) increasing the safety and efficiency of the protocol.

Our IR-PAR-CLIP protocol mainly follows earlier established protocols with several modifications (Fig. 1). To allow efficient crosslinking, photoactivatable modified nucleoside 4sU is added to cell culture media 15 h prior to collection, to allow for incorporation into the cellular RNAs (Fig. 1A). Cells are exposed to 365 nm UV light to crosslink the 4sU-containing RNAs with interacting proteins (Fig. 1B), collected and lysed (Fig. 1C). Clarified cell lysate is treated with RNase for initial fragmentation of the RNAs. At this step RNase treatment facilitates the IP of the protein of interest and reduces the contamination from other RBPs interacting with the same mRNA (Fig. 1D). For the IP of the endogenous protein, here we used an anti-IGF2BP3 antibody coupled to protein G magnetic beads. Following the IP, a second RNase treatment is performed while the crosslinked protein–RNA complexes are still coupled to the beads. This treatment further shortens the RNA footprints to map the RBP-binding sites with high resolution. As both RNase I and RNase T1 used in this work leave a 2′,3′-cyclic phosphate, the crosslinked RNA footprints have to be dephosphorylated to allow 3′ adapter ligation (Fig. 1E). Next, the preadenylated IR-dye-conjugated DNA adapter is ligated to the RNA fragments (Fig. 1F; Supplemental Fig. 1A). The IR-dye allows visualization of ligated fragments at attomolar amounts (Zarnegar et al. 2016) and the random sequence at the 5′ end of the adapter helps to reduce the ligation bias (König et al. 2010; McGlincy and Ingolia 2017). The protein–RNA-adapter complexes are then eluted from the beads and resolved on SDS–PAGE which is visualized at a near-infrared light imager (here, LI-COR Odyssey CLx). The protein–RNA-adapter complexes are size selected on a gel (Supplemental Fig. 1B), extracted from the gel fragments, and treated with proteinase K to digest the crosslinked protein leaving the small peptide remnant. The peptide–RNA-adapter complexes are then size-selected on a denaturing RNA gel. The efficiency of RNase treatment can be already estimated during size selection (Fig. 1G; Supplemental Fig. 1C). Next, the purified peptide–RNA-adapter complexes are reverse transcribed with the primer containing flexible hexa-ethyleneglycol spacer. It allows efficient circular ligation and prevents the rolling-circle amplification during final library amplification (Ingolia 2010; McGlincy and Ingolia 2017). The cDNA is separated from the unreacted primer and no-insert products on a denaturing gel (Fig. 1H; Supplemental Fig. 1D) and ligated in a circular ligation reaction. The cDNA library circles are then amplified and indexed in a library construction PCR and separated from the excess of the primer on a gel (Fig. 1I; Supplemental Fig. 1E). The detailed step-by-step protocol is attached as Supplemental Material, the library schema is shown in Supplemental Figure 1A, and the most crucial optimization steps including the effect of RNase treatment on RBP targets identification are described below.

Optimization of the immunoprecipitation of the endogenous IGF2BP3

The CLIP methods rely on immunoprecipitation of the protein of interest for the isolation of specific RBP–RNA complexes from cells. For higher efficiency and obtaining cleaner IPs, tagging the protein of interest has been a common strategy. The addition of a tag to the protein of interest can affect protein levels and function, and the selection of the tag and its position in the protein sequence may require optimization. The availability of IP-compatible antibodies recognizing the protein of interest allows the characterization of the protein in various cell types at its endogenous levels and without manipulating its native structure. Earlier studies indicated that tagging IGF2BP3 might impact its association with polysomes and was suggested to impact its function (Bell et al. 2013). To be able to map the interaction

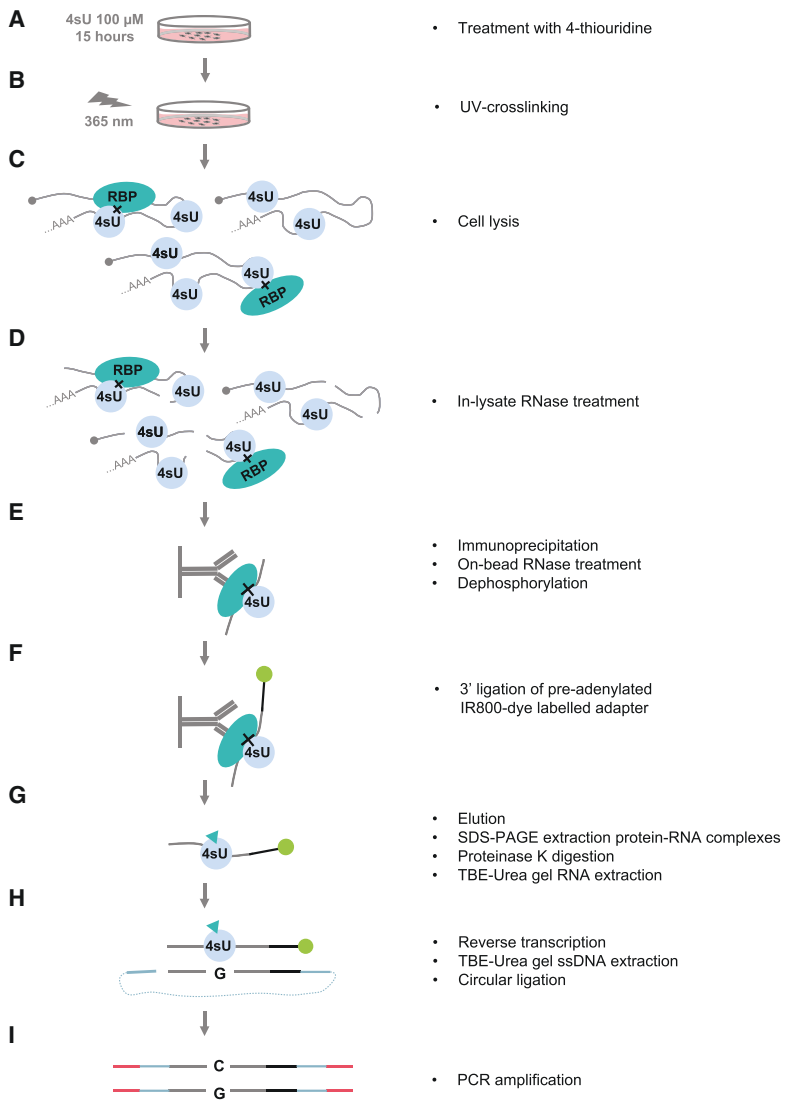

FIGURE 1. Schematic of the infrared PAR-CLIP. (*A*) Mammalian cells are treated with 100 µM 4sU for 15 h to achieve maximum 4sU incorporation into RNA. (*B*) Exposure to 365 nm UV light crosslinks RNA to interacting proteins. (*C*) Cells are lysed and (*D*) the lysate is treated with RNase to make proteins more accessible for immunoprecipitation. (*E*) Protein of interest is immobilized on the magnetic beads via immunoprecipitation. The RNA–protein complexes are treated with RNase to obtain short RNA fragments to map the protein binding site with high resolution. RNA fragments are dephosphorylated for the subsequent DNA-adapter ligation. (*F*) 3′ Ligation of the preadenylated DNA adapter. For the visualization of the RNA–protein complexes, the IR800CW dye is azide-conjugated to the 3′end of the adapter. (*G*) The RNA–protein complexes are eluted from the beads, resolved on the SDS–PAGE, and visualized in the infrared channel. The RNA–protein complexes are eluted from the gel and the protein is digested with the proteinase K. RNA fragments are recovered with acidic phenol and size selected on the TBE-Urea gel. (*H*) RNA fragment is reverse transcribed from the primer complementary to the adapter sequence. The resulting ssDNA is purified on the TBE-Urea gel and circularized in a circular ligation reaction. (*I*) The library is amplified in PCR reaction introducing Illumina barcode and adapter sequences. The library schema is shown in detail in Supplemental Figure 1A.

of endogenous IGF2BP3 with its targets in mammalian cells, we characterized the IP-compatible antibody from Proteintech (14642-1-AP). As the PAR-CLIP approaches involve the purification of the cross-linked RBP–RNA complexes from gels, the purity of the IP samples is highly crucial. We performed the IPs in the presence of high salt for stringency. The colloidal Coomassie staining of the SDS–PAGE gel of the IP eluates revealed that Proteintech anti-IGF2BP3 antibody showed a single major band corresponding to the size of IGF2BP3 (Fig. 2A). It is advisable to visualize the gels with highly sensitive protein staining approaches in addition to western blotting to assess the purity of the eluates for PAR-CLIP experiments.

When isolating the endogenous protein, the specificity of the antibody has to be tested to ensure that it does not recognize other proteins with similar molecular weights. One of the most important challenges of the PAR-CLIP experiments for endogenous IGF2BP3 is the high sequence conservation between IGF2BP paralogs. Therefore, the cross-reactivity of the polyclonal antibody has to be considered. We used the HCT116 colorectal carcinoma cell line that has low levels of IGF2BP1, but high IGF2BP2 expression (Mongroo et al. 2011; Nusinow et al. 2020; Lu et al. 2021). To test whether the anti-IGF2BP3 antibody recognizes IGF2BP2, we analyzed HCT116 CRISPR–Cas9 knockouts of IGF2BP2 and IGF2BP3. By using siRNA depletion of IGF2BP2 in IGF2BP3 KO HCT116 cells, we found that the Proteintech anti-IGF2BP3 antibody partially recognizes IGF2BP2 resulting in ~20% contamination which has to be considered when interpreting the data (Fig. 2C). We corroborated these results by performing mass spectrometry analyses following IP of IGF2BP3 using the Proteintech antibody (Fig. 2D; Supplemental Table 1). As IGF2BP paralogs form RNA-bridged complexes, we performed the RNase treatment prior to the IPs and applied extensive high salt washes similar to our PAR-CLIP experiments. The peptide intensity of the next most abundant contaminant ATP6V1A protein [catalytic subunit of the V1 complex of vacuolar(H+)-ATPase] was more than 100 times lower than that of IGF2BP3 and, as

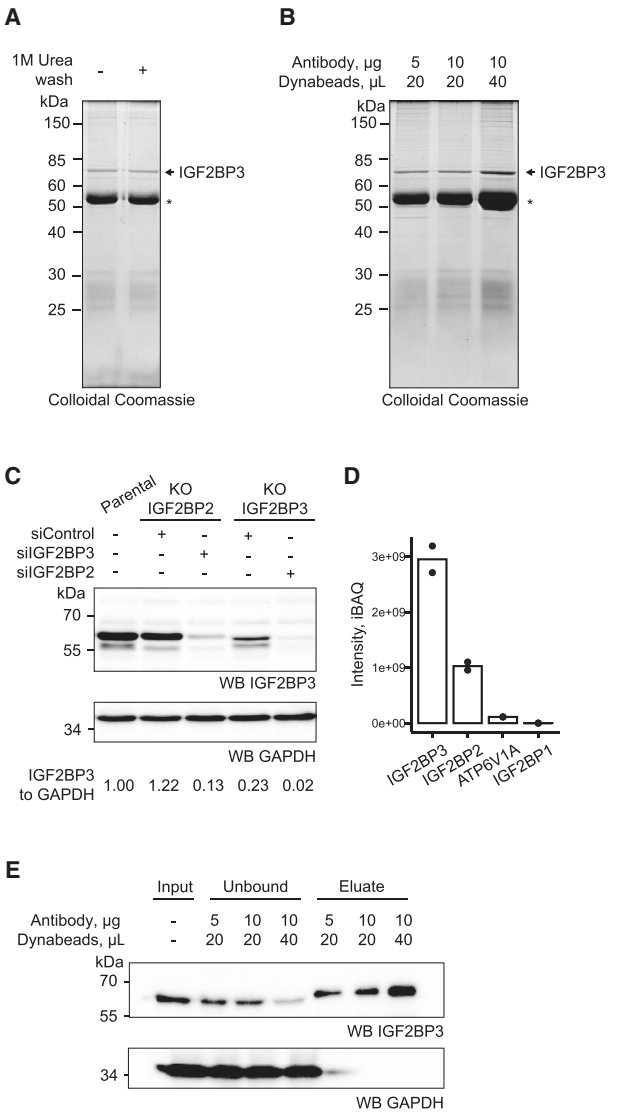

FIGURE 2. Optimization of immunoprecipitation of endogenous IGF2BP3. (*A*,*B*) Eluates from the immunoprecipitation reactions of IGF2BP3 from 25 mln HCT116 cells (~2.5 mg of total protein) with Proteintech (14642-1-AP) anti-IGF2BP3 antibody coupled to protein G Dynabeads at indicated amounts resolved on SDS–PAGE and stained with a Colloidal Coomassie. * IgG heavy chain. (*C*) Western blot of the IGF2BP2 and IGF2BP3 CRISPR–Cas9 knockout HCT116 treated with the siRNA against IGF2BP3 and IGF2BP2, respectively, to deplete the remaining paralog. (*D*) Mass spectrometry intensities in the eluate of the immunoprecipitation of IGF2BP3 with Proteintech (14642-1-AP) anti-IGF2BP3 antibody. (*E*) Western blot of the IP described in (*B*). The input, unbound fraction, and eluates were loaded at a 1:1:1 ratio.

the protein has no known RNA-binding activity, it should not crosslink to RNA.

Isolating most of the protein from cell lysates is crucial as the unbound portion of the protein might be present in complexes that are not as accessible to IP, and an incomplete IP might affect the interpretation of the data. For the IP experiments, we coupled the antibody to magnetic beads (Dynabeads, Thermo Fisher). We tested the ratio of Dynabeads to antibody to identify conditions that capture the highest amount of IGF2BP3 from cell lysates (Fig. 2B, E). Using 4 µg antibody for 16 µL of Dynabeads per 1 mg of total protein within the lysate resulted in ~75% depletion of the protein and was selected for further experiments (Fig. 2B,E). Based on these results, we decided to use Proteintech anti-IGF2BP3 antibody for our subsequent experiments.

The infrared labeled 3′ adapter provides a robust and sensitive alternative to radioactive labeling

Traditionally, radioactive isotopes have been used to visualize crosslinked protein–RNA complexes and RNA fragments at various steps of CLIP protocols. The use of radioactive isotopes presents challenges in the widespread application of the method. They represent a health hazard and require a high safety level laboratory space. Moreover, radioactive isotopes decay causing a variation of the signal across experiments. To overcome these challenges, we used an infrared dye labeling strategy for PAR-CLIP experiments. We used IR800CW (LI-COR) as it provides high sensitivity with low fluorescence background. A similar strategy has been successfully implemented in other CLIP methods (Zarnegar et al. 2016; Kaczynski et al. 2019). In our protocol, we used the 5′ preadenylated 3′ DNA adapter labeled at the 3′ end with an azide-conjugated infrared dye. 5′ adenylation of the adapter and blocking of the 3′ end of the sequence with the azide-conjugated dye ensures the single direction of ligation (Fig. 3A; Supplemental Fig. 1A). The described 3′ adapter contains the following features: (i) Illumina adapter sequence, (ii) 5-nt unique molecular identifier (UMI) that is used to remove the PCR duplicates during analysis, and (iii) 5-nt index sequence. Adapter-ligated RNAs containing different index sequences can be pooled together before the reverse transcription reaction (König et al. 2010).

The infrared detection of the IR800CW dye displayed high sensitivity, as 100 attomoles of the adapter visualized on the gel displayed sufficient signal intensity for detection (Fig. 3B). The SDS–PAGE of crosslinked protein–RNA-adapter complexes showed little background and displayed distinct bands for the two proteins we tested based on their different molecular weights (MOV10 [114 kDa] and IGF2BP3 [64 kDa]). The crosslinked RNA-adapter fragments add ~30–50 kDa to the apparent molecular weight of the protein depending on the size of the RNA conjugate at different RNase treatment conditions. The appearance of RNase-sensitive high molecular weight products confirmed that the observed complexes result from the adapter-crosslinked RNA footprints (Fig. 3C). Additionally, those gels allowed us to estimate the efficiency of RNase cleavage and the yield of the isolated complexes. Altogether, we established a modified IR-PAR-CLIP protocol that

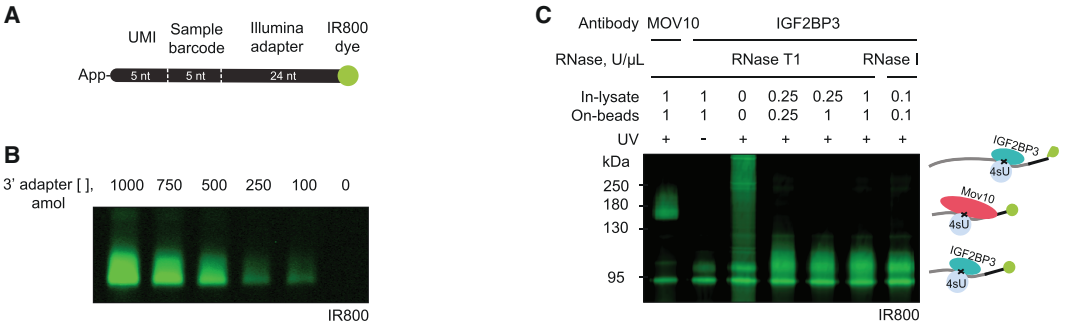

FIGURE 3. Infrared adapter ligation allows visualization of RNA–protein complexes with high sensitivity. (*A*) Schematic of the DNA adapter. The preadenylated DNA adapter contains the UMI, sample barcode, and Illumina adapter sequence. The IR800CW dye is azide-conjugated to the 3′end of the adapter. (*B*) The infrared adapter can be detected at the TBE-Urea gel starting from 100 attomoles (~1 pg DNA). (*C*) SDS–PAGE of the RNA–protein complexes after infrared adapter ligation. Immunoprecipitation of endogenous MOV10 (114 kDa) or IGF2BP3 (64 kDa) proteins was done in 4sU-crosslinked lysates. The control without crosslinking shows a gel background. The crosslinked RNA-adapter fragments add ~30–50 kDa to the apparent molecular weight of the protein depending on the RNase treatment conditions.

allowed us to visualize crosslinked RNA–protein conjugates with high sensitivity.

RNase treatment impacts the identification of IGF2BP3-binding sites and mRNA targets

In the PAR-CLIP method, RBP–RNA complexes are subjected to RNA fragmentation by RNase treatment at two distinct steps: (i) RNase treatment of the lysate to decrease copurification of additional RBPs in RNA-bridged RNP complexes and (ii) RNase treatment on beads to allow for size selection. To fragment the crosslinked RNAs in CLIP experiments, RNase I and RNase T1 are most commonly used. The sequence preferences of RNases and differences in digestion efficiency can introduce a bias into the PAR-CLIP data and affect conclusions. While RNase I has a low sequence preference, RNase T1 preferentially digests after guanosines and can therefore introduce a stronger bias (Kishore et al. 2011; Gerashchenko and Gladyshev 2017). Interestingly, although PAR-CLIP produces short reads that are more prone to be affected by the RNase sequence preferences, most PAR-CLIP protocols use RNase T1 (Hafner et al. 2010; Friedersdorf and Keene 2014; Danan et al. 2016), while RNase I is more commonly used in iCLIP and eCLIP protocols (König et al. 2010; Conway et al. 2016; Van Nostrand et al. 2016; Buchbender et al. 2020)

To systematically address the effect of RNase cleavage on the results of IGF3BP3 PAR-CLIP, we tested RNase T1 and RNase I at several concentrations. In all of the libraries, the reads preferentially mapped to the 3′UTR regions in agreement with known IGF2BP3-binding preferences in cancer cells (Fig. 4A; Hafner et al. 2010; Palanichamy et al. 2016; Huang et al. 2018) and the IGF2BP3 libraries contained on average 2000 times more crosslinked read clusters compared to the IgG control sample (Fig. 4B,C). In PAR-CLIP, two RNase treatment steps are usually performed: first treatment in the lysate intended to partially digest the RNA, facilitate the IP and reduce the co-IP of other RBPs bound to the same mRNA and the second treatment after the IP to shorten the RNA footprints for better identification of the binding motifs. For RNase I, we tested the in-lysate concentrations of 0.05 and 0.1 U/µL with a constant on-beads concentration of 0.025 U/µL and the on-beads concentrations of 0.05 and 0.025 U/µL with a constant in-lysate concentration of 0.05 U/µL. In this concentration range, we observed that the increase of the RNase concentration both in-lysate and on-beads improved the yield of the unique reads and the number of identified clusters (Fig. 4B,C) while the lower RNase concentrations only slightly increased the lengths of the aligned deduplicated reads (Fig. 4D). Similarly, the combination of RNase T1 concentrations of 1 U/µL in-lysate and on-beads resulted in higher numbers of the aligned reads and identified clusters than 0.25 U/µL (Fig. 4B–D). The efficiency of RNase treatment depends on multiple parameters including cell type, the nature of interactions between the protein of interest and its targets, and the concentration of this protein in the cells. Therefore, optimization of the RNase treatment for a particular experiment may be required.

To reveal whether treatment with various RNases impacts the results, we compared the PAR-CLIP coverage for IGF2BP3 obtained with RNase I and RNase T1. Strikingly, the coverage profiles on 3′UTRs differed for multiple targets. The representative examples of *TP53*, *MYC*, and *HMGA2* show that RNase I digestion results in broader coverage than RNase T1 and can possibly identify different binding sites (Fig. 5A). Indeed, the analysis of overrepresented 4-nt motifs identified CAGU as the most significant motif for each RNase I concentration tested (Fig. 5B; Supplemental Fig. 2A). This sequence was not identified in RNase T1-treated samples where the strongest motif was CAUU in agreement with previously published IGF2BP3 PAR-CLIP data obtained with RNase T1 digestion (Fig. 5B; Supplemental Fig. 2A; Hafner et al. 2010).

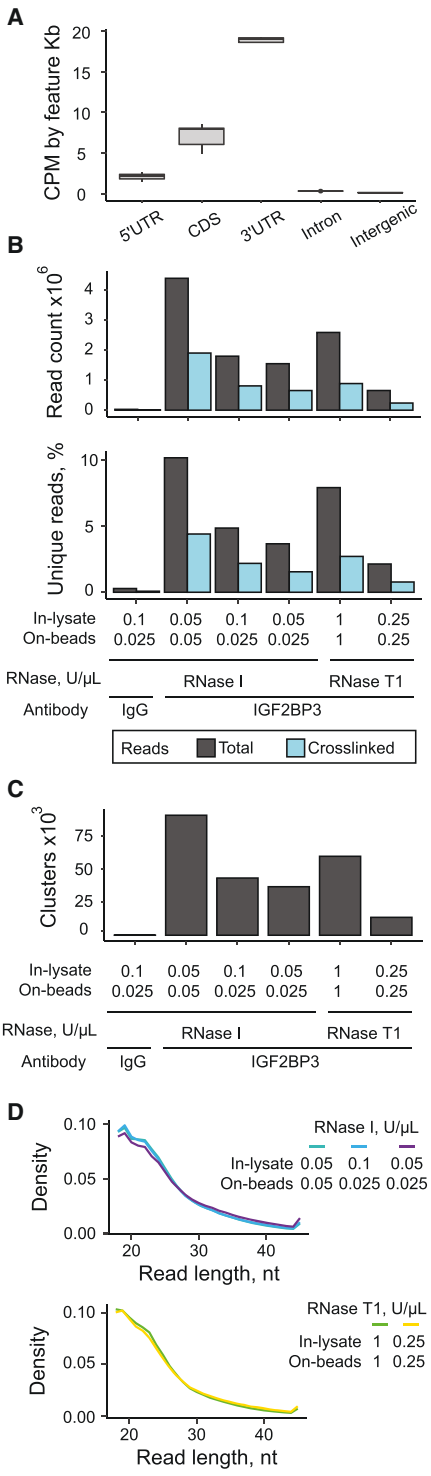

FIGURE 4. Effect of RNase treatment conditions on the recovery of crosslinked RNA fragments. (*A*) Read alignment of the libraries made in this study to genome features. (*B*) Counts and percentages of the unique deduplicated reads in the final libraries depending on RNase treatment conditions. (*C*) The number of clusters identified with PARalyzer depending on RNase treatment conditions. (*D*) Distribution of lengths of deduplicated reads within the 18–45 nt range.

Moreover, RNase I treatment allowed us to identify ~1.5 times more IGF2BP3-bound targets compared to RNase T1 including most of the targets identified with RNase T1 (Fig. 5C; Supplemental Fig. 2B; Supplemental Table 2). Interestingly, highly intersecting sets of targets were identified in all RNase I concentration conditions despite having up to a two-times difference in the number of aligned crosslinked deduplicated reads (Fig. 4B) or the number of identified clusters (Fig. 4C). The number of targets identified with RNase I increased with increasing RNase I concentration. In contrast, a similar number of targets was identified with the two tested RNase T1 treatment conditions (1 or 0.25 U/µL) although the number of aligned crosslinked deduplicated reads in 1 U/µL condition was ~4 times higher than in 0.25 U/µL (Fig. 4B), as was the number of the identified clusters (Fig. 4C). To exclude the possibility that the higher number of targets obtained in samples with the RNase I treatment resulted from the different number of useful reads, we compared the results of the samples treated with RNase T1 at 1/1 U/µL with the ones treated with RNase I 0.1/0.025 U/µL. At those concentrations, RNase T1 produced a slightly higher number of aligned crosslinked deduplicated reads and identified clusters compared to RNase I, but the number of identified targets was still 1.4 times higher in RNase I sample. Most of the targets that we identified only in RNase I conditions were not found in RNase T1 due to lower coverage at the cluster (less than 10 counts per million [CPM]) (e.g., *PARK7*, *SRPRB*; Fig. 5D) and several examples had less than 50% of T to C transitions at the covered positions (e.g., *FABP5*; Fig. 5D). Although the number of targets identified using two RNase T1 concentrations was similar, more than 30% of the targets were identified only in one of the conditions. This can be explained by the RNase T1 cleavage bias resulting in pronounced differences in the recovered footprints for samples treated with different enzyme concentrations. The differences between the RNase treatment conditions were also evident in the Pearson correlation matrix of the IGF2BP3 IR-PAR-CLIP coverage (Supplemental Fig. 2C), with RNase I conditions showing higher correlation coefficients compared to RNase T1. Altogether, our results revealed that RNase I treated samples yielded a higher number of IGF2BP3 RNA targets with higher confidence.

IR-PAR-CLIP identifies novel IGF2BP3 RNA targets in colon cancer cell lines

IGF2BP3 expression is elevated in colon cancers and was shown to be associated with increased tumor angiogenesis, growth, and poor prognosis (Lochhead et al. 2012; Shantha Kumara et al. 2015; Xu et al. 2019; Yang et al. 2020). Several mechanisms were suggested for the function of IGF2BP3 in promoting tumorigenesis in colon cancers including regulation of mRNA localization, translation,

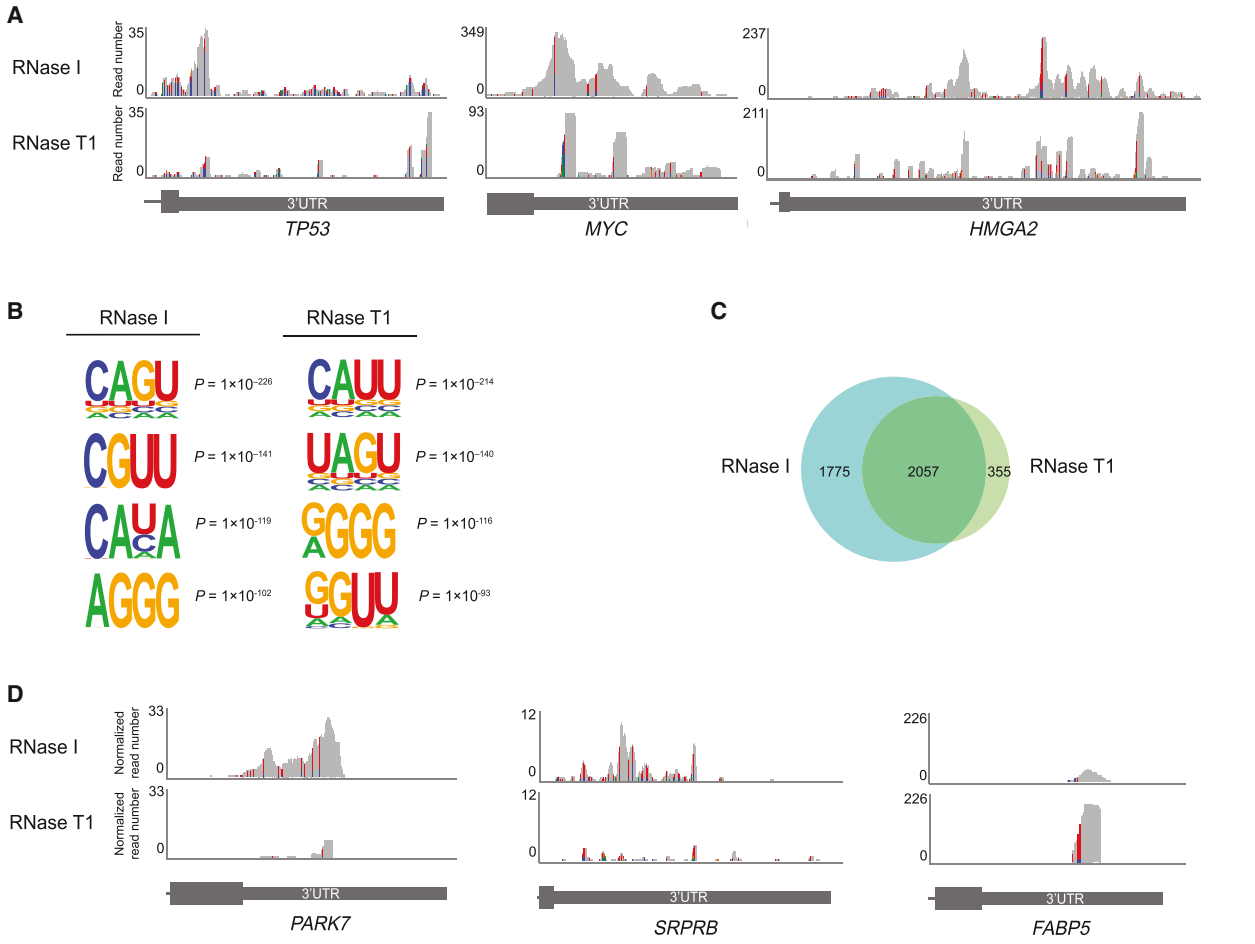

FIGURE 5. RNase selection affects IR-PAR-CLIP coverage, motif and target prediction results. (*A*) Examples of IGF2BP3 PAR-CLIP read coverage of 3′UTRs of *TP53*, *MYC*, and *HMGA2* transcripts. (*B*) 4-nt IGF2BP3-binding motifs identified by HOMER in IR-PAR-CLIP of HCT116. (*C*) Overlap of IGF2BP3 targets identified in this study with RNase I and RNase T1. Concentrations of RNases used for this figure in-lysate and on-beads: RNase I 0.05 U/µL, RNase T1 1 U/µL. (*D*) Examples of IGF2BP3 PAR-CLIP library-size normalized read coverage of 3′UTRs of *PARK7*, *SRPRB*, and *FABP5* transcripts. Transitions color code: (A) green, (C) blue, (G) brown, (T) red.

and stabilization of oncogenic transcripts (Rivera Vargas et al. 2014; Deforzh et al. 2016; Ennajdaoui et al. 2016; Li et al. 2020). Therefore, thorough identification of IGF2BP3 targets in colon cancers is important for understanding its function.

In this work, we identified the mRNA targets of IGF2BP3 in the colorectal carcinoma cell line HCT116 using our optimized IR-PAR-CLIP method. We compared our results obtained with both RNase I and RNase T1 (4181 targets) with IGF2BP3 targets identified by the PAR-CLIP method in HEK293 (Hafner et al. 2010), by other CLIP approaches in human pluripotent stem cells (Conway et al. 2016), B-acute lymphoblastic leukemia (B-ALL) (Palanichamy et al. 2016), hepatocellular carcinoma (HepG2) (ENCODE [Dunham et al. 2012]), and pancreatic ductal adenocarcinoma (PL45 and Panc1) (Ennajdaoui et al. 2016) (6456 targets) (Supplemental Table 2). This comparison revealed 2863 common targets identified in the analyzed cell types and 1318 novel targets only identified in HCT116 cells (Fig. 6A). The IGF2BP3 target pool might differ depending on cell line-specific factors, the most prominent factor being differences in transcriptome composition and the expression level of transcripts. Therefore, our results highlight the importance of the identification of IGF2BP3 targets in various cancers in order to reveal their role in tumorigenesis.

The GO term analysis of all the IGF2BP3 targets in HCT116 cells showed that the IGF2BP3-bound transcripts belong to multiple functional categories (biological process) involved in mRNA processing and metabolism, RNA localization and targeting to the endoplasmic reticulum, response to proteotoxic stress and chromatin modifications (Fig. 6B; Supplemental Table 3). These categories were highly similar to previously published data indicating that IGF2BP3 interacts with a core set of RNAs independent of the tissue or cell type. Interestingly, the 1318 targets characteristic only for HCT116 included transcripts

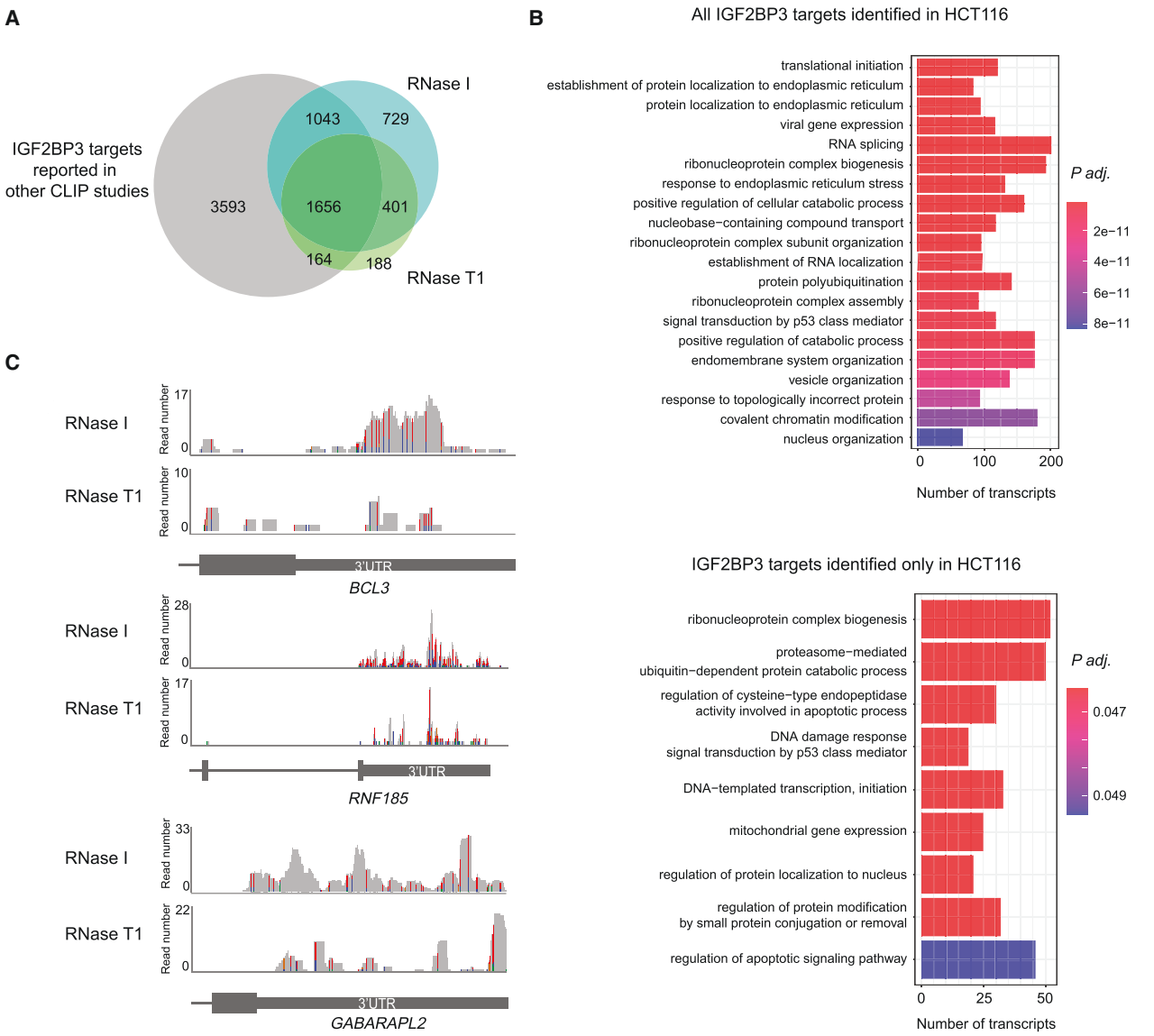

FIGURE 6. Novel IGF2BP3 RNA targets identified by IR-PAR-CLIP in HCT116 colorectal carcinoma cell line. (*A*) Overlap of IGF2BP3 targets identified in this study with RNase I and RNase T1 with the aggregated list of IGF2BP3 targets identified in the HEK 293 (Hafner et al. 2010), human pluripotent stem cells (Conway et al. 2016), B-ALL (Palanichamy et al. 2016), hepatocellular carcinoma (HepG2) (ENCODE [Dunham et al. 2012]), and pancreatic ductal adenocarcinoma (PL45 and Panc1) (Ennajdaoui et al. 2016). Concentrations of RNases used for this figure in-lysate and on-beads: RNase I 0.05 U/µL, RNase T1 1 U/µL. (*B*) Gene Ontology (GO) term analysis of biological process (BP) categories enriched in HCT116 targets identified in this work with both RNase I and RNase T1 (HCT116 all) or when the previously identified targets (A) are excluded (HCT116 only). For visualization, the GO enrichment results were simplified by clustering using the *simplify* function from the clusterProfiler R package. (*C*) Examples of IGF2BP3 PAR-CLIP read coverage of 3′UTRs of *BCL3*, *GABARAPL2*, and *RNF185* transcripts. Transitions color code: (A) green, (C) blue, (G) brown, (T) red.

playing a role in DNA-damage response and apoptotic pathway regulation (e.g., *CDK4*, *BAX*, *CASP2*, *BCL3*, *BCL10*), proteasome-mediated degradation (e.g., *USP7*, *CUL3*, *TRIM2*, *PSMA6*, *PSMA5*, *PSMD8*), and autophagy (e.g., *LAMTOR1*, *GABARAPL2*) and included numerous components of transcription initiation mediated by DNA polymerases I and II (e.g., *POLR1A*, *POLR1B*, *POLR1C*, *POLR2D*, *MED4*, *MED14*, *MED20*, *MED24*, *TAF4*, *TAF9*) (Fig. 6B,C) suggesting that IGF2BP3 might be involved in the regulation of these processes in colon cancer.

DISCUSSION

Emerging data reveal the importance of posttranscriptional mechanisms in cellular adaptation and development (Becker et al. 2018; Rendleman et al. 2018). Multiple

RBPs bind and regulate the fate of different mRNA targets depending on the cellular state and developmental stage. This has been linked to the differences in mRNA abundance, RNA modifications, and posttranslational modification of the RBPs as well as the interactions of RBPs with other proteins (Hüttelmaier et al. 2005; Hafner et al. 2013; Huang et al. 2018). Therefore, identifying mRNA targets bound to RBPs at different cellular, metabolic, or developmental states is of crucial importance. Identifying the RNAs that are directly bound to the RBP of interest is challenging. Isolating ribonucleoprotein complexes from cells requires stringent conditions, which might lead to the loss of transient interactions between RBP and RNAs (Riley and Steitz 2013). To identify RNAs interacting with the RBP of interest and map the binding sites with high confidence, CLIP methods are widely used (Lee and Ule 2018; Hafner et al. 2021). Those methods rely on crosslinking of RNAs to the RBP of interest in their native environment in cells before their isolation from cells by IP. Originally, UV light at 254 nm has been used for crosslinking approaches. However, due to the low efficiency of crosslinking at this wavelength, PAR-CLIP approaches relying on the introduction of photoactivatable nucleosides have been developed (Hafner et al. 2010; Danan et al. 2016).

The IGF2BP family of RBPs plays an important role in posttranscriptional regulation by controlling mRNA localization, stability, and translation (Nielsen et al. 1999; Ladd et al. 2001; Fallini et al. 2011; Mizutani et al. 2016). IGF2BP3 is one of the three paralogs of the IGF2BP family. Due to its high expression in aggressive tumors and its role in regulating the stability of mRNAs that promote cell growth and metastasis, IGF2BP3 has been widely studied. According to previously published data (Dunham et al. 2012; Conway et al. 2016; Palanichamy et al. 2016) and our current study (Fig. 6A), IGF2BP3 binds to multiple mRNAs and the RNA target pool can vary dramatically depending on the cell type similar to many other RBPs (Van Nostrand et al. 2020). In this paper, we developed and applied a modified PAR-CLIP protocol IR-PAR-CLIP for the identification of transcripts interacting with endogenous IGF2BP3 (Fig. 1).

In IR-PAR-CLIP, we optimized or modified four important steps of the protocol. (i) We replaced radioactive isotopes with IR fluorescence tags to visualize the RNA fragments. (ii) We developed a streamlined approach to test antibody specificity for IGF2BP paralogs and optimized the IP protocol for human IGF2BP3. (iii) We implemented circular ligation to the PAR-CLIP protocol to increase efficiency and reduce sequence bias during library preparation. (iv) We tested the biases introduced by the RNases used to fragment the RNAs during PAR-CLIP and optimized RNase cleavage. Altogether, using our optimized IR-PAR-CLIP method, we revealed 1318 novel RNA targets of IGF2BP3s in colon cancer cells with high confidence.

The CLIP approaches rely on the IP of the RBP–RNA complexes from cells to identify their direct target RNAs. IP of the RBP of interest using specific antibodies against the protein is an attractive approach that does not require the attachment of affinity tags to the RBP of interest. Even though the CRISPR–Cas9 gene editing methods have become more reliable, efficient, and accessible, ensuring homozygous insertion of the tag to both alleles of the gene of interest requires clonal selection and careful further characterization of various clones, which still poses a challenge. Moreover, the addition of the tag may alter protein expression levels, localization, and function. Thus, performing IPs with antibodies against the protein of interest is preferable if such antibodies are available. In this case, the specificity of the antibody is of crucial importance as contamination with another RBP may impact the experimental outcome. We found that visualizing the IP eluates via unbiased sensitive protein staining methods such as colloidal Coomassie allows careful assessment of the specificity of the antibodies (Fig. 2A). Another possible challenge when performing IPs for endogenous proteins is the affinity of the antibody of interest for paralogs of the RBP. Many RBPs have closely related paralogs in mammalian cells including IGF2BP3. The sequence identity among the IGF2BP paralogs is ∼73%. To test the specificity of the anti-IGF2BP3 antibody, we used IGF2BP3 and IGF2BP2 knockout cell lines together with siRNA depletion of the second paralog (Fig. 2C). Moreover, we performed mass spectrometry analyses with the eluates of the IPs using the anti-IGF2BP3 antibody. We found that the anti-IGF2BP3 antibody partially recognizes the IGF2BP2 paralog and in the MS analyses IGF2BP2 might cover a maximum of 20% of the total reads obtained with IGF2BP3 antibody (Fig. 2D). In the future, the use of monoclonal antibodies raised against the diverging sequences might help to increase the selectivity of antibodies for IGF2BP3 paralogs.

In the PAR-CLIP method, the crosslinked RBP–RNA complexes are subjected to size selection at distinct stages to further purify the complexes and increase the stringency in the protocol. Traditionally, the RBP–RNA complexes and the isolated fragments have been visualized by radioactive isotopes using autoradiography. Even though highly sensitive, this method is tedious due to the need for permits, the possibility of contamination, and the long exposure times of radioactive labels. Moreover, due to the decay of the radioactive isotopes the signal varies from experiment to experiment. Here, we optimized the use of IR fluorescence tags to label the RNAs at the 3′ end by the use of IR800-dye labeled adapters. The IR-labeled 3′ adapter could be visualized at a 100 attomole range (Fig. 3B). According to our estimations, ∼2 femtomole of IGF2BP3- or MOV10-RNA-3′adapter complexes could be isolated from 25 million HCT116 cells and visualized with more than sufficient intensity (Fig. 3C). Our results suggest that IR-PAR-CLIP offers a sensitive, reliable, and convenient

alternative to radioactive isotopes to visualize RNAs at different steps of the PAR-CLIP protocol.

The low input amounts present a challenge in the CLIP methods. To increase the efficiency of the library preparation, recent protocols have used reverse transcriptases with high processivity and optimized the size selection and the reaction clean-up steps to find effective ways to get rid of the excess of the unreacted adapter, RT primer, and no-insert products (Zarnegar et al. 2016; Van Nostrand et al. 2017; Lee and Ule 2018; Buchbender et al. 2020; Anastasakis et al. 2021). In order to increase the efficiency in IR-PAR-CLIP, here we used highly processive reverse transcriptase Superscript IV and implemented the on-bead ligation of a preadenylated 3′ DNA adapter. We used the adapter sequence that contains the UMIs and index sequences allowing deduplication and multiplexing of samples (König et al. 2010). To additionally increase the efficiency and to reduce the ligation bias, we implemented a circular ligation strategy using the reverse transcription primer with an optimized sequence containing the carbon linker which facilitates circular ligation and prevents rolling circle amplification (Ingolia 2010; König et al. 2010; McGlincy and Ingolia 2017). Recently, omitting the RNA size selection step and performing the size selection during the first step of the two-step PCR approach was shown to increase the efficiency of PAR-CLIP library preparation (Anastasakis et al. 2021). We did not implement this change to the current protocol as we used the denaturing RNA gels to control for the efficiency of the RNase cleavage and separate the ligated RNA fragments from the longer non-crosslinked RNAs and no-insert products. Additionally, the separation of longer, potentially non-crosslinked RNAs on a denaturing gel allowed us to omit the transfer to the nitrocellulose membrane, as this step was stated to decrease the efficiency of the recovery of the crosslinked fragments (Anastasakis et al. 2021). In future protocols, if the RNA size selection is omitted, the use of ssDNA exonuclease in combination with 5′ deadenylase may be beneficial to reduce the contamination with the unreacted adapter as described in McGlincy and Ingolia (2017). To further increase the efficiency of the protocol, the bead-based size selection methods can be optimized for purifying the reverse transcription product, as implemented in eCLIP (Van Nostrand et al. 2016) and iCLIP2 protocols (Buchbender et al. 2020). With the described IR-PAR-CLIP approach, we were able to amplify the IGF2BP3 PAR-CLIP library obtained from 125 million cells at 16 cycles. The final library contained ∼10% of aligned deduplicated reads and resulted in the identification of 80,000 IGF2BP3-binding clusters and ∼4000 mRNA targets. We observed that different RNA fragmentation conditions lead to variations in the number of identified clusters within one order of magnitude and are, therefore, an important step in the protocol that requires optimization.

Optimization of the RNase treatment in the PAR-CLIP is crucial as too short reads will not allow unique genomic mapping while too long reads complicate the precise mapping of the binding sites. Importantly, different nucleases display preferences in their cleavage sequence, and this can introduce biases when one is assigning the binding sites (Kishore et al. 2011). Even though micrococcal nuclease (MNase), RNase A, and RNase I have been implemented in some PAR-CLIP protocols, currently RNase T1 is the most frequently used nuclease for PAR-CLIP experiments in the literature (Kishore et al. 2013; Danan et al. 2016; Garzia et al. 2017; Anastasakis et al. 2021). In CLIP approaches, RNase T1 was shown to introduce a sequence bias, because it preferentially cleaves after guanosines (Haberman et al. 2017). RNase I, which does not have any described nucleotide preferences, was often used in recent CLIP papers (Conway et al. 2016; Haberman et al. 2017; Lee and Ule 2018). Here, we tested whether RNase I or RNase T1 treatment impacts the number of identified targets as well as the sequences identified by IR-PAR-CLIP of IGF2BP3 (Figs. 4, 5). We optimized limited RNase digestion for the two RNases and subjected the IGF2BP3 IR-PAR-CLIP libraries to next-generation sequencing. We found that in samples treated with RNase I, there were around 3800 RNA targets identified in our analyses. In contrast, only approximately 2500 RNAs were identified when libraries were prepared using RNase T1. Importantly, around 2000 of those RNAs were common between RNase I and T1 treated samples indicating that RNase I treatment does not fail to recover targets. Most of the targets that did not pass the selection criteria in RNase T1-treated samples displayed a too low number of reads per cluster compared to the samples subjected to RNase I treatment. Moreover, we also observed that T to C transition sites were not covered for some targets to pass the selection criteria during the analyses. In summary, RNase I outperformed RNase T1 in the identification of IGF2BP3 targets in colon cancer cells.

Intriguingly, the IGF2BP3 interaction motifs identified for RNase I and RNase T1 treated samples showed distinct differences in the top four most reliably predicted motifs. Upon RNase T1 treatment, the motif with the highest score, CAUU, was identical to that identified earlier for IGF2BP3 in HEK293 cells following RNase T1 treatment (Hafner et al. 2010). Instead, in HCT116 cells treated with RNase I, the top scoring motif was CAGU (Fig. 5B; Supplemental Fig. 2A). The motifs obtained with RNase T1 might be depleted of some G-containing sequences if the RNA is digested inside of the recognition motif. Therefore, for PAR-CLIP protocols RNase treatment conditions have to be selected carefully with the preference to be given to the RNases that have low sequence specificity, like RNase I.

Our IR-PAR-CLIP method allowed us to identify 1318 novel mRNAs bound to IGF2BP3s in a colorectal carcinoma cell line (HCT116). Many of these genes are involved in the

regulation of cell cycle, apoptosis, and proteostasis and have cancer-associated functions, suggesting that by regulating their stability or translation IGF2BP3 might contribute to cancer progression (Fig. 6A). For many RBPs, the identity of the targets highly depends on the cell type and condition, therefore the identification of RBP targets in various cellular contexts using the most sensitive methods is crucial for understanding their function and mechanism of action. We anticipate that our framework can be used to identify the targets of other RBPs in a variety of cell types or tissues.

MATERIALS AND METHODS

IR-PAR-CLIP

The crosslinking, proteinase treatment, and size selection parts of the protocol are based on the published PAR-CLIP protocol (Hafner et al. 2010; Danan et al. 2016), the ligation of the IR 3′ adapter is adapted from irCLIP methods (Zarnegar et al. 2016), and the library preparation strategy from iCLIP (König et al. 2010) and ribosome profiling protocols (Ingolia et al. 2009; Ingolia 2010; McGlincy and Ingolia 2017). The detailed step-by-step protocol is provided in the Supplemental Material.

Preadenylation of the 3′ adapter and conjugation of the infrared dye

The 3′ adapter was ordered as RNase-Free HPLC purified oligonucleotide phosphorylated at the 5′ end and containing azide (NHS ester) at the 3′ end with the following sequence: /5Phos/NNNNNATCGTAGATCGGAAGAGCACACGTCTGAA/3AzideN/ (McGlincy and Ingolia 2017). A total of 250 pmol of the oligo was preadenylated in a 50 µL reaction using the 5′ DNA Adenylation Kit (NEB) according to the manufacturer's instructions. The reaction was incubated at 65°C for 2 h. Then the oligonucleotide was purified using Oligo Clean & Concentrator columns (Zymo), and IRdye-800CW-DBCO (LiCor) was conjugated via "click" chemistry at 37°C for 2 h as described in Zarnegar et al. (2016) and Kaczynski et al. (2019).

Cell culture

HCT116 conditionally expressing Tet-OsTIR1 were obtained from the Masato Kanemaki lab (Natsume et al. 2016). The cells were tested for mycoplasma contamination and mycoplasma contamination was not detected. The HCT116 cells were cultured in McCoy's 5A (modified) medium (Sigma) with 10% fetal bovine serum (Gibco), 2 mM glutamine (Sigma), 1% Pen/Step (Sigma). 4sU (Sigma) was added to the cell culture media 15 h prior to collection at 100 µM. For IR-PAR-CLIP, five 15 cm (diameter) dishes of cells per condition were plated with 3.5 million HCT116 cells per dish so that they reach 60% confluency at the time of collection, resulting in approximately 125 million cells per condition. Cells were put on ice and washed with 10 mL of ice-cold PBS (Sigma). PBS was completely aspirated and 1 mL of PBS was added to prevent cells from drying. Crosslinking was performed with the UV light at 365 nm with 0.15 J/cm^2. Upon crosslinking, cells were collected via scraping, then were pelleted, frozen in liquid nitrogen, and stored at −80°C.

Cell lysis, in-lysate RNase treatment, and immunoprecipitation

Cell pellets from 125 million cells per condition were lysed in 1250 µL of ice-cold lysis buffer (25 mM HEPES pH 7.3, 150 mM NaCl, 0.5% NP-40, 0.5 mM EDTA, 10% glycerol, 0.1% SDS, 0.2% sodium deoxycholate, 1× protease inhibitors cocktail, 0.1 mM DTT), by incubation on ice for 15 min with intermittent vortexing and passing three times through the 27G needle. The lysate was clarified by centrifugation for 20 min at 20,000*g* at +4°C. A total of 1100 µL of the supernatant was taken for the in-lysate RNase digestion on a rotator for 15 min at room temperature. The RNase I (Ambion) was used at 0.1 or 0.05 U/µL and RNase T1 (Thermo Scientific) at 1 or 0.25 U/µL. For IP, 50 µg of Proteintech anti-IGF2BP3 antibody (14642-1-AP, lot 00090203) or Proteintech IgG control (30000-0-AP) was coupled to the 200 µL of protein G Dynabeads (Invitrogen) in 1 mL of lysis buffer for 20 min, rotating at room temperature, washed three times with 1 mL of the lysis buffer, resuspended in the original bead volume (200 µL) and added to 1 mL of the RNase treated lysate. The IP was incubated on a rotator at +4°C for 4 h, washed twice, and resuspended in 1 mL of the lysis buffer. To test the sensitivity of protein-crosslinked-RNA-3′ adapter fragments to RNase, one dish of HCT116 per condition was used as described above and all reaction volumes were scaled down proportionally. MOV10 IP was performed using Proteintech anti-MOV10 antibody (10370-1-AP, lot00001954).

On-beads RNase treatment, dephosphorylation, 3′ adapter ligation, and SDS–PAGE of protein–RNA complexes

For the on-beads, RNase treatment RNase I (Ambion) was added at 0.05 or 0.025 U/µL and RNase T1 (Thermo Scientific) at 1 or 0.25 U/µL. The combinations of in-lysate and on-beads RNase concentrations are indicated in the Results section. For RNase treatment, the samples were incubated on the rotator for 15 min at room temperature and cooled on ice for 5 min. Then the beads were washed three times with 1 mL of ice-cold high salt wash buffer (25 mM HEPES pH 7.3, 400 mM NaCl, 0.5% NP-40, 0.5 mM EDTA, 10% glycerol, 1× protease inhibitors cocktail, 0.1mM DTT), with 3 min incubations on ice after each wash step. For dephosphorylation of the crosslinked RNA fragments, the beads were washed once with 1 mL of PNK wash buffer (20 mM Tris-HCl pH 6.5, 10 mM $MgCl_2$, 0.2% Tween20, 0.1 mM DTT), resuspended in 200 µL of dephosphorylation mix (1× PNK buffer pH 6.5 [70 mM Tris-HCl pH 6.5, 10 mM $MgCl_2$, 1 mM DTT], 100 U T4 polynucleotide kinase [NEB], 20 U SUPERase·In [Invitrogen]) and incubated at 37°C for 30 min with shaking at 1100 rpm. Afterward, the beads were kept on ice and washed once with 1 mL of PNK wash buffer, incubated in 1 mL of high salt wash buffer for 5 min on ice, and washed once more with 1 mL of PNK wash buffer. For 3′ adapter ligation, the beads were resuspended in 200 µL of the ligation reaction mix

(20% PEG8000, 1× T4 RNA ligase reaction buffer [NEB], 1000 U T4 RNA ligase 2 truncated KQ [NEB], 50 pmol 5′ preadenylated IR-dye-conjugated DNA adapter, and 20 U SUPERase·In) and incubated at 25°C for 3 h with shaking at 1100 rpm in the dark. Next, the beads were transferred on ice and washed once with 1 mL of PNK wash buffer, incubated in 1 mL of high salt wash buffer for 5 min on ice, resuspended in 1 mL of PNK wash buffer, and transferred to the new low-bind RNase-free 1.5 mL tube. The PNK wash buffer was removed, and the crosslinked protein–RNA complexes were eluted in 40 µL of 1× SDS sample buffer without DTT at +70°C for 10 min. DTT at 20 mM concentration was added to the collected eluates, and the samples were heated at +70°C for 10 min and stored at −80°C. Next, the crosslinked protein–RNA complexes were resolved on a 10-well 4%–12% NuPAGE Novex Bis-Tris gel (Invitrogen) in 1× MOPS-SDS running buffer (Invitrogen) at 200 V for 65 min. The gel was visualized at 800 nm using LI-COR Odyssey CLx near-infrared imager, and RBP–RNA complexes were size selected using the imager's grid. The bands corresponding to IGF2BP3–RNA complexes were excised from the gel and transferred to a low-bind RNase-free tube.

Proteinase K digestion, 3′ adapter-ligated RNA extraction, and size selection

For the samples with the RNase treatment conditions in-lysate and on-beads: RNase I 0.05 U/µL, RNase T1 1 U/µL proteinase K digestion was performed as described in Acosta-Alvear et al. (2018). The gel piece was transferred to a nuclease-free water pre-equilibrated Pur-A-Lyzer Midi Dialysis Tube (MWCO 3.5 kDa, Sigma), with 400 µL 1× MOPS-SDS running buffer (Invitrogen), and electroelution was performed at 100 V for 2 h. The polarity of the electric current was reversed for 120 sec, the sample was transferred to the new 2 mL low-bind RNase-free tube with an equal volume of 2× Proteinase K buffer (100 mM HEPES pH 7.3, 100 mM NaCl, 20 mM EDTA, 2% SDS) and proteinase K (Invitrogen) at a final concentration of 1.2 mg/mL, and incubated for 30 min at +55°C. For the samples with RNase treatment conditions: RNase I 0.05 U/µL in-lysate and 0.025 U/µL on-beads, RNase I 0.01 U/µL in-lysate and 0.025 U/µL on-beads, and RNase T1 0.25 U/µL in-lysate and on-beads gel extraction and protein digestion were performed as described in Anastasakis et al. (2021). Gel pieces were transferred to a 1.5 mL low-bind RNase-free tube, frozen at −80°C, thawed at +55°C and crashed with a single-use RNase-free pellet pestle. Gel slurry was boiled in 2× proteinase K buffer with 50 mM DTT at +95°C for 2 min and was subsequently incubated three times with fresh addition of proteinase K at 2.4 mg/mL, 1.5 mg/mL, and 2.4 mg/mL in 2× proteinase K buffer at +50°C for 30 min with shaking at 1100 rpm. Extracted 3′ adapter-ligated RNA fragments were separated from the gel by centrifugation at 10,000*g* for 10 min through a Spin-X centrifuge filter (Costar). For all samples, RNA was extracted with 1 mL of acidic phenol–chloroform–isoamyl alcohol (25:24:1, pH 4.0), isopropanol precipitated, resuspended 1× TBE-Urea dye (Invitrogen), denatured by heating at +75°C for 2 min, and resolved on a 10-well 15% TBE-Urea gel (Invitrogen) in 1× TBE running buffer (Invitrogen) at 180 V for 70 min. The gel was visualized at 800 nm using LI-COR Odyssey CLx near-infrared imager and the 3′ adapter-ligated RNA fragments were size selected using the imager's grid.

Reverse transcription, circular ligation, library construction PCR, and sequencing

Gel pieces were transferred to a 1.5 mL low-bind RNase-free tube, frozen at −80°C, thawed at +55°C, and crashed with a single-use RNase-free pellet pestle. 3′ adapter-ligated RNA fragments were extracted from the gel during overnight incubation rotating in 300 µL of RNA elution buffer at +4°C (10 mM Tris-HCl pH 7.0, 0.3 M NaOAc pH 5.5, 2 mM EDTA, 20 U SUPERase·In). Extracted complexes were separated from the gel fragments by centrifugation at 10,000*g* for 10 min through a Spin-X centrifuge filter, ethanol precipitated and resuspended in 11.5 µL of nuclease-free water. For reverse transcription, 1 µL of 1 µM reverse transcription primer (/5Phos/RNAGATCGGAAGAGCGTCGTGTAGGGAAAGAG/iSp18/GTGACTGGAGTTCAGACGTGTGCTC) was added to the sample. The sample was incubated at +70°C for 10 min and transferred on ice. Then the components of the reverse transcription mix were added to the sample making a final volume of 20 µL (1× Superscript IV buffer, dNTPs 0.2 mM each, 5 mM DTT, 10 U SUPERase·In, 200 U Superscript IV [Invitrogen]); the reaction was performed at +55°C for 20 min and inactivated at +80°C for 5 min. A total of 2.2 µL of 1 M NaOH was added, and RNA was hydrolyzed in 30 min incubation at 98°C. The reaction was neutralized by the addition of 2.2 µL of 1 M HCl. The reverse transcription reaction was purified on Oligo Clean & Concentrator columns (Zymo) according to the manufacturer's instructions and eluted in 6 µL of nuclease-free water. cDNA was mixed with 6 µL of 2× TBE-Urea dye, denatured by heating at +75°C for 2 min, and resolved on a 10-well 10% TBE-Urea gel (Invitrogen) in 1× TBE running buffer at 180 V for 70 min. The gel was stained with SYBR Gold (Invitrogen) and visualized, and the reverse transcription product was separated from the unreacted primer and no-insert products. Gel extraction was performed similarly to the 3′ adapter-ligated RNA fragments using DNA elution buffer (10 mM Tris-HCl pH 8.0, 0.3 M NaOAc pH 5.5). After ethanol precipitation, the pellet was resuspended in 10 µL of circular ligation reaction mix (1× CircLigase II buffer, 2.5 mM $MnCl_2$, 50 U CircLigase II [Lucigen]). Circular ligation was performed at +60°C for 2 h, and the enzyme was inactivated through heating at +80°C for 10 min. To determine the number of cycles required for the PCR amplification for the library construction, a series of small-scale PCR reactions was performed with NEB Phusion polymerase and index primers (NEB, E6609S). The reaction mix of 65 µL (1× High Fidelity buffer, dNTPs 0.2 mM each, 500 nM NEB Universal primer, 500 nM NEB Index primer, 2.8 µL circularization reaction, 1.3 U Phusion polymerase) was aliquoted to six PCR tubes (10 µL) and run according to the following program: 98°C, 30 sec; 20 cycles of 98°C, 10 sec; 65°C, 10 sec; 72°C, 10 sec. The tubes were removed at the end of extension at cycles 10, 12, 14, 16, 18, and 20 and the products were resolved on 10-well 6% TBE gel (Invitrogen) in 1× TBE running buffer at 180 V for 40 min and stained with SYBR Gold. For the library construction PCR, the cycle number was selected where the bright product band appeared. Typically, the number of cycles was 16–18 for IGF2BP3 IP and 22–23 for IgG control. The reaction composition and conditions were the same as for the PCR designed to determine the cycles; additionally, the final extension was performed for 5 min at 72°C. Libraries were ethanol precipitated, resolved on a 10-well 6% TBE gel similarly to the cycle selection PCR, and separated from the no-insert library and unreacted primers.

Gel extraction was performed similarly to the extraction after the reverse transcription reaction, but the gel pieces were not heated higher than +30°C. After ethanol precipitation, pellets were resuspended in 10 µL of nuclease-free water. Library size distribution and quantity were determined using the Agilent Bioanalyzer 2100 with the High Sensitivity DNA Kit (Agilent) and via qPCR with the NEBNext Library Quant Kit for Illumina (NEB). Libraries were sequenced on a NovaSeq 6000 S1 at SR100 mode (Illumina) at the Vienna BioCenter NGS facility producing 55 million reads per sample on average.

Computational analysis

For the demultiplexed data sets, UMIs were extracted and adapter sequences were trimmed using UMI-tools v1.1.1 (Smith et al. 2017). The reads were size and quality trimmed using Trimmomatic v0.30 (Bolger et al. 2014) to have a length between 18 and 45 nt. The reads then were mapped to the GENCODE human genome assembly GRCh38.p13 with bowtie v0.12.7 (Langmead et al. 2009), allowing up to three mismatches and deduplicated using UMI-tools v1.1.1. IGF2BP3-binding clusters were called with PARalyzer v1.5 (Corcoran et al. 2011) (ini file is available in Supplemental Material). Genes that have at least one cluster containing more than 10 CPM and more than 50% of T to C conversions per read were selected as IGF2BP3 targets. The enrichment of 4-nt motifs in IGF2BP3-binding clusters was analyzed with HOMER v4.11 (Heinz et al. 2010), findMotifsGenome.pl command using exome as a background. The Pearson correlation between the IGF2BP3 IR-PAR-CLIP conditions was calculated for the 50-nt coverage windows using the multiBamSummary and plotCorrelation tools from deepTools (Ramírez et al. 2016). Sequencing data processing was conducted using the HPC of the Center for Integrative Bioinformatics Vienna (CIBIV), Austria. The published lists of IGF2BP3 targets were obtained from Conway et al. (2016), Palanichamy et al. (2016), and Ennajdaoui et al. (2016). The ENCODE eCLIP IGF2BP3 target list was downloaded from the POSTAR3 (Zhao et al. 2022) (source data: ENCODE project [ENCSR993OLA], Dunham et al. 2012). For data from Conway et al. (2016), the gene was selected as IGF2BP3 target if CDS or 3′UTR peak coverage was four times higher than in SMIinput in IGF2BP3 eCLIP, and not more than two times higher in the IgG control. The IGF2BP3 PAR-CLIP data (GSM545209, SRR048962) (Hafner et al. 2010) were analyzed in parallel with the data from the current study with the same parameters used for bowtie alignments, peak calling, and target identification. GO term analysis was performed with clusterProfiler v3.18.1 (Yu et al. 2012).

Optimization of IGF2BP3 immunoprecipitation

To test the IGF2BP3 immunoprecipitation conditions, one 15 cm (diameter) dish of 60% confluent HCT116 (~25 million cells) per condition was washed in ice-cold PBS, scraped, pelleted, and resuspended in 250 µL of ice-cold lysis buffer. Cells were lysed by incubation with the lysis buffer on ice for 15 min with intermittent vortexing and passing the cell suspension three times through the 27G needle. The lysate was clarified by centrifugation for 20 min at 20,000 and treated with 0.2 U/µL RNase I (Ambion) rotating at room temperature for 15 min. For IP, from one 15 cm (diameter) dish 5 µg of Proteintech (14642-1-AP, lot 00090203) antibody was coupled to Dynabeads, as described before in 1 µg:4 µL antibody:beads ratio. The lysates were rotated at +4°C for 4 h for the IP. The flowthrough was removed using a magnetic rack, and the IP-ed complexes were washed five times in one volume (250 µL) of ice-cold high salt wash buffer with 3-min incubations on ice. For the urea wash, urea was added to the buffer during the first wash to a final concentration of 1 M. Protein was eluted in 25 µL of sample buffer as described in the section "On-beads RNase treatment, dephosphorylation, 3′ adapter ligation, and SDS–PAGE of protein–RNA complexes" above. The eluate was resolved on SDS–PAGE in tris-glycine SDS buffer and analyzed with colloidal Coomassie staining (Dyballa and Metzger 2009) or western blotting with anti-IGF2BP3 (Proteintech, 14642-1-AP) and anti-GAPDH (Proteintech, 10494-1-AP) antibodies.

Establishment of IGF2BP2 and IGF2BP3 knockout cell lines and siRNA depletion

For knockout cell line generation, gRNA sequences (IGF2BP2: 5′GAGCTGCCGGAGGTCGTCGG 3′; IGF2BP3: 5′ACGCGTAGC CAGTCTTCACC 3′) were cloned into the pSpCas9 (BB)-2A-GFP (PX458) (plasmid #48138; Addgene) (Ran et al. 2013). Cells were transiently transfected using jetOPTIMUS reagent (Tamar, 101000051), and GFP-positive single-cell clones were FACS sorted at BD FACSAria IIIu at Max Perutz Labs BioOptics FACS Facility. For siRNA knockdown, cells were transfected with ON-TARGETplus Human IGF2BP2 (Dharmacon, L-017705-00-0005) or IGF2BP3 (Dharmacon, L-003976-00-0005) SMARTpool siRNAs using DharmaFECT 2 (Dharmacon, T-2002-01). ON-TARGETplus nontargeting siRNA #1 (Dharmacon, D-001810-01-05) was used as a control.

Mass spectrometry of IGF2BP3 immunoprecipitation

For mass spectrometry of IGF2BP3 immunoprecipitation, three 15 cm (diameter) dishes of 60% confluent HCT116 per condition were washed in ice-cold PBS, scraped, pelleted, and resuspended in 750 µL of ice-cold lysis buffer. The IP was performed as described in the section "Optimization of IGF2BP3 immunoprecipitation" above using 30 µg of Proteintech anti-IGF2BP3 antibody (14642-1-AP, lot 00090203) per sample. RNA was digested using 1 U/µL RNase T1 (Thermo Scientific). Protein was eluted in 50 µL of sample buffer, resolved on a 10-well 4%–12% NuPAGE Novex Bis-Tris gel (Invitrogen) in 1× MOPS-SDS running buffer (Invitrogen), and stained with colloidal Coomassie (Dyballa and Metzger 2009). The band corresponding to IGF2BP3 was cut from the gel, submitted for tandem mass spectrometry, and analyzed with MaxQuant 1.6.17.0 at the Max Perutz Labs Mass Spectrometry Facility.

DATA DEPOSITION

All raw and processed sequencing data generated in this study have been deposited in the Gene Expression Omnibus database, https://www.ncbi.nlm.nih.gov/geo/ (accession no. GSE229653).

SUPPLEMENTAL MATERIAL

Supplemental material is available for this article.

ACKNOWLEDGMENTS

We are grateful to the Vienna BioCenter Next-Generation Sequencing Facility for deep sequencing services, and to Markus Hartl and the Max Perutz Labs Mass Spectrometry Facility for performing mass spectrometry. We thank Robert Happel, Arndt von Haeseler, and the Center for Integrative Bioinformatics Vienna (CIBIV) for support with sequencing data analysis. We are grateful to Thomas Kapral and Bojan Zagrovic for their help with the analyses of the published IGF2BP3 data. We thank Roland Foisner and Nana Naetar-Kerenyi for their input on CRISPR–Cas9 editing, and Diego Acosta-Alvear for great suggestions and invaluable input. G.E.K. acknowledges funding from the Austrian Science Fund (FWF-SFB F79). A.A. is supported by the DOC Fellowship Programme of the Austrian Academy of Sciences.

Received May 11, 2023; accepted July 26, 2023.

REFERENCES

Acosta-Alvear D, Elif Karagöz G, Fröhlich F, Li H, Walther TC, Walter P. 2018. The unfolded protein response and endoplasmic reticulum protein targeting machineries converge on the stress sensor IRE1. *Elife* **7:** e43036. doi:10.7554/eLife.43036

Anastasakis DG, Jacob A, Konstantinidou P, Meguro K, Claypool D, Cekan P, Haase AD, Hafner M. 2021. A non-radioactive, improved PAR-CLIP and small RNA CDNA library preparation protocol. *Nucleic Acids Res* **49:** e45. doi:10.1093/nar/gkab011

Ascano M Jr, Mukherjee N, Bandaru P, Miller JB, Nusbaum JD, Corcoran DL, Langlois C, Munschauer M, Dewell S, Hafner M, et al. 2012. FMRP targets distinct mRNA sequence elements to regulate protein expression. *Nature* **492:** 382–386. doi:10.1038/nature11737

Barberán-Soler S, Vo JM, Hogans RE, Dallas A, Johnston BH, Kazakov SA. 2018. Decreasing miRNA sequencing bias using a single adapter and circularization approach. *Genome Biol* **19:** 105. doi:10.1186/s13059-018-1488-z

Becker K, Bluhm A, Casas-Vila N, Dinges N, Dejung M, Sayols S, Kreutz C, Roignant JY, Butter F, Legewie S. 2018. Quantifying post-transcriptional regulation in the development of *Drosophila melanogaster*. *Nat Commun* **9:** 4970. doi:10.1038/s41467-018-07455-9

Bell JL, Wächter K, Mühleck B, Pazaitis N, Köhn M, Lederer M, Hüttelmaier S. 2013. Insulin-like growth factor 2 mRNA-binding proteins (IGF2BPs): post-transcriptional drivers of cancer progression? *Cell Mol Life Sci* **70:** 2657–2675. doi:10.1007/s00018-012-1186-z

Bolger AM, Lohse M, Usadel B. 2014. Trimmomatic: a flexible trimmer for Illumina sequence data. *Bioinformatics* **30:** 2114–2120. doi:10.1093/bioinformatics/btu170

Buchbender A, Mutter H, Reymond Sutandy FX, Körtel N, Hänel H, Busch A, Ebersberger S, König J. 2020. Improved library preparation with the new ICLIP2 protocol. *Methods* **178:** 33–48. doi:10.1016/J.YMETH.2019.10.003

Conway AE, Van Nostrand EL, Pratt GA, Aigner S, Wilbert ML, Sundararaman B, Freese P, Lambert NJ, Sathe S, Liang TY, et al. 2016. Enhanced CLIP uncovers IMP protein-RNA targets in human pluripotent stem cells important for cell adhesion and survival. *Cell Rep* **15:** 666–679. doi:10.1016/j.celrep.2016.03.052

Corcoran DL, Georgiev S, Mukherjee N, Gottwein E, Skalsky RL, Keene JD, Ohler U. 2011. PARalyzer: definition of RNA binding sites from PAR-CLIP short-read sequence data. *Genome Biol* **12:** R79. doi:10.1186/gb-2011-12-8-r79

Dai N, Zhao L, Wrighting D, Krämer D, Majithia A, Wang Y, Cracan V, Borges-Rivera D, Mootha VK, Nahrendorf M, et al. 2015. IGF2BP2/IMP2-deficient mice resist obesity through enhanced translation of *Ucp1* mRNA and other mRNAs encoding mitochondrial proteins. *Cell Metab* **21:** 609–621. doi:10.1016/j.cmet.2015.03.006

Danan C, Manickavel S, Hafner M. 2016. PAR-CLIP: a method for transcriptome-wide identification of RNA binding protein interaction sites. *Methods Mol Biol (Clifton, N.J.)* **1358:** 153–173. doi:10.1007/978-1-4939-3067-8_10

Deforzh E, Vargas TR, Kropp J, Vandamme M, Pinna G, Polesskaya A. 2016. IMP-3 protects the mRNAs of cyclins D1 and D3 from GW182/AGO2-dependent translational repression. *Int J Oncol* **49:** 2578–2588. doi:10.3892/ijo.2016.3750

Dimitriadis E, Trangas T, Milatos S, Foukas PG, Gioulbasanis I, Courtis N, Nielsen FC, Pandis N, Dafni U, Bardi G, et al. 2007. Expression of oncofetal RNA-binding protein CRD-BP/IMP1 predicts clinical outcome in colon cancer. *Int J Cancer* **121:** 486–494. doi:10.1002/ijc.22716

Dunham I, Kundaje A, Aldred SF, Collins PJ, Davis CA, Doyle F, Epstein CB, Frietze S, Harrow J, Kaul R, et al. 2012. An integrated encyclopedia of DNA elements in the human genome. *Nature* **489:** 57–74. doi:10.1038/nature11247

Dyballa N, Metzger S. 2009. Fast and sensitive colloidal Coomassie G-250 staining for proteins in polyacrylamide gels. *J Vis Exp* doi:10.3791/1431

Ennajdaoui H, Howard JM, Sterne-Weiler T, Jahanbani F, Coyne DJ, Uren PJ, Dargyte M, Katzman S, Draper JM, Wallace A, et al. 2016. IGF2BP3 modulates the interaction of invasion-associated transcripts with RISC. *Cell Rep* **15:** 1876–1883. doi:10.1016/j.celrep.2016.04.083

Fallini C, Zhang H, Su Y, Silani V, Singer RH, Rossoll W, Bassell GJ. 2011. The survival of motor neuron (SMN) protein interacts with the mRNA-binding protein HuD and regulates localization of poly(A) mRNA in primary motor neuron axons. *J Neurosci* **31:** 3914–3925. doi:10.1523/JNEUROSCI.3631-10.2011

Friedersdorf MB, Keene JD. 2014. Advancing the functional utility of PAR-CLIP by quantifying background binding to mRNAs and lncRNAs. *Genome Biol* **15:** R2. doi:10.1186/gb-2014-15-1-r2

Garzia A, Meyer C, Morozov P, Sajek M, Tuschl T. 2017. Optimization of PAR-CLIP for transcriptome-wide identification of binding sites of RNA-binding proteins. *Methods* **118–119:** 24–40. doi:10.1016/j.ymeth.2016.10.007

Gerashchenko MV, Gladyshev VN. 2017. Ribonuclease selection for ribosome profiling. *Nucleic Acids Res* **45:** e6. doi:10.1093/nar/gkw822

Gregersen LH, Schueler M, Munschauer M, Mastrobuoni G, Chen W, Kempa S, Dieterich C, Landthaler M. 2014. MOV10 is a 5′ to 3′ RNA helicase contributing to UPF1 mRNA target degradation by translocation along 3′ UTRs. *Mol Cell* **54:** 573–585. doi:10.1016/j.molcel.2014.03.017

Haberman N, Huppertz I, Attig J, König J, Wang Z, Hauer C, Hentze MW, Kulozik AE, Le Hir H, Curk T, et al. 2017. Insights into the design and interpretation of ICLIP experiments. *Genome Biol* **18:** 7. doi:10.1186/s13059-016-1130-x

Hafner M, Landthaler M, Burger L, Khorshid M, Hausser J, Berninger P, Rothballer A, Ascano M Jr, Jungkamp AC, Munschauer M, et al. 2010. Transcriptome-wide identification of RNA-binding protein and microRNA target sites by PAR-CLIP. *Cell* **141:** 129–141. doi:10.1016/j.cell.2010.03.009

Hafner M, Renwick N, Brown M, Mihailović A, Holoch D, Lin C, Pena JTG, Nusbaum JD, Morozov P, Ludwig J, et al. 2011. RNA-ligase-dependent biases in miRNA representation in deep-sequenced small RNA CDNA libraries. *RNA* **17:** 1697–1712. doi:10.1261/rna.2799511

Hafner M, Max KEA, Bandaru P, Morozov P, Gerstberger S, Brown M, Molina H, Tuschl T. 2013. Identification of mRNAs bound and regulated by human LIN28 proteins and molecular requirements for RNA recognition. *RNA* **19:** 613–626. doi:10.1261/rna.036491.112

Hafner M, Katsantoni M, Köster T, Marks J, Mukherjee J, Staiger D, Ule J, Zavolan M. 2021. CLIP and complementary methods. *Nat Rev Methods Primers* **1:** 20. doi:10.1038/s43586-021-00018-1

Hammer NA, Hansen TVO, Byskov AG, Meyts ER-D, Grøndahl ML, Bredkjær HE, Wewer UM, Christiansen J, Nielsen FC. 2005. Expression of IGF-II mRNA-binding proteins (IMPs) in gonads and testicular cancer. *Reproduction* **130:** 203–212. doi:10.1530/rep.1.00664

Hanniford D, Ulloa-Morales A, Karz A, Berzoti-Coelho MG, Moubarak RS, Sánchez-Sendra B, Kloetgen A, Davalos V, Imig J, Wu P, et al. 2020. Epigenetic silencing of *CDR1as* drives IGF2BP3-mediated melanoma invasion and metastasis. *Cancer Cell* **37:** 55–70.e15. doi:10.1016/j.ccell.2019.12.007

Hansen TVO, Hammer NA, Nielsen J, Madsen M, Dalbaeck C, Wewer UM, Christiansen J, Nielsen FC. 2004. Dwarfism and impaired gut development in insulin-like growth factor II mRNA-binding protein 1-deficient mice. *Mol Cell Biol* **24:** 4448–4464. doi:10.1128/mcb.24.10.4448-4464.2004

Heinz S, Benner C, Spann N, Bertolino E, Lin YC, Laslo P, Cheng JX, Murre C, Singh H, Glass CK. 2010. Simple combinations of lineage-determining transcription factors prime *cis*-regulatory elements required for macrophage and B cell identities. *Mol Cell* **38:** 576–589. doi:10.1016/j.molcel.2010.05.004

Huang H, Weng H, Sun W, Qin X, Shi H, Wu H, Zhao BS, Mesquita A, Liu C, Yuan CL, et al. 2018. Recognition of RNA N^6-methyladenosine by IGF2BP proteins enhances mRNA stability and translation. *Nat Cell Biol* **20:** 285–295. doi:10.1038/s41556-018-0045-z

Huang W, Li Y, Zhang C, Zha H, Zhou X, Fu B, Guo J, Wang G. 2020. IGF2BP3 facilitates cell proliferation and tumorigenesis via modulation of JAK/STAT signalling pathway in human bladder cancer. *J Cell Mol Med* **24:** 13949–13960. doi:10.1111/jcmm.16003

Hüttelmaier S, Zenklusen D, Lederer M, Dictenberg J, Lorenz M, Meng XH, Bassell GJ, Condeelis J, Singer RH. 2005. Spatial regulation of β-actin translation by Src-dependent phosphorylation of ZBP1. *Nature* **438:** 512–515. doi:10.1038/nature04115

Ingolia NT. 2010. Genome-wide translational profiling by ribosome footprinting. *Methods Enzymol* **470:** 119–142. doi:10.1016/S0076-6879(10)70006-9

Ingolia NT, Ghaemmaghami S, Newman JRS, Weissman JS. 2009. Genome-wide analysis *in vivo* of translation with nucleotide resolution using ribosome profiling. *Science* **324:** 218–223. doi:10.1126/science.1168978

Jønson L, Christiansen J, Hansen TVO, Vikeså J, Yamamoto Y, Nielsen FC. 2014. IMP3 RNP safe houses prevent miRNA-directed *HMGA2* mRNA decay in cancer and development. *Cell Rep* **7:** 539–551. doi:10.1016/j.celrep.2014.03.015

Kaczynski T, Hussain A, Farkas M. 2019. Quick-irCLIP: interrogating protein-RNA interactions using a rapid and simple cross-linking and immunoprecipitation technique. *MethodsX* **6:** 1292–1304. doi:10.1016/j.mex.2019.05.014

Kishore S, Jaskiewicz L, Burger L, Hausser J, Khorshid M, Zavolan M. 2011. A quantitative analysis of CLIP methods for identifying binding sites of RNA-binding proteins. *Nat Methods* **8:** 559–567. doi:10.1038/nmeth.1608

Kishore S, Gruber AR, Jedlinski DJ, Syed AP, Jorjani H, Zavolan M. 2013. Insights into SnoRNA biogenesis and processing from PAR-CLIP of SnoRNA core proteins and small RNA sequencing. *Genome Biol* **14:** R45. doi:10.1186/gb-2013-14-5-r45

König J, Zarnack K, Rot G, Curk T, Kayikci M, Zupan B, Turner DJ, Luscombe NM, Ule J. 2010. iCLIP reveals the function of HnRNP particles in splicing at individual nucleotide resolution. *Nat Struct Mol Biol* **17:** 909–915. doi:10.1038/nsmb.1838

Ladd AN, Charlet-B N, Cooper TA. 2001. The CELF family of RNA binding proteins is implicated in cell-specific and developmentally regulated alternative splicing. *Mol Cell Biol* **21:** 1285–1296. doi:10.1128/mcb.21.4.1285-1296.2001

Laggai S, Kessler SM, Boettcher S, Lebrun V, Gemperlein K, Lederer E, Leclercq IA, Mueller R, Hartmann RW, Haybaeck J, et al. 2014. The *IGF2* mRNA binding protein p62/IGF2BP2-2 induces fatty acid elongation as a critical feature of steatosis. *J Lipid Res* **55:** 1087–1097. doi:10.1194/jlr.M045500

Langmead B, Trapnell C, Pop M, Salzberg SL. 2009. Ultrafast and memory-efficient alignment of short DNA sequences to the human genome. *Genome Biol* **10:** R25. doi:10.1186/gb-2009-10-3-r25

Lecanda A, Nilges BS, Sharma P, Nedialkova DD, Schwarz J, Vaquerizas JM, Leidel SA. 2016. Dual randomization of oligonucleotides to reduce the bias in ribosome-profiling libraries. *Methods* **107:** 89–97. doi:10.1016/j.ymeth.2016.07.011

Lee FCY, Ule J. 2018. Advances in CLIP technologies for studies of protein-RNA interactions. *Mol Cell* **69:** 354–369. doi:10.1016/j.molcel.2018.01.005

Li K, Huang F, Li Y, Li D, Lin H, Ni R, Zhang Q, Zhao M, Huang S, Zou L, et al. 2020. Stabilization of oncogenic transcripts by the IGF2BP3/ELAVL1 complex promotes tumorigenicity in colorectal cancer. *Am J Cancer Res* **10:** 2480–2494.

Licatalosi DD, Mele A, Fak JJ, Ule J, Kayikci M, Chi SW, Clark TA, Schweitzer AC, Blume JE, Wang X, et al. 2008. HITS-CLIP yields genome-wide insights into brain alternative RNA processing. *Nature* **456:** 464–469. doi:10.1038/NATURE07488

Lochhead P, Imamura Y, Morikawa T, Kuchiba A, Yamauchi M, Liao X, Qian ZR, Nishihara R, Wu K, Meyerhardt JA, et al. 2012. Insulin-like growth factor 2 messenger RNA binding protein 3 (IGF2BP3) is a marker of unfavourable prognosis in colorectal cancer. *Eur J Cancer* **48:** 3405–3413. doi:10.1016/j.ejca.2012.06.021

Lu S, Han L, Hu X, Sun T, Xu D, Li Y, Chen Q, Yao W, He M, Wang Z, et al. 2021. N^6-methyladenosine reader IMP2 stabilizes the ZFAS1/OLA1 axis and activates the Warburg effect: implication in colorectal cancer. *J Hematol Oncol* **14:** 188. doi:10.1186/s13045-021-01204-0

McGlincy NJ, Ingolia NT. 2017. Transcriptome-wide measurement of translation by ribosome profiling. *Methods* **126:** 112–129. doi:10.1016/j.ymeth.2017.05.028

Mizutani R, Imamachi N, Suzuki Y, Yoshida H, Tochigi N, Oonishi T, Suzuki Y, Akimitsu N. 2016. Oncofetal protein IGF2BP3 facilitates the activity of proto-oncogene protein EIF4E through the destabilization of EIF4E-BP2 mRNA. *Oncogene* **35:** 3495–3502. doi:10.1038/onc.2015.410

Mongroo PS, Noubissi FK, Cuatrecasas M, Kalabis J, King CE, Johnstone CN, Bowser MJ, Castells A, Spiegelman VS, Rustgi AK. 2011. IMP-1 displays cross-talk with K-Ras and modulates colon cancer cell survival through the novel proapoptotic protein CYFIP2. *Cancer Res* **71:** 2172–2182. doi:10.1158/0008-5472.CAN-10-3295

Müeller-Pillasch F, Lacher U, Wallrapp C, Micha A, Zimmerhackl F, Hameister H, Varga G, Friess H, Büchler M, Beger HG, et al. 1997. Cloning of a gene highly overexpressed in cancer coding for a novel KH-domain containing protein. *Oncogene* **14:** 2729–2733. doi:10.1038/sj.onc.1201110

Natsume T, Kiyomitsu T, Saga Y, Kanemaki MT. 2016. Rapid protein depletion in human cells by auxin-inducible degron tagging with short homology donors. *Cell Rep* **15:** 210–218. doi:10.1016/J.CELREP.2016.03.001

Nielsen J, Christiansen J, Lykke-Andersen J, Johnsen AH, Wewer UM, Nielsen FC. 1999. A family of insulin-like growth factor II mRNA-

binding proteins represses translation in late development. *Mol Cell Biol* **19:** 1262–1270. doi:10.1128/mcb.19.2.1262

Nusinow DP, Szpyt J, Ghandi M, Rose CM, Robert McDonald E III, Kalocsay M, Jané-Valbuena J, Gelfand E, Schweppe DK, Jedrychowski M, et al. 2020. Quantitative proteomics of the cancer cell line encyclopedia. *Cell* **180:** 387–402.e16. doi:10.1016/j.cell.2019.12.023

Palanichamy JK, Tran TM, Howard JM, Contreras JR, Fernando TR, Sterne-Weiler T, Katzman S, Toloue M, Yan W, Basso G, et al. 2016. RNA-binding protein IGF2BP3 targeting of oncogenic transcripts promotes hematopoietic progenitor proliferation. *J Clin Invest* **126:** 1495–1511. doi:10.1172/JCI80046

Ramírez F, Ryan DP, Grüning B, Bhardwaj V, Kilpert F, Richter AS, Heyne S, Dündar F, Manke T. 2016. DeepTools2: a next generation web server for deep-sequencing data analysis. *Nucleic Acids Res* **44:** W160–W165. doi:10.1093/NAR/GKW257

Ran FA, Hsu PD, Wright J, Agarwala V, Scott DA, Zhang F. 2013. Genome engineering using the CRISPR-Cas9 system. *Nat Protoc* **8:** 2281–2308. doi:10.1038/nprot.2013.143

Regué L, Minichiello L, Avruch J, Dai N. 2019. Liver-specific deletion of IGF2 mRNA binding protein-2/IMP2 reduces hepatic fatty acid oxidation and increases hepatic triglyceride accumulation. *J Biol Chem* **294:** 11944–11951. doi:10.1074/jbc.RA119.008778

Ren F, Lin Q, Gong G, Du X, Dan H, Qin W, Miao R, Xiong Y, Xiao R, Li X, et al. 2020. Igf2bp3 maintains maternal RNA stability and ensures early embryo development in zebrafish. *Commun Biol* **3:** 94. doi:10.1038/s42003-020-0827-2

Rendleman J, Cheng Z, Maity S, Kastelic N, Munschauer M, Allgoewer K, Teo G, Zhang YBM, Lei A, Parker B, et al. 2018. New insights into the cellular temporal response to proteostatic stress. *Elife* **7:** e39054. doi:10.7554/eLife.39054

Riley KJ, Steitz JA. 2013. The 'observer effect' in genome-wide surveys of protein-RNA interactions. *Mol Cell* **49:** 601–604. doi:10.1016/j.molcel.2013.01.030

Rivera Vargas T, Boudoukha S, Simon A, Souidi M, Cuvellier S, Pinna G, Polesskaya A. 2014. Post-transcriptional regulation of cyclins D1, D3 and G1 and proliferation of human cancer cells depend on IMP-3 nuclear localization. *Oncogene* **33:** 2866–2875. doi:10.1038/onc.2013.252

Ross J, Lemm I, Berberet B. 2001. Overexpression of an mRNA-binding protein in human colorectal cancer. *Oncogene* **20:** 6544–6550. doi:10.1038/sj.onc.1204838

Samanta S, Pursell B, Mercurio AM. 2013. IMP3 protein promotes chemoresistance in breast cancer cells by regulating breast cancer resistance protein (ABCG2) expression. *J Biol Chem* **288:** 12569–12573. doi:10.1074/jbc.C112.442319

Shantha Kumara HMC, Kirchoff D, Caballero OL, Su T, Ahmed A, Herath SAC, Njoh L, Cekic V, Simpson AJ, Cordon-Cardo C, et al. 2015. Expression of the cancer testis antigen IGF2BP3 in colorectal cancers; IGF2BP3 holds promise as a specific immunotherapy target. *Oncoscience* **2:** 607–614. doi:10.18632/oncoscience.174

Smith T, Heger A, Sudbery I. 2017. UMI-tools: modeling sequencing errors in unique molecular identifiers to improve quantification accuracy. *Genome Res* **27:** 491–499. doi:10.1101/gr.209601.116

Van Nostrand EL, Pratt GA, Shishkin AA, Gelboin-Burkhart C, Fang MY, Sundararaman B, Blue SM, Nguyen TB, Surka C, Elkins K, et al. 2016. Robust transcriptome-wide discovery of RNA-binding protein binding sites with enhanced CLIP (ECLIP). *Nat Methods* **13:** 508–514. doi:10.1038/nmeth.3810

Van Nostrand EL, Shishkin AA, Pratt GA, Nguyen TB, Yeo GW. 2017. Variation in single-nucleotide sensitivity of ECLIP derived from reverse transcription conditions. *Methods* **126:** 29–37. doi:10.1016/J.YMETH.2017.08.002

Van Nostrand EL, Freese P, Pratt GA, Wang X, Wei X, Xiao R, Blue SM, Chen JY, Cody NAL, Dominguez D, et al. 2020. A large-scale binding and functional map of human RNA-binding proteins. *Nature* **583:** 711–719. doi:10.1038/s41586-020-2077-3

Vong YH, Sivashanmugam L, Leech R, Zaucker A, Jones A, Sampath K. 2021. The RNA-binding protein Igf2bp3 is critical for embryonic and germline development in zebrafish. *PLoS Genet* **17:** e1009667. doi:10.1371/journal.pgen.1009667

Xu W, Sheng Y, Guo Y, Huang Z, Huang Y, Wen D, Liu C, Cui L, Yang Y, Du P. 2019. Increased IGF2BP3 expression promotes the aggressive phenotypes of colorectal cancer cells *in vitro* and *vivo*. *J Cell Physiol* **234:** 18466–18479. doi:10.1002/jcp.28483

Yang Z, Wang T, Wu D, Min Z, Tan J, Yu B. 2020. RNA N^6-methyladenosine reader IGF2BP3 regulates cell cycle and angiogenesis in colon cancer. *J Exp Clin Cancer Res* **39:** 203. doi:10.1186/s13046-020-01714-8

Yaniv K, Fainsod A, Kalcheim C, Yisraeli JK. 2003. The RNA-binding protein Vg1 RBP is required for cell migration during early neural development. *Development* **130:** 5649–5661. doi:10.1242/dev.00810

Yu G, Wang L-G, Han Y, He Q-Y. 2012. ClusterProfiler: an R package for comparing biological themes among gene clusters. *OMICS* **16:** 284–287. doi:10.1089/omi.2011.0118

Zarnegar BJ, Flynn RA, Shen Y, Do BT, Chang HY, Khavari PA. 2016. irCLIP platform for efficient characterization of protein-RNA interactions. *Nat Methods* **13:** 489–492. doi:10.1038/nmeth.3840

Zhang Q, Yaniv K, Oberman F, Wolke U, Git A, Fromer M, Taylor WL, Meyer D, Standart N, Raz E, et al. 1999. Vg1 RBP intracellular distribution and evolutionarily conserved expression at multiple stages during development. *Mech Dev* **88:** 101–106. doi:10.1016/S0925-4773(99)00162-8

Zhao W, Lu D, Liu L, Cai J, Zhou Y, Yang Y, Zhang Y, Zhang J. 2017. Insulin-like growth factor 2 mRNA binding protein 3 (IGF2BP3) promotes lung tumorigenesis via attenuating P53 stability. *Oncotarget* **8:** 93672–93687. doi:10.18632/oncotarget.21280

Zhao W, Zhang S, Zhu Y, Xi X, Bao P, Ma Z, Kapral TH, Chen S, Zagrovic B, Yang YT, et al. 2022. POSTAR3: an updated platform for exploring post-transcriptional regulation coordinated by RNA-binding proteins. *Nucleic Acids Res* **50:** D287–D294. doi:10.1093/nar/gkab702

See the following page for ***Meet the First Author***

Optimized infrared photoactivatable ribonucleoside-enhanced crosslinking and immunoprecipitation (IR-PAR-CLIP) protocol identifies novel IGF2BP3-interacting RNAs in colon cancer cells

Aleksandra S. Anisimova and G. Elif Karagöz

RNA 2023 29: 1818-1836 originally published online August 15, 2023
Access the most recent version at doi:10.1261/rna.079714.123

Figure S1

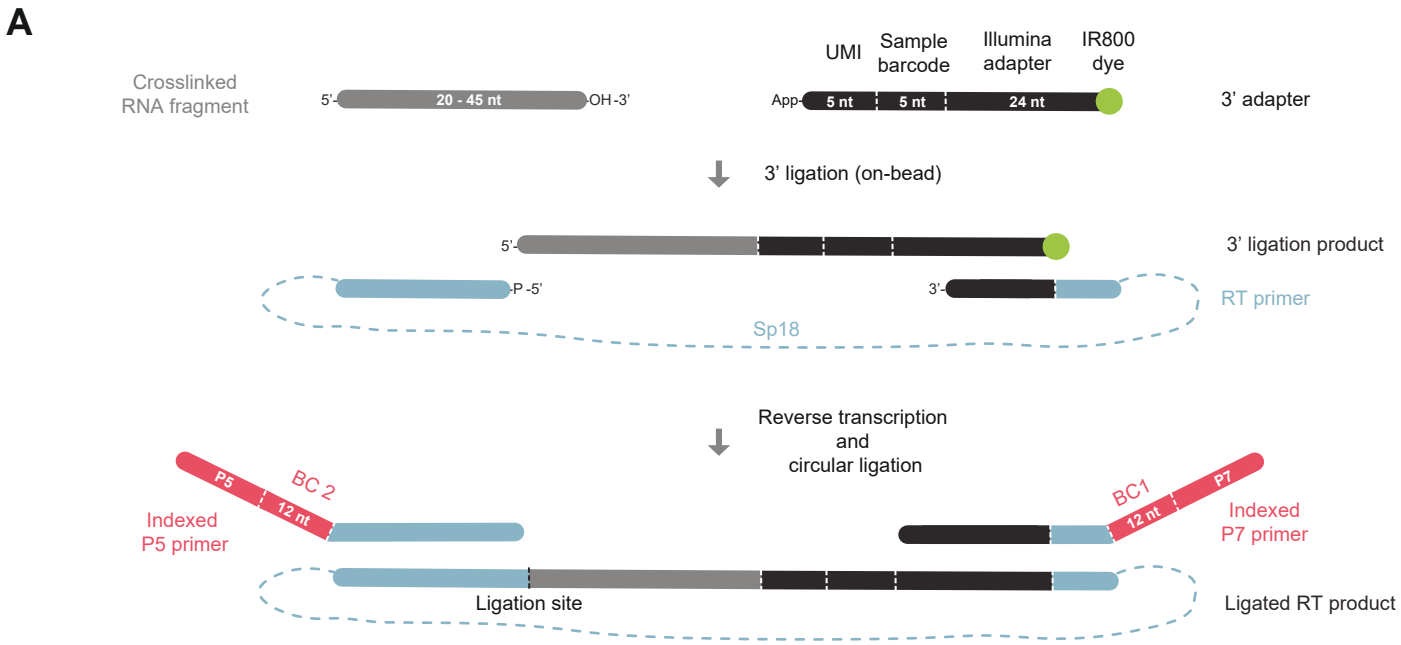
A
Crosslinked RNA fragment
5'-
20 - 45 nt
-OH-3'
UMI
Sample barcode
Illumina adapter
IR800 dye
App-
5 nt
5 nt
24 nt
3' adapter
3' ligation (on-bead)
5'-
3' ligation product
-P-5'
3'-
RT primer
Sp18
Reverse transcription and circular ligation
P5
BC 2
12 nt
Indexed P5 primer
BC1
12 nt
P7
Indexed P7 primer
Ligation site
Ligated RT product

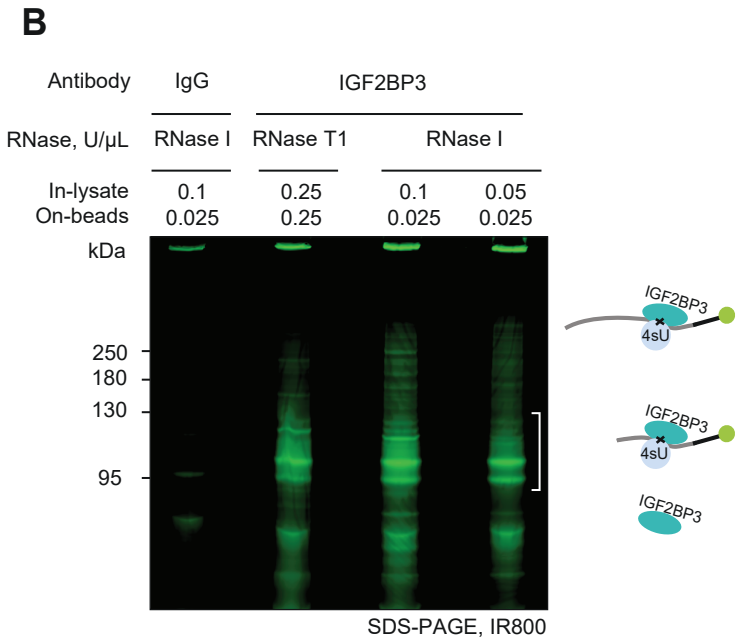
B
Antibody
IgG
IGF2BP3
RNase, U/µL
RNase I
RNase T1
RNase I
In-lysate
On-beads
0.1
0.025
0.25
0.25
0.1
0.025
0.05
0.025
kDa
250
180
130
95
IGF2BP3
4sU
SDS-PAGE, IR800

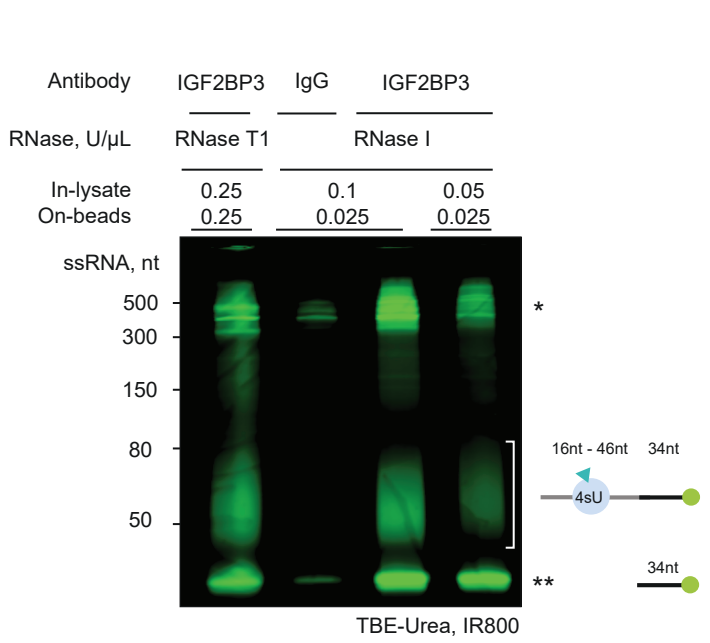
C
Antibody
IGF2BP3
IgG
IGF2BP3
RNase, U/µL
RNase T1
RNase I
In-lysate
On-beads
0.25
0.25
0.1
0.025
0.05
0.025
ssRNA, nt
500
300
150
80
50
*
**
16nt - 46nt
34nt
4sU
34nt
TBE-Urea, IR800

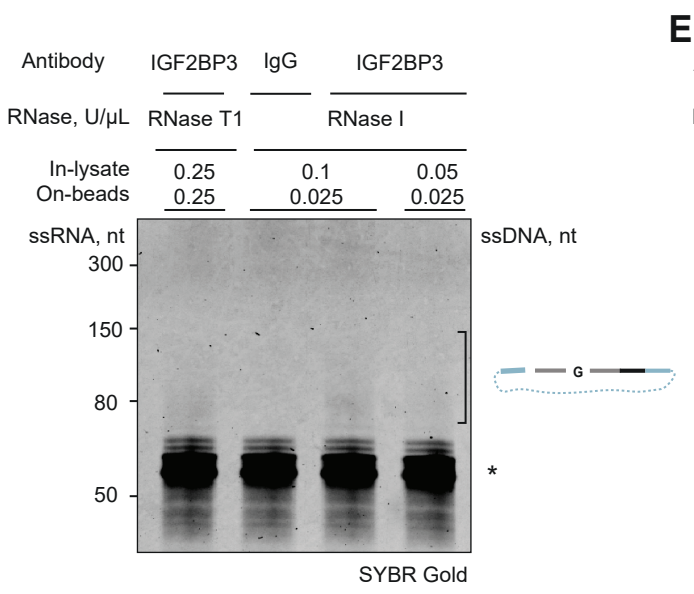
D
Antibody
IGF2BP3
IgG
IGF2BP3
RNase, U/µL
RNase T1
RNase I
In-lysate
On-beads
0.25
0.25
0.1
0.025
0.05
0.025
ssRNA, nt
300
150
80
50
ssDNA, nt
G
*
SYBR Gold

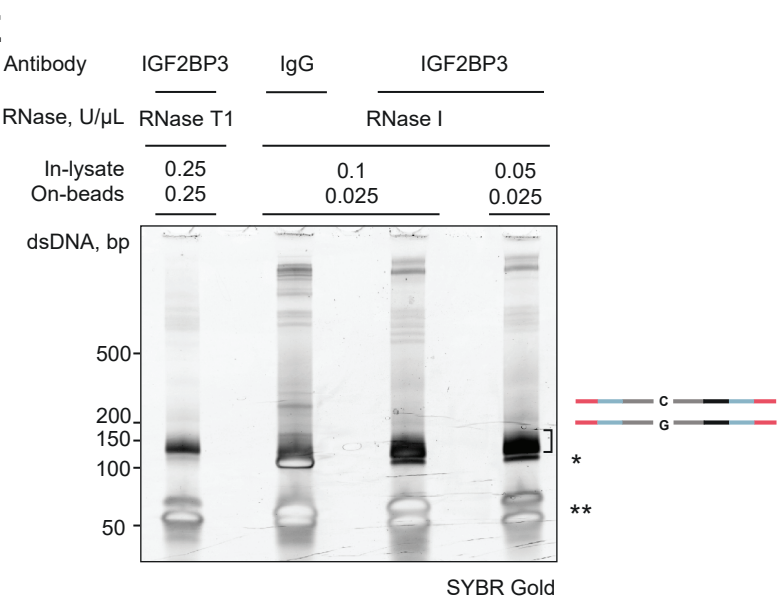
E
Antibody
IGF2BP3
IgG
IGF2BP3
RNase, U/µL
RNase T1
RNase I
In-lysate
On-beads
0.25
0.25
0.1
0.025
0.05
0.025
dsDNA, bp
500
200
150
100
50
C
G
*
**
SYBR Gold

Figure S2

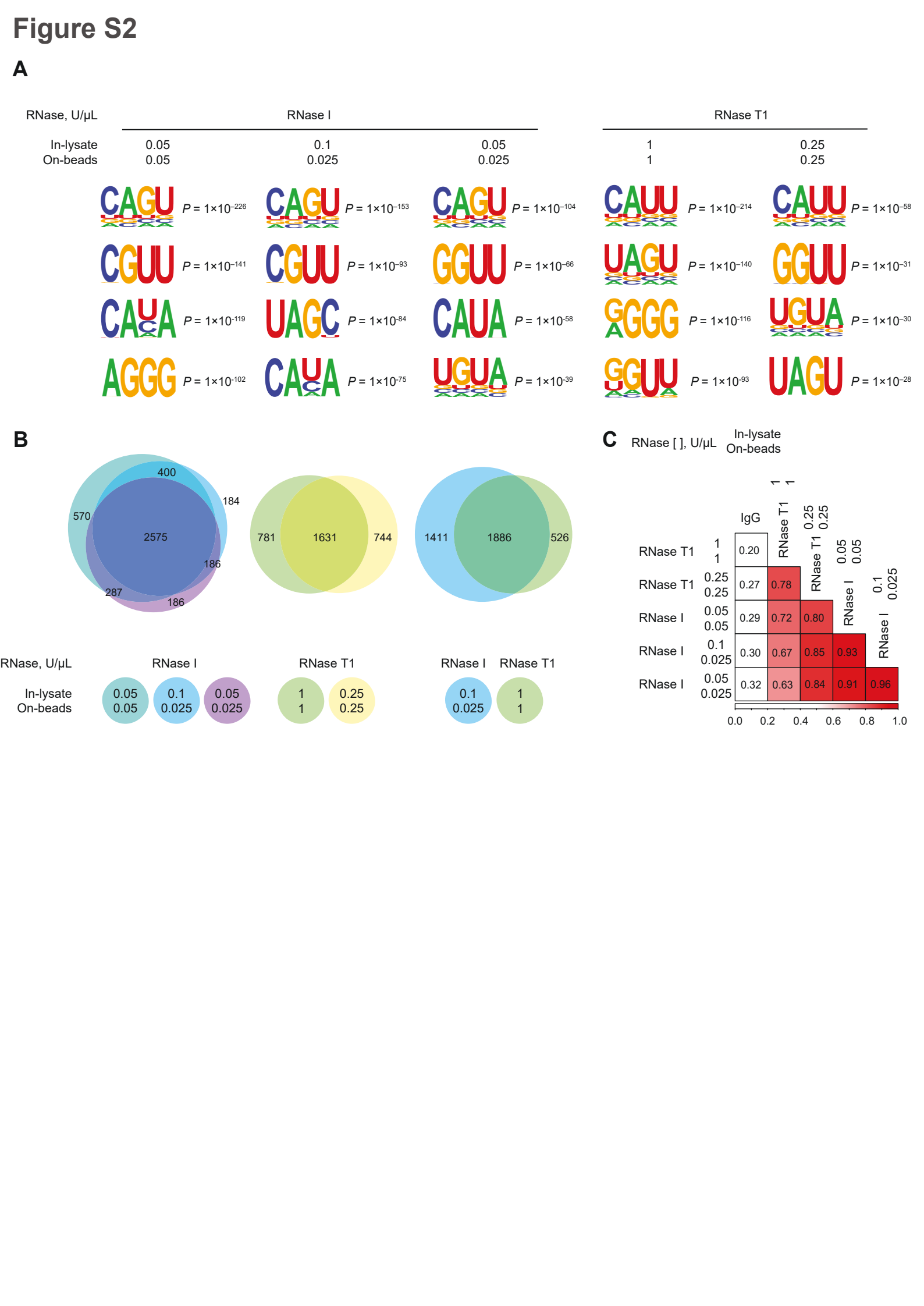
A
RNase, U/μL
RNase I
RNase T1
In-lysate
On-beads
0.05
0.05
0.1
0.025
0.05
0.025
1
1
0.25
0.25
P = 1×10−226
P = 1×10−153
P = 1×10−104
P = 1×10−214
P = 1×10−58
P = 1×10−141
P = 1×10−93
P = 1×10−66
P = 1×10−140
P = 1×10−31
P = 1×10−119
P = 1×10−84
P = 1×10−58
P = 1×10−116
P = 1×10−30
P = 1×10−102
P = 1×10−75
P = 1×10−39
P = 1×10−93
P = 1×10−28
B
400
184
570
2575
186
287
186
781
1631
744
1411
1886
526
RNase, U/μL
RNase I
RNase T1
RNase I
RNase T1
In-lysate
On-beads
0.05
0.05
0.1
0.025
0.05
0.025
1
1
0.25
0.25
0.1
0.025
1
1
C
RNase [ ], U/μL
In-lysate
On-beads
IgG
RNase T1
1
1
RNase T1
0.25
0.25
RNase I
0.05
0.05
RNase I
0.1
0.025
RNase T1
1
1
0.20
RNase T1
0.25
0.25
0.27
0.78
RNase I
0.05
0.05
0.29
0.72
0.80
RNase I
0.1
0.025
0.30
0.67
0.85
0.93
RNase I
0.05
0.025
0.32
0.63
0.84
0.91
0.96
0.0
0.2
0.4
0.6
0.8
1.0

Supplementary figures

Supplemental Figure 1. Gel-based size selection steps of the infrared PAR-CLIP protocol. A. Schema of the IR-PAR-CLIP library. The crosslinked RNA fragment is ligated to the infra-red dye-conjugated 3' adapter containing a 5 nt unique molecular identifier (UMI) and a sample barcode (BC). The complementary strand is transcribed using the reverse transcription (RT) primer complementary to the adapter sequence and containing an 18-atom hexa-ethyleneglycol spacer (Sp18). The library is amplified in a PCR reaction with the indexed primers. The use of the Unique Dual Index barcodes is recommended (BC 1, BC 2). **B.** SDS-PAGE of the RNA-IGF2BP3 complexes after infrared adapter ligation. Different RNase conditions are tested and immunoprecipitation of IGF2BP3 is compared to the IgG control. Note that higher in-lysate concentration of RNase results in a higher output of eluted complexes. **C.** TBE-Urea gel of the recovered RNA-adapter fragments crosslinked to the protein remnant left after proteinase K treatment. *RNA-protein complexes insufficiently digested with proteinase K (as we did not observe these bands when the proteinase K-treated peptide-RNA-adapter complexes were purified with electroelution before the RNA gel), ** unligated adapter. **D.** TBE-Urea gel of the reverse transcription reaction product. Although the reverse transcription product is hardly visible on SYBR-Gold stained gel, this step is important to separate the product from * the unreacted primer. **E.** TBE gel of the library construction PCR product. The libraries obtained with anti-IGF2BP3 antibody were amplified with 18 PCR cycles, while the IgG control library was amplified with 23 cycles. * no-insert product, ** unreacted primers. Brackets show the region excised from the gel.

Supplemental Figure 2. Effect of RNase concentration on IR-PAR-CLIP coverage, motif, and target prediction results. A. 4-nucleotide IGF2BP3-binding motifs identified by HOMER in IR-PAR-CLIP of HCT116. **B.** Overlap of IGF2BP3 targets identified in this study with different RNase I and RNase T1 treatment conditions. **C.** Pearson correlation matrix of the IGF2BP3 IR-PAR-CLIP coverage for the tested RNase I and RNase T1 treatment conditions.

2.2 Dual regulation of the unfolded protein response by IGF2BP3 during ER stress

2.2.1 Preamble

This study addresses the main research question of my PhD thesis. In this paper, I investigated the role of IGF2BP3 in post-transcriptional regulation during ER stress. Using IR-PAR-CLIP, I demonstrated that under ER stress conditions, IGF2BP3 binds transcripts encoding key UPR effectors. To determine how IGF2BP3 influences these targets, I analyzed the effect of IGF2BP3 depletion on the transcriptome under ER stress and distinguished between its impact on transcription and mRNA stability. The results revealed a dual regulatory mechanism: IGF2BP3 indirectly promotes transcriptional activation of the UPR, while at the same time destabilizes many of its bound transcripts to reduce translational burden. These two outcomes act in balance to support the cellular stress response. Finally, I investigated the molecular mechanism behind IGF2BP3-mediated destabilization and found that ER stress enhances association of IGF2BP3 with the mRNA decapping complex and the ER stress sensor IRE1, consistent with its role in promoting mRNA decay.

This manuscript was sent for revision in *Genes & Development* on September 2nd, 2025.

The earlier version of the manuscript is published in *bioRxiv* on March 31st, 2025:

doi: https://doi.org/10.1101/2025.03.29.646117

2.2.2 Contribution statement

I was involved in conceptualization and experimental design and performed all experimental work and data analyses, except for the experiments listed below. The data in Supp. Fig. 1A are reanalyzed data from Acosta-Alvear and Karagöz et al., 2018 [112]. The co-immunoprecipitation of GFP-IGF2BP3 experiment shown in Supp. Fig. 1B and the mapping of the IGF2BP3-EDC3 interaction site shown in Fig. 5 I-K were done by Elif Karagöz. The proteomics data was generated by the Max Perutz Labs Proteomics Facility. I was involved in the writing and editing of the manuscript.

Dual regulation of the unfolded protein response by IGF2BP3 during ER stress

Aleksandra S Anisimova[1,2], Harald Hornegger[1,2], Irmgard Fischer[1], Gijs A Versteeg[1,3], Stefan L Ameres[1,4], G Elif Karagöz[1,5,#]

1. Max Perutz Labs, Vienna BioCenter Campus, Dr.-Bohr-Gasse 9, 1030, Vienna, Austria.
2. Vienna BioCenter PhD Program, a Doctoral School of the University of Vienna and the Medical University of Vienna, A-1030 Vienna, Austria.
3. University of Vienna, Center for Molecular Biology, Department of Microbiology, Immunobiology, and Genetics, Dr.-Bohr-Gasse 9, 1030, Vienna, Austria.
4. University of Vienna, Center for Molecular Biology, Department of Biochemistry and Cell Biology, Dr.-Bohr-Gasse 9, 1030, Vienna, Austria.
5. Medical University of Vienna, Center for Medical Biochemistry, Dr.-Bohr-Gasse 9, 1030, Vienna, Austria.

Correspondence: guelsuen.karagoez@meduniwien.ac.at

Abstract

Misfolded protein accumulation in the endoplasmic reticulum (ER) perturbs cellular homeostasis, causing pathological ER stress. While a transcriptional response is paramount for the Unfolded Protein Response (UPR), which counters ER protein-folding overload, multiple UPR-linked mRNAs are post-transcriptionally regulated. However, the mechanisms mediating this regulation remain unclear. Here, we reveal specific interactions between the conserved RNA-binding protein IGF2BP3 and transcripts encoding UPR effectors. During ER stress, IGF2BP3 destabilizes many of its target transcripts, including UPR effectors. Mechanistically, ER stress enhances IGF2BP3's association with the mRNA decapping complex and the ER stress sensor RNase IRE1, correlating with a shift toward mRNA destabilization. Unexpectedly, prolonged depletion of IGF2BP3 inhibits UPR via decreased transcription of UPR target genes. Together, our findings suggest that IGF2BP3 contributes to proteostasis during ER stress through dual mechanisms: directly promoting mRNA degradation to reduce translation and folding burden and indirectly supporting transcriptional activation of the UPR.

Introduction

Protein-folding homeostasis is paramount for robust cell function. Underlining the importance of this homeostasis, various stress-response pathways surveil and react to protein-folding perturbations. In the endoplasmic reticulum (ER), a critical site for the folding of secreted and transmembrane proteins, protein-folding homeostasis is maintained by a conserved signaling cascade known as the “Unfolded Protein Response” (UPR). In metazoans, the UPR is driven by three parallel ER-tethered sensor/transducers: IRE1, PERK, and ATF6. Each sensor monitors the accumulation of misfolded proteins in the ER and takes corrective actions to restore homeostasis.

The UPR increases protein folding and degradation capacity in the ER through transcriptional upregulation of chaperones, foldases, ER-associated degradation (ERAD), and ER-phagy components [1-11]. However, if homeostasis is not achieved in a timely manner, the UPR initiates cell death programs that eliminate defective cells for the benefit of the organism [12, 13]. Together with the magnitude and duration of the ER stress, the interplay between the UPR branches sets molecular timers that govern the decision to either repair the damaged cell or eliminate it as a potential threat. These factors heavily depend on cell identity as well as metabolic and cellular state [12, 13].

Whlie the UPR-driven transcriptional response is essential for maintaining ER homeostasis, cells also utilize a variety of post-transcriptional mechanisms to adapt to ER stress [14-17]. The early response to ER stress converges on the shutdown of global translation by the ER-tethered kinase PERK, which reduces global protein synthesis [Harding, 1999 #420;Harding, 2000 #418;Walter P., 2011 #1;Holcik, 2005 #1923]. During translational shutdown, some translationally silenced mRNAs are protected from turnover, whereas others are degraded [18-20]. Under such conditions, the UPR sensor IRE1 cleaves ER-localized mRNAs via regulated IRE1-dependent decay of messenger RNAs (RIDD), proposed to decrease protein folding load in the ER [21, 22]. Apart from its role in tuning protein synthesis into the ER, RIDD protects cells from apoptosis via opposing the transcriptional upregulation of the death receptor 5 (DR5) mRNA expression induced by the PERK-ATF4 branch. Therefore, while it is clear that posttranscriptional mechanisms contribute to life-and-death decisions during ER stress, the mechanistic details of how this is achieved have been poorly understood.

RNA-binding proteins (RBPs) mediate post-transcriptional mechanisms that facilitate adaptation to developmental and metabolic changes or cellular perturbations [23, 24]. Using immunoprecipitation coupled to mass spectrometry analyses (IP-MS/MS) of the UPR sensor IRE1, we previously revealed that it is associated with a highly conserved RBP, IGF2BP3, in a stress-dependent manner [25]. IGF2BPs are a conserved family of RBPs that regulate mRNA fate by controlling target mRNA stability, localization, and translation (reviewed in [26]). IGF2BPs were proposed to protect mRNAs from degradation by competing with microRNA binding [27, 28]. More recently, IGF2BP family members have been shown to function as readers of m6A and m7G mRNA modifications. While all IGF2BPs guard m6A-modified mRNAs from decay, IGF2BP1 and IGF2BP3 facilitate the degradation of mRNAs harboring m7G modifications [29, 30]. Among the

three IGF2BP paralogs in mammalian cells, IGF2BP1 and IGF2BP3 are expressed at high levels during early development [31-33], regulate mRNAs involved in cell growth and migration [28, 34-38], therefore are necessary for healthy embryo development. Notably, expression of all IGF2BP paralogs is upregulated in various cancers, and this strongly correlates with poor patient outcomes, enhanced tumor growth, drug resistance, and metastasis [35, 39, 40].

Several studies show that during proteotoxic stress induced by heat shock or arsenite treatment, IGF2BPs promote mRNA stability by preventing mRNA degradation. Moreover, they facilitate target mRNA translation once the stress is relieved [29, 41, 42]. Given these data, IGF2BPs may mediate post-transcriptional regulation in response to organelle-specific stress. However, whether IGF2BP3 responds to ER stress and contributes to restoring ER homeostasis remains unclear.

In this study, we assessed the role of IGF2BP3 in regulating UPR-associated transcripts. Our data show that the stress-dependent association of IGF2BP3 with IRE1 is conserved across cell lines, revealing that IGF2BP3 binds to prominent UPR-effector transcripts. Using genome-wide transcriptome and mRNA stability analyses, we demonstrate that IGF2BP3 regulates the UPR at both the post-transcriptional and transcriptional levels, thereby forming a unique gene regulatory network that modulates the UPR.

Results

IGF2BP3 associates with IRE1 during ER stress

To decipher post-transcriptional mechanisms regulating mRNA fate during ER stress, we focused on the primary post-transcriptional regulator, the ER-tethered RNase IRE1, which binds to and cleaves the ER-bound mRNAs during ER stress. In previous work, we mapped the IRE1 interactome by IP-MS/MS in HEK293T and multiple myeloma cells and identified select RBPs associated with IRE1 [25]. We hypothesized that the RBPs interacting with IRE1 during ER stress regulate the stability of UPR-relevant mRNAs associated with IRE1. Among those RBPs, IGF2BP3 stood out as it was also recovered in IRE1 IP-MS/MS under denaturing conditions after RNA-protein cross-linking, which suggested a robust association with IRE1 and RNA-containing complexes (**Supp. Fig. 1A**).

To test whether ER stress-induced increase in IGF2BP3 association with IRE1 extended across different cell types, we performed IPs followed by Western Blot analyses in mouse embryonic fibroblasts expressing GFP-tagged IRE1. To address whether IGF2BP3 and IRE1 are bridged by RNAs we performed these IPs under native conditions and tested whether RNase will disrupt the interaction. IGF3BP3's interaction with IRE1 increased 2-fold after 4 h of ER stress compared to unstressed controls and was sensitive to RNase treatment (**Fig. 1A, B**). Consistent with this result, we also recovered IRE1 using reciprocal IGF2BP3 pull-downs in HEK293T cells in an ER stress-dependent manner (**Supp. Fig. 1B**).

From these results, we concluded that IRE1 and IGF2BP3 form complexes during ER stress. It is plausible that IGF2BP3 interacts with the ER-targeted mRNAs and this way is partially localized to the ER membrane during stress. The fact that these complexes were identified in multiple cell types makes it likely that they are universal cellular complexes with potential importance for general cellular biology.

IGF2BP3 interacts with the UPR target mRNAs

The mRNAs interacting with IGF2BP3 under steady-state conditions have been well established [38, 43, 44], but it is unclear whether proteotoxic stress modulates IGF2BP3 interactions with its target mRNAs. To this end, we defined IGF2BP3-interacting mRNAs during ER stress in HCT116 cells using Infra-Red Photoactivatable Ribonucleoside-enhanced Crosslinking and Immunoprecipitation (IR-PAR-CLIP) [43]. Due to extensive RNase cleavage and presence of T to C (T-C) transitions that mark the crosslink position this approach allows nucleotide-resolution detection of RBP-interaction sites in target RNAs [44]. IGF2BP3 IR-PAR-CLIP was performed under homeostatic conditions, during early response (1 h), and at peak response (4 h) time points after UPR induction by tunicamycin (TM). As UPR target genes are transcriptionally upregulated under these conditions, we performed total transcriptome sequencing in parallel to account for changes in transcript levels.

On average IGF2BP3 IR-PAR-CLIP produced 45-times more unique deduplicated reads comparing to the IgG controls with ~50% of the reads containing T-C transitions (**Supp. Fig. 1C**). To determine IGF2BP3-bound transcripts we performed T-C aware peak calling using PARalyzer [45]. Transcripts that had at least one cluster of IGF2BP3-croslinked reads containing more than 25 gene counts per million (CPM) and more than 50% of T-C conversions per read were considered IGF2BP3-bound. After correction for transcript levels (IR-PAR-CLIP CPM > transcriptome CPM) IR-PAR-CLIP identified 2313 IGF3BP3-bound transcripts under homeostatic conditions (**Supp. Fig. 1D, Supp. Table 1**). A short ER stress induction (1 hour) did not significantly alter neither the levels of the hallmark UPR-target transcripts nor IGF2BP3 binding; however, a 4-hour treatment led to strong UPR induction (**Fig. 1C**). Under these conditions, IGF2BP3 interacted with a transcript set largely overlapping that observed under control conditions, with 157 additional transcripts that only interacted during ER stress (**Supp. Fig. 1D**). These transcripts were enriched in those involved in ER stress response and proteasomal degradation (**Supp. Fig. 1E**). We further defined a list of 2470 IGF2BP3-bound transcripts present in either control or ER stress (4 h) conditions (**Supp. Table 1**). Gene ontology analyses of those mRNAs revealed that regulation of transcription, protein degradation, differentiation, intracellular communication, and response to ER stress were the top-enriched biological processes (**Supp. Fig. 1F**).

In agreement with the published data, our IGF2BP3 IR-PAR-CLIP analyses showed that under homeostatic conditions, IGF2BP3 binds to most of its target mRNAs through their 3' UTRs (**Supp. Fig. 1G**) [43, 44]. While IGF2BP3's binding preference for 3' UTRs was not affected by ER stress, the IGF2BP3-binding motifs showed distinct differences (**Supp. Fig. 1H**). The top five 5

nt-long motifs enriched in IGF2BP3-bound IR-PAR-CLIP reads included those with CA-rich sequences common among IGF2BP3 binding motifs [38, 46]. Three motifs (UCCAG, AGCCU, and UGCCA) were common for both conditions. In contrast, upon stress, novel ACUGU and ACCUG motifs were highly enriched in comparison to a canonical CAUU-containing motif [44]. These results indicated that IGF2BP3 associates with novel sequences during ER stress.

Next, we tested whether ER stress modulates IGF2BP3 interactions with its target transcripts. Upon ER stress induction, the number of IGF2BP3-bound reads derived from UPR-induced genes increased. These UPR targets included genes encoding for the master transcription factors XBP1, ATF4, CHOP (*DDIT3*), and major chaperones BiP (*HSPA5*) and DNAJB9 (**Fig. 1D**). At the same time, IGF2BP3 showed reduced binding to some of its canonical targets, such as *HMGA2* mRNA [28] (**Fig. 1D**). To assess the binding of IGF2BP3 to the UPR-target genes we defined 228 genes that were upregulated at least 2-fold upon ER stress induction as "UPR-induced" transcripts. To account for changes in the mRNA levels, we next compared ER stress-induced changes in transcript levels with the changes in IGF2BP3-bound transcripts (**Fig. 1E**) and calculated an "IGF2BP3 binding" score by normalizing the IR-PAR-CLIP reads to the transcript levels (**Fig. 1F, Supp. Fig. 1I**). These analyses revealed that IGF2BP3 binds UPR-induced targets to a similar extent under both homeostatic and ER stress conditions, suggesting that the observed increase in IGF2BP3-bound reads for most genes during ER stress results from increased transcription of UPR target genes. However, while IGF2BP3-bound reads increased linearly for multiple UPR targets with increased expression, mRNAs such as *HSPA5* showed preferential binding of IGF2BP3 during ER stress (**Fig. 1C, E, G, Supp. Fig. 1I**). Moreover, we identified novel IGF2BP3 targets, such as *DDIT3,* which were only expressed during ER stress (**Fig. 1C, G**).

Supporting our IP-MS/MS data, IGF2BP3 was bound to one-third of the transcripts interacting with IRE1 during ER stress (**Supp. Fig. 1J**). The IGF2BP3-binding sites did not overlap with IRE1 RIDD cleavage sites on most of the common IRE1 and IGF2BP3-bound mRNAs. Those analyses suggested that IGF2BP3 binding does not compete with IRE1 for the same sites (**Supp. Fig. 1K**). To sum up, we found that IGF2BP3 interacts with transcripts encoding UPR target genes during ER stress, identifying IGF2BP3 as a potential post-transcriptional regulator of the UPR.

IGF2BP3 depletion dampens UPR signaling

Based on our findings above, we hypothesized that IGF2BP3 might post-transcriptionally regulate UPR-induced mRNAs. We, therefore, set out to identify which transcripts might be functionally regulated by IGF2BP3. To this end, IGF2BP3 was depleted in colon carcinoma HCT116 cells by CRISPR/Cas9-mediated knockout (**Supp. Fig. 2A**), after which transcriptome analyses were performed under homeostatic and ER-stress conditions (**Supp. Table 2**). IGF2BP3 knockout resulted in moderate changes in the total transcriptome (**Fig. 2A**). Specifically, it led to the downregulation of genes involved in regulation of transcription, cell proliferation and migration, development, and response to growth factors, consistent with

previous reports [40, 43, 47, 48] (**Supp. Fig. 2B**). To address the effect of IGF2BP3 depletion on the cellular response to ER stress, we defined 288 UPR target transcripts as those upregulated by more than two-fold upon ER stress including those bound by IGF2BP3 (58 transcripts) (**Fig. 2B**) and followed their levels upon IGF2BP3 depletion. Transcriptome analysis showed that the levels of the UPR target transcripts were lower in IGF2BP3 knockouts compared to the parental cells during ER stress (**Fig. 2B, C**). While IGF2BP3 depletion had only a moderate impact on individual UPR effector transcripts (**Fig. 2B**), changes were evident when analyzed for the whole group (**Fig. 2 C**). In contrast, the levels of other IGF2BP3-bound transcripts were less affected by IGF2BP3 CRISPR/Cas9-mediated knockout (**Fig. 2A, C**). Thus, IGF2BP3 specifically impacts UPR target transcripts during ER stress (**Fig. 2B, C**).

To account for the adaptation of cells to long-term depletion of IGF2BP3 and to bypass the clonal selection, we used siRNA-based depletion as an orthogonal approach to validate our findings (**Supp. Table 2**). Using an siRNA pool against IGF2BP3, we obtained 75 percent depletion in 48 hours in HCT116 cells (**Supp. Fig. 2C, D**). The siRNA knockdown experiments confirmed the data obtained by the CRISPR/Cas9-based IGF2BP3 knockouts, indicating that depletion of IGF2BP3 dampens UPR signaling (**Fig. 2D**). Reverse transcription quantitative PCR (RT-qPCR) analyses of IGF2BP3-interacting transcripts confirmed these results even at milder, closer to physiological ER stress conditions, showing that IGF2BP3 knockout leads to a decrease in the levels of major UPR targets downstream of PERK (*ATF4*, *DDIT4*), IRE1 (*XBP1* spliced), and ATF6 (*HSPA5*) (**Fig. 2E**). Intriguingly, our analyses showed that during ER stress, depletion of IGF2BP3 not only reduced the levels of IGF2BP3-bound UPR targets but also affected those that are not its direct interactors (**Fig. 2B, C, D**). This suggested that IGF2BP3 depletion leads to the downregulation of the entire pathway, possibly due to secondary indirect effects. Altogether, our data showed that IGF2BP3 depletion tunes down UPR.

IGF2BP3 shapes the UPR through transcriptional feedback loops

As mentioned above, our genome-wide approaches revealed that in addition to IGF2BP3-bound transcripts, the levels of UPR targets that are not directly bound to IGF2BP3 also decreased upon IGF2BP3 depletion, suggesting a secondary indirect effect of IGF2BP3 depletion (**Fig. 2B, C, D**). As IGF2BP3 controls the stability of several mRNAs involved in transcriptional regulation, we hypothesized that transcriptional reprogramming might result in the indirect effects observed upon IGF2BP3 depletion.

To uncover the primary mechanism of IGF2BP3-mediated regulation during ER stress, we aimed to uncouple transcriptional reprogramming from post-transcriptional regulation. To unravel whether transcriptional reprogramming contributes to the changes in the transcript levels upon IGF2BP3 depletion, we used thiol (SH)-linked alkylation for the metabolic sequencing of RNA (SLAMseq) method (**Fig. 3A**). In SLAMseq, nascent transcripts are metabolically labelled, allowing assessment of *de novo* RNA synthesis [49]. We performed two hours of pulse labeling in HCT116 cells with s^4U, followed by total RNA extraction, alkylation, and mRNA 3′-end library preparation under homeostatic conditions and after subjecting cells to 5 hours of ER stress (with s^4U added for the last two hours) (**Supp. Table 3**). First, we followed

the changes in the transcript levels transcribed during the 2 hours of s^4U pulse (*de novo* transcriptome, T-C reads). SLAMseq analyses showed that siRNA-mediated depletion of IGF2BP3 decreased transcription of the UPR target genes (**Fig. 3B**) indicating that IGF2BP3 indirectly contributes to transcriptional reprogramming (**Fig. 3C**), potentially due to downregulation of a transcriptional regulator upon IGF2BP3 depletion. Indeed, several mRNAs encoding for transcription factors were downregulated upon IGF2BP3 depletion (**Supp. Fig. 3A**).

To systematically address the contribution of post-transcriptional regulation to the levels of the UPR target transcripts, we calculated the changes in mRNA stability by comparing the changes in the average T-C conversion rates per gene upon IGF2BP3 depletion (**Fig. 3D**). T-C conversion rate values reflect the relative abundance of pre-existing and *de novo* synthesized mRNA per given gene, and their decrease suggests stabilization. Those analyses showed that IGF2BP3 depletion increased the stability of IGF2BP3-bound transcripts including those encoding for the UPR target genes, particularly during ER stress. These data indicated that IGF2BP3 depletion controls UPR transcript levels at the post-transcriptional and transcriptional levels.

Supporting the notion that IGF2BP3 destabilizes its target mRNAs during stress, when transcription was inhibited by actinomycin D (ActD) treatment, IGF2BP3 depletion increased the levels of *XBP1* and *DDIT3* (CHOP) mRNAs during ER stress (**Fig. 3E, F**). Notably, the destabilization effect was specific to ER stress and was not observed during homeostatic conditions. These data suggested that IGF2BP3 regulates the UPR in two ways: 1. It binds to and destabilizes its target mRNAs during ER stress. 2. It indirectly upregulates the transcription of the UPR target genes. This transcriptional feedback loop allows differential regulation of UPR target transcripts by IGF2BP3 during ER stress. The transcriptional response is more potent, and this way, IGF2BP3 depletion dampens the response. This model explains how IGF2BP3 depletion leads to decreased levels of the UPR target transcripts, while its depletion increases the levels of its post-transcriptional targets. It is attractive to speculate that the IGF2BP3-driven dual regulatory mechanism allows cells to decrease protein folding burden while ensuring they elicit potent UPR during ER stress.

IGF2BP3 facilitates mRNA degradation during ER stress

Our transcriptomics and SLAMseq analyses showed that siRNA-mediated IGF2BP3 depletion resulted in both stabilization and destabilization of IGF2BP3-bound transcripts under homeostatic conditions. Most top-regulated transcripts encoded proteins involved in cell proliferation and motility (e.g., *HMGA2*, *CARM1, TRIB1*, *NACC2*) [50-53]. Notably, several of these target mRNAs encoded transcription factors (*ZNF385A*), regulators of gene expression (*HMGA2*, *CARM1, NACC2*), or RNA metabolism (*AGO2, ZFP36L1*), underlining that IGF2BP3-mediated post-transcriptional regulation impinges on potent gene regulatory networks to remodel the transcriptome.

The SLAM-seq analyses also revealed that, in contrast to the homeostatic conditions, IGF2BP3-binding destabilized majority of its target mRNAs during ER stress (**Fig. 3D**)**.** The observed

increase in IGF2BP3-mediated destabilization upon ER stress was specific for IGF2BP3-bound transcripts (**Fig. 4A**). In line with these analyses, IGF2BP3 destabilized a higher number of transcripts during ER stress compared to homeostatic conditions **(Fig. 4B, C**)**.** Together, these findings suggest that ER stress shifts IGF2BP3 function toward promoting the destabilization of its target transcripts.

Our data confirmed that IGF2BP3 regulates *HMGA2* (stabilized by IGF2BP3) [28] and *ZFP36L1* (destabilized by IGF2BP3) [47], as reported in earlier studies (**Fig. 4B, D, E)**. *HMGA2* encodes a nonhistone chromatin factor that controls gene expression by altering chromatin architecture [54]. In line with the published work, depletion of IGF2BP3 resulted in lower levels of *HMGA2* mRNA under homeostatic conditions, supporting the notion that IGF2BP3 binding stabilizes *HMGA2* mRNA (**Fig. 4B, C, D**). The SLAMseq analyses confirmed that IGF2BP3 binding stabilizes *HMGA2* under those conditions, as IGF2BP3 depletion did not result in decrease of *HMGA2* transcription (**Supp. Fig. 4A**). Surprisingly, *HMGA2* mRNA levels significantly decreased during ER stress (**Fig. 4D**). Using RT-qPCR analyses, we confirmed that IGF2BP3 did not stabilize *HMGA2* mRNA as efficiently during ER stress as under homeostatic conditions (**Fig. 4E**). These results were corroborated by actinomycin D chase experiments, which showed that IGF2BP3 depletion decreased the half-life of *HMGA2* mRNA under homeostatic conditions while not impacting it during ER stress (**Fig. 4F**). Notably, our IR-PAR-CLIP analyses showed that IGF2BP3 binding to *HMGA2* mRNA weakens during ER stress, which might explain the reduced protection of this mRNA (**Supp. Fig. 1I**).

Consistent with our data suggesting that IGF2BP3 switches to a degradative function during ER stress, we observed more pronounced destabilization of a subset of transcripts that IGF2BP3 also destabilizes under homeostatic conditions (**Fig. 4B, C, Supp. Fig. 4A**). Both the transcriptomics (**Fig. 4B, C, D, Supp. Fig. 4A**) and RT-qPCR data (**Fig. 4E**) showed that IGF2BP3 depletion increased the levels of a well-described target, *ZFP36L1* mRNA under homeostatic conditions supporting earlier work [47] that proposed IGF2BP3 facilitates *ZFP36L1* mRNA degradation. This effect was more pronounced during ER stress (**Fig. 4C, D, E**), with *ZFP36L1* mRNA showing an increased half-life upon IGF2BP3 depletion under stress conditions in actinomycin D chase experiments (**Fig. 4F**). These analyses indicated that ER stress modulates IGF2BP3 function, shifting the functional consequences of IGF2BP3 binding towards mRNA degradation. Altogether, we discovered that ER stress modulates IGF2BP3-target mRNA interactions and impacts how IGF2BP3 regulates its canonical targets.

ER stress promotes the association of IGF2BP3 with the mRNA decapping complex

The association of IGF2BP3 with the mRNA degradation machinery was previously proposed to regulate a subset of its target mRNAs [47, 48, 55]. Therefore, we employed proteomics to investigate whether changes in the IGF2BP3 interactome explain the increase in IGF2BP3-mediated degradation during ER stress. To this end, we immunoprecipitated IGF2BP3 from HCT116 cells. The proteomics analyses showed that IGF2BP3 co-IP recovered proteins involved in almost all distinct steps of mRNA metabolism including transcription (RNA Pol II subunits, transcription

factors), mRNA splicing (spliceosome components, SR proteins), export (THO complex subunits, MAGOH, RBM8A) and translation (ribosomal proteins) (**Supp. Fig. 5A, Suppl. Table 4**), supporting the model that IGF2BPs are loaded onto nascent transcripts in the nucleus and shuttle to the cytoplasm [56]. IGF2BP3 also interacted with signal recognition particle (SRP) components, showing that IGF2BP3 binds to mRNAs during active translation en route to the ER, which aligns with our data. Apart from those factors, our analyses identified an association of IGF2BP3 with the RNA degradation machinery (RNA deadenylation and decapping complex, exosome, XRN1) under both homeostatic conditions and during ER stress (**Fig. 5A, Supp. Fig. 5A, Suppl. Table 4**). These data supported the notion that IGF2BP3 accompanies its mRNA targets from synthesis to degradation.

To decrease the complexity in our experiments, we aimed to eliminate long-distance RNA-bridged interactors and treated the samples with RNases. RNase treatment reduced the abundance of many interactors, suggesting that they associate with IGF2BP3 through RNA-bridged interactions. However, most of IGF2BP3 interactors were still detected in the co-IP likely because a large portion of IGF2BP3s is embedded within mRNP complexes that are inaccessible to RNases (**Supp. Fig. 5B**). The highly RNase-sensitive interactors were enriched for proteins involved in mRNA splicing, maturation and export (**Supp. Fig. 5C**). RBPs and components of the mRNA degradation machinery showed variable RNase sensitivity. For instance, YBX1, HuR (ELAVL1), G3BP1/2, PABPC1, AGO2, and LSM complex were highly RNase sensitive. In contrast, RBPs FXR1/2, RNases IRE1 and XRN1, and the components of the decapping machinery (EDC3, EDC4, DCP1A, DCP2) were comparatively resistant, indicating that they are part of more compact assemblies with IGF2BP3 (**Supp. Fig. 5B, Suppl. Table 4**).

While ER stress caused only modest changes in IGF2BP3 binding to most interacting proteins, its association with a subset of proteins, including RNase IRE1, increased (**Fig. 5B**), supporting our initial findings (**Fig. 1A, Supp. Fig. 1A, B**). Notably, during ER stress, IGF2BP3 bound more strongly to all components of the mRNA decapping machinery (EDC3, EDC4, DCP1A, DCP2) (**Fig. 5B, C, Supp. Fig. 5D**), which is in line with the increase of IGF2BP3 pro-degradatory function during ER stress. We validated this finding by performing co-IP of split-GFP–tagged IGF2BP3 from HEK293T cells. EDC4 was recovered in the IGF2BP3 IP, and its interaction increased upon ER stress, supporting the endogenous co-IP–MS results (**Fig. 5D, E**). We further corroborated our findings by performing a reciprocal co-IP of another decapping complex component, EDC3, tagged with split-mNeonGreen (mNG), which recovered IGF2BP3 and confirmed its increased association with the decapping complex upon ER stress (**Fig. 5F, G**). These data suggested that increased interaction of IGF2BP3 with the mRNA decapping machinery might enable more efficient degradation of IGF2BP3 target mRNAs during ER stress.

To identify proteins mediating the specific interaction of IGF2BP3 with the mRNA decapping complex, we performed an AlphaFold2-Multimer *in silico* screen of pairwise protein-protein interactions between IGF2BP3 and confident interactors identified by proteomics analyses [57-59]. In AlphaFold, a high interface-predicted template modeling score (ipTM score > 0.6) indicates interfaces with high confidence interfaces. As our dataset contained many RBPs with disordered

segments, we used the average PEAK score. The average PEAK score quantifies the predicted error in the relative position of two residues, and is more sensitive in identifying regions of high confidence for proteins with smaller interaction surfaces and interactions involving disordered regions [57-59]. The AlphaFold2-Multimer screen identified 14 highly confident IGF2BP3 protein interactors with the average PEAK score > 0.75. EDC3 was the second top interactor of IGF2BP3 with an average PEAK score of 0.87 (**Fig. 5H**). To validate those findings, we performed AlphaFold3 [60] prediction with subdomains of IGF2BP3 and EDC3. IGF2BP3 comprises two N-terminal RNA-recognition motif (RRM) domains and four K Homology (KH) domains connected with two disordered linkers [46]. EDC3 comprises an N-terminal SM domain connected to the YjeF domain by a long disordered segment [61] (**Fig. 5I, J)**. The AlphaFold3 prediction of the complexes formed between IGF2BP3 and EDC3 subdomains revealed that the RRM2 domain of IGF2BP3 interacted with the YjeF domain of EDC3 with high confidence (ipTM = 0.72) (**Fig. 5I, J, K**). Importantly, our high-throughput AlphaFold2-Multimer predictions identified the same interaction surface between IGF2BP3 and EDC3 using the full-length proteins, increasing our confidence. In contrast, AlphaFold3 did not predict a confident interaction between other subdomains of both proteins (**Fig. 5I)**.

To experimentally validate the binding interface predicted by the structural models, we engineered a quadruple IGF2BP3 mutant (I88A, P90A, H91A, W94A) to impair its binding to EDC3 and called this IGF2BP3-4A mutant (**Fig. 5K**). We co-expressed GFP-tagged wild-type EDC3 with FLAG-tagged wild-type IGF2BP3 or IGF2BP3-4A in HCT116 IGF2BP3 KO cells and performed pulldown experiments to assess the interaction. Our data revealed that the IGF2BP3-4A mutant is largely impaired in its binding to EDC3 (**Fig. 5L, M**), indicating that the interaction surface identified by the Alphafold predictions is essential for mediating the binding of IGF2BP3 to EDC3. Altogether, we identified a novel interaction between IGF2BP3 and the mRNA decapping complex.

IGF2BP3's KH domains are responsible for RNA recognition, whereas its RRM domains bind RNA with relatively low affinity and specificity [46, 62]. In other RNA-binding proteins, the RRM domains also participate in protein–protein interactions [63]; we now show that RRM2 mediates IGF2BP3's binding to EDC3 and does not overlap with RNA-binding by the RRM1 domain [62] (**Fig. 5K**). Similarly, EDC3 dimerization is mediated by its YjeF domain, and the IGF2BP3 binding does not interfere with its self-association [64]. To summarize, our findings converge on the model that the increased association of IGF2BP3 with the mRNA decapping complex shifts its function towards promoting target transcript degradation during ER stress.

Discussion

Among its many essential functions, the ER is the site for the folding and maturation of secreted and transmembrane proteins, which form approximately one-third of the proteome. Cells need to rapidly adapt to changes in ER protein folding demands, as the separation of protein synthesis and folding in two distinct compartments poses a challenge. To overcome this, cells use diverse post-transcriptional and translational mechanisms to adjust the protein folding load in the ER. Here, we discovered that IGF2BP3-driven post-transcriptional mechanisms facilitate

mRNA degradation, as well as indirectly tune transcription to generate gene regulatory networks that control UPR signaling while relieving protein-folding load on the ER.

Based on our published proteomics data on the interaction of the ER stress sensor RNase IRE1 with IGF2BP3, here we explored the potential role of IGF2BP3 in post-transcriptional regulation of mRNA fate during ER stress. Our IR-PAR-CLIP analyses supported a model where IGF2BP3 predominantly binds to UPR target transcripts during ER stress, including those encoding the three master UPR transcription factors, XBP1, ATF4, and CHOP. Using complementary approaches to probe for post-transcriptional and transcriptional (RNA-Seq and SLAMseq) changes upon IGF2BP3 depletion, we discovered a dual regulatory role mediated by IGF2BP3-driven post-transcriptional control that maintains cellular homeostasis during ER stress. While IGF2BP3 destabilizes most of its target mRNAs under ER stress conditions, it stabilizes a subset of its target mRNAs, including key transcriptional regulators. Notably, the SLAMseq analyses revealed that an IGF2BP3-driven transcriptional feedback loop indirectly leads to the upregulation of many UPR genes. This IGF2BP3-driven dual regulation allows cells to downregulate the expression of most of the IGF3BP3 target transcripts while upregulating UPR targets essential for adaptation to ER stress. This helps cells to decrease cellular folding burden while enabling them to efficiently express UPR target mRNAs. While the transcription factor that drives the IGF2BP3-driven feedback mechanism is unknown, multiple transcription factors are downregulated upon IGF2BP3 depletion, making them potential candidates. Major UPR transcription factors, including XBP1s and ATF6N, are bZIP transcription factors that form heterodimers that combinatorially regulate the UPR [65]. It is also plausible that IGF2BP3-regulated bZIP transcription factors, such as FOSL2 or the ATF6 paralogue CREB3L2, might contribute to the transcriptional upregulation of UPR.

In addition to IGF2BP3-mediated regulation of UPR effector RNAs, our data revealed that ER stress leads to a functional switch in IGF2BP3, increasing its destabilizing function. IGF2BP3 stabilizes its target mRNAs during heat shock stress [29], suggesting that IGF2BP3 can drive opposing outcomes for its target transcripts depending on the cellular input. This dynamic and plastic response aligns with the cellular need to adjust transcript levels rapidly during proteotoxic stress. In line with these observations, we discovered that ER stress modulates IGF2BP3 interaction with its canonical targets. IGF2BP3 stabilizes *HMGA2* mRNA by protecting it from miRNA-driven degradation [28]. During ER stress, IGF2BP3 binding to *HMGA2* mRNA decreased, resulting in less efficient stabilization of *HMGA2* transcript, and notably, this correlated with lower levels of *HMGA2*. HMGA2 regulates many biological processes involved in embryonic development, stem cell maintenance, and tumorigenesis [54, 66, 67]. The resulting lower levels of HMGA2 during ER stress might interfere with early developmental processes, indicating a broader impact of stress-dependent regulation by IGF2BP3.

Our IP-MS/MS analyses of IGF2BP3 revealed that IGF2BP3 strongly associates with all the components of the mRNA decapping complex, an interaction that increases around 50% during ER stress. Moreover, a high-throughput AlphaFold2-multimer screen identified a novel interaction surface between EDC3 and IGF2BP3 with high confidence, and an IGF2BP3 mutant engineered to disrupt this interaction was impaired in its binding to EDC3, supporting these

findings. We speculate that the increased association of IGF2BP3 with the mRNA decapping complex and RNase IRE1 enhances the degradation of its targets during ER stress. Future work will provide insights into the mechanisms that mediate the preferred association of the mRNA decapping complex with IGF2BP3 during ER stress.

IGF2BP3 is an essential regulator of early development, and its overexpression in various tumors correlates with poor prognosis and cancer aggressiveness [40, 48, 68]. Similarly, physiological UPR contributes to development and differentiation, while cancer cells hijack this process to promote their growth [69]. We hypothesize that the dual-layered regulation we have uncovered allows cells to shift between opposing IGF2BP3 regulatory effects on UPR targets implying a cell state-specific regulation. While this regulatory plasticity may contribute to exquisite regulation during development, the balance may be tipped in cancer and impact UPR-driven cell fate decisions, presenting a novel avenue for therapeutic targeting. To sum up, we discovered a novel IGF2BP3-mediated dual regulatory mechanism that ensures an adaptive response to ER stress.

Declaration of interests

S.L.A. declare competing interests based on a granted patent related to SLAMseq. S.L.A. is co-founder, advisor, and member of the board of QUANTRO Therapeutics GmbH.

Acknowledgments

We are grateful to Niko Popitsch for support with the transcriptomics experiments and analyses of sequencing data. We are thankful to the Vienna BioCenter Next-Generation Sequencing Facility for deep sequencing services and Max Perutz Labs Proteomics Facility for mass spectrometry analyses. We thank Roland Foisner and Nana Naetar-Kerenyi for their input on CRISPR/Cas9 editing. We thank Sabina Omerbegovic and Erinc Hallacli for valuable assistance with co-immunoprecipitation experiments. RKO cells were a kind gift of the Johannes Züber lab. G.E.K. acknowledges funding from the Austrian Science Fund (FWF-SFB F79). For open access purposes, the author has applied a CC-BY public copyright license to any author-accepted manuscript version arising from this submission. A.S.A. is supported by the DOC Fellowship Programme of the Austrian Academy of Sciences.

Author Contributions

ASA and GEK conceived the project. ASA designed and performed most of the experiments. SLA, GV, and GEK supervised experimental procedures. HH and IF performed imaging experiments. ASA and GEK wrote the first draft, and all the authors edited the manuscript. GEK acquired funding.

Materials and methods

Mammalian cell culture

Mouse Embryonic Fibroblasts (MEF) expressing doxycycline-inducible GFP-IRE1 [70] were established in previous work [71]. HCT116 WT cells were a kind gift from the Manuela Baccarini Lab (Max Perutz Labs). HCT116 cells conditionally expressing doxycycline-inducible (tetON) OsTIR1 were obtained from the Masato Kanemaki lab [72]. RKO cells expressing doxycycline-inducible Cas9 were a kind gift from Johannes Zuber (IMP, Vienna, Austria) [73]. HEK293T cells expressing splitGFP-IGF2BP3 were a kind gift of Manuel Leonetti established using published protocols [74]. HEK293T cells expressing split mNeonGreen-EDC3 were a kind gift of Manuel Leonetti (Chen-Zuckerberg Biohub, USA [75]).

HCT116 cells were cultured in McCoy's 5A (modified) medium (Sigma, M9309) supplemented with 10% fetal bovine serum (Gibco, 10437028), 2 mM L-Glutamine (Sigma, G7513), 1% Pen/Step (Sigma, P0781). MEF and HEK293T cells were cultured in high-glucose DMEM media (Sigma, D5796) supplemented as above. RKO cells were cultured in RPMI-1640 media (Sigma, R8758) supplemented with 10% fetal bovine serum (Gibco, 10437028), 2 mM L-Glutamine (Sigma, G7513), 1% Pen/Step (Sigma, P0781), 1x non-essential amino acids (Thermo Scientific, 11140050), and 2 mM sodium pyruvate (Gibco, 11360070). All cell lines were cultured in a humidified incubator at 37°C and 5% CO2 and regularly tested for Mycoplasma infection with the EZ-PCR™ Mycoplasma Detection Kit (Biological Industries).

Western blotting

80% confluent cells were lysed with RIPA buffer (150 mM NaCl, 1% NP-40, 0.5% Sodium deoxycholate, 0.1% SDS, and 25 mM TRIS pH 7.4) with 1x EDTA-free protease inhibitor cocktail (Roche). Lysates were clarified using a table-top centrifuge at maximum speed (20,000 g) for 20 min at 4°C. Western blot samples were denatured at 95 °C for 5 min in 1x SDS sample buffer (50 mM Tris-HCl pH 6.8, 2% SDS, 0.1% Bromophenol blue, 10% glycerol, 20 mM DTT). Following denaturing, the samples were loaded onto a 10%, 12% or 15% sodium dodecyl sulfate (SDS) gel. Proteins were transferred onto a 0.2 µm nitrocellulose membrane (Amersham) using BioRad Trans-Blot Turbo Transfer System or with wet transfer in transfer buffer (25 mM TRIS, 190 mM glycine, 20% ethanol) for 110 min at 120 V. Membranes were stained with Ponceau S and blocked in 5% milk for 1 hour. The primary antibody (**Supp. Table 5**) was diluted in 2.5% milk and incubated overnight at 4 °C. The membrane was washed 5 times with TBST (20 mM TRIS, 150 mM NaCl, 0.1% Tween 20), and the membranes were incubated for 1 h with the secondary antibody (**Supp. Table 5**) diluted in 2.5% milk. After the incubation the membranes were washed 5 times with TBST. Membranes were developed with enhanced chemiluminescent (ECL) horse radish peroxidase substrate (WESTAR ETA C ULTRA 2.0, Cyanagen), imaged using BioRad ChemiDoc, and analyzed using ImageLab software (6.1.0).

Co-Immunoprecipitation of GFP-IRE1

Two ø15 cm dishes of 80% confluent MEF GFP-IRE1 cells were used per condition. To induce ER stress, cells were treated with 5 µg/mL tunicamycin (TM) for 4 hours (if other time is not indicated), DMSO in 1:1000 dilution was used a control. Cells were washed with ice-cold PBS

and collected by scraping and pelleting at 500 g at 4°C for 5 min. Cells were lysed in 250 µL of lysis buffer (25 mM HEPES pH 7.3, 150 mM NaCl, 1% NP-40, 1 mM EDTA, 10% Glycerol, 1x EDTA-free protease inhibitor cocktail, 0.4 U/µL RNasin RNase inhibitor) per condition by incubation on ice 10 min with intermittent vortexing. The lysate was clarified with two steps of centrifugation at 4°C 1,000 g for 5 min and 13,000 g for 15 min. The immunoprecipitation (IP) was performed with GFP-trap magnetic beads (ChromoTek). 40 µL of bead slurry was used for two ø15 cm dishes. The lysate was incubated with the GFP-trap beads for 2 hours at 4°C and the beads were washed 3 times with 1 mL of ice-cold lysis buffer. For RNase digestion 0.1 U/µL of RNase I (Ambion) and 1 U/µL of RNase T1 (EN0541) were added to the second wash. For the control (undigested) samples 1 U/µL of RNasin RNase inhibitor was added. Samples were incubated at room temperature for 10 min on a rotator. Proteins were eluted in 25 µL of 1x SDS sample buffer at +95 °C for 5 min, loaded on SDS-PAGE and analyzed by western blotting as described above with anti-IGF2BP3, anti-GFP and anti-GAPDH antibodies (**Supp. Table 5**).
For the GFP-IGF2BP3 co-IP from HEK293T followed by IRE1 western blotting same conditions were used as for MEF cells. One ø15 cm dish was used per condition; to induce ER stress, the cells were treated with 5 µg/mL TM for the indicated timelines or for 4 hours.

IR-PAR-CLIP of IGF2BP3

IGF2BP3 IR-PAR-CLIP library preparation and data processing

The detailed protocol for the infrared (IR) PAR-CLIP of IGF2BP3 is described in (Anisimova, Karagöz, 2023). 125 million (5x ø15 cm dishes) HCT116 inducible tetON OsTIR1 cells were used per condition. 100 µM 4sU (Sigma) was added to the cell culture media 15 h prior to collection. ER stress was induced with 5 µg/mL TM for 4 hours prior to collection. DMSO in 1:1000 dilution was used a control. IGF2BP3 was immunoprecipitated with anti-IGF2BP3 Proteintech antibody (14642-1-AP, lot 00088732). anti-IgG Proteintech antibody (30000-0-AP) was used as a control. RNase I (Ambion) was used for the in-lysate RNase digestion at 0.1 U/µL and for the on-bead digestion in 1 mL of the lysis buffer at 0.025 U/µL. IR-PAR-CLIP libraries were sequenced on a NovaSeq 6000 S1 on SR100 (Illumina) at the Vienna BioCenter NGS facility with 55 million reads per sample on average. UMIs were extracted and adapter sequences were trimmed using UMI-tools v1.1.1 (Smith et al. 2017). The reads were size- and quality-trimmed using Trimmomatic v0.30 (Bolger et al. 2014) to have a length between 18 and 45 nt. The reads were then mapped to human genome hg38 using GENCODE annotation (release 36) with bowtie v0.12.7 (Langmead et al. 2009), allowing up to three mismatches and deduplicated using UMI-tools v1.1.1. Gene counts were obtained using the FeatureCounts function of the Subread package v2.0.1[76]. Gene counts for protein coding genes were RLE normalized to calculate the counts per million values (CPM), filtered to only include genes with CPM higher than 5 in at least one third of the libraries, and the differential expression analysis was performed with edgeR glmQLFTest (Generalized Linear Model Quasi-Likelihood F-test) [77]. GO term analysis was performed with Enrichr webserver [78, 79]. Redundancy in GO terms was reduced using GOSemSim [80] and rrvgo [81]. Full GO term enrichment lists are shown in supplementary materials.

IR-PAR-CLIP matching transcriptome library preparation and data processing

An aliquot of the lysate was taken before the in-lysate RNase digest for total RNA isolation and sequencing. Total RNA was isolated using peqGOLD TriFast (Peqlab, VWR) and transcriptome libraries were prepared with QuantSeq 3' mRNA-Seq Library Prep Kit (Lexogen). Libraries were sequenced on a NextSeq2000 P2 at SR100 mode (Illumina) at the Vienna BioCenter NGS facility with 30 million reads per sample on average. The quality-, adapter-, and polyA-trimmed reads were aligned to human genome hg38 using GENCODE annotation (release 36) with STAR v2.7.5c. As the reads originate from cross-linked PAR-CLIP samples and have T to C transitions, mismatches were allowed. Gene counts for protein coding genes were RLE normalized to calculate the counts per million values (CPM), filtered to only include genes with a CPM higher than 1 in at least half of the libraries. Differential expression analysis was performed with edgeR glmQLFTest [82].

IR-PAR-CLIP computational analysis

To estimate relative binding of IGF2BP3, IR-PAR-CLIP CPMs were divided to the matching total transcriptome QuantSeq CPMs. A pseudocount of 1 CPM was added to all samples and only genes with mean CPM for QuantSeq samples greater than 5 CPM were taken for the analysis. To identify IGF2BP3 target genes, IGF2BP3-binding clusters were called with PARalyzer v1.5 [45] (ini file is available in **Supp. Table 5**). Genes that had at least one cluster containing more than 25 CPM and more than 50% of T to C conversions per read in two replicates (number 2 and 3) per condition were selected as IGF2BP3 targets. Samples from replicate 1 were excluded from target identification due to lower final read number and therefore lower number of identified clusters and targets. The target lists were filtered to only include targets with PAR-CLIP CPMs higher than total transcriptome QuantSeq CPMs. PAR-CLIP genomic tracks were visualized using svist4get v1.2.20 [83]. The enrichment of 5-nt motifs in IGF2BP3 PAR-CLIP reads was analyzed with HOMER v4.11 [84], findMotifs.pl command using shuffled background. Sequencing data processing was done using the HPC of the Center for Integrative Bioinformatics Vienna (CIBIV) and Life Science Compute Cluster (LiSC) of the University of Vienna, Austria.

Establishment of IGF2BP3 knockout cell lines and siRNA knockdown

For IGF2BP3 knockout cell line generation, gRNA sequences (clones E4 and A3: 5′TGGCACCGACTGATAGAGCT 3′; clone D12: 5′ACGCGTAGCCAGTCTTCACC 3′) were cloned into the pSpCas9 (BB)-2A-GFP (PX458) (plasmid #48138; Addgene) [85]. HCT116 tetON OsTIR1 cells were transiently transfected using jetOPTIMUS reagent (Tamar, 101000051), and GFP-positive single-cell clones were FACS sorted at BD FACSAria IIIu at Max Perutz Labs BioOptics FACS Facility. HCT116 cells do not express IGF2BP1 [86]. For siRNA knockdown, HCT116 cells (WT or tetON OsTIR1) or RKO iCas9 were transfected with IGF2BP3 (Dharmacon, L-003976-00-0005) SMARTpool siRNAs using DharmaFECT 2 (Dharmacon, T-2002-01) at 75 nM for 48 hours. ON-TARGETplus nontargeting siRNA pool (Dharmacon, D-001810-10-05) was used as a control.

Total transcriptome sequencing (RNA-Seq) of IGF2BP3 KO HCT116 cells

HCT116 tetON OsTIR1 IGF2BP3 KO clones E4, A3, and D12 (in duplicates) and parental cells (four replicates) were treated with 5 µg/mL TM for 4 hours (1:1000 DMSO was used as a control). Total RNA was isolated using peqGOLD TriFast (Peqlab, VWR), treated with RNase-

free DNase I (NEB), and re-purified with peqGOLD TriFast (Peqlab, VWR). RNA precipitation was done using the isopropanol method. Total RNA sequencing libraries were prepared with NEBNext Poly(A) mRNA Magnetic Isolation Module (NEB, E7490L) and NEBNext Ultra II Directional RNA Library Prep Kit (NEB, E7765L) by Vienna BioCenter NGS facility sequenced on a NovaSeq S4 on PE100 (Illumina) with 55 million reads per sample on average. The quality- and adapter-trimmed reads were aligned to human genome hg38 using GENCODE annotation (release 36) with STAR v2.7.5c allowing up to two mismatches per read. Gene counts for protein coding genes were RLE normalized to calculate the counts per million values (CPM), filtered to only include genes with CPM higher than 5 in at least half of the libraries, and differential expression analysis was performed with edgeR glmQLFTest [82].

RNA-Seq of HCT116 cells upon siRNA-mediated depletion of IGF2BP3

HCT116 WT cells were depleted of IGF2BP3 using siRNA pools as described in "Establishment of IGF2BP3 knockout cell lines and siRNA knockdown" section. ER stress was induced with 5 µg/mL TM for 4 hours prior to collection. One ~80% confluent well of a 6-well plate per condition (three biological replicates per condition) was washed with ice-cold PBS (Sigma) supplemented with 100 mg/mL cycloheximide, lysed on a plate on ice with 350 µL of ice-cold lysis buffer (20 mM HEPES pH 7.3, 150 mM KCl, 5 mM MgCl2, 1% Triton X-100, 100 mg/mL cycloheximide, 1 mM DTT, 1x EDTA-free protease inhibitor cocktail), scraped, and transferred to 1.5 mL RNase-free tube. Cell lysates were passed three times through the 27G needle, incubated on ice for 10 min with intermittent vortexing, and clarified on a table-top centrifuge at maximum speed (20,000 g) for 20 min at 4°C. Total RNA was extracted from 15 µL of the lysate using KingFisher Flex Purification System (Thermo) with the High-Performance RNA Isolation kit (Molecular Tools Shop, Vienna BioCenter). RNA-Seq libraries were prepared with NEBNext Poly(A) mRNA Magnetic Isolation Module (NEB, E7490L) and NEBNext Ultra II Directional RNA Library Prep Kit (NEB, E7765L) and sequenced on a NovaSeq SP on SR100 (Illumina) with 30 million reads per sample on average. The quality- and adapter-trimmed reads were aligned to human genome hg38 using GENCODE annotation (release 36) with STAR v2.7.5c allowing up to two mismatches per read. Gene counts for protein coding genes were filtered to include genes with coding sequence length-normalized CPM values higher than 5 in at least one third of the libraries. Differential expression analysis was performed with edgeR glmQLFTest [82].

Establishment of doxycycline-inducible IGF2BP3 knockout RKO cell lines

RKO-Dox-Cas9 (iCas9) cell lines for doxycycline-inducible knockout IGF2BP3 were established using lentiviral transduction with lentiviral particles (produced as described in [87] containing Dual-sgRNA_hU6-mU6 vectors described in [73] expressing two sgRNAs against IGF2BP3 (5′ TGGCACCGACTGATAGAGCT 3′ and 5′ GAAGATACTTTCTAGGTCCG 3′) or against non-coding locus AAVS1 (5' CGCTGTGCCCCGATGCACAC 3' and 5′ GGCGCGTCGCTCGCTCGCTC 3′) from human and mouse U6 promoters and eBFP2 from a PGK promoter. The eBFP2-positive cells were FACS sorted at BD FACSMelody™ Cell Sorter at Max Perutz Labs BioOptics FACS Facility.

Comparison of the RKO transcriptome upon doxycycline-inducible Cas9- and siRNA-mediated depletion of IGF2BP3IGF2BP3 depletion was induced in RKO iCas9 cells with 250

ng/mL doxycycline for 72 hours. siRNA-mediated depletion was performed in RKO iCas9 as described in the “Establishment of IGF2BP3 knockout cell lines and siRNA knockdown” section. RKO transcriptome was obtained using SLAMseq protocol [49]. 4-thiouridine (s^4U) was added to cell culture media at 250 μM 2 hours prior collection. Total RNA was extracted using the KingFisher Flex Purification System (Thermo) with the High-Performance RNA Isolation kit (Molecular Tools Shop, Vienna BioCenter). During the isolation RNA was treated with RNase-free DNase I (NEB). Samples were prepared according to the standard SLAMseq protocol described in [49]. Briefly, total RNA was alkylated with 10 mM iodoacetamide in alkylation buffer (50 mM sodium phosphate buffer pH 8.0, 50% DMSO) at 50°C for 15 min and purified using the KingFisher Flex Purification System. Sequencing libraries were prepared with NEBNext Poly(A) mRNA Magnetic Isolation Module (NEB, E7490L) and NEBNext Ultra II Directional RNA Library Prep Kit (NEB, E7765L) and sequenced on a NovaSeq SP on SR100 (Illumina) at the Vienna BioCenter NGS facility with 30 million reads per sample on average. The quality- and adapter-trimmed reads were aligned to human genome hg38 using GENCODE annotation (release 36) with STAR v2.7.5c allowing up to five mismatches per read. Total gene counts for protein coding genes were analyzed and genes were filtered to include those with coding sequence length-normalized CPM > 5 in at least half of the libraries. Differential expression analysis was performed with edgeR glmQLFTest [82]. The data were processed using the HPC of the Center for Integrative Bioinformatics Vienna (CIBIV).

Identification of siRNA pool off-targets from siRNA knockdown experiments

To exclude possible siRNA off-target genes we compared changes in gene expression upon doxycycline-inducible knockout and siRNA-mediated depletion of IGF2BP3 in RKO iCas9 cells. Genes were considered off-targets if changes in their levels were more than 20% upon siRNA-mediated depletion, but less than 10% upon doxycycline-inducible knockout. Significance was not considered for this analysis due to overall small amplitude of changes. The identified off-targets are listed in **Supp. Table 2**. These genes were excluded from analyses of experiments where IGF2BP3 was depleted with siRNA pools.

SLAMseq of HCT116 upon siRNA-mediated depletion of IGF2BP3

HCT116 WT cells were depleted of IGF2BP3 using siRNA pools as described in “Establishment of IGF2BP3 knockout cell lines and siRNA knockdown” section. ER stress was induced in using a 5 hour-long treatment with 5 μg/mL TM (1:1000 DMSO was used as a control). 4-thiouridine (s^4U) was added to cell culture media at 250 μM 2 hours prior collection. Total RNA was extracted using the KingFisher Flex Purification System (Thermo) with the High-Performance RNA Isolation kit (Molecular Tools Shop, Vienna BioCenter). During the isolation RNA was treated with RNase-free DNase I (NEB). SLAMseq samples were prepared according to the standard SLAMseq protocol described in [49]. Briefly, total RNA was alkylated with 10 mM iodoacetamide in alkylation buffer (50 mM sodium phosphate buffer pH 8.0, 50% DMSO) at 50°C for 15 min and purified using the KingFisher Flex Purification System. Sequencing libraries were prepared with NEBNext Poly(A) mRNA Magnetic Isolation Module (NEB, E7490L) and NEBNext Ultra II Directional RNA Library Prep Kit (NEB, E7765L) and sequenced on a NovaSeq SP on SR100 (Illumina) at the Vienna BioCenter NGS facility with 30 million reads per sample on average. The SLAMseq fastq files were trimmed and aligned to human genome hg38

using the nf-core/slamseq analysis pipeline v1.0.0 [88, 89] with default parameters. Genes were filtered to only include those with both total and T-C CPM > 5 for at least half of the samples. The differential expression analysis was performed with edgeR glmQLFTest [82]). Sample siControl ER stress replicate 3 was a clear outlier on a PCA plot and was excluded from analysis. The data were processed using the Life Science Compute Cluster (LiSC) of the University of Vienna.

RNA isolation and RT-qPCR

Total RNA was isolated using the KingFisher Flex Purification System (Thermo) with the High-Performance RNA Isolation kit (Molecular Tools Shop, Vienna BioCenter). During the isolation RNA was treated with DNase I (M0303S, NEB). cDNA was prepared with LunaScript RT SuperMix (NEB) and amplified in a qPCR reaction with 2x Hot Start qPCR master mix (Molecular Tools Shop, Vienna BioCenter) using BioRad CFX 384 Touch machine. The qPCR primers are listed in **Supp. Table 5**. mRNA levels were calculated relative to *RPL6* levels.

Co-Immunoprecipitation of endogenous IGF2BP3 followed by mass spectrometry

One ø15 cm dish of 80% confluent HCT116 WT cells was used per condition. To induce ER stress, cells were treated with 5 µg/mL tunicamycin (TM) for 4 hours, and DMSO at 1:1000 dilution was used as a control. Cells were washed with ice-cold PBS and collected by scraping and pelleting at 500 g at 4°C for 5 min. Cells were lysed in 250 µL of lysis buffer (25 mM HEPES pH 7.3, 150 mM NaCl, 0.5% NP-40, 0.5 mM EDTA, 10% Glycerol, 1x EDTA-free protease inhibitor cocktail, 1x PhosSTOP) per condition by incubation on ice 15 min with intermittent vortexing. The lysate was clarified by centrifugation at 20,000 g for 20 min at 4°C. 10 µg of Proteintech anti-IGF2BP3 antibody (14642-1-AP, lot 00088732) or Proteintech IgG control (30000-0-AP) was coupled to the 40 µL of protein G Dynabeads (Invitrogen) in 1 mL of lysis buffer for 20 min, rotating at room temperature, washed three times with 1 mL of the lysis buffer, resuspended in the original bead volume (40 µL) and added to 200 µL of the clarified lysate. Beads were washed five times with 1 mL of wash buffer (25 mM HEPES pH 7.3, 150 mM NaCl, 0.5 mM EDTA, 10% Glycerol). Each wash was incubated on ice for 3 min. For RNase digestion 0.1 U/µL of RNase I (Ambion) and 1 U/µL of RNase T1 (EN0541) were added to the second wash. Samples were incubated at room temperature for 10 min on a rotator. The control (undigested) samples were kept on ice. The proteins were eluted from the beads with 20 µL 100 mM glycine pH 2.0 three times and the pooled supernatant was adjusted to alkaline using about 20 µL 1M Tris pH 8.0. Disulfide bonds were reduced with 3.2 µL of 250 mM dithiothreitol (DTT) for 30 min at room temperature before adding 3.2 µL of 500 mM iodoacetamide and incubating for 30 min at room temperature in the dark. Remaining iodoacetamide was quenched with 1.6 µL of 250 mM DTT for 10 min. Proteins were digested with 300 ng trypsin (Trypsin Gold, Promega) in 3 µL 50 mM ammonium bicarbonate at 37°C overnight. The digest was stopped by the addition of 10% trifluoroacetic acid (TFA) to a final concentration of 0.5%. The peptides were desalted using C18 Stagetips [90].

Liquid chromatography-mass spectrometry analysis

Peptides were separated on a Vanquish Neo nano-flow chromatography system (Thermo-Fisher), using a trap-elute method for sample loading (Acclaim PepMap C18, 2 cm × 0.1 mm, 5 µm, Thermo-Fisher), and a C18 analytical column (Acclaim PepMap C18, 50 cm × 0.075 mm, 2 µm, Thermo-Fisher), applying a segmented linear gradient from 2% to 35% and finally 80% solvent B (80 % acetonitrile, 0.1 % formic acid; solvent A 0.1 % formic acid) at a flow rate of 230 nL/min over 120min. Eluting peptides were analyzed on an Exploris 480 Orbitrap mass spectrometer (Thermo-Fisher Scientific) coupled to the column with a FAIMS pro ion-source (Thermo-Fisher Scientific) using coated emitter tips (PepSep, MSWil) with the following settings: The mass spectrometer was operated in DDA mode with two FAIMS compensation voltages (CV) set to -45 or -60 and 1.5 s cycle time per CV. The survey scans were obtained in a mass range of 350-1500 m/z, at a resolution of 60k at 200 m/z, and a normalized AGC target at 100%. The most intense ions were selected with an isolation width of 1.4 m/z, fragmented in the HCD cell at 30% collision energy, and the spectra recorded for max. 50 ms at a normalized AGC target of 100% and a resolution of 15k. Peptides with a charge of +2 to +6 were included for fragmentation, the peptide match feature was set to preferred, the exclude isotope feature was enabled, and selected precursors were dynamically excluded from repeated sampling for 45 seconds.

Proteomics data analysis

The RAW MS data were analyzed with FragPipe (20.0), using MSFragger (4.1) [91]. IonQuant (1.10.27) [92] and Philosopher (5.0.0) [93] . The default FragPipe workflow for label free quantification (LFQ-MBR) was used, except “Normalize intensity across runs” was turned off. Cleavage specificity was set to Trypsin/P, with two missed cleavages allowed. The protein FDR was set to 1%. A mass of 57.02146 (carbamidomethyl) was used as fixed cysteine modification; methionine oxidation and protein N-terminal acetylation were specified as variable modifications. MS2 spectra were searched against the human 1 protein per gene reference proteome from Uniprot (Proteome ID: UP000005640, release 2024_01), concatenated with a database of 382 common laboratory contaminants (release 2023.03, https://github.com/maxperutzlabs-ms/perutz-ms-contaminants).

Computational analysis was performed using Python and the in-house developed Python library MsReport (version 0.0.24, [94]). LFQ protein intensities reported by FragPipe were log2-transformed and normalized across samples using the ModeNormalizer from MsReport. The missing normalized LFQ intensity values were imputed by drawing random values from a normal distribution after filtering out contaminants, proteins with less than 2 peptides and less than 2 quantified values in at least one group. Differences between groups were statistically evaluated using the LIMMA 3.52.1 [95] at 5% FDR (Benjamini-Hochberg). The in-house Python library XlsxReport (0.1.0) was used to create a formatted Excel file summarizing the results of protein quantification. Proteins were filtered to only include those that have at least 6 identified peptides and 24 spectral count events, both summed across all samples. Proteins were considered IGF2BP3 interactors if their normalized LFQ values were enriched more than 4 times over IgG control, *P* value adj. < 0.05 at least in one treatment condition. GO term analysis was performed with Enrichr webserver [78]. Redundancy in GO terms was reduced using GOSemSim [79, 80] and rrvgo [81]. Full GO term enrichment lists are shown in supplementary materials.

Co-Immunoprecipitation of GFP-IGF2BP3 and mNeonGreen-EDC3

One ø15 cm dish of 80% confluent HEK293T split GFP-IGF2BP3 or split mNeonGreen-EDC3 cells was used per condition. Parental HEK293T split GFP cells were used as a background control. To induce ER stress, cells were treated with 5 µg/mL tunicamycin (TM) for 4 hours (if other time is not indicated), DMSO in 1:1000 dilution was used a control. Cells were washed with ice-cold PBS and collected by scraping and pelleting at 500 g at 4°C for 5 min. Cells were lysed in 250 µL of lysis buffer (25 mM TrisHCl pH 7.4, 100 mM KCl, 0.5% NP-40, 10% Glycerol, 1x EDTA-free protease inhibitor cocktail, 1 U/µL Murine RNase inhibitor (NEB)) per condition by incubation on ice for 10 min. The lysate was clarified by centrifugation at 4°C 20,000 g for 20 min. The GFP-IGF2BP3 IP was performed using 40 µL of GFP-trap magnetic beads (ChromoTek) per condition. 20 µL of mNeonGree-trap magnetic beads (ChromoTek) per condition were used for mNeonGreen-EDC3. The lysate was incubated with the beads beads for 1 hour at 4°C with addition of 2 U/µL of RNase I (Ambion) and the beads were washed 5 times with 0.2 mL of ice-cold lysis buffer. Proteins were eluted in 25 µL of 1x SDS sample buffer at +95 °C for 5 min, loaded on SDS-PAGE and analyzed by western blotting as described above with anti-IGF2BP3, anti-EDC4, and anti-EDC3 antibodies (**Supp. Table 5**).

***In silico* screening of IGF2BP3 protein-protein interactions**

Protein-protein interaction screening of IGF2BP3 was performed using the AlphaFold2 Multimer [57-59] via the HT-ColabFold pipeline [96] . To this end pairwise interactions were analyzed for full length IGF2BP3 (O00425, IF2B3_HUMAN) versus IGF2BP3 interactors identified using co-IP-MS. In total 1213 predictions were made. PEAKscore was used to evaluate the prediction of the interaction. It represents the inverse, scaled (0-1) minimum Precision Alignment Error (PAE) between analyzed chains. HT-ColabFold screening was done using the HPC of the Center for Integrative Bioinformatics Vienna (CIBIV) and Life Science Compute Cluster (LiSC) of the University of Vienna, Austria.

The interactions between the separate domains of IGF2BP3 and EDC3 were analyzed using AlphaFold 3 [60]. The domain separation was defined using the following boundaries: IGF2BP3 (O00425, IF2B3_HUMAN) RRM1/2 – aa 1-195, linker1-KH1/2 – aa 160-350, KH1/2-linker2 – aa 196-405, linker2-KH3/4 - aa 343-579; EDC3 (Q96F86, EDC3_HUMAN) SM – aa 1-68, YjeF - aa 283-487.

Co-Immunoprecipitation of GFP-EDC3 and 3xFLAG-IGF2BP3 WT and 4A mutant

One well of 6-well plate was used per condition. ~70% confluent HCT116 tetON OsTIR1 IGF2BP3 KO cells clone A3 were transfected with transient expression plasmids expressing free eGFP (pEGFP-C1) or eGFP-EDC3 (pT7-EGFP-C1-HsEDC3) and 3xFLAG-hsIGF2BP3 WT or 4A mutant (this study). pT7-EGFP-C1-HsEDC3 was a gift from Elisa Izaurralde (Addgene plasmid # 25032). Cells were transfected with a total of 1 µg of DNA with jetOptimus reagent (Polyplus) according to the manufacturer's instructions. Cells were washed with ice-cold PBS and lysed in 200 µL of lysis buffer (25 mM TrisHCl pH 7.4, 100 mM KCl, 0.5% NP-40, 10% Glycerol, 1x EDTA-free protease inhibitor cocktail, 1 U/µL Murine RNase inhibitor (NEB)) per condition by incubation on ice for 10 min. The lysate was clarified by centrifugation at 4°C 20,000 g for 20 min. The lysate was incubated with the 20 µL GFP-trap beads for 1 hour at 4°C

with addition of 2 U/µL of RNase I (Ambion) and the beads were washed 5 times with 0.2 mL of ice-cold lysis buffer. Proteins were eluted in 25 µL of 1x SDS sample buffer at +95 °C for 5 min, loaded on SDS-PAGE and analyzed by western blotting as described above with anti-GFP and anti-FLAG antibodies (**Supp. Table 5**).

Data deposition

Next-generation sequencing data have been deposited in GEO with the following identifiers:
GSE289214 – RNA-Seq of HCT116 cells upon IGF2BP3 CRISPR/Cas9 knockout in control and ER stress conditions
GSE289023 – IR-PAR-CLIP of IGF2BP3 in HCT116 cells in control and ER stress conditions
GSE289024 – transcriptome (QuantSeq) of HCT116 cells in control and ER stress conditions matching IR-PAR-CLIP samples
GSE289424 – transcriptome (RNA-Seq) of HCT116 cells upon IGF2BP3 siRNA knockdown knockout in control and ER stress conditions
GSE289482 – SLAMseq of HCT116 cells upon IGF2BP3 knockdown in control and endoplasmic reticulum (ER) stress conditions
GSE289480 – SLAMseq of doxycycline-inducible knockout and siRNA-mediated depletion of IGF2BP3 in RKO iCas9 cells.

Mass spectrometry proteomics data have been deposited at the ProteomeXchange Consortium via the PRIDE partner repository [97] with the dataset identifier PXD060548.

Figure Legends

Figure 1. IGF2BP3 interacts with the UPR target mRNAs.
A. Western blot of IGF2BP3 showing its association with IRE1 after immunoprecipitation of GFP-IRE1 from mouse embryonic fibroblasts treated with ER stress-inducing drug tunicamycin at 5 µg/mL for 4 hours with or without RNase in the washes **B.** Quantification of A. **C.** Barplots showing normalized read count numbers (CPM) for IGF2BP3-bound reads (IR-PAR-CLIP) and total transcript levels (QuantSeq) of selected UPR target genes upon ER stress induction with TM at 5 µg/mL for 1 and 4 hours. Values are the mean ± s.d of n=3 biological replicates. *P* values were calculated by two-sided Student's t-test. **D.** Volcano plot showing changes in IGF2BP3 IR-PAR-CLIP CPM upon ER stress treatment. *P* values were calculated by edgeR glmQLFTest. **E.** Scatter plot comparing changes in IGF2BP3 IR-PAR-CLIP read counts with the total transcriptome changes (QuantSeq) upon ER stress treatment. **F.** Boxplot showing changes in IGF2BP3 binding (IR-PAR-CLIP CPM / QuantSeq CPM) to all genes and UPR upregulated genes (upregulated more than two-fold in ER stress than in control, *P* value adj. < 0.05, total RNA-Seq) upon ER stress and control conditions. *P* values were calculated by two-sided Wilcoxon test. **G.** Representative IGF2BP3 IR-PAR-CLIP coverage examples. Where not indicated otherwise, ER stress was induced with tunicamycin at 5 µg/mL for 4 hours. **P* < 0.05; ***P* < 0.01; ****P* < 0.001; *****P* < 0.0001.

Supplementary Figure 1.

A. Histogram showing the distribution of fold changes in normalized peptide intensity values of IRE1 interaction partners upon ER stress (crosslinking mass spectrometry data from Acosta-Alvear, Karagöz et al., 2018 [25]). Proteins identified in IgG or non-crosslinking controls were excluded from the analysis (n = 126). **B.** Western blot of IRE1 showing its association with IGF2BP3 after immunoprecipitation of GFP-IGF2BP3 from HEK293T cells treated with ER stress-inducing drug tunicamycin (TM) at 5 µg/mL for 4 hours. **C.** Barplots showing numbers of total and T-C containing unique deduplicated IR-PAR-CLIP read counts per library before normalization. **D.** Venn diagram showing the intersection of IGF2BP3 IR-PAR-CLIP targets in DMSO control and ER stress conditions (4-hour treatment with 5 µg/mL tunicamycin). **E.** GO term analysis of 157 IGF2BP3-bound transcripts identified in only in ER stress conditions **F.** GO term analysis of 2470 IGF2BP3-bound transcripts identified in either control or ER stress conditions. **G.** Feature length-normalized aggregated IGF2BP3 IR-PAR-CLIP coverage of genomic features. **H.** 5nt-long consensus motifs enriched in IGF2BP3 IR-PAR-CLIP reads over scrambled control in control and ER stress conditions (4 hr). Motif enrichment analysis was performed using HOMER software. **I.** Volcano plot showing changes in IGF2BP3 binding (IR-PAR-CLIP CPM / QuantSeq CPM) upon ER stress and control conditions. n=3 biological replicates. *P* values were calculated by edgeR glmQLFTest. **J.** Venn diagram showing the intersection between IGF2BP3 and IRE1 PAR-CLIP targets [25] in control and ER stress conditions. **K.** IGF2BP3 IR-PAR-CLIP coverage of IRE1 targets *XBP1* and *CD59*.

Figure 2. IGF2BP3 depletion dampens the unfolded protein response.

A. Volcano plot of transcriptome (RNA-seq) changes upon IGF2BP3 KO in control (left panel) and ER stress conditions (right panel). *P* values were calculated by edgeR glmQLFTest. **B.** Volcano plot of transcriptome (RNA-seq) changes upon ER stress treatment showing the selection of IGF2BP3-bound UPR targets (left panel), and volcano plot upon IGF2BP3 KO in ER stress conditions with highlighted UPR targets (upregulated more than two-fold in ER stress than in control, *P* value adj. < 0.05, total RNA-Seq) and IGF2BP3-bound UPR targets (right panel). *P* values were calculated by edgeR glmQLFTest. **C.** Boxplot showing changes in transcript levels upon IGF2BP3 KO for IGF2BP3-bound transcripts, UPR targets, and IGF2BP3-bound UPR targets. *P* values were calculated by two-sided Wilcoxon test. **D.** Boxplot showing changes in transcript levels upon siRNA-mediated IGF2BP3 for IGF2BP3-bound transcripts, UPR targets, and IGF2BP3-bound UPR targets. *P* values were calculated by two-sided Wilcoxon test. **E.** RT-qPCR analyses of IGF2BP3 KO and parental cells treated with 100 ng/mL for 7 hours. n=4 biological replicates. *P* values were calculated by two-sided Student's t-test. **P* < 0.05; ***P* < 0.01; ****P* < 0.001; *****P* < 0.0001.

Supplementary Figure 2.

A. Western blot of parental and IGF2BP3 KO HCT116 cell lines (clones A3, D12 and E4). * marks IGF2BP2 isoforms recognized by polyclonal anti-IGF2BP3 antibody. **B.** GO term analysis of genes downregulated in IGF2BP3 KO comparing to parental cells during ER stress. edgeR glmQLFTest *P* value adj. < 0.05. **C.** Western blot showing depletion of IGF2BP3 after 48-hour treatment with siRNA against IGF2BP3 compared to control siRNA. **D.** Quantification of C.

Figure 3. IGF2BP3 shapes the UPR through transcriptional feedback loops.

A. Design of thiol (SH)-linked alkylation for the metabolic sequencing of RNA (SLAMseq) experiment. IGF2BP3 is depleted for 48 hours using siRNA. For the last 5 hours before collection cells were treated with tunicamycin at 5 µg/mL or with DMSO as a control. In the last 2 hours 100 µM 4-thiouridine (s^4U) was added to the cells to label the newly synthesized mRNA. **B.** Boxplot showing changes in *de novo* transcripts levels of UPR targets (transcribed during 2-hour s^4U pulse) T-C (SLAMseq T-C CPM) upon siRNA-mediated depletion of IGF2BP3. *P* values were calculated by two-sided Wilcoxon test. **C.** Barplots showing SLAMseq *de novo* (T-C) CPM values for selected UPR target genes (*XBP1*, *DDIT4*, and *DDIT3*). Values are the mean ± s.d of n=4 biological replicates. *P* values were calculated by two-sided Student's t-test. **D.** Boxplot showing changes in estimated transcript stability upon siRNA-mediated IGF2BP3 depletion for IGF2BP3-bound transcripts and IGF2BP3-bound UPR targets. The changes in transcript stability were assessed by analyzing the differences in average T-C conversion rates per gene following IGF2BP3 depletion. T-C conversion rate values indicate the relative abundance of both pre-existing and newly synthesized mRNA for a given gene, with a decrease in these values suggesting increased stabilization. *P* values were calculated by two-sided Wilcoxon test. **E.** RT-qPCR analyses of degradation rates for UPR target *XBP1* (spliced) upon siRNA-mediated depletion of IGF2BP3. HCT116 cells were treated with tunicamycin at 250 ng/mL for 4 hours and the transcription was blocked with 5 µg/mL ActD for indicated time points. Values are the mean ± s.e. of n=4 biological replicates. *P* values were calculated by paired two-sided Student's t-test. **F.** Barplots showing results of RT-qPCR analyses of *XBP1* (spliced) total mRNA level (relative to RPL6) in unstressed cells and cells treated with tunicamycin at 250 ng/mL for 4 hours. Arrows indicate the 1-hour ActD treatment time point selected for boxplot representation in E**.** *P* values were calculated by two-sided Student's t-test. *$P < 0.05$; **$P < 0.01$; ***$P < 0.001$; ****$P < 0.0001$.

Supplementary Figure 3.

A. Table showing $\log_2$(IGF2BP3 depletion / control) values for transcriptional regulators (GO:0140110) that were downregulated more than 10% or 5% upon IGF2BP3 CRISPR/Cas9- or siRNA-mediated depletion, respectively, under ER stress conditions.

Figure 4. IGF2BP3 facilitates the degradation of its target mRNAs during ER stress.

A. Boxplot showing changes in total transcript levels (RNA-seq) upon siRNA-mediated depletion of IGF2BP3 for all genes and IGF2BP3-bound transcripts in control and ER stress conditions. **B.** Volcano plots of total transcriptome changes (RNA-seq) upon siRNA-mediated IGF2BP3 depletion with regulated genes highlighted (ΔRNA-seq > 20% and *P* value adj. < 0.05). * marks the genes encoding transcriptional regulators. **C.** Barplots showing total RNA-seq CPM values normalized to siControl conditions for selected genes regulated by IGF2BP3. Values are the mean ± s.d of n=3 biological replicates. *P* values were calculated by paired two-sided Student's t-test. **D.** Barplots showing total RNA-seq CPM values for *HMGA2* and *ZFP36L1*. Values are the mean ± s.d of n=3 biological replicates. *P* values were calculated by paired two-sided Student's t-test. **E.** Barplots showing results of RT-qPCR analyses of *HMGA2* and *ZFP36L1* (mRNA levels relative to *RPL6*) in unstressed cells and cells treated with tunicamycin at 5 µg/mL for 6 hours upon siRNA-mediated depletion of IGF2BP3. Values are the mean ± s.d. of n=3 biological

replicates. *P* values were calculated by two-sided Student's t-test. **F**. RT-qPCR analyses of degradation rates for *HMGA2* and *ZFP36L1* upon siRNA-mediated depletion of IGF2BP3. HCT116 cells were treated with tunicamycin at 5 µg/mL for 3 hours and the transcription was blocked with ActD for indicated time points. Values are the mean ± s.e. of n=3 biological replicates. *P* values were calculated by paired two-sided Student's t-test. **P* < 0.05; ***P* < 0.01; ****P* < 0.001; *****P* < 0.0001.

Supplementary Figure 4.
A. Barplots showing SLAMseq *de novo* (T-C CPM) transcript levels for selected transcripts regulated by IGF2BP3. Values are the mean ± s.d of n=4 biological replicates. *P* values were calculated by two-sided Student's t-test.

Figure 5. ER stress promotes the association of IGF2BP3 with mRNA decapping complex.
A. Volcano plot of co-IP–MS analysis of endogenous IGF2BP3 upon ER stress (tunicamycin, 5 µg/mL, 4 h) using IGF2BP3 antibody versus IgG control. IGF2BP3 interaction partners (4 times enriched over IgG control, *P* value adj. < 0.05) are shown in dark gray. **B.** Volcano plot comparing IGF2BP3 interactome in control and ER stress conditions. **C.** Normalized LFQ values for selected examples of IGF2BP3 interacting proteins that increase interaction with IGF2BP3 upon ER stress. Values are the mean ± s.d. of n=3 biological replicates. **D.** Western blot showing association of EDC4 with IGF2BP3 after immunoprecipitation of GFP-IGF2BP3 from HEK293T cells treated with ER stress-inducing drug tunicamycin (TM) at 5 µg/mL for 4 hours. * plausible IGF2BP isoforms recognized by the polyclonal IGF2BP3 antibody. Values are the mean ± s.d. of n=3 biological replicates. *P* values were calculated by two-sided Student's t-test. **P* < 0.05. **E.** Quantification of D. **F**. Western blot showing association of IGF2BP3 with EDC3 after immunoprecipitation of mNeonGreen-EDC3 from HEK293T cells treated with ER stress-inducing drug tunicamycin (TM) at 5 µg/mL for 4 hours. * split-mNeonGreen-EDC3 degradation product. **G.** Quantification of F. **H.** Violin plot of AlphaFold2-Multimer [57-59] PEAK scores predicting putative protein-protein interactions between full-length IGF2BP3 and IGF2BP3 interaction partners identified using co-IP-MS. **I.** Matrix showing AlphaFold3 ipTM scores between separate domains of IGF2BP3 and EDC3. **J.** Domain architecture of IGF2BP3 and EDC3. **K.** Predicted structural model (AlphaFold3) [60]of IGF2BP3 RRM1/2 domains (cyan) interacting with EDC3 YjeF domain (violet) through RRM2. RNA interacting with RRM1 is shown in yellow to highlight the RNA interaction interface [62]. IGF2BP3 residues I88, P90, H91, W94 are shown in red. **L**. Western blot showing association of IGF2BP3 with EDC3 after immunoprecipitation of GFP-EDC3 from HCT116 IGF2BP3 KO cells expressing 3xFLAG-IGF2BP3 WT or 4A (I88A, P90A, H91A, W94A) mutant. **M.** Quantification of L.

Supplementary Figure 5.
A. GO term enrichment analysis of IGF2BP3 interaction partners (4 times enriched over IgG control at least in one treatment condition, *P* value adj. < 0.05). **B.** Volcano plots comparing IGF2BP3 interactome with and without RNase treatment. **C.** GO term enrichment analysis of IGF2BP3-interacting proteins that decreased their association with IGF2BP3 upon RNase treatment (*P* value adj. < 0.05). **D.** GO term enrichment analysis of IGF2BP3-interacting proteins that increased their association with IGF2BP3 upon ER stress for more than 20%.

Figure 6. Model of IGF2BP3 function and regulation in ER stress conditions.

Depending on the transcript identity, IGF2BP3 binding to its target mRNAs can either promote their degradation or increase stability. Under homeostatic conditions, there is an equal balance between stabilization and degradation by IGF2BP3. ER stress increases the pro-degradation function of IGF2BP3 and degradation of its target transcripts, including the UPR effector mRNAs, likely through increased interaction of IGF2BP3 with mRNA decapping complexes and ER stress sensor RNase IRE1. Upon ER stress, IGF2BP3 indirectly elicits potent UPR by regulating an unidentified transcription factor. This dual-layered regulation allows IGF2BP3 to specifically upregulate UPR targets while broadly driving degradation of other transcripts to decrease ER folding load until stress is relieved.

References

1. Sriburi, R., Jackowski, S., Mori, K. & Brewer, J.W. XBP1: a link between the unfolded protein response, lipid biosynthesis, and biogenesis of the endoplasmic reticulum. *J Cell Biol* **167**, 35-41 (2004).
2. Bommiasamy, H. *et al.* ATF6alpha induces XBP1-independent expansion of the endoplasmic reticulum. *J Cell Sci* **122**, 1626-1636 (2009).
3. Schuck, S., Prinz, W.A., Thorn, K.S., Voss, C. & Walter, P. Membrane expansion alleviates endoplasmic reticulum stress independently of the unfolded protein response. *The Journal of cell biology* **187**, 525-536 (2009).
4. Lee, A.H., Iwakoshi, N.N. & Glimcher, L.H. XBP-1 regulates a subset of endoplasmic reticulum resident chaperone genes in the unfolded protein response. *Molecular and cellular biology* **23**, 7448-7459 (2003).
5. Acosta-Alvear, D. *et al.* XBP1 controls diverse cell type- and condition-specific transcriptional regulatory networks. *Mol Cell* **27**, 53-66 (2007).
6. Travers, K.J. *et al.* Functional and genomic analyses reveal an essential coordination between the unfolded protein response and ER-associated degradation. *Cell* **101**, 249-258 (2000).
7. Bernales, S., McDonald, K.L. & Walter, P. Autophagy counterbalances endoplasmic reticulum expansion during the unfolded protein response. *PLoS Biol* **4**, e423 (2006).
8. Grumati, P. *et al.* Full length RTN3 regulates turnover of tubular endoplasmic reticulum via selective autophagy. *Elife* **6** (2017).
9. Khaminets, A. *et al.* Regulation of endoplasmic reticulum turnover by selective autophagy. *Nature* **522**, 354-358 (2015).
10. Fumagalli, F. *et al.* Translocon component Sec62 acts in endoplasmic reticulum turnover during stress recovery. *Nat Cell Biol* **18**, 1173-1184 (2016).
11. Schuck, S., Gallagher, C.M. & Walter, P. ER-phagy mediates selective degradation of endoplasmic reticulum independently of the core autophagy machinery. *J Cell Sci* **127**, 4078-4088 (2014).
12. Lin, J.H. *et al.* IRE1 signaling affects cell fate during the unfolded protein response. *Science (New York, N.Y.)* **318**, 944-949 (2007).
13. Lu, Y., Liang, F.X. & Wang, X. A synthetic biology approach identifies the mammalian UPR RNA ligase RtcB. *Mol Cell* **55**, 758-770 (2014).
14. Harding, H.P., Zhang, Y. & Ron, D. Protein translation and folding are coupled by an endoplasmic-reticulum-resident kinase. *Nature* **397**, 271-274 (1999).
15. Harding, H.P., Zhang, Y., Bertolotti, A., Zeng, H. & Ron, D. Perk is essential for translational regulation and cell survival during the unfolded protein response. *Molecular cell* **5**, 897-904 (2000).
16. Walter P. & D., R. The unfolded protein response: from stress pathway to homeostatic regulation. *Science* **334**, 1081-1086 (2011).
17. Holcik, M. & Sonenberg, N. Translational control in stress and apoptosis. *Nat Rev Mol Cell Biol* **6**, 318-327 (2005).
18. Buchan, J.R., Nissan, T. & Parker, R. Analyzing P-bodies and stress granules in Saccharomyces cerevisiae. *Methods in enzymology* **470**, 619-640 (2010).

19. Buchan, J.R. & Parker, R. Eukaryotic stress granules: the ins and outs of translation. *Mol Cell* **36**, 932-941 (2009).
20. Protter, D.S. & Parker, R. Principles and Properties of Stress Granules. *Trends Cell Biol* **26**, 668-679 (2016).
21. Hollien, J. & Weissman, J.S. Decay of endoplasmic reticulum-localized mRNAs during the unfolded protein response. *Science* **313**, 104-107 (2006).
22. Le Thomas, A. *et al.* Decoding non-canonical mRNA decay by the endoplasmic-reticulum stress sensor IRE1α. *Nature Communications* **12**, 1-15 (2021).
23. Hentze, M.W., Castello, A., Schwarzl, T. & Preiss, T. A brave new world of RNA-binding proteins. *Nat Rev Mol Cell Biol* **19**, 327-341 (2018).
24. Gebauer, F., Schwarzl, T., Valcarcel, J. & Hentze, M.W. RNA-binding proteins in human genetic disease. *Nat Rev Genet* **22**, 185-198 (2021).
25. Acosta-Alvear, D. *et al.* The unfolded protein response and endoplasmic reticulum protein targeting machineries converge on the stress sensor IRE1. *Elife* **7** (2018).
26. Degrauwe, N., Suva, M.L., Janiszewska, M., Riggi, N. & Stamenkovic, I. IMPs: an RNA-binding protein family that provides a link between stem cell maintenance in normal development and cancer. *Genes Dev* **30**, 2459-2474 (2016).
27. Muller, S. *et al.* IGF2BP1 enhances an aggressive tumor cell phenotype by impairing miRNA-directed downregulation of oncogenic factors. *Nucleic Acids Res* **46**, 6285-6303 (2018).
28. Jønson, L. *et al.* IMP3 RNP safe houses prevent miRNA-directed HMGA2 mRNA decay in cancer and development. *Cell reports* **7**, 539-551 (2014).
29. Huang, H. *et al.* Recognition of RNA N 6-methyladenosine by IGF2BP proteins enhances mRNA stability and translation. *Nature Cell Biology* **20**, 285-295 (2018).
30. Liu, C. *et al.* IGF2BP3 promotes mRNA degradation through internal m(7)G modification. *Nat Commun* **15**, 7421 (2024).
31. Leeds, P. *et al.* Developmental regulation of CRD-BP, an RNA-binding protein that stabilizes c-myc mRNA in vitro. *Oncogene* **14**, 1279-1286 (1997).
32. Mueller-Pillasch, F. *et al.* Expression of the highly conserved RNA binding protein KOC in embryogenesis. *Mech Dev* **88**, 95-99 (1999).
33. Mori, H. *et al.* Expression of mouse igf2 mRNA-binding protein 3 and its implications for the developing central nervous system. *J Neurosci Res* **64**, 132-143 (2001).
34. Noubissi, F.K. *et al.* CRD-BP mediates stabilization of betaTrCP1 and c-myc mRNA in response to beta-catenin signalling. *Nature* **441**, 898-901 (2006).
35. Bell, J.L. *et al.* Insulin-like growth factor 2 mRNA-binding proteins (IGF2BPs): post-transcriptional drivers of cancer progression? *Cellular and Molecular Life Sciences* **70**, 2657-2675 (2013).
36. Yaniv, K. & Yisraeli, J.K. The involvement of a conserved family of RNA binding proteins in embryonic development and carcinogenesis. *Gene* **287**, 49-54 (2002).
37. Huttelmaier, S. *et al.* Spatial regulation of beta-actin translation by Src-dependent phosphorylation of ZBP1. *Nature* **438**, 512-515 (2005).
38. Conway, A.E.E. *et al.* Enhanced CLIP Uncovers IMP Protein-RNA Targets in Human Pluripotent Stem Cells Important for Cell Adhesion and Survival. *Cell Reports* **15**, 666-679 (2016).
39. Hansen, T.V. *et al.* Dwarfism and impaired gut development in insulin-like growth factor II mRNA-binding protein 1-deficient mice. *Mol Cell Biol* **24**, 4448-4464 (2004).
40. Lederer, M., Bley, N., Schleifer, C. & Huttelmaier, S. The role of the oncofetal IGF2 mRNA-binding protein 3 (IGF2BP3) in cancer. *Semin Cancer Biol* **29**, 3-12 (2014).
41. Stöhr, N. *et al.* ZBP1 regulates mRNA stability during cellular stress. *The Journal of Cell Biology* **175**, 527-534 (2006).

42. Weidensdorfer, D. *et al.* Control of c-myc mRNA stability by IGF2BP1-associated cytoplasmic RNPs. *RNA* **15**, 104-115 (2009).
43. Anisimova, A.S. & Karagöz, G.E. Optimized infrared photoactivatable ribonucleoside-enhanced crosslinking and immunoprecipitation (IR-PAR-CLIP) protocol identifies novel IGF2BP3-interacting RNAs in colon cancer cells. *RNA (New York, N.Y.)* **29**, 1818-1836 (2023).
44. Hafner, M. *et al.* Transcriptome-wide identification of RNA-binding protein and microRNA target sites by PAR-CLIP. *Cell* **141**, 129-141 (2010).
45. Corcoran, D.L. *et al.* PARalyzer: definition of RNA binding sites from PAR-CLIP short-read sequence data. *Genome Biol* **12**, R79 (2011).
46. Schneider, T. *et al.* Combinatorial recognition of clustered RNA elements by the multidomain RNA-binding protein IMP3. *Nat Commun* **10**, 2266 (2019).
47. Ennajdaoui, H. *et al.* IGF2BP3 Modulates the Interaction of Invasion-Associated Transcripts with RISC. *Cell Reports* **15**, 1876-1883 (2016).
48. Mizutani, R. *et al.* Oncofetal protein IGF2BP3 facilitates the activity of proto-oncogene protein eIF4E through the destabilization of EIF4E-BP2 mRNA. *Oncogene* **35**, 3495-3502 (2016).
49. Herzog, V.A. *et al.* Thiol-linked alkylation of RNA to assess expression dynamics. *Nature Methods* **14**, 1198-1204 (2017).
50. An, W., Kim, J. & Roeder, R.G. Ordered cooperative functions of PRMT1, p300, and CARM1 in transcriptional activation by p53. *Cell* **117**, 735-748 (2004).
51. Frietze, S., Lupien, M., Silver, P.A. & Brown, M. CARM1 regulates estrogen-stimulated breast cancer growth through up-regulation of E2F1. *Cancer Res* **68**, 301-306 (2008).
52. Singh, K. *et al.* TRIB1 confers therapeutic resistance in GBM cells by activating the ERK and Akt pathways. *Sci Rep* **13**, 12424 (2023).
53. Xuan, C. *et al.* RBB, a novel transcription repressor, represses the transcription of HDM2 oncogene. *Oncogene* **32**, 3711-3721 (2013).
54. Pfannkuche, K., Summer, H., Li, O., Hescheler, J. & Droge, P. The high mobility group protein HMGA2: a co-regulator of chromatin structure and pluripotency in stem cells? *Stem Cell Rev Rep* **5**, 224-230 (2009).
55. Latifkar, A. *et al.* IGF2BP2 promotes cancer progression by degrading the RNA transcript encoding a v-ATPase subunit. *Proc Natl Acad Sci U S A* **119**, e2200477119 (2022).
56. Pan, F., Huttelmaier, S., Singer, R.H. & Gu, W. ZBP2 facilitates binding of ZBP1 to beta-actin mRNA during transcription. *Mol Cell Biol* **27**, 8340-8351 (2007).
57. Mirdita, M. *et al.* ColabFold: making protein folding accessible to all. *Nat Methods* **19**, 679-682 (2022).
58. Evans, R. *et al.* Protein complex prediction with AlphaFold-Multimer. *bioRxiv*, 2021.2010.2004.463034 (2022).
59. Jumper, J. *et al.* Highly accurate protein structure prediction with AlphaFold. *Nature* **596**, 583-589 (2021).
60. Abramson, J. *et al.* Accurate structure prediction of biomolecular interactions with AlphaFold 3. *Nature* **630**, 493-500 (2024).
61. Tritschler, F. *et al.* A divergent Sm fold in EDC3 proteins mediates DCP1 binding and P-body targeting. *Mol Cell Biol* **27**, 8600-8611 (2007).
62. Jia, M., Gut, H. & Chao, J.A. Structural basis of IMP3 RRM12 recognition of RNA. *RNA* **24**, 1659-1666 (2018).
63. Maris, C., Dominguez, C. & Allain, F.H. The RNA recognition motif, a plastic RNA-binding platform to regulate post-transcriptional gene expression. *FEBS J* **272**, 2118-2131 (2005).
64. Ling, S.H. *et al.* Crystal structure of human Edc3 and its functional implications. *Mol Cell Biol* **28**, 5965-5976 (2008).

65. Yamamoto, K. *et al.* Transcriptional induction of mammalian ER quality control proteins is mediated by single or combined action of ATF6alpha and XBP1. *Dev Cell* **13**, 365-376 (2007).
66. Ashar, H.R., Chouinard, R.A., Jr., Dokur, M. & Chada, K. In vivo modulation of HMGA2 expression. *Biochim Biophys Acta* **1799**, 55-61 (2010).
67. Vignali, R. & Marracci, S. HMGA Genes and Proteins in Development and Evolution. *Int J Mol Sci* **21** (2020).
68. Xu, W. *et al.* Increased IGF2BP3 expression promotes the aggressive phenotypes of colorectal cancer cells in vitro and vivo. *Journal of Cellular Physiology* **234**, 18466-18479 (2019).
69. Salvagno, C., Mandula, J.K., Rodriguez, P.C. & Cubillos-Ruiz, J.R. Decoding endoplasmic reticulum stress signals in cancer cells and antitumor immunity. *Trends Cancer* **8**, 930-943 (2022).
70. Li, H., Korennykh, A.V., Behrman, S.L. & Walter, P. Mammalian endoplasmic reticulum stress sensor IRE1 signals by dynamic clustering. *Proceedings of the National Academy of Sciences of the United States of America* **107**, 16113-16118 (2010).
71. Karagoz, G.E. *et al.* An unfolded protein-induced conformational switch activates mammalian IRE1. *Elife* **6** (2017).
72. Natsume, T., Kiyomitsu, T., Saga, Y. & Kanemaki, M.T. Rapid Protein Depletion in Human Cells by Auxin-Inducible Degron Tagging with Short Homology Donors. *Cell Reports* **15**, 210-218 (2016).
73. de Almeida, M. *et al.* AKIRIN2 controls the nuclear import of proteasomes in vertebrates. *Nature* **599**, 491-496 (2021).
74. Leonetti, M.D., Sekine, S., Kamiyama, D., Weissman, J.S. & Huang, B. A scalable strategy for high-throughput GFP tagging of endogenous human proteins. *Proc Natl Acad Sci U S A* **113**, E3501-3508 (2016).
75. Cho, N.H. *et al.* OpenCell: Endogenous tagging for the cartography of human cellular organization. *Science* **375**, eabi6983 (2022).
76. Liao, Y., Smyth, G.K. & Shi, W. featureCounts: an efficient general purpose program for assigning sequence reads to genomic features. *Bioinformatics* **30**, 923-930 (2014).
77. Robinson, M.D., McCarthy, D.J. & Smyth, G.K. edgeR: a Bioconductor package for differential expression analysis of digital gene expression data. *Bioinformatics (Oxford, England)* **26**, 139-140 (2010).
78. Chen, E.Y. *et al.* Enrichr: interactive and collaborative HTML5 gene list enrichment analysis tool. *BMC Bioinformatics* **14**, 128 (2013).
79. Kuleshov, M.V. *et al.* Enrichr: a comprehensive gene set enrichment analysis web server 2016 update. *Nucleic Acids Res* **44**, W90-97 (2016).
80. Yu, G. *et al.* GOSemSim: an R package for measuring semantic similarity among GO terms and gene products. *Bioinformatics* **26**, 976-978 (2010).
81. Sayols, S. rrvgo: a Bioconductor package for interpreting lists of Gene Ontology terms. *MicroPubl Biol* **2023** (2023).
82. Robinson, M.D. & Oshlack, A. A scaling normalization method for differential expression analysis of RNA-seq data. *Genome Biol* **11**, R25 (2010).
83. Egorov, A.A. *et al.* svist4get: a simple visualization tool for genomic tracks from sequencing experiments. *BMC Bioinformatics* **20**, 113 (2019).
84. Heinz, S. *et al.* Simple combinations of lineage-determining transcription factors prime cis-regulatory elements required for macrophage and B cell identities. *Mol Cell* **38**, 576-589 (2010).
85. Ran, F.A. *et al.* Genome engineering using the CRISPR-Cas9 system. *Nature Protocols* **8**, 2281-2308 (2013).

86. Mongroo, P.S. *et al.* IMP-1 displays cross-talk with K-Ras and modulates colon cancer cell survival through the novel proapoptotic protein CYFIP2. *Cancer Res* **71**, 2172-2182 (2011).
87. Hornegger, H. *et al.* IGF2BP1 phosphorylation in the disordered linkers regulates ribonucleoprotein condensate formation and RNA metabolism. *Nat Commun* **15**, 9054 (2024).
88. Neumann, T. *et al.* Quantification of experimentally induced nucleotide conversions in high-throughput sequencing datasets. *BMC Bioinformatics* **20**, 258 (2019).
89. Ewels, P.A. *et al.* The nf-core framework for community-curated bioinformatics pipelines. *Nat Biotechnol* **38**, 276-278 (2020).
90. Rappsilber, J., Mann, M. & Ishihama, Y. Protocol for micro-purification, enrichment, pre-fractionation and storage of peptides for proteomics using StageTips. *Nat Protoc* **2**, 1896-1906 (2007).
91. Kong, A.T., Leprevost, F.V., Avtonomov, D.M., Mellacheruvu, D. & Nesvizhskii, A.I. MSFragger: ultrafast and comprehensive peptide identification in mass spectrometry-based proteomics. *Nat Methods* **14**, 513-520 (2017).
92. Yu, F., Haynes, S.E. & Nesvizhskii, A.I. IonQuant Enables Accurate and Sensitive Label-Free Quantification With FDR-Controlled Match-Between-Runs. *Mol Cell Proteomics* **20**, 100077 (2021).
93. da Veiga Leprevost, F. *et al.* Philosopher: a versatile toolkit for shotgun proteomics data analysis. *Nat Methods* **17**, 869-870 (2020).
94. Hollenstein, D.M. *et al.* Chemical Acetylation of Ligands and Two-Step Digestion Protocol for Reducing Codigestion in Affinity Purification-Mass Spectrometry. *J Proteome Res* **22**, 3383-3391 (2023).
95. Ritchie, M.E. *et al.* limma powers differential expression analyses for RNA-sequencing and microarray studies. *Nucleic Acids Research* **43**, e47-e47 (2015).
96. Hohmann, U. *et al.* A molecular switch orchestrates the nuclear export of human messenger RNA. *bioRxiv*, 2024.2003.2024.586400 (2024).
97. Perez-Riverol, Y. *et al.* The PRIDE database resources in 2022: a hub for mass spectrometry-based proteomics evidences. *Nucleic Acids Res* **50**, D543-D552 (2022).

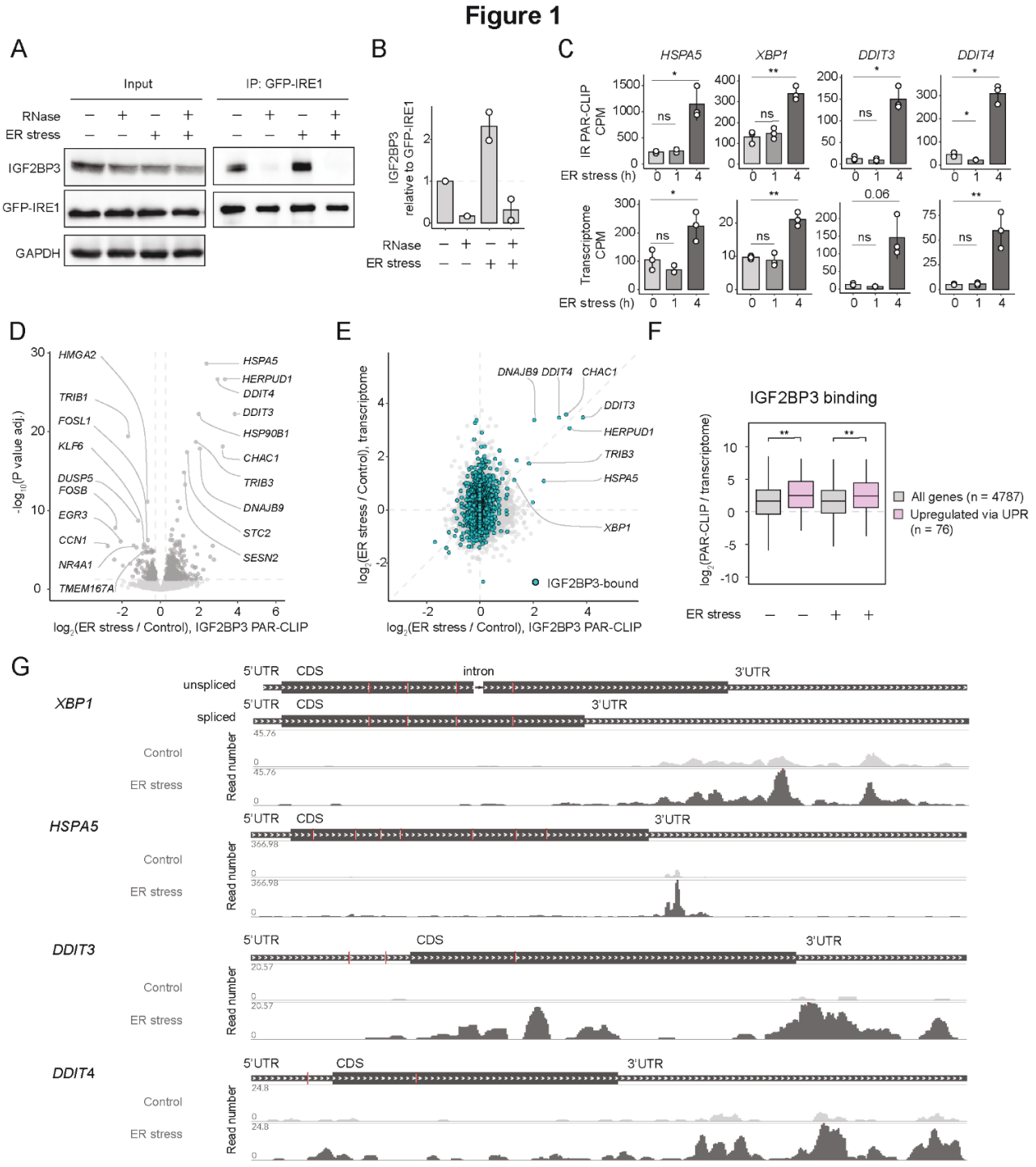

Figure 1. IGF2BP3 interacts with the UPR target mRNAs.

A. Western blot of IGF2BP3 showing its association with IRE1 after immunoprecipitation of GFP-IRE1 from mouse embryonic fibroblasts treated with ER stress-inducing drug tunicamycin at 5 µg/mL for 4 hours with or without RNase treatment **B.** Quantification of Figure 1A. **C.** Barplots showing normalized read count numbers (CPM) for IGF2BP3-bound reads (IR-PAR-CLIP) and total transcript levels (QuantSeq) of selected UPR target genes upon ER stress induction with tunicamycin at 5 µg/mL for 1 and 4 hours. Values are the mean ± s.d of n=3 biological replicates. *P* values were calculated by two-sided Student's t-test. **D.** Volcano plot showing changes in IGF2BP3 IR-PAR-CLIP CPM upon ER stress treatment. *P* values were calculated by edgeR glmQLFTest. **E.** Scatter plot comparing changes in IGF2BP3 IR-PAR-CLIP read counts with the total transcriptome changes (QuantSeq) upon ER stress treatment. **F.** Boxplot showing changes in IGF2BP3 binding

(IR-PAR-CLIP CPM / QuantSeq CPM) to all genes and UPR upregulated genes (upregulated more than two-fold in ER stress than in control, *P* value adj. < 0.05, total RNA-Seq) upon ER stress and control conditions. *P* values were calculated by two-sided Wilcoxon test. **G.** Representative IGF2BP3 IR-PAR-CLIP coverage examples. Where not indicated otherwise, ER stress was induced with tunicamycin at 5 µg/mL for 4 hours. **P* < 0.05; ***P* < 0.01; ****P* < 0.001; *****P* < 0.0001.

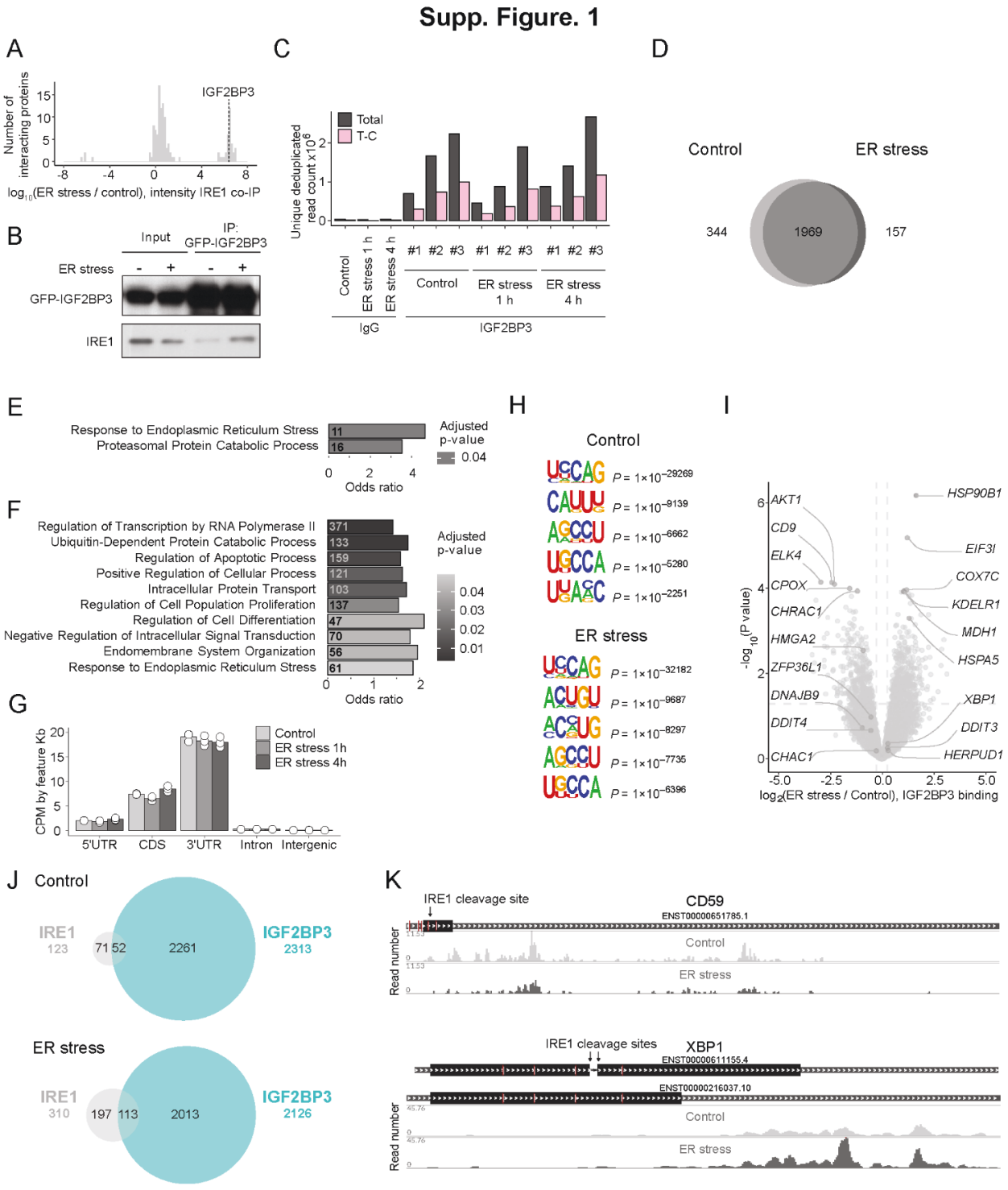

Supplementary Figure 1.

A. Histogram showing the distribution of fold changes in normalized peptide intensity values of IRE1 interaction partners upon ER stress (crosslinking mass spectrometry data from Acosta-Alvear, Karagöz et al., 2018 [1]). Proteins identified in IgG or non-crosslinking controls were excluded from the analysis (n = 126). **B.** Western blot of IRE1 showing its association with IGF2BP3 after immunoprecipitation of GFP-IGF2BP3 from HEK293T cells treated with ER stress-inducing drug tunicamycin (TM) at 5 µg/mL for 4 hours. **C.** Barplots showing numbers of total and T-C containing unique deduplicated IR-PAR-CLIP read counts per library before normalization. **D.** Venn diagram showing the intersection of IGF2BP3 IR-PAR-CLIP targets in DMSO control and ER stress conditions (4-hour treatment with 5 µg/mL tunicamycin). **E.** GO term analysis of 157 IGF2BP3-

bound transcripts identified in only in ER stress conditions **F.** GO term analysis of 2470 IGF2BP3-bound transcripts identified in either control or ER stress conditions. **G.** Feature length-normalized aggregated IGF2BP3 IR-PAR-CLIP coverage of genomic features. **H.** 5nt-long consensus motifs enriched in IGF2BP3 IR-PAR-CLIP reads over scrambled control in control and ER stress conditions (4 hr). Motif enrichment analysis was performed using HOMER software. **I.** Volcano plot showing changes in IGF2BP3 binding (IR-PAR-CLIP CPM / QuantSeq CPM) upon ER stress and control conditions. n=3 biological replicates. *P* values were calculated by edgeR glmQLFTest. **J.** Venn diagram showing the intersection between IGF2BP3 and IRE1 PAR-CLIP targets [1] in control and ER stress conditions. **K.** IGF2BP3 IR-PAR-CLIP coverage of IRE1 targets *XBP1* and *CD59*.

Figure 2

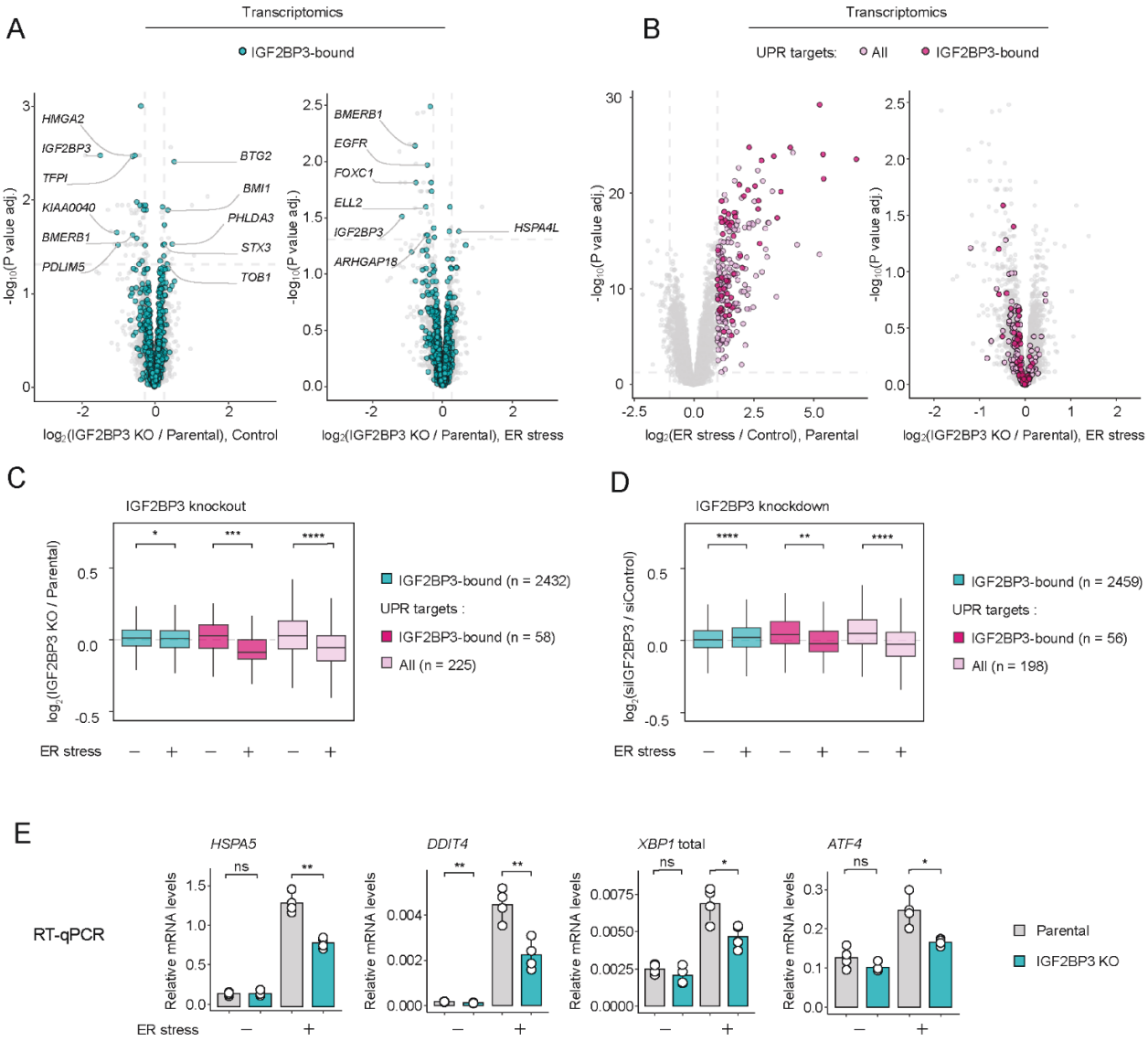

Figure 2. IGF2BP3 depletion dampens the unfolded protein response.
A. Volcano plot of the changes in the transcriptome (RNA-seq) upon IGF2BP3 KO in control (left panel) and ER stress conditions (right panel). *P* values were calculated by edgeR glmQLFTest. **B.** Volcano plot of the changes in the transcriptome (RNA-seq) upon ER stress treatment showing the selection of IGF2BP3-bound UPR targets (left panel), and volcano plot of the changes in the transcriptome upon IGF2BP3 KO in ER stress conditions with highlighted UPR targets (light pink) and IGF2BP3-bound UPR targets (dark pink) (right panel). *P* values were calculated by edgeR glmQLFTest. **C.** Boxplot showing changes in transcript levels upon IGF2BP3 KO for IGF2BP3-bound transcripts, UPR targets, and IGF2BP3-bound UPR targets. *P* values were calculated by a two-sided Wilcoxon test. **D.** Boxplot showing changes in transcript levels upon siRNA-mediated IGF2BP3 for IGF2BP3-bound transcripts, UPR targets, and IGF2BP3-bound UPR targets. *P* values were calculated by two-sided Wilcoxon test. **E.** RT-qPCR analyses of IGF2BP3 KO and parental cells treated with 100 ng/mL for 7 hours. n=4 biological replicates. *P* values were calculated by a two-sided Student's t-test. **P* < 0.05; ***P* < 0.01; ****P* < 0.001; *****P* < 0.0001.

Supp. Figure. 2

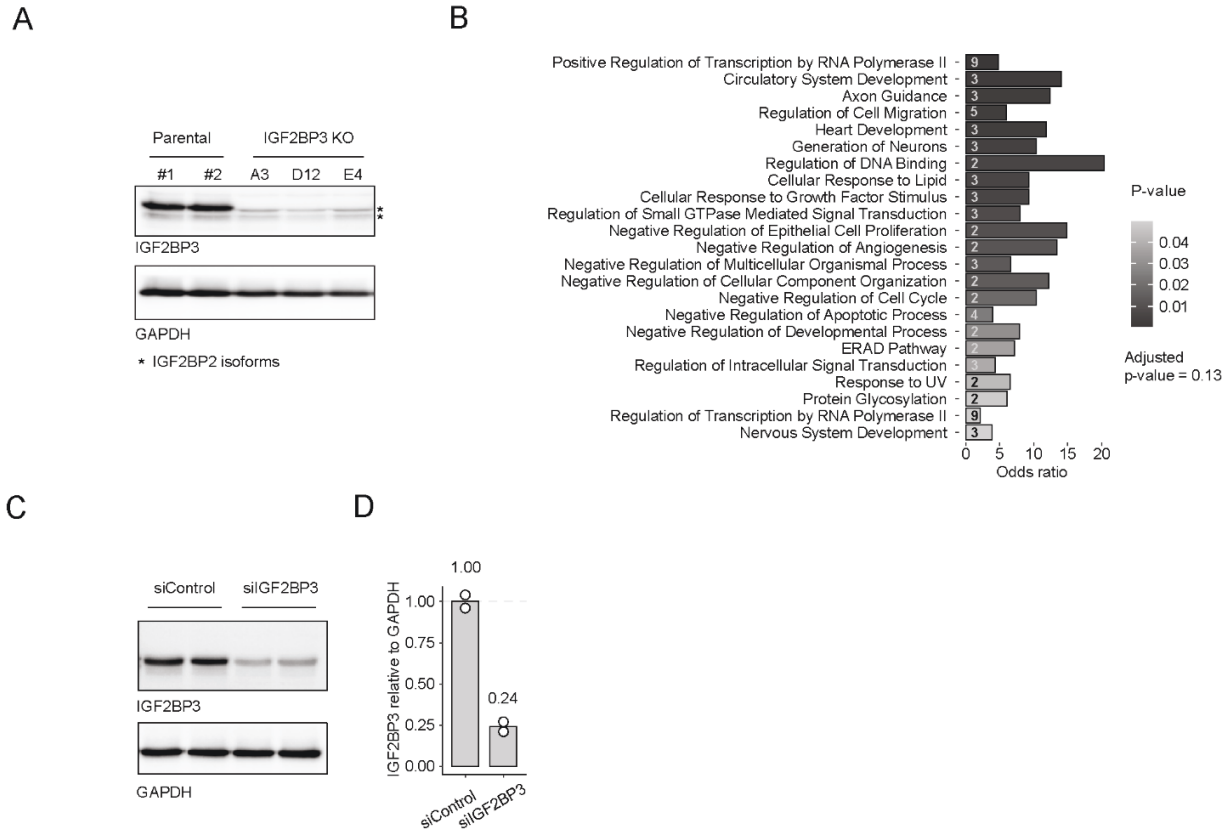

Supplementary Figure 2.
A. Western blot of parental and IGF2BP3 KO HCT116 cell lines (clones A3, D12 and E4). * marks IGF2BP2 isoforms recognized by polyclonal anti-IGF2BP3 antibody. **B.** GO term analysis of genes downregulated in IGF2BP3 KO compared to parental cells during ER stress. edgeR glmQLFTest *P* value adj. < 0.05. **C.** Western blot showing depletion of IGF2BP3 after 48-hour treatment with siRNA against IGF2BP3 compared to control siRNA. **D.** Quantification of Supp.Fig. 2C.

Figure 3

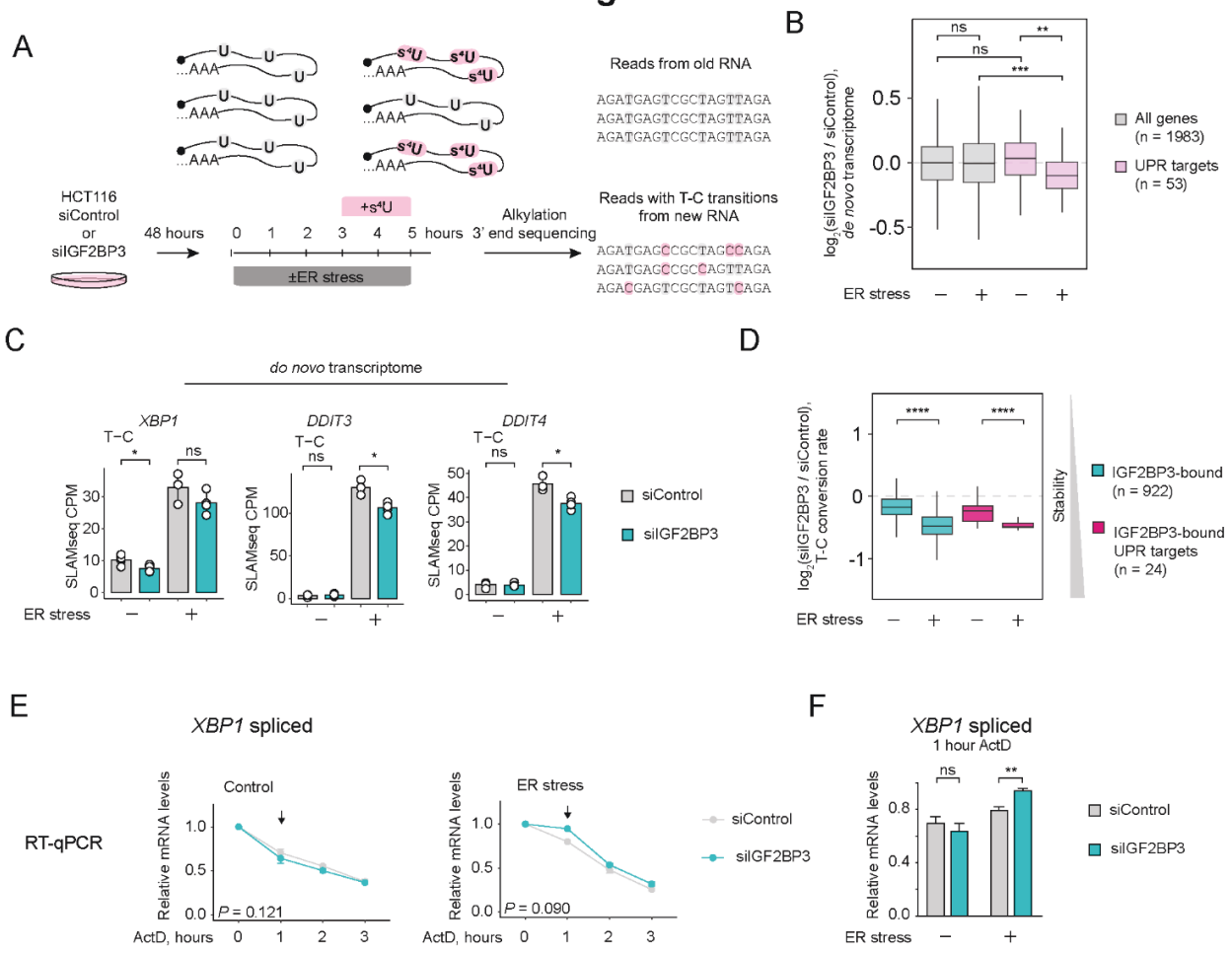

Figure 3. IGF2BP3 shapes the UPR through transcriptional feedback loops.
A. Design of thiol (SH)-linked alkylation for the metabolic sequencing of RNA (SLAMseq) experiment. IGF2BP3 is depleted for 48 hours using siRNA. For the last 5 hours before collection, cells were treated with tunicamycin at 5 µg/mL or with DMSO as a control. In the last 2 hours, 100 µM 4-thiouridine (s^4U) was added to the cells to label the newly synthesized mRNA. **B.** Boxplot showing changes in *de novo* transcripts levels of UPR targets (transcribed during 2-hour s^4U pulse) T-C (SLAMseq T-C CPM) upon siRNA-mediated depletion of IGF2BP3. *P* values were calculated by a two-sided Wilcoxon test. **C.** Barplots showing SLAMseq *de novo* (T-C) CPM values for selected UPR target genes (*XBP1*, *DDIT4*, and *DDIT3*). Values are the mean ± s.d of n=4 biological replicates. *P* values were calculated by a two-sided Student's t-test. **D.** Boxplot showing changes in estimated transcript stability upon siRNA-mediated IGF2BP3 depletion for the IGF2BP3-bound transcripts and the IGF2BP3-bound UPR targets. The changes in transcript stability were assessed by analyzing the differences in average T-C conversion rates per gene following IGF2BP3 depletion. T-C conversion rate values indicate the relative abundance of both pre-existing and newly synthesized mRNA for a given gene, with a decrease in these values suggesting increased stabilization. *P* values were calculated by a two-sided Wilcoxon test. **E.** RT-qPCR analyses of degradation rates of *XBP1* (spliced) mRNA upon siRNA-mediated depletion of IGF2BP3. HCT116 cells were treated with tunicamycin at 250 ng/mL for 4 hours, and the transcription was blocked with 5 µg/mL ActD at the indicated time points. Values are the mean ± s.e. of n=4 biological replicates. *P* values were calculated by a paired two-sided Student's t-test. **F.** Barplots showing results of RT-qPCR analyses of *XBP1* (spliced) total mRNA level (relative to RPL6) in unstressed cells and cells treated with tunicamycin at 250 ng/mL for 4 hours. Arrows indicate the 1-hour ActD treatment time point selected for boxplot representation in E**.** *P* values were calculated by two-sided Student's t-test. **P* < 0.05; ***P* < 0.01; ****P* < 0.001; *****P* < 0.0001.

Supp. Figure. 3

A

SYMBOL	logFC, IGF2BP3 CRISPR/Cas9 KO	logFC, IGF2BP3 siRNA KD
ETS1	-0.73	-0.09
KLF12	-0.59	-0.43
FOXD1	-0.59	-0.43
SOX9	-0.57	-0.08
HOXB8	-0.45	-0.09
ZNF70	-0.39	-0.08
ARNT2	-0.36	-0.19
ZNF134	-0.35	-0.07
NR2F2	-0.33	-0.28
HOXB9	-0.33	-0.12
BHLHA15	-0.27	-0.08
RCOR2	-0.25	-0.31
TCF7	-0.24	-0.13
RREB1	-0.23	-0.23
SMAD3	-0.23	-0.28
FOSL2	-0.22	-0.11
MEIS2	-0.22	-0.09
NPAS2	-0.22	-0.21
HR	-0.21	-0.24
UXT	-0.20	-0.08
TCF7L1	-0.19	-0.08
PLAGL2	-0.19	-0.40
FOSL1	-0.18	-0.12
FHL3	-0.17	-0.07
KLF4	-0.17	-0.37
MEIS3	-0.17	-0.41
SMARCD3	-0.16	-0.09
TCFL5	-0.15	-0.14
ZNF320	-0.15	-0.11
TBL1X	-0.15	-0.18
ZNF749	-0.14	-0.15
TEAD2	-0.14	-0.18
CREB3L2	-0.14	-0.12

Supplementary Figure 3. A. Table showing $\log_2$(IGF2BP3 depletion / control) values for transcriptional regulators (GO:0140110) that were downregulated more than 10% or 5% upon IGF2BP3 CRISPR/Cas9- or siRNA-mediated depletion, respectively, under ER stress conditions.

Figure 4

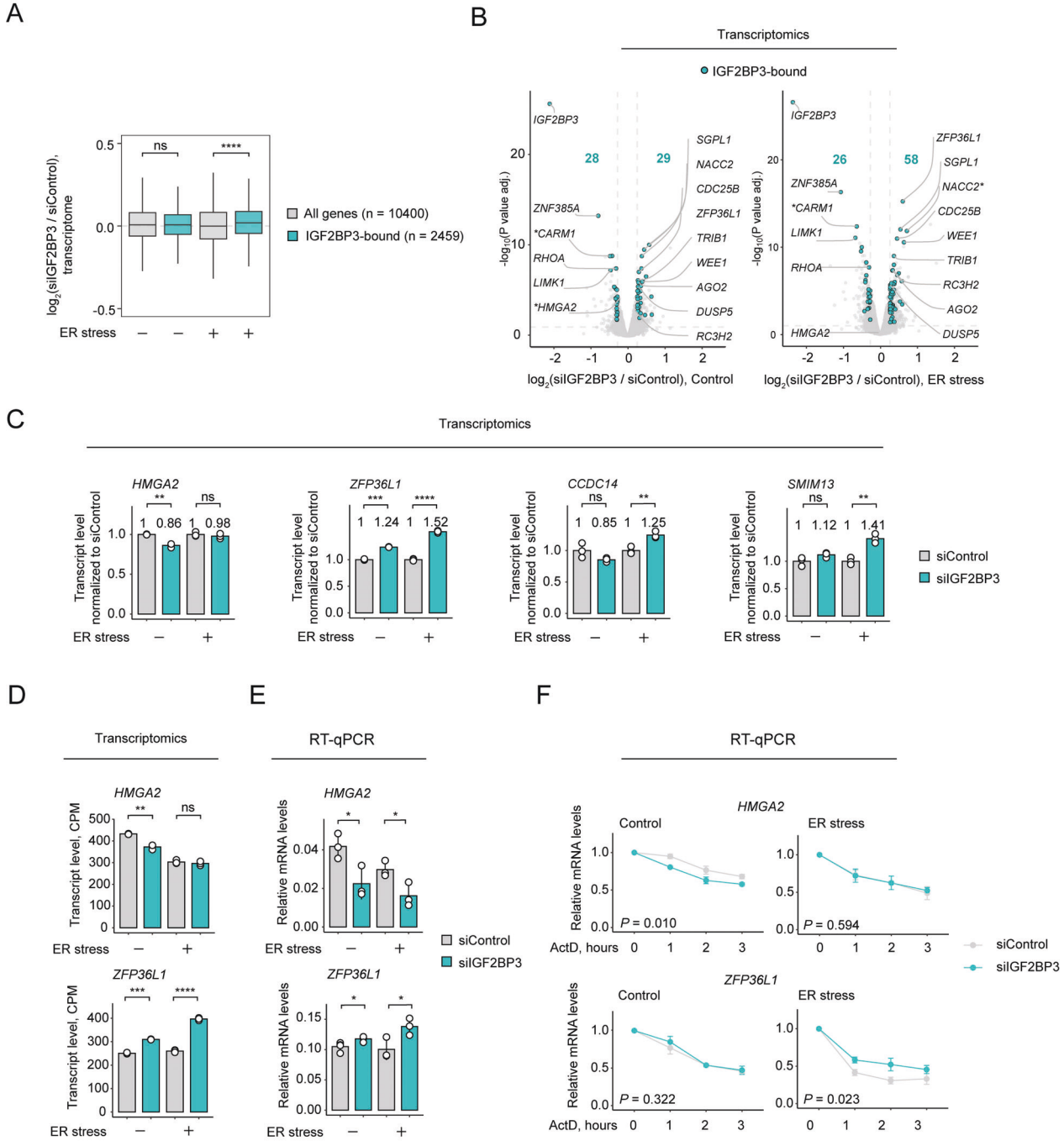

Figure 4. IGF2BP3 facilitates the degradation of its target mRNAs during ER stress. A. Boxplot showing changes in total transcript levels (RNA-seq) upon siRNA-mediated depletion of IGF2BP3 for all genes and IGF2BP3-bound transcripts in control and ER stress conditions. **B.** Volcano plots of total transcriptome changes (RNA-seq) upon siRNA-mediated IGF2BP3 depletion with regulated genes highlighted (ΔRNA-seq > 20% and *P* value adj. < 0.05). * marks the genes encoding transcriptional regulators. **C.** Barplots showing total RNA-seq CPM values normalized to siControl conditions for selected genes regulated by IGF2BP3. Values are the mean ± s.d of n=3 biological replicates. *P* values were calculated by paired two-sided Student's t-test. **D.** Barplots showing total RNA-seq CPM values for *HMGA2* and *ZFP36L1*. Values are the mean ± s.d of n=3 biological replicates. *P* values were calculated by paired two-sided Student's t-test. **E.** Barplots showing results of RT-qPCR analyses of *HMGA2* and *ZFP36L1* (mRNA levels relative to *RPL6*) in unstressed cells and cells treated with tunicamycin at 5 µg/mL for 6 hours upon siRNA-mediated depletion of IGF2BP3. Values are the mean ± s.d. of n=3

biological replicates. *P* values were calculated by two-sided Student's t-test. **F**. RT-qPCR analyses of degradation rates for *HMGA2* and *ZFP36L1* upon siRNA-mediated depletion of IGF2BP3. HCT116 cells were treated with tunicamycin at 5 µg/mL for 3 hours and the transcription was blocked with ActD for indicated time points. Values are the mean ± s.e. of n=3 biological replicates. *P* values were calculated by paired two-sided Student's t-test. **P* < 0.05; ***P* < 0.01; ****P* < 0.001; *****P* < 0.0001.

Supp. Figure. 4

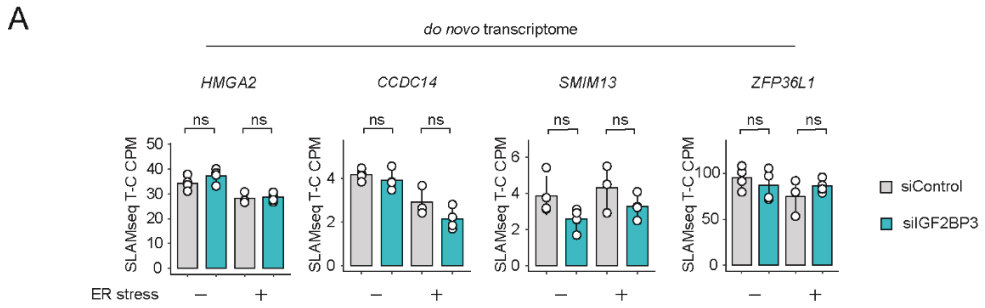

Supplementary Figure 4.
A. Barplots showing SLAMseq *de novo* (T-C CPM) transcript levels for selected transcripts regulated by IGF2BP3. Values are the mean ± s.d of n=4 biological replicates. *P* values were calculated by two-sided Student's t-test.

Figure 5

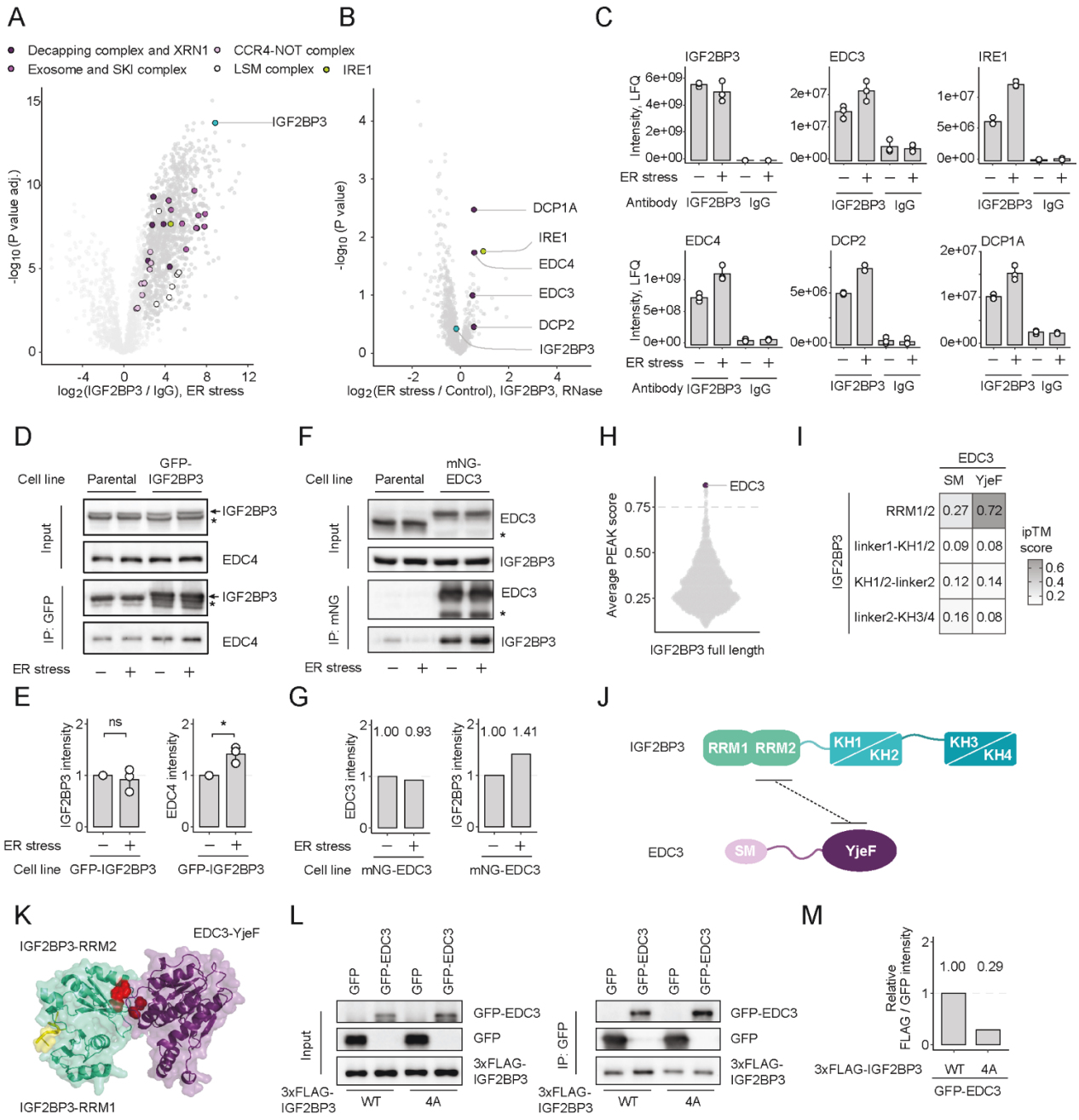

Figure 5. ER stress promotes the association of IGF2BP3 with mRNA decapping complex.
A. Volcano plot of co-IP–MS analysis of endogenous IGF2BP3 upon ER stress (tunicamycin, 5 µg/mL, 4 h) using IGF2BP3 antibody versus IgG control. IGF2BP3 interaction partners (4 times enriched over IgG control, *P* value adj. < 0.05) are shown in dark gray. **B.** Volcano plot comparing IGF2BP3 interactome in control and ER stress conditions. **C.** Normalized LFQ values for selected examples of IGF2BP3 interacting proteins that increase interaction with IGF2BP3 upon ER stress. Values are the mean ± s.d. of n=3 biological replicates. **D.** Western blot showing association of EDC4 with IGF2BP3 after immunoprecipitation of GFP-IGF2BP3 from HEK293T cells treated with ER stress-inducing drug tunicamycin (TM) at 5 µg/mL for 4 hours. * plausible IGF2BP isoforms recognized by the polyclonal IGF2BP3 antibody. Values are the mean ± s.d. of n=3 biological replicates. *P* values were calculated by a two-sided Student's t-test. **P* < 0.05. **E.** Quantification of the intensity of the IGF2BP3 and EDC4 bands in Figure 5D. **F**. Western blot showing association of IGF2BP3 with EDC3 via immunoprecipitation of mNeonGreen-EDC3 from HEK293T cells under control conditions and upon treatment with ER stress-inducing drug tunicamycin at 5 µg/mL for 4 hours. * split-mNeonGreen-EDC3 degradation product. **G.** Quantification

of the intensity of IGF2BP3 and EDC3 bands in the Western Blots in Figure 5F. **H.** Violin plot of AlphaFold2-Multimer [2-4]. PEAK scores predicting putative protein-protein interactions between full-length IGF2BP3 and IGF2BP3 interaction partners identified using co-IP-MS. **I.** Matrix showing AlphaFold3 ipTM scores between separate domains of IGF2BP3 and EDC3. **J.** Domain architecture of IGF2BP3 and EDC3. **K.** Predicted structural model (AlphaFold3) [5] of IGF2BP3 RRM1/2 domains (cyan) interacting with EDC3 YjeF domain (violet) through RRM2. RNA interacting with RRM1 is shown in yellow to highlight the RNA interaction interface [6]. IGF2BP3 residues I88, P90, H91, and W94 are shown as red spheres. **L**. Western blot showing association of IGF2BP3 with EDC3 after immunoprecipitation of GFP-EDC3 from HCT116 IGF2BP3 KO cells expressing 3xFLAG-IGF2BP3 WT or 4A (I88A, P90A, H91A, W94A) mutant. **M.** Quantification of co-IP efficiency calculated as the ratio of the band intensity of IGF2BP3 to EDC3 in Western Blots shown in Figure 5L.

Supp. Figure. 5

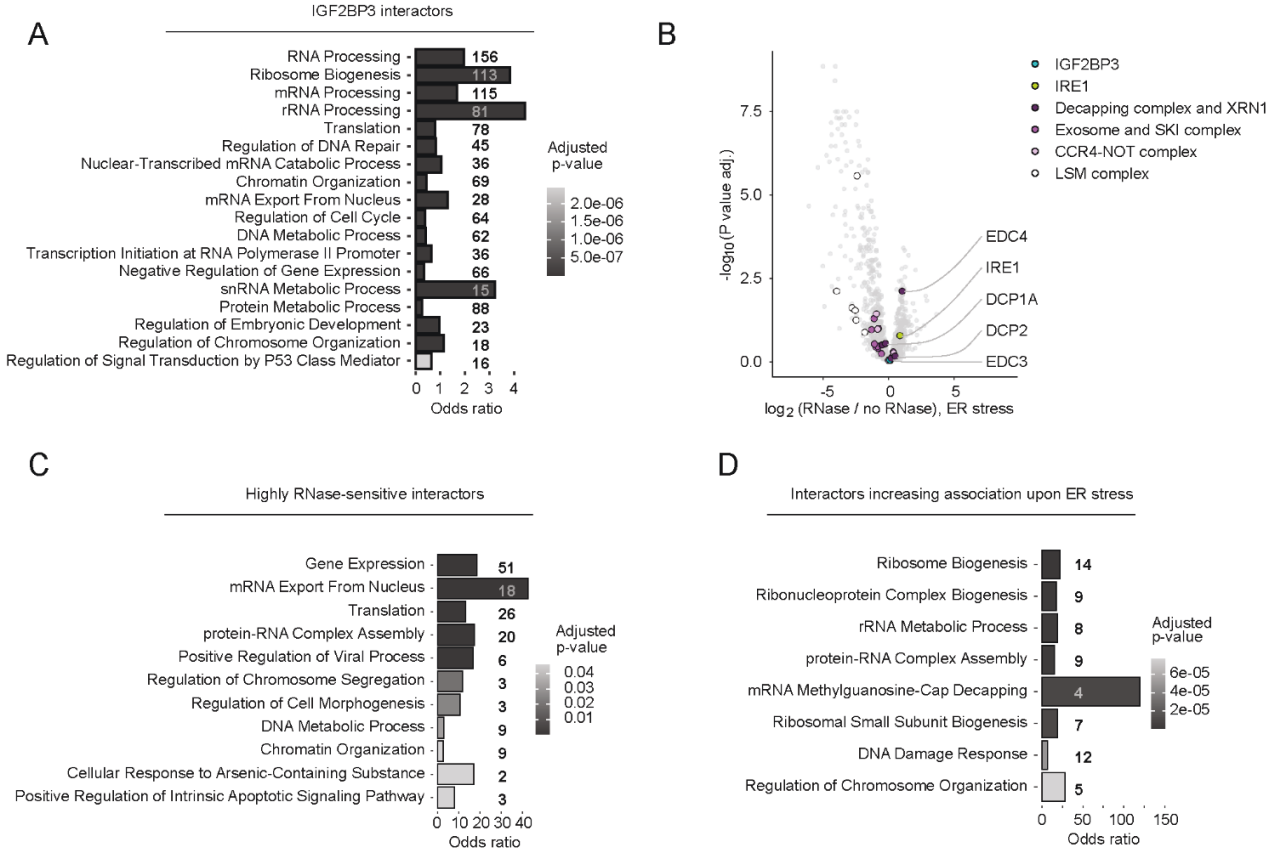

Supplementary Figure 5.

A. GO term enrichment analysis of IGF2BP3 interaction partners (4 times enriched over IgG control at least in one treatment condition, *P* value adj. < 0.05). **B.** Volcano plots comparing IGF2BP3 interactome with and without RNase treatment. **C.** GO term enrichment analysis of IGF2BP3-interacting proteins that decreased their association with IGF2BP3 upon RNase treatment (*P* value adj. < 0.05). **D.** GO term enrichment analysis of IGF2BP3-interacting proteins that increased their association with IGF2BP3 upon ER stress by more than 20%.

Figure 6

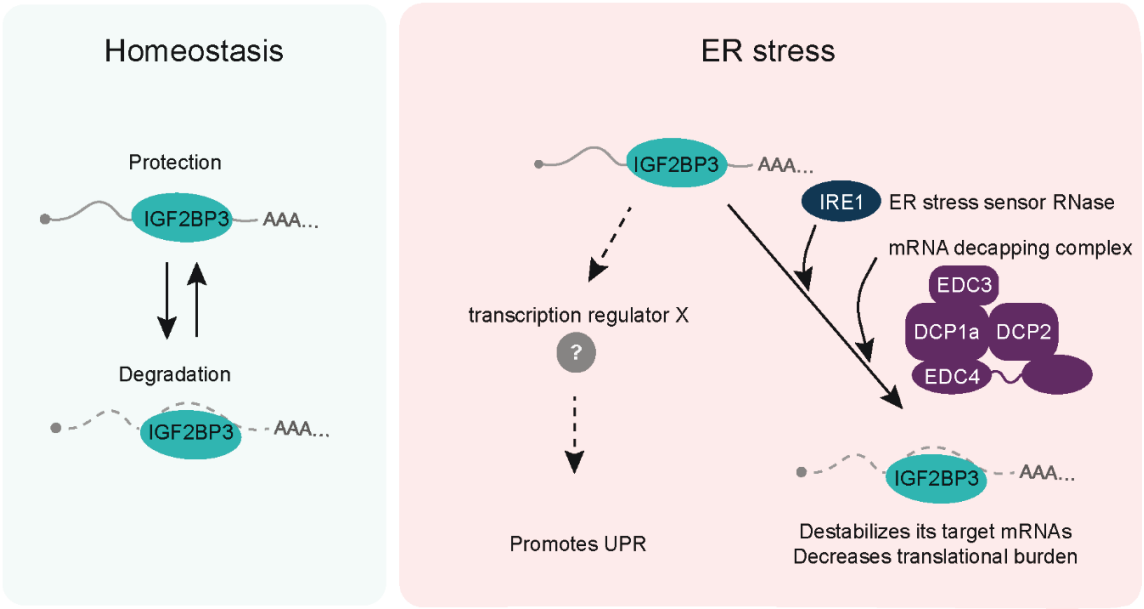

Figure 6. Model of IGF2BP3 function and regulation in ER stress conditions.

Depending on the transcript identity, IGF2BP3 binding to its target mRNAs can either promote their degradation or increase stability. Under homeostatic conditions, there is an equal balance between stabilization and degradation by IGF2BP3. ER stress increases the pro-degradation function of IGF2BP3 and degradation of its target transcripts, including the UPR effector mRNAs, likely through increased interaction of IGF2BP3 with mRNA decapping complexes and ER stress sensor RNase IRE1. Upon ER stress, IGF2BP3 indirectly elicits potent UPR by regulating an unidentified transcription factor. This dual-layered regulation allows IGF2BP3 to specifically upregulate UPR targets while broadly driving degradation of other transcripts to decrease ER folding load until stress is relieved.

Figure References

1. Acosta-Alvear, D. *et al.* The unfolded protein response and endoplasmic reticulum protein targeting machineries converge on the stress sensor IRE1. *Elife* **7** (2018).
2. Mirdita, M. *et al.* ColabFold: making protein folding accessible to all. *Nat Methods* **19**, 679-682 (2022).
3. Evans, R. *et al.* Protein complex prediction with AlphaFold-Multimer. *bioRxiv*, 2021.2010.2004.463034 (2022).
4. Jumper, J. *et al.* Highly accurate protein structure prediction with AlphaFold. *Nature* **596**, 583-589 (2021).
5. Abramson, J. *et al.* Accurate structure prediction of biomolecular interactions with AlphaFold 3. *Nature* **630**, 493-500 (2024).
6. Jia, M., Gut, H. & Chao, J.A. Structural basis of IMP3 RRM12 recognition of RNA. *RNA* **24**, 1659-1666 (2018).

2.3 IGF2BP1 phosphorylation in the disordered linkers regulates ribonucleoprotein condensate formation and RNA metabolism

2.3.1 Preamble

In this work, we investigated how IGF2BP1 is regulated under stress conditions. Using proteomics, we identified stress-dependent phosphorylation sites in IGF2BP1. To examine their role, we generated phosphomimetic mutants in two disordered linkers (S181E and Y396E) and analyzed their effect on IGF2BP1 condensate formation. Although the condensation of the mutants differed from that of the wild-type, their RNA-binding affinity *in vitro* remained unchanged. Structural analyses revealed that linker 1 binds RNA through its RGG/RG motif, and the S181E mutation weakens this interaction. In contrast, linker 2 associates with IGF2BP1's folded domains, and this interaction is disrupted by the Y396E mutation. Mutations at these phosphorylation sites further changed the size and dynamics of IGF2BP1-containing stress granules *in vivo* and affected both IGF2BP1's RNA target binding and its impact on the transcriptome during stress. The obtained results show that phosphorylation at the disordered linkers changes protein-protein and protein-RNA interaction properties of IGF2BP1 and contributes to IGF2BP-mediated regulation during stress.

This manuscript was published in *Nature Communications* on October 20th, 2024.

2.3.2 Contribution statement

I was involved in conceptualization, contributed to the mass spectrometry experiments, and establishment of cell lines expressing fluorescently tagged IGF2BP1 and its mutants. I performed transcriptomics and RNA immunoprecipitation sequencing (RIP-seq) library preparation and analyzed the data.

nature communications

Article

https://doi.org/10.1038/s41467-024-53400-4

IGF2BP1 phosphorylation in the disordered linkers regulates ribonucleoprotein condensate formation and RNA metabolism

Received: 20 November 2023

Accepted: 11 October 2024

Published online: 20 October 2024

Check for updates

Harald Hornegger[1,2,3], Aleksandra S. Anisimova[1,2,3], Adnan Muratovic[1], Benjamin Bourgeois[4,5], Elena Spinetti[6,7], Isabell Niedermoser[1,2], Roberto Covino[7,8], Tobias Madl[4,5] & G. Elif Karagöz[1,2]

The insulin-like growth factor 2 mRNA binding protein 1 (IGF2BP1) is a conserved RNA-binding protein that regulates RNA stability, localization and translation. IGF2BP1 is part of various ribonucleoprotein (RNP) condensates. However, the mechanism that regulates its assembly into condensates remains unknown. By using proteomics, we demonstrate that phosphorylation of IGF2BP1 at S181 in a disordered linker is regulated in a stress-dependent manner. Phosphomimetic mutations in two disordered linkers, S181E and Y396E, modulate RNP condensate formation by IGF2BP1 without impacting its binding affinity for RNA. Intriguingly, the S181E mutant, which lies in linker 1, impairs IGF2BP1 condensate formation in vitro and in cells, whereas a Y396E mutant in the second linker increases condensate size and dynamics. Structural approaches show that the first linker binds RNAs nonspecifically through its RGG/RG motif, an interaction weakened in the S181E mutant. Notably, linker 2 interacts with IGF2BP1's folded domains and these interactions are partially impaired in the Y396E mutant. Importantly, the phosphomimetic mutants impact IGF2BP1's interaction with RNAs and remodel the transcriptome in cells. Our data reveal how phosphorylation modulates low-affinity interaction networks in disordered linkers to regulate RNP condensate formation and RNA metabolism.

RNA-binding proteins (RBPs) play important roles in post-transcriptional control of RNA[1–6]. IGF2BPs are a conserved family of RBPs that regulate RNA localization, translation and stability[7–11]. There are three IGF2BP paralogs (IGF2BP1-3) in mammals. Discovered in chicken embryos, IGF2BP1 was the founding member of the IGF2BP family[12,13]. IGF2BP1 is highly conserved in sequence and function across species (Supplemenetary Fig. 1A). It is highly expressed during mid to late embryogenesis and its expression decreases in adult tissues. In line with embryonic functions, *Igf2bp1* knockout mice show developmental abnormalities[14]. However, IGF2BP1 expression is not restricted to early development, and it is detected later in differentiated gonads and the kidneys. Consistent with post-developmental functions, loss of IGF2BP1 in intestinal epithelial cells impairs intestinal homeostasis in adults[15,16]. IGF2BP1 is highly expressed in various tumors and its overexpression correlates with tumor aggressiveness[9,17]. Importantly, IGF2BP1 depletion impairs tumor growth, indicating that inhibition

[1]Max Perutz Laboratories Vienna, Vienna BioCenter, Vienna, Austria. [2]Medical University of Vienna, Vienna, Austria. [3]Vienna BioCenter PhD Program, Doctoral School of the University of Vienna and Medical University of Vienna, Vienna, Austria. [4]Otto Loewi Research Center, Medicinal Chemistry, Medical University of Graz, Graz, Austria. [5]BioTechMed-Graz, Graz, Austria. [6]Institute of Biophysics, Goethe University Frankfurt, Frankfurt am Main, Germany. [7]Frankfurt Institute for Advanced Studies, Frankfurt am Main, Germany. [8]Institute of Computer Science, Goethe University Frankfurt, Frankfurt am Main, Germany.
e-mail: guelsuen.karagoez@meduniwien.ac.at

may have therapeutic potential in cancer cells[18,19]. This link to disease underlines the importance of obtaining a mechanistic understanding of how IGF2BP1 exerts its function.

IGF2BP1 is a canonical multi-domain RBP, which contains six RNA-binding domains: two RNA recognition motif (RRM) domains and four hnRNP K homology (KH) domains that are linked by two intrinsically disordered regions (Fig. 1A). The KH domains are arranged into pseudodimers (KH1-2, and KH3-4). RNA recognition by IGF2BP1 is mediated by the KH domains, which interact with single-stranded RNAs through 4 nucleotide long recognition motifs[20]. In contrast, the RRM domains provide little specificity and promiscuously recognize dinucleotide sequences, as shown for the IGF2BP3 paralog[21,22]. These multivalent interactions increase the specificity and affinity of IGF2BPs for substrate RNAs[20,21,23].

Genome-wide cross-linking and immunoprecipitation (CLIP) studies identified a large number of IGF2BP1 targets, suggesting roles in cell growth, migration, synaptic plasticity in healthy tissues, as well as tumor growth and metastasis in cancer cells[9,17,24–27]. These data also revealed that IGF2BP1 binds to the coding regions, 5′-untranslated regions (UTRs), and 3′-UTRs of target RNAs, with the highest number of binding sites residing in 3′-UTRs[28,29]. Since the binding sites for IGF2BP1 and microRNAs overlap, it was proposed that IGF2BP1 can stabilize RNAs by competing with the microRNA binding sites[19]. IGF2BP1 also binds to and stabilizes N^6 methyl adenosine-modified RNAs during heat shock stress[8]. Although IGF2BP1 has been proposed to stabilize RNAs, binding to a subset of its target RNAs correlates with destabilization[30]. However, what regulates these distinct functional outputs remains largely unknown

IGF2BP1 assembles into various ribonucleoprotein granules (RNP) to regulate RNA fate. In neurons, IGF2BP1 is part of transport granules, which transport select mRNAs from soma to neurites to regulate site-specific protein synthesis[7]. During cellular stress, IGF2BP1 is sequestered into stress granules that have been proposed to protect mRNAs from degradation until translation resumes. Intriguingly, IGF2BP1 also localizes to P-bodies, which are sites of RNA recapping and degradation[8]. Yet, the regulation of IGF2BP1 assembly into RNP granules with opposite functions is not well understood.

One well-defined mechanism that regulates IGF2BP1 function is through its phosphorylation. In the best-studied example, phosphorylation of IGF2BP1 controls its binding to the ß-actin-encoding *ACTB*

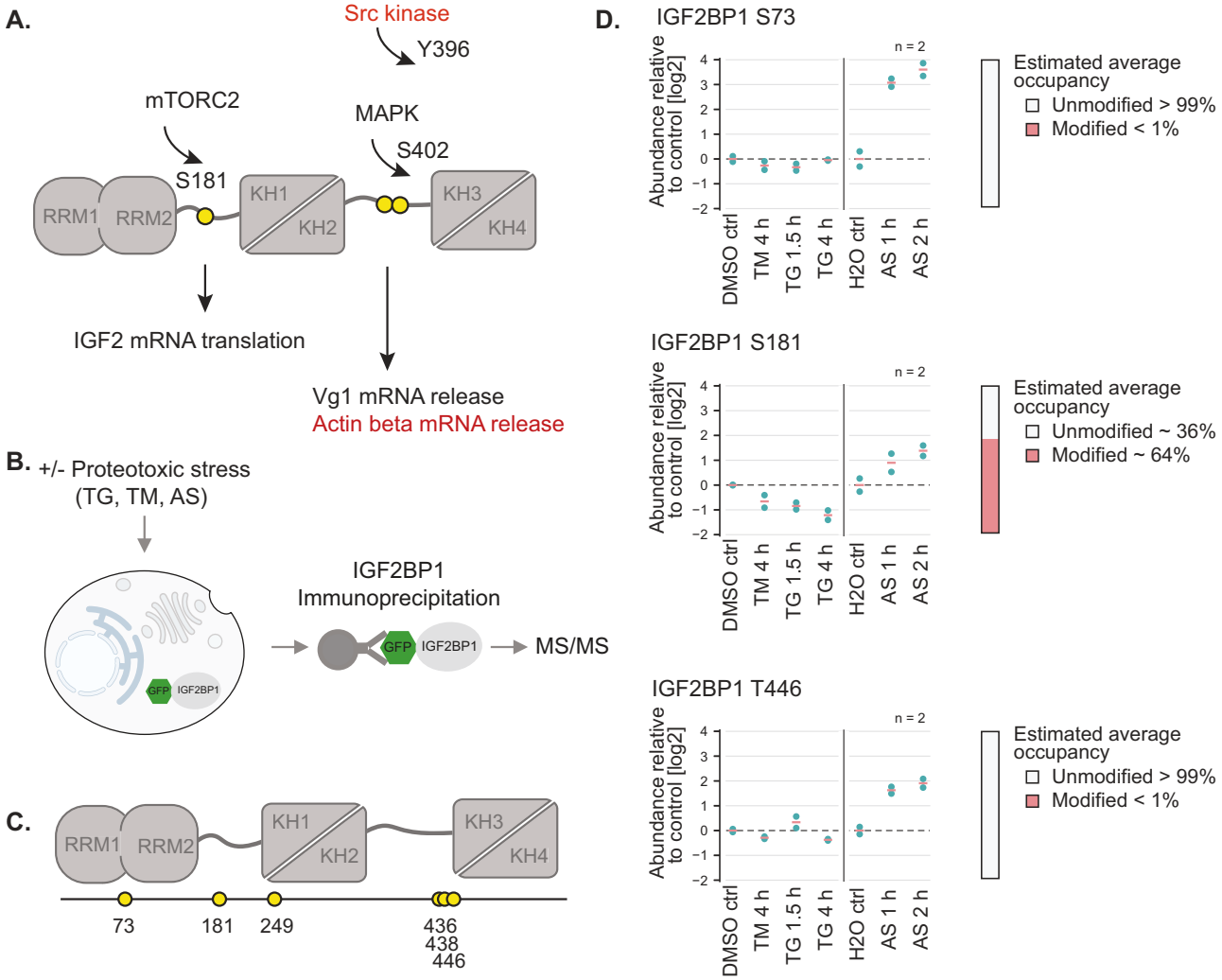

Fig. 1 | IGF2BP1 is phosphorylated at distinct sites in a stress-dependent manner. A Schematic depiction of IGF2BP1 domain architecture. IGF2BP1 consists of 6 RNA binding domains: two RRM domains and four KH domains, which are arranged as pseudo-dimers connected via two linkers. The well-studied phosphorylation sites (S181, Y396, S402), the respective kinases and the effect of the phosphorylation are also depicted. **B** Schematic overview of the workflow for mass spectrometry experiments to determine the stress-regulated phosphorylation sites in IGF2BP1. **C** Representation of IGF2BP1 phosphorylation sites identified by MS analyzes. **D** Relative abundance of the indicated IGF2BP1 phosphorylation sites in cells exposed to various forms of proteotoxic stress compared to the control conditions. Tunicamycin (TM) and thapsigargin (TG) induces ER stress, whereas sodium arsenite (AS) leads to oxidative stress. The time-points on the bottom indicate length of exposure to the stress-inducing drug.

mRNA, providing a regulatory switch to allow for spatial control of *ACTB* mRNA translation[7]. IGF2BP1 binds to the 3′-UTR of the *ACTB* mRNA and prevents its translation. Phosphorylation of IGF2BP1 at Y396 by the Src kinase, which is localized to the leading edge of the cell or axons, releases IGF2BP1 from *ACTB* mRNAs, allowing their translation at those sites[7]. In contrast, the phosphorylation of IGF2BP1 at S181 was suggested to enhance its binding to the 5′-UTR *of IGF2* mRNA, thereby increasing *IGF2* mRNA translation[31,32]. Importantly, S181 phosphorylation regulates stabilization of IGF2BP1 target RNAs and impacts dendritic branching in hippocampal neurons underlining its functional importance[33,34]. Yet, although IGF2BP1 phosphorylation at distinct sites has been suggested to impact RNA binding, the mechanistic details of IGF2BP1 regulation by phosphorylation remains only partially understood. Moreover, whether IGF2BP1 is regulated by other phosphorylation events has yet to be examined.

Here, we map stress-regulated phosphorylation sites in IGF2BP1 by targeted mass spectrometry analyzes to uncover mechanisms that control IGF2BP1 outputs. Using in vitro reconstitution, biochemistry, and structural methods, we dissect how IGF2BP1 phosphorylation in its disordered linker regions regulates function. We show that phosphorylation of the disordered linkers regulates the propensity of IGF2BP1 to form RNP granules in vitro and in cells by modulating low affinity interaction networks. Our data reveal how disordered regions provide highly tunable regulation of RNP condensate formation through a single phosphorylation event.

Results

IGF2BP1 is phosphorylated during proteotoxic stress

IGF2BP1 stabilizes a subset of RNAs during proteotoxic stress and we therefore tested whether IGF2BP1 is regulated through phosphorylation under those conditions[8,35]. To this end, we mapped phosphorylation sites in IGF2BP1 by mass spectrometry (MS) in mammalian cells under control conditions and under conditions where the cells were exposed to proteotoxic stress (Fig. 1B). To compare IGF2BP1 phosphorylation sites under various forms of proteotoxic stress, we exposed the cells to oxidative stress using sodium arsenite (1 or 2 hours) or endoplasmic reticulum (ER) stress using tunicamycin (4 hours) or thapsigargin (1.5 and 4 hours).

To increase specificity and stringency in our analyzes, we enriched for IGF2BP1 by immunoprecipitation from HEK293 cells engineered by CRISPR/Cas9 gene editing to express GFP-tagged IGF2BP1 using split-GFP technology[36]. We obtained a sequence coverage with identified peptides covering 78.7% of the IGF2BP1 amino acid sequence. Peptides covering the disordered linker 2, spanning from amino acids 347 to 423, were not detected in the MS analyzes. This likely resulted from the low complexity nature of this region, which may be inaccessible to tryptic digestion to generate MS-compatible peptides. To overcome this problem, we used different peptidases. The linker 2 region possesses several prolines and treatment with ProAlanase, a peptidase which cleaves after prolines, yielded 87.9% coverage of the whole IGF2BP1 sequence, including the linker 2 in vitro and in cells (Supplementary Data 1).

The subsequent MS analyzes identified several IGF2BP1-derived phosphopeptides whose levels increased or decreased in a stress-dependent manner (Fig. 1C-D, Supplementary Fig. 1B). The identified phosphopeptides mapped to the RRM1 domain (aa S73), disordered linker 1 (aa S181), KH1 (aa T249), KH2 and KH3 domains (aa S436, S438, T446) (Fig. 1C, Supplementary Fig. 1B). The ratio of signal intensities of phosphorylated to unmodified peptides was relatively low (< 1% of total protein) for most of the identified phosphopeptides (S73, T249, S436, S438, T446). The most prominent phosphorylation site we identified mapped to S181 (aa 176-QPRQGSPVAAGA-187 and >64% of total peptide signals), the intensity of which increased by around two-fold during oxidative stress induced by arsenite treatment. In contrast, the signal of the phosphorylated peptide at S181 decreased two-fold when cells were treated with ER stress-inducing drugs, indicating that this phosphorylation event depends on stress type. In line with the published results[7], we detected phosphorylation of the recombinant IGF2BP1 at Y396 by the Src kinase in vitro. However, we did not identify any phosphorylated peptides mapping to the linker 2 under control conditions or under arsenite and thapsigargin-induced stress in cells (> 95% of detected peptides were not phosphorylated; please see materials and methods) (Supplementary Fig. 1C, D).

Multiple amino acid sequence alignments revealed that S181 is highly conserved from fish to mammals, suggesting its functional importance (Supplementary Fig. 1A). This site has previously been proposed to be phosphorylated in all three IGF2BP paralogs by mTORC2[31,32]. Notably, apart from mTORC2, kinase motif prediction algorithms derived from experimental data indicated that S181 might be phosphorylated by members of the CMGC kinase family (i.e. SRPK2 and DYRK3), suggesting that other kinases might be involved in this regulation[37]. Altogether, we found that IGF2BP1 is phosphorylated at multiple sites in a stress-dependent manner.

Phosphomimetic mutants do not impact IGF2BP1 interaction with RNA

Since S181 was the most prominent stress-regulated phosphorylation site identified by our MS approaches, we went on to dissect how it regulates IGF2BP1 function. Interestingly, phosphorylation of S181 in linker 1 is proposed to increase its binding to RNAs, while phosphorylation of Y396 in disordered linker 2 was proposed to decrease it (Fig. 1A)[7,31,32]. However, how the phosphorylation of IGF2BP1 at these two well-described residues regulates its function remained only partially understood. To test whether phosphorylation in the disordered regions impacts IGF2BP1 interaction with RNAs, we measured the binding affinity of model RNAs to wild-type IGF2BP1 and its phosphomimetic mutants (IGF2BP1 S181E and Y396E). For these experiments, we selected two IGF2BP1 target mRNAs based on the published CLIP data sets: i. the unfolded protein response transcription factor *XBP1*, ii. the translation initiation factor *EIF2A*. The CLIP data showed that IGF2BP1 crosslinks to a distinct region in the 3′-UTR of the *XBP1* (Supplementary Fig. 2A, B, Supplementary Table 1) and that *EIF2A* mRNA is enriched in several predicted IGF2BP1-binding motifs[29] (Supplementary Table 1). In addition, as a comparison, we designed model RNAs derived from the functionally well-described IGF2BP1 target RNAs such as *MYC*[38] and *ACTB*[7] (Supplementary Table 1).

IGF2BP binds to its RNA targets by six RNA-binding domains with conserved folds. The individual RNA-binding domains mediate low-affinity interactions with RNA with low specificity, and the combinatorial recognition of RNAs by multiple domains ensures specificity and results in high affinity[21,23]. This interaction involves the recognition of a cluster of distinct and regularly spaced RNA elements covering a ~100 nucleotide-long target RNA region[21]. We in vitro transcribed approximately 200 nt-long regions from the *MYC*, *XBP1* and *EIF2A* RNAs (Supplementary Table 1) and tested their binding to IGF2BP1 using Electrophoretic Mobility Shift Assays (EMSA). The affinities are represented as the apparent dissociation constants ($K_{1/2}$) representing the sum of interactions of IGF2BP1's individual domains with different RNA sequences, causing a shift from unbound to IGF2BP1-bound RNA (please see the materials and methods). IGF2BP1 interacted with RNAs derived from the 3′-UTR of *XBP1* and *EIF2A* with similar affinities (for *XBP1*, $K_{1/2}$ = 41.0 nM and for *EIF2A* $K_{1/2}$ = 48.2 nM) and bound to the *MYC*-derived RNA with a slightly higher affinity ($K_{1/2}$, wild-type: 14.4 nM) (Fig. 2A, Supplementary Fig. 2C-H, Supplementary Table 2).

Next, we tested whether introducing phosphomimetic mutations to IGF2BP1 at the linkers would impact RNA binding. IGF2BP1 phosphomimetic mutants S181E and Y396E bound to the *XBP1*-derived 201 nt RNA with a similar affinity as the wild-type IGF2BP1 (Fig. 2B, C, Supplementary. Fig. 2C, Supplementary Table 2) ($K_{1/2}$, S181E = 17.1 nM, $K_{1/2}$, Y396E = 22.9 nM). Similarly, the phosphomimetic mutants showed only small differences in their affinity for longer *MYC* and *EIF2A*

https://doi.org/10.1038/s41467-024-53400-4

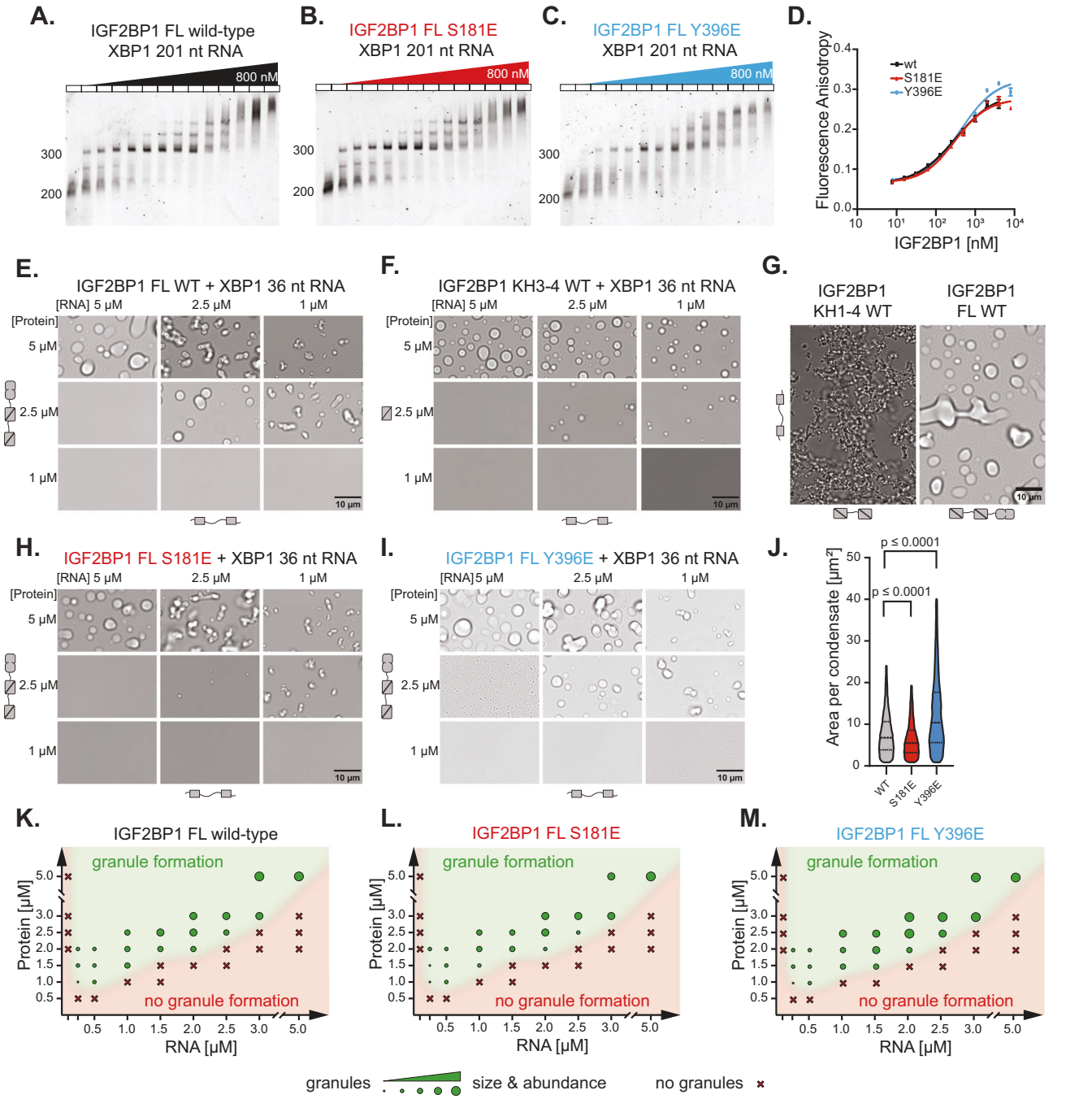

Fig. 2 | The phosphomimetic mutants alter the size of IGF2BP1 RNP condensates without impacting RNA binding. Electrophoretic Mobility Shift Assay (EMSA) of XBP1 201 nt RNA with IGF2BP1 wild-type (A), S181E (B) or Y396E (C) at concentrations from 0 to 800 nM. (D) Fluorescence anisotropy experiments of wild-type IGF2BP1 (black), S181E (red) and Y396E (blue) and 5′-fluorescein-labeled XBP1 36 nt RNA. Represented as mean, error bars indicating standard deviation (n = 3 technical replicates). The curves represent the fit of the Hill equation (see Materials and Methods). X-axis in log-scale. (E) RNP granule formation of wild-type IGF2BP1 with XBP1 36 nt RNA at different concentrations after 90 min. The protein (left) and RNA (bottom) valency is depicted by the number of folded domains and the number of predicted binding motifs. (F) RNP granule formation assay of IGF2BP1 KH3-4 pseudodimers under the same conditions as Fig. 2E. Valencies depicted as in Fig. 2E. (G) RNP granule formation assay of 5 µM IGF2BP1 KH1-4 with 5 µM XBP1 36 nt RNA after 90 min incubation in comparison to RNP granules formed by 5 µM full length IGF2BP1 with 5 µM XBP1 36 nt RNA at similar conditions (150 mM NaCl). Scale bar is 10 µm. Valencies are depicted for the protein (bottom) and RNA (left). (H) RNP granule formation of IGF2BP1 S181E and (I) IGF2BP1 Y396E with XBP1 36 nt RNA after 90 min of incubation. Scale bar is 10 µm. Valencies depicted as in Fig. 2E. (J) Violin plot of the area per condensate after 90 min with 5 µM IGF2BP1 full-length wild-type (black), S181E (red) and Y396E (blue) with 5 µM XBP1 36 nt RNA. Two-tailed Mann-Whitney test was used to compare wild-type with S181E ($p \le 0.0001$) and Y396E ($p \le 0.0001$). (K) Phase diagram for RNP granule formation by IGF2BP1 wild-type, (L) IGF2BP1 S181E and (M) IGF2BP1 Y396E with XBP1 36 nt RNA at different protein and RNA concentrations after 90 min of incubation. Granule size and abundance is represented by the circle sizes.

-derived model RNAs (*EIF2A*, $K_{1/2}$, wild-type: 48.2 nM, $K_{1/2}$, S181E: 35.4 nM, $K_{1/2}$, Y396E: 40.2 nM and *MYC*, $K_{1/2}$, wild-type: 14.4 nM, $K_{1/2}$, S181E: 17.8 nM, $K_{1/2}$, Y396E: 16.7 nM) (Supplementary Fig. 2D-J, Supplementary Table 2).

As a complementary quantitative approach, we set up fluorescence anisotropy assays to measure the affinity of IGF2BP1 for shorter RNAs. By truncating the 3′-UTR of the *XBP1* mRNA, we identified a 36 nt-long RNA composed of two predicted IGF2BP1 recognition motifs (Supplementary Fig. 2B, Supplementary Table 1). Fluorescence anisotropy assays showed that wild-type IGF2BP1 bound to the 5′-fluorescein-tagged 36 nt-long *XBP1*-derived RNA with an order of magnitude lower affinity than the 201 nt-long version (Fig. 2D, Supplementary Table 2, $K1_{/2}$, wild-type: 311.7 nM). We speculate that the lower affinity is due to a reduced number of binding sites in the RNA, resulting in decreased avidity by the RNA-binding domains. IGF2BP1 phosphomimetic mutants S181E and Y396E bound to *XBP1*-derived 36 nt-long RNA at a comparable affinity (Fig. 2D, Supplementary Table 2, $K1_{/2}$, S181E: 310.1 nM, $K_{1/2,}$ Y396E: 423.3 nM) to the wild-type IGF2BP1. Altogether these data indicated that the phosphomimetic mutants do not significantly impact IGF2BP1s interaction with model RNAs. These findings are consistent with previous data showing that canonical folded RNA-binding domains in IGF2BPs drive their interaction with target RNAs[21–23,39–41].

IGF2BP1 forms RNA-mediated RNP granules in vitro

IGF2BP1 function has been associated with its assembly into RNP granules[42–44]. Therefore, we investigated whether its phosphorylation impacts formation of IGF2BP1 RNP condensates. To test this possibility, we aimed to reconstitute RNP condensates formed by IGF2BP1 and RNAs. Many RNP granules form through phase transitions driven by multivalent interactions between RBPs and RNAs[45–47]. To allow the formation of a multivalent interaction network between IGF2BP1 and RNAs, we used the *XBP1*-derived 36 nt-long RNA, which contains two predicted IGF2BP1-binding motifs (Supplementary Fig. 2B, Supplementary Table 1). We incubated IGF2BP1 with this RNA at different concentrations and stoichiometry and monitored whether they formed RNP condensates visible as droplets by bright-field microscopy (Fig. 2E).

Under physiological pH and salt conditions, 2.5 μM IGF2BP1 and 1 μM *XBP1* 36 nt RNA readily formed RNP condensates (Fig. 2E, Supplementary Fig. 3A, B). Likewise, IGF2BP1 formed condensates at the same protein and RNA concentrations with other model RNAs with similar sequence lengths and number of predicted binding motifs derived from *ACTB, MYC*, and *EIF2A* (Supplementary Fig. 3C, Supplementary Table 1). The sequence properties of the RNA had an impact on the morphology of the IGF2BP1-RNP condensates consistent with the published work[47]. The RNAs with a higher propensity to form secondary structures, such as *ACTB* (free energy of −8.50 kcal/mol, Vienna RNAfold WebServer[48]), formed irregular networks. In contrast, *EIF2A* RNA that was not predicted to form secondary structures formed condensates with droplet-like morphology (Supplementary Fig. 3C, D, Supplementary Table 1)[49].

Increasing concentration of the IGF2BP1 and RNA resulted in the formation of larger condensates, whereas excess RNA abrogated condensate formation (Fig. 2E, Supplementary Fig. 3B) as shown for other condensates. Charge repulsion due to excess RNA was proposed to contribute to condensate dissolution by RNAs[50]. It is also plausible that the excess RNA occupies individual RNA-binding domains and breaks the multivalent interaction network. While most RNAs we tested did not lead to condensate formation at stoichiometric concentrations with IGF2BP1, the *XBP1*-derived RNA did. We hypothesize that *XBP1*-derived RNA might have additional non-canonical binding sites that drive phase separation even at stoichiometric concentrations. Altogether, we show that IGF2BP1-RNA interactions can mediate phase separation in vitro.

IGF2BP1's KH34 domains drive condensate formation

The KH domains drive RNA recognition in IGF2BPs, and the differences in their binding specificity contribute to substrate recognition by IGF2BPs[21,23,51]. As RNA binding drives the condensate formation by IGF2BP1, we next mapped which RNA-binding domains in IGF2BP1 contribute to RNP condensate formation. We first measured the affinity of IGF2BP1's individual domains for model RNAs. We found that KH3-4 dimers bound to a model *ACTB*-derived RNA (ACTB 28 nt)[39] and the *XBP1*-derived 36 nt-long RNA (Supplementary Table 1) at around 1.5 μM affinity (Supplementary Fig. 3E, F, Supplementary Table 2). Instead, KH1-2 bound to the same RNAs with an affinity of >15 μM. Likewise, the RRM1-2 dimer displayed very low apparent binding affinities for both of those RNAs (< 100 μM) (Supplementary Fig. 3E, F). These data are consistent with the earlier work indicating that KH3-4 domains in IGF2BPs bind to RNA with the highest affinity[41]. Introducing GEEG mutations, which impede the RNA interaction of the respective KH domain[51,52], into the RNA-binding motif in the KH3 domain in KH3-4 decreased binding affinity to *XBP1*-derived 36 nt-long RNA by 10-fold (Supplementary Fig. 3G, Supplementary Table 2, $K1_{/2}$ = 16.0 μM). In contrast, the KH3-4 mutant in which the binding site in KH4 is mutated, bound to RNA with a similar affinity as the wild-type KH3-4 dimers ($K_{1/2}$ = 2.1 μM) (Supplementary Fig. 3G). These data suggest that KH3 provides the major RNA binding site since in the KH3-4 construct.

A KH1-4 construct lacking the linker 1 bound to the *ACTB* and *XBP1*-derived short RNAs with similar affinity as the full-length IGF2BP1 (Supplementary Fig. 3E, F, Supplementary Table 2, *ACTB*: $K_{1/2}$ = 75.2 nM, full-length IGF2BP1: $K_{1/2}$ = 68.6 nM; *XBP1*: $K_{1/2}$ = 204.0 nM, full-length IGF2BP1: $K_{1/2}$ = 311.7 nM;). These data suggest that the binding of KH1-2 and KH3-4 domains to RNAs with two binding sites leads to an avidity effect. This can be due to the increased effective concentration for the subsequent binding events after the first KH dimer binds the RNA. Moreover, the incomplete dissociation because of proximal binding sites might increase the apparent affinity[53] (Supplementary Fig. 3H). To characterize this further, we mutated the KH3 and KH4 RNA-binding motifs to GEEG in the full-length IGF2BP1. Both the EMSA assays and fluorescent anisotropy experiments showed that full-length IGF2BP1 KH3-4 GEEG double mutant bound to RNA with similar affinity as the wild-type IGF2BP1 (Supplementary Fig. 3I,J, Supplementary Table 2, $K1_{/2}$ mutant: *XBP1*-derived 36 nt-long RNA: 185.8 nM; *XBP1*-derived 201 nt-long RNA: 64.7 nM). This indicates that multivalent interactions formed by the simultaneous binding of RRM1-2 and KH1-2 dimers to RNA results in an avidity effect that significantly enhances the affinity compared to the individual dimers. Interestingly, the EMSA assays performed with the *XBP1*-derived 201 nt-long RNA showed that compared to wild-type IGF2BP1, the IGF2BP1 KH3-4 GEEG double mutant displayed differences in the high molecular weight assemblies formed at higher protein concentrations (> 250 nM, Supplementary Fig. 3J). From these data, we concluded that the impaired RNA-binding of KH3-4 pseudodimers results in a different mode of RNA recognition by the mutant.

In line with the fluorescence anisotropy experiments, which showed the role of the KH3-4 in RNA recognition by the IGF2BP1, the KH3-4 domains alone formed condensates in the presence of RNA (Fig. 2F). Importantly, impairing RNA binding to either KH3 or KH4 domains through GEEG mutations abolished condensate formation (Supplementary Fig. 4A). We propose that this is by impairing their ability to form multivalent interactions required for condensate formation. These data revealed that KH3-4 domains are sufficient to build the multivalency that drives IGF2BP1 RNP condensate formation. Consistent with these results, bright-field microscopy analysis showed that the full-length IGF2BP1 KH3-4 GEEG mutant did not form condensates under the same conditions (Supplementary Fig. 4B). These data indicated that even though this mutant binds to RNA with high affinity (Supplementary Fig. 3I, J, Supplementary Table 2, K_D:185.8 nM), the low RNA-binding affinities of the individual KH1-2 and RRM1-2

domains (Supplementary Fig. 3E, F, Supplementary Table 2) do not allow the formation of networks that are necessary for condensate formation under the same conditions. Supporting this, KH1-2 domains alone did not form condensates under conditions where KH3-4 formed droplets (Supplementary Fig. 4C). Notably, a model RNA with a single IGF2BP1-binding motif did not mediate condensate formation when incubated with KH1-4, validating that multiple binding sites in both the RNA and protein are required for condensate formation (Supplementary Fig. 4D). Remarkably, KH1-4 formed mesh-like networks upon incubation with the *XBP1*-derived 36 nt-long RNA under conditions where full-length IGF2BP1 formed droplets (Fig. 2G). These findings indicated that IGF2BP1-RNA granules form via phase separation coupled to percolation[54]. These data also suggested that promiscuous RNA interactions by the RRM1-2 domains increases the dynamics in IGF2BP1-RNA interactions and possibly the valency in the network. In the presence of 250 mM NaCl, KH1-4 formed condensates similar to full-length IGF2BP1 (Supplementary Fig. 4E). We speculate that presence of a high concentration of salt weakens the interaction of KH1-4 with RNA, increasing their binding dynamics. In summary, our data revealed that binding of the KH3-4 pseudodimers to RNA drives IGF2BP1 condensate formation. We speculate that once the condensates are formed, due to the high protein and RNA concentration in the condensed phase, the RRM1-2 and KH1-2 pseudodimers can form additional contacts with RNA.

Phosphomimetic mutations modulate IGF2BP1 dynamics in RNP granules

After establishing that IGF2BP1 assembled into condensates together with RNA, we next tested whether phosphomimetic mutants S181E and Y396E would display differences in the formation of RNP condensates compared to wild-type IGF2BP1. To this end, we used fluorescence microscopy to quantify the size and area of the condensates formed by wild-type IGF2BP1 and its phosphomimetic mutants at 90 min after induction of condensate formation by the addition of RNA. Quantification of the IGF2BP1-RNA condensates (Supplementary Fig. 3A, see materials and methods) revealed that the average size of condensates and the total area of condensates formed by the S181E mutant were smaller compared to the wild-type IGF2BP1, indicating that the IGF2BP1 S181E mutant is impaired in condensate formation (Fig. 2H, J, Supplementary Fig. 4F-I, Supplementary Table 3, median area per condensate: wild-type: 7.0 μm, S181E: 5.7 μm, mean total area: wild-type: 7753 μm^2, S181E: 4691 μm^2, at 5 μM protein and RNA concentration). While IGF2BP1 S181E is largely impaired in condensate formation at 2.5 μM when incubated with stoichiometric amounts of *XBP1*-derived 36 nt-long RNA (Fig. 2H), the presence of 5% mCherry-labeled construct leads to the formation of small condensates (Supplementary Fig. 4F-I). We observed that the mCherry-tag enhances the phase separation propensity of IGF2BP1. This effect was prominent when 2.5 μM IGF2BP1 full-length S181E was incubated with 2.5 μM *XBP1*-derived 36 nt-long RNA (Supplementary Fig. 4G), likely because the saturating concentration of this protein is very close to 2.5 μM. Thus, we used sub-stochiometric amounts of mCherry-labeled IGF2BP1 to quantify the condensate area. Intriguingly, in contrast to the S181E mutant, the Y396E mutant formed larger condensates with a larger total area under the same experimental conditions (Fig. 2I, J, Supplementary Fig. 4 F, H, I, Supplementary Table 3, median area per droplet: Y396E 10.8 μm, mean total area: Y396E 9298 μm^2, at 5 μM protein and RNA concentration). Similarly, incubation of *XBP1*-derived 36 nt-long RNA with KH1-4 Y396E mutant led to the formation of condensates with regular droplet-like shape compared to the condensates formed by the wild-type KH1-4 under the same conditions (250 mM NaCl). These data confirmed that the Y396E mutation impacts condensate formation, and this effect does not depend on RRM1-2 domains in IGF2BP1 (Supplementary Fig. 4J). Notably, the impact of S181E and Y396E of the phosphomimetic mutants on the morphology of the IGF2BP1-RNP condensates were identical for four different model RNAs, where the condensates formed by the S181E constructs were smaller and irregular. In contrast, Y396E formed of larger and round droplet-like granules (Supplementary Fig. 5A-I).

We next tested whether phosphomimetic mutants affect the condensation threshold of IG2BP1 RNP condensates. We generated phase diagrams of wild-type IGF2BP1 and its phosphomimetic mutants at different protein and RNA concentrations to address this possibility. Surprisingly, all of the three constructs showed similar threshold concentrations for condensate formation (Fig. 2K-M), with the only difference being IGF2BP1 Y396E, which shows condensate formation at 1.5 μM protein and RNA concentration, while the wild-type did not. The diagram indicated that phase transitions occur at RNA concentrations above 125 nM which coincides with the binding affinity of IGF2BP1 to RNA. At the same time, the saturation concentration of the protein is above 0.5 μM indicating that at low concentrations the percolation required for condensate formation depends on an excess of protein. However, at all the conditions close to the saturation threshold, S181E mutant formed smaller condensates compared to the wild-type IGF2BP1 (Fig. 2K-M). These data indicated that while the phosphomimetic mutants do not impact the saturation concentration, they modulate biophysical properties of the condensates.

Polymers that undergo phase separation coupled to percolation form clusters in sub-saturation concentrations[55]. Thus, we investigated whether the phosphomimetic mutations affect the formation of pre-percolation clusters by using Dynamic Light Scattering (DLS). At low protein and RNA concentrations under the saturation threshold (250-800 nM), we observed particles with around 100 nm hydrodynamic radius for wild-type IGF2BP1 and the phosphomimetic mutants (Supplementary Fig. 5J). Under most conditions, the particles with a hydrodynamic radius (R_{hyd}) around 100 nm were most abundant species but at higher protein and RNA concentrations we observed larger clusters (R_{hyd} > 1000 nm) for all three constructs. Remarkably, under the conditions where we used 2:1 protein to RNA ratio, we observed even larger clusters (R_{hyd} > 10000 nm), which is in line with the phase separation assays (Supplementary Fig. 4F, Supplementary Fig. 5J). These data highlighted that the phase separation of IGF2BP1 with RNA is coupled to the formation of clusters at sub-saturation conditions and driven by similar types of interactions. Based on our data, we hypothesize that the effect of the phosphomimetic mutants on the condensate size is not primarily a result of a shift in the saturation concentration but due to changes in the low-affinity interaction network that define the biophysical properties of these RNP granules.

Next, we used turbidity assays to monitor the kinetics of condensate formation following the addition of RNA to the protein. The turbidity assays showed that IGF2BP1 S181E mutant formed condensates with slower kinetics, indicating that phase separation is impaired for this mutant (Supplementary Fig. 5K, Supplementary Table 4, wild-type: $t_{1/2}$ = 167 s, S181E: $t_{1/2}$ = 252 s). Moreover, the condensates formed by the IGF2BP1 S181E mutant showed lower scattering intensity compared to the wild-type protein (Supplementary Fig. 5K, Supplementary Table 4, wild-type: OD_{480} = 0.068, S181E: OD_{480} = 0.035), consistent with the microscopy data that showed the formation of smaller condensates (Fig. 2H, J). In contrast, the Y396E mutant had slightly faster formation kinetics compared to the wild-type IGF2BP1 with similar scattering intensity (Supplementary Fig. 5K, Supplementary Table 4, Y396E: $t_{1/2}$ = 115 s, OD_{480} = 0,064,). We cannot exclude the possibility that IGF2BP1 phosphomimetic mutants slightly impact the threshold concentrations close to the phase boundary and this might affect the kinetics of granule formation in this assay. To sum up, our data indicate that phosphomimetic mutations in the IGF2BP1 disordered linker regions impact the formation of RNP condensates in opposing directions and in a context-dependent manner.

Protein dynamics in condensates impact fusion and growth and affect condensate size[56]. Moreover, the dynamics of the condensate components often correlate with their function[57,58]. We hypothesized that the differences in the sizes and morphology of IGF2BP1 condensates formed by the phosphomimetic mutants might stem from differences in the dynamics of IGF2BP1 molecules in the condensates. Fluorescence recovery after photobleaching (FRAP) experiments measure protein diffusion and mobility in condensates and are widely used to determine the nature of protein interactions in the condensates[59,60]. To test whether IGF2BP1 phosphomimetic mutants had different diffusion dynamics in RNP condensates by FRAP experiments, we formed IGF2BP1-RNA condensates with sub-stochiometric mCherry-tagged IGF2BP1 and monitored the recovery of mCherry fluorescence in the condensates after photobleaching. To decouple condensate growth from fluorescence recovery and allow the formation of large condensates that are tractable for the FRAP measurements, we incubated IGF2BP1 with RNAs for 90 min before performing the photobleaching experiments. The FRAP data revealed that mCherry-IGF2BP1 fluorescence did not recover even 15 min after photobleaching, indicating that IGF2BP1 formed stable complexes with RNAs in the condensates. The long recovery time likely reflects the multivalent nature of IGF2BP1's interaction with RNA, which results in high residence times and long-lived interactions[61]. Consistent with this explanation, FRAP experiments showed that similar to wild-type IGF2BP1, the condensates formed by IGF2BP1 phosphomimetic mutants did not recover fluorescence intensity even after 15 min (Fig. 3A).

We hypothesized that due to competition with other RNAs and RBPs, IGF2BP1 might exhibit more dynamic interactions with RNAs in a cellular environment. Therefore, we reconstituted IGF2BP1-RNA granules under conditions that mimic the nature of RNP interactions in a complex environment. It has been recently shown that supplementing mammalian cell lysates with G3BP1, the RBP that drives stress granule assembly, results in the formation of RNP condensates, which closely resemble stress granules in protein and RNA composition[62]. IGF2BP1 is a component of the stress granules, and we used this method to reconstitute IGF2BP1-containing RNP condensates in cell lysates obtained from HEK293 cells expressing GFP-tagged IGF2BP1. The addition of recombinant G3BP1 to cell lysates induced the formation of condensates that were positive for GFP fluorescence, indicating that recombinant G3BP1 leads to the formation of IGF2BP1-containing RNP condensates in cell lysates (Fig. 3B). We confirmed these results by adding recombinant mCherry-tagged IGF2BP1 after the formation of stress granules. We found that the mCherry-tagged IGF2BP1 was sequestered into G3BP1 induced-RNP condensates (Fig. 3B). We used this experimental setup to assess the dynamics of wild-type mCherry-IGF2BP1 and its phosphomimetic mutants S181E and Y396E in RNPs by FRAP experiments. We found that wild-type IGF2BP1 formed condensates with a mobile fraction of 68.8 % 100 min after the induction of RNP condensate formation with a recovery half-time of 21.6 sec (Fig. 3C, D, Supplementary Table 5). Intriguingly, FRAP experiments performed with the IGF2BP1 S181E mutant showed an almost two-fold increase in recovery half-time (37.5 s), and a slight decrease in the mobile fraction (62.2 %) compared to the wild-type IGF2BP1. In contrast, the IGF2BP1 Y396E mutant showed a faster recovery (15.5 s) and a slightly higher mobile fraction (74.1 %) than the wild-type. These data revealed that while the S181E mutant forms more stable interactions in the RNP condensates, the Y396E forms more dynamic ones. These data showed a correlation between the size of RNP condensates, the mobility and dynamic population of IGF2BP1 wild-type and the phosphomimetic mutants. Therefore, we hypothesize that the S181E mutant forms a more stable interaction with RNAs, and the decreased dynamics leads to the formation of smaller condensates by the S181E mutant. Instead, the Y396E mutant leads to increased dynamics and results in the formation of larger condensates.

Phosphomimetic mutants impact the size and number of IGF2BP1 RNP granules in cells

To study the impact of the phosphomimetic mutations on IGF2BP1's assembly into RNPs in cells, we established mammalian cell lines stably expressing mCherry-tagged wild-type human IGF2BP1 or its phosphomimetic mutants using a lentiviral transduction approach. We selected two mammalian cell lines for these experiments: U2OS cells (human osteosarcoma) and HCT116 cells (colon carcinoma cells). HCT116 cells do not express IGF2BP1. To exclude the possibility of functional redundancy between IGF2BP paralogs, we knocked out IGF2BP2/3 in HCT116 cells using CRISPR-cas9 gene editing (Supplementary Fig. 6A). As IGF2BP1 expression levels might impact condensate formation, we used fluorescence-activated cell sorting (FACS) to select cells that expressed mCherry-tagged wild-type IGF2BP1 and its phosphomimetic mutants at similar levels. For the HCT116 cells, we used FACS to select single clones to ensure similar expression levels between wild-type and the mutants (Supplementary Fig. 6B, C, Supplementary Data 2). In addition, we studied U2OS cells due to their extended morphology, which is well-suited for microscopy experiments. To monitor stress granules and IGF2BP1 condensates simultaneously, we used engineered U2OS cells expressing GFP-tagged stress granule marker G3BP1[63]. We picked a population of U2OS cells where mCherry-IGF2BP1 and its mutants were expressed similarly to the wild-type protein levels (Supplementary Fig. 6D, E, Supplementary Data 3).

We assessed whether, similar to the in vitro results, IGF2BP1 phosphomimetic mutants impact RNP condensate formation in cells by studying IGF2BP1's assembly into stress granules. Treatment of cells with sodium arsenite resulted in stress granule formation, evidenced by IGF2BP1 sequestration into G3BP1 positive RNP granules (Supplementary Fig. 6F). Quantification of the number, size and total area of mCherry-IGF2BP1 positive granules revealed that HCT116 cells expressing wild-type and phosphomimetic mutants showed similar total granule area per cell (Fig. 3E, F, Supplementary Table 6, median total area per cell, wild-type: 10.3 μm^2, S181E: 10.3 μm^2, Y396E: 10.2 μm^2). Notably, the S181E mutant formed a higher number of condensates per cell (Fig. 3G, Supplementary Table 6, mean condensate number, wild-type: 5.7, S181E: 7.2) with a slightly smaller area per condensate (Fig. 3H, Supplementary Table 6, median condensate area, wild-type: 1.1 μm^2, S181: 1.0 μm^2) indicating that similar to what we found in vitro, the S181E forms smaller condensates in cells (Fig. 3H, Supplementary Table 6). These results were similar in both HCT116 and U2OS cell lines, with the differences being more pronounced in the HCT116 cell line. U2OS cells expressing the S181E mutant showed a lower total area of condensates and higher number of condensates (Supplementary Fig. 6G-J, Supplementary Table 6, median total area per cell, wild-type: 34.2 μm^2, S181E: 27.1 μm^2, mean number of condensates per cell, wild-type: 18.5, S181E: 20.7). The IGF2BP1 Y396E mutant did not display a large difference in size of the condensates but showed higher number of condensates in HCT116 cells (Fig. 3E-H, Supplementary Table 6, median condensate area, Y396E: 1.1 μm^2, mean condensate number per cell, Y396E: 6.3). Instead, condensates formed by the Y396E mutant in U2OS cells were smaller compared to those formed by wild-type IGF2BP1 (Supplementary Fig. 6G-J, Supplementary Table 6, median condensate area, wild-type = 0.98 μm^2, Y396E = 0.80 μm^2). We speculate that the expression of the wild-type IGF2BP1 and other IGF2BP paralogs, as well as cell-type dependent differences in signaling cascades, could result in the heterogeneity observed in U2OS cells. Overall, we found that the S181E mutation impacts the formation of IGF2BP1-containing granules in cells.

To further characterize the properties of IGF2BP1 in RNP granules in cells, we performed FRAP experiments in U2OS cells expressing mCherry-labeled wild-type IGF2BP1 and its phosphomimetic mutants, S181E and Y396E. Both the S181E and the Y396E mutants displayed reduced levels of dynamic population in stress granules compared to

https://doi.org/10.1038/s41467-024-53400-4

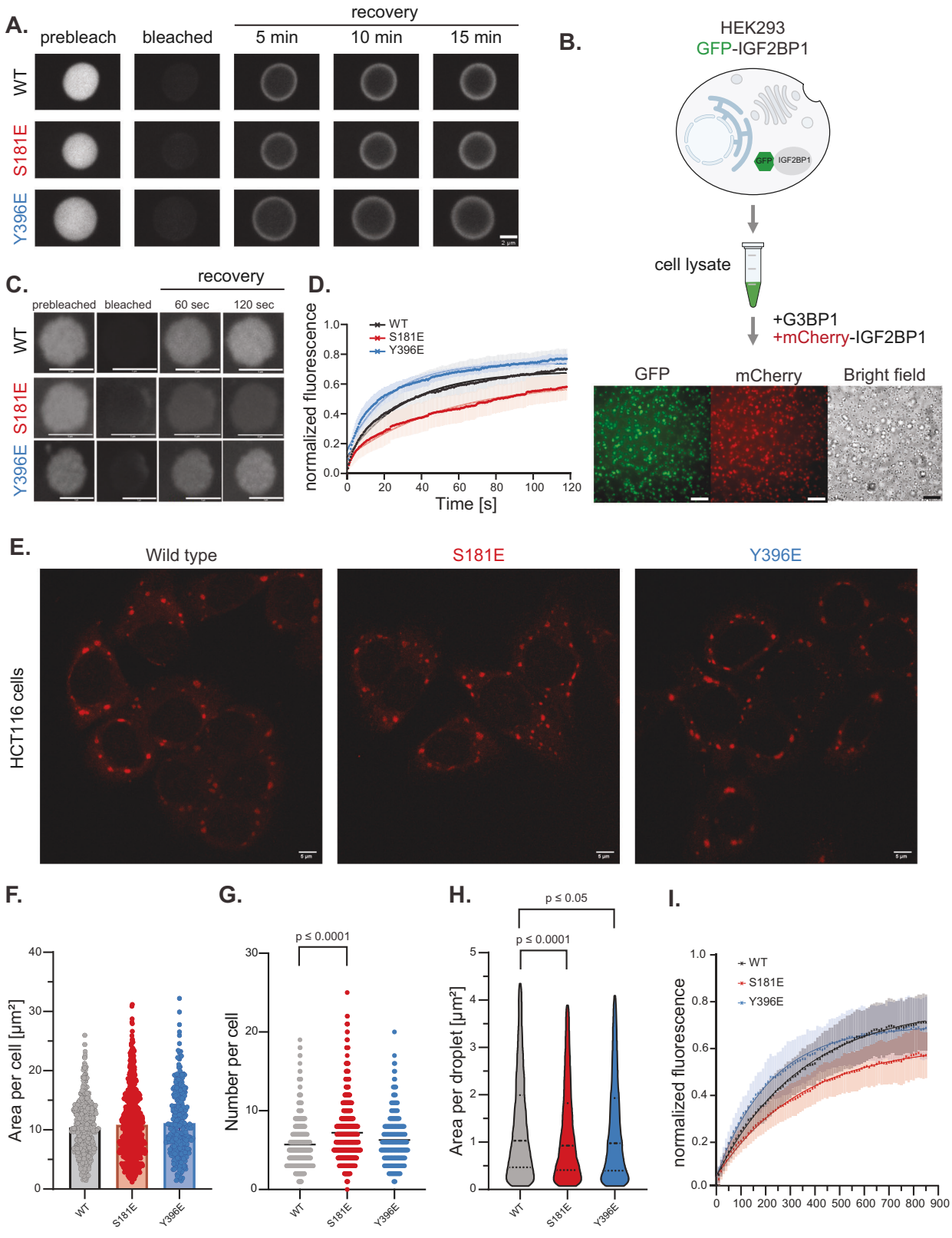

the wild-type IGF2BP1 (% dynamic population wild-type= 77.9, S181E = 61.3 Y396E = 69.4) (Fig. 3I, Supplementary Table 7). This data was inconsistent with the stress granules formed in the lysates, where the Y396E mutant displayed a higher dynamic population than the wild-type IGF2BP1 (Fig. 3D, Supplementary Table 5). In cells, the S181E mutant showed similar recovery half-time as the wild-type IGF2BP1, in contrast the Y396E recovered faster (Fig. 3I, Supplementary Table 7, $t1_{/2}$ [s] wild-type= 241.7, S181E = 240.0, Y396E = 151.3). We speculate that the composition and the relative stoichiometry of the components in stress granules formed in vitro compared to the ones formed in cells, resulting in the differences observed here. Moreover, it is plausible that stress-induced phosphorylation of the Y396E mutant at different sites might contribute to the differences observed here. Altogether, our data show that the IGF2BP1 phosphomimetic mutants impact

Fig. 3 | Phosphomimetic mutants affect formation and dynamics of IGF2BP1 RNP condensates in cells. (A) Representative images of Fluorescence Recovery After Photobleaching (FRAP) of condensates formed by 5 μM full-length IGF2BP1 wild-type, S181E and Y396E and 5% mCherry-labeled IGF2BP1 constructs in the presence of 5 μM XBP1 36 nt RNA after 90 min incubation. Scale bar is 2 μm. (B) Schematic depiction of G3BP1-induced RNP granule formation in lysates and representative images of the incorporation IGF2BP1 into RNP granules. Scale bar is 20 μm. (C) Representative images of FRAP experiments with mCherry-IGF2BP1 wild-type, S181E and Y396E mutants in RNP granules after 100 min incubation. Scale bar is 5 μm. (D) Recovery curves of FRAP experiments with mCherry-IGF2BP1 wild-type (black), S181E (red) and Y396E (blue) mutants in G3BP1-induced granules after 100 min incubation. Data represented as mean with error margins indicating the standard deviation. Curves represent the fit to a one-phase association equation (see Materials and Methods). n = 10 for wild-type, n = 11 for S181E, n = 13 for Y396E. (E) Representative fluorescence images of fixed HCT116 cells expressing mCherry-IGF2BP1 wild-type, S181E or Y396E. Cells were fixed 60 min after stress induction by 500 μM arsenite. Scale bar is 5 μm. Quantification of condensates in HCT116 cells represented as scatter plots: (F) total area of condensates per single cell (n = 449 for wild-type, n = 741 for S181E, n = 278 for Y396E, bar represents mean value; two-tailed t-test was for statistical analyzes) (G) number of condensates per single cell (bar represents mean value; two-tailed t-test was used to compare wild-type with S181E ($p \leq 0.0001$) and Y396E) (H) area per condensate (bars represent the median and 25 % and 75 % quartiles; two-tailed Mann-Whitney test was used to compare wild-type with S181E ($p \leq 0.0001$) and Y396E ($p \leq 0.05$)). (I) Recovery curves of FRAP experiments of arsenite induced stress granules in U2OS cells expressing mCherry-IGF2BP1 wild-type (black), S181E (red) and Y396E (blue). Represented as mean, error margins indicate the standard deviation. Curves represent the fit to a one-phase association equation. n = 17 for wild-type, n = 16 for S181E, n = 14 for Y396E.

IGF2BP1 dynamics, thereby modulating the size of IGF2BP1 condensates in cells.

IGF2BP1 adopts a compact conformation in solution

We aimed to elucidate how the phosphorylation of IGF2BP1 at the disordered linkers mechanistically impacts its condensation into RNP granules. We hypothesized that linkers might contact each other or the folded domains contributing to multivalency in condensates and that phosphorylation of the linkers could affect these interactions. Thus, we monitored the conformational status of IGF2BP1 by small-angle X-ray Scattering (SAXS) analyzes. SAXS is a solution scattering method that provides low-resolution structural information on the overall shape of molecules. Analysis of SAXS scattering curves (Supplementary Fig. 7A) showed that IGF2BP1 displays a maximal extension (D_{max}) of around 20 nm and a radius of gyration (R_g) of 4.18 nm. For flexible molecules such as IGF2BP1, scattering curves represent an average of conformational states sampled by the protein. The Kratky plot of IGF2BP1 highlighted the presence of flexibility in the protein as the curve does not converge to the s-axis (Supplementary Fig. 7B). This is a consequence of a lack of structure in the linker regions. We further analyzed SAXS data using the ensemble optimization method (EOM) to extract information about those states[64]. EOM generates a random pool of structures based on the protein's available structural data and amino acid sequence. EOM then selects the ensemble of structures that best fits the experimental SAXS data. To generate models for EOM for IGF2BP1, we provided high-resolution structures for the individual domains with the flexible linkers. The comparison of the radius of gyration (R_G) and maximal distance (D_{max}) distributions of the random pool of structures compared to the selected ensembles revealed that the selected ensemble displayed more compact structures compared to the random pool (Fig. 4A, B). These analyzes suggest that IGF2BP1 is in a conformational equilibrium between extended and compact states in solution, with a higher number of molecules found in the compact state at any given time. These data also indicate the presence of low-affinity intramolecular contacts within the molecule, leading to its compaction.

Next, to assess whether phosphomimetic linker mutants impact the overall conformation of IGF2BP1 in solution, we used SAXS analyzes. The SAXS data revealed that the scattering curves of the wild-type IGF2BP1 were very similar to the phosphomimetic mutants (Supplemenetary Fig. 7A). In line with this data, EOM analyzes of the phosphomimetic mutants showed comparable distributions of D_{max} and R_g values (Supplementary Fig. 7C, D). The similarity of D_{max} and R_g values indicated that wild-type IGF2BP1 and phosphomimetic mutants share a comparable overall conformational ensemble. These data revealed that the negative charges introduced to the disordered linkers do not result in significant conformational changes in the protein. As SAXS data provides low-resolution information on a conformational ensemble, we next used orthogonal methods to study the impact of phosphorylation on the conformation and self-assembly of the linkers.

IGF2BP1 linkers do not form condensates in isolation

Disordered regions contribute to the phase separation of proteins. Therefore, the phosphorylation of the linkers could regulate condensate formation through modulating self-association between these regions. To monitor the condensation propensity of the linkers in isolation, we performed coarse-grained Molecular Dynamic (MD) simulations of the disordered linkers and their corresponding phosphomimetic mutants (Fig. 4C-D). We ran 10 μs long Martini 3[65] simulations of 33 copies of the polypeptide chains of each linker in explicit solvent. These MD simulations revealed that over a 10 μs time scale, neither the wild-type linker, nor the phosphomimetic mutants assembled into clusters. A more detailed analysis of the intermolecular contact interactions revealed that linker 2 has a slightly higher tendency to engage in low-affinity, short-lived interactions. The wild-type linker 1 and its phosphomimetic mutant show the same lack of intermolecular interactions (Supplementary Fig. 7E). Interestingly, the phosphomimetic mutation in linker 2 significantly promotes the formation of intermolecular interactions (Supplementary Fig. 7F). While introduction of the phosphomimetic mutant Y396E to linker 2 does not lead to condensate formation, it might provide an additional source of low-affinity interactions to drive IGF2BP1 condensation with a liquid-like behavior.

Our in vitro microscopy experiments showed that the linkers did not form condensates at high protein concentrations (150 μM) even in the presence of a crowding agent supporting the MD simulations (Supplementary Fig. 7G). To dissect this further experimentally, we performed Nuclear Magnetic Resonance spectroscopy (NMR) experiments. For NMR analyzes, we produced ^{15}N-isotope labeled proteins. ^{1}H-^{15}N Heteronuclear Single Quantum Coherence (HSQC) experiments revealed a small dispersion of backbone amide signals, thus validating the disordered nature of the linker segments (Supplementary Fig. 8A-D). We assessed the self-association of the isolated disordered linkers by monitoring their NMR signal intensity at different linker concentrations. For monomeric non-self-associating molecules, NMR signal intensity increases linearly with increases in protein concentration. In contrast, if the linkers stably associate with each other, this would broaden the NMR signals and a drop in signal intensity. We acquired HSQC spectra of the linker 1 at protein concentrations ranging from 25-200 μM (Supplementary Fig. 8E). Our data revealed that the signal intensity of the backbone amide groups increased linearly with increased protein concentration, and there was no deviation from the predicted intensities. These data indicated that linker 1 does not stably self-associate under the conditions we tested. We made similar observations with linker 2 under the same experimental conditions, suggesting that both linkers do not form stable clusters or condensates under those experimental conditions (Supplementary

https://doi.org/10.1038/s41467-024-53400-4

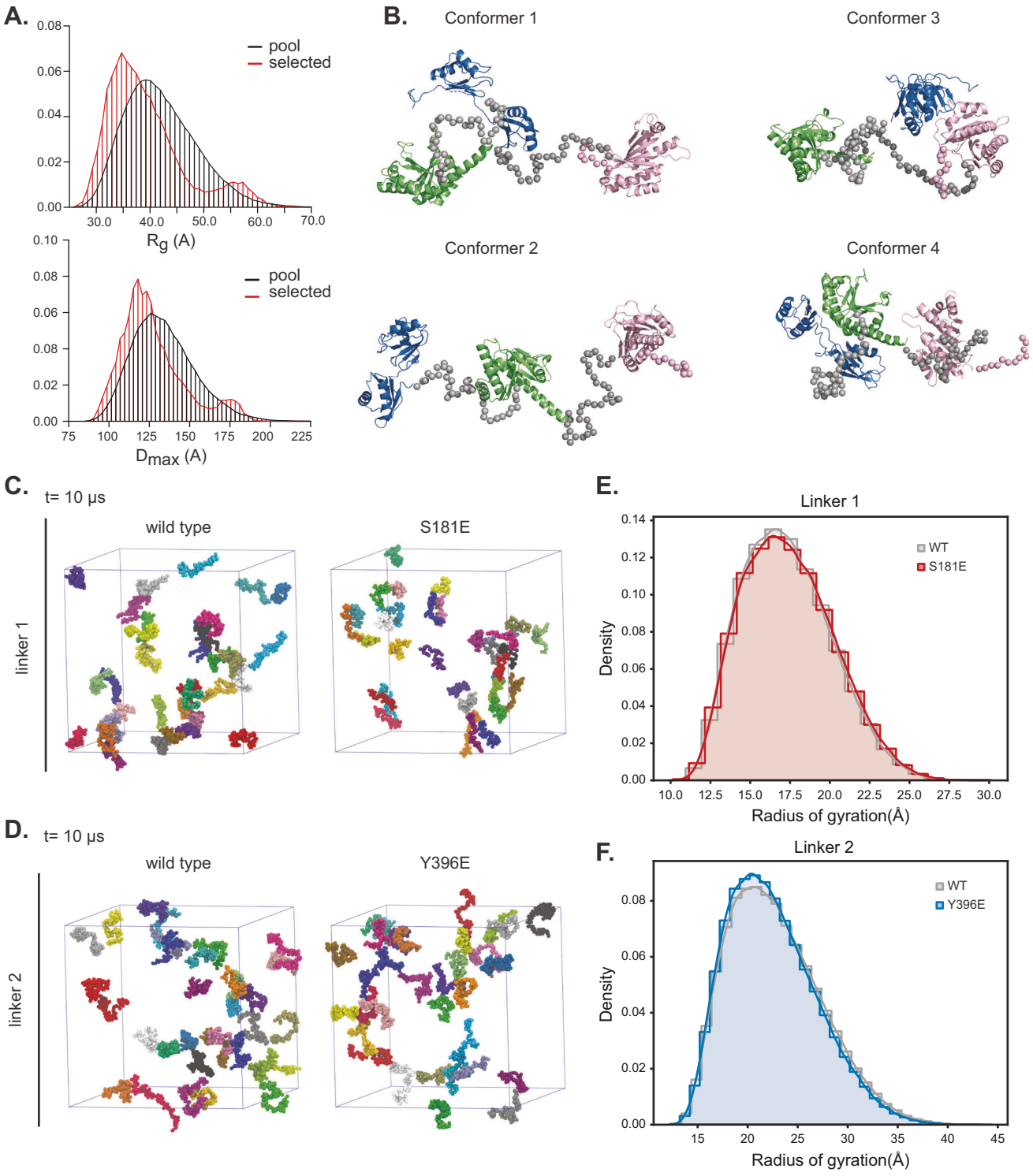

Fig. 4 | IGF2BP1 adopts a compact conformation in solution. (A) Comparison of radius of gyration (R_g, top) and maximum extension (D_{max}, bottom) distribution of random conformations of IGF2BP1 (black) and selected pool (red) that best fit the experimental SAXS data based on EOM analyzes. (B) IGF2BP1 structural conformers that best fit the experimental SAXS data (linkers are shown as gray spheres). The RRM1-2, KH1-2 and KH3-4 domains are colored in blue, green and pink, respectively. (C) Snapshot of coarse-grained Martini 3 Molecular Dynamics simulations of linker 1 and its mutant S181E at 10 μs. Each simulation box contains 33 copies of the polypeptide, depicted in different colors and sphere representation. Water and ions are not shown for clarity. (D) Snapshot of coarse-grained Martini 3 Molecular Dynamics simulations of linker 2 and its phosphomimetic mutant Y396E at 10 μs. Each simulation box contains 33 copies of the polypeptide, depicted in different colors and sphere representation. Water and ions are not shown for clarity. (E) R_g probability density distribution of linker 1 and its phosphomimetic mutant during MD simulations. (F) R_g probability density distribution of linker 2 and its phosphomimetic mutant during MD simulations.

Fig. 8F). To sum up, together with the MD simulations, the NMR data suggest that while the linkers do not drive phase separation on their own, linker 2 phosphomimetic mutant Y396E might form low-affinity contacts with other copies in trans. We anticipate that this might contribute to the changes in the dynamics of the condensates formed by Y396E mutant compared to the wild-type IGF2BP1.

IGF2BP1 linkers adopt an extended conformation

The amino acid properties of interdomain linkers determine their effective solvation volume and impact the conformational space of linear multi-domain proteins[66]. Importantly, linker compaction could regulate phase separation properties in multi-domain proteins[66]. As the linkers we tested did not have a propensity to self-associate, we next tested whether they form short distance intramolecular contacts that underlie the compaction we measured by SAXS analyzes. These contacts might impact the phase separation propensity of IGF2BP1. In MD simulations, we calculated the frequency of contacts formed within the same polymer chain (intra-molecular, cis-interactions). The contact maps obtained (Supplementary Fig. 9A, B) indicated that cis-contacts are rarely established among residues separated by more than four amino acids within the disordered linker 1 and linker 2, and do not occur in the phosphomimetic mutants. These results highlight how cis-interactions are sparse in the wild-type as well as in the phosphomimetic mutants. We observed no long-range interaction within the chains. This was reflected in the lack of trans-interactions in our simulation box. In line with these observations, the distributions of the R_g of the linkers (linker 1 and linker 2) and the phosphomimetic mutants in MD simulations revealed that both linker 1 and linker 2 and their phosphomimetic mutants adopt expanded conformations with similar median R_g values (Fig. 4E-F, Supplementary Table 8). Notably, both linker 1 and linker 2 display higher R_g values compared to an ideal polymer (i.e., an Analytical Flory Random Coil)[67] with perfectly balanced polymer-solvent and polymer-polymer interactions and with the same amino acid sequence for each linker. These higher R_g distribution values correspond to a polymer model where polymer-solvent interactions are more prominent than polymer-polymer interactions (Supplementary Fig. 9C,D). The MD simulations suggested that the linkers form an extended solvent-exposed conformation. Based on these data and the NMR experiments, we excluded the possibility that the differences in linker compaction led to the different phase separation propensities observed for the IGF2BP1 phosphomimetic mutants.

The linkers form low-affinity interactions with the folded domains and RNA

Besides compaction and self-association of the linkers, transient interactions between the linkers and folded domains could lead to the IGF2BP1 compaction observed in SAXS experiments. To test whether the linkers can interact with the folded domains of the protein, we performed ^{1}H-^{15}N HSQC experiments for the titration series of the ^{15}N-labeled linkers with the NMR invisible domains (RRM1-2, KH1-2, and KH3-4). Interactions between the linkers and domains are expected to induce chemical shift perturbations (CSPs) and/or peak broadening, reducing signal intensity for amino acids close to the interaction surface. We used a three-dimensional sequential assignment strategy to assign the signals in the NMR spectra of the linkers. We could unambiguously assign 70–80% of the signals in both linkers.

The titration of linker 1 with the folded domains showed very low CSPs (< 0.015 ppm) that were consistently alike for both the wild-type and S181E mutant protein (Fig. 5A, Supplementary Fig. 10A-I). Therefore, we concluded that linker 1 does not interact with the folded domains of the protein. Besides forming protein-protein interactions, the disordered linkers could form contacts with RNA, which could modulate the phase separation propensity of IGF2BP1. The RGG motifs in RNA-binding proteins mediate RNA-protein interactions[68]. Linker 1 contains an RGG-RG motif which is in the vicinity of S181 that shows evolutionary conservation in mammals and some vertebrate species (Supplementary Fig. 1A). Therefore, we investigated whether linker 1 could contribute to protein-RNA interactions by measuring HSQC spectra of linker 1 in the presence of a model RNA (12xUG) that is recognized by RGG containing proteins through formation of an RNA quadruplex[69] and a 10 nt RNA derived from *XBP1*. Titration of the wild-type linker 1 with the 12xUG RNA resulted in large chemical shift perturbations and a decrease in signal intensity of the residues around the RGG-RG motif (G170, G172 and G175, Fig. 5B-D and Supplementary Fig. 10J, K). Notably, the linker 1 phosphomimetic mutant S181E was impaired in binding to RNA, evident in lower CSPs and a lower drop in the signal intensity around the phosphorylation site upon its titration with the 12xUG RNA. We observed similar, albeit weaker, CSPs of the identical residues upon titration of the linker 1 with the 10nt *XBP1* RNA, indicating that this RNA bound to linker 1 with a much lower affinity (Supplementary Fig. 10L-P). The difference between the wild-type and the S181E mutant was more pronounced due to low-affinity interactions (Supplementary Fig. 10L-P). Our data suggest that impairing non-specific RNA binding by linker 1 via phosphorylation tunes the formation of IGF2BP1-containing RNP condensates.

Next, we assessed whether linker 2 interacts with the folded domains of IGF2BP1 through NMR experiments. The NMR analyzes revealed that titration of wild-type linker 2 with RRM1-2 as well as the KH1-2 domains showed small CSPs around aa S388-P395 (aa 388-SSVTGAP-395) (CSP > 0.015) (Supplementary Fig. 11A-F) indicating that linker 2 interacts with these domains with a low affinity in the millimolar range. Importantly, titration of the linker 2 phosphomimetic Y396E mutant with both domains displayed reduced CSPs in this region. These data demonstrate that the Y396E mutation modulates the low-affinity binding of linker 2 to RRM1-2 and KH1-2 domains.

Titration of linker 2 with KH3-4 domains displayed the largest CSPs observed for all folded domains, revealing that linker 2 most strongly interacts with KH3-4 dimers (Fig. 5E-G, Supplementary Fig. 11G-H). Nevertheless, the fluorescence anisotropy experiments showed that a construct containing linker 2 and the KH3-4 domains (linker 2-KH3-4) bound to RNA with a similar affinity to the KH3-4 domains alone. This result indicates that the low-affinity interaction between linker 2 and the KH3-4 domains does not impair RNA binding (Supplementary Fig. 11I, Supplementary Table 2). The KH3-4 pseudodimers bound to a largely hydrophobic region in linker 2 covering Q361-F376 (aa 361-QSHLIPGLNLAAVGLF-376). Notably, of all IGF2BP1 domains, this segment only bound to KH3-4, emphasizing the specificity of this interaction. In addition, KH3-4 domains bound to a region covering the Y396 phosphorylation site (aa V390-M400). The linker 2 Y396E phosphomimetic mutant showed reduced CSPs upon KH3-4 binding close to the mutation site, yet the interaction of KH3-4 with the hydrophobic segment (aa Q361-F376) was not affected by the Y396E mutation. In summary, linker 2 forms low-affinity contacts with KH3-4 pseudodimers, which are weakened in the Y396E phosphomimetic mutant. Notably, MD simulations on linker 2 showed that the Y396E mutant had an increased propensity to self-associate compared to the wild-type protein. It is plausible that the reformation of the low-affinity interaction network by the linker 2 impacts condensates formed by the phosphomimetic mutant Y396E.

The NMR data revealed that while linker 1 binds to RNA, linker 2 forms low-affinity interactions with the folded domains in IGF2BP1, and both interactions are modulated in the relevant phosphomimetic mutants. We anticipate that these low-affinity interactions are more pronounced in the condensed phase with high protein and RNA concentration (up to 20 mM)[70], resulting in the prominent effect of these mutants in IGF2BP1 RNP condensates.

https://doi.org/10.1038/s41467-024-53400-4

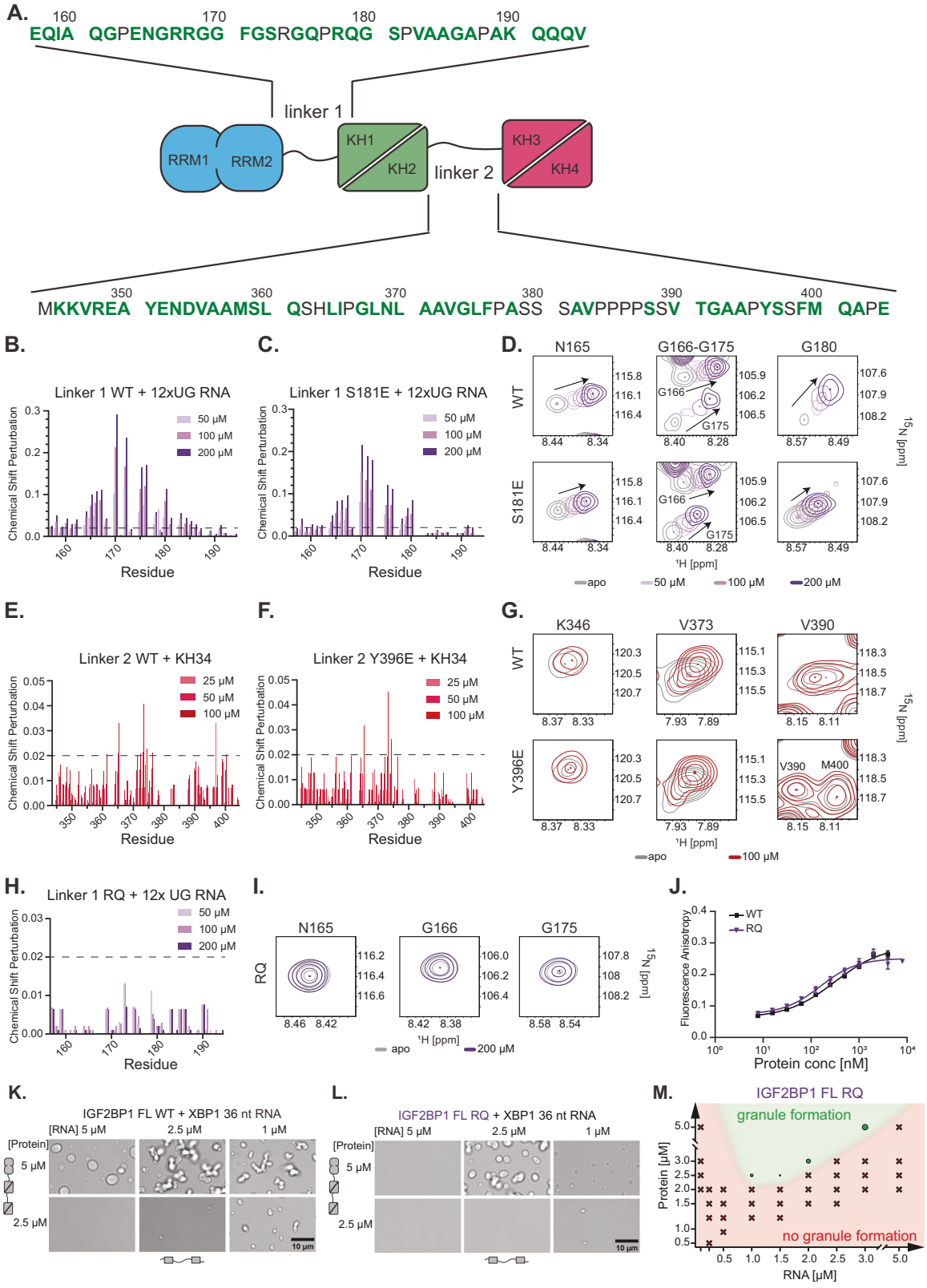

Impairing low-affinity RNA interactions in linker 1 impacts IGF2BP1 phase separation

Based on our NMR data, which showed that the RGG-motif-mediated RNA interactions are weakened in the S181E mutant, we speculated that the loss of low-affinity RNA-protein interactions in S181E impacts the formation of RNP condensates. This model would predict that impairing low-affinity RNA interactions mediated by the RGG motif in the linker 1 would phenocopy the S181E phosphomimetic mutant in its capacity to form RNP condensates. To test this model, we impaired the interaction of the RGG motif with RNAs by mutating four arginine residues at the positions 167, 168, 174, and 178 to glutamine, and for simplicity, we called this mutant IGF2BP1 RQ mutant (Supplementary Table 9). To investigate the effect of the RQ mutations on the RNA binding by the linker 1, we performed HSQC titration experiments with a model RNA

Fig. 5 | Disordered linkers form low-affinity contacts to regulate IGF2BP1 phase separation. (A) Amino acid sequence of wild-type linker 1 and linker 2. (B) Chemical Shift perturbation (CSP) analyzes of ^{15}N-labeled wild-type linker 1 in the absence (black) and presence of various concentrations of 12xUG RNA in ^{15}N-^{1}H HSQC experiments. (C) CSP analyzes of ^{15}N-labeled linker 1 S181E mutant in the absence and presence of various concentrations of 12xUG RNA. (D) Select backbone amide signals in the HSQC spectrum of wild-type linker 1 and the S181E mutant in the absence and the presence of various concentrations of 12xUG RNA. (E) CSP analyzes of ^{15}N-labeled wild-type linker 2 in the absence and presence of different concentrations of KH3-4. (F) CSP analyzes of ^{15}N-labeled linker 2 Y396E mutant in the absence and presence of various concentrations of KH3-4. (G) Representative signals of ^{15}N-labeled wild-type linker 2 and Y396E in the absence and presence of 100 μM KH3-4. (H) CSP analyzes of ^{15}N-labeled linker 1 RQ mutant in the absence and presence of various concentrations of 12xUG RNA. (I) Representative backbone amide signals from the linker 1 RQ mutant in absence and the presence 200 μM of 12xUG RNA from HSQC spectra. (J) Fluorescence anisotropy experiments measuring binding of wild-type IGF2BP1 (black) and IGF2BP1 RQ (purple) to 5′-fluorescein labeled XBP1 36 nt RNA. Data is represented as mean with error bars indicating the standard deviation (n = 3). The curves represent the fit of the Hill equation (see Materials and Methods). X-axis is represented in log-scale. (K) Comparison of the RNP granule formation of wild-type IGF2BP1 and (L) IGF2BP1 RQ in the presence of XBP1 36 nt RNA after 90 min of incubation. The protein and RNA concentrations are indicated in the figures. The valency of the protein (left) is depicted by the number of folded domains. The valency of the RNA (bottom) is depicted as the number and position of binding motifs. (M) Phase diagram of RNP granule formation of IGF2BP1 RQ with XBP1 36 nt RNA at different protein and RNA concentrations after 90 min of incubation.

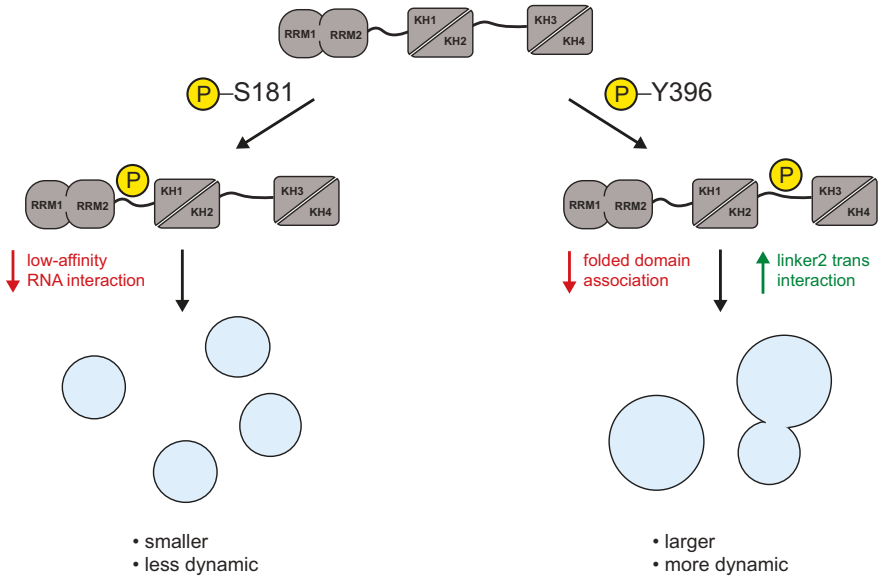

Fig. 6 | Phosphorylation of IGF2BP1 in disordered linkers impacts RNP condensates. Model depicting how phosphorylation affects IGF2BP1 RNP condensates.

(12xUG). We showed that the RQ mutant linker 1 was abolished entirely in binding to this model RNA (Fig. 5H, I, Supplementary Fig. 11J). The EMSA data revealed that the binding of IGF2BP1 RQ mutant to the *XBP1*-derived 201 nt-long RNA was not affected by the abrogation of low-affinity protein-RNA interactions in the linker 1 (Supplementary Fig. 11K, L, Supplementary Table 2). Accordingly, fluorescence anisotropy experiments did not indicate any observable difference in the RQ mutant's affinity to the *XBP1*-derived 36 nt RNA (Fig. 5J).

Remarkably, compared to the IGF2BP1 wild-type, the RQ mutant was largely impaired in RNP condensate formation in the presence of the *XBP1*-derived RNA (Fig. 5K-M). This effect was even more notable when we investigated the granule formation with the *MYC*-derived RNA (Supplementary Fig. 11M, N) where we could not observe condensates at any concentration used in these experiments. In summary, these data show that abrogating low-affinity protein-RNA interactions of the RGG/RG motif in linker 1 has no observable effect on the apparent binding affinity but impacts the RNP granule formation. Notably, the RQ mutant phenocopied the behavior of the S181E mutant, supporting the notion that low-affinity RNA interactions through the linker 1 regulate phase separation of IGF2BP1.

Based on our data, we hypothesize that the proteotoxic stress-dependent phosphorylation of S181 increases the rigidity and decreases the size of IGF2BP1-containing granules by abrogating low-affinity protein-RNA interactions. In contrast, Y396E phosphorylation increases the dynamics and size of these condensates by modulating low-affinity protein interaction networks (Fig. 6).

Disordered linkers contribute to RNA regulation by IGF2BP1

While phosphorylation of the disordered linkers was shown to contribute to the posttranscriptional RNA regulation by IGF2BP1, our knowledge has been limited to select targets. To have a global view of the regulation of RNA metabolism by IGF2BP1 phosphorylation in cells, we performed transcriptomics analyzes in HCT116 cells that solely express wild-type mCherry-IGF2BP1 or its phosphomimetic mutants. To identify whether the linker mutations impact IGF2BP1's binding to RNAs in an unbiased manner, we employed RNA immunoprecipitation sequencing (RIP-seq) experiments under control conditions and upon exposure of the cells to arsenite stress. We immunoprecipitated mCherry-IGF2BP1 and its mutants (S181E and Y396E) using RFP-TRAP magnetic beads and isolated the associated RNAs for deep sequencing. We used nonengineered HCT116 cells as a control to account for the unspecific interaction of the cellular RNA with the beads. To determine the possible function of low-affinity RNA interactions by the linker 1, we engineered HCT116 cells to express mCherry-IG2BP1 RQ mutant using lentiviral transduction and characterized its binding to RNAs. To circumvent differences in the transcriptome that might arise from clonal selection, for those experiments, we selected a population using a very narrow gate for mCherry signal in the FACS experiments to ensure comparable expression levels of the wild-type mCherry-IGF2BP1 and its mutants (Supplementary 12A, Supplementary Data 4).

The transcriptomics data showed that the levels of several RNAs significantly (adjusted p-value < 0.05) increased or decreased more than 20% in HCT116 cells expressing IGF2BP1 mutants compared to the

wild-type in control conditions and upon induction of stress via arsenite treatment. These data validated the regulatory role of the disordered linkers for IGF2BP1 function to control RNA metabolism in cells. Principle component analyzes clustered mCherry-IGF2BP1 wild-type with the RQ mutant, whereas mCherry-IGF2BP1 S181E mutant clustered together with the Y396E mutant, underlining the regulatory role of the distinct sites S181 and Y396 in the linkers (Supplementary Fig. 12B, Supplementary Data 5).

The phosphomimetic mutants did not impact the RNA-binding affinity of IGF2BP1 for several model RNA substrates in our in vitro assays. While these assays are robust in providing quantitative information on these select substrates, we sought to obtain a genome-wide global overview of whether the phosphomimetic mutations impact the RNA-binding capacity of IGF2BP1 in cells. We compared the RIP-seq data from wild-type IGF2BP1 and its mutants toward this goal. To define the high confidence IGF2BP1-binding transcripts, we set an arbitrary cut-off of 4-fold enrichment of the IGF2BP1-bound RNAs compared to the total RNA levels. Moreover, we set a threshold of 4-fold enrichment of RNAs in the RIP-seq data compared to the background to eliminate unspecific RNA interactions. The RIP-seq analyzes showed that wild-type mCherry-IGF2BP1 and its mutants bound approximately 1400 RNAs under control conditions, aligning with the published data (Supplementary Fig. 12C)[8,71]. Gene Ontology term analyzes of IGF2BP1-bound RNAs confirmed IGF2BP1's regulatory role in development and metabolism[28,72] (Supplementary Fig. 12D). While 462 of these RNAs did not show stress-dependent differences in their binding to IGF2BP1, approximately 1000 RNAs only bound to IGF2BP1 during control conditions, and about 250 RNAs only during arsenite treatment (Supplementary Fig. 12E). These analyzes revealed that the arsenite stress impacts IGF2BP1's interaction with select RNA targets. Notably, the IGF2BP1 mutants bound to a largely overlapping set of RNAs as the wild-type protein under control conditions (1200 shared target RNAs), while only 200 RNAs interacted with either wild-type IGF2BP1 or the linker mutants (Supplementary Fig. 12E).

The differences in the RNA expression levels might impact IGF2BP1 binding to RNA. To circumvent this problem, we defined an RNA-binding score by normalizing the RIP-seq levels to the RNA-seq levels. The fold-change in the RNA-binding score for mCherry-IGF2BP1 versus its mutants revealed a set of RNAs differentially binding to wild-type or mutant IGF2BP1 (Fig. 7A, Supplementary Data 5). In general, the phosphomimetic mutants bound to fewer RNAs during arsenite stress compared to the wild-type IGF2BP1 (Fig. 7A, Supplementary Fig. 12E). The IGF2BP1 RQ mutant showed less regulatory potential, where the mutation only impacted IGF2BP1's interaction with a small number of RNAs (Fig. 7A, Supplementary Fig. 12E). Our analyzes revealed that while wild-type IGF2BP1 and its mutants bind to similar RNAs, the differences are instead in the "strength" of binding. Importantly, in most cases, the mutants showed decreased binding to the RNA targets compared to the wild-type IGF2BP1 (Fig. 7A, B, Supplementary Fig. 12E).

Intriguingly, the differentially regulated targets by the phosphomimetic mutants included several RNAs with a regulatory potential (Fig. 7B). For example, the Y396E phosphomimetic mutant showed largely impaired RNA-binding to the canonical IGF2BP1 target RNA HMGA2, where the other mutants showed similar binding efficiency as the wild-type protein. In contrast, all the mutants showed impaired interaction with the PABPC1 and PHC3 mRNAs compared to the wild-type IGF2BP1 (Fig. 7B). Interestingly, unlike most RNAs that showed decreased binding to IGF2BP1 during arsenite stress, select RNAs, including GARS1, showed preferential IGF2BP1 binding under stress conditions (Fig. 7B). We also observed increased binding capacity of the linker mutants to a small group of RNA targets (see CCDC127) compared to the wild-type IGF2BP1. To sum up, our data show distinct differences in RNA-binding properties of the IGF2BP1 phosphomimetic mutants in cells.

While for select RNAs, the changes in the IGF2BP1 binding efficiency correlated with a decrease in the RNA levels, for others, increased IGF2BP1 binding led to target destabilization (see LIPA, Fig. 7B), suggesting that IGF2BP1-binding causes opposing outcomes for its targets. Importantly, the changes in IGF2BP1-binding did not lead to changes in the RNA levels for several RNAs. IGF2BP1 regulates the stability, translation, and localization of its targets[8,25,35,73]. One possible explanation for these results might be that IGF2BP1 regulates the translation or localization of those targets. These data also suggest that the significant differences in the transcriptome in cells expressing IGF2BP1 mutants compared to the wild-type IGF2BP1 are the consequence of the remodeling of the transcriptome by a subset of IGF2BP1 RNA targets that encode for proteins involved in the regulation of transcription or RNA metabolism, such as HMGA2 and PABPC1. In summary, our data validate the regulatory potential of the disordered linkers in controlling RNA metabolism in cells.

Discussion

Posttranslational modifications (PTMs) regulate protein function in a reversible, tunable manner that allows exquisite spatiotemporal control[74]. PTMs regulate many RBPs by modulating target RNA binding, interaction with partners, or subcellular localization, thereby contributing to the control of RNA metabolism in cells[75–77]. It has become increasingly clear that PTMs regulate assembly of RBPs into biomolecular condensates by phase separation. Using mass spectrometry, we mapped steady-state and stress-induced phosphorylation sites in IGF2BP1.

Targeted proteomics identified stress-dependent phosphorylation sites in IGF2BP1. Apart from the S181 site, whose phosphorylation decreased approximately two-fold during ER stress, ER stress only mildly impacted the phosphorylation status of IGF2BP1. Notably, the oxidative stress increased phosphorylation at various sites throughout the protein, including a two-fold increase in S181 phosphorylation, revealing the context-dependent nature of this phosphorylation event. IGF2BP1 residue S181 was previously proposed to be phosphorylated by mTORC2[31,32]. Importantly, recent data also predicted that the S181 site is phosphorylated by the CMKG kinase family[37]. Several members of the CMGC kinase family are activated during oxidative stress, and the family member DYRK3 partitions to stress granules and regulates their disassembly[78]. Under the induced ER stress conditions used here, cells did not form stress granules, suggesting their formation might be necessary for stress-induced IGF2BP1 phosphorylation at this site. Apart from prominent S181 phosphorylation (64% of the total protein pool), most of the identified phosphorylation sites in IGF2BP1 were only modified at sub-stoichiometric levels (<1%). Those sites might be regulated in a spatial or cell-type-specific manner and could be present at a higher frequency in other cell types.

In the absence of RNA, purified IGF2BP1 displayed monodisperse, monomeric behavior. In contrast, in the presence of RNAs with multiple IGF2BP1-binding motifs, IGF2BP1 assembled into RNP condensates. By systematically analyzing IGF2BP1 truncation mutants, we revealed that the KH3-4 domains in IGF2BP1 drive the formation of RNP condensates. These data align with experiments in which only RNA-binding mutants of KH3-4 domains impaired IGF2BP assembly into stress granules in cells[43]. Minimal IGF2BP1 RNP condensates consisting of RNA and IGF2BP1 were highly rigid due to the multivalent interaction of the RNA with the multidomain IGF2BP1. Like other biological systems involving multidomain RBPs that mediate specific multivalent engagement with RNAs, we anticipate that IGF2BP1 RNP condensates form via phase separation coupled to percolation[54,66]. Notably, while full-length IGF2BP1 formed droplets, KH1-4 domains formed meshed networks. These data showed that binding KH1-4 domains to RNAs mainly results in percolation without phase separation. These data revealed that RRM domains contribute to the coupling of percolation with phase separation, ultimately

https://doi.org/10.1038/s41467-024-53400-4

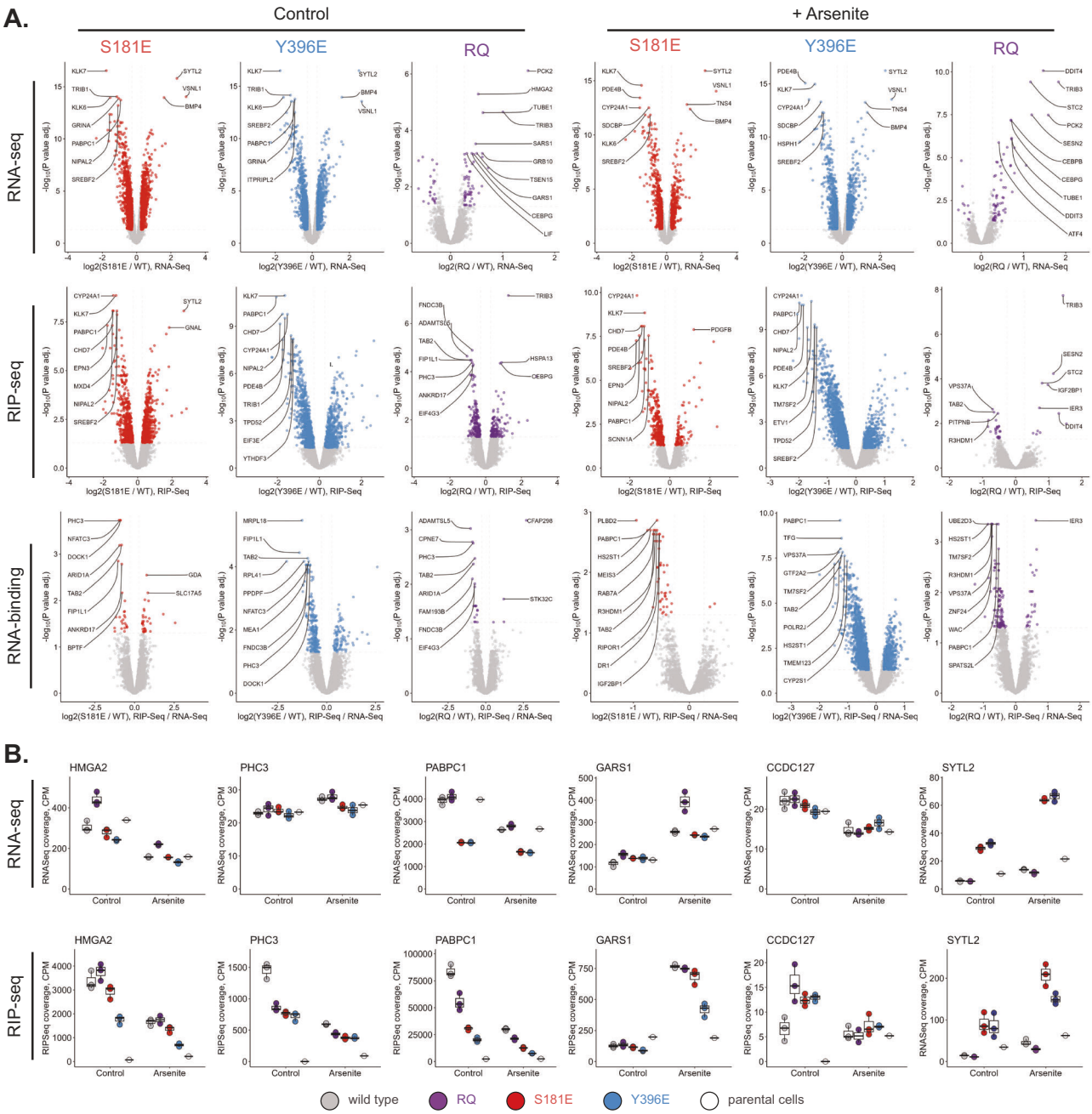

Fig. 7 | Phosphomimetic mutants impact IGF2BP1's interaction with RNA in cells. (A) Volcano plots showing changes in total transcriptome (RNA-Seq), IGF2BP1-bound transcript levels (RIP-Seq) and IGF2BP1 mRNA binding (RIP-Seq normalized to RNA-Seq) in HCT116 cells expressing mCherry-IGF2BP1 mutants S181E, Y396E, and RQ comparing to mCherry-IGF2BP1 wild-type. Arsenite stress was induced with a 2-hour treatment with 500 μM of sodium arsenite. Differentially regulated genes (fold change compared to the wild-type more than 20% with edgeR glmQLFTest[101] FDR-adjusted p value less than 0.05, n = 3 biological replicates) are highlighted, and their number is indicated in a figure. (B) RNA-Seq and RIP-Seq counts per million (CPM) graphs for selected genes. n = 3 biological replicates, data are shown as boxplots with all individual data points (center is a median, bounds of box are Q1 and Q3, and whiskers extend to ±1.5 × IQR, all individual data values are shown as dots). Source data are available in Supplementary Data 5.

leading to condensate formation. Our data suggest that the competing non-specific interactions of the highly promiscuous RRM1-2 pseudodimers increase the dynamics in RNA-protein interactions in IGF2BP1 condensates. In line with these observations, IGF2BP1 RNP condensates formed in vitro in cell lysates displayed increased dynamics compared to the RNP condensates reconstituted from minimal components. We anticipate that other RBPs compete with the available RNA-binding sites in cells, weakening the interactions between RBPs and RNAs and increasing the dynamics of RNA-protein interactions within condensates.

Systematic biochemical analyzes with truncation and point mutants revealed that the IGF2BP1 KH3-4 domains bind to RNA with the highest affinity, with KH3 showing the most substantial contribution. In contrast to what was shown for the IGF2BP1 chicken homolog ZBP1, we did not observe the looping of RNA around the KH3-4 domains, which results in an avidity effect by increasing the effective concentration for interactions with the second binding site for both the *ACTB*- and *XBP1*-derived RNAs[39,41]. However, we observed an avidity effect driven by the multivalent binding of the KH3-4 and KH1-2 domains to RNA. Importantly, RNA-binding mutants of the KH3 and

KH4 domains in full-length IGF2BP1 are bound tightly to RNA through multivalent interactions driven by RRM1-2 and KH1-2 domains. These data support earlier findings for the IGF2BP3 paralog, underlining the importance of combinatorial recognition of the IGF2BP targets[20,21]. We propose that the KH3-4 domains dock onto the RNA with a medium affinity and fast kinetics, and an avidity effect driven by the KH1-2 and RRM1-2 domains increases the affinity and specificity of IGF2BP1 binding to its targets. Phosphomimetic mutants of IGF2BP1 linkers bound to short model RNAs containing two IGF2BP1 binding motifs with an affinity similar to the wild-type protein. Notably, phosphomimetic mutants showed slight differences in their binding to the 200 nt-long *EIF2A*- and *XBP1*-derived RNAs but not for the *MYC*-derived RNA in EMSA. These data suggested the possibility of RNA-dependent differences in IGF2BP1-RNA interactions depending on phosphorylation. Altogether, our data converge on the model that linker phosphorylation does not abolish IGF2BP1's interaction with RNAs, yet might modulate IGF2BP1-RNA assemblies in cells as proposed earlier[7,32].

Combining cell biology and in vitro reconstitution methods, we found that IGF2BP1 phosphomimetic mutations introduced to the disordered linkers (S181, Y396) modulate its assembly into RNP granules. Intriguingly, while phosphomimetic mutant S181E at linker 1 decreases the dynamics and the size of IGF2BP1 RNP condensates, phosphomimetic mutant Y396E showed an opposite effect in vitro highlighting the regulatory potential of these sites. Notably, the phosphomimetic mutants did not largely impact the critical concentration of protein and RNAs for phase separation. This aligns with our findings that RNA interactions with folded domains drive IGF2BP1 phase separation. Using structural methods, we dissected how phosphomimetic mutants modulate the conformational state of IGF2BP1 and, thereby, the formation of RNP condensates. We hypothesized that linkers might be regulating IGF2BP1 condensation by three possible mechanisms: (i) self-association, (ii) interaction with folded domains, or (iii) interaction with RNAs. The NMR experiments, in vitro reconstitution, and MD simulations showed that linker 1 and linker 2 do not display a propensity to form condensates by themselves. Notably, the probability contact map derived from the MD simulations showed that linker 2 forms short-lived contacts with other linker 2 copies in trans, and the Y396E mutant showed an increased number of contacts compared to the wild-type, indicating that the mutation increases the propensity of linker 2 to self-associate. In addition, using NMR spectroscopy, we found that linker 2 forms low affinity contacts with all the folded domains in IGF2BP1, showing the strongest binding to the KH3-4 dimers. Notably, all folded domains bound weakly to the C-terminal segment (aa V390-M400) in linker 2 covering the Y396 phosphorylation site and those interactions were impaired for the Y396E phosphomimetic mutant. Those data uncovered that the molecular contacts between linker 2 and the folded domains were partially impaired in the Y396E mutant. Together with the MD simulations, these data suggest that the low-affinity interaction network of the linker 2 is rewired for the Y396E phosphomimetic mutant. The in vitro FRAP experiments showed that the IGF2BP1 Y396E mutant is more dynamic in condensates than the wild-type protein, consistent with the droplet-like morphology of the Y396E condensates. Our data suggest that changes in the low-affinity interaction networks formed by linker 2 increase IGF2BP1 dynamics in RNP condensates and facilitate condensate formation, resulting in the larger condensates we observed in vitro. Notably, the IGF2BP1 Y396E mutant expressed in cells formed smaller condensates with reduced dynamics. Increased compositional heterogeneity and complexity of the RNPs in cells compared to the in vitro experiments might cause these differences compared to the in vitro results.

The NMR experiments revealed that while linker 1 does not interact with folded domains of the IGF2BP1, it formed low-affinity contacts with RNA through its RGG/RG motif. We propose that these low-affinity contacts increase the dynamics of IGF2BP1 in the RNP condensates. Significantly, these low-affinity interactions were impaired in the phosphomimetic mutant S181E. In vitro FRAP experiments showed that IGF2BP1 S181E displayed lower mobile fraction and dynamics than wild-type protein, indicating that it forms more stable assemblies in the condensates compared to the wild-type IGF2BP1. Our results converge on the model that IGF2BP1 S181 phosphorylation impairs low-affinity non-specific interactions of the linker with the RNA. Lack of competing low-affinity interactions result in more stable binding of S181E with RNA in the condensates, observed as decreased dynamics of IGF2BP1 in FRAP experiments. We speculate that decreased dynamics interfere with condensate growth and lead to the formation of smaller condensates, which we observed in vitro and cells for the S181E mutant. While phosphomimetic mutations do not completely recapitulate the biophysical properties of the phosphorylation of serine or tyrosine residues, perturbing the amino acid composition of the linker by a single point mutation has profound effects on IGF2BP1-RNP formation in vitro and in cells. Future studies using genetic code expansion to introduce phosphorylated residues at distinct sites in IGF2BP1 might reveal whether there are distinct differences between phosphorylation compared to the phosphomimetic mutants introduced here[79].

Remarkably, the RIP-seq analyzes revealed that compared to the wild-type IGF2BP1, the phosphomimetic mutants were less efficient in binding to thousands of target RNAs, with a more substantial effect observed during arsenite stress. Using genome-wide transcriptomics approaches, we found that the expression of IGF2BP1 phosphomimetic mutants in mammalian cells resulted in significant changes in the expression levels of several IGF2BP1-target RNAs. While we lack IGF2BP1 separation-of-function mutants to precisely decipher the role of RNP condensate formation in regulating mRNA metabolism, our data show the functional importance and the regulatory capacity of the linker regions for IGF2BP1-dependent posttranscriptional regulation in cells. In addition to phosphorylation, RGG sequences are methylated by protein arginine methyltransferase 1 (PRMT1), which can impact RNA binding of linker 1[80]. Therefore, the linkers might be subjected to more intricate regulation in cells in a context and tissue-specific manner.

Our findings highlight a highly tunable regulatory mechanism where modulation of low affinity interactions through phosphorylation could, in turn, impact the physical properties of RBPs in RNP condensates as observed for other systems[45,77,81]. Our data exemplify how the effects of PTMs are amplified in the condensate environment, thus providing an increased regulatory capacity to control biomolecular interactions in membrane-less organelles.

Methods

In vitro construct cloning

All mCherry-IGF2BP1 constructs were cloned into a pET-47 plasmid with an N-terminal mCherry using Gibson assembly. Single point mutations were generated through site-directed mutagenesis as well as Gibson assembly. IGF2BP1 (Uniprot: Q9NZI8) mutation involved changing the wild-type Ser181 or Tyr396 residues to glutamic acid. In order to establish U2OS and HCT116 cell lines stably expressing IGF2BP1, a vector that contains hPGK promoter was used. The promoter, together with NheI restriction site was introduced into the pLX303 expression vector using XheI and BsrgI restriction enzymes. mCherry-tagged mutants of IGF2BP1 were amplified with pLX303_IGF2BP1_R(5'-CTCGCTAGCTCACTTCCTCCGTGCC-'3)and pLX303_mCherry_F (5'-CTCACCGGTGCCACCATGGTGAGCAAGG-'3) primers and incorporated into the modified pLX303 using the AgeI and NheI restriction sites. Sequencing confirmed IGF2BP1 integration.

Cell culture

U2OS cell lines used in this study were grown in DMEM high glucose medium (Sigma) with 10% Fetal Bovine Serum (Gibco), 2 mM

Glutamine (Sigma), 1% Pen/Step (Sigma). HCT116 conditionally expressing Tet-OsTIR1 were obtained from Masato Kanemaki Lab (Natsume et al. 2016) and grown in McCoy's 5 A (Modified) medium supplemented as above. The cells were maintained at 37 °C, with 5% CO2, and were used for all biochemical experiments, live cell imaging, and Immunofluorescence. The cells were tested for mycoplasma contamination which was not detected.

Establishment of IGF2BP2 and IGF2BP3 knockout cell lines

For knockout cell line generation, gRNA sequences (IGF2BP2: 5'-GAGCTGCCGGAGGTCGTCGG-3'; IGF2BP3: 5'-ACGCGTAGCCAGTCTTCACC-3') were cloned into the pSpCas9 (BB)−2A-GFP (PX458) (plasmid #48138; Addgene, (Ran et al. 2013)). Cells were transiently transfected using jetOPTIMUS reagent (Tamar, 101000051) and GFP-positive single-cell clones were FACS sorted at BD FACSAria IIIu at Max Perutz Labs BioOptics FACS Facility.

Mass spectrometry– Sample Preparation

For mass spectrometry of IGF2BP1, we used HEK293T cells expressing IGF2BP1 tagged with split-GFP at the endogenous locus. These cells were the kind gift of Manuel Leonetti (Chan Zuckerberg BioHub, USA[82]). Briefly, the cells were generated by integrating GFP^{1-10} into HEK293T cells by lentiviral integration. This cell line was then used to introduce GFP^{11} into the IGF2BP1 using CRISPR-Cas9 gene editing approaches[83]. For the immunoprecipitation experiments, HEK293T cells were treated with the respective diluent as a control (DMSO for thapsigargin and tunicamycin or PBS for sodium arsenite). To induce stress, cells were treated with 250 μM sodium arsenite for 1 and 2 h, with 5 μg/mL tunicamycin for 4 h and with 250 nM thapsigargin for 1.5 and 4 h. IGF2BP1 was immunoprecipitated from HEK293T cells by GFP-trap magnetic beads (ChromoTek). The cells were lysed using cold lysis buffer (20 mM HEPES pH 7.4, 150 mM NaCl, 0.5 mM EDTA, 0.1% SDS, 0.5% Triton X-100, 0.2% Deoxycholate, 2x Complete™, EDTA-free Protease Inhibitor Cocktail (Roche), 0.5 mM PMSF and 1x PhosSTOP™ phosphatase inhibitor (Roche)). 25 μL of bead slurry was used for around 50 million HEK293T cells. The lysate was incubated with the GFP-trap beads for 2 h at 4 °C to allow binding of the protein. After binding, the beads were washed 5 times with 1 mL of ice-cold wash buffer (20 mM HEPES, 500 mM NaCl, 0.5 mM EDTA, 0.1% SDS, 0.5% Triton X-100, 0.2% Deoxycholate, 1x Complete™, EDTA-free Protease Inhibitor Cocktail (Roche)). Protein was eluted in 50 μL of 1x SDS sample buffer (50 mM Tris-HCl pH 6.8, 2% SDS, 0.1% Bromophenol blue, 10% glycerol+ 20 mM DTT) at +70 °C for 10 min. The eluate was loaded on SDS-PAGE and stained by Colloidal Coomassie[84]. The band corresponding to IGF2BP1 was cut and subjected to mass spectrometry analyzes at the Max Perutz Labs Mass Spectrometry Facility.

For mass spectrometry of IGF2BP3, HEK293T cells expressing IGF2BP3-tagged with split-GFP at the endogenous locus and HCT116 cells were used. IGF2BP3 from HEK293T split-GFP cell lines were immunoprecipitated under same experimental conditions as IGF2BP1. For the immunoprecipitation experiments, both cell lines were treated with DMSO or PBS as control. To induce stress, cells were treated with 250 μM of sodium arsenite for 1 or 2 hours, or 250 nM of thapsigargin for 1.5 or 4 hours or 5 μg/ml tunicamycin for 4 hours. For mass spectrometry of IGF2BP3 from HCT116 cells, we used antibodies against endogenous IGF2BP3. For immunoprecipitation three 15 cm (diameter) dishes of 60% confluent HCT116 per condition (around 50 million cells) were washed in ice-cold PBS, scraped, pelleted, and resuspended in 750 μL of ice-cold lysis buffer (25 mM HEPES pH 7.3, 150 mM NaCl, 0.5% NP-40, 0.5 mM EDTA, 10% Glycerol, 0.1% SDS, 0.2% Sodium Deoxycholate, 2x Complete™, EDTA-free Protease Inhibitor Cocktail (Roche), and 1x PhosSTOP™ phosphatase inhibitor (Roche)). Cells were lysed by incubation with the lysis buffer on ice for 15 min with intermittent vortexing and passing the cell suspension three times through a 25 G needle. The lysate was clarified using two-step centrifugation for 5 min at 1,000 g and for 15 min at 13,000 g, and treated with 1 U/μL RNase T1 (Thermo Scientific) rotating at room temperature for 15 min. For IP from three 15 cm (diameter) dish 30 μg of anti-IGF2BP3 antibody was coupled to Dynabeads in 1 μg: 4 μL antibody: beads ratio. We used the MBL antibody (RN009P, lot 005) for the samples treated with tunicamycin and the respective 0.001% DMSO controls, and the Proteintech (14642-1-AP, lot 00090203) antibody for the thapsigargin, 0.0002% DMSO, arsenate and untreated control samples. The lysates were rotated at +4 °C for 4 hours for the IP. The unbound fraction was removed using a magnetic rack and the immunoprecipitated complexes were washed five times in 1 mL of ice-cold high salt wash buffer (25 mM HEPES pH 7.3, 400 mM NaCl, 0.5% NP-40, 0.5 mM EDTA, 10% Glycerol, 1x protease inhibitors cocktail) with 3-min incubations on ice. Protein was eluted in 50 μL of 1x SDS sample buffer (50 mM Tris-HCl pH 6.8, 2% SDS, 0.1% Bromophenol blue, 10% glycerol) without DTT at +70 °C for 10 min. DTT at 20 mM concentration was added to the collected eluates and the samples were heated at +70 °C for 10 min. Samples were separated by SDS-PAGE and stained with colloidal Coomassie. The band corresponding to IGF2BP3 was cut from the gel and submitted for tandem mass spectrometry at the Max Perutz Labs Mass Spectrometry Facility.

Mass Spectrometry – Sample processing

Coomassie stained gel bands were excised, cut into small pieces and destained with a mixture of acetonitrile (ACN) and 50 mM ammonium bicarbonate (ABC). After shrinking the gel pieces in ACN, 20 mM dithiothreitol (DTT) was added to reduce disulfide bridges. After washing with ABC and ACN, free SH-groups were subsequently alkylated in 50 mM iodoacetamide. The in-gel digestion with trypsin was carried out overnight at 37 °C and was stopped by adding 10% formic acid to an end concentration of approximately 5%. Peptides were extracted from the gel with 5% formic acid by repeated sonication.

Mass Spectrometry - Nano LC-MS/MS Analysis

Peptides were separated on an Ultimate 3000 RSLC nano-HPLC system using a pre-column for sample loading (Acclaim PepMap C18, 2 cm × 0.1 mm, 5 μm), and a C18 analytical column (Acclaim PepMap C18, 50 cm × 0.75 mm, 2 μm, all HPLC parts Thermo Fisher Scientific), applying a linear gradient from 2% to 35% solvent B (80% ACN, 0.08 % formic acid; solvent A 0.1 % formic acid) at a flow rate of 230 nL/min over 60 min. Eluting peptides were analyzed on a Q Exactive HF-X Orbitrap mass spectrometer coupled to the HPLC via Proxeon nanospray-source (all Thermo Fisher Scientific) equipped with coated emitter tips (New Objective).

The mass spectrometer was operated in data-dependent acquisition mode. Survey scans were obtained in a mass range of 375-1500 m/z with lock mass on, at a resolution of 120000 at 200 m/z and a normalized AGC target of 3E6. The 10 most intense ions were selected with an isolation width of 1.6 m/z, for max. 200 ms at a normalized AGC target of 1E5, and then fragmented in the HCD cell at 28% normalized collision energy. MS/MS Spectra were recorded at a resolution of 30000. Peptides with a charge of +1 or >+6 were excluded from fragmentation; the peptide match feature was set to "preferred" and the exclude isotope feature was enabled. Selected precursors were dynamically excluded from repeated sampling for 30 s.

For the parallel reaction monitoring (PRM) analysis survey scans were acquired in a mass range of 375-1500 m/z with lock mass off, at a resolution of 30000 at 200 m/z and a normalized AGC target of 3E6. The PRM parameters - precursor m/z and retention time - were built based on the gel samples measured with DDA. Precursors of 33 peptides of interest (14 phosphorylated peptides and their unmodified counterparts plus 5 reference peptides) were isolated in a 0.7 m/z window and fragmented with 28% HCD collision energy. Orbitrap resolution was set to 30000, the normalized AGC target to 2E5. Maximal injection time for modified peptides was set to 200 ms.

MS data analysis for identification of phosphorylation sites

The RAW MS data were analyzed with FragPipe (20.0), using MSFragger (3.8)[85], IonQuant (1.9.8)[86], and Philosopher (5.0.0)[87]. The default FragPipe workflow for label free quantification (LFQ-MBR) was used, except that "Add MaxLFQ", "Match between runs (MBR), and "Normalize intensity across runs" were turned off. Cleavage specificity was set to Trypsin/P, with two missed cleavages allowed. The protein FDR was set to 1%. A mass of 57.02146 (carbamidomethyl) was used as fixed cysteine modification; methionine oxidation, protein N-terminal acetylation, and serine/threonine/tyrosine phosphorylation were specified as variable modifications. MS2 spectra were searched against the *H. sapiens* reference proteome from Uniprot (Proteome ID: UP000005640, release 2023.03) containing 20598 entries, concatenated with a database of 379 common laboratory contaminants (in house database).

Computational analysis was conducted using Python along with two in-house Python libraries, "MsReport" (version 0.0.20) and "XlsxReport" (version 0.0.6)[88]. To compile a list of confidently identified phosphorylation sites for IGF2BP1, IGF2BP2, and IGF2BP3, we utilized the individual "ion.tsv" tables generated by FragPipe. Initially, the ion tables were concatenated and non-phosphorylated peptide ions were filtered out. Subsequently, multiple phosphorylated peptide ions were selected, and separate entries were generated for each phosphorylated site by duplication. The specific site localization probability was then extracted for each of the duplicated site entry. Entries with a peptide probability lower than 95% or a phosphorylation site localization probability less than 80% were removed. The expanded ion table was summarized by aggregating entries of individual phosphorylation sites, and the best peptide probability and site localization probability for each site were extracted. Total spectral counts were calculated as the sum of all PSMs (peptide spectrum matches) identifying specific phosphorylation site, excluding LC-MS runs with PRM measurements.

MS data analysis of PRM measurements for phosphorylation site quantification

LC-MS runs with PRM measurements were analyzed in Skyline (22.2.0.351)[89]. A list containing the 33 peptides targeted by PRM and the raw LC-MS files were imported into Skyline. All peptides and their transitions were validated manually based on retention time, relative ion intensities, and mass accuracy. Extracted ion chromatograms (XICs) were generated for the product ions of all selected peptides, and peak areas were exported from Skyline. The intensity of each peptide was calculated by summing the XICs of the three most intense, interference-free transitions. Subsequently, peptide intensities across different samples were normalized using four reference peptides. First, the sum of the reference peptide intensities was calculated for each sample. Next, these summed intensities were divided by the average across all samples to derive normalization factors. Finally, peptide intensities of each sample were divided by the respective normalization factor. To ensure reliable data, peptides with incomplete quantification or exhibiting an average coefficient of variation exceeding 2 between the two replicates were excluded from further analysis. The intensities of modified peptides covering the same phosphorylated protein site were summed to create site-level intensities. The intensities of the corresponding unmodified peptide counterparts of each site were also summarized to create site level counter intensities. Estimated site occupancy was calculated as "Site intensity" / ("Site intensity" + "Counter intensity") * 100. For plotting, site-level intensities were log2 transformed and normalized to the average intensity of the respective control samples.

In vitro phosphorylation of IGF2BP1 by Src kinase

5 μM IGF2BP1 full-length wild-type were incubated with 0.5 μM Src (Merck 23-042), 1 mM ATP, 2 mM $MgCl_2$, 150 mM NaCl, 25 mM HEPES pH 7.3 and 0.5 mM TCEP for 2 h at room temperature. Control sample was incubated without Src. Samples were subsequently flash frozen in liquid nitrogen.

ProAlanase digest of recombinant Src-treated IGF2BP1 for LC-MS/MS peptide mapping

1.5 μg of purified recombinant IGF2BP1 were denatured in 6 M urea and 50 mM TEAB, pH 8. Disulfide bridges were reduced with 10 mM dithiothreitol and free thiols subsequently alkylated with 20 mM iodoacetamide. Remaining iodoacetamide was quenched with 5 mM DTT before adjusting the pH to 1.5 using 30 mM HCl – this step also diluted the urea concentration to 0.3 M to allow for efficient digestion. ProAlanase (Promega) was added in a 1:50 ratio of enzyme to protein and the sample incubated at 37 °C for 1.5 h. The resulting peptides were digested using C18 Stagetips[90].

ProAlanase digest of immuno-enriched IGF2BP1 for LC-MS/MS peptide mapping

For the ProAlanase digestion analysis, cells were treated as described in "Mass spectrometry– Sample Preparation". Control, thapsigargin and arsenite treated cells were prepared in duplicates. After removing the final wash, the beads were resuspended in 1 M urea in 50 mM ammonium bicarbonate. Disulfide bridges were reduced with 10 mM DTT and free thiols subsequently alkylated with 20 mM iodoacetamide. Remaining iodoacetamide was quenched with 5 mM DTT. 100 mM glycine was added to the beads until pH 2 was reached and the urea concentration was diluted to 0.3 M. 300 ng ProAlanase (Promega) were added to the beads and incubated for 2 h at 37 °C. The supernatant was desalted using C18 Stagetips[90].

Nano LC-MS/MS analysis of ProAlanase digested samples

Peptides were separated on a Vanquish Neo nano-flow chromatography system (Thermo Fisher), using a trap-elute method for sample loading (Acclaim PepMap C18, 2 cm × 0.1 mm, 5 μm, Thermo Fisher), and a C18 analytical column (Acclaim PepMap C18, 50 cm × 0.75 mm, 2 μm, Thermo Fisher), applying a segmented linear gradient from 2% to 35% and finally 80% solvent B (80 % acetonitrile, 0.1 % formic acid; solvent A 0.1 % formic acid) at a flow rate of 230 nL/min over 60 min.

Eluting peptides were analyzed on an Exploris 480 Orbitrap mass spectrometer (Thermo Fisher), which was coupled to the column with a Nanospray Flex ion-source (Thermo Fisher) using coated emitter tips (PepSep, MSWil). The mass spectrometer was operated in data-dependent acquisition mode. Survey scans were obtained in a mass range of 375–2000 m/z, at a resolution of 120,000 at 200 m/z and a normalized AGC target of 3E6 and a cycle time of 2 s. The most intense ions were selected for fragmentation with an isolation width of 1.4 m/z, for max. 200 ms injection time at a normalized AGC target of 200%, and then fragmented in the HCD cell at 30% normalized collision energy. MS/MS Spectra were recorded at a resolution of 30,000. Peptides with a charge of >+6 were excluded from fragmentation. Selected precursors were dynamically excluded from repeated sampling for 20 s. In addition, target peptides covering the IGF2BP1 site Y396 (unmodified and phosphorylated) were added to an inclusion list to increase the likelihood of fragmentation.

Data analysis for identification of phosphorylation sites in ProAlanase digested samples

The RAW MS data were analyzed with FragPipe (22.0/22.0), using MSFragger (3.8/4.1)[85], IonQuant (1.9.8/1.10.27)[86], and Philosopher (5.0.0/5.1.1)[87]. The default FragPipe workflow for label free quantification and identification of phosphopeptides (LFQ-phospho) was used, except that "Normalize intensity across runs" was turned off. Cleavage specificity was specified to cut C-terminal to proline and alanine, with five missed cleavages allowed. The protein FDR was set to 1%. A mass of 57.02146 (carbamidomethyl) was used as fixed cysteine modification; methionine oxidation, protein N-terminal acetylation, and serine/

threonine/tyrosine phosphorylation were specified as variable modifications. MS2 spectra were searched against the *E. coli* reference proteome (UniProt, UP000000625, release 2024.01) and the IGF2BP1 recombinant sequence or against the *H. sapiens* reference proteome (UniProt, UP000005640, release 2024.01), in both cases concatenated with a database of 379 common laboratory contaminants (https://github.com/maxperutzlabs-ms/perutz-ms-contaminants).

Downstream computational analysis and reporting was conducted using Python with two in-house libraries, "MsReport" (version 0.0.24) and "XlsxReport" (version 0.0.6)[88], as described above. Extracted ion chromatograms were generated in Skyline-daily (24.0.9.197)[89].

Estimation of the linker 2 phosphorylation levels from in vitro and in vivo results

The intact mass spectrometry analyzes of in vitro phosphorylated IGF2BP1 by SRC kinase showed an approximate 1:1 ratio of unmodified to single phosphorylated protein (Supplementary Data 1). Peptide mapping from these samples revealed that the Y396 phosphopeptides showed 10–20% of the signal of the unmodified peptide (please see Supplementary Fig 1C). In the samples, where we IP-ed IGF2BP1 from cells, we detected the unmodified peptide with 2 to 5 E10 intensity (Supplementary Fig. 1D). Under the conservative assumption that phosphopeptides display 10% signal of the unmodified peptide, under those conditions phosphopeptides found in 100% stoichiometry of total protein would be expected to have an intensity in the range of 2–5E9. Similarly, at 1% stoichiometry, we would expect 2–5E7 signal intensity for the phosphopeptides. The lowest IGF2BP1 peptide signal detected in those experiments was in the range of 1E7, meaning that it would have been possible to detect the phosphopeptides at 1% stoichiometry at that intensity in our experiments. Altogether, our data suggest that the abundance of the phosphorylated Y396 is probably below 1%, if it is present at all.

Protein Expression and Purification

Full-length IGF2BP1 constructs were cloned into a pGEX-6P-2 vector containing an N-terminal GST-tag and a 3 C cleavage site. These proteins were expressed in Rosetta (DE3) cells grown to an OD of ~0.7 and induced with 400 μM IPTG. Cells were grown over night at 20 °C, resuspended in GST lysis buffer (25 mM HEPES pH 7.2, 1 M NaCl, 5% glycerol, 2 mM DTT, 0.5 mM PMSF, 2 mM EDTA), pelleted and frozen in liquid nitrogen.

mCherry-IGF2BP1 constructs were cloned into a pET-47b vector with an N-terminal mCherry- and a C-terminal Deca-His-tag with a 3 C cleavage site and expressed in Rosetta (DE3) cells. Shorter IGF2BP1 proteins (RRM1-2, KH1-4, KH1-2, KH3-4) were cloned into a pET-47b vector with an N-terminal Hexa -His-Tag and expressed in BL21 cells. His-tagged proteins were induced with 800 μM IPTG and cells were resuspended in His lysis buffer (25 mM HEPES pH 7.2, 1 M NaCl, 5% glycerol, 5 mM beta-mercaptoethanol, 0.5 mM PMSF, 20 mM Imidazole).

Linker peptides were cloned into a pET-21 vector with an N-terminal His- and SUMO-tag. These proteins were expressed in BL21 cells by growing them in to an OD of ~0.7, induction with 1 mM IPTG and incubation for 3.5 h at 25 °C. The cells were than resuspended in phosphate lysis buffer (20 mM phosphate buffer pH 7.2, 1 M NaCl, 5% glycerol, 5 mM beta-mercaptoethanol, 0.5 mM PMSF, 20 mM Imidazole). The obtain ^{15}N labeled linker proteins, the cells were grown in M9 minimal medium supplemented with $^{15}NH_4Cl$. To get ^{13}C-^{15}N-labeled proteins, glucose was replaced with ^{13}C-glucose.

Proteins were purified by resuspending the pellet in lysis buffer and lysing the cells in a EmulsiFlex C3 homogenizer. After pelleting non-soluble cell debris by centrifugating the lysate at 40,000 g for 30 min at 4 °C, the supernatant was loaded onto the respective affinity column. Full-length proteins were loaded onto two serially connected GST HiTrap HP 5 mL columns, washed with GST wash buffer (25 mM HEPES pH 7.2, 500 mM NaCl, 5% glycerol, 2 mM DTT, 0.5 mM PMSF, 2 mM EDTA), and eluted with a gradient of 20 mM reduced glutathione in GST wash buffer. His-tagged or His-SUMO-tagged protein were purified on a HisTrap HP 5 mL column by washing them with His wash buffer (25 mM HEPES pH 7.2, 500 M NaCl, 5% glycerol, 5 mM beta-mercaptoethanol, 0.5 mM PMSF, 20 mM Imidazole) and eluted with a gradient of 1 M Imidazole in wash buffer. Bound nucleotides were removed by loading the proteins onto a Heparin HiTrap HP 5 mL column after diluting the NaCl concentration to 100 mM (with wash buffer without NaCl), washing them with wash buffer (25 mM HEPES pH 7.2, 100 mM NaCl, 5 % glycerol, 2 mM DTT, 0.5 mM PMSF, 2 mM EDTA, which was excluded when purifying His-tagged proteins) and eluting them with a gradient of 1 M NaCl in wash buffer. The GST- and His- buffer was cleaved off by incubating the eluted protein with GST-3C or His-3C overnight at 4 °C. For cleaving off the SUMO-tag, proteins were incubated with SENP. The respective tag and the 3 C protease were extracted by running the cleaved protein over a GST HiTrap 5 mL or HisTrap HP 5 mL column by using the same buffers as in the affinity purification. For KH1/2 the His-tag was not removed and thus the overnight incubation with protease and the negative His-affinity purification was omitted. The flow through was pooled and further purified via size exclusion chromatography (SEC). Full-length and KH1/2, KH1/4, KH3/4 (no DTT in the buffer) and all respective constructs were eluted with SEC buffer (25 mM HEPES, 150 mM NaCl, 2 mM DTT). Linker constructs were eluted in phosphate SEC buffer (20 mM phosphate buffer pH 7.2, 150 mM NaCl). Protein concentration was measured by using a Nanodrop (full length proteins, linker) or BCA assay (shorter constructs).

In vitro transcription and RNA purification

The RNAs *XBP1* 201 nt, *EIF2A* 200 nt and *MYC* 191 nt were produced by adding a T7 promoter sequence (TAATACGACTCACTATAGGG) and using the HiScribe T7 RNA Synthesis Kit (NEB E2040S). Template DNA was digested by adding DNase I and incubation for 15 min at 37 °C. RNA was denatured by boiling it for 5 min in denaturing buffer (10 m urea, 1 mM EDTA, 0.1% SDS, 0.5 mg/mL xylene cyanol, 0.5 mg/mL bromophenol blue) and run on a 6% acrylamide, 10 M urea TBE (89 mM Tris, 89 mM borate, 2 mM EDTA) denaturing gel in 1x TBE buffer for 2 h at 100 V. The gel was stained with SYBR Gold and the bands containing the RNA with the correct size cut out. The RNA was extracted by crushing the gels with a pestle and shaking in RNase-free H_2O with 1x SUPERaseIn for 1 h at room temperature. The gel pieces were separated by centrifugation in Spin-X filter tubes for 5 min at 20.000 g. The RNA was further purified via Phenol-Chloroform extraction by mixing the RNA sample first with a 1:1 volume of phenol, vortexing and centrifugation for 2 min at 20,000 g then taking off the supernatant and mixing it with a 1:1 volume of chloroform, vortexing and centrifugation for 1 min at 20,000 g. The supernatant is then mixed with a 10: 1 volume of 3 M sodium acetate and 1: 1 volume of ice-cold isopropanol. After precipitating the RNA overnight at −80 °C, the RNA was washed twice with ice-cold 80% ethanol and centrifugation for 30 min at 20,000 g and 4 °C, dried for 10 min and resuspended in RNase free H_2O. The RNA concentration was determined by using a Nanodrop.

EMSA Assays

To investigate protein-RNA interaction via Electrophoretic Mobility Shift Assays, proteins were thawed and centrifuged for 15 min at 20000 g and 4 °C. RNA was refolded by heating up to 95 °C and cooling down to 25 °C in steps of 2 °C/min. The protein and RNA was mixed in EMSA buffer (25 mM HEPES pH7.3, 150 mM NaCl, 5% glycerol, 2 mM EDTA, 10 μg/mL Heparin, 0.5 mM TCEP) to the specified concentrations. All samples were incubated on ice for 30 min. A 5% TBE gel with 5% glycerol was prepared by pre-running it for 30 min at 210 V in 0.5x TBE buffer at 4 °C. 10 μL per sample and 0.5 μL ladder (RiboRuler low range SM1831) were loaded onto the gel and run for 30 min at

210 V in 0.5x TBE buffer at 4 °C. RNA was stained with SYBR Gold and the gel was imaged with BioRad ChemiDoc or iBright CL1500 and quantified with the corresponding software supplied by the manufacturer. RNA binding was determined by using mean intensities and defining the sample with 0 nM protein as 0 and the gel background as 1 on the y-axis. $K_{1/2}$'s were calculated in GraphPad Prism by using the Hill equation (1) $Y=Y_{free}+Y_{bound}/(1+10\hat{}((\log10(K_{1/2})-\log10(x))*n))$

Fluorescence anisotropy assays

Proteins were thawed and centrifuged for 15 min at 20,000 g and 4 °C. To be able to measure fluorescence anisotropy the corresponding RNAs were obtained from IDTDNA with a 5′ fluorescein tag. The sample with the highest concentration was prepared in anisotropy buffer (25 mM HEPES 7.3; 150 mM NaCl, 0.025% Tween 20, 10 μg/mL Heparin, 2 mM EDTA, 0.5 mM TCEP) with 10 nM of fluorescence labeled RNA. A concentration series was created by diluting the sample 1:1 with 10 nM RNA in anisotropy buffer. Subsequently, the samples were incubated on ice for 30 min. The fluorescence anisotropy was measured in a cuvette using an Edinburgh Instruments FS5 spectrofluorometer at threes wavelengths (515, 520, and 525 nm) with a slit width of 5 nm at 20 °C with an excitation wavelength of 485 nm, a slit width 5 nm and a dwell time of 1 s. The G-factor, which was measured once for every experiment and then used to calculate the anisotropy for each sample in the experiment, was determined in the beginning of the experiment by measuring 10 nM RNA in anisotropy buffer. The fluorescence anisotropy value was calculated by the manufacturer's software. $K_{1/2}$'s were calculated in GraphPad Prism by using a dose response curve to fit the data using a model following the Hill equation (1) $Y=Y_{free}+Y_{bound}/(1+10\hat{}((\log10(K_{1/2})-\log10(x))*n))$

RNP granule formation

To investigate the formation of RNP granules, proteins were thawed and centrifuged for 15 min at 20,000 g and 4 °C. RNA was refolded by heating up to 95 °C and cooling down to 25 °C in steps of 2 °C/min. The proteins were diluted in RNase free buffer (25 mM HEPES pH 7.3, 150 mM NaCl, 0.5 mM TCEP). RNP granule formation was induced by the addition of the RNA with the respective final concentration. Right after RNA addition and mixing 50 μL of the sample were pipetted into the well of a Greiner sensoplate, black, 96-well, glass bottom plate which was coated with 1% Pluronic F-127 by washing the well with 200 μL H_2O, then incubation with 1% Pluronic F-127 for 2 h at room temperature, four times washing with 200 μL H_2O, and once washing with 100 μL buffer. The plate was incubated on the microscope for 90 min to allow droplet formation while avoiding moving and disturbing the granules. To determine the formation of RNP granules for the phase diagram, 20 μL of each sample were prepared and granule formation induced by adding RNA. These samples were pipetted into a 384-well plate that was similarly coated with 1% Pluronic F-127 and incubated for 90 min. To avoid evaporation in these low volume sample, the wells were covered with mineral oil (CAS: 8042-47-5). RNP formation was qualified by the presence of droplet- or mesh-like condensates. The samples were imaged with a Zeiss Axio Observer Z1 in bright field mode, EC Plan–Neofluar 100x/1.3 Oil M27, Orca Flash 4.0 LT+ Camera, VIS-LED at 50% intensity and 20 ms exposure time.

For the quantification of the condensates, 5% of the respective N-terminal mCherry-labeled IGF2BP1 construct was used in the samples. To avoid non-specific interaction of the mCherry-labeled proteins with the glass bottom, the wells were coated with 2 mg/mL BSA in addition to 1% Pluronic F-127 by washing the well with 200 μL H_2O, then incubation with 100 μL 1% Pluronic F-127 for 2 h at room temperature, twice washing with 200 μL H_2O, incubation 100 μL 2 mg/mL BSA in PBS, twice washing with PBS and once washing with 100 μL buffer. RNP granule formation was induced by the addition of the RNA with the respective final concentration. Right after RNA addition and mixing 50 μL of the sample were pipetted into the well. Imaging was carried out at the microscope setting describe above with additional acquisition of fluorescence images with a Colibri 7 lamp using the 567 nm LED module and a Zeiss filter set 90 HE, 80% intensity and 250 ms exposure time. Four adjacent tiles were imaged to increase to field of view area. Two fields of view were imaged and analyzed per well and the experiment was performed in triplicates. To analyze the data, the tiles were stitched together using the Zeiss ZEN Blue software and cropped to 3200 ×3200 pixels to have similar sized images. Condensate quantification was performed in ImageJ. Background was subtracted with a rolling ball radius of 200 and a sliding paraboloid, the "Default Dark" threshold was set and the image converted to a mask, watershed was used to separate very close condensates and finally the particles were analyzed with a minimum size of 200, outlines and a summary were created. The two-sided Welch's t test was used to determine statistical significance.

FRAP of RNP granules

To investigate the dynamics of IGF2BP1 in RNP granules, proteins were thawed and centrifuged for 15 min at 20000 g and 4 °C. RNA was refolded by heating up to 95 °C and cooling down to 25 °C in steps of 2 °C/min. The proteins were diluted in RNase free buffer (25 mM HEPES pH 7.3, 150 mM NaCl, 0.5 mM TCEP). IGF2BP1 full-length wild-type, S181E and Y396E were mixed with 5 % of the respective mCherry-labeled IGF2BP1 construct. A Greiner sensoplate, black, 96-well, glass bottom plate was coated with 1% Pluronic F-127 by washing the well with 200 μL H2O, then incubation with 1% Pluronic F-127 for 2 h at room temperature, twice washing with 200 μL H_2O, incubation 100 μL 2 mg/mL BSA in PBS, twice washing with PBS and once washing with 100 μL buffer. RNP granule formation was induced by the addition of the RNA with the respective final concentration. Right after RNA addition and mixing 50 μL of the sample were pipetted into the well. The plate was incubated at the microscope for 90 min to allow droplet formation and avoiding moving and disturbing the granules. FRAP was performed on a Zeiss Axio Observer equipped with a Yokogawa CSU-X1 Nipkow spinning disk unit, EC Plan–Neofluar 100x/1.30 Oil Iris objective, 561 nm DPSS laser, Visitron controller, ET605/70 emission filter and a pco.edge sCMOS camera. Images were acquired with 20% laser power and 100 ms exposure time. FRAP was performed with a time interval of 3 s, 3 images were taken before bleaching, then selected regions were bleached with 30% FRAP-Laser power for 1 ms per pixel in 5 cycles and 361 frames were taken in total per experiment.

Phase separation assay

To determine whether Linker 1 or Linker 2 can phase separate on their own, the proteins were thawed and centrifuged for 15 min at 20000 g and 4 °C. The proteins were diluted in buffer (25 mM HEPES pH 7.2, 150 mM NaCl). A Greiner sensoplate, black, 96-well, glass bottom plate was coated with 1% Pluronic F-127 by washing the well with 200 μL H2O, then incubation with 1% Pluronic F-127 for 2 h at room temperature, four times washing with 200 μL H2O, and once washing with 100 μL buffer. 25 μL protein dilution were pipetted into the well. 25 μL of 30% PEG 8000 in buffer were added and carefully mixed to induce phase separation. The plate was incubated on the microscope for 60 min to allow droplet formation. The wells were imaged with a Zeiss Axio Observer Z1 in bright field mode, EC Plan–Neofluar 100x/1.3 Oil M27, Orca Flash 4.0 LT+ Camera, VIS-LED at 50% intensity and 20 ms exposure time.

Turbidity assay

Proteins, RNA and the plate were prepared as described in "RNP granule formation". After induction of granule formation by adding RNA, 50 μL of the samples were pipetted into the plates, the plate put into the plate reader and the experiment started immediately. We used a BioTek Synergy H1 plate reader to measure turbidity. At first, the samples were shaken for 5 s to ensure homogenous distribution of the

granules, then the turbidity was monitored by measuring the absorbance of the sample at 480 nm 46 times with a time interval of 20 s. The data was analyzed with GraphPad Prism. The one-phase association equation (2) $Y = YO + (Plateau\text{-}YO)*(1\text{-}\exp(-K*x))$ was used to quantify condensate formation.

Dynamic light scattering (DLS)

Proteins, RNA and buffer (25 mM HEPES pH 7.3, 150 mM NaCl, 0.5 mM TCEP) were filter with Spin-X filter tubes for 5 min at 20000 g. Proteins were diluted with buffer to the final concentration ranging from 500 nM to 1 μM, and cluster formation was induced by adding RNA at concentrations ranging between 250 nM- 1 μM (please see figure legends Supplementary Figure 5J). The samples were pipetted into a 1536-well plate, covered with silica oil and centrifuged at 500 g for 1 min to remove air bubbles. The plate was incubated for 90 min at 25 °C in a Wyatt Dynapro II DLS plate reader. Data acquisition and processing was performed using the software DYNAMICS V7 from Wyatt. 20 acquisitions were recorded with 2 s acquisition time. Acquisitions that did not baseline within a ± 0.01 interval or showed aggregation or vibration artefacts were discarded. The data was measured in technical triplicates and the resulting curves from three experiments were fitted with the Raynals online tool at the EMBLEM website (https://spc.embl-hamburg.de/app/raynals)[91]. Data is represented as mean of these fits, error bars show the standard deviation. Numbers of curve fits averaged per figure: 500-250: WT 6, S181E 5, Y396E 6; 600-300: WT 7, S181E 8, Y396E 7; 800-400: WT 5, S181E 5, Y396E 5; 600-600: WT 5, S181E 9, Y396E 7, 800-800: WT 5, S181E 9, Y396E 8; 1000-1000: WT 6, S181E 6, Y396E 5).

MD simulations

We performed molecular dynamics (MD) simulations of linker 1 wild-type, linker 1 S181E, linker 2 wild-type, and linker 2 Y396E using the Martini 3 force field with rescaled protein-water interactions[65]. We set the scaling parameter λ = 1.06. All linkers were modeled as polypeptide chains with no secondary structure (coils) using UCSF Chimera[92] and then martinised. Each simulation box (30x30x30 nm^3) was set up with 33 randomly placed copies of the same polypeptide chain, water and 0.15 M NaCl. We performed an energy minimization using the steepest descent algorithm. Then we equilibrated the system by running a 10 ps-long simulation using a 1 fs time step and restraining the position of protein backbone beads by using harmonic potentials with force-constants of 1000 kJ mol^{-1} nm^{-2}. Afterwards, we ran another 2.1 ns without restraints in the NVT ensemble and a final equilibration of 21 ns in the NPT ensemble, in both equilibration steps we used a 30 fs time step ns. After equilibration, we ran the production phase using a 20 fs time step. The temperature in the simulation box was controlled by a velocity rescale thermostat[93](reference temperature T_ref = 300 K, coupling time constant tau_T = 1 ps). The Parrinello–Rahman barostat [Parrinello, 1981] (reference pressure p_ref = 1 bar; coupling time constant τ_p = 24 ps) was used for the last equilibration step and for the production run. The simulations were performed using the Martini 3.0 forcefield[94] and the GROMACS 2020.5 software[95].

The contact maps for cis-interactions were calculated using the Contact Map Explorer Python analysis package [https://contact-map.readthedocs.io/en/latest/index.html] (version 0.7.0). For each simulation, we calculated all the contacts between all atoms of the same polypeptide at each frame of the trajectory (ignoring atoms of 2 neighboring residues in each direction). A contact is defined between two atoms that are within a distance of 0.45 nm. The contributions from all chains at each frame were summed up in a single matrix and normalized by the number of frames and chains. For the final plots, the results were shown in a matrix where a value of contact frequency p corresponds to each pair of residues, where p is the max value of the contact frequencies computed for every atom in the residue pair.

The radius of gyration probability distributions computed from MD simulations were compared to the Analytical Flory Random Coil (AFRC) distribution[67]. AFRC is an analytical model of unfolded polypeptides that behave as ideal chains, so it is suitable to be used as a reference. We computed the AFRC counterparts of linker 1, linker 2 and their phosphomimetic mutants using the AFRC model available via Google Colab notebook: (https://colab.research.google.com/drive/1WHw8ous7IgcKd2LKYuJLeBTlkdEYoRAk?usp=sharing).

SAXS experiments

SAXS samples were prepared at concentrations > 10 mg/ml in a 250 μL volume and each experiment performed in duplicates. All samples were measured at beamline BM29 at the ESRF facility in Grenoble. A Superdex 200 Increase 10/300 GL size exclusion column was equilibrated with SAXS buffer (25 mM HEPES, 150 mM NaCl, 0.5 mM TCEP). Samples were applied to the column and run with 0.5 ml/min. 1300 Frames with 0.5 frames per second were acquired. We used the ATSAS 3.1.3 data analysis software for data processing. SEC-coupled SAXS data was analyzed with CHROMIXS. 25 frames for buffer and sample were selected and averaged. The buffer subtracted data was analyzed and plotted in PRIMUSQT.

SAXS analyzes and EOM calculations

The data were processed with the SAXSQuant software (version 3.9), and de-smeared using the programs GNOM[96] and GIFT (PCG software). EOM analysis was performed with the ATSAS 2.5 package (EMBL, Hamburg). EOM calculations were carried out using the EOM program[64] and using default settings. A random pool of 100,000 independent structures was generated using the primary sequence and the available structure of IGF2BP1 domains. All disordered regions were randomized. Using the built-in genetic algorithm and using the default settings, a subset of a few independent structures were selected that described the experimental SAXS best and used to prepare the figures showing R_G/D_{max} distributions.

NMR Experiments

NMR spectra were recorded on a 600 MHz Bruker Avance Neo 600 spectrometer. ^{1}H-^{15}N Heteronuclear Single Quantum Coherence (HSQC) experiments were performed by thawing the proteins and centrifuging for 15 min at 20,000 g and 4 °C. The proteins were diluted with 20 mM phosphate buffer pH 7.2, 150 mM NaCl, 10% D_2O to the desired concentration. For the titration experiments with the folded domains, His-RRM1-2, His-KH1-2 or His-KH3-4 were prepared as above. The sample with the highest protein concentration was prepared first, measured and then diluted 1: 1 with 50 μM ^{15}N-Linker 1 or 25 μM ^{15}N-Linker 2 for higher dilution samples. All HSQC experiments with Linker 1 were performed at 15 °C. All experiments with 12xUG RNA or XBP1 10 nt RNA were performed in RNase free buffer with 25 mM HEPES pH 7.3, 150 mM NaCl. Experiments with 15N-labeled KH1-4 and L2-KH3-4 were conducted in 25 mM HEPES pH 7.2, 150 mM NaCl, 2 mM DTT. For all His-RRM1-2 experiments 2 mM DTT was used.

The spectra were processed and phased using NMRPipe[97] and further analyzed with CCPNMR Version 3[98]. Chemical shift perturbations were calculated with the following formula:

$$CSP = \sqrt{\left(\delta H^2 + 0.14 * \delta N^2\right)} \quad (3)$$

δH and δN are the chemical shift differences compared to the apo protein. Peaks unresolved in the concentrations used for the titration experiments were excluded from the analysis.

Peaks were assigned by obtaining HNCO, HNCACO, HNCACB, HNCOCACB, HNCANNH and HNCOCANNH spectra of 300 μM ^{13}C-^{15}N-Linker 1 wild-type and 300 μM ^{13}C-^{15}N-Linker 2 wild-type and the respective HSQC spectra. Peak assignments were performed in

CCPNMR. NMR assignments are available in Biological Magnetic Resonance Bank.

Stress granule reconstitution in cell lysates

Split-GFP tagged IGF2BP1 cells were seeded in a 15 cm dish and grown until they reached 90% confluency. Cells were washed with ice cold PBS, and harvested by scraping. Subsequently cells were centrifuged at 1123 g for 4 min. PBS was removed by aspiration, and cell pellet was flash-frozen. In order to lyse the cells, they were thawed and flash-frozen three times. Next, 500ul of lysis buffer, composed of 25 mM Tris pH 7, 0.5% NP-40, 1x Protease inhibitor cocktail, 2,5% murine RNAse inhibitor, 100 mM NaCl and 2 mM DTT, was added. After the addition of the lysis buffer, the cells were further resuspended using a 25 G needle 10 times. Next, two centrifugation steps ensued, first at 1500 g for 5 min, then 16,000 g for 8 min. Supernatants were transferred to a new tube, lysate concentration was measured using a BCA kit (ThermoFisher) and concentration was adjusted to 5 mg/ml using the lysate buffer. 20uM of purified G3BP1 were added to induce LLPS followed by a 40 min incubation step. Afterwards, 5uM of mCherry-tagged IGF2BP1 was spiked in, gently mixed and incubated for 20 min. The μ-Slide Angiogenesis with ibiTreat 20 ul was used as an imaging vessel. Fluorescence recovery after photobleaching (FRAP) experiments were performed on a Zeiss Axio Observer, using a Plan-Apochromat 63x/1.4 Oil DIC III objective with a Yokogawa CSU-X1 Nipkow spinning disk (50 µm pinholes, spacing 253 µm, 5000 rpm). Imaging was conducted for 3 min with 150 ms exposure time, with a time interval of 500 ms. Three pre-bleach images were taken. 70% of FRAP laser power was used, and a 40% excitation laser.

Transfection of packaging cells

Plasmids used for transfection were purified using an endotoxin-free plasmid kit from Qiagen. Transfections were performed using 1100 ng of DNA in total, with 500 ng of plasmid of interest, 500 ng pCMVR8.74 (Addgene plasmid # 22036), and 100 ng of pCMV-VSV-G (Addgene plasmid # 8454). Supplement free DMEM was used to mix DNA and Polyethylenimine (PEI) in a 1:3 ratio. HEK293T HiEX cell were used as packaging cells. 2×10^5 cells were seeded in a 6-well plate a day before transfection and grown in a fully supplemented DMEM. The Plasmid mixture containing a transfection reagent was added dropwise onto the cells and they were incubated for 48 h.

Transduction of U2OS (GFP-G3BP1) and HCT116 cells (ΔIGF2BP2, ΔIGF2BP3)

After a 48 h incubation, virus was collected from the supernatant with a syringe and sterile filtered. U2OS and HCT116 cells were seeded a day before in fully supplemented medium. The sterile filtered virus was mixed with fully supplemented DMED with 8ug/ml Polybrene at a 1:50 ratio. Cells were grown for 48 h up to 15 cm dishes. The BD Melody Fluorescence Activated Cell Sorting (FACS) system was used to sort U2OS cells in purity mode and gated for high and low expression. The high-expressing population was used for further experiments. HCT116 cells were sorted in a single-cell sorting mode, gated for high and low expression. Three clones were selected for further characterization. None of the cell lines are authenticated. The cell lines were not tested for Mycoplasma contamination.

Western blotting

80% confluent cells were lysed with RIPA buffer (150 mM NaCl, 1% NP-40, 0.5% Sodium deoxycholate, 0.1% SDS, and 25 mM TRIS pH 7.4) containing 1x Protease inhibitor (Roche). The protein concentration was determined using a commercially available BCA kit (ThermoFisher). 10 μg of protein containing lysate in sample buffer was denatured at 95 °C for 5 min. Following denaturing, the samples were loaded onto the 10% sodium dodecyl sulfate (SDS) gel. Proteins were transferred onto a Nitrocellulose membrane (Amersham) in transfer buffer (25 mM TRIS, 190 mM glycine, 20% ethanol) for 110 min at 120 V. Membranes were stained with Ponceau S and blocked in 5% milk for 1 h, or in LI-COR blocking buffer (part number: 927-60001). The primary antibody was diluted in 2.5% milk (Table 1) and incubated overnight at 4 °C, or in case of the LI-COR secondary antibody in the blocking buffer. The membrane was washed 5 times with TBST (20 mM TRIS, 150 mM NaCl, 0.1% Tween 20), and the secondary antibody was applied and incubated for 1 h, which was diluted in 2.5% milk (Table 1). LI-COR secondary antibody was diluted in the manufacturers antibody diluent (927-65001). After the incubation the membranes were washed 5 times with TBST and an enhanced chemiluminescent (ECL) horse radish peroxidase substrate (ThermoFisher) was added. In case of LI-COR secondary antibodies, after the TBST washes, the membrane was washed three more times with 1x TBS. Membranes were imaged using a BioRad Chemidock, and analyzed using the manufacturers image analysis software (Biorad Image Lab), or using LICOR Odyssey CLx fluorescence imager, and analyzed using Fiji.

Table 1 | Antibodies and dilutions used for Western Blot analysis

Antibodies and dilutions used				
Antibody	Dilution	Manufacturer	Catalog number	Lot number
Anti-IGF2BP1	1:2500	Proteintech	22803-1-AP	00018571
Anti-GAPDH	1:20000	Proteintech	10494-1-AP	00113796
Anti-Rabbit IgG HRP conjugate	1:20000	Promega	W401B	0000573275
Anti-Rabbit IgG IRdye 800CW secondary antibody	1:20000	LI-COR	926-32211	D30307-15

Immunofluorescence and Image analyzes

20.000 U2OS and HCT116 cells were seeded in an Ibidi μSlide 8 well dish one day before the experiment and incubated at 37 °C with 5% CO_2. In order to induce the stress granule formation, cells were stressed with 500 uM of Sodium arsenite (As) for 30 or 60 min. Afterwards cells were washed with PBS and fixed with ice-cold Methanol for 5 min. After the fixation the slide was washed 3 more times with PBS and incubated with blocking buffer (5% BSA in TBST) for 1 h. In the case of HCT116 cells, the primary ChromoTek RFP-Booster Alexa Fluor 568 (rb2AF568) was incubated overnight. Following the incubation, three washes with PBS ensued and the sample was imaged in PBS using a Zeiss inverse point LSM980 scanning confocal microscope. The objective used was an oil 63x Plan-Apochromat objective with 1.4 NA. The software used for microscope operation is Zeiss ZEN v3.3. The fluorophores were excited with 488 nm and 561 nm lasers respectively and image analysis was done in Fiji/ImageJ. Cell pose was used in order to get the individual cells in the image, which were saved as an ROI. Cells that touch the image border were excluded, gaussian blur was applied (σ=2), background was subtracted using a rolling ball algorithm with a radius 5, and an auto-threshold "Yen" was applied, after which the particles were analyzed, from sizes 10 pixels to infinity.

Live cell imaging and FRAP analyzes

Live U2OS cells expressing GFP-tagged G3BP1 and mCherry-tagged IGF2BP1 were imaged using a Nikon Ti2-E, inverse microscope with a Nikon Perfect Focus System, and a Yokogawa CSU-X1-A1 Nipkow spinning disk (50µm pinholes, spacing 253 µm, 5000 rpm). CFI Plan Apo 60x/1.42 Oil, WD 0.15 mm objective was used. Cells were imaged in Ibidi 8-well μSlide (80826). 20000 cells were seeded a day before the experiment in fully supplemented DMEM, and were treated with 500 uM Sodium arsenite in Gibco Imaging DMEM (11880-028) for 60 min before imaging. Cells were incubated at 37 °C, 5% CO_2 during

imaging. The fluorescence recovery after photobleaching (FRAP) experiment was conducted with 100% 561 nm laser power and with 10 ms bleach time per pixel. Images were acquired with 25% 561 nm laser power 500 ms exposure time and a gain of 150. 90 timepoints were recorded during the recovery with a 10 s interval and 3 frames pre-bleach. To be able to follow the recovery, a z-stack containing 6 slices with a spacing of 0.5 μm around bleached layer was acquired at each timepoint. Image processing was conducted in Fiji/ImageJ. Respective z-stacks were combined to a single image via Z projection of the Max intensity. Then the bleached ROI and two ROIs of the similar size with stress granules that were not bleached for bleaching correction. Two ROIs within a cell without stress granules were selected to be used as background- The bleaching factor for each timepoint was calculated by dividing the mean intensity at a given timepoint by the mean intensity of timepoint zero. The background intensity was calculated by mean of both background ROIs corrected for bleaching. The fluorescence of the bleached ROIs was normalized to the background and the mean intensity of the three pre-bleach images for all timepoints after bleaching. The resulting curve was fitted using the one phase association equation (2) $Y = YO + (Plateau\text{-}YO)*(1\text{-}\exp(-K*x))$ in GraphPad PRISM.

Immunoprecipitation for LC MS/MS analysis

HEK293 cells expressing spit-GFP tagged IGF2BP1 were seeded in 15 cm dishes and grown until they reached 80% confluency (10^6 cells). Cells were washed with ice-cold PBS, scraped, centrifuged (1123 g, 4 min) and the pellet flash frozen. On the day of the experiment, the pellets were thawed and 750ul of lysis buffer (consisting of 20 mM HEPES pH 7.4, 150 mM NaCl, 0.5 mM EDTA, 0.1% SDS, 0.5% Triton X-100, 0.2% Deoxycholate, 1x protease inhibitor cocktail, 1x phosphatase inhibitor cocktail, 10 ug/mL RNase A, 10 U/μL RNase T1). Cells were lysed by vortexing for 15 min (3 s in 2 min intervals). The lysate was centrifuged at 20.000 g for 15 min. 50 ul Chromotek GFP-Trap magnetic beads (gtma-20) were used per 15 cm dish. Lysates were incubated at 4 °C for 2 h rotating. The supernatant was removed by pipetting, while the beads were magnetized using a magnetic rack. The beads were washed five times with wash buffer 1 (20 mM HEPES pH 7.4, 500 mM NaCl, 0.5 mM EDTA, 0.1% SDS, 0.5% Triton X-100, 0.2% Deoxycholate) and five times with wash buffer 2 (20 mM HEPES pH 7.4, 500 mM NaCl, 0.5 mM EDTA. The samples were submitted on-beads for mass-spectrometry analysis at the Max Perutz Labs Mass Spectrometry Facility.

RNA immunoprecipitation (RIP-Seq) and total transcriptome (RNA-Seq) sequencing and analysis

HCT116 cells stably expressing mCherry-tagged wild-type IGF2BP1 or S181E, Y396E, and RQ mutants (in triplicates, dishes plated and grown independently) and parental HCT116 cells were seeded in 10 cm dishes and grown until they reached 80% confluency. To induce stress cells were treated with 500 μM sodium arsenite (Sigma) for two hours before collection. PBS was added to the control cells. Cells were washed with ice-cold PBS, scraped, centrifuged (1123 g, 4 min) and the pellet flash frozen and stored at −80 °C. On the day of the experiment, the pellets were thawed and 150 μL of lysis buffer (25 mM HEPES pH 7.3, 150 mM NaCl, 5 mM $MgCl_2$, 0.5% NP-40, 1 mM DTT). 1x protease inhibitor cocktail (Roche), 1x phosphatase inhibitor PhosSTOP (Roche) and 1 U / μL of Murine RNase Inhibitor (New England Biolabs) were added for lysis. Cells were lysed by vortexing for 20 min (3 s with 2-minute intervals). The lysate was centrifuged at 20.000 g for 15 min. 20 μL of RPF-Trap magnetic agarose (rtma) were used per 10 cm dish. Lysates were incubated at 4 °C for 1 h rotating, and then washed three times with lysis buffer and twice with wash buffer (25 mM HEPES pH 7.3, 150 mM NaCl, 1 mM MgCl2, 0.5% NP40). Then the beads were resuspended in 150 μL of wash buffer containing 0.1% SDS and 2 mg/mL proteinase K (Ambion), and incubated at 55 °C for 30 min. The eluate was collected and purified with an RNA cleanup kit (Zymo Research). The purified RNA samples were rRNA depleted using human riboPOOL probes (siTOOLs) according to the manufacturer's instructions. The RNA was then purified with an RNA cleanup kit (Zymo Research) and treated with 0.2 U of RNase-free DNase I (NEB) at 37 °C for 15 min, re-purified with an RNA cleanup kit (Zymo Research), and used for library preparation with NEBNext Ultra Directional RNA Library Prep Kit for Illumina (NEB).

For total transcriptome sequencing total RNA was extracted from 5 μL aliquot of clarified cell lysate (IP input) using the KingFisher Flex Purification System (Thermo) with the High-Performance RNA Isolation kit (Molecular Tools Shop, Vienna BioCenter). During the isolation RNA was treated with RNase-free DNase I (NEB). PolyA mRNA was isolated using NEBNext Poly(A) mRNA Magnetic Isolation Module (NEB) and used for library preparation with NEBNext Ultra Directional RNA Library Prep Kit for Illumina (NEB).

Both RIP- and RNA-Seq libraries were sequenced on NovaSeqX 1.5B at SingleRead 100 mode at the Vienna BioCenter NGS facility producing ~35 million reads per sample. BCL files were converted to demultiplexed fastq files with bcl2fastq v2.20.0.422. The quality of fastq files was checked with fastqc 0.11.9. The fastq files were trimmed and aligned to human genome hg38 using GENCODE annotation (release 46) with STAR v2.7.11b[99] allowing for the two mismatches. Gene counts were obtained using FeatureCounts function of the Subread package v2.0.6[100]. Total gene counts for protein coding genes were TMM normalized to calculate the counts per million values (CPM), filtered to only include genes with CPM higher than 10 in at least half of the libraries, and the differential expression analysis was performed with edgeR glmQLFTest (Generalized Linear Model Quasi-Likelihood F-test)[101]. IGF2BP1 targets were defined as genes with RIP-Seq CPMs at least 2-fold higher than RNA-Seq CPMs and 4-fold higher than the background RIP-Seq CPMs from parental cells. For the GO term analysis GOrilla service was used[102]. Sequencing data processing was done using the Life Science Compute Cluster (LiSC) of the University of Vienna.

Reporting summary

Further i nformation on research design is available in the Nature Portfolio Reporting Summary linked to this article.

Data availability

The source data are provided with this paper. All raw and processed sequencing data generated in this study have been deposited in the Gene Expression Omnibus database with the accession number GSE272875 (IGF2BP1 RNA-Seq and RIP-Seq data). The mass spectrometry proteomics data have been deposited to the ProteomeXchange Consortium (http://proteomecentral.proteomexchange.org) via the PRIDE partner repository[103] with the dataset identifier PXD045761 (mass spectrometry data of IGF2BP1 from HEK293T cells) and PXD056497 (mass spectrometry data of ProAlanase digested IGF2BP1 from HEK293T cells). The NMR signal assignments are deposited with BMRB ID 52567 (wild-type IGF2BP1 linker1 157-194) and 52568 (wild-type IGF2BP1 linker2 344-404) Source data are provided with this paper.

References

1. Dreyfuss, G., Kim, V. N. & Kataoka, N. Messenger-RNA-binding proteins and the messages they carry. *Nat Rev Mol Cell Biol* **3**, 195–205 (2002).
2. Glisovic, T., Bachorik, J. L., Yong, J. & Dreyfuss, G. RNA-binding proteins and post-transcriptional gene regulation. *FEBS Lett* **582**, 1977–1986 (2008).
3. Kishore, S., Luber, S. & Zavolan, M. Deciphering the role of RNA-binding proteins in the post-transcriptional control of gene expression. *Brief Funct Genomics* **9**, 391–404 (2010).

4. Gerstberger, S., Hafner, M., Ascano, M. & Tuschl, T. Evolutionary conservation and expression of human RNA-binding proteins and their role in human genetic disease. *Adv Exp Med Biol* **825**, 1–55 (2014).
5. Gerstberger, S., Hafner, M. & Tuschl, T. A census of human RNA-binding proteins. *Nat Rev Genet* **15**, 829–845 (2014).
6. Schneider-Lunitz, V., Ruiz-Orera, J., Hubner, N. & van Heesch, S. Multifunctional RNA-binding proteins influence mRNA abundance and translational efficiency of distinct sets of target genes. *PLoS Comput Biol* **17**, e1009658 (2021).
7. Huttelmaier, S. et al. Spatial regulation of beta-actin translation by Src-dependent phosphorylation of ZBP1. *Nature* **438**, 512–515 (2005).
8. Huang, H. et al. Recognition of RNA N(6)-methyladenosine by IGF2BP proteins enhances mRNA stability and translation. *Nat Cell Biol* **20**, 285–295 (2018).
9. Huang, X. et al. Insulin-like growth factor 2 mRNA-binding protein 1 (IGF2BP1) in cancer. *J Hematol Oncol* **11**, 88 (2018).
10. Nielsen, J. et al. A family of insulin-like growth factor II mRNA-binding proteins represses translation in late development. *Mol Cell Biol* **19**, 1262–1270 (1999).
11. Nielsen, J., Kristensen, M. A., Willemoes, M., Nielsen, F. C. & Christiansen, J. Sequential dimerization of human zipcode-binding protein IMP1 on RNA: a cooperative mechanism providing RNP stability. *Nucleic Acids Res.* **32**, 4368–4376 (2004).
12. Kislauskis, E. H., Zhu, X. & Singer, R. H. Sequences responsible for intracellular localization of beta-actin messenger RNA also affect cell phenotype. *J Cell Biol* **127**, 441–451 (1994).
13. Ross, A. F., Oleynikov, Y., Kislauskis, E. H., Taneja, K. L. & Singer, R. H. Characterization of a beta-actin mRNA zipcode-binding protein. *Mol Cell Biol* **17**, 2158–2165 (1997).
14. Hansen, T. V. et al. Dwarfism and impaired gut development in insulin-like growth factor II mRNA-binding protein 1-deficient mice. *Mol Cell Biol* **24**, 4448–4464 (2004).
15. Hammer, N. A. et al. Expression of IGF-II mRNA-binding proteins (IMPs) in gonads and testicular cancer. *Reproduction* **130**, 203–212 (2005).
16. Singh, V. et al. The mRNA-binding protein IGF2BP1 maintains intestinal barrier function by up-regulating occludin expression. *J Biol Chem* **295**, 8602–8612 (2020).
17. Singh, V., Walter, V., Elcheva, I., Imamura Kawasawa, Y. & Spiegelman, V. S. Global role of IGF2BP1 in controlling the expression of Wnt/beta-catenin-regulated genes in colorectal cancer cells. *Front Cell Dev Biol* **11**, 1236356 (2023).
18. Wallis, N. et al. Small molecule inhibitor of Igf2bp1 represses Kras and a pro-oncogenic phenotype in cancer cells. *RNA Biol* **19**, 26–43 (2022).
19. Muller, S. et al. IGF2BP1 enhances an aggressive tumor cell phenotype by impairing miRNA-directed downregulation of oncogenic factors. *Nucleic Acids Res* **46**, 6285–6303 (2018).
20. Korn, S. M., Ulshofer, C. J., Schneider, T. & Schlundt, A. Structures and target RNA preferences of the RNA-binding protein family of IGF2BPs: An overview. *Structure* **29**, 787–803 (2021).
21. Schneider, T. et al. Combinatorial recognition of clustered RNA elements by the multidomain RNA-binding protein IMP3. *Nat Commun* **10**, 2266 (2019).
22. Jia, M., Gut, H. & Chao, J. A. Structural basis of IMP3 RRM12 recognition of RNA. *RNA* **24**, 1659–1666 (2018).
23. Biswas, J. et al. The structural basis for RNA selectivity by the IMP family of RNA-binding proteins. *Nat Commun* **10**, 4440 (2019).
24. Degrauwe, N. et al. The RNA Binding Protein IMP2 Preserves Glioblastoma Stem Cells by Preventing let-7 Target Gene Silencing. *Cell Rep.* **15**, 1634–1647 (2016).
25. Glass, M. et al. IGF2BP1, a Conserved Regulator of RNA Turnover in Cancer. *Front Mol Biosci* **8**, 632219 (2021).
26. Noubissi, F. K. et al. CRD-BP mediates stabilization of betaTrCP1 and c-myc mRNA in response to beta-catenin signalling. *Nature* **441**, 898–901 (2006).
27. Lederer, M., Bley, N., Schleifer, C. & Huttelmaier, S. The role of the oncofetal IGF2 mRNA-binding protein 3 (IGF2BP3) in cancer. *Semin Cancer Biol* **29**, 3–12 (2014).
28. Conway, A. E. et al. Enhanced CLIP uncovers IMP protein-RNA targets in human pluripotent stem cells important for cell adhesion and survival. *Cell Rep.* **15**, 666–679 (2016).
29. Hafner, M. et al. Transcriptome-wide identification of RNA-binding protein and microRNA target sites by PAR-CLIP. *Cell* **141**, 129–141 (2010).
30. Hammerle, M. et al. Posttranscriptional destabilization of the liver-specific long noncoding RNA HULC by the IGF2 mRNA-binding protein 1 (IGF2BP1). *Hepatology* **58**, 1703–1712 (2013).
31. Dai, N. et al. mTOR phosphorylates IMP2 to promote IGF2 mRNA translation by internal ribosomal entry. *Genes Dev* **25**, 1159–1172 (2011).
32. Dai, N., Christiansen, J., Nielsen, F. C. & Avruch, J. mTOR complex 2 phosphorylates IMP1 cotranslationally to promote IGF2 production and the proliferation of mouse embryonic fibroblasts. *Genes Dev* **27**, 301–312 (2013).
33. Urbanska, A. S. et al. ZBP1 phosphorylation at serine 181 regulates its dendritic transport and the development of dendritic trees of hippocampal neurons. *Sci Rep.* **7**, 1876 (2017).
34. Lambrianidou, A. et al. mTORC2 deploys the mRNA binding protein IGF2BP1 to regulate c-MYC expression and promote cell survival. *Cell Signal* **80**, 109912 (2021).
35. Stohr, N. et al. ZBP1 regulates mRNA stability during cellular stress. *J Cell Biol.* **175**, 527–534 (2006).
36. Kamiyama, D. et al. Versatile protein tagging in cells with split fluorescent protein. *Nat Commun* **7**, 11046 (2016).
37. Johnson, J. L. et al. An atlas of substrate specificities for the human serine/threonine kinome. *Nature* **613**, 759–766 (2023).
38. Bernstein, P. L., Herrick, D. J., Prokipcak, R. D. & Ross, J. Control of c-myc mRNA half-life in vitro by a protein capable of binding to a coding region stability determinant. *Genes Dev* **6**, 642–654 (1992).
39. Chao, J. A. et al. ZBP1 recognition of beta-actin zipcode induces RNA looping. *Genes Dev* **24**, 148–158 (2010).
40. Patel, V. L. et al. Spatial arrangement of an RNA zipcode identifies mRNAs under post-transcriptional control. *Genes Dev* **26**, 43–53 (2012).
41. Nicastro, G. et al. Mechanism of beta-actin mRNA Recognition by ZBP1. *Cell Rep.* **18**, 1187–1199 (2017).
42. Mateu-Regue, A. et al. Single mRNP Analysis Reveals that Small Cytoplasmic mRNP Granules Represent mRNA Singletons. *Cell Rep.* **29**, 736–748 e734 (2019).
43. Zeng, W. J. et al. Initiation of stress granule assembly by rapid clustering of IGF2BP proteins upon osmotic shock. *Biochim Biophys Acta Mol Cell Res.* **1867**, 118795 (2020).
44. Tiruchinapalli, D. M. et al. Activity-dependent trafficking and dynamic localization of zipcode binding protein 1 and beta-actin mRNA in dendrites and spines of hippocampal neurons. *J Neurosci* **23**, 3251–3261 (2003).
45. Yang, P. et al. G3BP1 Is a Tunable Switch that Triggers Phase Separation to Assemble Stress Granules. *Cell* **181**, 325–345 e328 (2020).
46. Guillen-Boixet, J. et al. RNA-Induced Conformational Switching and Clustering of G3BP Drive Stress Granule Assembly by Condensation. *Cell* **181**, 346–361 e317 (2020).
47. Zhang, H. et al. RNA Controls PolyQ Protein Phase Transitions. *Mol Cell* **60**, 220–230 (2015).
48. Gruber, A. R., Lorenz, R., Bernhart, S. H., Neubock, R. & Hofacker, I. L. The Vienna RNA websuite. *Nucleic Acids Res.* **36**, W70–W74 (2008).

49. Ma, W., Zhen, G., Xie, W. & Mayr, C. In vivo reconstitution finds multivalent RNA-RNA interactions as drivers of mesh-like condensates. *Elife* **10**, e64252 (2021).
50. Banerjee, P. R., Milin, A. N., Moosa, M. M., Onuchic, P. L. & Deniz, A. A. Reentrant Phase Transition Drives Dynamic Substructure Formation in Ribonucleoprotein Droplets. *Angew Chem Int Ed Engl* **56**, 11354–11359 (2017).
51. Wachter, K., Kohn, M., Stohr, N. & Huttelmaier, S. Subcellular localization and RNP formation of IGF2BPs (IGF2 mRNA-binding proteins) is modulated by distinct RNA-binding domains. *Biol Chem* **394**, 1077–1090 (2013).
52. Hollingworth, D. et al. KH domains with impaired nucleic acid binding as a tool for functional analysis. *Nucleic Acids Res*. **40**, 6873–6886 (2012).
53. Erlendsson, S. & Teilum, K. Binding Revisited-Avidity in Cellular Function and Signaling. *Front Mol Biosci* **7**, 615565 (2020).
54. Mittag, T. & Pappu, R. V. A conceptual framework for understanding phase separation and addressing open questions and challenges. *Mol Cell* **82**, 2201–2214 (2022).
55. Kar, M. et al. Phase-separating RNA-binding proteins form heterogeneous distributions of clusters in subsaturated solutions. *Proc Natl Acad Sci USA* **119**, e2202222119 (2022).
56. Kettel, P. et al. Stress-induced clustering of the UPR sensor IRE1 is driven by disordered regions within its ER lumenal domain Authors. *bioRxiv*, 2023.2003. 2030.534746 (2023).
57. Boke, E. et al. Amyloid-like Self-Assembly of a Cellular Compartment. *Cell* **166**, 637–650 (2016).
58. Shin, Y. & Brangwynne, C. P. Liquid phase condensation in cell physiology and disease. *Science* **357**, eaaf4382 (2017).
59. Taylor, N. O., Wei, M. T., Stone, H. A. & Brangwynne, C. P. Quantifying Dynamics in Phase-Separated Condensates Using Fluorescence Recovery after Photobleaching. *Biophys J* **117**, 1285–1300 (2019).
60. Klionsky, D. J. et al. Guidelines for the use and interpretation of assays for monitoring autophagy (3rd edition). *Autophagy* **12**, 1–222 (2016).
61. Vauquelin, G. & Charlton, S. J. Long-lasting target binding and rebinding as mechanisms to prolong in vivo drug action. *Br J Pharmacol* **161**, 488–508 (2010).
62. Freibaum, B. D., Messing, J., Yang, P., Kim, H. J. & Taylor, J. P. High-fidelity reconstitution of stress granules and nucleoli in mammalian cellular lysate. *Journal of Cell Biology* **220**, e202009079 (2021).
63. Kedersha, N., Tisdale, S., Hickman, T. & Anderson, P. Real-time and quantitative imaging of mammalian stress granules and processing bodies. *Methods in enzymology* **448**, 521–552 (2008).
64. Bernado, P., Mylonas, E., Petoukhov, M. V., Blackledge, M. & Svergun, D. I. Structural characterization of flexible proteins using small-angle X-ray scattering. *J Am Chem Soc* **129**, 5656–5664 (2007).
65. Thomasen, F. E., Pesce, F., Roesgaard, M. A., Tesei, G. & Lindorff-Larsen, K. Improving Martini 3 for Disordered and Multidomain Proteins. *J Chem Theory Comput* **18**, 2033–2041 (2022).
66. Harmon, T. S., Holehouse, A. S., Rosen, M. K. & Pappu, R. V. Intrinsically disordered linkers determine the interplay between phase separation and gelation in multivalent proteins. *Elife* **6**, e30294 (2017).
67. Alston, J. J., Ginell, G. M., Soranno, A. & Holehouse, A. S. The analytical Flory random coil is a simple-to-use reference model for unfolded and disordered proteins. *bioRxiv* (2023).
68. Thandapani, P., O'Connor, T. R., Bailey, T. L. & Richard, S. Defining the RGG/RG motif. *Mol Cell* **50**, 613–623 (2013).
69. Roschdi, S. et al. An atypical RNA quadruplex marks RNAs as vectors for gene silencing. *Nat Struct Mol Biol* **29**, 1113–1121 (2022).
70. Kim, T. H. et al. Phospho-dependent phase separation of FMRP and CAPRIN1 recapitulates regulation of translation and deadenylation. *Science* **365**, 825–829 (2019).
71. Hafner, M., Lianoglou, S., Tuschl, T. & Betel, D. Genome-wide identification of miRNA targets by PAR-CLIP. *Methods* **58**, 94–105 (2012).
72. Stohr, N. & Huttelmaier, S. IGF2BP1: a post-transcriptional "driver" of tumor cell migration. *Cell Adh Migr* **6**, 312–318 (2012).
73. Wu, B., Buxbaum, A. R., Katz, Z. B., Yoon, Y. J. & Singer, R. H. Quantifying Protein-mRNA Interactions in Single Live Cells. *Cell* **162**, 211–220 (2015).
74. Deribe, Y. L., Pawson, T. & Dikic, I. Post-translational modifications in signal integration. *Nat Struct Mol Biol* **17**, 666–672 (2010).
75. Velazquez-Cruz, A., Banos-Jaime, B., Diaz-Quintana, A., De la Rosa, M. A. & Diaz-Moreno, I. Post-translational control of RNA-binding proteins and disease-related dysregulation. *Front Mol Biosci* **8**, 658852 (2021).
76. Tsai, W. C. et al. Arginine demethylation of G3BP1 promotes stress granule assembly. *J Biol Chem* **291**, 22671–22685 (2016).
77. Hofweber, M. & Dormann, D. Friend or foe-Post-translational modifications as regulators of phase separation and RNP granule dynamics. *J Biol Chem* **294**, 7137–7150 (2019).
78. Wippich, F. et al. Dual specificity kinase DYRK3 couples stress granule condensation/dissolution to mTORC1 signaling. *Cell* **152**, 791–805 (2013).
79. Beranek, V. et al. Genetically encoded protein phosphorylation in mammalian cells. *Cell Chem Biol* **25**, 1067–1074 e1065 (2018).
80. Li, W. J. et al. Profiling PRMT methylome reveals roles of hnRNPA1 arginine methylation in RNA splicing and cell growth. *Nat Commun* **12**, 1946 (2021).
81. Ranganathan, S., Dasmeh, P., Furniss, S. & Shakhnovich, E. Phosphorylation sites are evolutionary checkpoints against liquid-solid transition in protein condensates. *Proc Natl Acad Sci USA* **120**, e2215828120 (2023).
82. Cho, N. H. et al. OpenCell: Endogenous tagging for the cartography of human cellular organization. *Science* **375**, eabi6983 (2022).
83. Leonetti, M. D., Sekine, S., Kamiyama, D., Weissman, J. S. & Huang, B. A scalable strategy for high-throughput GFP tagging of endogenous human proteins. *Proc Natl Acad Sci USA* **113**, E3501–E3508 (2016).
84. Dyballa, N. & Metzger, S. Fast and sensitive colloidal coomassie G-250 staining for proteins in polyacrylamide gels. *J Vis Exp* **30**, e1431 (2009).
85. Kong, A. T., Leprevost, F. V., Avtonomov, D. M., Mellacheruvu, D. & Nesvizhskii, A. I. MSFragger: ultrafast and comprehensive peptide identification in mass spectrometry-based proteomics. *Nat Methods* **14**, 513–520 (2017).
86. Yu, F., Haynes, S. E. & Nesvizhskii, A. I. IonQuant enables accurate and sensitive label-free quantification with FDR-controlled match-between-runs. *Mol Cell Proteomics* **20**, 100077 (2021).
87. da Veiga Leprevost, F. et al. Philosopher: a versatile toolkit for shotgun proteomics data analysis. *Nat Methods* **17**, 869–870 (2020).
88. Hollenstein, D. M. et al. Chemical acetylation of ligands and two-step digestion protocol for reducing codigestion in affinity purification-mass spectrometry. *J Proteome Res*. **22**, 3383–3391 (2023).
89. MacLean, B. et al. Skyline: an open source document editor for creating and analyzing targeted proteomics experiments. *Bioinformatics* **26**, 966–968 (2010).
90. Rappsilber, J., Ishihama, Y. & Mann, M. Stop and go extraction tips for matrix-assisted laser desorption/ionization, nanoelectrospray, and LC/MS sample pretreatment in proteomics. *Anal Chem* **75**, 663–670 (2003).

91. Burastero, O. et al. Raynals, an online tool for the analysis of dynamic light scattering. *Acta Crystallogr D Struct Biol* **79**, 673–683 (2023).
92. Pettersen, E. F. et al. UCSF Chimera–a visualization system for exploratory research and analysis. *J Comput Chem* **25**, 1605–1612 (2004).
93. Bussi, G., Donadio, D. & Parrinello, M. Canonical sampling through velocity rescaling. *J Chem Phys*. **126**, 014101 (2007).
94. Souza, P. C. T. et al. Martini 3: a general purpose force field for coarse-grained molecular dynamics. *Nat Methods* **18**, 382–388 (2021).
95. Lindahl, E., MJ;, A., Hess, B. & van der Spoel, D. *GROMACS 2020.5 Source code*. (2021).
96. Svergun, D. Determination of the regularization parameter in indirect-transform methods using perceptual criteria. *J. Appl. Cryst.* **25**, 495–503 (1992).
97. Delaglio, F. et al. NMRPipe: a multidimensional spectral processing system based on UNIX pipes. *J Biomol NMR* **6**, 277–293 (1995).
98. Skinner, S. P. et al. CcpNmr AnalysisAssign: a flexible platform for integrated NMR analysis. *J Biomol NMR* **66**, 111–124 (2016).
99. Dobin, A. et al. STAR: ultrafast universal RNA-seq aligner. *Bioinformatics* **29**, 15–21 (2013).
100. Liao, Y., Smyth, G. K. & Shi, W. featureCounts: an efficient general purpose program for assigning sequence reads to genomic features. *Bioinformatics* **30**, 923–930 (2014).
101. Robinson, M. D. & Oshlack, A. A scaling normalization method for differential expression analysis of RNA-seq data. *Genome Biol* **11**, R25 (2010).
102. Eden, E., Navon, R., Steinfeld, I., Lipson, D. & Yakhini, Z. GOrilla: a tool for discovery and visualization of enriched GO terms in ranked gene lists. *BMC Bioinformatics* **10**, 48 (2009).
103. Perez-Riverol, Y. et al. The PRIDE database resources in 2022: a hub for mass spectrometry-based proteomics evidences. *Nucleic Acids Res*. **50**, D543–D552 (2022).

Acknowledgements

We are grateful to the late Thomas Peterbauer at the Max Perutz Labs Biooptics Light Microscopy Facility for his help and support. We thank Mila Asparuhova, Gizem Celebi and Isabell Niedermoser for their technical support and help. We appreciate the support from Julia Scholz in image analysis. We thank Gijs Versteeg and his lab for their help with lentiviral transduction and providing us with the expression plasmids. We thank Kitti Csalyi and Thomas Sauer at Max Perutz Labs Biooptics FACS facility for their help. We thank Georg Kontaxis for his continuing support with NMR measurements. Proteomics analyzes were performed by the Mass Spectrometry Facility at Max Perutz Labs using the VBCF instrument pool. We are grateful to Max Perutz Labs Mass spectrometry facility, Markus Hartl, Dorothea Anrather, Wei-qiang Chen and David Hollenstein for their help and support with measurements, data analyzes and experimental design. We are grateful to Thomas Leonard for his help with SEC-SAXS measurements and his invaluable input in data analyzes. We thank Jeffrey A. Chao for providing us the MBP-tagged IGF2BP1 full-length. We thank Arthur Sedivy from the Vienna BioCenter ProTech Facility for his value support with DLS measurement and analysis. This research was funded in whole or in part by the Austrian Science Fund (FWF) [FWF-SFB F79 and FWF-W 1261] to GEK. For open access purposes, the author has applied a CC BY public copyright license to any author accepted manuscript version arising from this submission.E.S. and R.C. acknowledge support and funding by the Frankfurt Institute of Advanced Studies, the LOEWE Center for Multiscale Modeling in Life Sciences of the state of Hesse, the Collaborative Research Center 1507 "Membrane-associated Protein Assemblies, Machineries, and Supercomplexes" (Project-ID Project ID 450648163 – P09), and the International Max Planck Research School on Cellular Biophysics (to R.C.), the Centre for Scientific Computing of the Goethe University and the Jülich Supercomputing Centre for computational resources and support. The research of T.M. was supported by Austrian Science Fund (FWF) grants P28854, I3792, DOC-130, and DK-MCD W1226; Austrian Research Promotion Agency (FFG) grants 864690 and 870454; the Integrative Metabolism Research Center Graz; the Austrian Infrastructure Program 2016/2017; the Styrian Government (Zukunftsfonds, doc.fund program); the City of Graz; and BioTechMed-Graz (flagship project). The GFP-G3BP1 engineered cell lines are kind gift of Witold Szaflarski, Pavel Ivanov and Paul Anderson.

Author contributions

HH: Conceptualization. HH, ASA, AM, BB, ES and IN: Investigation, Methodology, Formal Analyzes and Visualization. TM, RC and GEK: Conceptualization, Funding acquisition and Supervision. HH and GEK wrote the original draft. All authors contributed to review and editing.

Competing interests

The authors declare no competing interests.

Additional information

Supplementary information The online version contains supplementary material available at https://doi.org/10.1038/s41467-024-53400-4.

Correspondence and requests for materials should be addressed to G. Elif Karagöz.

Peer review information *Nature Communications* thanks Stefan Hüttelmaier, and the other, anonymous, reviewer(s) for their contribution to the peer review of this work. A peer review file is available.

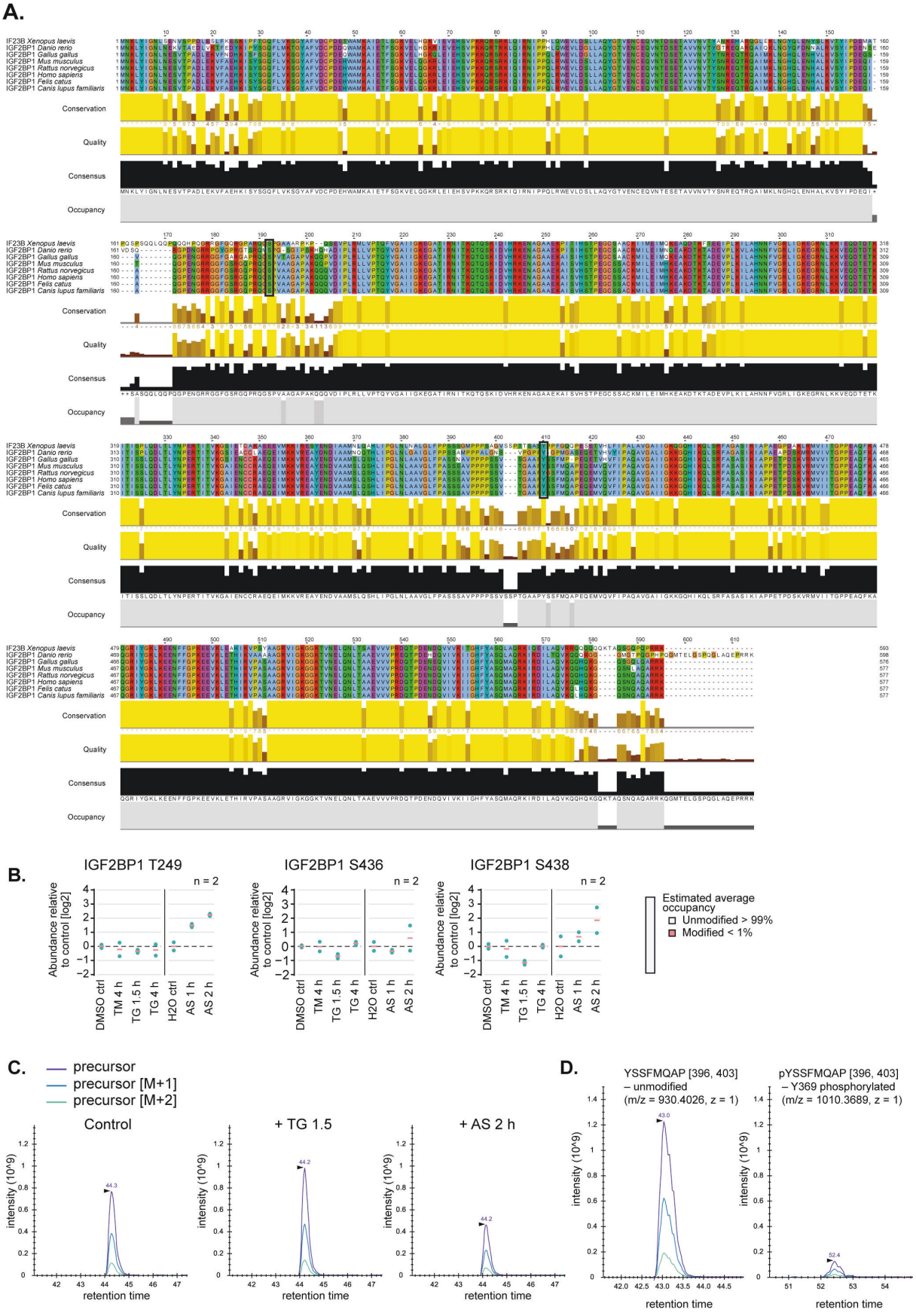

Supplementary Figure 1. IGF2BP1 phosphorylation sites S181 and Y396 are highly conserved
(A) Comparison of the IGF2BP1 primary protein sequence from*; Xenopus laevis; Danio rerio; Gallus gallus; Mus musculus; Rattus norvegicus; Homo sapiens; Felis catus and Canis lupus familiaris.* (B)

Relative abundance of the indicated IGF2BP1 phosphorylation sites in cells exposed to various forms of proteotoxic stress compared to the control conditions. Tunicamycin (TM) and thapsigargin (TG) induces ER stress, whereas sodium arsenite (AS) leads to oxidative stress. The time-points on the bottom indicate length of exposure to the stress-inducing drug. (C) Extracted ion chromatogram of LC-MS/MS peaks of the YSSFMQAP peptide obtained from IGF2BP1 isolated from mammalian cells under control, thapsigargin, and arsenite conditions (D) Extracted ion chromatogram of LC-MS/MS peaks of unmodified (left) and phosphorylated (right) YSSFMQAP peptides obtained from *in vitro* purified IGF2BP1 after ProAlanase treatment. The in vitro phosphorylation was performed by Src kinase treatment, please see materials and methods

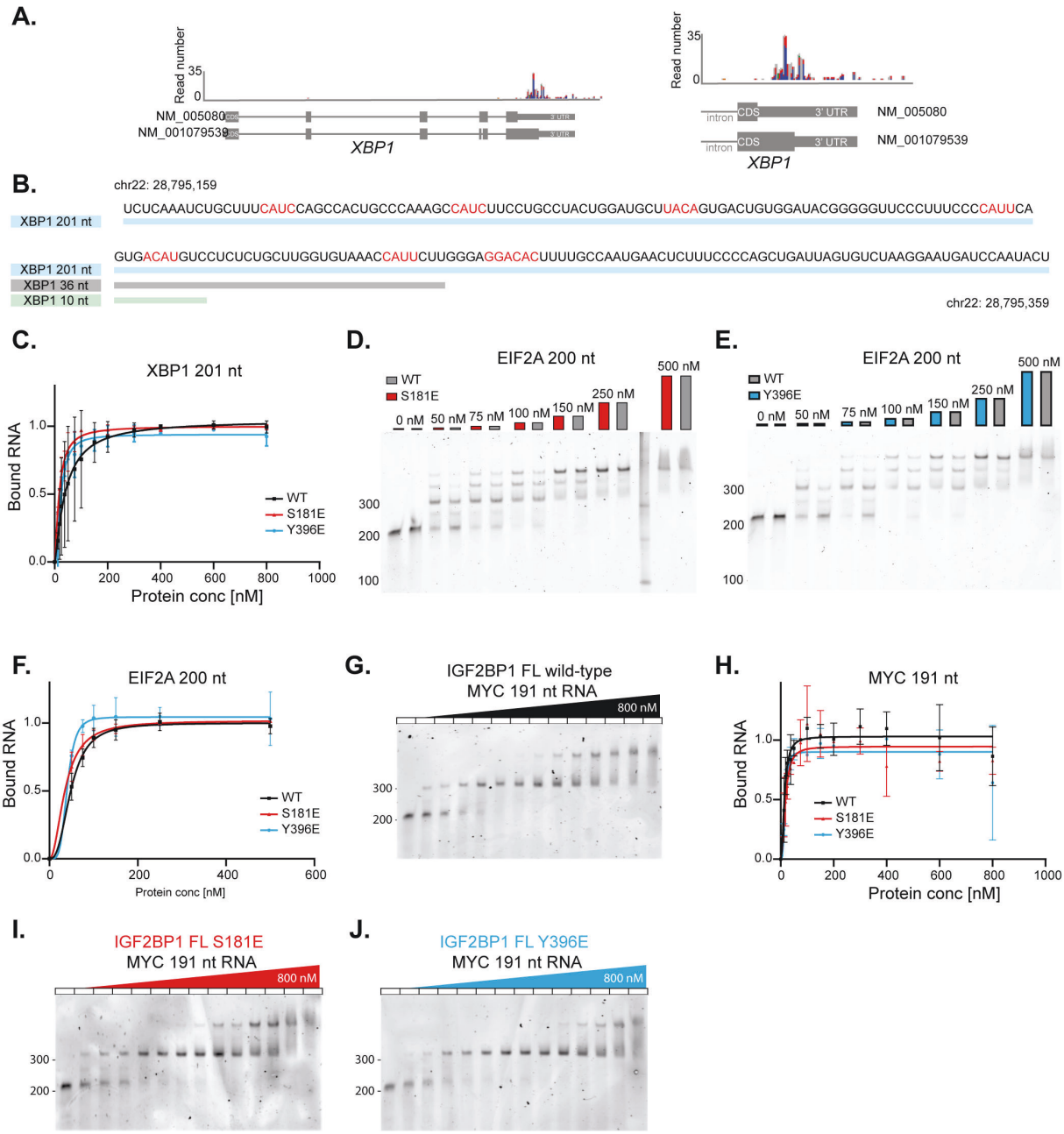

Supplementary Figure 2. Phosphomimetic mutations do not affect IGF2BP1 binding to model RNAs
(A) IGF2BP1 binding sites in XBP1 identified by analyzing PAR-CLIP data published by Hafner et al. 2010. (B) Sequence of the XBP1-derived RNAs: XBP1 201 nt (blue), XBP1 36 nt (grey) and XBP1 10 nt RNA (green) with genome annotation. Predicted RNA binding motifs are highlighted in red. (C) Quantification of EMSA assays with IGF2BP1 full-length wild-type (black), S181E (red) and Y396E (blue) and XBP1 201 nt RNA from Fig. 2 (A-C) in duplicates. RNA binding is represented by the depletion of free RNA. Mean intensity from 0 nM protein sample was used to define 0 while the mean intensity of gel background represents 1. Dose response equation was used for curve fitting and calculation of K_D. Error bars represent the standard deviation. (D) (E) EMSA assays assessing IGF2BP1 full-length wild-type (black), S181E (red) and Y396E (blue) interaction with EIF2A 200 nt RNA. (F) Quantification of EMSA assays of IGF2BP1 full-length wild-type (black), S181E (red) and Y396E (blue) with EIF2A 200 nt RNA from Fig. Supp. 2 (D, E) in duplicates. Dose response equation was used for curve fitting and calculation of $K_{1/2}$. Error bars represent the standard deviation. (G) EMSA assays assessing IGF2BP1 full-length wild-type (black) interaction with MYC 191. (H) Quantification of EMSA assays of IGF2BP1 full-length wild-type (black), S181E (red) and Y396E (blue) with MYC 191 nt RNA from Fig. Supp. 2 (G, I, J) in

duplicates as described in Supp. Fig. 2C. EMSA assays assessing (I) S181E (red) and (J) Y396E (blue) interaction with MYC 191 nt RNA.

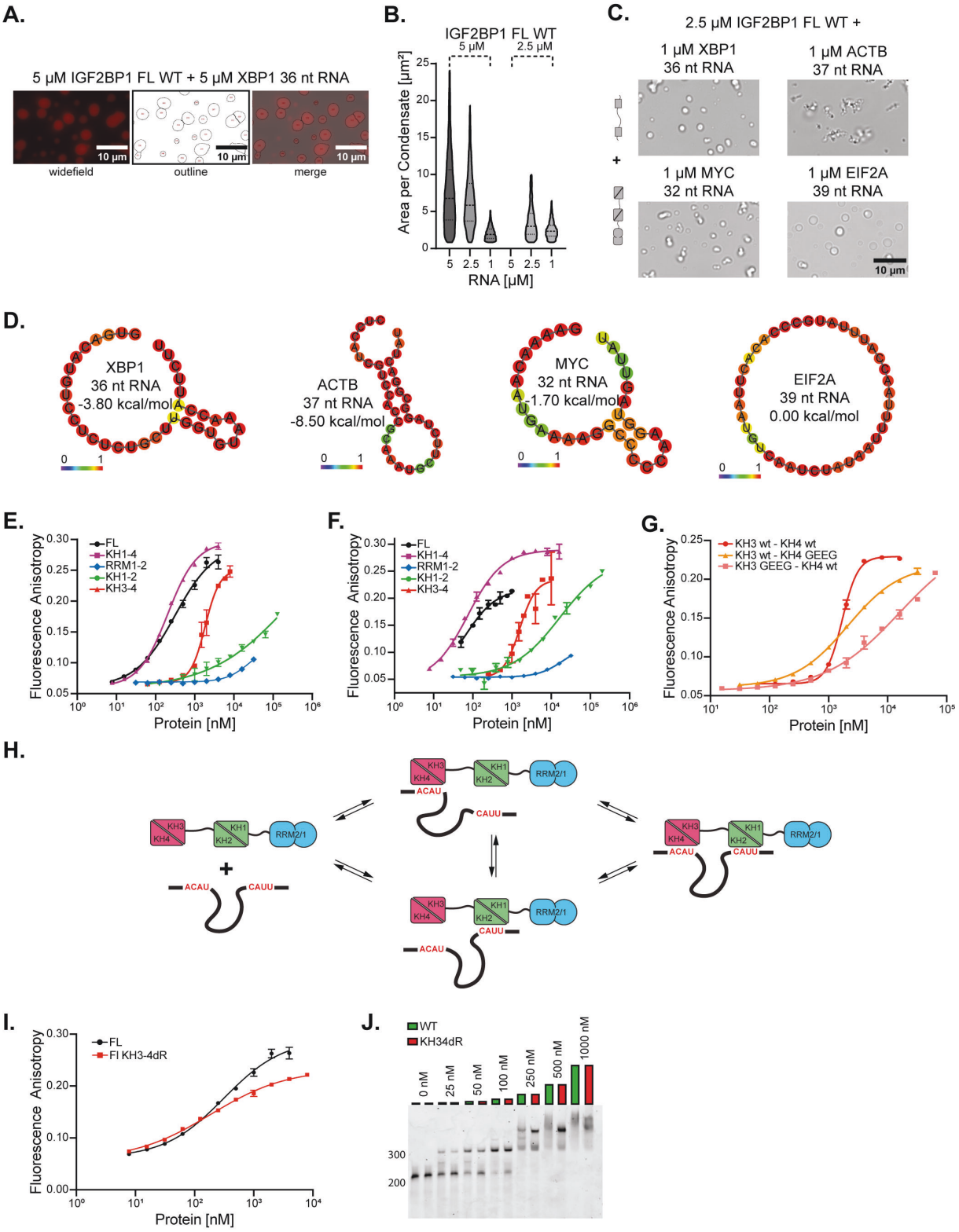

Supplementary Figure 3. KH3-4 domains drive RNA binding and RNP granule formation

(A) Representative images, outlines and overlay of the quantification of granules containing 5 µM IGF2BP1 with 5 % mCherry-IGF2BP1 and 5 µM XBP1 36 nt RNA after 90 min of incubation. (B) Violin plots of the area per condensate of IGF2BP1 full-length wild-type with XBP1 36 nt RNA at different protein and RNA concentrations. Dashed line represents median, the dotted lines 25 % and 75 % quartiles. (C) RNP granule formation assays of IGF2BP1 full-length wild-type with XBP1 36 nt, ACTB 37 nt, MYC 32 nt and EIF2A 39 nt RNA. Scale bar is 10 µm. Protein and RNA valency (left) is depicted as folded domains and the number of binding motifs. Secondary structure and minimum free energy thereof

predicted via the Vienna RNAfold Webserver [1] of the (D) XBP1 36 nt RNA, MYC 32 nt RNA, ACTB 37 nt RNA and EIF2A 39 nt RNA. (E) Fluorescence anisotropy assays (FA) to measure binding of full-length IGF2BP1 (black), IGF2BP1 KH1-4 (purple), IGF2BP1 RRM1-2 (blue), IGF2BP1 KH1-2 (green) and IGF2BP1 KH3-4 (red) to XBP1 36 nt RNA. X-axis in log-scale. (F) FA to measure binding of IGF2BP1 full-length and truncation mutants to ACTB RNA, the color-code is same as Supp. Figure 3D. (G) FA of IGF2BP1 KH3-KH4 (red), IGF2BP1 KH3-KH4GEEG (orange) and KH3GEEG-KH4 (pink) with XBP1 36 nt. X-axis in log-scale. (H) The model shows the avidity effect of IGF2BP1 interacting with XBP1-derived RNA. (I) FA of full-length IGF2BP1 (black) and full-length IGF2BP1 KH3GEEG-KH4GEEG (KH3-4dR, red) with XBP1 36 nt RNA. X-axis represented in log-scale. (J) EMSA assay of full-length IGF2BP1 (black) and full-length IGF2BP1 KH3GEEG-KH4GEEG (KH3-4dR, red) with XBP1 201 nt RNA. (I) RNP granule formation assays of 5 μM IGF2BP1 KH3-4 mutant KH3-GEEG and IGF2BP1 KH3-4 mutant KH4-GEEG with 5 μM XBP1 36 nt RNA.

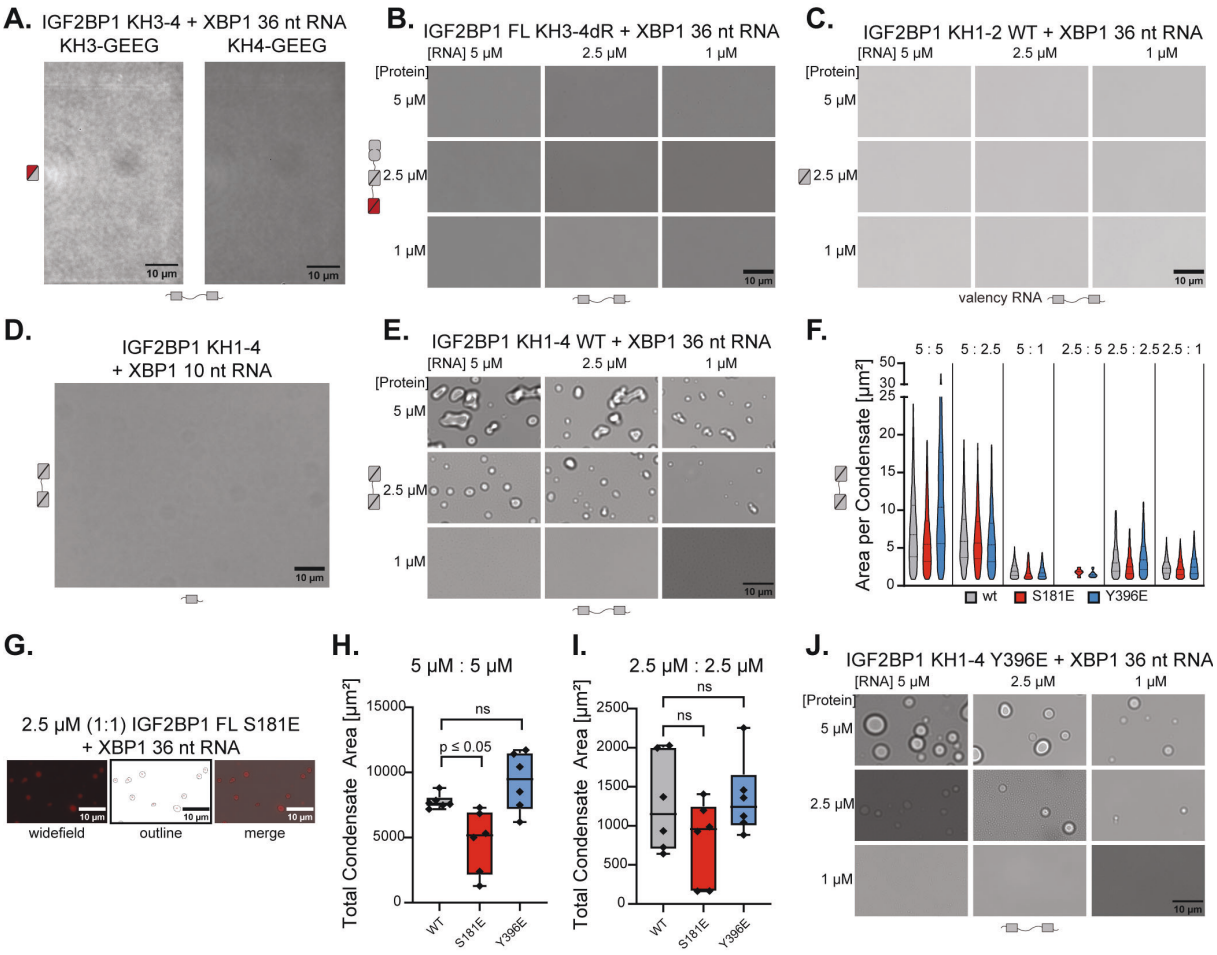

Supp. Figure 4. Mutantions affect granule formation of IGF2BP1

(A) RNP granule formation assays of 5 µM IGF2BP1 KH3-4 mutant KH3-GEEG and IGF2BP1 KH3-4 mutant KH4-GEEG with 5 µM XBP1 36 nt RNA. Protein (left) and RNA valency (bottom) is depicted as folded domains and the number of binding motifs. GEEG mutations indicated in red. (B) RNP granule formation assays of: IGF2BP1 full-length KH3-4dR (double mutant) with XBP1 36 nt RNA (C) 6XHis-IGF2BP1 KH1-2 and XBP1 36 nt RNA (D) 25 µM IGF2BP1 KH1-4 with 25 µM XBP1 10 nt RNA (30 min incubation) (E) IGF2BP1 KH1-4 wild-type and XBP1 36 nt RNA (250 mM NaCl). (F) Violin plots of the area per condensate for IGF2BP1 full-length wild-type, S181E and Y396E with XBP1 36 nt RNA at different protein and RNA concentrations. The dashed line represents the median value, the dotted lines the upper and lower quartiles. (G) Representative fluorescence microscopy images of condensates formed by full-length IGF2BP1 S181E, 5 % mCherry-IGF2BP1 S181E and XBP1 36 nt RNA (2.5 µM, 1:1). Box plots of total condensate area per field of view in (H) 5 µM protein + 5 µM RNA and (I) 2.5 µM protein + 2.5 µM RNA (see Supplementary Table 3). Two-tailed Welch's t-test was used for statistical analyses. (J) RNP granule formation assays of IGF2BP1 KH1-4 Y396E and XBP1 36 nt RNA (250 mM NaCl).

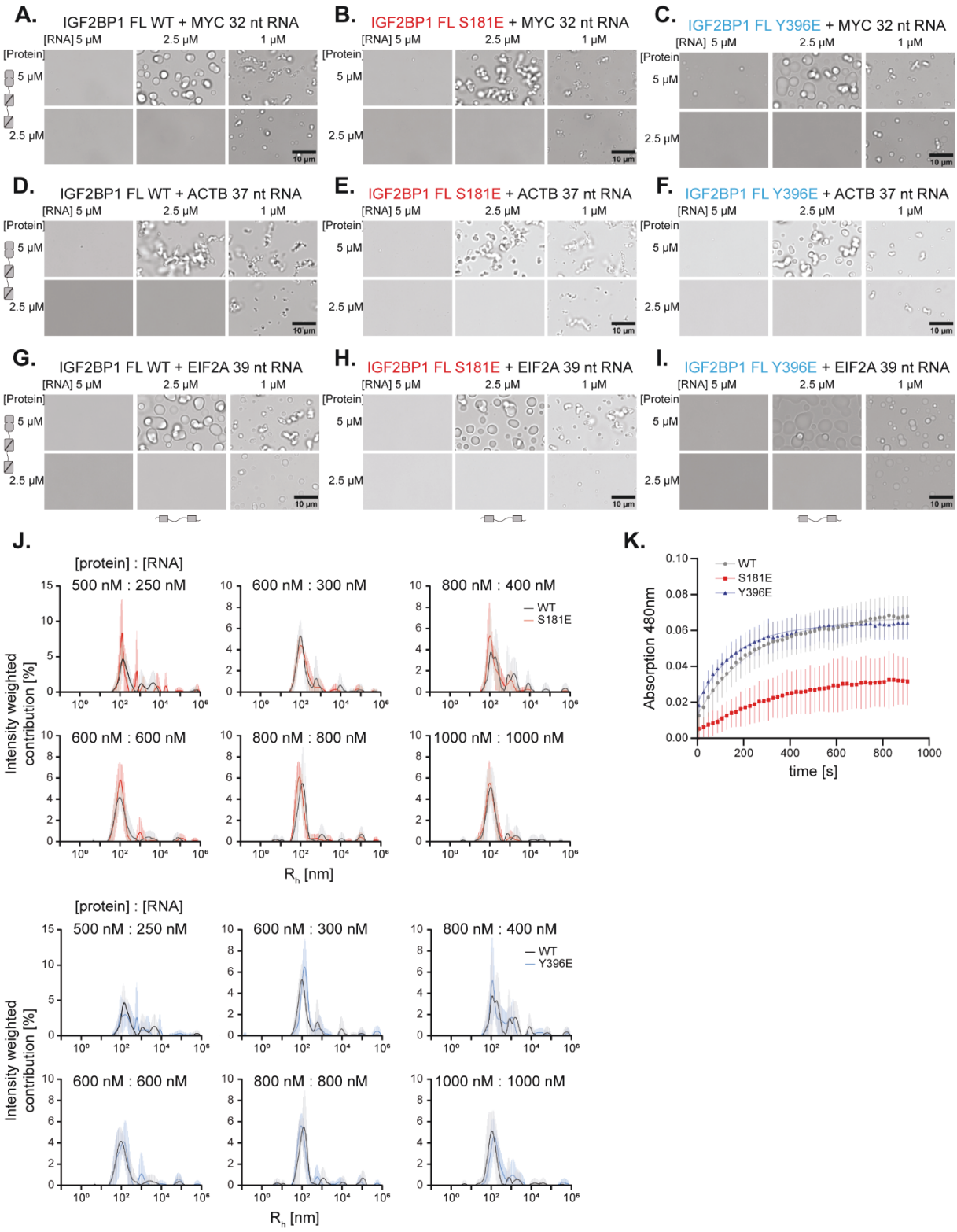

Supplementary Figure 5. IGF2BP1 phosphomimetic mutants display similar effects on RNP condensate formation in the presence of different model RNAs

(A) Brightfield images of IGF2BP1 wild-type, (B) S181E and (C) Y396E with MYC 32 nt RNA. Scale bar is 10 µm. (D) Brightfield images of IGF2BP1 wild-type, (E) S181E and (F) Y396E with ACTB 37 nt RNA. Scale bar is 10 µm. (G) Brightfield images of IGF2BP1 wild-type, (H) S181E and (I) Y396E with EIF2A 39 nt RNA. Scale bar is 10 µm. The valency (left, per row) is depicted as folded domains. (J) Distributions of hydrodynamic radii as their intensity weighted contribution in [%] of IGF2BP1 wild-type (black), S181E (red) and Y396E (blue) with XBP1 36 nt RNA at depicted protein and RNA concentrations. Data recorded in three independent experiments as technical triplicates. n is between 5 and 9, see Methods for details.

(K) Turbidity assay monitoring condensate formation kinetics at 5 μM IGF2BP1 full-length wild-type (grey), S181E (red) and Y396E (blue) and 5 μM XBP1 36 nt RNA. Error bars represent the standard deviation (WT n = 10, S181E n=11, Y396E n=10) . The data is fitted to a one-phase association equation.

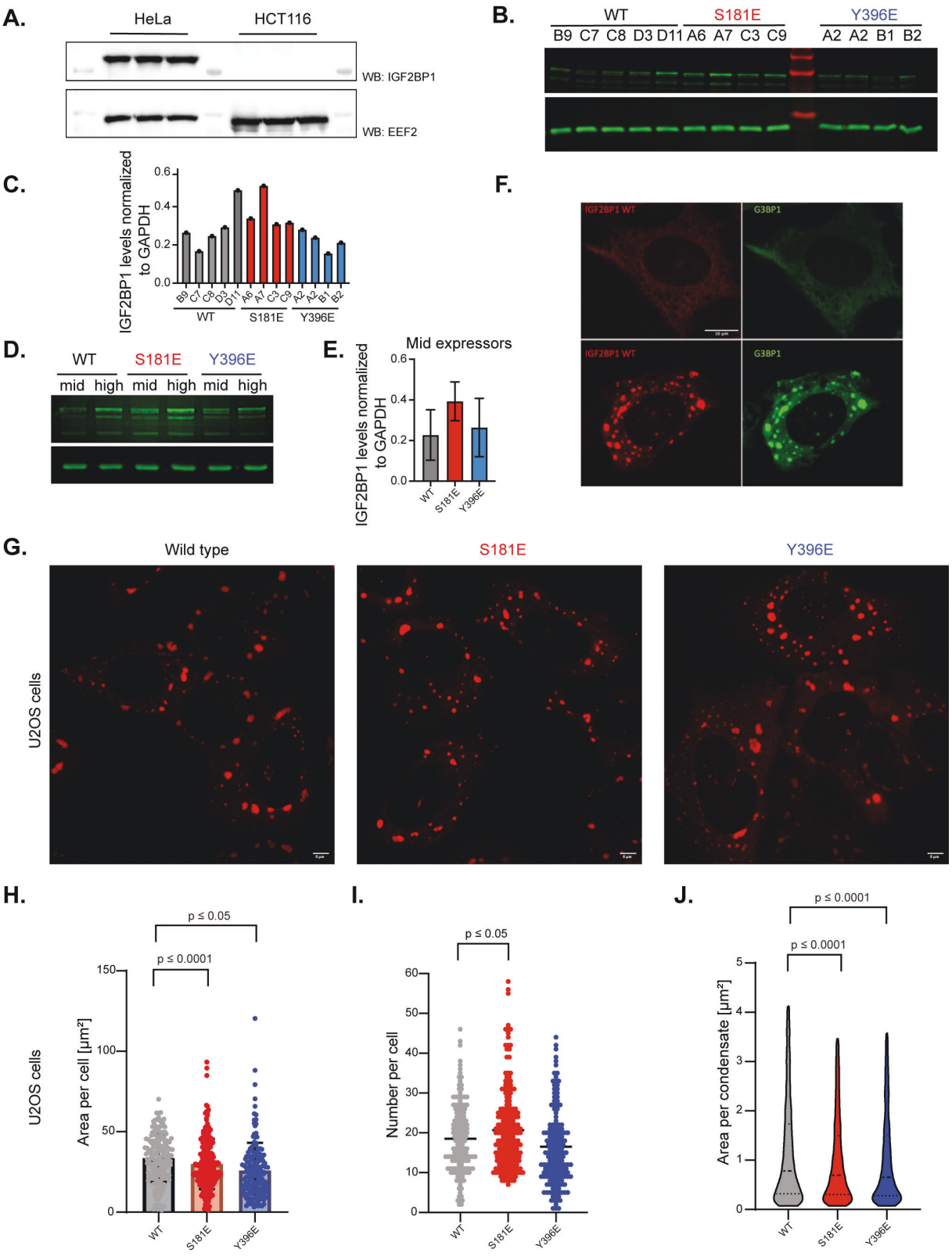

Supplementary Figure 6. IGF2BP1 phosphomimetic mutants affect granule sizes and numbers in cells (A) Western Blot analyses of IGF2BP1 expression in HeLa and HCT116 cells (Anti-IGF2BP1 antibody, MBL, RN001M; Anti-EEF2 antibody, Proteintech, 20107-1-AP). (B) Western Blot analyses of expression level of mCherry-IGF2BP1 wild-type, S181E and Y396E mutants expressed in single clone isolated from HCT116 cells by FACS. The IDs of clones are indicated on the WB. IGF2BP1 is stained by a fluorescently labeled anti-mCherry antibody. (C) Quantification of Western Blots from HCT116 cells. The IGF2BP1 band intensities were normalized to bands for the GAPDH control by the LI-COR system for

quantification. (D) Western Blot analyses of expression level of mCherry-IGF2BP1 wild-type, S181E and Y396E mutants expressed in U2OS cells. Mid and high indicate the expression levels identified by FACS. IGF2BP1 is stained by a fluorescently labeled anti-mCherry antibody. (E) Quantification of Western Blots from U2OS cells. The IGF2BP1 bands were normalized to GAPDH control. The LI-COR system was used for quantification. (F) Fluorescence microscopy images of fixed U2OS cells expressing mCherry-IGF2BP1 full-length wild-type and GFP-G3BP1 before (top row) and after (bottom row) treatment with 500 µM arsenite for 30 min. (G) Representative images of fluorescence microscopy from fixed U2OS cells expressing m-Cherry-IGF2BP1 full-length wild-type, m-Cherry-IGF2BP1 full-length S181E or m-Cherry-IGF2BP1 full-length Y396E stressed with 500 µM arsenite for 60 min. Scale bar is 5 µm. Quantification of condensates in U2OS cells represented as scatter plots: (H) total area of condensates per single cell (n = 162 for wild-type, n=230 for S181E, n=162 for Y396E; bar represents the mean value; two-tailed t-test was used to compare wild-type with S181E and Y396E) (I) number of condensates per single cell (bar represents the mean value; two-tailed t-test was used to compare wild-type with S181E and Y396E) and (J) area per condensate (the dashed line represents the median value, the dotted lines represent the 25 % and 75 % quartiles; two-tailed Mann-Whitney test was used to compare wild-type with S181E and Y396E).

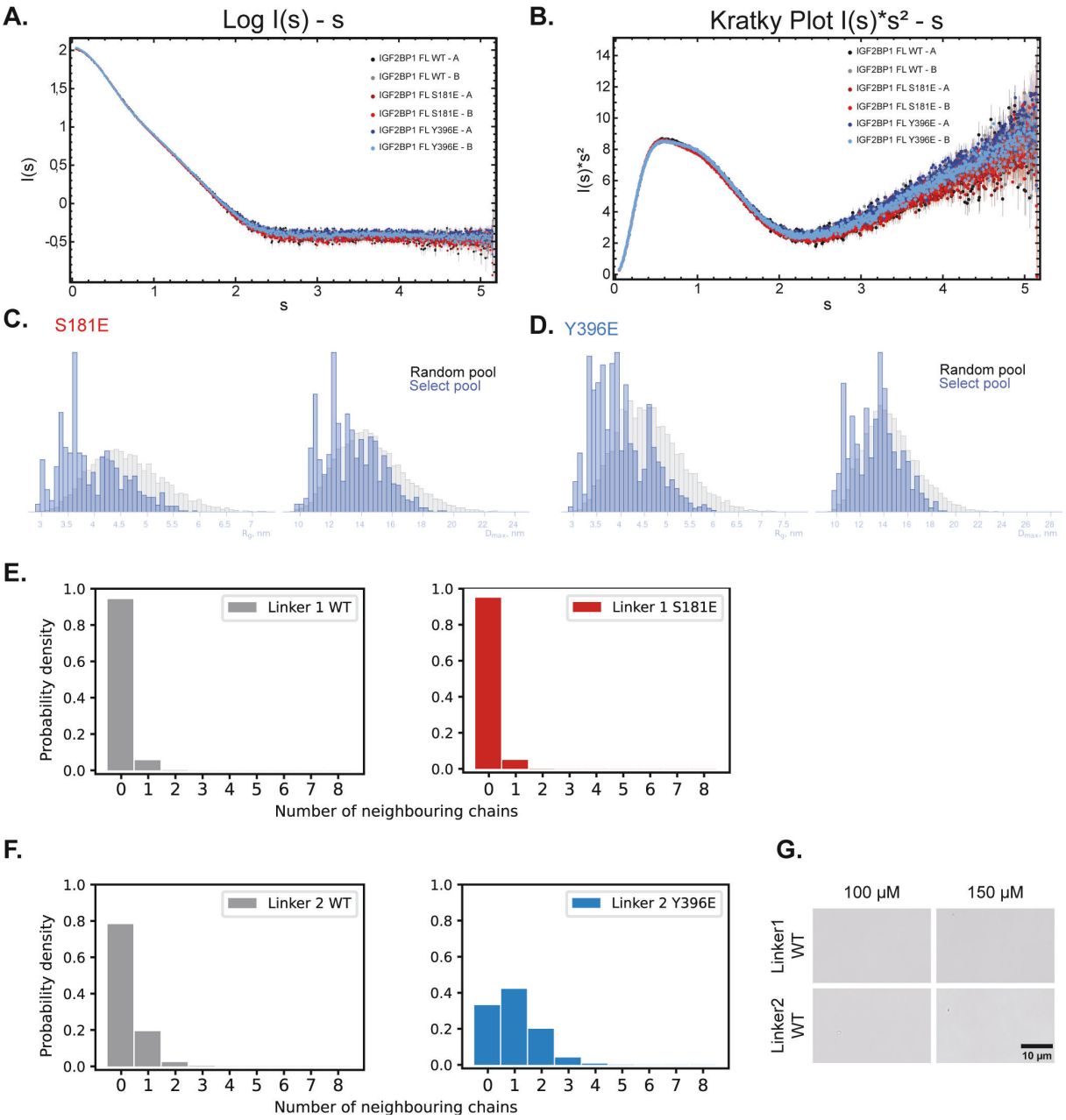

Supplementary Figure 7. IGF2BP1 forms a compact conformation in solution
(A) Intensity plot I(s) - s of SEC-SAXS data from IGF2BP1 full-length wild-type (black), IGF2BP1 full-length S181E (red), IGF2BP1 full-length Y396E (blue) in duplicates (A, B). Y-axis is represented in $\log_{10}$ scale. (B) Kratky plot $I(s)*s^2$ – s of SEC-SAXS data from IGF2BP1 full-length wild-type (black), IGF2BP1 full-length S181E (red), IGF2BP1 full-length Y396E (blue) in duplicates (A, B). (C) Comparison of R_g and D_{max} distribution of random conformations of IGF2BP1 S181E and selected pool that best fit the experimental SAXS data based on EOM analyses. (D) Comparison of R_g and D_{max} distribution of random conformations of IGF2BP1 Y396E and selected pool that best fit to the experimental SAXS data based on EOM analyses. (E) Probability distribution of pairwise contacts in MD simulations of Linker1 WT, Linker 1 S181E as well as (F) Linker2 WT and Linker2 Y396E. (G) Brightfield images of linker 1 (100 µM) and linker 2 (150 µM) and 15 % PEG8000 after 60 min incubation. Scale bar = 10 µm.

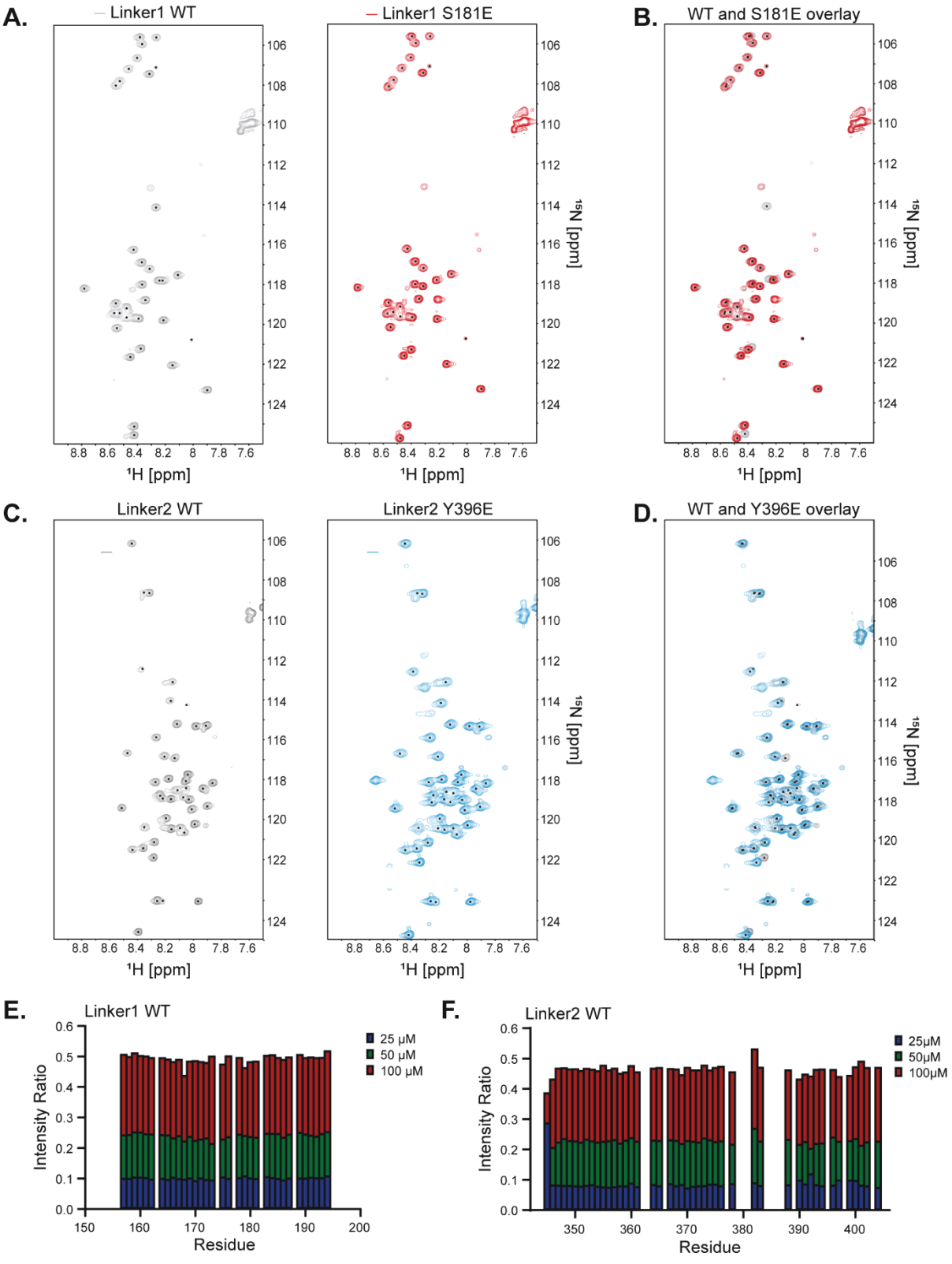

Supp. Figure 8. IGF2BP1 linkers do not strongly self-associate in solution
(A) HSQC spectra of ^{15}N-labeled linker 1 wild-type (grey) and ^{15}N-labeled linker 1 S181E (red) at 200 µM. Black dots represent assigned peaks. (B) Overlay of the HSQC spectra of linker 1 wild-type and linker 1 S181E (red). (C) HSQC spectra of ^{15}N-labeled linker 2 wild-type (grey) and ^{15}N-labeled Linker 2 Y396E (blue) at 200 µM. (D) Overlay of the HSQC spectra of linker 2 wild-type and linker 2 Y396E (blue). Black dots represent assigned peaks. (E) Plot of the intensity ratios of 100 µM, 50 µM and 25 µM to 200

μM ^{15}N-labeled linker 1 wild-type in HSQC. (F). Plot of the intensity ratios of 100 μM, 50 μM and 25 μM to 200 μM ^{15}N-labeled linker 2 wild-type in HSQC.

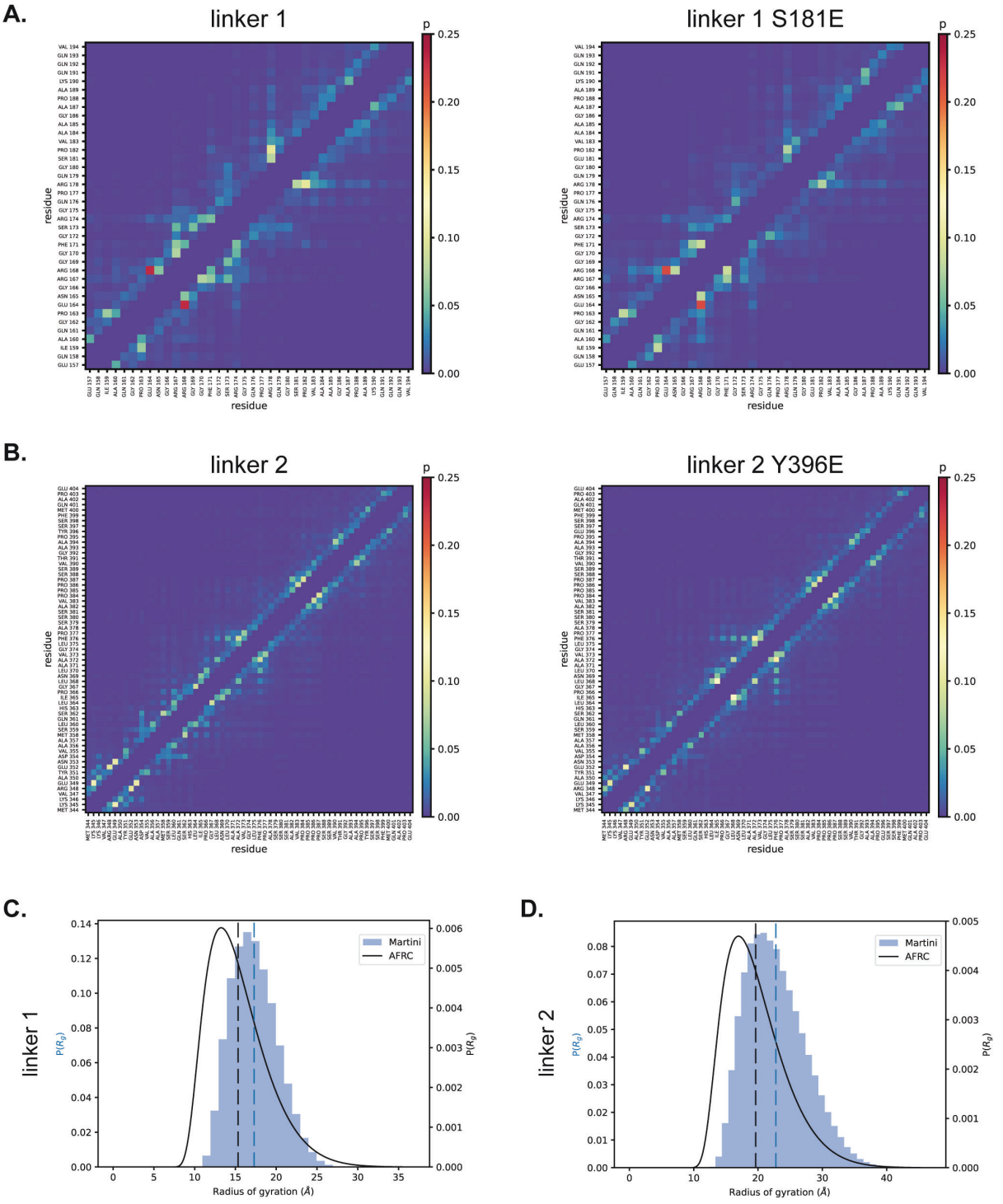

Supp. Figure 9. IGF2BP1 linkers do not display strong intermolecular interactions
(A) Contact map for cis-interactions of linker 1 and its phosphomimetic mutant S181E during MD simulations. (B) Contact map for cis-interactions of linker 2 and its phosphomimetic mutant Y396E during MD simulations. Value p measures the frequency of contact formation over the whole MD simulation. (C) Rg probability distribution of linker 1 and (D) linker 2 (filled blue steps) overlayed to the probability distribution computed for an ideal polypeptide with the same amino acidic sequence (black line). Dashed lines indicate the mean of the distribution.

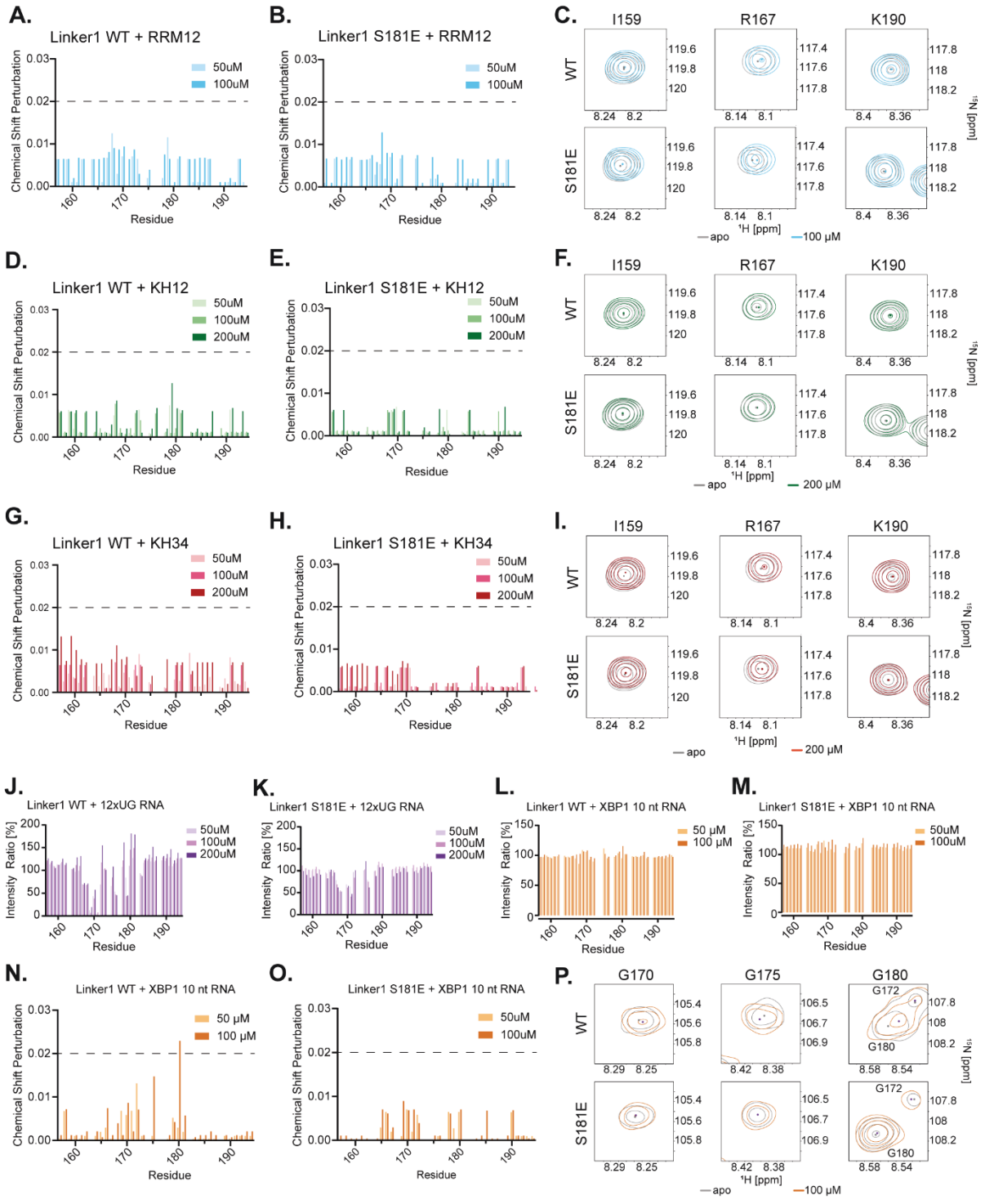

Supplementary Figure 10. Phosphomimetic mutation S181E in the linker1 affects low-affinity RNA interactions

(A) CSP analyses of ^{15}N-labeled linker 1 wild-type in the absence and presence of different concentrations of RRM1-2. (B) CSP analyses of ^{15}N-labeled linker 1 S181E with different concentrations of RRM1-2 (C) Representative HSQC signals in the ^{15}N-labeled linker 1 wild-type and S181E in the absence and presence of 100 µM RRM1-2 (D) CSP analyses of ^{15}N-labeled linker 1 wild-type with different concentrations of KH1-2. (E) CSP analyses of ^{15}N-labeled linker 1 S181E with different concentrations of KH1-2. (F) Representative peaks of ^{15}N-labeled linker 1 wild-type and S181E in the absence and presence of 200 µM KH1-2. (G) CSP analyses of ^{15}N-labeled linker 1 wild-type with different concentrations of KH3-4. (H) CSP analyses of ^{15}N-labeled linker 1 S181E with different concentrations of KH3-4. (I) Representative HSQC signals from ^{15}N-labeled linker 1 wild-type and

S181E in the absence and presence 200 μM KH3-4. (J) Intensity plots of signals in ^{15}N-labeled linker 1 wild-type in the presence of different concentrations of 12xUG RNA in HSQC normalized to signals in the apo spectrum. (K) Intensity plots of ^{15}N-labeled linker 1 S181E with different concentrations of 12xUG RNA in HSQC normalized to signals in the apo spectrum. (L) Intensity plots of ^{15}N-labeled linker 1 wild-type with different XBP1 10 nt RNA concentrations in HSQC normalized to signals in the apo spectrum. (M) Intensity plots of ^{15}N-labeled Linker 1 S181E with different concentrations of XBP1 10 nt RNA in HSQC normalized to apo spectrum. (N) CSP analyses of ^{15}N-labeled Linker 1 wild-type with different concentrations of XBP1 10 nt RNA. (O) CSPs of ^{15}N-labeled linker 1 S181E with different concentrations of XBP1 10 nt RNA. (P) Representative peaks of ^{15}N-labeled linker 1 wild-type and S181E in the absence and presence of 100 μM of XBP1 10 nt RNA.

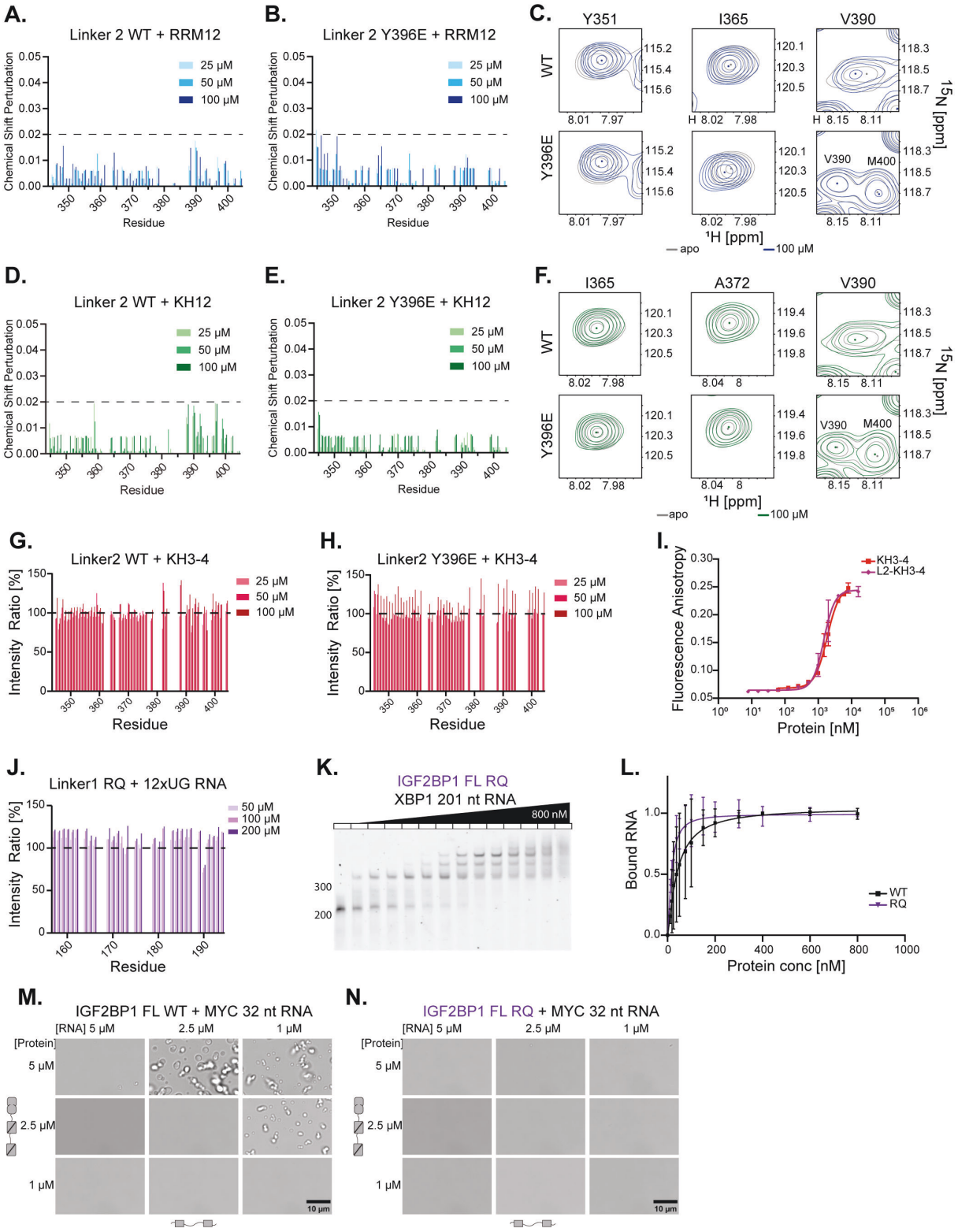

Supp. Figure 11. RGG motif in Linker 1 mediates low-affinity RNA interactions and regulates condensate formation

(A) CSP analyses of ^{15}N-labeled linker 2 wild-type in the absence and presence of various concentrations of RRM1-2 determined. (B) CSP analyses of ^{15}N-labeled linker 2 Y396E with different concentrations of RRM1-2. (C) Representative HSQC signals in ^{15}N-labeled linker 2 wild-type and Y396E in the absence and presence of 100 µM RRM1-2. (D) CSP analyses of ^{15}N-labeled linker 2 wild-type with different concentrations of KH1-2 (E) CSP analyses of ^{15}N-labeled linker 2 Y396E with different concentrations of KH1-2 (F) Representative HSQC signals in ^{15}N-labeled linker 2 wild-type and Y396E in the absence and presence of 100 µM KH1-2 (G) Intensity plots of ^{15}N-labeled wild-type linker 2 in the presence of different concentrations of KH3-4 normalized to linker 2 signals in the apo spectrum. (H)

Intensity plots of ^{15}N-labeled linker 2 Y396E in the presence of different concentrations of KH3-4 normalized to linker 2 Y396E signals in the apo spectrum. (I) Fluorescence anisotropy assays to assess binding of IGF2BP1 KH3-4 wild-type (red) and IGF2BP1 linker 2 KH3-4 wild-type (purple) to 5'-fluorescein labeled XBP1 36 nt. X-axis represented in log-scale. (J) Intensity plots of ^{15}N-labeled linker 1 RQ in the presence of different concentrations of 12x UG RNA in HSQC normalized to linker 1 RQ signals in the apo spectrum. (K) Electrophoretic Mobility Shift Assay (EMSA) to assess the binding of IGF2BP1 RQ with XBP1 201 nt RNA at concentrations ranging from 0 to 800 nM. (L) Quantification of EMSA assays of IGF2BP1 full-length wild-type (black) (from Fig. 2A) and IGF2BP1 RQ (purple) with XBP1 201 nt RNA (from Supplementary Figure 9K) in duplicates. Dose response equation was used for curve fitting and calculation of $K_{1/2}$. Error bars represent the standard deviation. (M) Bright field images of condensates formed by IGF2BP1 wild-type and (N) IGF2BP1 RQ with MYC 32 nt RNA. Scale bar is 10 µm. The valency of the protein (left) is depicted by the number of folded domains. The valency of the RNA (bottom) is depicted as the number and position of binding motifs.

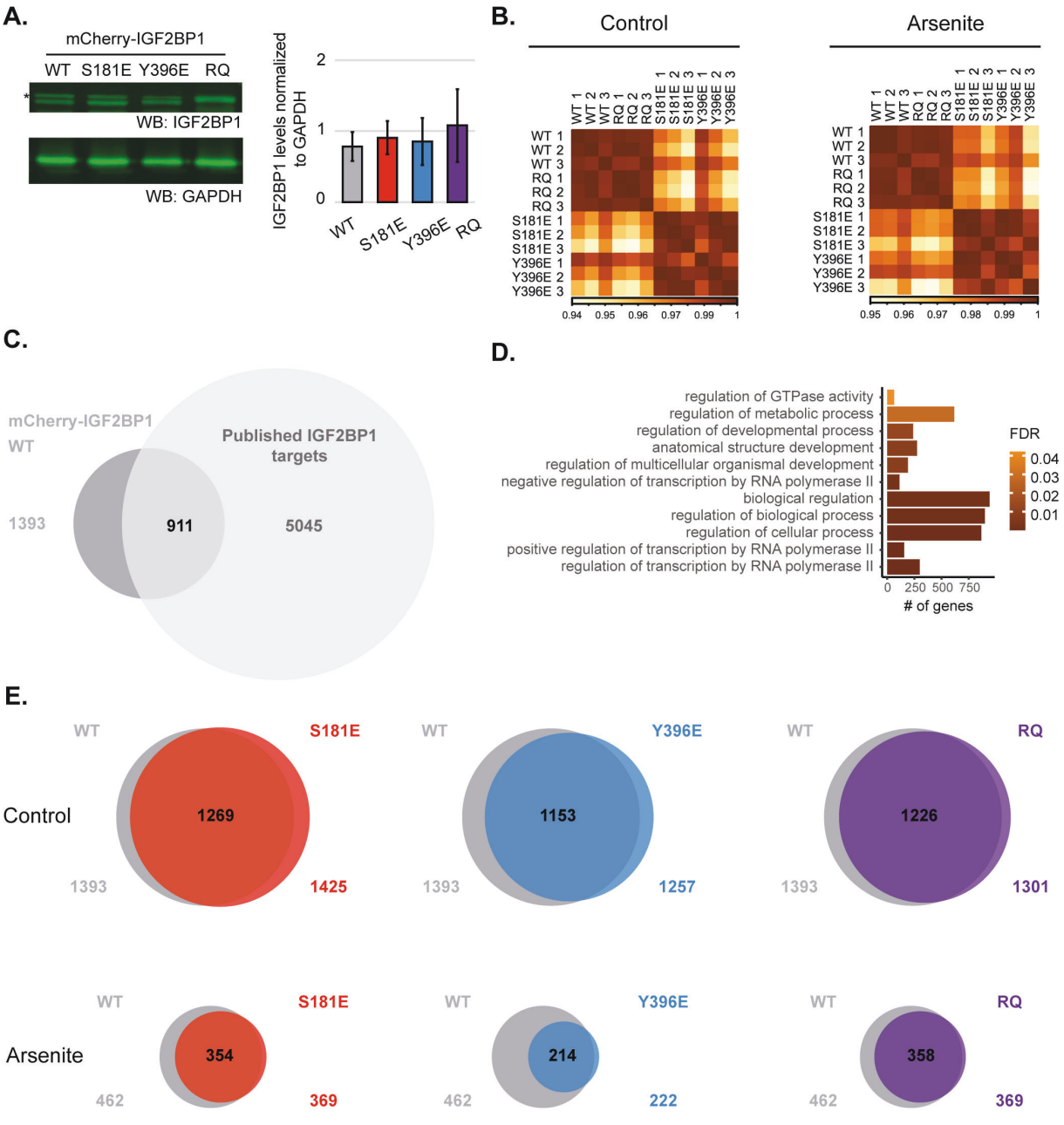

Supplementary Figure 12. Total transcriptome (RNA-Seq) and RNA immunoprecipitation sequencing (RIP-seq) of IGF2BP1 S181E, Y396E, and RQ mutants.

(A) Western Blot analyses of expression level of mCherry-IGF2BP1 wild-type and S181E, Y396E, and RQ mutants in a FACS-sorted narrow gate population of HCT116 cells used for transcriptomics and RIP-Seq experiments. n=3 technical replicates, data are presented as mean values +/- SD. (B) Pearson correlation matrices of total transcriptome of HCT116 cells expressing mCherry-IGF2BP1 wild-type or S181E, Y396E, and RQ mutants. Arsenite stress was induced with 2-hour treatment with 500 µM of sodium arsenite. (C) Venn diagram showing the intersection between the mRNA transcript targets identified in this study in control conditions for mCherry-IGF2BP1 (2-fold enrichment of RIP-Seq CPM compared to RNA-Seq CPM and 4-fold enrichment of RIP-Seq CPM compared to the background RIP-Seq (parental HCT116 cells) and the reported IGF2BP1 targets (PAR-CLIP PARalyzer-identified targets from HEK293 cells [2] with more than 5 binding sites [3]) (D) GO-term biological process enrichment analysis of mCherry-IGF2BP1 mRNA transcript targets identified in this study in control conditions. For visualization purposes the list of GO term was simplified using REVIGO [4] .(E) Venn diagrams showing

the intersection between the mRNA transcript targets identified for mCherry-IGF2BP1 wild-type and S181E, Y396E, and RQ mutants. Source data are available in Supplementary File 2.

	Sequence
XBP1 201 nt	UCUCAAAUCUGCUUU**CAUC**CAGCCACUGCCCAAAGC**CAUC**U UCCUGCCUACUGGAUGCU**UACA**GUGACUGUGGAUACGGGG GUUCCCUUUCCC**CAUU**CAGUG**ACAU**GUCCUCUCUGCUUGG UGUAAAC**CAUU**CUUGGGA**GGAC**ACUUUUGCCAAUGAACUCU UUCCCCAGCUGAUUAGUGUCUAAGGAAUGAUCCAAUACU
EIF2A 200 nt	AGAAAAUUCAGAAAGA**AACA**GCCCUUCUCCAGGAGCUGGAA GAUUUGGAAUUGGGUAUUUAAAGAUUCACGGAAAGCAAGUU GAUGACCAGAAAUCAGUGCAAA**CACAU**CUUCUGUUAAACC**C** **AUU**GGUA**UACACA**GAAUAUUCCUGUGCC**CACA**CUUAAUGUC AAUCUAUAAUUUUAAC**CAUU**UAUCCAAGAUUCUACU
MYC 191 nt [8]	UGCGUGACCAGAUCCCGGAGUUGGAA**AACA**AUGAAAAGGCC CCCAAGG**UAGU**UAUCCUUAAAAAAGC**CACA**G**CAUACAUC**CU GUCCGUCCAAGCAGAGGAGCAAAAGCU**CAUU**UCUGAAGA**GG** **AC**UUGUUGCGGAAACGACGAG**AACAGU**UGA**AACACA**AACUU G**AACA**GCUACGGAACUCUUGUGCGUAA
XBP1 36 nt	GUG**ACAU**GUCCUCUCUGCUUGGUGUAAAC**CAUU**CUU
XBP1 10 nt	GUG**ACAU**GUC
MYC 32 nt [9]	GAA**AACA**AUGAAAAGGCCCCCAAGG**UAGU**UAU
ACTB 28 nt [10]	ACC**GGAC**UGUUACCAACACC**CACA**CCCC
ACTB 37 nt [11]	CUC**CAUC**GUCCACCGCAAAUGCUUCUAGGC**GGAC**UAU
EIF2A 39 nt	GCC**CACA**CUUAAUGUCAAUCUAUAAUUUUAAC**CAUU**UAU
12xUG	UGUGUGUGUGUGUGUGUGUGUG

Supplementary Table 1: Sequences of model RNAs
RNAs were used in the following experiments: Fig. 2A-M, Fig. 5H-M, Fig. Supp. 2C-J, Fig. Supp. 3A-G, I, J, Fig. Supp. 4A-J, Fig. Supp. 5A-K, Fig. Supp. 10J-P, Fig. Supp. 11I-N. Putative binding sites in **bold** [5-8].

EMSA					
XBP1 201 nt RNA	$K_{1/2}$ [nM]		95% CI		R^2
wild-type	41.01		20.87 to 174.8		0.7774
S181E	17.06		14.33 to 20.16		0.9727
Y396E	22.91		19.05 to 27.81		0.9519
RQ	17.00		12.08 to 22.95		0.9114
KH34dR	64.74		43,42 to 131,4		0,9739
EIF2A 200 nt RNA	$K_{1/2}$ [nM]		95% CI		R^2
wild-type	48.19		42.00 to 53.61		0.9686
S181E	35.42		23.25 to 43.23		0.9869
Y396E	40.17		14.90 to ???		0.9585
MYC 191 nt RNA	$K_{1/2}$ [nM]		95% CI		R^2
wild-type	14.36		8.902 to 20.02		0.831
S181E	17.78		10.76 to 27.61		0.7757
Y396E	16.70		12.31 to 21.90		0.8105
Fluorescence Anisotropy					
XBP1 36 nt RNA	$K_{1/2}$[nM]	95% CI	Hill-Coeff.	95% CI	R^2
wild-type	311.7	258.2 to 390.5	0.8640	0.7525 to 0.9900	0.9932
S181E	310.1	256.3 to 377.5	1.049	0.8728 to 1.258	0.9855
Y396E	423.3	344.8 to 530.7	0.9587	0.7963 to 1.150	0.9862
RQ	113.8	97.76 to 132.7	0.8618	0.7680 to 0.9690	0.9928
KH1-4 wild-type	204.0	188.4 to 221.6	1.174	1.073 to 1.285	0.9984
RRM1-2 wild type	25928	13310 to ???	1.410	0.8336 to 2.258	0.9340
KH1-2 wild-type*	-	-			-
KH3-4 wild-type	1850	1661 to 2151	2.338	1.741 to 3.112	0.9832
L2-KH3-4 wild-type	1470	1318 to 1640	2.620	2.042 to 3.392	0.9809
Full-length KH3 GEEG KH4 GEEG	185.8	157.4 to 223.2	0.6683	0.6089 to 0.7328	0.9957
KH3 wild-type KH4 GEEG	2.122	1.980 to 2.286	0.9702	0.9142 to 1.029	0.9988
KH3 GEEG KH4 wild-type	15.69	9.738 to 33.85	0.6979	0.5827 to 0.8249	0.9906
ACTB 28 nt RNA	$K_{1/2}$[nM]	95% CI	Hill-Coeff.	95% CI	R^2
Full-length wild-type	68.55	56.88 to 87.17	1.116	0.7966 to 1.471	0.9818
KH1-4 wild-type	75.18	65.69 to 86.12	0.9804	0.8803 to 1.096	0.9953
RRM1-2 wild type	19839	11390 to 287085	1.368	0.8564 to 2.067	0.9449
KH1-2 wild-type	16670	10009 to 44411	0.7285	0.5232 to 0.9849	0.9793
KH3-4 wild-type	1574	1175 to 2575	2.109	1.024 to 4.634	0.9285

Supplementary Table 2: Fit-values of binding experiments

$K_{1/2}$ values of different full-length IGF2BP1 constructs binding to different RNAs from EMSA and Fluorescence Anisotropy assays in Fig. 2A-D, Fig. Supp. 2C-J, Fig. Supp. 3E-G, I J, Fig. Supp. 11I, K, L; *not enough data points for a reasonable fit

	Median area per condensate [µm²]	25% Percentile	75% Percentile	Mean total area of condensates [µm²]
IGF2BP1 wild-type	7.022	3.955	11.28	7753
IGF2BP1 S181E	5.716	3.306	9.342	4691
IGF2BP1 Y396E	10.790	5.758	18.52	9298

Supplementary Table 3: Quantification of *in vitro* RNP granule formation
Area per condensate of IGF2BP1 full-length constructs with XBP1 36 nt RNA (5 µM protein plus 5 µM RNA) in Fig. 2J and total condensate area in the same conditions (Fig. Supp. 4H).

	$t_{1/2}$ [s]	95% CI	OD_{480}	95% CI	R^2
IGF2BP1 wild-type	167	138.4 to 205.7	0.06775	0.06531 to 0.07082	0.6448
IGF2BP1 S181E	251.6	171.8 to 431.4	0.03505	0.03130 to 0.04282	0.3264
IGF2BP1 Y396E	115.3	97.98 to 136.8	0.06358	0.06230 to 0.06501	0.6495

Supplementary Table 4: Turbidity curve over 15 min of different IGF2BP1 constructs with XBP1 36 nt RNA based on Fig. Supp. 5K.

	Dynamic pop. [%]	95% CI	$t_{1/2}$ [s]	95% CI	R^2
IGF2BP1 wild-type	68.81	67.35 to 70.46	21.58	19.44 to 24.09	0.5531
IGF2BP1 S181E	62.15	60.04 to 64.70	37.46	33.58 to 42.22	0.6744
IGF2BP1 Y396E	74.07	73.75 to 74.40	15.50	15.04 to 15.98	0.9079

Supplementary Table 5: The analyses of the FRAP curves of different IGF2BP1 constructs in G3BP1 induced SGs in Fig. 3D.

HCT116 cells	Median area per condensate [µm²]	25% Percentile	75% Percentile	Total number of condensates
wild-type	1.142	0.4985	2.286	5272
S181E	1.026	0.4404	2.148	6719
Y396E	1.093	0.4336	2.248	3927
RQ	1.276	0.5518	2.217	3826
HCT116 cells	Median total area per cell [µm²]	25% Percentile	75% Percentile	Mean number of condensates per cell
wild-type	10.26	6.907	13.55	5.71
S181E	10.26	6.496	14.82	7.205
Y396E	10.15	6.811	15.22	6.291
RQ	8.648	6.011	11.67	5.927
U2OS cells	Median area per condensate [µm²]	25% Percentile	75% Percentile	Total number of condensates
wild-type	0.976	0.369	2.408	2980
S181E	0.824	0.333	1.981	4463
Y396E	0.803	0.304	2.097	2685
U2OS cells	Median total area per cell [µm²]	25% Percentile	75% Percentile	Mean number of condensates per cell
wild-type	34.19	22.87	44.3	18.54
S181E	27.12	19.68	39.74	20.66
Y396E	22.79	13.53	33.97	16.52

Supplementary Table 6: Area per condensate of IGF2BP1 full-length constructs expressed in HCT116 and U2OS cells based on experiments in Fig.3 E-H, Fig. Supp. 6G-J.

	Dynamic pop. [%]	95% CI	$t_{1/2}$ [s]	95% CI	R^2
IGF2BP1 wild-type	77.86	75.54 to 80.56	241.7	221.1 to 266.0	0.801
IGF2BP1 S181E	61.32	59.37 to 63.61	240.0	217.8 to 266.6	0.7869
IGF2BP1 Y396E	69.36	67.90 to 70.96	151.3	138.1 to 166.5	0.7347

Supplementary Table 7: The analyses of the FRAP curves of different IGF2BP1 constructs in U2OS cells (Fig. 3I).

	Method	<Rg> (Å)	<Ree> (Å)
Linker 1 WT	CALVADOS	16.3 $\pm$ 0.1	39.1 $\pm$ 0.4
Linker 1 WT	Martini	17.3	-
Linker 1 WT	AFRC	15.31	35.81
Linker 1 S181E	CALVADOS	16.25$\pm$ 0.09	39.0 $\pm$ 0.4
Linker 1 S181E	Martini	17.4	-
Linker 1 S181E	AFRC	15.32	35.8
Linker 2 WT	CALVADOS	22.3 $\pm$ 0.1	52.7 $\pm$ 0.7
Linker 2 WT	Martini	22.8	-
Linker 2 WT	AFRC	19.63	45.76
Linker 2 Y396E	CALVADOS	22.2 $\pm$ 0.1	52.7 $\pm$ 0.6
Linker 2 Y396E	Martini	22.5	-
Linker 2 Y396E	AFRC	19.62	45.75

Supplementary Table 8: The radius of gyration values of the linkers and their mutants based on the MD simulations in Fig. 4C-F.

	Sequence
Full-length wild-type	GPLGSPGIPGMNKLYIGNLNESVTPADLEKVFAEHKISYSGQFLVKSGYAF VDCPDEHWAMKAIETFSGKVELQGKRLEIEHSVPKKQRSRKIQIRNIPPQL RWEVLDSLLAQYGTVENCEQVNTESETAVVNVTYSNREQTRQAIMKLNG HQLENHALKVSYIPDEQIAQGPENGRRGGFGSRGQPRQGSPVAAGAPAK QQQVDIPLRLLVPTQYVGAIIGKEGATIRNITKQTQSKIDVHRKENAGAAEK AISVHSTPEGCSSACKMILEIMHKEAKDTKTADEVPLKILAHNNFVGRLIGK EGRNLKKVEQDTETKITISSLQDLTLYNPERTITVKGAIENCCRAEQEIMKK VREAYENDVAAMSLQSHLIPGLNLAAVGLFPASSSAVPPPPSSVTGAAPYS SFMQAPEQEMVQVFIPAQAVGAIIGKKGQHIKQLSRFASASIKIAPPETPDS KVRMVIITGPPEAQFKAQGRIYGKLKEENFFGPKEEVKLETHIRVPASAAG RVIGKGGKTVNELQNLTAAEVVVPRDQTPDENDQVIVKIIGHFYASQMAQR KIRDILAQVKQQHQKGQSNQAQARRK
Full-length S181E	GPLGSPGIPGMNKLYIGNLNESVTPADLEKVFAEHKISYSGQFLVKSGYAF VDCPDEHWAMKAIETFSGKVELQGKRLEIEHSVPKKQRSRKIQIRNIPPQL RWEVLDSLLAQYGTVENCEQVNTESETAVVNVTYSNREQTRQAIMKLNG HQLENHALKVSYIPDEQIAQGPENGRRGGFGSRGQPRQGEPVAAGAPAK QQQVDIPLRLLVPTQYVGAIIGKEGATIRNITKQTQSKIDVHRKENAGAAEK AISVHSTPEGCSSACKMILEIMHKEAKDTKTADEVPLKILAHNNFVGRLIGK EGRNLKKVEQDTETKITISSLQDLTLYNPERTITVKGAIENCCRAEQEIMKK VREAYENDVAAMSLQSHLIPGLNLAAVGLFPASSSAVPPPPSSVTGAAPYS SFMQAPEQEMVQVFIPAQAVGAIIGKKGQHIKQLSRFASASIKIAPPETPDS KVRMVIITGPPEAQFKAQGRIYGKLKEENFFGPKEEVKLETHIRVPASAAG RVIGKGGKTVNELQNLTAAEVVVPRDQTPDENDQVIVKIIGHFYASQMAQR KIRDILAQVKQQHQKGQSNQAQARRK
Full-length Y396E	GPLGSPGIPGMNKLYIGNLNESVTPADLEKVFAEHKISYSGQFLVKSGYAF VDCPDEHWAMKAIETFSGKVELQGKRLEIEHSVPKKQRSRKIQIRNIPPQL RWEVLDSLLAQYGTVENCEQVNTESETAVVNVTYSNREQTRQAIMKLNG HQLENHALKVSYIPDEQIAQGPENGRRGGFGSRGQPRQGSPVAAGAPAK QQQVDIPLRLLVPTQYVGAIIGKEGATIRNITKQTQSKIDVHRKENAGAAEK AISVHSTPEGCSSACKMILEIMHKEAKDTKTADEVPLKILAHNNFVGRLIGK EGRNLKKVEQDTETKITISSLQDLTLYNPERTITVKGAIENCCRAEQEIMKK VREAYENDVAAMSLQSHLIPGLNLAAVGLFPASSSAVPPPPSSVTGAAPES SFMQAPEQEMVQVFIPAQAVGAIIGKKGQHIKQLSRFASASIKIAPPETPDS KVRMVIITGPPEAQFKAQGRIYGKLKEENFFGPKEEVKLETHIRVPASAAG RVIGKGGKTVNELQNLTAAEVVVPRDQTPDENDQVIVKIIGHFYASQMAQR KIRDILAQVKQQHQKGQSNQAQARRK
Full-length RQ	GPLGSPGIPGMNKLYIGNLNESVTPADLEKVFAEHKISYSGQFLVKSGYAF VDCPDEHWAMKAIETFSGKVELQGKRLEIEHSVPKKQRSRKIQIRNIPPQL RWEVLDSLLAQYGTVENCEQVNTESETAVVNVTYSNREQTRQAIMKLNG HQLENHALKVSYIPDEQIAQGPENGQQGGFGSQGQPQQGSPVAAGAPA KQQQVDIPLRLLVPTQYVGAIIGKEGATIRNITKQTQSKIDVHRKENAGAAE KAISVHSTPEGCSSACKMILEIMHKEAKDTKTADEVPLKILAHNNFVGRLIG KEGRNLKKVEQDTETKITISSLQDLTLYNPERTITVKGAIENCCRAEQEIMK KVREAYENDVAAMSLQSHLIPGLNLAAVGLFPASSSAVPPPPSSVTGAAPY SSFMQAPEQEMVQVFIPAQAVGAIIGKKGQHIKQLSRFASASIKIAPPETPD SKVRMVIITGPPEAQFKAQGRIYGKLKEENFFGPKEEVKLETHIRVPASAA GRVIGKGGKTVNELQNLTAAEVVVPRDQTPDENDQVIVKIIGHFYASQMAQ RKIRDILAQVKQQHQKGQSNQAQARRK

mCherry-IGF2BP1 full-length wild-type	MVSKGEEDNMAIIKEFMRFKVHMEGSVNGHEFEIEGEGEGRPYEGTQTA KLKVTKGGPLPFAWDILSPQFMYGSKAYVKHPADIPDYLKLSFPEGFKWE RVMNFEDGGVVTVTQDSSLQDGEFIYKVKLRGTNFPSDGPVMQKKTMG WEASSERMYPEDGALKGEIKQRLKLKDGGHYDAEVKTTYKAKKPVQLPG AYNVNIKLDITSHNEDYTIVEQYERAEGRHSTGGMDELYKMNKLYIGNLNE SVTPADLEKVFAEHKISYSGQFLVKSGYAFVDCPDEHWAMKAIETFSGKV ELQGKRLEIEHSVPKKQRSRKIQIRNIPPQLRWEVLDSLLAQYGTVENCEQ VNTESETAVVNVTYSNREQTRQAIMKLNGHQLENHALKVSYIPDEQIAQG PENGRRGGFGSRGQPRQGSPVAAGAPAKQQQVDIPLRLLVPTQYVGAIIG KEGATIRNITKQTQSKIDVHRKENAGAAEKAISVHSTPEGCSSACKMILEIM HKEAKDTKTADEVPLKILAHNNFVGRLIGKEGRNLKKVEQDTETKITISSLQ DLTLYNPERTITVKGAIENCCRAEQEIMKKVREAYENDVAAMSLQSHLIPGL NLAAVGLFPASSSAVPPPPSSVTGAAPYSSFMQAPEQEMVQVFIPAQAVG AIIGKKGQHIKQLSRFASASIKIAPPETPDSKVRMVIITGPPEAQFKAQGRIY GKLKEENFFGPKEEVKLETHIRVPASAAGRVIGKGGKTVNELQNLTAAEVV VPRDQTPDENDQVIVKIIGHFYASQMAQRKIRDILAQVKQQHQKGQSNQA QARRKDLEVLFQ
mCherry-IGF2BP1 full-length S181E	MVSKGEEDNMAIIKEFMRFKVHMEGSVNGHEFEIEGEGEGRPYEGTQTA KLKVTKGGPLPFAWDILSPQFMYGSKAYVKHPADIPDYLKLSFPEGFKWE RVMNFEDGGVVTVTQDSSLQDGEFIYKVKLRGTNFPSDGPVMQKKTMG WEASSERMYPEDGALKGEIKQRLKLKDGGHYDAEVKTTYKAKKPVQLPG AYNVNIKLDITSHNEDYTIVEQYERAEGRHSTGGMDELYKMNKLYIGNLNE SVTPADLEKVFAEHKISYSGQFLVKSGYAFVDCPDEHWAMKAIETFSGKV ELQGKRLEIEHSVPKKQRSRKIQIRNIPPQLRWEVLDSLLAQYGTVENCEQ VNTESETAVVNVTYSNREQTRQAIMKLNGHQLENHALKVSYIPDEQIAQG PENGRRGGFGSRGQPRQGEPVAAGAPAKQQQVDIPLRLLVPTQYVGAIIG KEGATIRNITKQTQSKIDVHRKENAGAAEKAISVHSTPEGCSSACKMILEIM HKEAKDTKTADEVPLKILAHNNFVGRLIGKEGRNLKKVEQDTETKITISSLQ DLTLYNPERTITVKGAIENCCRAEQEIMKKVREAYENDVAAMSLQSHLIPGL NLAAVGLFPASSSAVPPPPSSVTGAAPYSSFMQAPEQEMVQVFIPAQAVG AIIGKKGQHIKQLSRFASASIKIAPPETPDSKVRMVIITGPPEAQFKAQGRIY GKLKEENFFGPKEEVKLETHIRVPASAAGRVIGKGGKTVNELQNLTAAEVV VPRDQTPDENDQVIVKIIGHFYASQMAQRKIRDILAQVKQQHQKGQSNQA QARRKDLEVLFQ
mCherry-IGF2BP1 full-length Y396E	MVSKGEEDNMAIIKEFMRFKVHMEGSVNGHEFEIEGEGEGRPYEGTQTA KLKVTKGGPLPFAWDILSPQFMYGSKAYVKHPADIPDYLKLSFPEGFKWE RVMNFEDGGVVTVTQDSSLQDGEFIYKVKLRGTNFPSDGPVMQKKTMG WEASSERMYPEDGALKGEIKQRLKLKDGGHYDAEVKTTYKAKKPVQLPG AYNVNIKLDITSHNEDYTIVEQYERAEGRHSTGGMDELYKMNKLYIGNLNE SVTPADLEKVFAEHKISYSGQFLVKSGYAFVDCPDEHWAMKAIETFSGKV ELQGKRLEIEHSVPKKQRSRKIQIRNIPPQLRWEVLDSLLAQYGTVENCEQ VNTESETAVVNVTYSNREQTRQAIMKLNGHQLENHALKVSYIPDEQIAQG PENGRRGGFGSRGQPRQGSPVAAGAPAKQQQVDIPLRLLVPTQYVGAIIG KEGATIRNITKQTQSKIDVHRKENAGAAEKAISVHSTPEGCSSACKMILEIM HKEAKDTKTADEVPLKILAHNNFVGRLIGKEGRNLKKVEQDTETKITISSLQ DLTLYNPERTITVKGAIENCCRAEQEIMKKVREAYENDVAAMSLQSHLIPGL NLAAVGLFPASSSAVPPPPSSVTGAAPESSFMQAPEQEMVQVFIPAQAVG AIIGKKGQHIKQLSRFASASIKIAPPETPDSKVRMVIITGPPEAQFKAQGRIY

	GKLKEENFFGPKEEVKLETHIRVPASAAGRVIGKGGKTVNELQNLTAAEVV VPRDQTPDENDQVIVKIIGHFYASQMAQRKIRDILAQVKQQHQKGQSNQA QARRKDLEVLFQ
KH1-4 wild-type	GPGVDIPLRLLVPTQYVGAIIGKEGATIRNITKQTQSKIDVHRKENAGAAEK AISVHSTPEGCSSACKMILEIMHKEAKDTKTADEVPLKILAHNNFVGRLIGK EGRNLKKVEQDTETKITISSLQDLTLYNPERTITVKGAIENCCRAEQEIMKK VREAYENDVAAMSLQSHLIPGLNLAAVGLFPASSSAVPPPPSSVTGAAPYS SFMQAPEQEMVQVFIPAQAVGAIIGKKGQHIKQLSRFASASIKIAPPETPDS KVRMVIITGPPEAQFKAQGRIYGKLKEENFFGPKEEVKLETHIRVPASAAG RVIGKGGKTVNELQNLTAAEVVVPRDQTPDENDQVIVKIIGHFYASQMAQR KIRDILAQVKQQHQKGQSNQAQARRK
KH1-4 Y396E	GPGVDIPLRLLVPTQYVGAIIGKEGATIRNITKQTQSKIDVHRKENAGAAEK AISVHSTPEGCSSACKMILEIMHKEAKDTKTADEVPLKILAHNNFVGRLIGK EGRNLKKVEQDTETKITISSLQDLTLYNPERTITVKGAIENCCRAEQEIMKK VREAYENDVAAMSLQSHLIPGLNLAAVGLFPASSSAVPPPPSSVTGAAPES SFMQAPEQEMVQVFIPAQAVGAIIGKKGQHIKQLSRFASASIKIAPPETPDS KVRMVIITGPPEAQFKAQGRIYGKLKEENFFGPKEEVKLETHIRVPASAAG RVIGKGGKTVNELQNLTAAEVVVPRDQTPDENDQVIVKIIGHFYASQMAQR KIRDILAQVKQQHQKGQSNQAQARRK
RRM1-2 wild type	GPGMNKLYIGNLNESVTPADLEKVFAEHKISYSGQFLVKSGYAFVDCPDEH WAMKAIETFSGKVELQGKRLEIEHSVPKKQRSRKIQIRNIPPQLRWEVLDS LLAQYGTVENCEQVNTESETAVVNVTYSNREQTRQAIMKLNGHQLENHAL KVSYIPDEQIAQ
KH1-2 wild-type	GPGVDIPLRLLVPTQYVGAIIGKEGATIRNITKQTQSKIDVHRKENAGAAEK AISVHSTPEGCSSACKMILEIMHKEAKDTKTADEVPLKILAHNNFVGRLIGK EGRNLKKVEQDTETKITISSLQDLTLYNPERTITVKGAIENCCRAEQEIMKK VREAYENDVAAMSLQSHLIPGLN
KH3-4 wild-type	GPGEQEMVQVFIPAQAVGAIIGKKGQHIKQLSRFASASIKIAPPETPDSKVR MVIITGPPEAQFKAQGRIYGKLKEENFFGPKEEVKLETHIRVPASAAGRVIG KGGKTVNELQNLTAAEVVVPRDQTPDENDQVIVKIIGHFYASQMAQRKIRD ILAQVKQQHQKGQSNQAQARRK
L2-KH3-4 wild-type	GPGMKKVREAYENDVAAMSLQSHLIPGLNLAAVGLFPASSSAVPPPPSSV TGAAPYSSFMQAPEQEMVQVFIPAQAVGAIIGKKGQHIKQLSRFASASIKIA PPETPDSKVRMVIITGPPEAQFKAQGRIYGKLKEENFFGPKEEVKLETHIR VPASAAGRVIGKGGKTVNELQNLTAAEVVVPRDQTPDENDQVIVKIIGHFY ASQMAQRKIRDILAQVKQQHQKGQSNQAQARRK
Full-length KH3 GEEG KH4 GEEG	GPLGSPGIPGMNKLYIGNLNESVTPADLEKVFAEHKISYSGQFLVKSGYAF VDCPDEHWAMKAIETFSGKVELQGKRLEIEHSVPKKQRSRKIQIRNIPPQL RWEVLDSLLAQYGTVENCEQVNTESETAVVNVTYSNREQTRQAIMKLNG HQLENHALKVSYIPDEQIAQGPENGRRGGFGSRGQPRQGSPVAAGAPAK QQQVDIPLRLLVPTQYVGAIIGKEGATIRNITKQTQSKIDVHRKENAGAAEK AISVHSTPEGCSSACKMILEIMHKEAKDTKTADEVPLKILAHNNFVGRLIGK EGRNLKKVEQDTETKITISSLQDLTLYNPERTITVKGAIENCCRAEQEIMKK VREAYENDVAAMSLQSHLIPGLNLAAVGLFPASSSAVPPPPSSVTGAAPYS SFMQAPEQEMVQVFIPAQAVGAIIGEEGQHIKQLSRFASASIKIAPPETPDS KVRMVIITGPPEAQFKAQGRIYGKLKEENFFGPKEEVKLETHIRVPASAAG RVIGEEGKTVNELQNLTAAEVVVPRDQTPDENDQVIVKIIGHFYASQMAQR KIRDILAQVKQQHQKGQSNQAQARRK

KH3-4 KH3 wild-type KH4 GEEG	GPGEQEMVQVFIPAQAVGAIIGKKGQHIKQLSRFASASIKIAPPETPDSKVR MVIITGPPEAQFKAQGRIYGKLKEENFFGPKEEVKLETHIRVPASAAGRVIG EEGKTVNELQNLTAAEVVVPRDQTPDENDQVIVKIIGHFYASQMAQRKIRD ILAQVKQQHQKGQSNQAQARRK
KH3 GEEG KH4 wild-type	GPGEQEMVQVFIPAQAVGAIIGEEGQHIKQLSRFASASIKIAPPETPDSKVR MVIITGPPEAQFKAQGRIYGKLKEENFFGPKEEVKLETHIRVPASAAGRVIG KGGKTVNELQNLTAAEVVVPRDQTPDENDQVIVKIIGHFYASQMAQRKIRD ILAQVKQQHQKGQSNQAQARRK
Linker1 wild-type	ATYEQIAQGPENGRRGGFGSRGQPRQGSPVAAGAPAKQQQV
Linker1 S181E	ATYEQIAQGPENGRRGGFGSRGQPRQGEPVAAGAPAKQQQV
Linker1 RQ	ATYEQIAQGPENGQQGGFGSQGQPQQGSPVAAGAPAKQQQV
Linker2 wild-type	ATYMKKVREAYENDVAAMSLQSHLIPGLNLAAVGLFPASSSAVPPPPSSVT GAAPYSSFMQAPE
Linker2 Y396E	ATYMKKVREAYENDVAAMSLQSHLIPGLNLAAVGLFPASSSAVPPPPSSVT GAAPESSFMQAPE

Supplementary Table 9: Amino acid sequences of all recombinant IGF2BP1 protein constructs used in this study.

Supplementary References

1. Gruber, A.R. *et al.* The Vienna RNA Websuite. Nucleic Acids Res., vol. 36, no. suppl_2, pp. W70–W74, Jul (2008).
2. Hafner, M. et al. Transcriptome-wide identification of RNA-binding protein and microRNA target sites by PAR-CLIP. Cell 141, 129-141 (2010).
3. Zhao, W. et al. POSTAR3: An updated platform for exploring post-transcriptional regulation coordinated by RNA-binding proteins. Nucleic Acids Res 50, D287–D294 (2022).
4. Supek, F., Bošnjak, M., Škunca, N. & Šmuc, T. REVIGO Summarizes and Visualizes Long Lists of Gene Ontology Terms. PLoS One 6, e21800 (2011).
5. Conway, A.E. *et al.* Enhanced CLIP Uncovers IMP Protein-RNA Targets in Human Pluripotent Stem Cells Important for Cell Adhesion and Survival. *Cell Rep* 15, 666-679 (2016).
6. Schneider, T. *et al.* Combinatorial recognition of clustered RNA elements by the multidomain RNA-binding protein IMP3. *Nat Commun* 10, 2266 (2019).
7. Hafner, M. *et al.* Transcriptome-wide identification of RNA-binding protein and microRNA target sites by PAR-CLIP. *Cell* 141, 129-141 (2010).
8. Anisimova A.S. and Karagöz G.E. Optimized infrared photoactivatable ribonucleoside-enhanced crosslinking and immunoprecipitation (IR-PAR-CLIP) protocol identifies novel IGF2BP3-interacting RNAs in colon cancer cells. RNA, vol. 29, no. 11, pp. 1818–1836 (2023).
9. Bernstein P.L. *et al.* Control of c-myc mRNA half-life in vitro by a protein capable of binding to a coding region stability determinant. Genes Dev vol. 6, no. 4, pp. 642–654 (1992).
10. Chao, J.A. *et al.* ZBP1 recognition of beta-actin zipcode induces RNA looping. *Genes Dev* 24, 148-158 (2010).
11. Hüttelmaier S. et al. Spatial regulation of β-actin translation by Src-dependent phosphorylation of ZBP1. Nature vol. 438 no. 7067, pp. 512–515 (2005).

3 Discussion

Maintaining protein homeostasis in the ER is essential for cellular function, and, not surprisingly, its disruption contributes to pathology of numerous diseases, including cancer, diabetes, and neurodegeneration (reviewed in [74–80]). To cope with ER stress, cells activate the UPR, which adjusts protein folding capacity to match the cellular need and initiates apoptosis if adaptation fails. While transcriptional regulation through UPR is essential for restoring homeostasis and has been extensively studied, much less is known about how post-transcriptional mechanisms shape the transcriptome during stress. System-level data revealed that post-transcriptional mechanisms are engaged during ER stress, yet how this is achieved at the mechanistic level has been poorly understood.

In this thesis, I aimed to uncover how a specific RBP, IGF2BP3, contributes to post-transcriptional regulation during ER stress. Using unbiased proteomics methods, our previous work identified that IGF2BP3 associates with the ER stress sensor IRE1 in an ER stress-dependent manner [112]. Yet, whether IGF2BP3 regulates mRNA fate during ER stress remained unclear.

Here, I showed that IGF2BP3 binds and regulates UPR effector mRNAs. Notably, I found that during ER stress, IGF2BP3 promotes degradation of its target mRNAs, decreasing their levels. In parallel, it indirectly facilitates transcription of UPR target genes, and its depletion dampens the UPR. These findings establish IGF2BP3 as a previously unrecognized regulator of ER proteostasis and open new perspectives on how RBPs integrate mRNA metabolism regulation with stress signaling.

3.1 IGF2BP3 binds UPR effectors and reduces association with its canonical targets during ER stress

Using unbiased RNA-crosslinking co-immunoprecipitation of IRE1, we revealed that the RBP IGF2BP3 associates with IRE1 in an ER stress-dependent manner through protein-RNA interactions. Guided by this finding, we hypothesized that IGF2BP3 may bind IRE1 mRNA targets and contribute functionally to the cellular response to ER stress. To test this hypothesis, we first set out to identify which transcripts IGF2BP3 binds under ER stress conditions. While several studies have mapped IGF2BP3 targets in unstressed cells [125,149,165], it remained unclear whether ER stress alters its

binding properties. Moreover, because some of the UPR-induced genes are only expressed during stress, such targets could not have been detected previously.

To define IGF2BP3 target transcripts and its binding sites, I established immunoprecipitation conditions that enable efficient extraction of endogenous IGF2BP3 and optimized the PAR-CLIP protocol [149,175]. Instead of radioactive labeling, I used a safe and highly sensitive infrared dye to visualize RNA fragments crosslinked to IGF2BP3, and established the RNase treatment conditions to achieve the best binding site coverage. Specifically, the use of RNase I, which has low sequence specificity, was crucial for obtaining high-quality coverage profiles. I performed the experiments in the HCT116 colorectal carcinoma cell line, as it does not express IGF2BP1, which could mask IGF2BP3 function due to redundancy. Moreover, both UPR activation and IGF2BP expression contribute to colorectal cancer progression[176–178]. As a result, I developed an IR-PAR-CLIP protocol, which provided the basis for the subsequent analysis of IGF2BP3 binding changes during ER stress.

In order to define whether ER stress alters IGF2BP3 binding, I used the IR-PAR-CLIP to compare the binding profiles of endogenous IGF2BP3 in unstressed cells and upon ER stress induction. The analysis of IGF2BP3-bound transcripts upon ER stress identified one-third of the UPR-target transcripts as specific IGF2BP3 binding targets, including *HSPA5* (encoding major ER chaperone BiP), *XBP1* (the main IRE1 target), and *DDIT3* (encoding pro-apoptotic transcription factor CHOP). At the same time, IGF2BP3 showed reduced binding to its canonical targets such as *HMGA2*, which encodes an oncogenic transcriptional regulator [179]. These data indicated that IGF2BP3's target spectrum changes during ER stress. Consistent with its association with UPR effectors, IGF2BP3 also bound approximately one-third of IRE1 targets. Initially, we hypothesized that IGF2BP3 might protect IRE1 targets from cleavage and subsequent degradation. However, the binding sites of IGF2BP3 did not overlap with IRE1 binding and cleavage positions, contradicting this idea. In addition, we observed ER stress-dependent differences in IGF2BP3 binding motifs. Whether these differences result from changes in IGF2BP3 binding preferences or from target transcript abundance remains to be determined. Altogether, the binding of IGF2BP3 to UPR effectors and the changes in its canonical interactions under stress suggest that IGF2BP3 may contribute to transcriptome remodeling during ER stress.

3.2 IGF2BP3 shapes the UPR transcriptome via a dual mechanism

The results of the IR-PAR-CLIP experiment revealed that IGF2BP3 binds multiple UPR effector transcripts, making it plausible that IGF2BP3 regulates them and therefore contributes to the post-transcriptional regulation of the UPR. However, previous studies show that binding of an RBP to an mRNA does not necessarily lead to a functional outcome [180]. Moreover, IGF2BP3 has versatile functions ranging from mRNA stabilization, degradation, and translational regulation, all of which depend on mRNA sequence as well as cellular context [151,156,162,165]. Therefore, to understand the functional role of IGF2BP3 during ER stress, I next dissected changes in the transcriptome upon IGF2BP3 depletion.

3.2.1 Depletion of IGF2BP3 dampens the UPR

First, to determine the functional role of IGF2BP3 in the UPR, we analyzed the effect of its depletion on the total transcriptome during ER stress. Although we did not observe significant changes for individual UPR effectors, depletion of IGF2BP3 resulted in consistent and significant downregulation of the set of UPR-upregulated genes. We further confirmed our findings using RT-qPCR experiments under milder, closer to physiological ER stress conditions, where the effect of IGF2BP3 on total levels of individual UPR effector transcripts was more pronounced and statistically significant. It should be noted that we did not observe IGF2BP3-mediated regulation of IRE1 RIDD targets, suggesting that IGF2BP3 does not modulate cleavage of these targets by IRE1. As multiple UPR-upregulated transcripts are suboptimal substrates of IRE1 [112], the possibility remains that IGF2BP3 may regulate their interaction with IRE1 and cleavage. Surprisingly, IGF2BP3 depletion resulted in reduced levels across all three UPR branches, even for transcripts not directly bound by IGF2BP3. This indicates that the observed effect may not be mediated solely through direct IGF2BP3 binding and stabilization of the UPR targets, but rather through rewiring of the transcriptional UPR program. Therefore, in the next experiment, we aimed to uncouple the transcriptional and post-transcriptional changes occurring upon IGF2BP3 depletion and to track the stability of IGF2BP3-bound transcripts.

3.2.2 Experimental approaches to address mRNA stability regulation during ER stress

Several experimental strategies have been employed to investigate mRNA stability in the context of ER stress. The first relies on blocking transcription with DNA intercalating agents, such as actinomycin D (ActD), and following the degradation rates [31,32,109,181]. While it allows for direct monitoring of transcript decay rates, it has several important limitations. Blocking transcription simultaneously with ER stress induction prevents proper UPR activation and expression of the stress-induced transcripts. This setup can therefore only be used to monitor transcripts already present before stress, such as RIDD targets [31,32,109], it will not capture the regulation events mediated via the transcriptional UPR branches. To overcome this limitation, ActD chase can be applied after ER stress induction [181]. However, this method is still not optimal to monitor changes in half-lives of long-lived mRNAs, as prolonged ActD treatment drastically changes the transcriptome of treated cells.

A second frequently used approach estimates the regulation of transcript half-lives by comparing the changes in total and nascent transcriptomes. To capture nascent transcription during the UPR, previous studies have employed run-on RNA sequencing, which detects RNAs associated with RNA polymerase at a given moment [82,109]. While these methods are considered the gold standard for mapping polymerase positions, their protocols are extensive, and estimates of nascent transcription rates may be biased by polymerase pausing and gene length. Additionally, because they provide only a snapshot of transcription, they might miss changes in some dynamically regulated UPR targets.

Taking these limitations into account, we reasoned that thiol(SH)-linked alkylation for the metabolic sequencing of RNA (SLAMseq) would provide the most suitable approach to test whether IGF2BP3 affects transcription or mRNA stability during ER stress [182]. SLAMseq allows direct comparison of nascent and total transcriptomes within a defined time frame. It relies on treating cells with 4-thiouridine (s^4U), which is incorporated into newly transcribed mRNAs and results in T-C transitions in the final library. In our experimental setup, ER stress was induced, and after 3 hours a 2-hour s^4U pulse was applied. This approach allowed us to directly assess IGF2BP3-mediated effects on transcription and to estimate mRNA stability across the entire transcriptome,

including UPR-induced transcripts. Importantly, this setup does not interfere with the transcription of UPR target genes and thus the natural progression of the UPR throughout the experiment.

3.2.3 SLAMseq reveals a dual mechanism through which IGF2BP3 functions during ER stress

SLAMseq analysis showed that IGF2BP3 depletion caused a more substantial decrease in nascent mRNA levels compared to the total transcript levels for UPR targets. This suggested two conclusions. First, that the observed dampening of the UPR upon IGF2BP3 depletion occurs primarily at the transcriptional level. Second, because reduced transcription does not result in a substantial decrease in total transcript levels, an additional layer of regulation likely operates at the level of mRNA stability. To further address whether IGF2BP3 depletion results in the stabilization of UPR targets, we analyzed SLAMseq data by calculating the T-C conversion rate values. They represent the ratio of the number of T-C conversions to the total coverage at Ts for a given gene, and reflect the relative abundance of newly synthesized and pre-existing mRNAs. Therefore, a decrease in T-C conversion rate indicates increased stabilization. Using this analysis, we found that under ER stress IGF2BP3 depletion leads to stabilization of its target RNAs, including UPR-induced transcripts. These findings were further supported by monitoring mRNA decay upon ActD treatment followed by RT-qPCR. Altogether, the IGF2BP3 depletion analysis results suggested the following model: IGF2BP3 indirectly supports transcription of the UPR targets, while ER stress shifts its direct function toward promoting mRNA degradation. For most IGF2BP3 targets, this leads to a decrease in their total levels; however, UPR target levels are partially rescued due to an increase in their transcription. At the total transcript level, this results in small changes that we could detect only when UPR-upregulated genes were analyzed as a group. Strikingly, the decrease in UPR target levels was more prominent under milder, closer-to-physiological ER stress conditions. This suggests that stronger ER stress is required to enhance pro-degradatory functions of IGF2BP3. Therefore, in an organism or cancer context, IGF2BP3 could be expected to promote UPR.

How IGF2BP3 supports the transcription of UPR target genes remains unclear. One possibility is that it acts through the regulation of a transcription factor involved in the

pathway. The major UPR transcription factors, XBP1s and ATF6(N), belong to the basic-leucine zipper (bZIP) family and function as heterodimers that in combination regulate transcription of UPR target genes [183,184]. In this context, IGF2BP3-regulated bZIP proteins such as FOSL2 or the ATF6 paralog CREB3L2 may also participate in reinforcing transcriptional activation of the UPR. It should be noted that the dampening of the UPR that we observe is not limited to a single branch. Although a more detailed analysis is required to understand whether a particular UPR branch is particularly susceptible to IGF2BP3 depletion, this may be complicated due to the cross-talk between branches. One also cannot exclude the possibility that IGF2BP3 acts via a transcriptional regulator not previously linked to the UPR. We were unable to identify such a regulator from the current data, and experiments under milder stress conditions may be necessary. Altogether, our data demonstrate that by influencing transcriptional networks, RBPs can extend post-transcriptional regulation beyond their direct targets and support stress adaptation.

Our depletion experiments, coupled with mRNA stability assays, show that ER stress shifts IGF2BP3 function towards promoting the destabilization of its targets. Under homeostatic conditions, IGF2BP3 binding can either promote mRNA stability or facilitate degradation, depending on the target identity. However, under ER stress, the pro-degradatory outcome of IGF2BP3 binding becomes more prominent. Functionally, this shift may help cells decrease overall mRNA concentration, reducing the translational and, therefore, folding burden under stress conditions that perturb proteostasis. This hypothesis can be addressed in future transcriptomic experiments with the addition of spike-in normalization.

Another consequence involves in the regulation of specific IGF2BP3 targets, which might contribute to UPR progression, including regulation of its transcriptional branches. Under homeostatic conditions, IGF2BP3 sequesters *HMGA2* into RISC-depleted mRNPs, protecting it from degradation [126]. According to our data, ER stress results in the release of *HMGA2* mRNA from IGF2BP3 and subsequent destabilization. HMGA2 is an architectural protein that regulates gene expression through changing chromatin structure [185–187]. One possible model is that HMGA2-mediated remodeling of chromatin facilitates the initiation of the UPR, while its levels decrease due to a negative feedback loop during UPR progression. In this case, IGF2BP3 depletion

would dampen the UPR, in agreement with our data. HMGA2 depletion experiments should be performed to address this hypothesis further.

In addition to transcriptional regulators such as HMGA2, multiple IGF2BP3-bound transcripts encoding post-transcriptional regulators showed increased degradation during stress. Among them were a previously described target of IGF2BP3, the *ZFP36L1* mRNA [165], which encodes a post-transcriptional repressor of the tristetraprolin (TTP) family, and AGO2. Functionally, it is not clear how destabilization of transcripts encoding post-transcriptional regulators contributes to cellular physiology. However, this can result in changes to the relative activity of different mRNA degradation pathways and contribute to selective remodeling of the transcriptome.

3.3 ER stress increases the association of IGF2BP3 with mRNA decapping complex

Having established that IGF2BP3 promotes mRNA degradation during ER stress, we next asked how this effect is achieved at the molecular level. Because IGF2BP3 is an RBP and cannot directly degrade its targets, we reasoned that it might act as an adaptor that delivers them to degrading enzymes. To test this hypothesis, we set out to determine protein interaction partners of IGF2BP3. We performed co-immunoprecipitation of endogenous IGF2BP3 followed by mass spectrometry, which revealed interactors that showed increased association upon ER stress. Among them, GO term analysis revealed all components of the mRNA decapping complex (EDC4, EDC3, DCP1A, DCP2). Moreover, we also recovered IRE1, supporting our initial findings. These proteins appeared relatively resistant to RNase treatment, possibly reflecting their incorporation into tight mRNP complexes with IGF2BP3. However, in GFP-IRE1 co-immunoprecipitation experiments, the interaction with IGF2BP3 proved sensitive to RNase. Together, these results suggest that both protein-protein and protein-RNA interactions may contribute to the association of IGF2BP3 with its partners. The exact molecular basis of these interactions, however, remains to be established.

In cells, mRNA decapping complex accumulates in the P-bodies. It has been reported that IGF2BP3 partially localizes to P-bodies, mediating translational silencing of its

mRNA targets [156]. Nevertheless, it remains unclear which interactions recruit IGF2BP3 to P-bodies. Apart from P-body localization, previous studies have also suggested an association of IGF2BP3 with other mRNA degradation machinery, such as exosome [162]. Moreover, the functional link between IGF2BP3 binding and AGO2 recruitment to their targets to promote mRNA degradation was established [165]. However, in contrast to the mRNA decapping complex proteins, our data show strong RNase sensitivity for both the exosome and AGO2.

To determine which protein-protein interactions may drive IGF2BP3 pro-degradative function upon ER stress, we performed an unbiased AlphaFold2 Multimer screen, predicting the pairwise interactions between IGF2BP3 and all proteins identified in the IGF2BP3 co-immunoprecipitation experiment. This approach has proven powerful for predicting direct protein-protein interactions within large lists of potential interactors in multiple studies (e.g., for the identification of molecular mechanisms of fertilization [188] and PIWI-piRNA complex assembly [189]). Remarkably, among all 1213 proteins recovered in IGF2BP3 co-immunoprecipitants, the mRNA decapping complex component EDC3 showed the highest probability to interact with IGF2BP3 directly. EDC3 is a decapping coactivator that supports the active conformation of the DCP1-DCP2 decapping enzyme. While the N-terminal LSm domain interacts with DCP1/2, the C-terminal YjeF-N domain dimerizes, supporting the assembly and integrity of the complex [190–192]. We further mapped the interaction to occur between the RRM2 domain of IGF2BP3 and the YjeF domain of EDC3, and confirmed it by co-immunoprecipitation of IGF2BP3 mutated at the predicted EDC3 interaction site. Importantly, the interaction site does not overlap with either the RNA-binding site on the RRM2 of IGF2BP3 or the self-association surface on the YjeF of EDC3, and therefore should not interfere with these functions. Instead, we propose that IGF2BP3 delivers its targets for decapping through its interaction with EDC3. Additionally, multivalent interactions between IGF2BP3, mRNAs, and the decapping complex may contribute to the formation of higher-order mRNPs.

Taken together, these results point to a role of IGF2BP3 as an adaptor that connects its mRNA targets with the decapping machinery via EDC3. Consistent with our findings, the interaction between EDC3 and the adaptor RBP TTP has been shown to facilitate decapping of TTP targets. However, the exact interaction surface between the two

proteins has not yet been identified [193]. This highlights the ability of EDC3 to bridge different RBPs with the decapping complex and supports the mechanism proposed for IGF2BP3.

Our results demonstrate a direct interaction between IGF2BP3 and the mRNA decapping complex, and reveal that this association increases during ER stress. However, the mechanism behind this increase remains to be established. One possibility is that it is mediated via the regulation of the protein-protein interaction between IGF2BP3 and EDC3. Further experiments are planned to test whether an IGF2BP3 mutation that reduces its interaction with EDC3 prevents the ER stress-induced increase in IGF2BP3 association with the mRNA decapping complex. It will also be essential to determine whether disrupting this interaction impairs IGF2BP3-mediated destabilization of its targets.

Adaptor RBPs often rely on their IDRs to deliver mRNAs to degradation machineries, and these interactions can be dynamically regulated by phosphorylation. For example, phosphorylation of TTP by p38 MAP kinase disrupts its binding to CCR4-NOT and increases stability of its targets [194,195]. More broadly, this concept has been demonstrated for the IDRs of multiple RBPs [196]. In line with these findings, our Alphafold2-Multimer screen predicted the interaction between the second IDR linker of IGF2BP3 and CNOT9, a component of the CCR4-NOT complex. IDRs have also been implicated in the interaction of adaptor RBPs with the mRNA decapping complex, as shown for TTP, whose IDR binds directly to DCP2[197]. Altogether, these findings raise the possibility that the effect of ER stress on IGF2BP3 association with the mRNA decapping complex could also be regulated by phosphorylation.

In our work presented in Section 2.3, we demonstrated that oxidative stress changes phosphorylation of IGF2BP3 paralog IGF2BP1 at several sites, which differentially regulate its mRNA binding, protein interactions, and condensation properties. Similar to IGF2BP1, our preliminary data suggest that IGF2BP3 phosphorylation is modulated by ER stress. However, due to protease cleavage specificity, we could not obtain the coverage of either the IGF2BP3-EDC3 interaction surface or its IDRs. Therefore, optimization of mass spectrometry sample preparation is necessary to identify the potential phosphorylation sites that may be involved in regulation of IGF2BP3-mRNA

decapping complex interaction upon ER stress. In addition, EDC3 itself can be phosphorylated, which influences its localization to P-bodies and their dynamics [198]. Thus, phosphorylation of either IGF2BP3 or EDC3, or both, could contribute to the enhanced association of IGF2BP3 with the decapping complex during ER stress. Future experiments will be required to address these possibilities.

The different outcomes of IGF2BP3 binding have been linked to modifications of target mRNAs, where m6A-modified transcripts were proposed to be stabilized by IGF2BP3, while m7G-modified transcripts were targeted for degradation. Although no transcriptome-wide profiling has been performed to address changes in m6A and m7G modifications upon ER stress, it is plausible that these modifications respond dynamically to ER stress conditions. Indeed, m6A modification profiles are highly sensitive to heat shock and contribute to the regulation of mRNA metabolism [199,200]. Moreover, m6A modification plays a crucial role in cell survival under ER stress by inhibiting CHOP expression [201]. In this scenario, increased m7G modification of IGF2BP3 targets could enhance their degradation under ER stress, with IGF2BP3-EDC3 interaction stabilizing their association with the mRNA decapping complex. To test this hypothesis, further experiments, including m7G sequencing and analysis of mRNA stability upon mutation of m7G sites are required.

3.4 Concluding remarks

Our results identify IGF2BP3 as an adaptor protein that, upon ER stress, delivers its target transcripts to the mRNA decapping machinery, promoting their degradation while indirectly supporting the transcription of UPR targets. Physiologically, such dual regulation may help cells balance protein load and transcriptional output during ER stress. Considering that IGF2BP3 expression peaks in embryonic and malignant tissues, this mechanism is likely to operate in a tissue-specific manner and may contribute to the variability in stress response outcomes observed during development and tumorigenesis.

4 Limitations of the study and future directions

4.1 Identifying potential post-transcriptional regulators of the UPR

To identify potential post-transcriptional regulators of transcripts relevant for the progression of the ER stress response, we relied on crosslinking co-immunoprecipitation of IRE1 coupled with mass spectrometry [112]. This approach allowed us to identify RBPs that associate with IRE1 and its mRNA targets in an unbiased manner and was most appropriate for identifying modulators of IRE1 selectivity. Nevertheless, we could have missed the potential regulators if they were more sensitive to RNase treatment. Technical limitations of mass spectrometry could also prevent the identification of potential candidates. In addition, because not every transcript contributing to the UPR outcome is an IRE1 target, RBPs acting on such mRNAs could have been missed. Unbiased functional genomics approaches coupled with transcriptomics [55] could be an effective alternative or a valuable addition to our strategy. These methods allow systematic depletion of virtually any protein followed by transcriptomic profiling. Applied in our context, they could reveal RBPs that influence UPR-relevant transcripts, enabling the identification of regulators of UPR that are not captured by IRE1 interaction-based assays.

4.2 Contribution of IGF2BP1 and IGF2BP2 to ER stress regulation

The IGF2BP family comprises three paralogs that share approximately two-thirds of their binding targets and, in certain cases, exhibit similar regulatory effects, suggesting they may compensate for each other.[151]. Although mass spectrometry of IRE1 interaction partners identified IGF2BP3 as the only confident interactor that increased its association with IRE1 upon ER stress, IGF2BP1 and IGF2BP2 were also detected in the immunoprecipitation. We have not further probed IGF2BP1 and IGF2BP2 associations with IRE1 upon ER stress using western blot analyses. To avoid the possibility of functional redundancy, the HCT116 colorectal carcinoma cell line was selected, as it does not express IGF2BP1. Compared with IGF2BP3, siRNA-mediated depletion of IGF2BP2 had a negligible effect on the levels of UPR-upregulated transcripts, while CRISPR/Cas9 knockout experiments were unsuccessful due reduced cellular viability and high variability among the IGF2BP2 knockout clones. These data were not included in this thesis, and further studies are needed to systematically assess potential redundancy among the paralogs.

4.3 SLAMseq strategies to differentiate between transcriptional and post-transcriptional regulation

To differentiate between transcriptional and post-transcriptional changes upon IGF2BP3 depletion during ER stress, we performed a SLAMseq experiment with a 2-hour s^4U pulse. By calculating changes in the incorporation of s^4U, this approach directly detects changes in the nascent transcriptome allowing us to track transcriptional regulation [202]. Additionally, by comparing the ratios of total and T-C (newly transcribed) coverage, it estimates the changes on the level of mRNA stability [203]. In contrast, an alternative, catabolic mode of SLAMseq, involving a long pulse of s^4U followed by a washout, is tailored to determine mRNA half-lives directly, but does not allow addressing transcriptional changes [182]. Although we supported our SLAMseq results with an ActD chase RT-qPCR experiment, an additional catabolic SLAMseq experiment would expand and strengthen our findings. It should also be noted, that a 2-hour pulse is too long to address post-transcriptional regulation of mRNAs with short half-lives, as such transcripts will undergo complete turnover and will be replaced by newly transcribed molecules during the pulse. Both ActD chase and catabolic SLAMseq experiments could be performed with shorter time intervals to capture stability changes in transcripts with rapid turnover.

4.4 Limitations of IGF2BP3 long-term depletion and perspectives for acute degradation approaches

Both IGF2BP3 depletion approaches used in this work require substantial time, leading to cellular adaptation and transcriptional rewiring, which complicates the identification of the direct molecular mechanism of IGF2BP3 function. To overcome this limitation, acute depletion of IGF2BP3 using a targeted degradation system could be advantageous. In the course of this work, we developed two different degron systems to deplete IGF2BP3, however, both of them had their limitations incompatible with our research question. First, we endogenously tagged IGF2BP3 with the auxin-inducible degron (mAID) in cells expressing E3 ligase OsTIR1. In this system, treatment of cells with the plant hormone auxin brings tagged protein into the proximity of OsTIR1, resulting in protein ubiquitination and degradation [204]. With this approach, we achieved > 95% depletion of mAID-IGF2BP3 after 9 hours of treatment. Unfortunately, despite controlled expression of OsTIR1 from the doxycycline-inducible promoter designed to

minimize background degradation of the tagged protein, mAID-IGF2BP3 levels were reduced approximately 4-fold compared with the untagged control, making it impossible to detect IGF2BP3-mediated changes upon depletion. Moreover, treatment of cells with auxin resulted in substantial transcriptome changes, with effect sizes comparable to those expected upon IGF2BP3 depletion. It is possible that a newer version of the mAID system will overcome these limitations [205].

In the second approach, we endogenously tagged IGF2BP3 with an engineered haloalkane dehalogenase HaloTag, which covalently binds chloroalkane-containing ligands [206,207]. The proteolysis-targeting chimera compounds have been designed to bind HaloTag (HaloPROTACs) and target the fusion protein to the endogenous E3 ligase Hippel-Lindau (VHL) for ubiquitination and degradation [208,209]. Using an effective and commercially available compound, HaloPROTAC3 [209], we achieved 75% depletion of HaloTag-IGF2BP3 after 5 hours of treatment. To our surprise, HaloPROTAC3 induced ER stress independently of HaloTag-IGF2BP3 expression, preventing us from using it to study the UPR. These results were published and are summarized in Section 5.1. Recently, more efficient HaloPROTAC-E compound has been developed that requires lower concentrations to deplete HaloTag fusion proteins [210]. It has proved promising in our preliminary experiments, as even high concentrations of HaloPROTAC-E did not activate the UPR, and future experiments are planned with this compound to test effects of the acute depletion of IGF2BP3.

4.5 IGF2BP3 function in post-transcriptional regulation may extend beyond mRNA stability regulation

Previous studies have shown that IGF2BP3 can influence both mRNA stability [151,162] and translation [156]. This work focuses in particular on the role of IGF2BP3 in regulation of mRNA stability during ER stress. Nevertheless, we have addressed the possibility of translation regulation with a ribosome profiling experiment, that is published in the *bioRxiv* version of the manuscript (Section 2.2). Upon IGF2BP3 depletion, ribosome occupancy decreased modestly on several targets, including *DDIT3* (which encodes the pro-apoptotic transcription factor CHOP), indicating that IGF2BP3 contributes to its expression under ER stress. We also observed reduced translation of transcripts normally translationally upregulated during ER stress, mirroring the dampening of

transcriptional UPR branches upon IGF2BP3 loss and suggests general downregulation of the UPR.

Previous work suggests that IGF2BP3 inhibits translation of its targets, which can be detected at the bulk protein level [156]. Because our ribosome profiling experiments did not include spike-in controls for normalization of ribosome footprints and transcript levels, we could not quantify absolute changes. These data would be particularly important for testing our hypothesis that IGF2BP3-mediated degradation of mRNAs during ER stress contributes to the reduction of translational burden.

4.6 Physiological importance of IGF2BP3 role during ER stress

Our model of IGF2BP3 action during ER stress suggests that it facilitates UPR activation and helps cells adapt by reducing protein synthesis. However, IGF2BP3 depletion decreased activation of both pro-survival and pro-apoptotic UPR branches, making the final outcome difficult to predict. We cannot exclude the possibility that the effect varies depending on context, including cell type, the state of the transcriptome, and the extent and type of stress. Answering this question will require future experiments addressing how IGF2BP3 impacts fitness and viability in different cell types and under various ER stress conditions.

5 Appendix

In the appendix, I included results that I obtained and contributed to during my thesis work, but that are not part of the main story. These two studies contribute to the field of ER proteostasis regulation and are an important part of my PhD work.

5.1 HaloPROTAC3 treatment activates the unfolded protein response of the endoplasmic reticulum in nonengineered mammalian cell lines

5.1.1 Preamble

Investigating the depletion phenotypes is crucial for defining protein function. However, the most commonly used depletion approaches, such as CRISPR/Cas9 knockout or siRNA-mediated depletion, require long time frames (more than 24 hours) and often lead to the accumulation of indirect effects, making it difficult to understand the direct function of the studied protein. To address this limitation, the degrader compounds have been developed to induce rapid degradation of their protein targets. In this manuscript, I tested whether the heterobifunctional degrader HaloPROTAC3 could be used to achieve acute depletion of HaloTag-IGF2BP3. Using this system, we achieved ~75% depletion within 5 hours. Strikingly, HaloPROTAC3 induced the UPR not only in cells expressing HaloTag-IGF2BP3 but also in the parental non-engineered cell line. I further confirmed that HaloPROTAC3-mediated UPR induction occurs in mammalian cell lines of different origins. These findings provide important guidance for future studies using HaloPROTAC3 and highlight the importance of developing diverse degrader compounds.

This manuscript was published in *Molecular Biology of the Cell* on May 7th, 2025.

5.1.2 Contribution statement

I contributed to the conceptualization of this project, performed the experiments, analyzed the data, and was involved in the writing and editing of the manuscript.

HaloPROTAC3 treatment activates the unfolded protein response of the endoplasmic reticulum in nonengineered mammalian cell lines

Aleksandra S. Anisimova[a,b], and G Elif Karagöz[a,c,*]
[a]Max Perutz Labs Vienna, Vienna BioCenter, Vienna, Austria.; [b]Vienna BioCenter PhD Program, Doctoral School of the University of Vienna and Medical University of Vienna, Vienna, Austria.; [c]Medical University of Vienna, Vienna, Austria.

ABSTRACT **Proteins fused to HaloTag, an engineered haloalkane dehalogenase, can be depleted by a heterobifunctional degrader compound HaloPROTAC3. The binding of HaloPROTAC3 to both the HaloTag and the E3 ligase von Hippel-Lindau (VHL) brings them into proximity and mediates the degradation of the HaloTag fusion proteins. Here, we generated a colon cancer cell line HCT116 expressing HaloTag fused to the RNA-binding protein IGF2BP3 to study its function. HaloPROTAC3 treatment depleted 75% of HaloTag-IGF2BP3 in 5 h. Transcriptomics revealed that HaloPROTAC3 treatment resulted in the destabilization of IGF2BP3 target mRNAs and activated the unfolded protein response (UPR). Surprisingly, we found that HaloPROTAC3 results in UPR activation in nonengineered mammalian cells. Our data demonstrate that HaloPROTAC3 causes mild endoplasmic reticulum stress independent of IGF2BP3 function and shall guide future studies using the HaloPROTAC3 protein depletion strategy.**

SIGNIFICANCE STATEMENT

- Proteolysis-targeting chimeras (PROTACs) are degrader compounds that recruit the target proteins to the E3 ubiquitin ligases for subsequent degradation by the ubiquitin-proteasome system. PROTACs enable specific and temporal removal of proteins from the cell, yet their off-target effects of remain only partially uncovered.
- HaloPROTAC3 is a PROTAC that brings the engineered haloalkane dehalogenase HaloTag into the proximity of the E3 ligase VHL, allowing depletion of HaloTag fusion proteins. The authors report that HaloPROTAC3 treatment activated the UPR in nonengineered mammalian cells.
- This work will guide future studies using the HaloPROTAC3 as a protein depletion tool.

Monitoring Editor
Guillaume Thibault
Nanyang Technological University

Received: Aug 7, 2024
Revised: Mar 10, 2025
Accepted: Mar 14, 2025

New Methods

This article was published online ahead of print in MBoC in Press (http://www.molbiolcell.org/cgi/doi/10.1091/mbc.E24-08-0342) on March 19, 2025.
Author contributions: A.S.A. and G.E.K. conceived and designed the experiments; A.S.A. performed the experiments; A.S.A. analyzed the data; A.S.A. and G.E.K. drafted the article.
Conflicts of interest: The authors declare no competing financial interests.

*Address correspondence to: G Elif Karagöz (guelsuen.karagoez@meduniwien.ac.at).

Abbreviations used: ATF4, Activating Transcription Factor 4; CHOP, C/EBP homologous protein; CPM, counts per million; DDIT3, DNA Damage Inducible Transcript 3; DMSO, dimethyl sulfoxide; ER, endoplasmic reticulum; HMGA2, High Mobility Group AT-Hook 2; IGF2BP3, Insulin-like growth factor-2 messenger RNA-binding protein 3; IRE1, serine/threonine-protein kinase/endoribonuclease

INTRODUCTION

Targeted protein degradation enables specific and temporal removal of proteins from the cell by small-molecule degrader compounds (Tsai *et al.*, 2024). One class of such degrader compounds are proteolysis-targeting chimeras (PROTACs), which are heterobifunctional molecules that recruit the target proteins to the E3 ubiquitin ligases for their subsequent degradation by the ubiquitin-proteasome system (Bekes *et al.*, 2022; Tsai *et al.*, 2024). The most widely used E3 ligase for PROTAC-based approaches is the von Hippel-Lindau (VHL) due to the presence of its well-characterized small-molecule binders and its widespread expression in various tissues (Girardini *et al.*, 2019; Diehl and Ciulli, 2022). PROTACs provide a novel, powerful therapeutic approach for targets considered nontargetable by small molecules. While a large body of research focuses on the discovery of small molecules that specifically bind to the target of interest to generate target-specific PROTACs, fusing the protein of interest to a protein with established small-molecule binders has been an attractive strategy when target-specific PROTACs are not available with high potential as tool compounds in research.

One way such small-molecule degraders have recently been utilized in cell biology was for reversible and temporal depletion of a protein of interest. Temporally controlled protein depletion allows for the efficient depletion of essential proteins for cell viability. Moreover, short-term depletion largely eliminates indirect effects arising from long-term depletion of protein of interest enabling one to uncover protein function more accurately. To this end, short-term depletion strategies have been particularly powerful to unravel direct function of proteins involved in transcriptional and posttranscriptional mechanisms (Worner *et al.*, 2023; Ren *et al.*, 2024).

The HaloTag is an engineered haloalkane dehalogenase that specifically and irreversibly binds to chloroalkane linkers. Synthetic ligand variants, where the chloroalkane linker is attached to fluorescent dyes or affinity handles, enabled the HaloTag system as a versatile platform for a variety of applications ranging from imaging to handles for protein isolation (Los *et al.*, 2008; England *et al.*, 2015; Brannan *et al.*, 2016). Recently, HaloPROTACs have emerged as heterobifunctional PROTAC molecules (Buckley *et al.*, 2015; Tovell *et al.*, 2019). In addition to a chloroalkane linker that covalently binds to HaloTag, HaloPROTACs contain a small molecule that specifically binds to select E3 ligases. To date, HaloPROTACs engaging E3 ligases VHL, cereblon (CRBN), and cellular inhibitor of apoptosis protein 1 (cIAP1) have been developed (Buckley *et al.*, 2015; Caine *et al.*, 2020; Zhao *et al.*, 2021; Ody *et al.*, 2023). Yet, the HaloPROTAC3 that binds to VHL is most commonly used (Buckley *et al.*, 2015; Caine *et al.*, 2020; Zhao *et al.*, 2021). This way, HaloPROTACs bring the HaloTag (or its fusion proteins) into proximity of the E3 ligases, leading to their ubiquitination and degradation. This strategy has been successfully used for targeted protein degradation of HaloTag fusion proteins in cells (Buckley *et al.*, 2015; Caine *et al.*, 2020; Zhao *et al.*, 2021).

IGF2BP3 is an RNA-binding protein that controls mRNA stability, localization, and translation. IGF2BPs regulate many mRNAs involved in cellular growth, migration, and stemness (Yaniv and Yisraeli 2002; Conway *et al.*, 2016; Degrauwe *et al.*, 2016; Huang, Weng *et al.*, 2018). Furthermore, IGF2BPs are highly expressed in cancers where their upregulation correlates with tumor aggressiveness and poor patient outcomes (Ross *et al.* 2001; Dimitriadis *et al.*, 2007; Bell *et al.*, 2013; Samanta *et al.*, 2013; Degrauwe *et al.*, 2016; Xu *et al.*, 2019; Hanniford *et al.*, 2020; Huang *et al.*, 2020; Glass *et al.*, 2021). Consequently, revealing how IGF2BP3 regulates its mRNA targets and how this contributes to pathology is an active area of research. IGF2BP3 binds to and regulates mRNAs encoding for several transcription factors or regulators, including *MYC* and *HMGA2* (Jønson *et al.*, 2014; Huang, Zhang *et al.*, 2018). Long-term depletion of IGF2BP3 leads to transcriptional rewiring, and therefore it is very challenging to identify mRNAs regulated directly by IGF2BP3.

Here, we used the HaloPROTAC strategy to induce short-term depletion of IGF2BP3 in a colon cancer cell line (HCT116) and performed transcriptome analysis to decipher IGF2BP3 function. The treatment of cells with the small-molecule protein degrader HaloPROTAC3 resulted in the depletion of IGF2BP3 by 75% within 5 h. Transcriptomic analyses revealed that HaloPROTAC3 treatment led to the destabilization of canonical IGF2BP3 target mRNAs such as *HMGA2*. Notably, these data showed that HaloPROTAC3 treatment led to activation of the unfolded protein response (UPR), as indicated by the increased or decreased levels of the UPR target mRNAs. Validation experiments using real-time quantitative PCR (RT-qPCR) analyses showed that HaloPROTAC3 treatment induced the UPR in parental nonengineered colorectal carcinoma HCT116 cells, as well as in cervical carcinoma HeLa cells and human embryonic kidney HEK293T cells. Our data show that HaloPROTAC3 treatment induces mild endoplasmic reticulum (ER) stress in mammalian cells, activating the UPR. Our results should be taken into consideration when using HaloPROTAC3 for protein depletion in future studies.

RESULTS

HaloPROTAC3 treatment depletes HaloTag-IGF2BP3 in HCT116 cells

To study IGF2BP3 function and localization, we set out to attach a HaloTag to the N-terminus of IGF2BP3 in HCT116 cells using CRISPR-Cas9 gene editing. HCT116 cells express two IGF2BP paralogues, IGF2BP2 and IGF2BP3 (Mongroo *et al.*, 2011; Nusinow *et al.*, 2020; Anisimova and Karagöz, 2023). The paralogues are highly similar in amino acid sequence with high sequence identity and were suggested to bind to overlapping mRNA targets (Hafner *et al.* 2012; Bell *et al.*, 2013; Conway *et al.* 2016; Huang, Weng *et al.*, 2018). We first generated IGF2BP2 knockout (KO) HCT116 cells using CRISPR-Cas9 gene editing methods to overcome potential redundancy. We then tagged IGF2BP3 in its endogenous locus with an N-terminal HaloTag using CRISPR-Cas9 methods in IGF2BP2 KO HCT116 cells. Using PCR analyses of the genomic locus and Western blot analyses, we confirmed that in the engineered HCT116 cells the HaloTag was attached to the N-terminus of IGF2BP3 in both alleles (Supplemental Figure S1A). Western blot analyses showed that IGF2BP3 expression levels in parental cell lines were comparable with HaloTag-IGF2BP3, indicating that the HaloTag did not impact protein stability or expression (Figure 1, A and B).

inositol-requiring enzyme 1 α; PROTACs, proteolysis-targeting chimeras; RIDD, regulated IRE1α-dependent decay; RT-qPCR, real-time quantitative PCR; SLAM-seq, thiol(SH)-linked alkylation for the metabolic sequencing of RNA; TM, tunicamycin; UPR, unfolded protein response; VHL, E3 ligase von Hippel-Lindau; XBP1, X-Box Binding Protein 1.

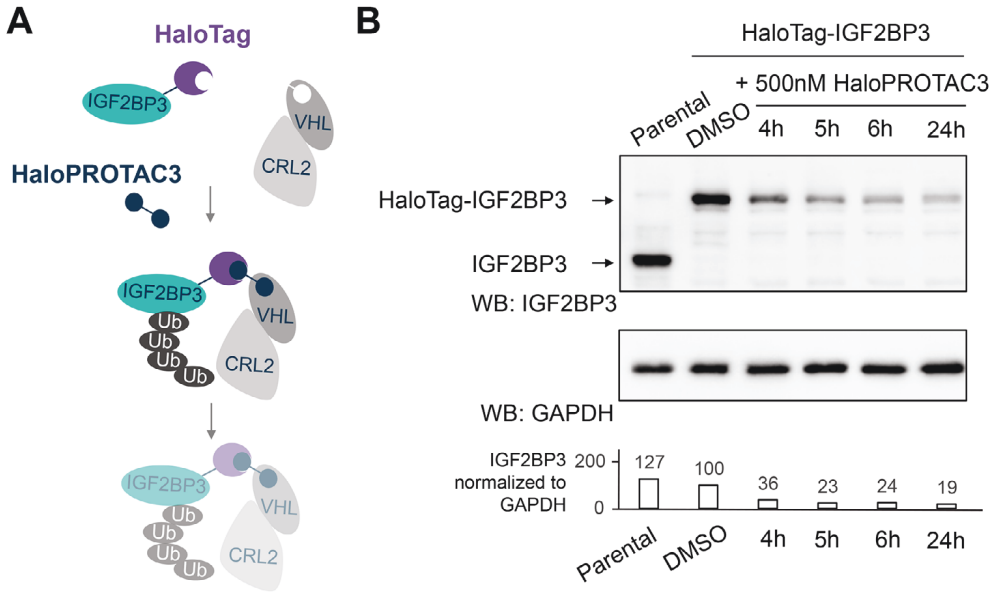

FIGURE 1: HaloPROTAC3 treatment depletes HaloTag-IGF2BP3 in HCT116 cells. (A) Schema of the HaloPROTAC3-mediated depletion of HaloTag-IGF2BP3 fusion. (B) Western blotting showing HaloPROTAC3-mediated depletion of HaloTag-IGF2BP3 in IGF2BP2 KO HCT116 cells. anti-IGF2BP3 (14642-1-AP, Proteintech) and anti-GAPDH (10494-1-AP, Proteintech) antibodies were used.

To achieve acute depletion of IGF2BP3 from mammalian cells, we used the HaloPROTAC3 strategy. We treated the cells with HaloPROTAC3 at 500 nM for different time spans, ranging from 4 to 24 h (Figure 1B). After 5 h, treatment with 500 nM HaloPROTAC3 led to around 75% depletion of IGF2BP3 in HCT116 cells. Therefore, we went on to study the function of IGF2BP3 under those conditions.

HaloPROTAC3 treatment leads to destabilization of IGF2BP3 target mRNAs and UPR induction in HCT116 cells expressing HaloTag-IGF2BP3

We performed global transcriptomics analyses using next-generation sequencing to reveal the transcripts regulated by IGF2BP3 in HCT116 cells. The transcriptomics data showed that HaloPROTAC3 treatment induced moderate changes in the HaloTag-IGF2BP3 HCT116 transcriptome (Figure 2, A and B; Supplemental Table S1). The levels of well-described IGF2BP3 mRNA target *HMGA2* decreased upon HaloPROTAC3 treatment (Figure 2, A and B; Supplemental Table S1), suggesting the destabilization of *HMGA2* upon depletion of HaloTag-IGF2BP3. These data recapitulated the published data on the direct IGF2BP3 targets via HaloPROTAC3-mediated depletion in HCT116 cells (Sheen *et al.*, 2015; Ennajdaoui *et al.*, 2016).

To characterize transcriptome changes upon short-term depletion of IGF2BP3 in HCT116 cells, we defined a group of genes whose total expression levels changed more than 20% with a *p*-value less than 0.1. This cutoff defined 178 down- and 160 upregulated genes upon HaloPROTAC3 treatment. Surprisingly, the gene ontology (GO) term analyses for upregulated genes upon HaloPROTAC3 treatment identified the UPR as the most prevalent biological process (Figure 2C). Instead, the genes down-regulated by HaloPROTAC3 did not converge on any particular biological pathway.

In mammals, the UPR is driven by three ER-tethered signaling sensors/transducers, IRE1, PERK, and ATF6 (Karagoz *et al.*, 2019). IRE1 is an ER-tethered kinase/RNase, which, upon activation, initiates nonconventional splicing of XBP1 mRNA through its RNase domain (Sidrauski and Walter, 1997; Tirasophon *et al.*, 1998; Wang *et al.*, 1998). Spliced XBP1 mRNA encodes for a potent transcription factor, XBP1s, which regulates the synthesis of downstream targets, including chaperones (*DNAJB9*) and lipid synthesis enzymes (Tirasophon *et al.*, 2000; Urano *et al.*, 2000). In addition, IRE1 cleaves mRNAs targeted to the ER by its RNase domain in a process called regulated IRE1-dependent decay (RIDD) (e.g., *BLOC1S1, DGAT2, TGOLN2, CD59*) (Hollien and Weissman, 2006; Hollien *et al.*, 2009b; Le Thomas *et al.*, 2021). PERK is an ER-tethered kinase that phosphorylates eIF2α upon activation, leading to transient translational shutdown during ER stress (Harding *et al.*, 1999; Harding *et al.*, 2000). Under those conditions, the transcription factor ATF4 is preferentially translated, which regulates the expression of UPR target genes including *DDIT3*. ATF6 is an ER-tethered transcription factor; during ER stress, it travels to the Golgi, where it is processed by the site 1 P and site 2 P proteases, releasing its transcription factor cytosolic domain from the Golgi (Yoshida *et al.*, 1998; Haze *et al.*, 1999). The processed ATF6 N-terminus (ATF6N) localizes to the nucleus to initiate transcription of its target genes, including *HSPA5* (Yoshida *et al.*, 2000). The transcriptomics data showed that apart from *HMGA2*, direct IRE1 RIDD mRNA targets (*TGOLN2, CD59, BCAM, DGAT2, TMEM19, and BLOC1S1*) (Hollien *et al.*, 2009a; Le Thomas *et al.*, 2021) were destabilized upon HaloPROTAC3 treatment suggesting the induction of IRE1 RNase activity (Figure 2, A and B). Moreover, the transcriptomics data showed specific enrichment of the downstream transcriptional targets of IRE1 driven by the UPR transcription factors XBP1s and ATF6 (e.g., *DNAJB9*, *HSPA5*, *XBP1*, *WFS1*) (Figure 2, A–C), while the transcriptional targets of the PERK-ATF4 branch (e.g., *DDIT3*, *PDIA4*) (Shoulders *et al.*, 2013) were not upregulated (Figure 2B).

To validate these data, we used RT-qPCR analyses to monitor the levels of the UPR targets XBP1s (spliced), *HSPA5*, *ATF4*, and *DDIT3* in HaloTag-IGF2BP3 HCT116 upon HaloPROTAC3 treatment. Additionally, in order to address to which extent HaloPROTAC3 induces the UPR, we used tunicamycin (TM) to induce ER

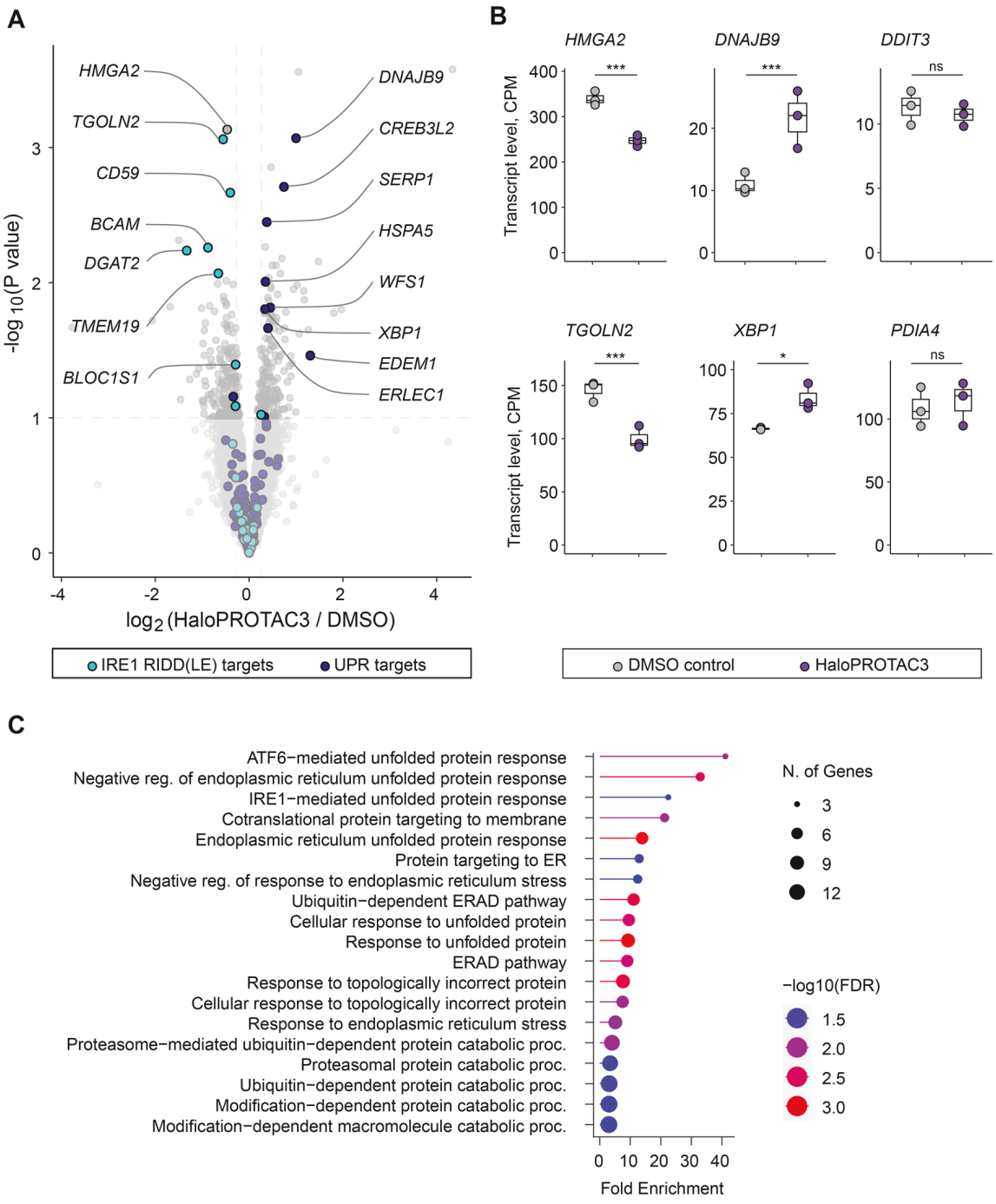

FIGURE 2: HaloPROTAC3 treatment leads to the destabilization of canonical IGF2BP3 targets and activation of the UPR. (A) Volcano plot showing transcriptome changes upon HaloPROTAC3-mediated depletion of HaloTag-IGF2BP3 (SLAMseq total gene counts per million (CPM), combining newly synthesized and pre-existed mRNAs). To deplete HaloTag-IGF2BP3 cells were treated with 500 nM HaloPROTAC3 for 7 h, DMSO was used as a control. IRE1 RIDD(LE) targets from (Le Thomas *et al.*, 2021) (lightblue) and UPR transcripts (GO:0006986, response to unfolded protein) (blue) are highlighted. (B) Boxplots showing total transcript levels (gene counts per million, CPM) upon HaloPROTAC3-mediated depletion of HaloTag-IGF2BP3. Differential expression analysis was reformed using edgeR glmQLFTest. *$P < 0.05$; **$P < 0.01$; ***$P < 0.001$. (C) GO term analysis of the genes differentially expressed upon treatment of HaloTag-IGF2BP3 expressing HCT116 with HaloPROTAC3. The genes were defined as differentially expressed when their fold change upon HaloPROTAC3 treatment was higher than 20% with edgeR (Robinson and Oshlack, 2010; Robinson *et al.*, 2010) *p*-value less than 0.1. $n = 3$ biological replicates. GO term analysis was performed with ShinyGo webserver (Ge *et al.*, 2020).

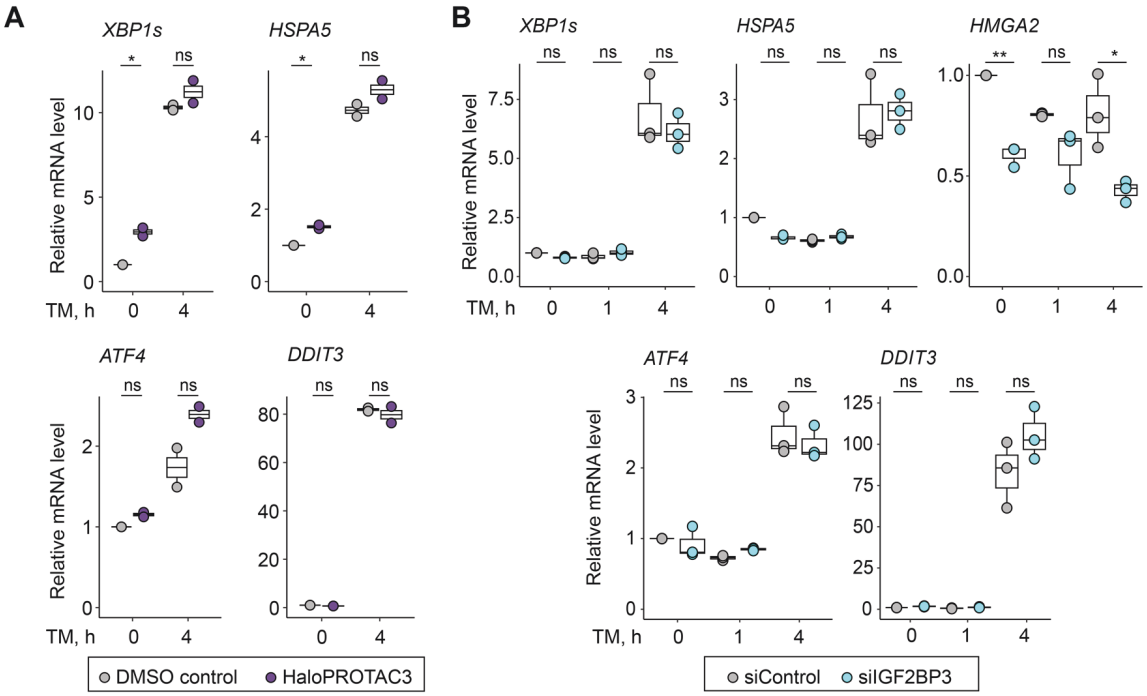

FIGURE 3: siRNA-mediated IGF2BP3 depletion does not result in the UPR activation. (A) RT-qPCR of HCT116 expressing HaloTag-IGF2BP3 upon HaloPROTAC3 treatment and ER stress induction with tunicamycin (TM). Cells were treated with 500 nM of HaloPROTAC3 for 7 h, DMSO was used as a control. In the last 3 h, DMSO or 5 μg/ml TM was added. The Cq values for the indicated mRNAs were normalized to *RPL6* mRNA levels and then to the control condition. $n = 2$ biological replicates. (B) RT-qPCR of HCT116 expressing HaloTag-IGF2BP3 upon siRNA-mediated depletion of HaloTag-IGF2BP3 and ER stress induction with TM. Cells were treated with 75 nM of siRNA against IGF2BP3 or nontargeting control for 48 h. ER stress was induced with 1 μg/ml TM, 4-h treatment with DMSO was used as a control condition. The Cq values for the indicated mRNAs were normalized to *RPL6* mRNA levels and then to the unstressed nontargeting siRNA condition. $n = 3$ technical replicates. $^*P < 0.05$; $^{**}P < 0.01$; one-sided Student's *t* test.

stress by inhibiting N-linked glycosylation in the ER. The RT-qPCR analyses confirmed the transcriptomics data showing that upon HaloPROTAC3 treatment the transcripts encoding for ATF6 and IRE1 target genes (*XBP1s, HSPA5*, and *ATF4* mRNAs) are upregulated (Figure 3A; Supplemental Figure S2A). The *XBP1s* mRNA levels increased 3-fold upon 7 h of HaloPROTAC3 treatment in comparison to the 12-fold increase observed by 3-h tunicamycin treatment (5 μg/ml). Therefore, our data indicated that HaloPROTAC3 treatment resulted in mild UPR activation compared with the ER stress–inducing drugs commonly used in the literature.

HaloPROTAC3 treatment leads to UPR activation in nonengineered mammalian cell lines

To confirm our findings, we used small interfering RNAs (siRNA) as an orthogonal strategy to deplete IGF2BP3. Using siRNAs, we depleted IGF2BP3 up to 85% after 48 h (Supplemental Figure S2, B and C) (Anisimova and Karagöz, 2023). Next, we tested the impact of IGF2BP3 depletion on select mRNAs using RT-qPCR. We focused on the UPR targets *XBP1s, HSPA5*, *ATF4*, *DDIT3*, and the canonical IGF2BP3 target *HMGA2*. While those experiments confirmed the destabilization of *HMGA2* upon IGF2BP3 depletion, surprisingly, siRNA depletion of IGF2BP3 did not lead to increased expression of the UPR targets (Figure 3B).

As the siRNA-based depletion strategy did not recapitulate the findings obtained by depleting IGF2BP3 by HaloPROTAC3, we wondered whether some of these effects on mRNA levels were independent of the IGF2BP3 function and are due to the indirect effect of the drug treatment. To test this, we treated nonengineered wild-type HCT116 cells with HaloPROTAC3 and performed RT-qPCR and Western blotting analyses for select UPR targets. The RT-qPCR data showed activation of the UPR target genes and decrease in the levels of IRE1's RIDD targets in those nonengineered cells upon 7 h of HaloPROTAC3 treatment. Importantly, the UPR induction of the nonengineered HCT116 cells upon HaloPROTAC3 treatment was at similar levels as in Halo-IGF2BP3 expressing cells (Figures 3A and 4A; Supplemental Figure S2A). At the protein level, we could observe accumulation of XBP1s protein, suggesting activation of the IRE1 branch of the UPR. In contrast, we could only detect CHOP (*DDIT3*) at the highest HaloPROTAC3 concentration (5 μM), while we could not detect the processing of ATF6 at all the concentrations tested (Figure 4B). These data suggested that the IRE1 branch is more sensitive to HaloPROTAC3 treatment compared with PERK and ATF6 branches. Our findings revealed that HaloPROTAC3 treatment induces mild ER stress and activates the UPR in HCT116 cells.

We next tested whether HaloPROTAC3 treatment induces UPR in other commonly used mammalian cell lines HeLa and HEK293T. To this end, we treated HCT116, HeLa, and HEK293T cells with two different batches of HaloPROTAC3 at two different concentrations (100 and 500 nM) (Figure 5, A–C). Next, we performed RT-qPCR analyses to test UPR activation. The HaloPROTAC3 treatment induced UPR in all tested cell lines, indicated by accumulation of *XBP1s* and *HSPA5* mRNAs. While HeLa cells responded similarly to HaloPROTAC3 as the HCT116 cells, the HEK293Ts werethe least sensitive. Importantly, these cell lines showed differences in their sensitivity to the ER stressor tunicamycin suggesting that their UPR

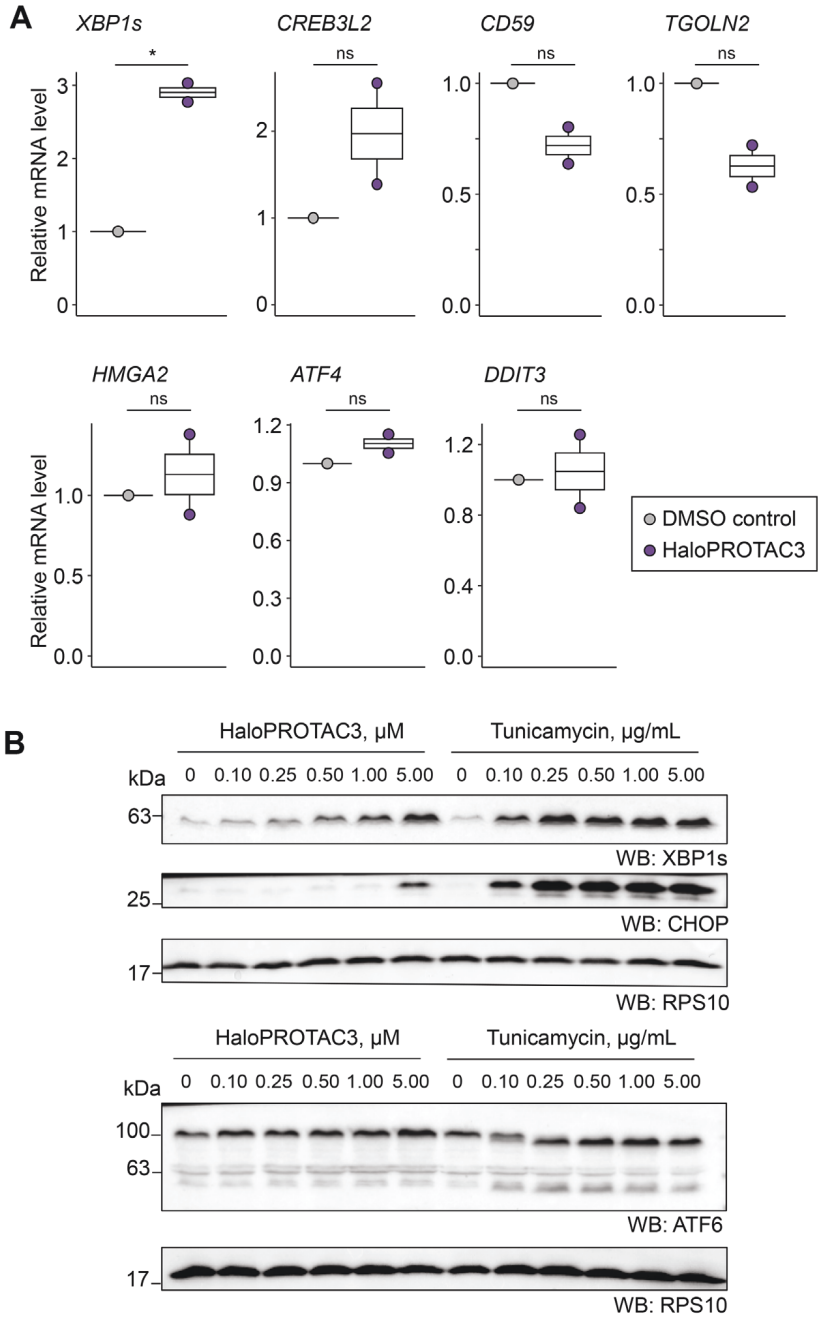

FIGURE 4: HaloPROTAC3 induces the UPR in nonengineered HCT116 cells. (A) RT-qPCR of nonengineered HCT116 cells upon HaloPROTAC3 treatment. Cells were treated with 500 nM of HaloPROTAC3 for 7 h, DMSO at 1:5000 dilution was used as a control. The Cq values for the indicated mRNAs were normalized to *RPL6* mRNA levels and then to the control condition. $n = 2$ biological replicates. $^{*}P < 0.05$; $^{**}P < 0.01$; one-sided Student's *t* test. (B) Western blotting of nonengineered HCT116 cells treated with HaloPROTAC3 or TM for 9 h at indicated concentrations. DMSO 1:1000 9-h treatment was used as a control.

signaling is wired differently (Supplemental Figure S3A). To sum up, we found that HaloPROTAC3 activates UPR in nonengineered mammalian cell lines.

HaloPROTAC3 treatment does not activate HIF-1

The overexpression of HIF-1 was shown to induce the UPR (Delbrel *et al.*, 2018). The E3 ligase VHL regulates the transcription factor HIF-1, and it has been shown that HIF-1 core target genes are upregulated upon VHL inhibition (Frost *et al.*, 2019). We speculated that the competition between HaloPROTAC3 and the endogenous VHL targets might lead to increased levels of HIF-1 and lead to the UPR activation phenotype observed here. To test this, we checked whether HaloPROTAC3 treatment results in the upregulation of HIF-1 target genes in HCT116 cells. Our transcriptomics data showed that under the tested conditions, the levels of most of the HIF-1 targets remained similar to control conditions, while some showed a slight decrease (Frost *et al.*, 2019). These data indicated that the HIF-1 activation is not the cause of the HaloPROTAC3-induced UPR activation in HCT116 cells (Figure 6, A and B; Supplemental Table S1).

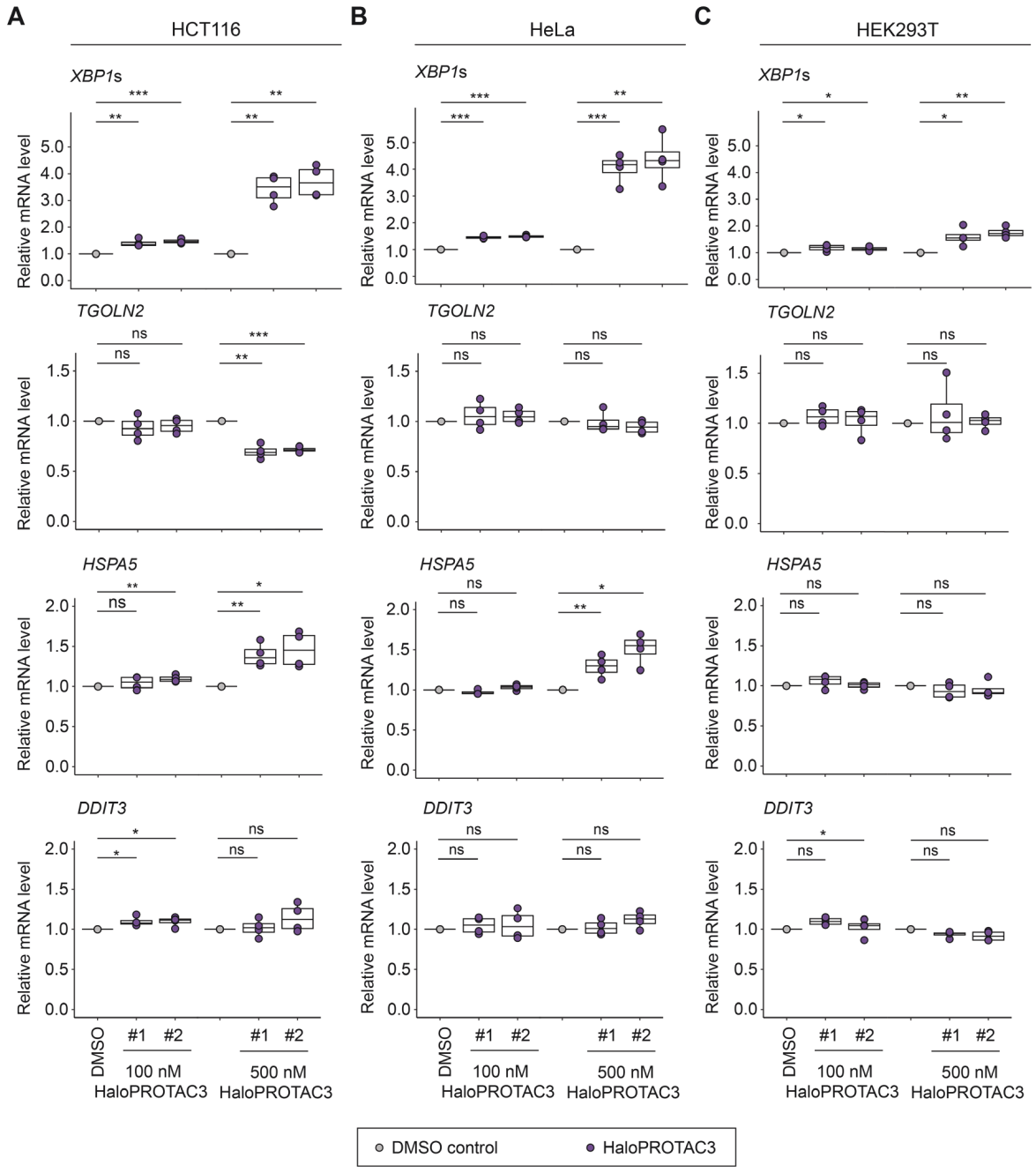

FIGURE 5: HaloPROTAC3 induces the UPR in nonengineered mammalian cell lines. RT-qPCR of nonengineered (A) HCT116, (B) HeLa, and (C) HEK293T cells upon HaloPROTAC3 treatment. Cells were treated with 100 or 500 nM of HaloPROTAC3 for 7 h, DMSO at 1:5000 or 1:1000 dilution was used as a control. Two batches of HaloPROTAC3 were tested (#1: CS2072A01 [batch # 0000441121] and #2: GA3110, Promega). The Cq values for the indicated mRNAs were normalized to *RPL6* mRNA levels and then to the control condition. $n = 4$ biological replicates. *$P < 0.05$; **$P < 0.01$; ***$P < 0.001$; ****$P < 0.0001$; one-sided Student's *t* test.

DISCUSSION

IGF2BPs regulate multiple mRNAs that are important for cell proliferation and growth, including several transcription factors. Therefore, their long-term depletion leads to the rewiring of transcriptional programs making the identification of mRNAs that are directly regulated by IGF2BPs highly challenging (Jønson *et al.*, 2014; Conway *et al.*, 2016; Ennajdaoui *et al.*, 2016; Busch *et al.* 2016; Huang, Weng *et al.*, 2018). Here, we used a PROTAC-based strategy for the depletion of IGF2BP3 from HCT116 cells using HaloPROTAC3. HaloPROTAC3 treatment led to around 75% depletion of HaloTag-IGF2BP3 in HCT116 cells in around 4 h. Global transcriptomics analyses revealed that HaloPROTAC3 treatment resulted in destabilization of the canonical mRNA targets of IGF2BP3, indicating that short-term protein depletion is a viable strategy to study IGF2BP3 function. It also revealed that HaloPROTAC3 treatment resulted in increased levels of the UPR target genes and decreased levels of the RIDD target mRNAs of the UPR sensor IRE1. Validation experiments using an orthogonal

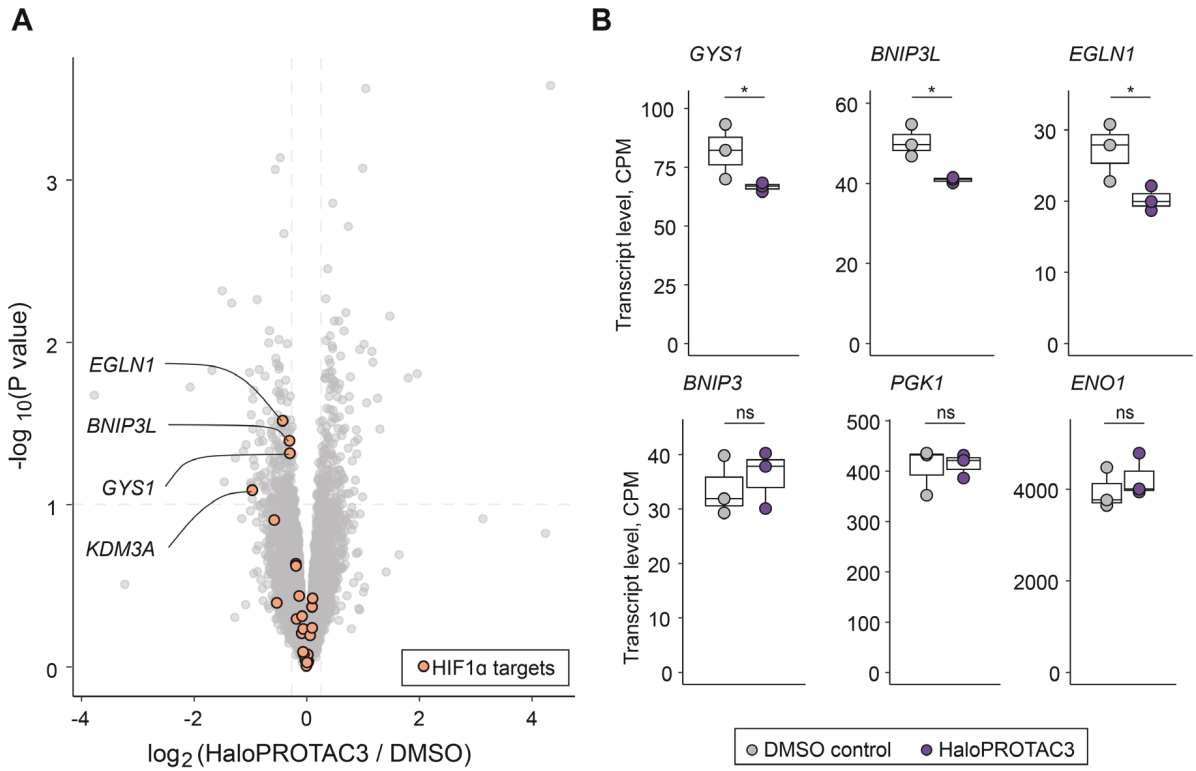

FIGURE 6: HaloPROTAC3 treatment did not upregulate the HIF-1 targets. (A) Volcano plot showing transcriptome changes upon HaloPROTAC3-mediated depletion of HaloTag-IGF2BP3 (SLAMseq total CPMs, combining new and old mRNAs). HCT116 cells were treated with 500 nM HaloPROTAC3 for 7 h, DMSO was used as a control. HIF-1 targets from (Frost *et al.*, 2019) (list of genes upregulated in VH032) (orange) are highlighted. (B) Boxplots showing total transcript levels (gene count per million, CPM) for selected genes. $n = 3$ biological replicates. Differential expression analysis was reformed using edgeR glmQLFTest. *$P < 0.05$; **$P < 0.01$; ***$P < 0.001$.

depletion strategy by siRNA knockdown of IGF2BP3 confirmed that depletion of IGF2BP3 results in the destabilization of its canonical target *HMGA2*. However, siRNA depletion of IGF2BP3 did not recapitulate the results on the UPR target genes obtained by the HaloPROTAC3 strategy. Importantly, HaloPROTAC3 treatment resulted in UPR induction in the parental HCT116 cells that do not express HaloTag fusion protein and in other mammalian cell lines of different tissue origin, HeLa and HEK293T. Altogether, our data revealed an indirect effect of HaloPROTAC3 inducing mild ER stress independent of IGF2BP3 in mammalian cells.

While we do not know how HaloPROTAC3 induces ER stress, our transcriptomics data suggest that it is not through interference with the VHL-mediated regulation of HIF-1. The genes that were most significantly upregulated during HaloPROTAC3 treatment mapped to the IRE1 branch of the UPR. Notably, in HCT116 cells apart from IRE1's transcriptional targets, the RIDD targets were also substantially down-regulated, even to a similar extent as they were down-regulated during the treatment of cells with potent ER stress–inducing drugs such as tunicamycin (Hollien *et al.*, 2009b; Le Thomas *et al.*, 2021). In contrast, we could not detect ATF6 processing to ATF6N by Western blotting. Therefore, we cannot conclude whether the increase of ATF6 targets (e.g., *HSPA5* and *WFS1*) is due to slight activation of ATF6 (undetectable by Western blotting) or whether they are induced by IRE1 consistent by earlier reports (Asada *et al.* 2011; Kondo *et al.*, 2011). It is plausible that by directly binding to IRE1 or IRE1-specific regulatory proteins such as ERdj4 (Amin-Wetzel *et al.*, 2017), HaloPROTAC3 induces its activation. However, further experiments are required to test these possibilities.

HaloPROTAC3 binds to the E3 ligase VHL with an IC_{50} of 0.54 ± 0.06 μM and the recommended HaloPROTAC3 concentration for depletion of endogenous proteins is 300 nM (Buckley *et al.*, 2015). As IGF2BP3 is a highly expressed protein, we used 500 nM HaloPROTAC3 in our experiments. In line with the IC_{50}, the treatment of cells with 500 nM HaloPROTAC3 enabled 75% depletion of IGF2BP3 from HCT116 cells. Therefore, we performed all the subsequent analyses under those conditions. The RT-qPCR and Western blot analyses of XBP1s show that 500 nM HaloPROTAC3 treatment leads to 25% XBP1s levels in HCT116 cells compared with what is achieved by the treatment of cells with 5 μg/ml tunicamycin for 4 h. Our data were reproduced by three different batches of HaloPROTAC3, indicating that this is not a batch effect but a reproducible effect of the drug on HCT116 cells.

The HaloPROTAC3 treatment only results in mild ER stress and does not largely impair the viability. However, induction of mild ER stress might functionally impact several biological processes. Moreover, with the depletion of the protein of interest, ER stress induction might show synergistic or antagonistic effects that either enhance or mask the phenotypes exhibited by the protein of interest. Therefore, our findings shall be considered when HaloPROTAC3 is used in future studies (Lin *et al.*, 2009). We anticipate our data will guide studies that aim to use the HaloPROTAC3 strategy to deplete proteins and future chemical efforts to engineer more potent versions or different PROTAC modalities.

MATERIALS AND METHODS

Request a protocol through *Bio-protocol*

Cell culture and drug treatment

Parental human colorectal carcinoma HCT116 cells conditionally expressing Tet-OsTIR1 were obtained from the Masato Kanemaki lab (Natsume *et al.*, 2016). The cells were tested for *Mycoplasma* contamination and *Mycoplasma* contamination was not detected. HCT116 WT cells were a kind gift from Prof. Manuela Baccarini (Max Perutz Labs). HEK293 Flp-In T-REx cells were obtained through Invitrogen. HeLa cells were a kind gift from Dr. Shotaro Otsuka (Max Perutz Labs). The HCT116 cells were cultured in McCoy's 5A (modified) medium (Sigma) with 10% FBS (Life Technologies), 2 mM glutamine (Sigma), 1% Pen/Step (Sigma). HEK293T and HeLa and cells were cultured DMEM (Sigma) with 10% FBS (Life Technologies), 2 mM glutamine (Sigma), 1% Pen/Step (Sigma). Where indicated cells were treated with thapsigargin (Sigma), tunicamycin (Sigma) or HaloPROTAC3 (three orders of: CS2072A01 [batches # 0000441121 and 0000369685] and GA3110, Promega). For siRNA knockdown, cells were transfected with ONTARGETplus Human IGF2BP3 (Dharmacon, L-003976-00-0005) SMARTpool siRNAs using DharmaFECT 2 (Dharmacon, T-2002-01) at 75 nM for 48 hours. ONTARGETplus nontargeting siRNA #1 (Dharmacon, D-001810-01-05) was used as a control.

Generation of HCT116 IGF2BP2 KO cells expressing IGF2BP3 endogenously tagged with HaloTag

Parental cell line origin and culture conditions. For IGF2BP2 KO cell line generation, gRNA sequence 5′-GAGCTGCCGGAGGTCG TCGG-3′ was cloned into the pSpCas9 (BB)-2A-GFP (PX458) (plasmid #48138, Addgene) (Ran *et al.*, 2013). HCT116 Tet-OsTIR1 cells were transiently transfected using jetOPTIMUS reagent (Tamar, 101000051), and GFP-positive single-cell clones were FACS sorted at BD FACSAria IIIu at Max Perutz Labs BioOptics FACS Facility.

Cloning of the homology directed repair template for HaloTag-IGF2BP3. To endogenously tag IGF2BP3 with HaloTag we have ordered (IDT) the sequence of N-terminal homology arms (629 bp before and 78 bp after the Cas9 cut site) of IGF2BP3 with SacI, SalI, BamI, and XhoI restriction sites. The gene block was amplified using gene block adapter primers. The IGF2BP3 homology arms were inserted into the pMK344 plasmid backbone (Addgene #121179) using SacI and XhoI restriction sites. HaloTag sequence was amplified from pHaloTag-EGFP plasmid (a gift from Thomas Leonard Lab) using SalI_HaloTag_F forward and BamHI_HaloTag_R reverse primers and inserted into the plasmid with N-terminal homology arms of IGF2BP3 using SalI and BamI restriction sites resulting in the homology directed repair (HDR) template. The PAM sites were mutated in the HDR template using site-directed mutagenesis with a primer pair (IGF2BP3_PAM_mut_F and IGF2BP3_PAM_mut_R).

Generation of the HCT116 IGF2BP2 KO HaloTag-IGF2BP3 cell line. To endogenously introduce the HaloTag-IGF2BP3 into HCT116 IGF2BP2 KO cells were transiently transfected with an equimolar mixture of the HaloTag-IGF2BP3 HDR template plasmid and pSpCas9 (BB)-2A-GFP (PX458) (plasmid #48138, Addgene) (Ran *et al.*, 2013) targeting the first exon of IGF2BP3 gene using the Fugene HD (Promega) reagent according to the manufacturer's instructions. Cells were cultured for additional 3 d, labeled with the Janelia Fluor 646 (GA1120, Promega) according to the rapid, no-wash labeling protocol of the manufacturer. The HaloTag-positive single-cell clones were FACS sorted at BD FACSAria IIIu at Max Perutz Labs BioOptics FACS Facility.

Genotyping of HCT116 IGF2BP2 KO HaloTag-IGF2BP3 clones. The initial screening of the HaloTag-positive single-cell clones was done using Western blot analysis with anti-IGF2BP3 (14642-1-AP, Proteintech) and anti-GAPDH (10494-1-AP, Proteintech) antibodies. HaloTag-IGF2BP3 positive clones that did not express the wild-type IGF2BP3 were further characterized with the PCR from the genomic DNA. The genomic DNA was isolated using the DirectPCR Lysis-Reagent Cell (Peqlab, VWR). To verify the insertion of the HaloTag-IGF2BP3, we used the primer pair targeting the 5′UTR of IGF2BP3 and HaloTag (HaloIGF2BP3_5UTR_2_F and HaloIGF2BP3_Halo_1_R). To distinguish between the homozygous and heterozygous insertion, we used the primer pair targeting 5′UTR and CDS of IGF2BP3 (HaloIGF2BP3_5UTR_1_F and HaloIGF2BP3_CDS_1_R). All mentioned sequences are listed in Supplemental File S1.

Transcriptomics of IGF2BP2 KO HaloTag-IGF2BP3 HCT116 cells upon HaloPROTAC3 treatment.

SLAMseq library preparation. For the transcriptomic analysis, two millioncells were plated per a 6-well plate 2 d before collection. Cells were treated with 500 nM HaloPROTAC3 for 7 h, DMSO in 1:5000 dilution was used as a control. Transcriptome sequencing was performed using thiol(SH)-linked alkylation for the metabolic sequencing of RNA (SLAMseq) protocol (Herzog *et al.*, 2017). The newly synthesized RNAs were labeled with 250 µM 4-thiouridine (4SU) (Sigma) for last 2 h of HaloPROTAC3 treatment. Cells and RNA were protected from light until 4SU was alkylated. Cells were washed with PBS and collected in 1 ml of peqGOLD TriFast (Peqlab, VWR). A total of 200 µl of chloroform:IAA (AppliChem) was added and samples were vortexed for 15 s and centrifuged at 16,000 × *g* for 15 min to separate the phases. DTT was added to the aqueous phase to 0.1 mM. RNA was precipitated by adding isopropanol (Sigma) in 1:1 ratio and 1 µl of 20 mg/ml glycogen (Thermo Fisher Scientific). RNA was incubated at the room temperature for 10 min, centrifuged at 20,000 × *g* for 20 min at 4°C and washed with 75% ethanol supplemented with 0.1 mM DTT. The RNA pellets were resuspended in nuclease-free water supplemented with 1 mM DTT and RNaseIn (N2515, Promega) at 1:50 dilution and incubated for 10 min at 55°C. A total of 10 µg of RNA was taken for alkylation reaction (10 µg of RNA, 5 µl of 100 mM iodoacetamide [Sigma] in ethanol, 50 mM $NaPO_4$ pH 8.0, 50% DMSO) and incubated at 50°C for 15 min. The reaction was quenched with 1 µl of 1 M DTT.

The RNA was precipitated using ethanol method, washed with 75% ethanol and resuspended in nuclease-free water. The sequencing libraries were prepared using QuantSeq 3′ mRNA-Seq Library Prep Kit FWD with UDI (Lexogen) and sequenced on a NovaSeq S1 XP lane at SR100 the Vienna BioCenter NGS facility producing ~40 million reads per sample.

SLAMseq data analysis. BCL files were converted to demultiplexed fastq files with bcl2fastq v2.20.0.422. The quality of fastq files was checked with fastqc 0.11.9. The fastq files were trimmed and aligned to human genome hg38 using the nf-core/slamseq analysis pipeline v1.0.0 (Neumann *et al.*, 2019, Ewels, 2020 #5564) with default parameters with the following changes: multimappers were excluded, T2C reads were called if at least one T2C transition was detected, and a variant fraction cutoff was 0.2. Total gene counts for protein coding genes were Relative Log Expression

(RLE) normalized to calculate the counts per million values (CPM) and the differential expression analysis was performed with edgeR (Robinson *et al.*, 2010). GO term analysis was performed with ShinyGo webserver (Ge *et al.*, 2020). The computational results of this work have been achieved using the Life Science Compute Cluster (LiSC) of the University of Vienna.

RNA isolation and RT-qPCR. For RT-qPCR analyses of HCT116 IGF2BP2 KO cells expressing HaloTag-IGF2BP3 total RNA was isolated using peqGOLD TriFast (Peqlab, VWR). Cells were grown in 24-well plates and collected at ~70% confluency. Cells were washed with PBS and collected in 0.1 ml of peqGOLD TriFast (Peqlab, VWR). A total of 50 µl nuclease-free water and 30 µl of chloroform:IAA (AppliChem) was added and samples were vortexed for 15 s and centrifuged at 16,000 × *g* for 15 min to separate the phases. RNA was precipitated by adding isopropanol (Sigma) in 1:1 ratio and 0.5 µl of 20 mg/ml glycogen (Thermo Fisher Scientific). RNA was incubated at the room temperature for 10 min, centrifuged at 20,000 × *g* for 20 min at 4°C and washed with 75% ethanol. RNA pellets were resuspended in 10 µl of DNase I reaction mix (1x DNase I buffer (NEB), 0.5 µl RNase-free DNase I (NEB), 0.1 µl RNaseIn (Promega)) and incubated for 10 min at 37°C. To stop DNase digestion EDTA was added at final concentration of 5 mM and the reaction was incubated for 10 min at 70°C. The RNA was precipitated using isopropanol method, washed with 75% ethanol and resuspended in nuclease-free water.

For RT-qPCR analyses of nonengineered HCT116 WT, HeLa and HEK293T cells total RNA was isolated using the KingFisher Flex Purification System (Thermo Fisher Scientific) with the High-Performance RNA Isolation kit (Molecular Tools Shop, Vienna BioCenter). During the isolation, RNA was treated with DNase I (M0303S, NEB).

cDNA was prepared with LunaScript RT SuperMix (NEB) and amplified in a qPCR reaction with 2x Hot Start qPCR master mix (Molecular Tools Shop, Vienna BioCenter) using BioRad CFX 384 Touch machine. The qPCR primers are listed in Supplemental File S1.

Western blotting. Cells at ~70% confluency were washed with PBS and lysed using RIPA buffer (25 mM Tris-HCl pH 7.4, 150 mM NaCl, 1% NP-40, 0.5% sodium deoxycholate, 0.1% SDS, 1× protease inhibitors cocktail [Roche]), lysed on ice for 20 min and the lysate was clarified by centrifugation at 20,000 × *g* for 20 min at 4°C. Proteins were separated by 15% SDS–PAGE, transferred to nitrocellulose membranes, and detected using Pierce ECL Western Blotting Substrate (Thermo Fisher Scientific). The following antibodies were used: anti-IGF2BP3 (14642-1-AP, Proteintech), anti-GAPDH (10494-1-AP, Proteintech), anti-XBP1s (E9V3E) (#40435, Cell Signaling Technology), anti-CHOP (L63F7) (#2895, Cell Signaling Technology), anti-RPS10 (ab151550, Abcam), anti-ATF6 (24169-1-AP, Proteintech), and anti-Rabbit IgG (H+L), HRP Conjugate (W4011, Promega).

Data availability

All raw and processed sequencing data generated in this study have been deposited in the Gene Expression Omnibus database, https://www.ncbi.nlm.nih.gov/geo/ (accession no. GSE274227).

ACKNOWLEDGMENTS

We are grateful to Stefan Ameres and Niko Popitsch for support with the transcriptomics experiment and analyses of the sequencing data and to the Vienna BioCenter Next-Generation Sequencing Facility for deep sequencing services. We thank Roland Foisner and Nana Naetar-Kerenyi for their input on CRISPR/Cas9 editing, Mila Asparuhova for the help with genotyping of HaloTag-IGF2BP3 HCT116 clones, and Dhaarsini Koneswarakantha for help with RT-qPCR. G.E.K. acknowledges funding from the Austrian Science Fund (FWF-SFB F79) and the Vienna Science and Technology Fund (WWTF-LS21-009). A.S.A. is supported by the DOC Fellowship Programme of the Austrian Academy of Sciences.

REFERENCES

Amin-Wetzel N, Saunders RA, Kamphuis MJ, Rato C, Preissler S, Harding HP, Ron D (2017). A J-protein co-chaperone recruits BiP to monomerize IRE1 and repress the unfolded protein response. Cell 171, 1625–1637.e13.

Anisimova AS, Karagöz GE (2023). Optimized infrared photoactivatable ribonucleoside-enhanced crosslinking and immunoprecipitation (iPAR-CLIP) protocol identifies novel IGF2BP3-interacting RNAs in colon cancer cells. RNA 29, 1818–1836.

Asada R, Kanemoto S, Kondo S, Saito A, Imaizumi K (2011). The signalling from endoplasmic reticulum-resident bZIP transcription factors involved in diverse cellular physiology. J Biochem 149, 507–518.

Bekes M, Langley DR, Crews CM (2022). PROTAC targeted protein degraders: The past is prologue. Nat Rev Drug Discov 21, 181–200.

Bell JL, Wächter K, Mühleck B, Pazaitis N, Köhn M, Lederer M, Hüttelmaier S (2013). Insulin-like growth factor 2 mRNA-binding proteins (IGF2BPs): post-transcriptional drivers of cancer progression? Cell Mol Life Sci 70, 2657–2675.

Brannan KW, Jin W, Huelga SC, Banks CA, Gilmore JM, Florens L, Washburn MP, Van Nostrand EL, Pratt GA, Schwinn MK, *et al.* (2016). SONAR discovers RNA-binding proteins from analysis of large-scale protein-protein interactomes. Mol Cell 64, 282–293.

Buckley DL, Raina K, Darricarrere N, Hines J, Gustafson JL, Smith IE, Miah AH, Harling JD, Crews CM (2015). HaloPROTACS: Use of small molecule PROTACs to induce degradation of HaloTag fusion proteins. ACS Chem Biol 10, 1831–1837.

Busch B, Bley N, Müller S, Glaß M, Misiak D, Lederer M, Vetter M, Strauß H-G, Thomssen C, Hüttelmaier S (2016). The oncogenic triangle of HMGA2, LIN28B and IGF2BP1 antagonizes tumor-suppressive actions of the let-7 family. Nucleic Acids Res 44, 3845–3864.

Caine EA, Mahan SD, Johnson RL, Nieman AN, Lam N, Warren CR, Riching KM, Urh M, Daniels DL (2020). Targeted protein degradation phenotypic studies using HaloTag CRISPR/Cas9 endogenous tagging coupled with HaloPROTAC3. Curr Protoc Pharmacol 91, e81.

Conway AEE, Nostrand ELV, Pratt GAA, Aigner S, Wilbert MLL, Sundararaman B, Freese P, Lambert NJJ, Sathe S, Liang TYY, *et al.* (2016). Enhanced CLIP uncovers IMP protein-RNA targets in human pluripotent stem cells important for cell adhesion and survival. Cell Rep 15, 666–679.

Degrauwe N, Suva ML, Janiszewska M, Riggi N, Stamenkovic I (2016). IMPs: An RNA-binding protein family that provides a link between stem cell maintenance in normal development and cancer. Genes Dev 30, 2459–2474.

Delbrel E, Soumare A, Naguez A, Label RBernard O, Bruhat A, Fafournoux P, Tremblais G, Marchant D, Gille T, *et al.* (2018). HIF-1alpha triggers ER stress and CHOP-mediated apoptosis in alveolar epithelial cells, a key event in pulmonary fibrosis. Sci Rep 8, 17939.

Diehl CJ, Ciulli A (2022). Discovery of small molecule ligands for the von Hippel-Lindau (VHL) E3 ligase and their use as inhibitors and PROTAC degraders. Chem Soc Rev 51, 8216–8257.

Dimitriadis E, Trangas T, Milatos S, Foukas PG, Gioulbasanis I, Courtis N, Nielsen FC, Pandis N, Dafni U, Bardi G, Ioannidis P (2007). Expression of oncofetal RNA-binding protein CRD-BP/IMP1 predicts clinical outcome in colon cancer. Int J Cancer 121, 486–494.

England CG, Luo H, Cai W (2015). HaloTag technology: A versatile platform for biomedical applications. Bioconjug Chem 26, 975–986.

Ennajdaoui H, Howard JM, Sterne-Weiler T, Jahanbani F, Coyne DJ, Uren PJ, Dargyte M, Katzman S, Draper JM, Wallace A, *et al.* (2016). IGF2BP3 modulates the interaction of invasion-associated transcripts with RISC. Cell Rep 15, 1876–1883.

Frost J, Ciulli A, Rocha S (2019). RNA-seq analysis of PHD and VHL inhibitors reveals differences and similarities to the hypoxia response. Wellcome Open Res 4, 17.

Ge SX, Jung D, Yao R (2020). ShinyGO: A graphical gene-set enrichment tool for animals and plants. Bioinformatics 36, 2628–2629.

Girardini M, Maniaci C, Hughes SJ, Testa A, Ciulli A (2019). Cereblon versus VHL: Hijacking E3 ligases against each other using PROTACs. Bioorg Med Chem 27, 2466–2479.

Glass M, Misiak D, Bley N, Muller SHagemann S, Busch B, Rausch A, Huttelmaier S (2021). IGF2BP1, a conserved regulator of RNA turnover in cancer. Front Mol Biosci 8, 632219.
Hafner M, Lianoglou S, Tuschl T, Betel D (2012). Genome-wide identification of miRNA targets by PAR-CLIP. Methods, 58, 94–105.
Hanniford D, Ulloa-Morales A, Karz ABerzoti-Coelho MGMoubarak RS, Sánchez-Sendra B, Kloetgen A, Davalos V, Imig J, Wu P, *et al.* (2020). Epigenetic silencing of CDR1as drives IGF2BP3-mediated melanoma invasion and metastasis. Cancer Cell 37, 55–70.e15.
Harding HP, Novoa I, Zhang Y, Zeng HWek R, Schapira M, Ron D (2000). Regulated translation initiation controls stress-induced gene expression in mammalian cells. Mol Cell 6, 1099–1108.
Harding HP, Zhang Y, Ron D (1999). Protein translation and folding are coupled by an endoplasmic-reticulum-resident kinase. Nature 397, 271–274.
Haze K, Yoshida H, Yanagi H, Yura T, Mori K (1999). Mammalian transcription factor ATF6 is synthesized as a transmembrane protein and activated by proteolysis in response to endoplasmic reticulum stress. Mol Biol Cell 10, 3787–3799.
Herzog VA, Reichholf B, Neumann T, Rescheneder P, Bhat P, Burkard TR, Wlotzka W, Haeseler Av, Zuber J, Ameres SL (2017). Thiol-linked alkylation of RNA to assess expression dynamics. Nat Methods 14, 1198–1204.
Hollien J, Lin JH, Li H, Stevens N, Walter P, Weissman JS (2009a). Regulated Ire1-dependent decay of messenger RNAs in mammalian cells. J Cell Biol 186, 323–331.
Hollien J, Weissman JS (2006). Decay of endoplasmic reticulum-localized mRNAs during the unfolded protein response. Science 313, 104–107.
Hollien J, Lin JH, Li H, Stevens N, Walter P, Weissman JS (2009b). Regulated Ire1-dependent decay of messenger RNAs in mammalian cells. J Cell Biol 186, 323–331.
Huang H, Weng H, Sun W, Qin X, Shi H, Wu H, Zhao BS, Mesquita A, Liu C, Yuan CL, *et al.* (2018). Recognition of RNA N 6-methyladenosine by IGF2BP proteins enhances mRNA stability and translation. Nat Cell Biol 20, 285–295.
Huang W, Li Y, Zhang C, Zha H, Zhou X, Fu B, Guo J, Wang G (2020). IGF2BP3 facilitates cell proliferation and tumorigenesis via modulation of JAK/STAT signalling pathway in human bladder cancer. J Cell Mol Med 24, 13949–13960.
Huang X, Zhang H, Guo X, Zhu Z, Cai H, Kong X (2018). Insulin-like growth factor 2 mRNA-binding protein 1 (IGF2BP1) in cancer. J Hematol Oncol 11, 88.
Jønson L, Christiansen J, Hansen TVO, Vikeså J, Yamamoto Y, Nielsen FC (2014). IMP3 RNP safe houses prevent miRNA-directed HMGA2 mRNA decay in cancer and development. Cell Rep 7, 539–551.
Karagoz GE, Acosta-Alvear D, Walter P (2019). The unfolded protein response: Detecting and responding to fluctuations in the protein-folding capacity of the endoplasmic reticulum. Cold Spring Harb Perspect Biol 11, a033886.
Kondo S, Saito A, Asada R, Kanemoto S, Imaizumi K (2011). Physiological unfolded protein response regulated by OASIS family members, transmembrane bZIP transcription factors. IUBMB Life 63, 233–239.
Le Thomas A, Ferri E, Marsters SHarnoss JM, Lawrence DA, Zuazo-Gaztelu I, Modrusan Z, Chan S, Solon M, Chalouni C, *et al.* (2021). Decoding non-canonical mRNA decay by the endoplasmic-reticulum stress sensor IRE1α. Nat Commun 12, 7310.
Lin JH, Li H, Zhang Y, Ron D, Walter P (2009). Divergent effects of PERK and IRE1 signaling on cell viability. PLoS One 4, e4170.
Los GV, Encell LP, McDougall MG, Hartzell DD, Karassina N, Zimprich C, Wood MG, Learish R, Ohana RF, Urh M, *et al.* (2008). HaloTag: A novel protein labeling technology for cell imaging and protein analysis. ACS Chem Biol 3, 373–382.
Mongroo PS, Noubissi FK, Cuatrecasas MKalabis J, King CE, Johnstone CN, Bowser MJ, Castells A, Spiegelman VS, Rustgi AK (2011). IMP-1 displays cross-talk with K-Ras and modulates colon cancer cell survival through the novel proapoptotic protein CYFIP2. Cancer Res 71, 2172–2182.
Natsume T, Kiyomitsu T, Saga Y, Kanemaki MT (2016). Rapid protein depletion in human cells by auxin-inducible Degron tagging with short homology donors. Cell Rep 15, 210–218.
Neumann T, Herzog VA, Muhar Mvon Haeseler A, Zuber J, Ameres SL, Rescheneder P (2019). Quantification of experimentally induced nucleotide conversions in high-throughput sequencing datasets. BMC Bioinformatics 20, 258.
Nusinow DP, Szpyt J, Ghandi M, Rose CM, McDonald ER, Kalocsay M, Jané-Valbuena J, Gelfand E, Schweppe DK, Jedrychowski M, *et al.* (2020). Quantitative proteomics of the cancer cell line encyclopedia. Cell 180, 387–402.e16.
Ody BK, Zhang J, Nelson SE, Xie Y, Liu R, Dodd CJ, Jacobs SE, Whitzel SL, Williams LA, Gozem S, *et al.* (2023). Synthesis and evaluation of cereblon-recruiting HaloPROTACs. Chembiochem 24, e202300498.
Ran FA, Hsu PD, Wright J, Agarwala V, Scott DA, Zhang F (2013). Genome engineering using the CRISPR-Cas9 system. Nat Protoc 8, 2281–2308.
Ren G, Ku WL, Ge G, Hoffman JA, Kang JY, Tang Q, Cui K, He Y, Guan Y, Gao B, *et al.* (2024). Acute depletion of BRG1 reveals its primary function as an activator of transcription. Nat Commun 15, 4561.
Robinson MD, Oshlack A (2010). A scaling normalization method for differential expression analysis of RNA-seq data. Genome Biol 11, R25.
Robinson MD, McCarthy DJ, Smyth GK (2010). edgeR: A Bioconductor package for differential expression analysis of digital gene expression data. Bioinformatics 26, 139–140.
Ross J, Lemm I, Berberet B (2001). Overexpression of an mRNA-binding protein in human colorectal cancer. Oncogene 20, 6544–6550.
Samanta S, Pursell B, Mercurio AM (2013). IMP3 protein promotes chemoresistance in breast cancer cells by regulating breast cancer resistance protein (ABCG2) expression. J Biol Chem 288, 12569–12573.
Sheen YS, Liao YHLin MHChu CYHo BYHsieh MCChen PCCha STJeng YMChang CC, *et al.* (2015). IMP-3 promotes migration and invasion of melanoma cells by modulating the expression of HMGA2 and predicts poor prognosis in melanoma. J Invest Dermatol 135, 1065–1073.
Shoulders MD, Ryno LM, Genereux JC, Moresco JJ, Tu PG, Wu C, Yates JR, 3rd, Su AI, Kelly JW, Wiseman RL (2013). Stress-independent activation of XBP1s and/or ATF6 reveals three functionally diverse ER proteostasis environments. Cell Rep 3, 1279–1292.
Sidrauski C, Walter P (1997). The transmembrane kinase Ire1p is a site-specific endonuclease that initiates mRNA splicing in the unfolded protein response. Cell 90, 1031–1039.
Tirasophon W, Lee K, Callaghan B, Welihinda A, Kaufman RJ (2000). The endoribonuclease activity of mammalian IRE1 autoregulates its mRNA and is required for the unfolded protein response. Genes Dev 14, 2725–2736.
Tirasophon W, Welihinda AA, Kaufman RJ (1998). A stress response pathway from the endoplasmic reticulum to the nucleus requires a novel bifunctional protein kinase/endoribonuclease (Ire1p) in mammalian cells. Genes Dev 12, 1812–1824.
Tovell H, Testa A, Maniaci C, Zhou H, Prescott AR, Macartney T, Ciulli A, Alessi DR (2019). Rapid and reversible knockdown of endogenously tagged endosomal proteins via an optimized HaloPROTAC degrader. ACS Chem Biol 14, 882–892.
Tsai JM, Nowak RP, Ebert BL, Fischer ES (2024). Targeted protein degradation: From mechanisms to clinic. Nat Rev Mol Cell Biol 25, 740–757
Urano F, Bertolotti A, Ron D (2000). IRE1 and efferent signaling from the endoplasmic reticulum. J Cell Sci 113 Pt 21, 3697–3702.
Wang XZ, Harding HP, Zhang Y, Jolicoeur EM, Kuroda M, Ron D (1998). Cloning of mammalian Ire1 reveals diversity in the ER stress responses. EMBO J 17, 5708–5717.
Worner K, Liu Q, Maschhoff KR, Hu W (2023). Identification of RNA-binding proteins' direct effects on gene expression via the degradation tag system. RNA 29, 1453–1457.
Xu W, Sheng Y, Guo Y, Huang Z, Huang YWen D, Liu C-Y, Cui L, Yang Y, Du P (2019). Increased IGF2BP3 expression promotes the aggressive phenotypes of colorectal cancer cells in vitro and vivo. J Cell Physiol 234, 18466–18479.
Yaniv K, Yisraeli JK (2002). The involvement of a conserved family of RNA binding proteins in embryonic development and carcinogenesis. Gene 287, 49–54.
Yoshida H, Haze K, Yanagi H, Yura T, Mori K (1998). Identification of the cis-acting endoplasmic reticulum stress response element responsible for transcriptional induction of mammalian glucose-regulated proteins. Involvement of basic leucine zipper transcription factors. J Biol Chem 273, 33741–33749.
Yoshida H, Okada T, Haze K, Yanagi HYura TNegishi M, Mori K (2000). ATF6 activated by proteolysis binds in the presence of NF-Y (CBF) directly to the cis-acting element responsible for the mammalian unfolded protein response. Mol Cell Biol 20, 6755–6767.
Zhao D, Yin Z, Soellner MB, Martin BR (2021). Scribble sub-cellular localization modulates recruitment of YES1 to regulate YAP1 phosphorylation. Cell Chem Biol 28, 1235–1241.e5.

Supplemental Materials

Molecular Biology of the Cell

Anisimova *et al*.

Fig. Supp. 1.

A

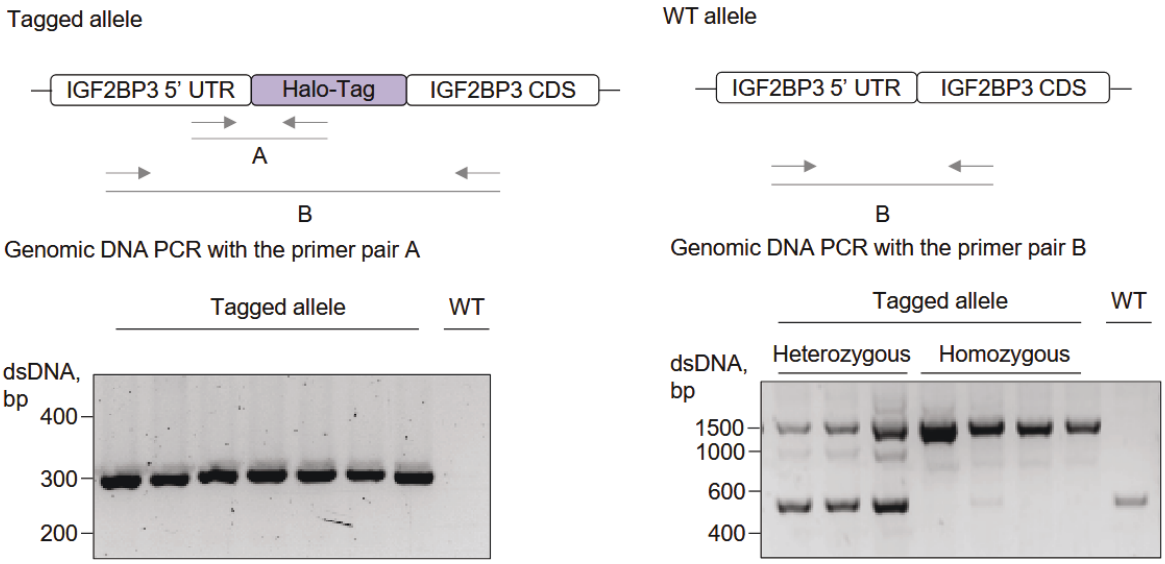
Tagged allele
IGF2BP3 5' UTR
Halo-Tag
IGF2BP3 CDS
A
B
Genomic DNA PCR with the primer pair A
Tagged allele
WT
dsDNA, bp
400
300
200
WT allele
IGF2BP3 5' UTR
IGF2BP3 CDS
B
Genomic DNA PCR with the primer pair B
Tagged allele
WT
Heterozygous
Homozygous
dsDNA, bp
1500
1000
600
400

Fig. Supp. 2

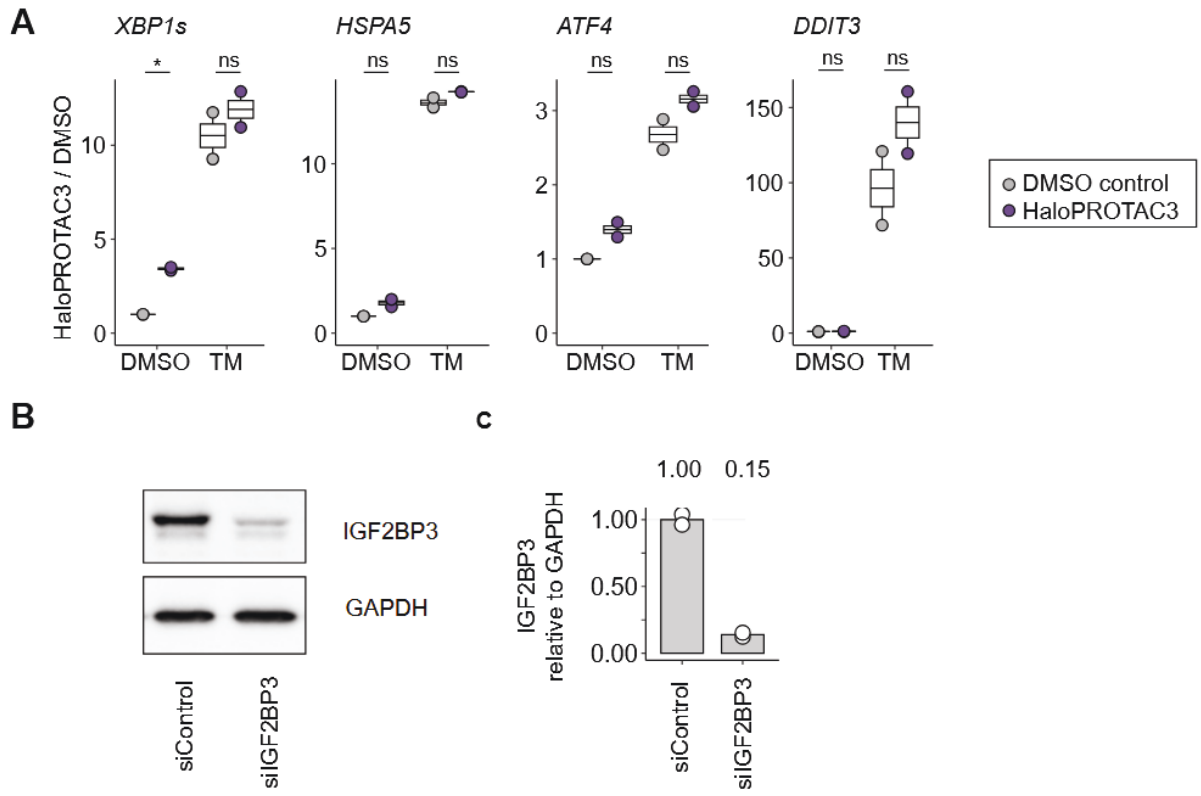
A
XBP1s
HSPA5
ATF4
DDIT3
HaloPROTAC3 / DMSO
*
ns
DMSO
TM
DMSO control
HaloPROTAC3
B
IGF2BP3
GAPDH
siControl
siIGF2BP3
c
1.00
0.15
IGF2BP3 relative to GAPDH
siControl
siIGF2BP3

Fig. Supp. 3.

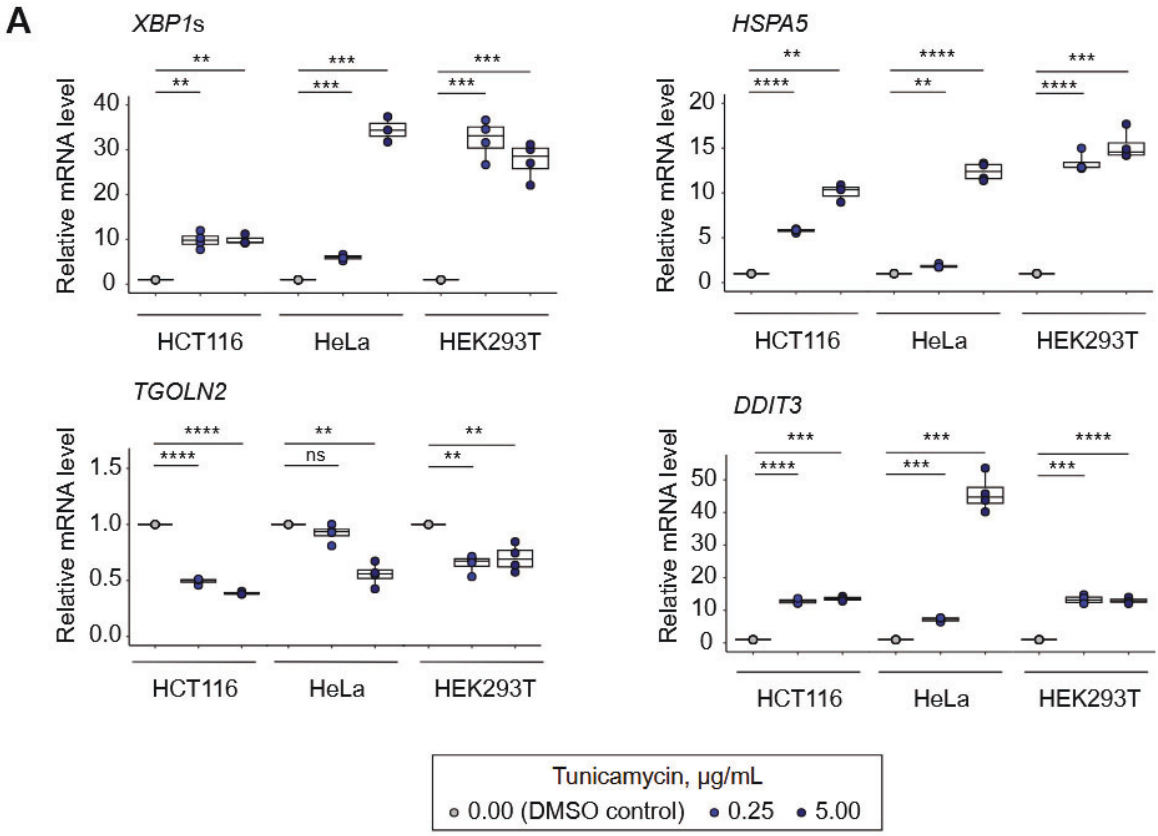
A
XBP1s
HSPA5
TGOLN2
DDIT3
Relative mRNA level
HCT116
HeLa
HEK293T
ns
Tunicamycin, µg/mL
0.00 (DMSO control)
0.25
5.00

Fig. Supp. 1. Genotyping of N-terminally tagged HaloTag-IGF2BP3 fusion alleles.
A. PCR-based genotyping of HaloTag-IGF2BP3 in HCT116 clones. Primer pair A amplifies a ~300 bp fragment from the clones modified with the HaloTag-IGF2BP3 fusion. No PCR product is expected from the parental cells harboring the WT IGF2BP3 allele. Primer pair B amplifies the
~500 bp fragment from the WT allele and ~1500 bp fragment from the HaloTag-IGF2BP3 fusion allele. Single ~1500 bp PCR product suggests that both IGF2BP3 alleles are tagged with HaloTag.

Fig. Supp. 2. RT-qPCR analyses confirms that HaloPROTAC3 treatment activates the UPR in HaloTag-IGF2BP3 expressing cells.
A. RT-qPCR of HCT116 expressing HaloTag-IGF2BP3 upon HaloPROTAC3 treatment and ER stress induction with tunicamycin (TM). Cells were treated with 500 nM of HaloPROTAC3 for 9 hours, DMSO was used as a control. In the last 5 hours, DMSO or 5 µg/mL of TM was added. The Cq values for the indicated mRNAs were normalized to *RPL6* mRNA levels and then to the control condition. n=2 biological replicates. **P* < 0.05; one s-sided Student's t-test.
B. Western blot analyses showing siRNA-mediated depletion of IGF2BP3 in IGF2BP2 KO HCT116 cells. The anti-IGF2BP3 (14642-1-AP, Proteintech) and anti-GAPDH (10494-1-AP, Proteintech) antibodies were used. **C.** Quantification of **B**, n=2 biological replicates.

Fig. Supp. 3. Non-engineered mammalian cell lines show variability in response to ER stress-inducing drug tunicamycin.
A. RT-qPCR of non-engineered HCT116, HeLa, and HEK293T cells upon tunicamycin (TM) treatment. Cells were treated with 0.25 µg/mL or 5.00 µg/mL of TM for 7 hours, DMSO at 1:1000 dilution was used as a control. The Cq values for the indicated mRNAs were normalized to *RPL6* mRNA levels and then to the control condition. n=4 biological replicates. **P* < 0.05; ***P* < 0.01;
****P* < 0.001; *****P* < 0.0001; one s-sided Student's t-test.

5.2 The coordinated action of UFMylation and ribosome-associated quality control pathway clears arrested nascent chains at the endoplasmic reticulum

5.2.1 Preamble

In this work, we investigated the mechanisms of ribosome-associated protein quality control (RQC) that take place when ribosomes stall at the ER membranes. Ribosome stalling results in arrested nascent polypeptides that have to be cleared to maintain proteostasis. How this is achieved has been extensively studied in the cytosol, but how cells clear stalled ribosomes bound to the translocon on the ER remains unclear. It has been discovered that the ribosomes stalled at the ER is marked by the ubiquitin-fold modifier UFM1 at the large ribosomal subunit protein RPL26. Importantly, this has been shown to facilitate the degradation of the arrested peptides. However, the exact sequence of events required for clearance of the incomplete peptides at the ER and the cross-talk between the UFMylation and the RQC machinery has remained unclear. Here, we show that the UFM1 E3 ligase complex binds to and UFMylates the 60S-peptidyl-tRNA complex, cooperating with the canonical RQC factors to promote degradation of arrested polypeptides and ensure proper protein quality control at the ER.

5.2.2 Contribution statement

I contributed to the conceptualization of this work, experimental work, data analyses, and editing of the manuscript. I supervised Master's student Ioanna Styliara for the FLAG-UFM1 co-immunoprecipitation mass spectrometry experiments, established protein depletion conditions and cell lines used in this study, performed depletion experiments combined with stalling induction using anisomycin, and polysome profiling experiments.

This manuscript is submitted to *EMBO Journal* on the 15th of May, 2025.

The earlier version of the manuscript is published on *bioRxiv* on January 19th, 2025:

doi: https://doi.org/10.1101/2025.01.17.633636

The coordinated action of UFMylation and ribosome-associated quality control pathway clears arrested nascent chains at the endoplasmic reticulum

Milica Mihailovic [1,2,*], Aleksandra S Anisimova [1,2,*], Bu Erte [3], Ni Zhan [3], Ioanna Styliara[1,4], Yasin Dagdas [3,5,#], G Elif Karagöz [1,5,#]

Affiliations

1. Max Perutz Laboratories Vienna, Vienna BioCenter, Vienna, Austria.
2. Vienna BioCenter PhD Program, Doctoral School of the University of Vienna and Medical University of Vienna, Vienna, Austria.
3. Gregor Mendel Institute (GMI), Vienna BioCenter, Vienna, Austria.
4. University of Vienna, Vienna, Austria.
5. Heidelberg University, Centre for Organismal Studies (COS), 69120 Heidelberg, Germany
6. Medical University of Vienna, Vienna, Austria.

Correspondence: guelsuen.karagoez@meduniwien.ac.at and yasin.dagdas@gmi.oeaw.ac.at
*: equal contribution

Abstract

Clearance of incomplete nascent polypeptides resulting from ribosomal stalling is essential for protein homeostasis. While ribosome-associated quality control (RQC) mechanisms that degrade these polypeptides are well-characterized in the cytosol, how stalled endoplasmic reticulum (ER)-bound ribosomes are cleared remains poorly understood. Stalled ER-bound ribosomes are marked by ubiquitin-fold modifier 1 (UFM1) on large ribosomal subunit protein RPL26, but the precise function and regulation of this process are unclear. Here, we demonstrate that canonical RQC factors associate with ribosomes stalled at the ER. Functional cellular assays using ER-targeted stalling reporters reveal that while ribosome splitting is a prerequisite for UFMylation of RPL26, the UFMylation persists without late RQC components that are involved in the clearance of arrested nascent chains (NEMF and LTN1). The UFM1 E3 ligase complex binds to and UFMylates the 60S-peptidyl-tRNA complex and, in concert with the canonical RQC pathway, facilitates the clearance of arrested polypeptides. Our findings reveal that UFMylation acts to maintain translational integrity at the ER.

Introduction

To maintain cellular protein homeostasis, protein translation is constantly monitored by quality control factors. Distinct secondary mRNA structures, incompletely processed mRNAs, rare codons, or translation into poly(A) tail can lead to prolonged translational pausing and ribosomal stalling [1–5]. Like a traffic jam, stalled ribosomes lead to ribosomal collisions and impaired translation [6,7]. Also, incomplete nascent polypeptides are prone to aggregation, perturbing homeostasis [2]. The highly conserved ribosome-associated quality control (RQC) pathway recognizes and recycles stalled ribosomes and degrades incomplete nascent chains to maintain proteostasis.

Cytosolic RQC mechanisms have been studied in depth (reviewed [8–11]). Collided ribosomes are recognized by the E3 ligase ZNF598, which ubiquitinates 40S ribosomal proteins and halts translation [5,12,13]. This is followed by the binding of the ribosome splitting factors ASC-1 complex/Pelo that recognize ubiquitinated stalled ribosomes [14,15] and split the leading ribosome to release the 60S-peptidyl-tRNA complex. After splitting, the 60S-peptidyl-tRNA complex is recognized by the NEMF/LTN1 complex. NEMF adds template-independent C-terminal alanine and threonine extensions (CAT-tails) to the stalled nascent chain, which facilitates the exposure of the nascent chains out of the ribosome tunnel for ubiquitination by the E3 ligase LTN1 [16–20]. Subsequently, the nascent chain is released from the ribosome after tRNA cleavage by ANKZF1, extracted from the 60S ribosomal subunit by AAA ATPase VCP, and finally targeted for proteasomal degradation [21–23]. The released 60S subunit is recycled and ready for translation initiation.

Translation into the endoplasmic reticulum (ER) membrane or the ER lumen poses topological and steric challenges for the RQC machinery to access the nascent chains on ER-bound ribosomes upon stalling. They also obstruct the translocon, hindering the synthesis and maturation of other proteins at the ER, which causes an additional burden on proteostasis [24,25]. Our understanding of RQC for the ER-bound ribosomes that co-translationally translocate nascent chains into the ER is less understood [26,27]. Recent studies showed that ribosomes stalled at the ER are marked by UFM1 (ubiquitin-fold modifier 1) at the large ribosomal subunit protein RPL26 [28,29]. Similarly to ubiquitination, UFMylation proceeds through a cascade of enzymatic reactions catalized by an E1-activating enzyme (UBA5), an E2-conjugating enzyme (UFC1), and a complex E3-ligating enzyme (UFM1 E3 ligase complex) [30–34]. The UFM1 E3 ligase complex consists of three components: UFL1, DDRGK1, and CDK5RAP3 (C53), and is tethered to the ER by the ER-membrane protein DDRGK1, providing specificity to the ER-bound ribosomes.

Accumulating evidence supports two, not necessarily mutually exclusive, models that explain the role of UFMylation in ER-localized translation. The first model suggests that ribosomal stalling at the ER induces RPL26 UFMylation, and UFMylation is involved in the clearance of stalled ribosomes and arrested polypeptides resulting from ribosomal stalling [28,35]. The second model proposes UFMylation releases 60S ribosomal subunit from the translocon following the canonical termination of translation at the ER [36,37]. Structural studies show preferential binding of UFL1 to empty 60S subunit and propose that simultaneous binding of UFL1 and tRNA is incompatible [36,37]. However, this binding mode does not explain how the depletion of UFMylation machinery results in the accumulation of nascent arrested polypeptides in cells [28,35]. To fill this gap in our knowledge, we dissected the interplay between the RQC and UFMylation machinery in clearing stalled ribosomes at the ER. We show that upon ribosomal stalling at the ER, UFL1 loads onto the 60S-peptidyl-tRNA complex. Through close collaboration with the RQC factors NEMF/LTN1, UFM1 E3 ligase complex facilitates clearance of the stalled peptides. Altogether, our findings underline the crucial role of the UFMylation-RQC crosstalk for clearing arrested incomplete polypeptides and ER-homeostasis.

Results

RQC factors associate with and act on UFMylated ribosomes

To discover regulators of UFMylated ribosomes, we purified them from mammalian cells and performed mass spectrometry (MS) analyses. To efficiently isolate UFMylated ribosomes, we generated an HCT116 cell line with endogenously tagged FLAG-UFM1 using the CRISPR-Cas9 gene editing approach. We then pelleted ribosomes by sucrose cushion sedimentation after inducing ribosomal stalling with anisomycin (ANS), which impairs peptidyl transferase activity of ribosomes [38]. UFMylated ribosomes were subsequently enriched by FLAG immunoprecipitation (Fig. 1A). The MS analyses showed the expected enrichment of UFM1 E3 ligase complex components (UFL1, CDKRAP53, DDRGK1) in FLAG-immunoprecipitated samples from FLAG-UFM1 cells treated with anisomycin, compared to the input, and normalized to untreated cells as control (Fig. 1B, full list in Supplementary table 1). Additionally, we found that the RQC component NEMF is specifically associated with UFMylated ribosomes in a stalling-dependent manner (Figure 1B, C).

The association of late RQC components with UFMylated ribosomes suggests that the cytosolic RQC machinery can also act on ribosomes stalled at the ER. To test whether the early RQC components recognize and split the ER-stalled ribosomes , we monitored the translational readthrough of well characterized stalling cytosolic or ER-targeted reporters [28] (Figure 1D) in a fluorescence-activated cell sorting (FACS) assay (Figure 1E, F). The ERK20 reporter consists of N-terminal signal sequence, N-glycosylation site, followed by EGFP and a poly-lysine stretch that mimics translation into polyA tail, and a C-terminal mCherry; while CytoK20 reporter has the same domain organization without the ER-targeting signal sequence and glycosylation site. To test whether early RQC machinery can access the ER-stalled ribosomes, we used siRNA to deplete ZNF598 and ASCC3, an ASC-1 complex component (Supplementary figure 1A), as depletion of ASCC3 leads to the 80% destabilization of the whole complex [14]. Both the cytosolic (as shown earlier [13]) and ER stalling reporters showed increased readthrough upon loss of ZNF598 and ASCC3 (Figure 1E-F). In contrast, control cytosolic CytoK0 and ER-targeted ERK0 reporters, which lack a stalling-inducing poly-lysine sequence, did not show a difference in readthrough upon depletion of the RQC components, as they don't recruit the RQC machinery. Importantly, the loss of Pelo, which acts specifically on ribosomes stalled at the 3'-end of the RNAs [24,39], did not impact the readthrough of our internal ribosomal stalling reporters validating our findings (Supplementary figure 1B). Altogether, these results suggest that early RQC factors ZNF598 and ASCC3 can access and act on stalled ribosomes at the ER.

RQC factors and UFMylation machinery collaborate to clear stalled peptides at the ER

After showing that early RQC components are essential for recognizing and splitting the ER-stalled ribosomes, we next tested the interplay between RQC factors and UFMylation machinery on the clearance of the model ER stalling substrate, ERK20. To deplete RQC factors, we used RKO cell lines that stably express doxycycline-inducible Cas9 (iCas9). Using lentiviral transduction, we introduced either specific guide RNAs (gRNAs) targeting the RQC components (ANKZF1, ASCC3, NEMF, LTN1) or the non-coding control locus AAVS1. In parallel, we used UFM1 iCas9 cells to impair UFMylation. Treatment of cells with doxycycline for 48 hours resulted in efficient depletion of the RQC factors or UFM1 (96% ANKZF1, 71% ASCC3, 75% NEMF and 69% LTN1 and 93% UFM1, Supplementary figure 1C). Importantly, we found that their depletion significantly stabilized the ER stalling reporter ERK20 (Figure 1G, H). Depletion of ASSC3 did not stabilize ERK20 reporter, since ASC-1 complex acts in

early RQC. In contrast, as expected, depletion of these genes did not cause accumulation of the control ER reporter ERK0 (Figure 1I, J).

We next tested the downstream degradation pathway of cytosolic and ER stalling reporters through proteasomal inhibition with MG132 and autophagy inhibition with bafilomycin treatment. Both reporters are stabilized by the inhibition of proteasome and autophagy machineries, yet the proteasomal inhibition showed a higher accumulation of the reporters indicating its major contribution to their clearance (Supplementary figure 1D). Taken together, we show that both the UFMylation and the RQC machinery are involved in clearing arrested nascent peptides on stalled ribosomes at the ER.

Recognition and splitting of the ER-stalled ribosomes precedes UFMylation

Next, we investigated the crosstalk between the RQC pathway and UFMylation. To reveal the order of events and the interdependence of these pathways, we first assessed whether the loss of RQC components impacts UFMylation of the ER-stalled ribosomes. To this end, we used RKO iCas9 cell lines expressing gRNAs against RQC components (Supplementary figure 1C). Under steady-state conditions, depletion of ZNF598, ASCC3, or PELO did not impact UFMylation levels (Figure 2A, lanes 1-4, Figure 2B). However, upon ANS treatment, we noticed a significant decrease in UFMylation levels upon depletion of ZNF598, ASCC3, or Pelo compared to control (AAVS1) (Figure 2C, lanes 1-3, Figure 2D). These results were corroborated in HCT116 cell line using siRNA depletion of RQC components (Supplementary figure 2A, B).This data indicated that ribosome splitting is required for UFMylation of ribosomes at RPL26. Additionally, we detected ZNF598-dependent ubiquitination of 40S ribosome protein RPS10 on disomes by polysome profiling in HCT116 cells treated with ANS, while UFMylation was mainly enriched in 60S fractions, suggesting that early RQC-mediated ubiquitination and UFMylation have different substrates (Supplementary figure 2C).

Notably, the depletion of RQC factors NEMF and LTN1, which facilitate ubiquitination and clearance of the nascent chain, increased RPL26 UFMylation levels under steady-state conditions (Figure 2A, lanes 5,6, Figure 2B), suggesting that RQC continuously surveils aberrant translation. We anticipate that depletion of NEMF and LTN1 impairs the clearance of the stalled ribosomes at the ER (as we showed in Figure 1G, H), leading to the accumulation of the UFMylated 60S-peptidyl-tRNA complex intermediates. Surprisingly, NEMF and LTN1 depletion did not largely impact RPL26 UFMylation upon ANS treatment (Figure 2C, lanes 5,6, Figure 2D). Compared to steady-state conditions in Figure 2A, this difference could be due to cell-wide ribosomal stalling induced by ANS treatment exhausting the UFMylation machinery. These data suggest that the UFMylation machinery acts at capacity, therefore, the depletion of NEMF and LTN1 during ANS treatment does not lead to a further increase.

To uncover ER-specific cross-talk between the RQC and UFMylation machinery, we induced ribosomal stalling in a more specific manner by expressing cytosolic or ER stalling reporters ERK20 and CytoK20 in HCT116 cells. As shown before [28], while ERK20 expression increased RPL26 UFMylation, CytoK20 did not (Figure 2E). The siRNA-mediated knockdowns of ZNF598, and ASCC3 resulted in a significant decrease in RPL26 UFMylation levels in cells expressing ERK20, compared to control siRNA, while PELO knockdown did not impact UFMylation (Figure 2E, lanes 1-4, Figure 2F). In contrast, cells expressing CytoK20 showed no difference in RPL26 UFMylation levels upon knockdowns of early RQC components

ZNF598, and ASCC3 (Figure 2E, lanes 5-8, Figure 2G). Similarly, their depletion did not impact UFMylation levels in cells expressing control ERK0 reporter (Supplementary figure 2D, E). Therefore, the depletion of ZNF598 and ASC-1 complex decreases UFMylation, specifically in cells expressing ER stalling reporter ERK20. We also noticed an increase in UFMylation upon NEMF depletion in RKO iCas9 cells expressing ERK20 reporter (Figure 2H, I) showing that UFMylation of RPL26 is not dependent on NEMF.

Given the conservation of the UFMylation system across eukaryotes, we proceeded to investigate the evolutionary conservation of this mechanism in plants. To this end, we evaluated the effect of RQC machinery on RPL26 UFMylation using *Arabidopsis thaliana* mutant lines. UFMylation levels were assessed upon ANS treatment in *ascc3*, *pelota*, *ltn1*, and *nemf* mutant lines compared to wt (Columbia Col-0 ecotype). Knocking out *ascc3* and *pelota* significantly decreased UFMylation levels upon stalling induction by ANS treatment compared to the wild-type (Figure 2J, K). Additionally, we noticed a slight decrease in nemf mutant line (Figure 2J, K). These results confirm our hypothesis that the order of events upon ribosome stalling at the ER is conserved across eukaryotes.

To sum up, we show that upon stalling at the ER, ribosomes are recognized by ZNF598 and split by ASC-1 complex. The ribosome splitting precedes and is required for UFMylation of the ER-bound ribosomes upon stalling. At the same time, the depletion of the late RQC components NEMF and LTN1, which are involved in the clearance of the arrested peptides on the 60S, does not impair the UFMylation of RPL26. These results indicate that the nascent polypeptide release is not necessary for the UFM1 E3 ligase complex to access and UFMylate the 60S. Taken together, we mechanistically show that translational stalling at the ER induces UFMylation of post-splitting 60S-peptidyl-tRNA complexes, and this mechanism is evolutionarily conserved in plants and mammals.

UFM1 E3 ligase complex binds nascent chain-associated 60S-peptidyl-tRNA complex at the ER

The cryo-electron microscopy structures of UFL1 complex bound to 60S ribosomes revealed that UFM1 E3 ligase complex forms extensive contacts with the 60S in a clamp-like architecture extending from tRNA-binding sites to the peptide exit tunnel with all the three subunits of complex contributing to this interaction [36,37]. Based on these structures, it was proposed that UFL1 binding blocks the tRNA-binding site and these two binding events are mutually exclusive. However, those structures cannot explain how the loss of the components of the UFM1 E3 ligase leads to the accumulation of ER stalling reporters. Namely, it is not clear how machinery that only works on post-termination ribosomes could result in the accumulation of the arrested nascent polypeptides (Fig. 1G, H). To this end, we next dissected whether binding of the UFM1 E3 ligase complex occurs before or after nascent chain release from ER-bound 60S subunits.

Depletion of the RQC factors involved in the nascent chain clearance increased UFMylation of RPL26, suggesting that the UFM1 E3 ligase complex can access and UFMylate nascent chain-associated 60S subunits (Figure 2A, B, H, I). The catalytic component of the UFM1 E3 ligase complex, UFL1, forms the central scaffold of the UFM1 E3 ligase complex and forms extensive contacts with both other components of the E3 ligase complex as well as the 60S. The structural model of UFL1 displays a short N-terminal α-helix followed by one partial

winged-helix (pWH), five WH motifs, a bipartite coiled-coil (CC) domain with a disordered region and a C-terminal globular domain (CTD), which contacts the 28S ribosomal RNA (rRNA) occluding all three tRNA-binding sites (Figure 3A, B). Based on our data and data from others [36,37], we hypothesized that the extensive contacts formed between the UFM1 E3 ligase complex and the 60S would allow for sufficient affinity for this interaction to occur even though the tRNA site is occupied. Notably, the structural models of the UFL1 show that CTD displays high degree of conformational freedom due it being connected to the rest of the protein with a disordered segment (Figure 3A). Overlaying the published structures of 60S ribosomes with UFL1 complex and NEMF/LTN1 shows a possibility of a hybrid state with a possible rearrangement of the CTD of UFL1 and NEMF/LTN1 at the P-site (Figure 3B). Supporting our data, deletion of the CTD of UFL1 does not entirely abolish UFMylation of the RPL26 in cells [36]. Therefore, we speculated that UFL1 could undergo conformational rearrangements to enable its binding to 60S-peptidyl-tRNA complex (Figure 3B).

To experimentally test this model, we assessed whether the UFL1 complex associates with the 60S-peptidyl-tRNA complex following ribosome splitting. To this end, we enriched nascent chain-bound ribosomes by immunoprecipitating ER stalling reporter ERK20 or control ER reporter ERK0 in RKO cells (Figure 3C). To enrich for the ribosome-associated nascent chains, we first isolated ribosomes via sucrose cushions and performed immunoprecipitation (Figure 3C). We found that UFL1 specifically associates with ERK20 on the nascent chain-bound ribosomes, while we did not observe UFL1 binding to ERK0 (Figure 3D). Quantification of three replicates showed a significant difference in binding between ERK0 and ERK20, showing that UFL1 binding depends on ribosome stalling at the ER (Figure 3E). Importantly, we also observed an enrichment of the UFMylated RPL26 in the eluates from ERK20-expressing cells (Figure 3D, lanes 3-5). These data indicated that UFL1 can bind and actively UFMylate 60S-peptidyl-tRNA complex with the arrested nascent chains at the ER.

To test whether the association of NEMF/LTN1 with the 60S is required for UFL1 binding to the 60S-peptidyl-tRNA complex at the ER, we conducted similar experiments upon NEMF depletion in RKO iCas9 cells expressing CytoK20 or ERK20 reporters (Figure 3C). IP analyses showed specific interaction of UFL1 with the ERK20-stalled ribosomes while it did not associate with the ribosomes stalled in the cytosol (CytoK20) (Figure 3F, G). Moreover, UFL1 binding was unaffected by NEMF depletion, supporting the evidence that UFMylation precedes the activity of the late RQC components (Figure 3G, right panel). Notably, upon NEMF depletion, EK20 pulldowns displayed higher levels of UFMylated RPL26, further supporting our model that UFL1 binds to and UFMylates 60S-peptidyl-tRNA complex before nascent chain release (Figure 3F, lanes 10,11). The UFM1 depletion did not impair association of UFL1 with ERK20 expressing ribosomes, indicating that this step precedes stabilization of UFL1-ribosome complexes via UFM1 attachment (Figure 3F, lanes 10, 12). We also noticed a NEMF-dependent association of LTN1 to the 60S-peptidyl-tRNA complexes both for cytosolic and ER-stalled ribosomes (Figure 3H), in accordance with previous data [40]. Interestingly, we show that LTN1 binding decreases upon UFM1 KO for ER-stalled ribosomes (Figure 3H). This can be explained by destabilization of the translocon-60S association by UFMylation of the 60S-peptidyl-tRNA complexes, thus allowing better access of LTN1 to the nascent chain (Figure 3B). In summary, we demonstrate that the UFM1 E3 ligase complex binds to 60S-peptidyl-tRNA on the ER following ribosomal stalling. This interaction does not depend on binding of the NEMF/LTN1 complex and facilitates the clearance of arrested polypeptides on ER stalled ribosomes.

Discussion

The best-described substrate of the UFMylation machinery is the large ribosomal subunit protein RPL26, initially discovered to be increasingly UFMylated upon ribosomal stalling at the ER [28,29]. However, the primary function of this event has remained poorly understood. Recent cryo-EM structures uncovered a novel function of the UFMylation machinery in recycling the 60S subunits after translational termination at the ER by releasing them from the translocon [36,37]. These structures also showed that UFL1 occupies the tRNA binding sites at the 60S, suggesting that the UFM1 E3 ligase binds to 60S subsequent to translation termination [36,37]. Therefore, the role of UFMylation in clearing ER-stalled ribosomes remained unclear.

Here, using IP-MS analyses, we found that RQC components are associated with the UFMylated ribosomes (Figure 1B, C). To confirm the role of RQC factors on clearing ER stalled ribosomes, we used genetic depletion of RQC machinery and found that ribosomes stalled upon ERK20 expression recruit the RQC E3 ligase ZNF598 and the ribosome splitting factor ASC-1 complex (Figure 1E, F, Figure 2E-I). Similar to RQC events upon cytosolic stalling, the stalled ribosomes at the ER required the activity of ANKZF1, NEMF and LTN1 for clearance of arrested polypeptides since the loss of these components stabilized the ER stalling reporter (Figure 1G, H). Likewise, impaired UFMylation specifically stabilized ERK20 substrate in line with the published work (Figure 1G, H) [28], indicating that both the RQC and the UFMylation machinery are involved in the clearance of the stalled ribosomes at the ER.

After demonstrating the role of the RQC and the UFMylation machinery in the clearance of the ER-stalled ribosomes, we assessed the sequence of events and interdependence of these pathways by testing the impact of the loss of RQC factors on RPL26 UFMylation upon ribosome stalling. The RPL26 UFMylation levels decreased upon knockdown or knockout of ZNF598 or ASCC3 in cells treated with anisomycin, a drug inducing ribosomal stalling (Figure 2 C, D, Supplementary figure 2A, B) as well as upon expression of the specific ER stalling reporter ERK20 (Figure 2E-I). Experiments performed in plants (*Arabidopsis thaliana*) validated those findings (Figure 2J, K), concluding that UFMylation happens on post-split 60S ribosomes upon ribosomal stalling at the ER and that this mechanism is conserved from plants to mammals.

Previous structural data showed that UFL1 mainly binds to the 60S ribosomal subunit in a way that excludes the binding of the 40S subunit, translocon, or tRNA [36,37]. These data cannot be reconciled with the data showing increased UFMylation of RPL26 upon ribosome stalling. We showed that UFL1 associates with ribosomes expressing ER stalling reporter ERK20, but not the cytosolic stalling reporter CytoK20 or the ER-targeted control reporter ERK0 (Figure 3D, E). Immunoprecipitation of the ribosome-attached ERK20 stalling reporter showed that these ribosomes were already UFMylated at RPL26, demonstrating that UFM1 E3 ligase can act on nascent chain-loaded ribosomes, contradicting the previous model (Figure 3D, E) [36,37]. Importantly, the depletion of NEMF and UFM1 did not impact UFL1 binding to the nascent chain-containing ribosomes (Figure 3F, G). Moreover, we readily detected UFMylated RPL26 in the nascent chain immunoprecipitates from NEMF KO cells, showing that UFMylation happens independently of NEMF binding (Figure 3F). Supporting our findings, single particle cryo-electron microscopy studies of the native UFM1 E3 ligase complexes isolated from cells showed a small population of 60S with a weak extra density in the peptide exit tunnel, which could possibly represent a nascent polypeptide chain [36]. To sum up, we found that the 60S-

peptidyl-tRNA complex formed upon ribosome splitting can serve as a substrate for UFM1 E3 ligase complex and that the NEMF/LTN1-dependent release of the nascent chain is not necessary for RPL26 UFMylation.

In cytosolic ribosomes, LTN1 binds close to the ribosome exit tunnel in the vicinity of the stalled nascent polypeptides emerging from the ribosome [40]. In the ER-bound ribosomes exit tunnel is occupied by the translocon [41,42]. The RQC pathway was proposed to act on ER-stalled ribosome through exposure of the nascent polypeptide in the cytosol at the ribosome-translocon contact site [43]. As depletion of the UFMylation machinery stabilizes the arrested nascent chains, and the binding of LTN1 to 60S at the ER is enhanced by UFMylation (Figure 3F, H), we speculate that, similar to what has been proposed for the post-termination empty 60S subunits, binding of the UFM1 E3 ligase complex destabilizes the 60S-translocon interactions and allows the E3 ligase LTN1 to access the arrested nascent chain for ubiquitination and subsequent degradation (Figure 3B).

Both ubiquitin proteosome system and lysosomal degradation was proposed be involved in clearance of stalled nascent peptides at the ER [28,33,35]. Notably, the previous work on the ERK20 reporter used here showed that it is mainly degraded by lysosomes and neither proteosome inhibition nor NEMF depletion stabilized the reporter [28]. However, we show a clear stabilization of the same reporter preferentially by proteosome inhibition (Supplementary figure 1D), and NEMF depletion (Figure 1G, H). Supporting our results, an alternative ER stalling reporter containing a folded VHP domain and a poly-lysine stretch, was degraded primarily by the proteasome, and showed a NEMF-dependent stabilization [35]. We therefore conclude that while RQC and ubiquitin proteosome system play the major role to clear stalled ribosomes, depending on the cell type and the expression level, the arrested polypeptides at the ER can be cleared by complementary degradation pathways including ER-phagy and lysosomal pathways [28,33].

Altogether, our data converge on the following model: stalling of the ER-bound ribosomes recruits canonical ribosome-associated quality control machinery. First, the E3 ligase ZNF598 recognizes the collided ribosomes and stabilizes them by ubiquitinating small subunit proteins [13]. This is followed by the binding of the ASC-1 complex that splits the leading ribosome, leaving a 60S-peptidyl-tRNA complex (Figure 4). The 60S-peptidyl-tRNA complex is then recognized and UFMylated by UFM1 E3 ligase independently of downstream RQC components' activities. RPL26 UFMylation allows better access of LTN1 to the nascent chain that gets ubiquitinated and targeted for downstream proteasomal degradation to restore cellular proteostasis. This process shows high evolutionary conservation in plants and mammals and highlights the importance of fine regulation and complementarity of ribosomal quality control processes.

Declaration of interests

The authors declare no competing interests.

Acknowledgements

We thank Kitti Csalyi and Thomas Sauer at Max Perutz Labs Biooptics FACS facility and Elisabeth Roitinger at Vienna BioCenter Proteomics Core Facility for their help. We are

thankful to Gijs Versteeg (Max Perutz Labs, Vienna) and Johannes Zuber (IMP, Vienna) for the help with the iCas9 RKO cel llines and lentiviral transduction, and to Yihong Ye (NIH, Bethesda) for CytoK0, CytoK20, ERK0, and ERK20 plasmids. This research was funded in whole or in part by the Austrian Science Fund (FWF) [FWF-W1261, FWF-DOC 177B] to GEK, the [FWF-SFB F79] and Vienna Science and Technology Fund, WWTF-LS21 Chemical Biology to GEK and YD and European Research Council Grant (Project number: 101043370) to YD. ASA and MM are supported by the DOC fellowship of Austrian Academy of Sciences. For open access purposes, the author has applied a CC BY public copyright license to any author-accepted manuscript version arising from this submission. Schemes are generated in BioRender.

References

1. Shoemaker, C. J. & Green, R. Translation drives mRNA quality control. *Nat Struct Mol Biol* **19**, 594–601 (2012).
2. Choe, Y.-J. *et al.* Failure of RQC machinery causes protein aggregation and proteotoxic stress. *Nature* **531**, 191–195 (2016).
3. Doma, M. K. & Parker, R. Endonucleolytic cleavage of eukaryotic mRNAs with stalls in translation elongation. *Nature* **440**, 561–564 (2006).
4. Letzring, D. P., Wolf, A. S., Brule, C. E. & Grayhack, E. J. Translation of CGA codon repeats in yeast involves quality control components and ribosomal protein L1. *RNA* **19**, 1208–1217 (2013).
5. Juszkiewicz, S. & Hegde, R. S. Initiation of Quality Control during Poly(A) Translation Requires Site-Specific Ribosome Ubiquitination. *Molecular Cell* **65**, 743-750.e4 (2017).
6. Chandrasekaran, V. *et al.* Mechanism of ribosome stalling during translation of a poly(A) tail. *Nat Struct Mol Biol* **26**, 1132–1140 (2019).
7. Tesina, P. *et al.* Molecular mechanism of translational stalling by inhibitory codon combinations and poly(A) tracts. *EMBO Journal* **39**, (2020).
8. Joazeiro, C. A. P. Ribosomal stalling during translation: Providing substrates for ribosome-associated protein quality control. *Annual Review of Cell and Developmental Biology* **33**, 343–368 (2017).
9. Joazeiro, C. A. P. Mechanisms and functions of ribosome-associated protein quality control. *Nat Rev Mol Cell Biol* **20**, 368–383 (2019).
10. Filbeck, S., Cerullo, F., Pfeffer, S. & Joazeiro, C. A. P. Ribosome-associated quality-control mechanisms from bacteria to humans. *Mol Cell* **82**, 1451–1466 (2022).
11. Inada, T. & Beckmann, R. Mechanisms of Translation-coupled Quality Control. *Journal of Molecular Biology* **436**, 168496 (2024).
12. Sundaramoorthy, E. *et al.* ZNF598 and RACK1 Regulate Mammalian Ribosome-Associated Quality Control Function by Mediating Regulatory 40S Ribosomal Ubiquitylation. *Mol Cell* **65**, 751-760.e4 (2017).
13. Juszkiewicz, S. *et al.* ZNF598 Is a Quality Control Sensor of Collided Ribosomes. *Mol Cell* **72**, 469-481.e7 (2018).
14. Juszkiewicz, S., Speldewinde, S. H., Wan, L., Svejstrup, J. Q. & Hegde, R. S. The ASC-1 Complex Disassembles Collided Ribosomes. *Mol Cell* **79**, 603-614.e8 (2020).
15. Hashimoto, S., Sugiyama, T., Yamazaki, R., Nobuta, R. & Inada, T. Identification of a novel trigger complex that facilitates ribosome-associated quality control in mammalian cells. *Sci Rep* **10**, 3422 (2020).

16. Shen, P. S. *et al.* Protein synthesis. Rqc2p and 60S ribosomal subunits mediate mRNA-independent elongation of nascent chains. *Science* **347**, 75–78 (2015).
17. Bengtson, M. H. & Joazeiro, C. A. P. Role of a ribosome-associated E3 ubiquitin ligase in protein quality control. *Nature* **467**, 470–473 (2010).
18. Kostova, K. K. *et al.* CAT-tailing as a fail-safe mechanism for efficient degradation of stalled nascent polypeptides. *Science* **357**, 414–417 (2017).
19. Chu, J. *et al.* A mouse forward genetics screen identifies LISTERIN as an E3 ubiquitin ligase involved in neurodegeneration. *Proc Natl Acad Sci U S A* **106**, 2097–2103 (2009).
20. Lyumkis, D. *et al.* Single-particle EM reveals extensive conformational variability of the Ltn1 E3 ligase. *Proc Natl Acad Sci U S A* **110**, 1702–1707 (2013).
21. Kuroha, K., Zinoviev, A., Hellen, C. U. T. & Pestova, T. V. Release of Ubiquitinated and Non-ubiquitinated Nascent Chains from Stalled Mammalian Ribosomal Complexes by ANKZF1 and Ptrh1. *Molecular Cell* **72**, 286-302.e8 (2018).
22. Brandman, O. *et al.* A ribosome-bound quality control complex triggers degradation of nascent peptides and signals translation stress. *Cell* **151**, 1042–1054 (2012).
23. Meyer, H., Bug, M. & Bremer, S. Emerging functions of the VCP/p97 AAA-ATPase in the ubiquitin system. *Nat Cell Biol* **14**, 117–123 (2012).
24. Izawa, T. *et al.* Roles of dom34:hbs1 in nonstop protein clearance from translocators for normal organelle protein influx. *Cell Rep* **2**, 447–453 (2012).
25. Phillips, B. P. & Miller, E. A. Ribosome-associated quality control of membrane proteins at the endoplasmic reticulum. *Journal of Cell Science* **133**, jcs251983 (2020).
26. Karagöz, G. E., Acosta-Alvear, D. & Walter, P. The unfolded protein response: Detecting and responding to fluctuations in the protein-folding capacity of the endoplasmic reticulum. *Cold Spring Harbor Perspectives in Biology* **11**, (2019).
27. Lakshminarayan, R. *et al.* Pre-emptive Quality Control of a Misfolded Membrane Protein by Ribosome-Driven Effects. *Curr Biol* **30**, 854-864.e5 (2020).
28. Wang, L. *et al.* UFMylation of RPL26 links translocation-associated quality control to endoplasmic reticulum protein homeostasis. *Cell Research* **30**, 5–20 (2020).
29. Walczak, C. P. *et al.* Ribosomal protein RPL26 is the principal target of UFMylation. *Proceedings of the National Academy of Sciences of the United States of America* **116**, 1299–1308 (2019).
30. Kumar, M. *et al.* Structural basis for UFM1 transfer from UBA5 to UFC1. *Nat Commun* **12**, 5708 (2021).
31. Komatsu, M. *et al.* A novel protein-conjugating system for Ufm1, a ubiquitin-fold modifier. *EMBO J* **23**, 1977–1986 (2004).
32. Gavin, J. M. *et al.* Mechanistic study of Uba5 enzyme and the Ufm1 conjugation pathway. *J Biol Chem* **289**, 22648–22658 (2014).
33. Stephani, M. *et al.* A cross-kingdom conserved er-phagy receptor maintains endoplasmic reticulum homeostasis during stress. *eLife* **9**, 1–105 (2020).
34. Tatsumi, K. *et al.* A Novel Type of E3 Ligase for the Ufm1 Conjugation System*. *Journal of Biological Chemistry* **285**, 5417–5427 (2010).
35. Scavone, F., Gumbin, S. C., Da Rosa, P. A. & Kopito, R. R. RPL26/uL24 UFMylation is essential for ribosome-associated quality control at the endoplasmic reticulum. *Proceedings of the National Academy of Sciences* **120**, e2220340120 (2023).
36. DaRosa, P. A. *et al.* UFM1 E3 ligase promotes recycling of 60S ribosomal subunits from the ER. *Nature* 1–8 (2024) doi:10.1038/s41586-024-07073-0.

37. Makhlouf, L. *et al.* The UFM1 E3 ligase recognizes and releases 60S ribosomes from ER translocons. *Nature* 1–8 (2024) doi:10.1038/s41586-024-07093-w.
38. Hansen, J. L., Moore, P. B. & Steitz, T. A. Structures of Five Antibiotics Bound at the Peptidyl Transferase Center of the Large Ribosomal Subunit. *Journal of Molecular Biology* **330**, 1061–1075 (2003).
39. Guydosh, N. R. & Green, R. Dom34 rescues ribosomes in 3' untranslated regions. *Cell* **156**, 950–962 (2014).
40. Shao, S., Brown, A., Santhanam, B. & Hegde, R. S. Structure and Assembly Pathway of the Ribosome Quality Control Complex. *Molecular Cell* **57**, 433–444 (2015).
41. Lewis, A. J., Zhong, F., Keenan, R. J. & Hegde, R. S. Structural analysis of the dynamic ribosome-translocon complex. *eLife* **13**, RP95814 (2024).
42. Voorhees, R. M., Fernández, I. S., Scheres, S. H. W. & Hegde, R. S. Structure of the Mammalian Ribosome-Sec61 Complex to 3.4 Å Resolution. *Cell* **157**, 1632–1643 (2014).
43. von der Malsburg, K., Shao, S. & Hegde, R. S. The ribosome quality control pathway can access nascent polypeptides stalled at the Sec61 translocon. *Mol Biol Cell* **26**, 2168–2180 (2015).
44. Natsume, T., Kiyomitsu, T., Saga, Y. & Kanemaki, M. T. Rapid Protein Depletion in Human Cells by Auxin-Inducible Degron Tagging with Short Homology Donors. *Cell Rep* **15**, 210–218 (2016).
45. de Almeida, M. *et al.* AKIRIN2 controls the nuclear import of proteasomes in vertebrates. *Nature* **599**, 491–496 (2021).
46. Hornegger, H. *et al.* IGF2BP1 phosphorylation in the disordered linkers regulates ribonucleoprotein condensate formation and RNA metabolism. *Nat Commun* **15**, 9054 (2024).
47. Ran, F. A. *et al.* Genome engineering using the CRISPR-Cas9 system. *Nat Protoc* **8**, 2281–2308 (2013).

Figure Legends

Figure 1. RQC and UFMylation machinery are needed to clear stalled peptides at the ER (A) Scheme of mass spectrometry analysis of UFMylated ribosomes. (B) Scatter plot of proteins enriched with UFMylated ribosomes upon 3h 4μM ANS treatment compared to untreated HCT116 FLAG-UFM1 cells. (C) Enrichment of FLAG-eluates from ANS treated HCT116 FLAG-UFM1 cells over FLAG-eluates from untreated control HCT116 FLAG-UFM1 cells normalized to respective cushion samples, shown as $\log_2$ fold change, identified by mass spectrometry experiment from (A). (D) Schematic representation of control (K0) and stalling (K20) cytosolic and ER reporters. (E and F) Readthrough of reporters from (D) shown by mCherry/GFP ratio measured by FACS after 24h expression in HCT116 cells upon siRNA-mediated knockdown of ZNF598 (E) or ASCC3 (F) compared to non-targeting control siRNA. (G and I) Reporter accumulation shown by FLAG immunoblot in RKO iCas9 KO cell lysates upon 48h dox treatment to induce AAVS1 (non-targeting control), ANKZF1, ASCC3, UFM1, NEMF or LTN1 knockout, upon 24h ERK20 (G) or ERK0 expression (I) normalized to RPS10 loading control. AP – arrested peptide, g – glycosylation, * - degradation products. (H) Quantification of (G). (J) Quantification of (I).

Figure 2. RPL26 is UFMylated on post-split 60S subunit upon ribosomal stalling at the ER (A and C) UFMylation levels visualized by UFM1 immunoblot in RKO iCas9 cells upon 48h dox treatment to induce RQC components or non-targeting AAVS1 knockout in untreated (A)

or 1h 4μM ANS treated cells (C). (B) Quantification of (A). (D) Quantification of (C). (E) UFMylation levels visualized by UFM1 immunoblot in HCT116 cells upon 72h siRNA-mediated knockdown of RQC components or non-targeting control, and 24h expression of ERK20 or CytoK20. (F and G) Quantification of (E) for cells expressing ERK20 (F) or CytoK20 (G) shown by FLAG signal normalized to loading control. (H) UFMylation levels visualized by RPL26 immunoblot in RKO iCas9 cells upon 48h dox treatment to induce non-targeting AAVS1 or NEMF knockout upon 24h expression of ERK20 reporter. (I) Quantification of (H). (J) 7-day-old *Arabidopsis* seedlings of wildtype (Col-0) and RQC component mutant (*ascc3*, *pelota*, *ltn1*, *nemf*, *rqc1*, *edf1*) were treated with either DMSO or 100 μM ANS for 16 hours. The UFMylation level was tested via immunoblotting using anti-UFM1 antibody, with UGPase was introduced as loading control. The data shown are representative of three biological replicates. (K) Quantification of (J) for ANS-treated samples. FL – full length, AP – arrested peptide, g – glycosylation, # - UFC1-UFM1 complex [30], * - degradation products.

Figure 3. UFL1 UFMylates nascent chain-bound 60S subunits (A) The cryostructural model of UFM1 E3 ligase complexes shows flexibility around the CTD region of UFL1 (pbd: 8ohd). (B) Left: The structure of UFM1 E3 ligase complex bound to 60S subunit (pbd: 8ohd), right: the structure of NEMF/LTN1 complex bound to peptidyl-tRNA-60S complex (pdb: 3j92, 8agw) docked on translocon (pdb:3j7r), middle: overlay of two structures shows a possible hybrid state with conformational rearrangements of UFL1 and DDRGK1. (C) Experimental approach for detecting interactors of nascent chain-associated ribosomes. (D) Ribosomal pellet was obtained by sucrose cushion centrifugation followed by GFP immunoprecipitation from RKO iCas9 parental cell line upon 24h expression of ERK0 or ERK20 reporter. Protein levels are analyzed by immunoblotting. (E) Quantification of UFL1 association normalized to eluate nascent chain levels from (D). (F) Ribosomal pellet was obtained by sucrose cushion centrifugation followed by GFP immunoprecipitation from RKO iCas9 AAVS1 (non-targeting control), NEMF or UFM1 KO cell line upon 24h expression of CytoK20 or ERK20 reporter. Protein levels are analyzed by immunoblotting. (G) Quantification of UFL1 association normalized to eluate nascent chain levels from (F) for cells expressing CytoK20 or ERK20. (H) Quantification of LTN1 association normalized to eluate nascent chain levels from (F). FL – full length, AP – arrested peptide, # - UFC1-UFM1 complex [30], * - degradation products.

Figure 4. UFMylation machinery acts together with RQC to clear arrested peptides at the ER Upon ribosomal stalling at the ER, ZNF598 recognizes and ubiquitinates 40S proteins, followed by ASC-1 complex-mediated splitting of the leading ribosome. The remaining 60S-peptidyl-tRNA complex is recognized and UFMylated by the UFM1 E3 ligase complex, independently of downstream RQC factors. UFMylation allows easier access to nascent chain that gets ubiquitinated by LTN1 with the help of NEMF. The nascent chain gets degraded by the proteasome and the 60S subunit is recycled.

Supplementary Figure 1. (A) Scatter plot of proteins enriched with UFMylated ribosomes upon 3h 4μM ANS treatment compared to untreated HCT116 FLAG-UFM1 cells, shown as $\log_2$ fold change of eluates over ribosome cushions (second replicate from Figure 1B). (B) Immunoblots showing knockdowns of RQC proteins Pelota, ASCC3, or ZNF598 upon 72h siRNA treatment in HCT116 cells. GAPDH is used as a loading control. (C) Readthrough of reporters from Fig. 1D shown by mCherry/GFP ratio measured by FACS after 24h expression in HCT116 cells upon siRNA-mediated knockdown of Pelota compared to non-targeting control siRNA. (D) Immunoblots showing knockouts of RQC proteins NEMF, LTN1, ASCC3,

ANKZF1, or UFM1 knockout upon 48h dox treatment in RKO cells. GAPDH or eEF2 are used as a loading control. (E) Immunoblots showing reporter accumulation upon 24h expression of CytoK20 or ERK20 in HCT116 cells after treatment with either 20 nM MG132 for 3h, 10 nM Baf for 16h, or untreated as a control. AP – arrested peptide, * - degradation products.

Supplementary Figure 2. (A) UFMylation levels visualized by UFM1 immunoblot in untreated or 1h 4μM ANS treated HCT116 cells upon 72h siRNA-mediated knockdown of RQC components or non-targeting control. (B) Quantification of (A). (C) Top: polysome profiles from HCT116 cells upon 72h knockdown of ZNF598 (right panel) or control siRNA (left panel). Bottom: immunoblots showing RPL26 and RPS10 protein levels from corresponding fractions. (D) UFMylation levels visualized by UFM1 immunoblot in HCT116 cells upon 72h siRNA-mediated knockdown of RQC components or non-targeting control, and 24h expression of ERK0. (E) Quantification of (D). # - UFC1-UFM1 complex, * - degradation products.

Materials and Methods

Mammalian cell culture

HCT116 tetON (doxycycline-inducible) OsTIR1 cells obtained the Masato Kanemaki lab [44] were cultured in McCoy's 5A (modified) medium (Sigma, M9309) supplemented with 10% fetal bovine serum (Gibco, 10437028), 2 mM L-Glutamine (Sigmam, G7513), 1% Pen/Step (Sigma, P0781). RKO-Dox-Cas9 cells (expressing doxycycline-inducible Cas9), a kind gift from from Johannes Zuber lab [45] were cultured in RPMI-1640 media (Sigma, R8758) supplemented with 10% fetal bovine serum (Gibco, 10437028), 2 mM L-Glutamine (Sigmam, G7513), 1% Pen/Step (Sigma, P0781), 1x non-essential amino acids (Thermo Scientific, 11140050), and 1 mM sodium pyruvate (Gibco, 11360070). Cell lines were grown in a humidified incubator at 37°C and 5% CO_2. All cell lines were regularly tested for *Mycoplasma* infection with the EZ-PCR™ Mycoplasma Detection Kit (Biological Industries).

Mammalian cell line generation

RKO-Dox-Cas9 (iCas9) cell lines for doxycycline inducible knockout of the genes encoding RQC components were established using lentiviral transduction with lentiviral particles (produced as described in [46] containing Dual-sgRNA_hU6-mU6 vectors described in [45] expressing two sgRNAs (Supplementary table 2) from human and mouse U6 promoters and eBFP2 from a PGK promoter. The eBFP2-positive cells were FACS sorted at BD FACSMelody™ Cell Sorter at Max Perutz Labs BioOptics FACS Facility.

To endogenously tag UFM1 with N-terminal 3xFLAG sequence human UFM1 N-terminal homology arms sequence was amplified using HindIII_UFM1_N_HAs_F and XhoI_UFM1_N_HAs_R primers. The UFM1 homology arms were inserted into the pMK344 plasmid backbone (Addgene #121179) using HindIII and XhoI restriction sites. To remove the BamHI site the plasmid was treated with HindIII and XbaI restriction enzymes and ligated through annealed overlapping oligos (pMK344_oligo_HindIII_XbaI_F/R). The BamHI and SalI restriction sites were

introduced to the homology arms using BamHI_UFM1_N-HA and SalI_UFM1_N-HA primers. The BSD-P2A-3xFLAG sequence was cloned using the pMK347 (BSD-P2A-mAID) plasmid (Addgene #121181) which was digested with the Esp3I and BamHI enzymes to remove P2A-mAID and ligated using P2A-3xFLAG template made from annealed oligos (3xFLAG_pMK347_F/R) with cohesive ends. The BSD-P2A-3xFLAG sequence was inserted into the plasmid with N-terminal homology arms of UFM1 using SalI and BamI restriction sites resulting in the HDR template. The PAM sites were mutated in the HDR template using site-directed mutagenesis with a primer pair UFM1_gRNA_517_PAM_mut_F/R. To clone the Hygro-P2A-3xFLAG HDR template Hygro-P2A-3xFLAG was amplified from pMK344 with KS_F and P2A_3xFLAG_BamHI_R primers and cloned to replace the BSD-P2A-3xFLAG in the final UFM1 HDR template with mutated PAM sites. All primer sequences are listed in Supplementary table 2.

To introduce the 3xFLAG tag to the N-terminus of the endogenous UFM1 HCT116 tetON OsTIR1 cells [44] were transiently transfected with 1:1:2 ratio mixture of the BSD-P2A-3xFLAG HDR, Hygro-P2A-3xFLAG HDR template plasmids and pSpCas9 (BB)-2A-GFP (PX458) (plasmid #48138, Addgene) [47] targeting the first exon of the UFM1 gene (Supplementary table 2) using the Fugene HD (Promega) reagent according to the manufacturer's instructions. 24 hours after transfection cell were collected by trypsinization and plated in 1:200 dilution in standard culture media (McCoy's 5A (modified) with 10% FBS, 2 mM L-Glutamine, 1% Pen/Step). On the next day the media was supplemented with 100 µg/mL of Hygromycin B Gold (InvivoGen, #ant-hg) and 10 µg/mL of Blasticidin S Hydrochloride (InvivoGen, #ant-bl-05). Cells were grown in selection media until visible colonies were formed and expanded in 96-well plates. The homozygous insertion was verified using western blotting with anti-UFM1 (ab108062, Abcam) and anti-GAPDH (10494-1-AP, Proteintech) antibodies and genotyped using DirectPCR Lysis-Reagent Cell (Peqlab, VWR) with hsUFM1_HAs_F, hsUFM1_HAs_R, HygR_F, and BSDR_F primers.

Co-Immunoprecipitation mass spectrometry of 3xFLAG-UFM1

For mass spectrometry of 3xFLAG-UFM1 co-immunoprecipitation (co-IP) ten 15 cm (diameter) dishes of 80% confluent 3xFLAG-UFM1 HCT116 per condition were used. Cell culture media was exchanged to fresh one 16 hours prior collection. To induce ribosome stalling cells were treated with 4 µM anisomycin for 3 h. Cells were washed with warm (37°C) PBS supplemented with 100 µg/mL cycloheximide, lysed on the plate with ice-cold lysis buffer (20 mM HEPES pH 7.3, 150 mM KCl, 5 mM $MgCl_2$, 1% Triton X-100, 100 mg/mL cycloheximide, 1 mM DTT, 1x EDTA-free protease inhibitor cocktail), scraped, and transferred to 2 mL RNase-free tubes. Cell lysates were further incubated on ice for 10 min with intermittent vortexing, passed three times through the 27G needle, and clarified on a table-top centrifuge at maximum speed (20,000 g) for 20 min at 4°C. Total RNA concentration in the lysate was estimated using OD A260 measurement on Nanodrop. The lysate concentrations were equalized and brought to 1.5 mL with lysis buffer. Polysomes were digested with 2.5 µg RNase A (Thermo

Scientific, EN0531) per 750 ng total RNA for 20 min at 25°C at 750 rpm. The reaction was quenched with 0.4 mg/mL heparin. 3 mL of the lysate was layered on top of 9 mL 25% sucrose cushion in gradient buffer (25% sucrose, 20 mM HEPES pH 7.3, 150 mM KCl, 5 mM $MgCl_2$, 100 mg/mL cycloheximide, 1x EDTA-free protease inhibitor cocktail). Ribosomes were pelleted by centrifugation at 100,000 g overnight at 4°C in a SW40Ti rotor. After the supernatant was removed, the ribosomal pellet was resuspended with 600 µL of resuspension buffer (10% glycerol, 20 mM HEPES pH 7.3, 150 mM KCl, 5 mM $MgCl_2$, 0.1% NP-40, 100 mg/mL cycloheximide, 1x EDTA-free protease inhibitor cocktail).

For co-IP 100 µg of Monoclonal ANTI-FLAG® M2 antibody (Sigma, F1804) was coupled to the 400 µL of protein G Dynabeads (Invitrogen) in 1 mL of lysis buffer without DTT and cycloheximide for 20 min rotating at room temperature, washed three times with 1 mL of 25% sucrose in gradient buffer supplemented with 0.1% NP-40, resuspended in the original bead volume and added to 500 µL of resuspended ribosomal pellet. The IP was incubated on a rotator at +4ºC for overnight, washed 4 times with wash buffer (10% glycerol, 20 mM HEPES pH 7.3, 150 mM KCl, 5 mM $MgCl_2$, 0.01% NP-40, 100 mg/mL cycloheximide, 1x EDTA-free protease inhibitor cocktail), followed by 5 washes with (20mM HEPES, KCl 150mM). The samples were eluted from beads using tryptic digestion and the peptides were submitted for mass spectrometry at Vienna BioCenter Proteomics Core Facility.

100 µL aliquot of ribosomal pellet sample was taken as an IP input control. It was filled with dH_2O up to 1 mL, 10 µL of 10% sodium deoxycholate were added and vortexed. Proteins were precipitated on ice for 10 min after addition of 200 µL of 50% TCA and centrifuged at 20,000 g for 20 min at 4°C. Pellet was washed twice with 1 mL of 100% acetone, all supernatant was discarded and the pellet was vacuum-dried briefly for 5 min at 45°C vacuum evaporator. Samples were prepared and tryptic digested, using the iST kit (PO 00001, PreOmics) according to the manufacturer's instructions. 250 ng of each peptide sample were submitted for mass spectrometry at Vienna BioCenter Proteomics Core Facility. For the IP analyses, we used a cut off of at least 10% coverage of a protein of interest.

Mammalian siRNA and plasmid transfections

For reporter accumulation experiments, RKO iCas9 cells were seeded in 6-well plates and treated with 450 nM doxycycline for 48 h to induce expression of Cas9. The cells were then transfected with 2 µg plasmid using jetOPTIMUS® reagent according to the manufacturer’s instructions (Avantor, 101000051). Cells were washed with cold PBS buffer and collected on plate in RIPA buffer (150 mM NaCl, 1% NP-40, 0.5% Sodium deoxycholate, 0.1% SDS, and 25 mM TRIS pH 7.4) with 1x EDTA-free protease inhibitor cocktail (Roche, 11873580001). Cell lysate was clarified on a table-top centrifuge at maximum speed (20,000 g) for 20 min at 4°C.

To test the effect of RQC components’ loss on UFMylation, HCT116 tetON OsTIR1 cells were seeded in 24-well plates and transfected with Dharmacon ON-TARGETplus Human siRNA SMARTpools at 10 nM against ASCC3 (L-012757-01-0005) and at 25 nM against PELO (L-019068-01-0005) and ZNF598 (L-007104-00-0005). ON-

TARGETplus Non-targeting Control Pool (D-001810-10-05) at 25 nM was used as a control. Cells were passed to 6-well plates and either transfected with 2 µg of plasmids containing CytoK0, CytoK20, ERK0, or ERK20 reporters [28] for 24 h using jetOPTIMUS® reagent (Avantor, 101000051) according to the manufacturer's instructions or treated with 4 µM anisomycin dissolved in DMSO for 1 h before collection.

RKO iCas9 cells were seeded in 10-cm dishes in media supplemented with 450 nM doxycycline for 48h to induce expression of Cas9. Cells were then either transfected with 10 µg of plasmids containing CytoK0, CytoK20, ERK0, or ERK20 reporters [28] for 24 h using jetOPTIMUS® reagent according to the manufacturer's instructions (Avantor, 101000051), or treated with 4µM anisomycin dissolved in DMSO for 1 h before collection.

Flow cytometry analysis

HCT116 tetON OsTIR1 cells were seeded in 24-well plates and transfected with Dharmacon ON-TARGETplus Human siRNA SMARTpools for 72 h total as described in "Mammalian siRNA and plasmid transfections". Cells were passed to 6-well plates and transfected with 2 µg of pEGFP-N1 plasmid containing CytoK0, CytoK20, ERK0, or ERK20 reporters [28] for 24 h using jetOPTIMUS® reagent according to the manufacturer's instructions (Avantor, 101000051). Cells were harvested in trypsin, resuspended in full media and analysed by flow cytometry (BD LSRFortessa™ Cell Analyser). Data was analysed in FlowJo software.

Cell lysis and immunoblotting

Clear cell lysates were collected in RIPA buffer with 1xEDTA-free protease inhibitor cocktail (Roche, 11873580001), clarified on a table-top centrifuge at maximum speed (20,000 g) for 20 min at 4°C, and analysed on 10%, 12% or 15% SDS-polyacrylamide gels, followed by a semi-dry transfer (BioRad blotter) or wet transfer (120V, 1 h 20 min on a BioRad blotter) on a 0.2 µm nitrocellulose membrane. Membrane was blocked in 1xTBS buffer with 0.1% Tween containing 5% milk for 1 h at room temperature. Primary antibody (listed in Supplementary table 2) was diluted in 2.5% milk 1x TBS-0.1% Tween buffer and incubated either 1 h at room temperature or at 4°C overnight, followed by three washes with 1x TBS-0.1% Tween buffer. Secondary antibody conjugated with horseradish peroxidase (Promega) was diluted in 2.5% milk 1x TBS-0.1% Tween buffer and incubated for 1 h at room temperature, followed by three washes with 2.5% milk 1x TBS-0.1% Tween buffer. The blots were developed using chemiluminescent detection on iBright ThermoFisher machine and quantified in iBright Analysis Software (ThermoFisher).

Immunoprecipitations

For detecting UFL1 binding to nascent chain-containing 60S ribosomes, RKO iCas9 cell lines expressing gRNA against AAVS1 (non-targeting control), NEMF, or UFM1 (gRNA sequences are listed in Supplementary table 2) were seeded in 10-cm dishes (2 dishes per condition) in media supplemented with 450 nM doxycycline for 48h to

induce expression of Cas9. Cells were then transfected with 10 µg of plasmids containing CytoK20, or ERK20 reporters [28] for 24 h using jetOPTIMUS® reagent according to the manufacturer's instructions (Avantor, 101000051). Cells were then washed in cold PBS supplemented with 100 µg/mL cycloheximide, lysed on the plate with ice-cold lysis buffer (20 mM HEPES pH 7.3, 120 mM KCl, 5 mM $MgCl_2$, 1% NP-40, 100 µg/mL cycloheximide, 0.5 mM DTT, 1x EDTA-free protease inhibitor cocktail). Cell lysates were further incubated on ice for 10 min with intermittent vortexing, passed three times through the 27G needle, and clarified on a table-top centrifuge at maximum speed (20,000 g) for 20 min at 4°C. 700 µL of the lysate was layered on top of 233 µL of sucrose cushion (1 M sucrose, 20 mM HEPES pH 7.3, 120 mM KCl, 5 mM $MgCl_2$, 100 µg/mL cycloheximide, 0.5 mM DTT). Ribosomes were pelleted by centrifugation at 100,000 g for 1,5 h at 4°C in a TLA100.3 rotor. After the supernatant was removed, the ribosomal pellet was resuspended with 150 µL of lysis buffer. Immunoprecipitations were performed with 40 µL of resuspended GFP-Trap® Magnetic Particles (ChromoTek, gtd-20) per condition, the mixture was incubated on a rotator at +4ºC for 1 h, washed 3 times with wash buffer (20 mM HEPES pH 7.3, 195 mM KCl, 5 mM $MgCl_2$, 0.5% NP-40, 100 µg/mL cycloheximide, 0,1 mM DTT, 1x EDTA-free protease inhibitor cocktail), and eluted in 30 µL of 1xSDS sample buffer without DTT. Samples were incubated at 70°C for 10 min, the eluate was separated from the magnetic particles, DTT was added to the final concentration of 10 mM, samples were incubated at 95°C for 5 min and loaded on a SDS-PAGE gel followed by Western blotting.

Plant experiments

All *Arabidopsis thaliana* lines used in this study originate from the Columbia (Col-0) ecotype. Mutant lines used in this study are listed in Supplementary table 2. Seedlings were grown in liquid 1/2 MS medium containing 1% sucrose under 16 h light/8 h dark photoperiod for 7 days with shaking at 80 rpm. 7-day-old seedling grown in liquid 1/2 MS medium were treated with 100 µM anisomycin (ANS) for 16 hours under continuous light with shaking at 80 rpm. An equal volume of pure dimethyl sulfoxide (DMSO) was added as control. Subsequently, seedlings were then frozen in liquid nitrogen after chemical treatment and homogenized for western blotting. The total protein was extracted with Grinding Buffer (50 mM Tris-HCl, 150 mM NaCl, 1 % Glycerol, 0.5 % NP-40, 1.5 mM $MgCl_2$, 1x protease inhibitor cocktail). The SDS loading buffer was added to lysates, and the samples then were boiled at 95°C for 10 minutes. 10 µg of sample was loaded per lane. SDS-PAGE was performed using gradient 4–20% Mini-PROTEAN TGX Precast Protein Gels (BioRad). Blotting on nitrocellulose membranes was performed using a semi-dry Turbo Transfer Blot System (BioRad). The membranes were blocked with 5 % skimmed milk in TBS and 0.1 % Tween 20 (TBS-T) for 1 hour at room temperature. Subsequently, the membranes were incubated with primary antibody, followed by incubation with secondary antibody conjugated to horseradish peroxidase (HRP). After three times 10 minutes washes with TBS-T, the immune-reaction was developed using ECL SuperSignal West Femto (Thermo) and detected with iBright Imaging System (Thermo). Protein bands intensity

was quantified using the iBright Imaging analysis System (Thermo). The average relative intensities and a standard error were calculated from three biological replicates.

Statistical analysis and reproducibility

All experiments were performed at least 3 times unless otherwise indicated in figure legends. Statistical analysis was performed in GraphPad Prism 10 software using Student t-test.

Figure 1

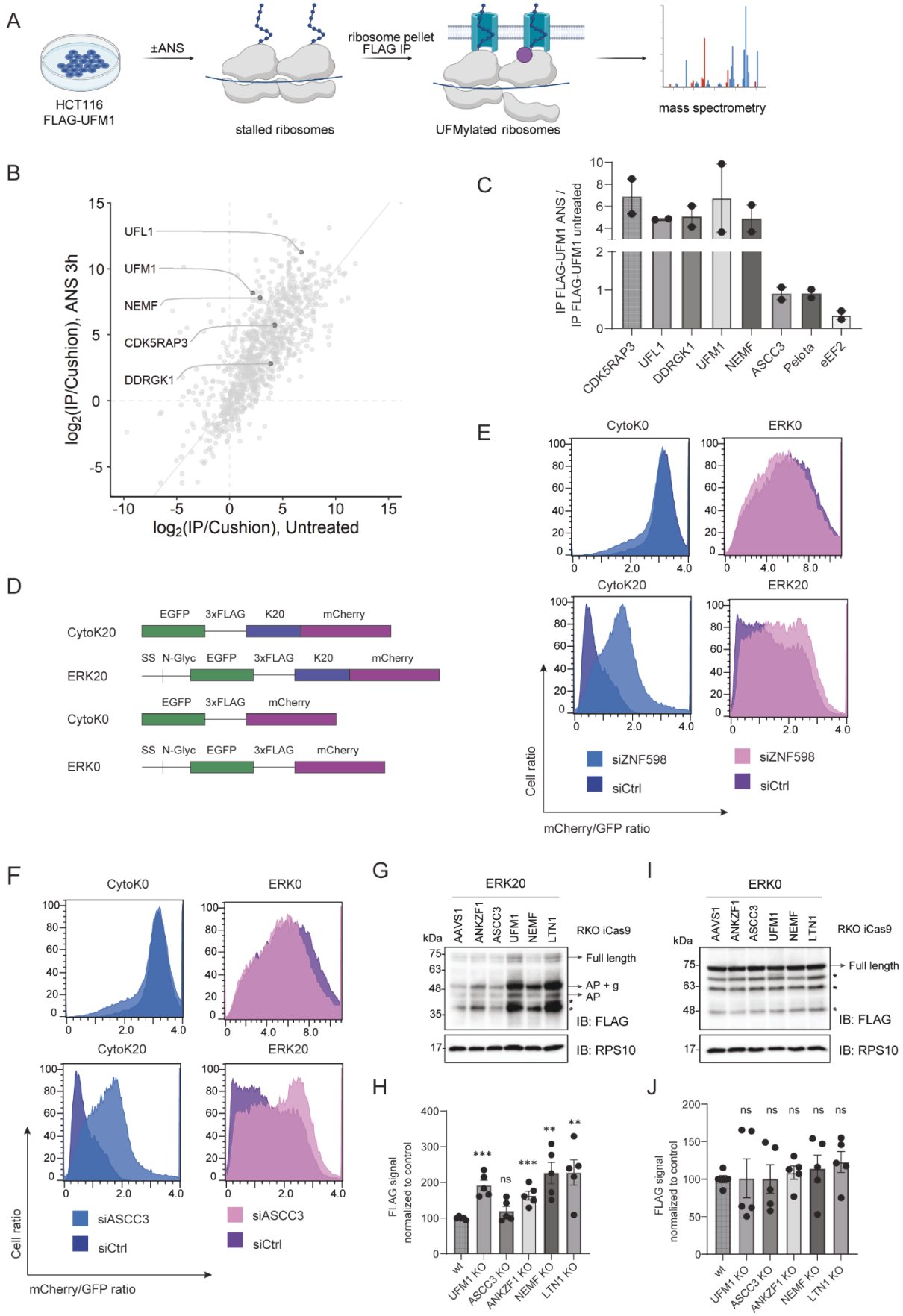

Figure 1. RQC and UFMylation machinery are needed to clear stalled peptides at the ER

(A) Scheme of mass spectrometry analysis of UFMylated ribosomes. (B) Scatter plot of

proteins enriched with UFMylated ribosomes upon 3h 4μM ANS treatment compared to untreated HCT116 FLAG-UFM1 cells. (C) Enrichment of FLAG-eluates with 10% coverage cut-off from ANS treated HCT116 FLAG-UFM1 cells over FLAG-eluates from untreated control HCT116 FLAG-UFM1 cells normalized to respective cushion samples, shown as $\log_2$ fold change, identified by mass spectrometry experiment from (A). (D) Schematic representation of control (K0) and stalling (K20) cytosolic and ER reporters. (E and F) Readthrough of reporters from (D) shown by mCherry/GFP ratio measured by FACS after 24h expression in HCT116 cells upon siRNA-mediated knockdown of ZNF598 (E) or ASCC3 (F) compared to non-targeting control siRNA. (G and I) Reporter accumulation shown by FLAG immunoblot in RKO iCas9 KO cell lysates upon 48h dox treatment to induce AAVS1 (non-targeting control), ANKZF1, ASCC3, UFM1, NEMF or LTN1 knockout, upon 24h ERK20 (G) or ERK0 expression (I) normalized to RPS10 loading control. AP – arrested peptide, g – glycosylation, * - degradation products. (H) Quantification of (G). (J) Quantification of (I).

Figure 2

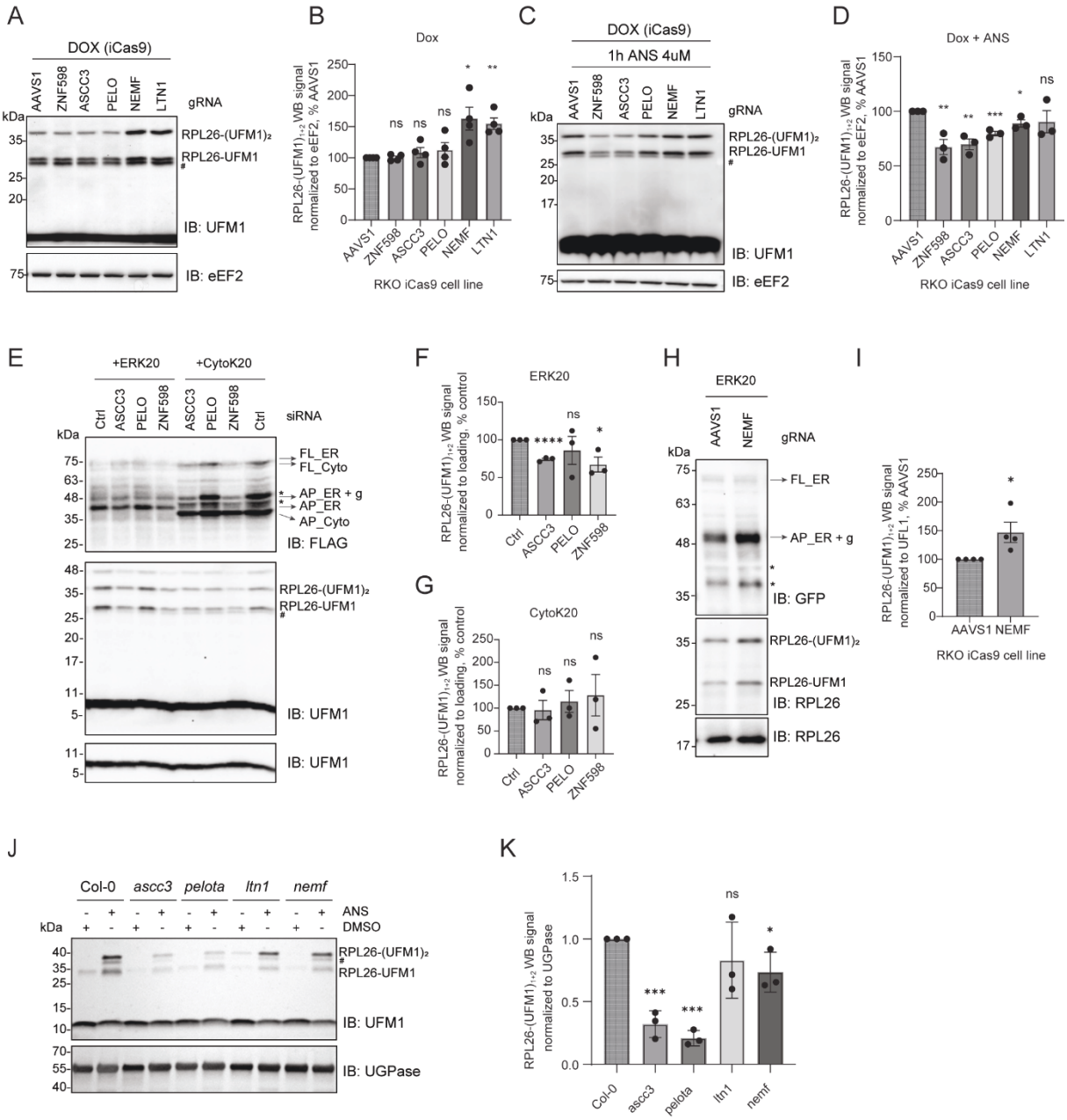

Figure 2. RPL26 is UFMylated on post-split 60S subunit upon ribosomal stalling at the ER (A and C) UFMylation levels visualized by UFM1 immunoblot in RKO iCas9 cells upon 48h dox treatment to induce RQC components or non-targeting AAVS1 knockout in untreated (A) or 1h 4μM ANS treated cells (C). (B) Quantification of (A). (D) Quantification of (C). (E) UFMylation levels visualized by UFM1 immunoblot in HCT116 cells upon 72h siRNA-mediated knockdown of RQC components or non-targeting control, and 24h expression of ERK20 or CytoK20. (F and G) Quantification of (E) for cells expressing ERK20 (F) or CytoK20 (G) shown by FLAG signal normalized to loading control. (H) UFMylation levels visualized by RPL26 immunoblot in RKO iCas9 cells upon 48h dox treatment to induce non-targeting AAVS1 or NEMF knockout upon 24h expression of ERK20 reporter. (I) Quantification of (H). (J) 7-day-old *Arabidopsis* seedlings of wildtype (Col-0) and RQC component mutant (*ascc3*, *pelota*, *ltn1*, *nemf*, *rqc1*, *edf1*) were treated with either DMSO or 100 μM ANS for 16 hours. The UFMylation level was tested via immunoblotting using anti-UFM1 antibody, with UGPase was introduced

as loading control. The data shown are representative of three biological replicates. (K) Quantification of (J) for ANS-treated samples. FL – full length, AP – arrested peptide, g – glycosylation, # - UFC1-UFM1 complex [30], * - degradation products.

Figure 3

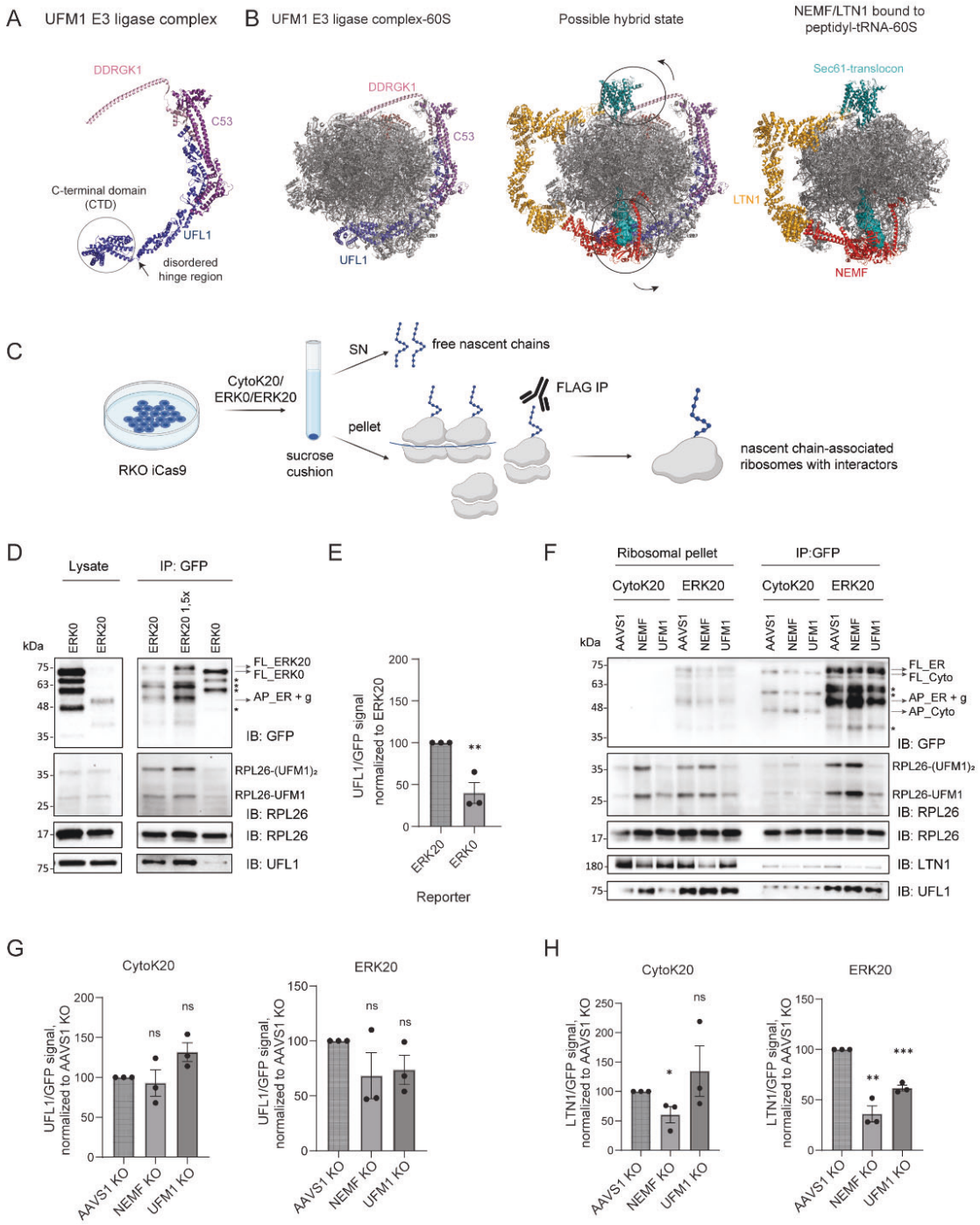

Figure 3. UFL1 UFMylates nascent chain-bound 60S subunits (A) The cryostructural model of UFM1 E3 ligase complexes shows flexibility around the CTD region of UFL1 (pbd: 8ohd). (B) Left: The structure of UFM1 E3 ligase complex bound to 60S subunit (pbd: 8ohd), right: the structure of NEMF/LTN1 complex bound to peptidyl-tRNA-60S complex (pdb: 3j92, 8agw) docked on translocon (pdb:3j7r), middle: overlay of two structures shows a possible hybrid state with conformational rearrangements of UFL1 and DDRGK1. (C) Experimental approach for detecting interactors of nascent chain-associated ribosomes. (D) Ribosomal pellet was

obtained by sucrose cushion centrifugation followed by GFP immunoprecipitation from RKO iCas9 parental cell line upon 24h expression of ERK0 or ERK20 reporter. Protein levels are analyzed by immunoblotting. (E) Quantification of UFL1 association normalized to eluate nascent chain levels from (D). (F) Ribosomal pellet was obtained by sucrose cushion centrifugation followed by GFP immunoprecipitation from RKO iCas9 AAVS1 (non-targeting control), NEMF or UFM1 KO cell line upon 24h expression of CytoK20 or ERK20 reporter. Protein levels are analyzed by immunoblotting. (G) Quantification of UFL1 association normalized to eluate nascent chain levels from (F) for cells expressing CytoK20 or ERK20. (H) Quantification of LTN1 association normalized to eluate nascent chain levels from (F). FL – full length, AP – arrested peptide, # - UFC1-UFM1 complex [30], * - degradation products.

Figure 4

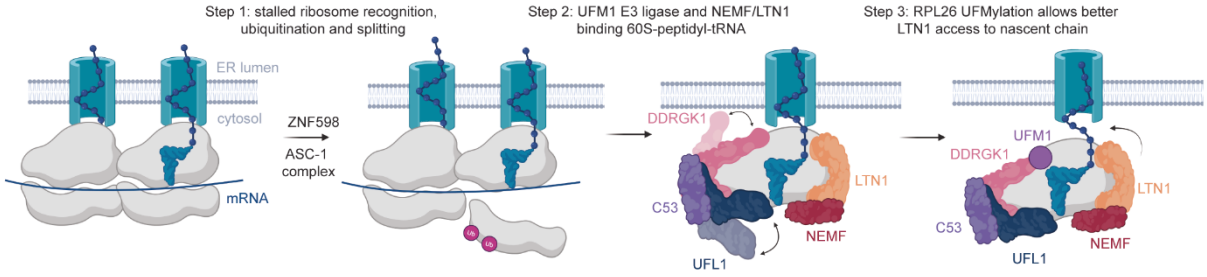

Figure 4. UFMylation machinery acts together with RQC to clear arrested peptides at the ER Upon ribosomal stalling at the ER, ZNF598 recognizes and ubiquitinates 40S proteins, followed by ASC-1 complex-mediated splitting of the leading ribosome. The remaining 60S-peptidyl-tRNA complex is recognized and UFMylated by the UFM1 E3 ligase complex, independently of downstream RQC factors. UFMylation allows easier access to nascent chain that gets ubiquitinated by LTN1 with the help of NEMF. The nascent chain gets degraded by the proteasome and the 60S subunit is recycled.

Supplementary figure 1

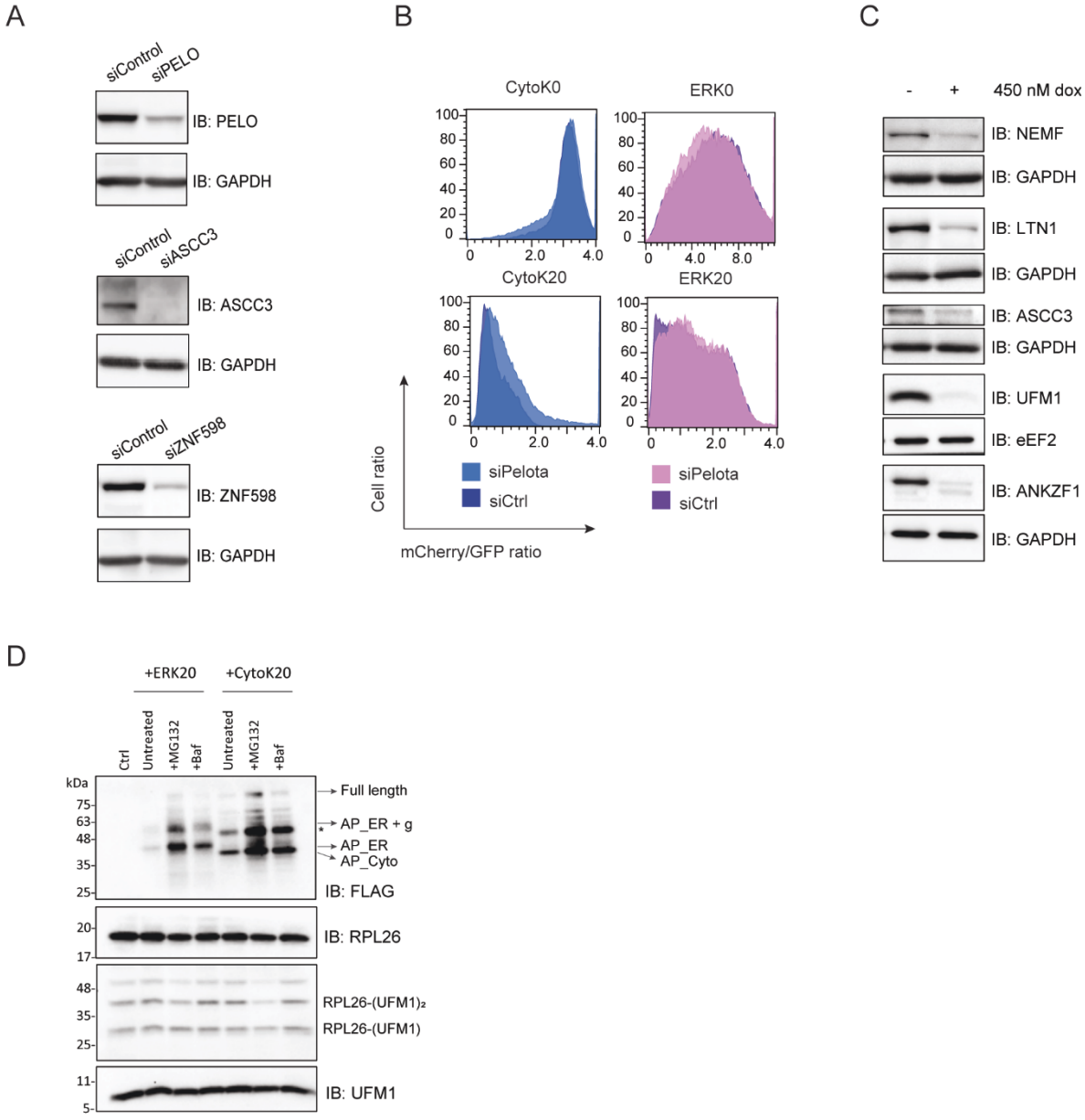

Supplementary Figure 1. (A) Scatter plot of proteins enriched with UFMylated ribosomes upon 3h 4μM ANS treatment compared to untreated HCT116 FLAG-UFM1 cells, shown as $\log_2$ fold change of eluates over ribosome cushions (second replicate from Figure 1B). (B) Immunoblots showing knockdowns of RQC proteins Pelota, ASCC3, or ZNF598 upon 72h siRNA treatment in HCT116 cells. GAPDH is used as a loading control. (C) Readthrough of reporters from Fig. 1D shown by mCherry/GFP ratio measured by FACS after 24h expression in HCT116 cells upon siRNA-mediated knockdown of Pelota compared to non-targeting control siRNA. (D) Immunoblots showing knockouts of RQC proteins NEMF, LTN1, ASCC3, ANKZF1, or UFM1 knockout upon 48h dox treatment in RKO cells. GAPDH or eEF2 are used as a loading control. (E) Immunoblots showing reporter accumulation upon 24h expression of CytoK20 or ERK20 in HCT116 cells after treatment with either 20 nM MG132 for 3h, 10 nM Baf for 16h, or untreated as a control. AP – arrested peptide, * - degradation products.

Supplementary figure 2

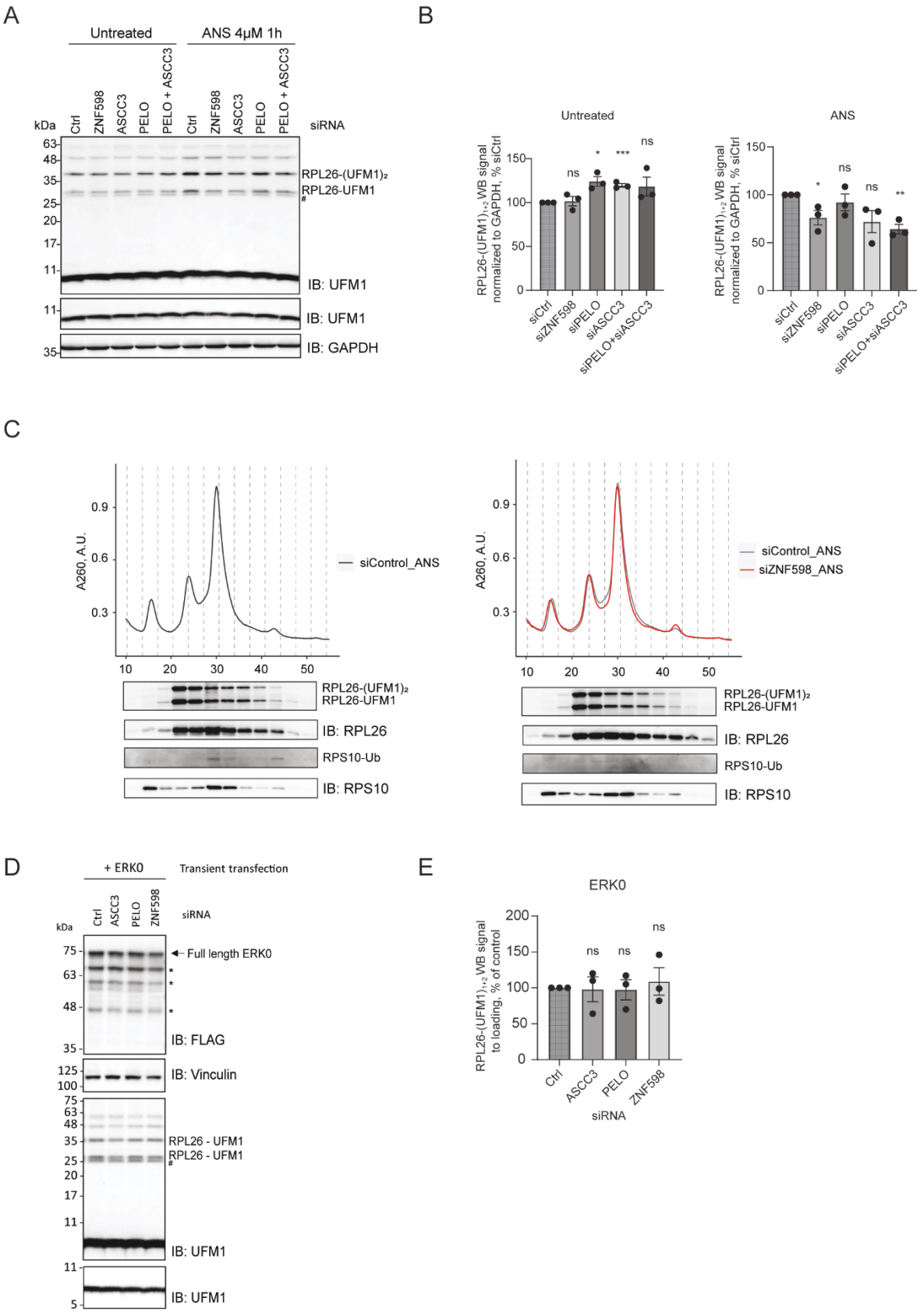

Supplementary Figure 2. (A) UFMylation levels visualized by UFM1 immunoblot in untreated or 1h 4µM ANS treated HCT116 cells upon 72h siRNA-mediated knockdown of RQC components or non-targeting control. (B) Quantification of (A). (C) Top: polysome profiles from

HCT116 cells upon 72h knockdown of ZNF598 (right panel) or control siRNA (left panel). Bottom: immunoblots showing RPL26 and RPS10 protein levels from corresponding fractions. (D) UFMylation levels visualized by UFM1 immunoblot in HCT116 cells upon 72h siRNA-mediated knockdown of RQC components or non-targeting control, and 24h expression of ERK0. (E) Quantification of (D). # - UFC1-UFM1 complex, * - degradation products.

Subject: EMBOJ-2025-121175: Receipt of New Manuscript by The EMBO Journal
From: contact@embojournal.org
Date: 15-May-25, 9:57 AM
To: milicam97@univie.ac.at

15th May 2025

Dear Mrs. Mihailovic,

Thank you for your submission to The EMBO Journal. This is to inform you that you are listed as a co-author of EMBOJ-2025-121175 with the title 'The coordinated action of UFMylation and the RQC pathways clears arrested polypeptides at the ER'.

Corresponding Author(s):

Dr. Gülsün Elif Karagöz

, Yasin Dagdas (yasin.dagdas@gmi.oeaw.ac.at)

Contributing Author(s):

Milica Mihailovic, Aleksandra S Anisimova, Bu Erte, Ni Zhan, Yasin Dagdas

Please note that as a contributing author, you have agreed to the submission and data reported. The corresponding author is responsible for communicating with the journal and managing communication between co-authors. Please contact the corresponding author directly with any queries you may have. If you are listed as a co-corresponding author of this manuscript, please note that our manuscript system is presently only able to recognize a primary corresponding author for communication purposes.

Sincerely,

The EMBO Journal
contact@embojournal.org

Content alerts: embopress.org/alertsfeeds
Follow us on Bluesky: @embojournal.org

5.3 Confirmation of manuscript status for “Dual regulation of the unfolded protein response by IGF2BP3 during ER stress”

From: genesdev@cshlbp.org
Subject: [EXTERN] Genes & Development GENESDEV/2025/353291 -- Manuscript Correspondence
Date: 2 September 2025 at 22:22
To: guelsuen.karagoez@meduniwien.ac.at

MS ID#: GENESDEV/2025/353291
MS TITLE: Dual regulation of the unfolded protein response by IGF2BP3 during ER stress

Dear Dr. Gulsun Elif Karagoz,

We have received the manuscript that you have submitted to Genes&Development (GENESDEV/2025/353291). Your paper has been sent out for review and you will be notified as soon as a decision has been reached.

Many Thanks,

Genes & Development
Editorial Office

6 References

1. Rapoport, T. A. Protein translocation across the eukaryotic endoplasmic reticulum and bacterial plasma membranes. *Nature 2007 450:7170* **450**, 663–669 (2007).

2. Shao, S. & Hegde, R. S. Membrane Protein Insertion at the Endoplasmic Reticulum. *Annu Rev Cell Dev Biol* **27**, 25 (2011).

3. Ghaemmaghami, S. *et al.* Global analysis of protein expression in yeast. *Nature 2003 425:6959* **425**, 737–741 (2003).

4. Stevens, F. J. & Argon, Y. Protein folding in the ER. *Semin Cell Dev Biol* **10**, 443–454 (1999).

5. Kleizen, B. & Braakman, I. Protein folding and quality control in the endoplasmic reticulum. *Curr Opin Cell Biol* **16**, 343–349 (2004).

6. Tu, B. P. & Weissman, J. S. Oxidative protein folding in eukaryotes: mechanisms and consequences. *J Cell Biol* **164**, 341 (2004).

7. Christianson, J. C. & Ye, Y. Cleaning up in the endoplasmic reticulum: ubiquitin in charge. *Nat Struct Mol Biol* **21**, 325 (2014).

8. Dayel, M. J., Horn, E. F. Y. & Verkman, A. S. Diffusion of green fluorescent protein in the aqueous-phase lumen of endoplasmic reticulum. *Biophys J* **76**, 2843–2851 (1999).

9. Kettel, P. & Karagöz, G. E. Endoplasmic reticulum: Monitoring and maintaining protein and membrane homeostasis in the endoplasmic reticulum by the unfolded protein response. *Int J Biochem Cell Biol* **172**, (2024).

10. Karagöz, G. E., Acosta-Alvear, D. & Walter, P. The Unfolded Protein Response: Detecting and Responding to Fluctuations in the Protein-Folding Capacity of the Endoplasmic Reticulum. *Cold Spring Harb Perspect Biol* **11**, a033886 (2019).

11. Wang, X. Z. *et al.* Cloning of mammalian Ire1 reveals diversity in the ER stress responses. *EMBO J* **17**, 5708–5717 (1998).

12. Tirasophon, W., Welihinda, A. A. & Kaufman, R. J. A stress response pathway from the endoplasmic reticulum to the nucleus requires a novel bifunctional protein kinase/endoribonuclease (Ire1p) in mammalian cells. *Genes Dev* **12**, 1812 (1998).

13. Noh, S. J., Kwon, C. S. & Chung, W. I. Characterization of two homologs of Ire1p, a kinase/endoribonuclease in yeast, in Arabidopsis thaliana. *Biochimica et Biophysica Acta (BBA) - Gene Structure and Expression* **1575**, 130–134 (2002).

14. Koizumi, N. *et al.* Molecular characterization of two Arabidopsis Ire1 homologs, endoplasmic reticulum-located transmembrane protein kinases. *Plant Physiol* **127**, 949–962 (2001).

15. Zhou, J. *et al.* The crystal structure of human IRE1 luminal domain reveals a conserved dimerization interface required for activation of the unfolded protein response. *Proc Natl Acad Sci U S A* **103**, 14343–14348 (2006).

16. Gardner, B. M. & Walter, P. Unfolded proteins are Ire1-activating ligands that directly induce the unfolded protein response. *Science* **333**, 1891–1894 (2011).

17. Karagöz, G. E. *et al.* An unfolded protein-induced conformational switch activates mammalian IRE1. *Elife* **6**, (2017).

18. Yoshida, H., Matsui, T., Yamamoto, A., Okada, T. & Mori, K. XBP1 mRNA Is Induced by ATF6 and Spliced by IRE1 in Response to ER Stress to Produce a Highly Active Transcription Factor. *Cell* **107**, 881–891 (2001).

19. Cox, J. S. & Walter, P. A Novel Mechanism for Regulating Activity of a Transcription Factor That Controls the Unfolded Protein Response. *Cell* **87**, 391–404 (1996).

20. Cox, J. S., Shamu, C. E. & Walter, P. Transcriptional induction of genes encoding endoplasmic reticulum resident proteins requires a transmembrane protein kinase. *Cell* **73**, 1197–1206 (1993).

21. Sidrauski, C. & Walter, P. The Transmembrane Kinase Ire1p Is a Site-Specific Endonuclease That Initiates mRNA Splicing in the Unfolded Protein Response. *Cell* **90**, 1031–1039 (1997).

22. Aragón, T. *et al.* Messenger RNA targeting to endoplasmic reticulum stress signalling sites. *Nature 2008 457:7230* **457**, 736–740 (2008).

23. Li, H., Korennykh, A. V., Behrman, S. L. & Walter, P. Mammalian endoplasmic reticulum stress sensor IRE1 signals by dynamic clustering. *Proc Natl Acad Sci U S A* **107**, 16113–16118 (2010).

24. Korennykh, A. V. *et al.* The unfolded protein response signals through high-order assembly of Ire1. *Nature 2008 457:7230* **457**, 687–693 (2008).

25. Yanagitani, K. *et al.* Cotranslational Targeting of XBP1 Protein to the Membrane Promotes Cytoplasmic Splicing of Its Own mRNA. *Mol Cell* **34**, 191–200 (2009).

26. Korennykh, A. V. *et al.* Structural and functional basis for RNA cleavage by Ire1. *BMC Biol* **9**, 47 (2011).

27. Peschek, J., Acosta-Alvear, D., Mendez, A. S. & Walter, P. A conformational RNA zipper promotes intron ejection during non-conventional XBP 1 mRNA splicing . *EMBO Rep* **16**, 1688–1698 (2015).

28. Lee, A. H., Chu, G. C., Iwakoshi, N. N. & Glimcher, L. H. XBP-1 is required for biogenesis of cellular secretory machinery of exocrine glands. *EMBO J* **24**, 4368–4380 (2005).

29. Lee, A.-H., Iwakoshi, N. N. & Glimcher, L. H. XBP-1 regulates a subset of endoplasmic reticulum resident chaperone genes in the unfolded protein response. *Mol Cell Biol* **23**, 7448–7459 (2003).

30. Acosta-Alvear, D. *et al.* XBP1 Controls Diverse Cell Type- and Condition-Specific Transcriptional Regulatory Networks. *Mol Cell* **27**, 53–66 (2007).

31. Hollien, J. & Weissman, J. S. Decay of Endoplasmic Reticulum-Localized mRNAs During the Unfolded Protein Response. *Science (1979)* **313**, 104–107 (2006).

32. Hollien, J. *et al.* Regulated Ire1-dependent decay of messenger RNAs in mammalian cells. *J Cell Biol* **186**, 323–31 (2009).

33. Lin, J. H. *et al.* IRE1 signaling affects cell fate during the unfolded protein response. *Science* **318**, 944–949 (2007).

34. Han, D. *et al.* IRE1α Kinase Activation Modes Control Alternate Endoribonuclease Outputs to Determine Divergent Cell Fates. *Cell* **138**, 562–575 (2009).

35. Upton, J. P. *et al.* IRE1α cleaves select microRNAs during ER stress to derepress translation of proapoptotic Caspase-2. *Science* **338**, 818–822 (2012).

36. Maurel, M., Chevet, E., Tavernier, J. & Gerlo, S. Getting RIDD of RNA: IRE1 in cell fate regulation. *Trends Biochem Sci* **39**, 245–254 (2014).

37. Ye, J. *et al.* ER stress induces cleavage of membrane-bound ATF6 by the same proteases that process SREBPs. *Mol Cell* **6**, 1355–1364 (2000).

38. Haze, K., Yoshida, H., Yanagi, H., Yura, T. & Mori, K. Mammalian transcription factor ATF6 is synthesized as a transmembrane protein and activated by proteolysis in response to endoplasmic reticulum stress. *Mol Biol Cell* **10**, 3787–3799 (1999).

39. HAZE, K. *et al.* Identification of the G13 (cAMP-response-element-binding protein-related protein) gene product related to activating transcription factor 6 as a transcriptional activator of the mammalian unfolded protein response. *Biochemical Journal* **355**, 19–28 (2001).

40. Bommiasamy, H. *et al.* ATF6alpha induces XBP1-independent expansion of the endoplasmic reticulum. *J Cell Sci* **122**, 1626–1636 (2009).

41. Nadanaka, S., Yoshida, H., Sato, R. & Mori, K. Analysis of ATF6 Activation in Site-2 Protease-deficient Chinese Hamster Ovary Cells. *Cell Struct Funct* **31**, 109–116 (2006).

42. Adachi, Y. *et al.* ATF6 Is a Transcription Factor Specializing in the Regulation of Quality Control Proteins in the Endoplasmic Reticulum. *Cell Struct Funct* **33**, 75–89 (2008).

43. Wang, Y. *et al.* Activation of ATF6 and an ATF6 DNA binding site by the endoplasmic reticulum stress response. *J Biol Chem* **275**, 27013–27020 (2000).

44. Yoshida, H., Haze, K., Yanagi, H., Yura, T. & Mori, K. Identification of the cis-acting endoplasmic reticulum stress response element responsible for transcriptional induction of mammalian glucose-regulated proteins. Involvement of basic leucine zipper transcription factors. *J Biol Chem* **273**, 33741–33749 (1998).

45. Harding, H. P., Calfon, M., Urano, F., Novoa, I. & Ron, D. Transcriptional and translational control in the mammalian unfolded protein response. *Annu Rev Cell Dev Biol* **18**, 575–599 (2002).

46. Harding, H. P., Zhang, Y. & Ron, D. Protein translation and folding are coupled by an endoplasmic-reticulum-resident kinase. *Nature 1999 397:6716* **397**, 271–274 (1999).

47. Shi, Y. *et al.* Identification and characterization of pancreatic eukaryotic initiation factor 2 alpha-subunit kinase, PEK, involved in translational control. *Mol Cell Biol* **18**, 7499–7509 (1998).

48. Harding, H. P. *et al.* An integrated stress response regulates amino acid metabolism and resistance to oxidative stress. *Mol Cell* **11**, 619–633 (2003).

49. Harding, H. P. *et al.* Regulated translation initiation controls stress-induced gene expression in mammalian cells. *Mol Cell* **6**, 1099–1108 (2000).

50. Scheuner, D. *et al.* Translational control is required for the unfolded protein response and in vivo glucose homeostasis. *Mol Cell* **7**, 1165–1176 (2001).

51. Fawcett, T. W., Martindale, J. L., Guyton, K. Z., Hai, T. & Holbrook, N. J. Complexes containing activating transcription factor (ATF)/cAMP-responsive-element-binding protein (CREB) interact with the CCAAT/enhancer-binding protein (C/EBP)-ATF

composite site to regulate Gadd153 expression during the stress response. *Biochemical Journal* **339**, 135–141 (1999).

52. Zinszner, H. *et al.* CHOP is implicated in programmed cell death in response to impaired function of the endoplasmic reticulum. *Genes Dev* **12**, 982–995 (1998).

53. Ron, D. & Walter, P. Signal integration in the endoplasmic reticulum unfolded protein response. *Nature Reviews Molecular Cell Biology 2007 8:7* **8**, 519–529 (2007).

54. Lu, M. *et al.* Opposing unfolded-protein-response signals converge on death receptor 5 to control apoptosis. *Science (1979)* **345**, 98–101 (2014).

55. Adamson, B. *et al.* A multiplexed single-cell CRISPR screening platform enables systematic dissection of the unfolded protein response. *Cell* **167**, 1867 (2016).

56. Benedetti, C., Fabbri, M., Sitia, R. & Cabibbo, A. Aspects of Gene Regulation during the UPR in Human Cells. *Biochem Biophys Res Commun* **278**, 530–536 (2000).

57. Lindner, P., Christensen, S. B., Nissen, P., Møller, J. V. & Engedal, N. Cell death induced by the ER stressor thapsigargin involves death receptor 5, a non-autophagic function of MAP1LC3B, and distinct contributions from unfolded protein response components. *Cell Communication and Signaling* **18**, 1–23 (2020).

58. Jin, S. *et al.* Loss of ATF6α in a human carcinoma cell line is compensated not by its paralogue ATF6β but by sustained activation of the IRE1 and PERK arms for tumor growth in nude mice. *Mol Biol Cell* **34**, ar20 (2023).

59. Van Schadewijk, A., Van'T Wout, E. F. A., Stolk, J. & Hiemstra, P. S. A quantitative method for detection of spliced X-box binding protein-1 (XBP1) mRNA as a measure of endoplasmic reticulum (ER) stress. *Cell Stress Chaperones* **17**, 275–279 (2012).

60. Iwawaki, T., Akai, R., Kohno, K. & Miura, M. A transgenic mouse model for monitoring endoplasmic reticulum stress. *Nat Med* **10**, 98–102 (2004).

61. Clark, E. M., Nonarath, H. J. T., Bostrom, J. R. & Link, B. A. Establishment and validation of an endoplasmic reticulum stress reporter to monitor zebrafish ATF6 activity in development and disease. *DMM Disease Models and Mechanisms* **13**, (2020).

62. Zhang, X., Szabo, E., Michalak, M. & Opas, M. Endoplasmic reticulum stress during the embryonic development of the central nervous system in the mouse. *International Journal of Developmental Neuroscience* **25**, 455–463 (2007).

63. Reimold, A. M. *et al.* An essential role in liver development for transcription factor XBP-1. *Genes Dev* **14**, 152–157 (2000).

64. Harding, H. P. *et al.* Diabetes Mellitus and Exocrine Pancreatic Dysfunction in Perk−/− Mice Reveals a Role for Translational Control in Secretory Cell Survival. *Mol Cell* **7**, 1153–1163 (2001).

65. Reimold, A. M. *et al.* Plasma cell differentiation requires the transcription factor XBP-1. *Nature 2001 412:6844* **412**, 300–307 (2001).

66. Hassler, J. R. *et al.* The IRE1α/XBP1s Pathway Is Essential for the Glucose Response and Protection of β Cells. *PLoS Biol* **13**, e1002277 (2015).

67. Scheuner, D. *et al.* Translational control is required for the unfolded protein response and in vivo glucose homeostasis. *Mol Cell* **7**, 1165–1176 (2001).

68. Rutkowski, D. T. *et al.* UPR Pathways Combine to Prevent Hepatic Steatosis Caused by ER Stress-Mediated Suppression of Transcriptional Master Regulators. *Dev Cell* **15**, 829–840 (2008).

69. Lee, A. H., Scapa, E. F., Cohen, D. E. & Glimcher, L. H. Regulation of hepatic lipogenesis by the transcription factor XBP1. *Science (1979)* **320**, 1492–1496 (2008).

70. Bertolotti, A. *et al.* Increased sensitivity to dextran sodium sulfate colitis in IRE1beta-deficient mice. *J Clin Invest* **107**, 585–593 (2001).

71. Chakrabarty, A. *et al.* sUPRa is a dual-color reporter for unbiased quantification of the unfolded protein response with cellular resolution. *Scientific Reports 2024 14:1* **14**, 1–17 (2024).

72. Valdés, P. *et al.* Control of dopaminergic neuron survival by the unfolded protein response transcription factor XBP1. *Proc Natl Acad Sci U S A* **111**, 6804–6809 (2014).

73. Wei, X. *et al.* The unfolded protein response is required for dendrite morphogenesis. *Elife* **4**, (2015).

74. Wu, J. & Kaufman, R. J. From acute ER stress to physiological roles of the Unfolded Protein Response. *Cell Death & Differentiation 2006 13:3* **13**, 374–384 (2006).

75. Chen, X., Shi, C., He, M., Xiong, S. & Xia, X. Endoplasmic reticulum stress: molecular mechanism and therapeutic targets. *Signal Transduction and Targeted Therapy 2023 8:1* **8**, 1–40 (2023).

76. Zhao, L. & Ackerman, S. L. Endoplasmic reticulum stress in health and disease. *Curr Opin Cell Biol* **18**, 444–452 (2006).

77. Hetz, C., Martinon, F., Rodriguez, D. & Glimcher, L. H. The unfolded protein response: Integrating stress signals through the stress sensor IRE1 α. *Physiol Rev* **91**, 1219–1243 (2011).

78. Hetz, C. & Mollereau, B. Disturbance of endoplasmic reticulum proteostasis in neurodegenerative diseases. *Nature Reviews Neuroscience 2014 15:4* **15**, 233–249 (2014).

79. Roussel, B. D. *et al.* Endoplasmic reticulum dysfunction in neurological disease. *Lancet Neurol* **12**, 105–118 (2013).

80. Oakes, S. A. Endoplasmic Reticulum Stress Signaling in Cancer Cells. *American Journal of Pathology* **190**, 934–946 (2020).

81. Kawai, T., Fan, J., Mazan-Mamczarz, K. & Gorospe, M. Global mRNA Stabilization Preferentially Linked to Translational Repression during the Endoplasmic Reticulum Stress Response. *Mol Cell Biol* **24**, 6773 (2004).

82. Woo, Y. M. *et al.* TED-Seq Identifies the Dynamics of Poly(A) Length during ER Stress. *Cell Rep* **24**, 3630-3641.e7 (2018).

83. Rendleman, J. *et al.* New insights into the cellular temporal response to proteostatic stress. *Elife* **7**, (2018).

84. Alzahrani, M. R. *et al.* Newly synthesized mRNA escapes translational repression during the acute phase of the mammalian unfolded protein response. *PLoS One* **17**, e0271695 (2022).

85. Kedersha, N. L., Gupta, M., Li, W., Miller, I. & Anderson, P. RNA-binding proteins TIA-1 and TIAR link the phosphorylation of eIF-2 alpha to the assembly of mammalian stress granules. *J Cell Biol* **147**, 1431–1441 (1999).

86. Mazroui, R. *et al.* Inhibition of ribosome recruitment induces stress granule formation independently of eukaryotic initiation factor 2α phosphorylation. *Mol Biol Cell* **17**, 4212–4219 (2006).

87. Kedersha, N. *et al.* Dynamic shuttling of TIA-1 accompanies the recruitment of mRNA to mammalian stress granules. *J Cell Biol* **151**, 1257–1268 (2000).

88. Kedersha, N. *et al.* Stress granules and processing bodies are dynamically linked sites of mRNP remodeling. *Journal of Cell Biology* **169**, 871–884 (2005).

89. Protter, D. S. W. & Parker, R. Principles and Properties of Stress granules. *Trends Cell Biol* **26**, 668 (2016).

90. Child, J. R., Chen, Q., Reid, D. W., Jagannathan, S. & Nicchitta, C. V. Recruitment of endoplasmic reticulum-targeted and cytosolic mRNAs into membrane-associated stress granules. *RNA* **27**, 1241–1256 (2021).

91. Mateju, D. & Chao, J. A. Stress granules: regulators or by-products? *FEBS J* **289**, 363–373 (2022).

92. Mazroui, R., Di Marco, S., Kaufman, R. J. & Gallouzi, I. E. Inhibition of the ubiquitin-proteasome system induces stress granule formation. *Mol Biol Cell* **18**, 2603–2618 (2007).

93. Stöhr, N. *et al.* ZBP1 regulates mRNA stability during cellular stress. *Journal of Cell Biology* **175**, 527–534 (2006).

94. Khong, A. *et al.* The Stress Granule Transcriptome Reveals Principles of mRNA Accumulation in Stress Granules. *Mol Cell* **68**, 808-820.e5 (2017).

95. Namkoong, S., Ho, A., Woo, Y. M., Kwak, H. & Lee, J. H. Systematic Characterization of Stress-Induced RNA Granulation. *Mol Cell* **70**, 175 (2018).

96. Bley, N. *et al.* Stress granules are dispensable for mRNA stabilization during cellular stress. *Nucleic Acids Res* **43**, e26 (2014).

97. Cairrão, F. *et al.* Pumilio protects Xbp1 mRNA from regulated Ire1-dependent decay. *Nature Communications 2022 13:1* **13**, 1–13 (2022).

98. Backlund, M., Paukku, K., Kontula, K. K. & Lehtonen, J. Y. A. Endoplasmic reticulum stress increases AT1R mRNA expression via TIA-1-dependent mechanism. *Nucleic Acids Res* **44**, 3095–3104 (2016).

99. Belot, A. *et al.* Endoplasmic reticulum stress controls iron metabolism through TMPRSS6 repression and hepcidin mRNA stabilization by RNA-binding protein HuR. *Haematologica* **106**, 1202–1206 (2021).

100. Pan, Y. X., Chen, H. & Kilberg, M. S. Interaction of RNA-binding proteins HuR and AUF1 with the human ATF3 mRNA 3′-untranslated region regulates its amino acid limitation-induced stabilization. *Journal of Biological Chemistry* **280**, 34609–34616 (2005).

101. Jungers, C. F. & Djuranovic, S. Modulation of miRISC-Mediated Gene Silencing in Eukaryotes. *Front Mol Biosci* **9**, 832916 (2022).

102. McMahon, M., Samali, A. & Chevet, E. Regulation of the unfolded protein response by noncoding RNA. *Am J Physiol Cell Physiol* **313**, C243–C254 (2017).

103. Bartoszewska, S. *et al.* Regulation of the unfolded protein response by microRNAs. *Cell Mol Biol Lett* **18**, 555–578 (2013).

104. Chitnis, N., Pytel, D. & Diehl, J. A. UPR-inducible miRNAs contribute to stressful situations. *Trends Biochem Sci* **38**, 447–452 (2013).

105. Efstathiou, S. *et al.* ER-associated RNA silencing promotes ER quality control. *Nature Cell Biology 2022 24:12* **24**, 1714–1725 (2022).

106. Reid, D. W., Chen, Q., Tay, A. S. L., Shenolikar, S. & Nicchitta, C. V. The unfolded protein response triggers selective mRNA release from the endoplasmic reticulum. *Cell* **158**, 1362–1374 (2014).

107. Moore, K. & Hollien, J. Ire1-mediated decay in mammalian cells relies on mRNA sequence, structure, and translational status. *Mol Biol Cell* **26**, 2873 (2015).

108. Gonzalez, T. N., Sidrauski, C., Dörfler, S. & Walter, P. Mechanism of non-spliceosomal mRNA splicing in the unfolded protein response pathway. *EMBO J* **18**, 3119–3132 (1999).

109. Le Thomas, A. *et al.* Decoding non-canonical mRNA decay by the endoplasmic-reticulum stress sensor IRE1α. *Nature Communications 2021 12:1* **12**, 1–15 (2021).

110. So, J. S. *et al.* Silencing of lipid metabolism genes through ire1α-mediated Mrna decay lowers plasma lipids in mice. *Cell Metab* **16**, 487–499 (2012).

111. Liu, S. *et al.* Mammalian IRE1α dynamically and functionally coalesces with stress granules. *Nature Cell Biology 2024 26:6* **26**, 917–931 (2024).

112. Acosta-Alvear, D. *et al.* The unfolded protein response and endoplasmic reticulum protein targeting machineries converge on the stress sensor IRE1. *Elife* **7**, (2018).

113. Bell, J. L. *et al.* Insulin-like growth factor 2 mRNA-binding proteins (IGF2BPs): post-transcriptional drivers of cancer progression? *Cellular and Molecular Life Sciences* **70**, 2657–2675 (2013).

114. Degrauwe, N., Suvà, M.-L., Janiszewska, M., Riggi, N. & Stamenkovic, I. IMPs: an RNA-binding protein family that provides a link between stem cell maintenance in normal development and cancer. *Genes Dev* **30**, 2459–2474 (2016).

115. Müeller-Pillasch, F. *et al.* Cloning of a gene highly overexpressed in cancer coding for a novel KH-domain containing protein. *Oncogene* **14**, 2729–2733 (1997).

116. Doyle, G. A. R. *et al.* The c-myc coding region determinant-binding protein: a member of a family of KH domain RNA-binding proteins. *Nucleic Acids Res* **26**, 5036–5044 (1998).

117. Mori, H. *et al.* Expression of mouse igf2 mRNA-binding protein 3 and its implications for the developing central nervous system. *J Neurosci Res* **64**, 132–143 (2001).

118. Mueller-Pillasch, F. *et al.* Expression of the highly conserved RNA binding protein KOC in embryogenesis. *Mech Dev* **88**, 95–99 (1999).

119. Leeds, P. *et al.* Developmental regulation of CRD-BP, an RNA-binding protein that stabilizes c-myc mRNA in vitro. *Oncogene 1997 14:11* **14**, 1279–1286 (1997).

120. Nielsen, J. *et al.* A family of insulin-like growth factor II mRNA-binding proteins represses translation in late development. *Mol Cell Biol* **19**, 1262–1270 (1999).

121. Vikesaa, J. *et al.* RNA-binding IMPs promote cell adhesion and invadopodia formation. *EMBO J* **25**, 1456–1468 (2006).

122. Hüttelmaier, S. *et al.* Spatial regulation of beta-actin translation by Src-dependent phosphorylation of ZBP1. *Nature* **438**, 512–515 (2005).

123. Noubissi, F. K. *et al.* CRD-BP mediates stabilization of betaTrCP1 and c-myc mRNA in response to beta-catenin signalling. *Nature* **441**, 898–901 (2006).

124. Yaniv, K. & Yisraeli, J. K. The involvement of a conserved family of RNA binding proteins in embryonic development and carcinogenesis. *Gene* **287**, 49–54 (2002).

125. Conway, A. E. E. *et al.* Enhanced CLIP Uncovers IMP Protein-RNA Targets in Human Pluripotent Stem Cells Important for Cell Adhesion and Survival. *Cell Rep* **15**, 666–679 (2016).

126. Jønson, L. *et al.* IMP3 RNP safe houses prevent miRNA-directed HMGA2 mRNA decay in cancer and development. *Cell Rep* **7**, 539–551 (2014).

127. Yisraeli, J. K. VICKZ proteins: a multi-talented family of regulatory RNA-binding proteins. *Biol Cell* **97**, 87–96 (2005).

128. Deshler, J. O., Highett, M. I. & Schnapp, B. J. Localization of Xenopus Vg1 mRNA by Vera protein and the endoplasmic reticulum. *Science* **276**, 1128–1131 (1997).

129. De Vasconcellos, J. F. *et al.* IGF2BP1 overexpression causes fetal-like hemoglobin expression patterns in cultured human adult erythroblasts. *Proc Natl Acad Sci U S A* **114**, E5664–E5672 (2017).

130. Christiansen, J., Kolte, A. M., Hansen, T. V. O. & Nielsen, F. C. IGF2 mRNA-binding protein 2: biological function and putative role in type 2 diabetes. *J Mol Endocrinol* **43**, 187–195 (2009).

131. Li, Y. *et al.* Rna M6a Methylation Regulates Glycolysis of Beige Fat and Contributes to Systemic Metabolic Homeostasis. *Advanced Science* **10**, 2300436 (2023).

132. Dai, N. *et al.* IGF2BP2/IMP2-deficient mice resist obesity through enhanced translation of Ucp1 mRNA and other mRNAs encoding mitochondrial proteins. *Cell Metab* **21**, 609–621 (2015).

133. Regué, L. *et al.* RNA m6A reader IMP2/IGF2BP2 promotes pancreatic β-cell proliferation and insulin secretion by enhancing PDX1 expression. *Mol Metab* **48**, 101209 (2021).

134. Christiansen, J., Kolte, A. M., Hansen, T. V. O. & Nielsen, F. C. IGF2 mRNA-binding protein 2: biological function and putative role in type 2 diabetes. *J Mol Endocrinol* **43**, 187–195 (2009).

135. Lederer, M., Bley, N., Schleifer, C. & Hüttelmaier, S. The role of the oncofetal IGF2 mRNA-binding protein 3 (IGF2BP3) in cancer. *Semin Cancer Biol* **29**, 3–12 (2014).

136. Huang, X. *et al.* Insulin-like growth factor 2 mRNA-binding protein 1 (IGF2BP1) in cancer. *J Hematol Oncol* **11**, 1–15 (2018).

137. Hamilton, K. E. *et al.* IMP1 promotes tumor growth, dissemination and a tumor-initiating cell phenotype in colorectal cancer cell xenografts. *Carcinogenesis* **34**, 2647–2654 (2013).

138. Gola, A. M., Bucci-Muñoz, M., Rigalli, J. P., Ceballos, M. P. & Ruiz, M. L. Role of the RNA binding protein IGF2BP1 in cancer multidrug resistance. *Biochem Pharmacol* **230**, 116555 (2024).

139. Vikesaa, J. *et al.* RNA-binding IMPs promote cell adhesion and invadopodia formation. *EMBO Journal* **25**, 1456–1468 (2006).

140. Müller, S. *et al.* The oncofetal RNA-binding protein IGF2BP1 is a druggable, post-transcriptional super-enhancer of E2F-driven gene expression in cancer. *Nucleic Acids Res* **48**, 8576 (2020).

141. Mongroo, P. S. *et al.* IMP-1 displays cross-talk with K-Ras and modulates colon cancer cell survival through the novel proapoptotic protein CYFIP2. *Cancer Res* **71**, 2172–2182 (2011).

142. Sparanese, D. & Lee, C. H. CRD-BP shields c-myc and MDR-1 RNA from endonucleolytic attack by a mammalian endoribonuclease. *Nucleic Acids Res* **35**, 1209–1221 (2007).

143. Wächter, K., Köhn, M., Stöhr, N. & Hüttelmaier, S. Subcellular localization and RNP formation of IGF2BPs (IGF2 mRNA-binding proteins) is modulated by distinct RNA-binding domains. *Biol Chem* **394**, 1077–1090 (2013).

144. Schneider, T. *et al.* Combinatorial recognition of clustered RNA elements by the multidomain RNA-binding protein IMP3. *Nature Communications 2019 10:1* **10**, 1–18 (2019).

145. Dagil, R. *et al.* IMP1 KH1 and KH2 domains create a structural platform with unique RNA recognition and re-modelling properties. *Nucleic Acids Res* **47**, 4334–4348 (2019).

146. Chao, J. A. *et al.* ZBP1 recognition of β-actin zipcode induces RNA looping. *Genes Dev* **24**, 148–158 (2010).

147. Kislauskis, E. H., Zhu, X. & Singer, R. H. Sequences responsible for intracellular localization of beta-actin messenger RNA also affect cell phenotype. *J Cell Biol* **127**, 441–451 (1994).

148. Ross, A. F., Oleynikov, Y., Kislauskis, E. H., Taneja, K. L. & Singer, R. H. Characterization of a beta-actin mRNA zipcode-binding protein. *Mol Cell Biol* **17**, 2158–2165 (1997).

149. Hafner, M. *et al.* Transcriptome-wide identification of RNA-binding protein and microRNA target sites by PAR-CLIP. *Cell* **141**, 129–41 (2010).

150. Weidensdorfer, D. *et al.* Control of c-myc mRNA stability by IGF2BP1-associated cytoplasmic RNPs. *RNA* **15**, 104–115 (2009).

151. Huang, H. *et al.* Recognition of RNA N 6-methyladenosine by IGF2BP proteins enhances mRNA stability and translation. *Nat Cell Biol* **20**, (2018).

152. Müller, S. *et al.* IGF2BP1 enhances an aggressive tumor cell phenotype by impairing miRNA-directed downregulation of oncogenic factors. *Nucleic Acids Res* **46**, 6285–6303 (2018).

153. Müller, S. *et al.* IGF2BP1 promotes SRF-dependent transcription in cancer in a m6A- and miRNA-dependent manner. *Nucleic Acids Res* **47**, 375–390 (2019).

154. Busch, B. *et al.* The oncogenic triangle of HMGA2, LIN28B and IGF2BP1 antagonizes tumor-suppressive actions of the let-7 family. *Nucleic Acids Res* **44**, 3845–3864 (2016).

155. Farina, K. L., Hüttelmaier, S., Musunuru, K., Darnell, R. & Singer, R. H. Two ZBP1 KH domains facilitate β-actin mRNA localization, granule formation, and cytoskeletal attachment. *J Cell Biol* **160**, 77 (2003).

156. Shan, T. *et al.* m6A modification negatively regulates translation by switching mRNA from polysome to P-body via IGF2BP3. *Mol Cell* **83**, 4494-4508.e6 (2023).

157. Prokipcak, R. D., Herrick, D. J. & Rosssnll, J. Purification and Properties of a Protein That Binds to the C-terminal Coding Region of Human c-myc mRNA*. *Journal of Biological Chemistry* **269**, 9261–9269 (1994).

158. Bernstein, P. L., Herrick, D. J., Prokipcak, R. D. & Ross, J. Control of c-myc mRNA half-life in vitro by a protein capable of binding to a coding region stability determinant. *Genes Dev* **6**, 642–654 (1992).

159. Barnes, T. *et al.* Identification of Apurinic/apyrimidinic endonuclease 1 (APE1) as the endoribonuclease that cleaves c-myc mRNA. *Nucleic Acids Res* **37**, 3946–3958 (2009).

160. Elcheva, I., Goswami, S., Noubissi, F. K. & Spiegelman, V. S. CRD-BP Protects the Coding Region of βTrCP1 mRNA from miR-183-Mediated Degradation. *Mol Cell* **35**, 240–246 (2009).

161. Goswami, S. *et al.* MicroRNA-340-mediated degradation of microphthalmia-associated transcription factor (MITF) mRNA is inhibited by coding region determinant-binding protein (CRD-BP). *Journal of Biological Chemistry* **290**, 384–395 (2015).

162. Liu, C. *et al.* IGF2BP3 promotes mRNA degradation through internal m7G modification. *Nat Commun* **15**, 7421 (2024).

163. Schmiedel, D. *et al.* The RNA binding protein imp3 facilitates tumor immune escape by downregulating the stress-induced ligands ULPB2 and MICB. *Elife* **5**, (2016).

164. Mizutani, R. *et al.* Oncofetal protein IGF2BP3 facilitates the activity of proto-oncogene protein eIF4E through the destabilization of EIF4E-BP2 mRNA. *Oncogene* **35**, 3495–3502 (2016).

165. Ennajdaoui, H. *et al.* IGF2BP3 Modulates the Interaction of Invasion-Associated Transcripts with RISC. *Cell Rep* **15**, 1876–1883 (2016).

166. Dai, N., Christiansen, J., Nielsen, F. C. & Avruch, J. mTOR complex 2 phosphorylates IMP1 cotranslationally to promote IGF2 production and the proliferation of mouse embryonic fibroblasts. *Genes Dev* **27**, 301–312 (2013).

167. Lambrianidou, A. *et al.* mTORC2 deploys the mRNA binding protein IGF2BP1 to regulate c-MYC expression and promote cell survival. *Cell Signal* **80**, (2021).

168. Dai, N. *et al.* mTOR phosphorylates IMP2 to promote IGF2 mRNA translation by internal ribosomal entry. *Genes Dev* **25**, 1159–1172 (2011).

169. Git, A. *et al.* Vg1RBP phosphorylation by Erk2 MAP kinase correlates with the cortical release of Vg1 mRNA during meiotic maturation of Xenopus oocytes. *RNA* **15**, 1121–1133 (2009).

170. Markmiller, S. *et al.* Context-Dependent and Disease-Specific Diversity in Protein Interactions within Stress Granules. *Cell* **172**, 590-604.e13 (2018).

171. Youn, J. Y. *et al.* High-Density Proximity Mapping Reveals the Subcellular Organization of mRNA-Associated Granules and Bodies. *Mol Cell* **69**, 517-532.e11 (2018).

172. Stöhr, N. *et al.* ZBP1 regulates mRNA stability during cellular stress. *Journal of Cell Biology* **175**, 527–534 (2006).

173. Hayes, J. D., Dinkova-Kostova, A. T. & Tew, K. D. Oxidative Stress in Cancer. *Cancer Cell* **38**, 167–197 (2020).

174. Cai, Y., Wang, Y., Mao, B., You, Q. & Guo, X. Targeting insulin-like growth factor 2 mRNA-binding proteins (IGF2BPs) for the treatment of cancer. *Eur J Med Chem* **268**, 116241 (2024).

175. Danan, C., Manickavel, S. & Hafner, M. PAR-CLIP: A Method for Transcriptome-Wide Identification of RNA Binding Protein Interaction Sites. *Methods Mol Biol* **1358**, 153–73 (2016).

176. Huang, J. *et al.* Unfolded protein response in colorectal cancer. *Cell Biosci* **11**, 26 (2021).

177. Martins, F. *et al.* Differential unfolded protein response regulation in KRAS silencing sensitive and innately resistant colorectal cancer cells. *Scientific Reports 2025 15:1* **15**, 1–15 (2025).

178. Spaan, C. N. *et al.* Expression of UPR effector proteins ATF6 and XBP1 reduce colorectal cancer cell proliferation and stemness by activating PERK signaling. *Cell Death & Disease 2019 10:7* **10**, 1–10 (2019).

179. Khazem, F. & Zetoune, A. B. Decoding high mobility group A2 protein expression regulation and implications in human cancers. *Discover Oncology 2024 15:1* **15**, 1–26 (2024).

180. Van Nostrand, E. L. *et al.* A large-scale binding and functional map of human RNA-binding proteins. *Nature 2020 583:7818* **583**, 711–719 (2020).

181. Rutkowski, D. T. *et al.* Adaptation to ER Stress Is Mediated by Differential Stabilities of Pro-Survival and Pro-Apoptotic mRNAs and Proteins. *PLoS Biol* **4**, e374 (2006).

182. Herzog, V. A. *et al.* Thiol-linked alkylation of RNA to assess expression dynamics. *Nature Methods 2017 14:12* **14**, 1198–1204 (2017).

183. Lee, K. *et al.* IRE1-mediated unconventional mRNA splicing and S2P-mediated ATF6 cleavage merge to regulate XBP1 in signaling the unfolded protein response. *Genes Dev* **16**, 452–466 (2002).

184. Vidal, R. L. *et al.* Enforced dimerization between XBP1s and ATF6f enhances the protective effects of the UPR in models of neurodegeneration. *Mol Ther* **29**, 1862–1882 (2021).

185. Reeves, R., Edberg, D. D. & Li, Y. Architectural transcription factor HMGI(Y) promotes tumor progression and mesenchymal transition of human epithelial cells. *Mol Cell Biol* **21**, 575–594 (2001).

186. Narita, M. *et al.* A Novel Role for High-Mobility Group A Proteins in Cellular Senescence and Heterochromatin Formation. *Cell* **126**, 503–514 (2006).

187. Ozturk, N., Singh, I., Mehta, A., Braun, T. & Barreto, G. HMGA proteins as modulators of chromatin structure during transcriptional activation. *Front Cell Dev Biol* **2**, 76938 (2014).

188. Deneke, V. E. *et al.* A conserved fertilization complex bridges sperm and egg in vertebrates. *Cell* **187**, 7066-7078.e22 (2024).

189. Portell-Montserrat, J. *et al.* Target RNA recognition drives PIWI∗ complex assembly for transposon silencing. *Mol Cell* **85**, 3288-3305.e6 (2025).

190. Arribas-Layton, M., Wu, D., Lykke-Andersen, J. & Song, H. Structural and functional control of the eukaryotic mRNA decapping machinery. *Biochim Biophys Acta* **1829**, 580 (2012).

191. Fromm, S. A. *et al.* The structural basis of Edc3-and Scd6-mediated activation of the Dcp1:Dcp2 mRNA decapping complex. *EMBO Journal* **31**, 279–290 (2012).

192. Mugridge, J. S., Tibble, R. W., Ziemniak, M., Jemielity, J. & Gross, J. D. Structure of the activated Edc1-Dcp1-Dcp2-Edc3 mRNA decapping complex with substrate analog poised for catalysis. *Nature Communications 2018 9:1* **9**, 1–10 (2018).

193. Fenger-Grøn, M., Fillman, C., Norrild, B. & Lykke-Andersen, J. Multiple processing body factors and the ARE binding protein TTP activate mRNA decapping. *Mol Cell* **20**, 905–915 (2005).

194. Marchese, F. P. *et al.* MAPKAP kinase 2 blocks tristetraprolin-directed mRNA decay by inhibiting CAF1 deadenylase recruitment. *Journal of Biological Chemistry* **285**, 27590–27600 (2010).

195. Clement, S. L., Scheckel, C., Stoecklin, G. & Lykke-Andersen, J. Phosphorylation of Tristetraprolin by MK2 Impairs AU-Rich Element mRNA Decay by Preventing Deadenylase Recruitment. *Mol Cell Biol* **31**, 256–266 (2011).

196. Stowell, J. A. W. *et al.* Phosphorylation-dependent tuning of mRNA deadenylation rates. *bioRxiv* 2024.10.18.618793 (2024) doi:10.1101/2024.10.18.618793.

197. Maciej, V. D. *et al.* Intrinsically disordered regions of tristetraprolin and DCP2 directly interact to mediate decay of ARE-mRNA. *Nucleic Acids Res* **50**, 10665–10679 (2022).

198. Bearss, J. J. *et al.* EDC3 phosphorylation regulates growth and invasion through controlling P-body formation and dynamics. *EMBO Rep* **22**, (2021).

199. Dierks, D. *et al.* Passive shaping of intra- and intercellular m6A dynamics via mRNA metabolism. *Elife* **13**, (2025).

200. Zhou, J. *et al.* Dynamic m6A mRNA methylation directs translational control of heat shock response. *Nature 2015 526:7574* **526**, 591–594 (2015).

201. Wei, J. *et al.* HRD1-mediated METTL14 degradation regulates m6A mRNA modification to suppress ER proteotoxic liver disease. *Mol Cell* **81**, 5052 (2021).

202. Muhar, M. *et al.* SLAM-seq defines direct gene-regulatory functions of the BRD4-MYC axis. *Science (1979)* **360**, 800–805 (2018).

203. Bhat, P. *et al.* SLAMseq resolves the kinetics of maternal and zygotic gene expression during early zebrafish embryogenesis. *Cell Rep* **42**, 112070 (2023).

204. Yesbolatova, A., Natsume, T., Hayashi, K. & Kanemaki, M. T. Generation of conditional auxin-inducible degron (AID) cells and tight control of degron-fused proteins using the degradation inhibitor auxinole. *Methods* **164–165**, 73–80 (2019).

205. Xing, D. *et al.* Systematic comparison and base-editing-mediated directed protein evolution and functional screening yield superior auxin-inducible degron technology. *Nature Communications 2025 16:1* **16**, 1–12 (2025).

206. England, C. G., Luo, H. & Cai, W. HaloTag technology: a versatile platform for biomedical applications. *Bioconjug Chem* **26**, 975–986 (2015).

207. Los, G. V. *et al.* HaloTag: a novel protein labeling technology for cell imaging and protein analysis. *ACS Chem Biol* **3**, 373–382 (2008).

208. Buckley, D. L. *et al.* HaloPROTACS: Use of Small Molecule PROTACs to Induce Degradation of HaloTag Fusion Proteins. *ACS Chem Biol* **10**, 1831 (2015).

209. Caine, E. A. *et al.* Targeted Protein Degradation Phenotypic Studies Using HaloTag CRISPR/Cas9 Endogenous Tagging Coupled with HaloPROTAC3. *Curr Protoc Pharmacol* **91**, (2020).

210. Tovell, H. *et al.* Rapid and Reversible Knockdown of Endogenously Tagged Endosomal Proteins via an Optimized HaloPROTAC Degrader. *ACS Chem Biol* **14**, 882–892 (2019).

7 Abbreviations

ABCB1	ATP binding cassette subfamily B member 1
ACTB	actin beta
ActD	actinomycin D
AGO2	Argonaute 2
AT1R	angiotensin II type 1 receptor
ATF3	activating transcription factor 4
ATF4	activating transcription factor 4
ATF6	activating transcription factor 6
BiP	binding immunoglobulin protein
BLOC1S1	biogenesis of lysosomal organelles complex-1 subunit 1
BTRC	β-transducin repeat containing E3 ubiquitin protein ligase
bZIP	basic leucine zipper
CCR4-NOT	Carbon Catabolite Repression 4 - Negative On TATA-less deadenylase complex
CD44	CD44 molecule (Indian blood group)
CD59	CD59 glycoprotein
CHOP	C/EBP homologous protein
CREB3L2	cAMP responsive element binding protein 3 like 2
DCP1A	mRNA decapping enzyme 1A
DCP2	mRNA decapping enzyme 2
DDIT3	DNA damage inducible transcript 3 (CHOP)
EDC3	enhancer of mRNA decapping 3
EDC4	enhancer of mRNA decapping 4
eIF2α	eukaryotic translation initiation factor 2 alpha
EIF4E-BP2	eukaryotic translation initiation factor 4E binding protein 2
ER	endoplasmic reticulum
ERAD	ER-associated degradation
FOSL2	FOS like 2, AP-1 transcription factor subunit
GFP	green fluorescent protein
HMGA2	high mobility group AT-hook 2

HSPA5	heat shock protein family A (Hsp70) member 5
IDR	intrinsically disordered region
IGF2	insulin-like growth factor 2
IGF2BP	insulin-like growth factor 2 mRNA-binding protein
IRE1	inositol-requiring enzyme 1
IR-PAR-CLIP	infrared photoactivatable-ribonucleoside-enhanced crosslinking and immunoprecipitation
KRAS	Kirsten rat sarcoma viral oncogene homolog
MAPK	mitogen-activated protein kinase
mAID	mini auxin-inducible degron
miRNA	microRNA
mRNP	messenger ribonucleoprotein
MITF	microphthalmia-associated transcription factor
MYC	myelocytomatosis oncogene
m6A	N6-methyladenosine
m7G	N7-methylguanosine
OsTIR1	Oryza sativa TIR1 (auxin receptor)
P-bodies	processing bodies
PAR-CLIP	photoactivatable-ribonucleoside-enhanced crosslinking and immunoprecipitation
PERK	PKR-like ER kinase
PROTAC	proteolysis-targeting chimera
RBP	RNA-binding protein
RIDD	regulated IRE1-dependent decay
RIP-seq	RNA immunoprecipitation sequencing
RISC	RNA-induced silencing complex
RNase	ribonuclease
RPL26	ribosomal protein L26
RQC	ribosome-associated quality control
RT-qPCR	reverse transcription quantitative PCR
s4U	4-thiouridine
SG	stress granule

SLAMseq	thiol(SH)-linked alkylation for the metabolic sequencing of RNA
SRF	serum response factor
TGOLN2	trans-Golgi network protein 2
T-C	thymidine-to-cytidine (conversion)
UCP1	uncoupling protein 1
UFM1	ubiquitin-fold modifier 1
UPR	unfolded protein response
UTR	untranslated region
VHL	von Hippel–Lindau (E3 ligase)
XBP1	X-box binding protein 1
XBP1s	spliced XBP1
XBP1u	unspliced XBP1
ZFP36L1	zinc finger protein 36 like 1